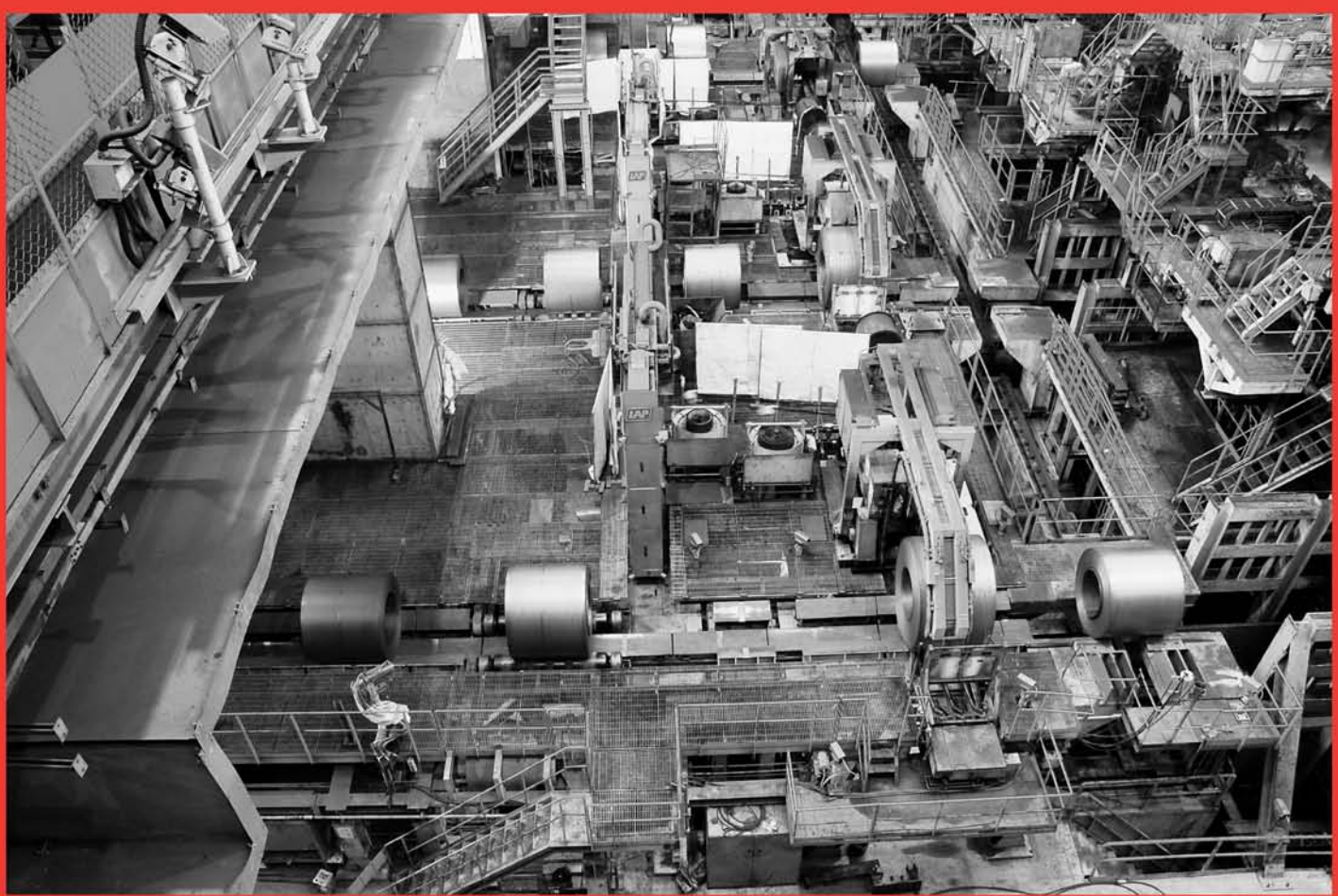
FLAT-ROLLED STEEL PROCESSES

Advanced Technologies



Edited by **Vladimir B. Ginzburg**

CRC Press
Taylor & Francis Group

FLAT-ROLLED STEEL PROCESSES

Advanced Technologies

Edited by **Vladimir B. Ginzburg**



CRC Press
Taylor & Francis Group
Boca Raton London New York

CRC Press is an imprint of the
Taylor & Francis Group, an **informa** business

CRC Press
Taylor & Francis Group
6000 Broken Sound Parkway NW, Suite 300
Boca Raton, FL 33487-2742

© 2009 by Taylor & Francis Group, LLC
CRC Press is an imprint of Taylor & Francis Group, an Informa business

No claim to original U.S. Government works
Printed in the United States of America on acid-free paper
10 9 8 7 6 5 4 3 2 1

International Standard Book Number-13: 978-1-4200-7292-1 (Hardcover)

This book contains information obtained from authentic and highly regarded sources. Reasonable efforts have been made to publish reliable data and information, but the author and publisher cannot assume responsibility for the validity of all materials or the consequences of their use. The authors and publishers have attempted to trace the copyright holders of all material reproduced in this publication and apologize to copyright holders if permission to publish in this form has not been obtained. If any copyright material has not been acknowledged please write and let us know so we may rectify in any future reprint.

Except as permitted under U.S. Copyright Law, no part of this book may be reprinted, reproduced, transmitted, or utilized in any form by any electronic, mechanical, or other means, now known or hereafter invented, including photocopying, microfilming, and recording, or in any information storage or retrieval system, without written permission from the publishers.

For permission to photocopy or use material electronically from this work, please access www.copyright.com (http://www.copyright.com/) or contact the Copyright Clearance Center, Inc. (CCC), 222 Rosewood Drive, Danvers, MA 01923, 978-750-8400. CCC is a not-for-profit organization that provides licenses and registration for a variety of users. For organizations that have been granted a photocopy license by the CCC, a separate system of payment has been arranged.

Trademark Notice: Product or corporate names may be trademarks or registered trademarks, and are used only for identification and explanation without intent to infringe.

Library of Congress Cataloging-in-Publication Data

Flat-rolled steel processes : advanced technologies / editor, Vladimir B. Ginzburg.
p. cm.
"A CRC title."
Includes bibliographical references and index.
ISBN 978-1-4200-7292-1 (alk. paper)
1. Rolling (Metal-work) I. Ginzburg, Vladimir B., 1935- II. Title.

TS340.F576 2009
672.3'2--dc22 2008049238

Visit the Taylor & Francis Web site at
http://www.taylorandfrancis.com

and the CRC Press Web site at
http://www.crcpress.com

Contents

Preface vii
Editor ix
Contributors xi

SECTION I New Concepts and Modernization of Rolling Mills

Chapter 1 A History of Minimills Producing Flat-Rolled Steel 3
John Stubbles

Chapter 2 Review of Casting and Rolling Lines with Thin- and Medium-Slab Casters 15
Vladimir B. Ginzburg

Chapter 3 Methodology and Results of Major Hot Strip Mill Modernization Projects 35
Wlodzimierz Boleslaw Filipczyk

Chapter 4 Plate Mill Upgrades for High-Strength Products 55
J. F. Evans and P. Sopp

Chapter 5 Roughing Mill Work Rolls for Hot Strip Production 63
Michael Windhager and Karl Heinz Ziehenberger

Chapter 6 High-Speed Steel Rolls: The Last Frontier in Hot Steel Rolling 71
Alberto Tremea, Angelo Biggi, Massimo Pellizzari, and Alberto Molinari

Chapter 7 Tunnel Furnace Roll Options and Energy Considerations 83
Robert J. Echlin, Daniel V. Miller, and Roman I. Pankiw

Chapter 8 Descaling of Hot-Rolled Strip 91
John B. Tiley and Per A. Munther

SECTION II Modeling of Flat Rolling Processes

Chapter 9 Modeling for Reheat Furnace Practices 99
Shaojie Chen

Chapter 10 Improvement of Schedules for Hot Rolling of Thin Wide Strips 115
Eduard Garber, Alexander Traino, and Irina Kozhevnikova

Chapter 11 Width Variation Behavior during Hot Rolling 127
Qiulin Yu

Chapter 12 Parameter Optimization and Uncertainty Quantification in Rolling 141
Arif S. Malik and Ramana V. Grandhi

Chapter 13 Simulation for the Dynamic Behavior of Strips Running on Hot Run-Out Tables 155
Yuji Ohara, Shin-ichiro Aoe, Hiromasa Hayashi, and Kazushige Ishino

Chapter 14 Laminar Flow-Cooling of Wide Heavy-Thickness Strip in a Hot Rolling Mill 161
Qiulin Yu

Chapter 15 Consideration of Microstructure Evolution in Hot Strip Mill Automation 171
Hans-Ulrich Löffler, Klaus Weinzierl, and Rüdiger Döll

Chapter 16 Novel Mathematical Models for Cold-Rolling Process 179
Eduard Garber, Alexander Traino, and Irina Kozhevnikova

Chapter 17 Elastohydrodynamic Lubrication of Cold-Rolling Lubricants and Its Mechanism in Nonconformal Rolling Contacts 191
Ian Burton

SECTION III Measurement, Automation, and Process Control

Chapter 18 Multivariable Hot Strip Mill Control 209
Gerald Hearns, T. Bilkhu, and Peter Reeve

Chapter 19 Finishing Mill Predictive Temperature Control 219
Gerald Hearns, Chris Fryer, and Peter Reeve

Chapter 20 Digital Visual Inspection of Coils 229
Mohammad B. Assar, Larry Romanauski, Matt Kremer, Margaret Krolikowski, Joe Franklin, Mike L. Elliott, and Randy A. Stankie

Chapter 21 Yield Improvement through Better Crop Optimization 239
Robert L. Ricciatti

Chapter 22 State-of-the-Art, Noncontact Infrared, Laser, and Microwave Intelligent Sensors and Systems for Steel Mills 245
François Reizine, Bingji Li, and John Nauman

Chapter 23 Cold-Rolling Mill Vibration and Its Impact on Productivity and Product Quality 255
Tom Farley

Chapter 24 IMPOC©: An Online Material Properties Measurement System 265
Klaus Herrmann and Matthias Irle

Chapter 25 Technologies for the Prediction and Control of Microstructural Changes and Mechanical Properties 271
Kazuhiro Ohara

Chapter 26 Metallurgical, Modeling, and Software Engineering Issues in the Further Development of the Steel Mill Level 2 Models 277
Bingji Li and John Nauman

SECTION IV Strip Profile and Flatness Control

Chapter 27 Methods of Describing, Assessing, and Influencing Shape Deviations in Strips 287
Gert Mücke, Paul Dieter Pütz, and Frank Gorgels

Chapter 28 Local Shape Defects in Cold Rolling: Simulation, Causes Identification, and Reduction 299
Yuli Liu, Jian Fan, and Mike Levick

Chapter 29 Fundamentals of Online Flatness Measuring Devices 319
Fabio Miani and Paolo Patrizi

Chapter 30 Recent Developments in Strip-Profile Calculation 329
Arif S. Malik and Ramana V. Grandhi

Chapter 31 Hot Band Profile Irregularities Related to Thermal Contour of Work Rolls 341
Eugene Nikitenko

Chapter 32 Analysis of the Transverse Temperature Distribution in the Hot Strip Mill of a Compact Strip Production Plant 349
Jie Zhang, Lili Tian, Paolo Patrizi, and Fabio Miani

Chapter 33 Innovations in Shape Measurement and Control for Cold-Rolled Flat Strip Products 355
Mark E. Zipf

Index 367

Preface

Technology for the production of flat steel products has a long history of development, and demonstrates all the signs of longevity. The last two decades have been especially successful in the introduction of new technology, significantly reducing production cost and further improving product quality. Among the most revolutionary technologies that were introduced during that time were

- Hot strip production plants that use the thin- and medium-slab casters in combination with conventional rolling mills
- Hot strip and plate production plants that use thin- and medium-slab casters in combination with reversing Steckel mill
- Cast strip production plants
- High-productivity reversing cold mill

Significant progress has been made in the development of automation and process control for rolling mills, including the development of systems for monitoring the quality of rolled products. Further advances have been made in mathematical modeling of various aspects of rolling process. A recent consolidation of the steel industry created favorable conditions for the implementation of new technology. It also created a better opportunity for the exchange of technological know-how between plants that belong to the same company. The purpose of this book is to familiarize a broad audience with the latest developments in the theory and practice of manufacturing flat-rolled steel products.

This book has its roots in a series of technical publications that review and summarize developments in the theory and practice of manufacturing flat-rolled steel products. In the United States, the history of these publications goes back to 1978 when the first book on this subject *Cold Rolling of Steel* was published by Marcel Dekker. The author of the book was William R. Roberts, an American expert in flat rolling and processing of steel. Following the success of the first publication, Marcel Dekker published two more books written by Roberts: *Hot Rolling of Steel* in 1983 and *Flat Processing of Steel* in 1988.

I was thrilled when shortly before his retirement Roberts endorsed my first book, which was part of the same series, *Steel-Rolling Technology—Theory and Practice* published by Marcel Dekker, Inc. in 1989, and the other three books that I wrote later, *High-Quality Steel Rolling—Theory and Practice* in 1993, *Flat Rolling Fundamentals* (jointly with R. Ballas) in 2000, and *Metallurgical Design of Flat Rolled Steels* in 2005.

Unlike the above seven books that were written by either one or two authors, this book assembles the works of 63 authors specializing in various areas of research and development of steel production technology and manufacturing of flat steel products. The contributors to this book are from nine countries: Austria, Canada, China, Germany, Italy, Japan, Russia, the United Kingdom, and the United States. Their names and affiliations are listed in the contributor list.

I wish to express my gratitude to all the authors for their contributions to this book and also for their cooperation during the technical editing of their chapters. I am also grateful to Allison Shatkin of CRC Press with whom I brainstormed the idea of this book and who worked very hard to reach the potential contributors. I am also thankful to Amy Blalock of CRC Press for her tireless communication with the authors. My special gratitude goes to my son, Gene, who made the computer versions of the figures for my chapter, and to my wife, Tatyana, for her continuous support.

Vladimir B. Ginzburg

Editor

Vladimir B. Ginzburg, PhD, is president of International Rolling Mill Consultants, Inc., Pittsburgh, Pennsylvania. He began his career in the steel industry in 1975 as a staff engineer at Wean United. In 1981, he became the vice president of research and development of Tippins Machinery Company, and in 1984, he formed his own company, International Rolling Mill Consultants, Inc.

During the subsequent 15 years, he has acted as an exclusive consultant to Wean United, United Engineering, and Danieli Wean United. Over the past 8 years, he has provided consulting services to companies both designing and manufacturing rolling mill equipment and to steel-producing companies. He also conducts Expertise-Sharing Seminars for rolling mill personnel, utilizing a highly interactive method.

Dr. Ginzburg is the author or coauthor of numerous articles, proceedings papers, and books including *Steel-Rolling Technology, High-Quality Steel Rolling, Flat Rolling Fundamentals,* and *Metallurgical Design of Flat Rolled Steels* (all titles, Marcel Dekker). Dr. Ginzburg holds over 60 U.S. and foreign patents related to steel rolling and casting technologies. A member of the Association of Iron and Steel Technology, Dr. Ginzburg received his MS (1961) in mechanical engineering from the All-Union Machinery Engineering Institute, Moscow, Russia. He received his PhD (1968) in technical science from Moscow Rail Transportation Institute, Russia. In 2000 he received the Tadeuzs Sendzimir Memorial Medal, the highest technical award issued by the Association of Iron and Steel Technology.

Contributors

Shin-ichiro Aoe
JFE R&D Corporation
Kawasaki, Japan

M. B. Assar
ArcelorMittal
Cleveland, Ohio

Angelo Biggi
INNSE Cilindri
Brescia, Italy

T. Bilkhu
Converteam Ltd.
Rugby, United Kingdom

Ian Burton
D.A. Stuart Company
Valley Forge, Pennsylvania

Shaojie Chen
Evraz Inc. NA
R&D Centre
Regina, Saskatchewan, Canada

Rüdiger Döll
Siemens AG
Erlangen, Germany

Robert J. Echlin
Duraloy Technologies, Inc.
Scottdale, Pennsylvania

M. L. Elliott
Benchmark Automation
Cleveland, Ohio

J. F. Evans
Siemens VAI Metals Technologies
Sheffield, United Kingdom

Jian Fan
Quad Engineering Inc.
Toronto, Ontario, Canada

Tom Farley
Innoval Technology Ltd.
Banbury, United Kingdom

Wlodzimierz Boleslaw Filipczyk
TMEIC-GE Automation Systems
Roanoke, Virginia

J. Franklin
ArcelorMittal
Cleveland, Ohio

Chris Fryer
Converteam Ltd.
Rugby, United Kingdom

Eduard Garber
Cherepovets State University
Cherepovets, Russia

Vladimir B. Ginzburg
International Rolling Mill Consultants, Inc.
Pittsburgh, Pennsylvania

Frank Gorgels
VDEh-Betriebsforschungsinstitut GmbH
Düsseldorf, Germany

Ramana V. Grandhi
Wright State University
Dayton, Ohio

Hiromasa Hayashi
JFE R&D Corporation
Kawasaki, Japan

Gerald Hearns
Converteam Ltd.
Rugby, United Kingdom

Klaus Herrmann
EMG Automation GmbH
Wenden, Germany

Matthias Irle
EMG Automation GmbH
Wenden, Germany

Kazushige Ishino
JFE R&D Corporation
Kawasaki, Japan

Irina Kozhevnikova
Cherepovets State University
Cherepovets, Russia

M. Kremer
ArcelorMittal
Cleveland, Ohio

M. Krolikowski
ArcelorMittal
Cleveland, Ohio

Mike Levick
Quad Engineering Inc.
Toronto, Ontario, Canada

Bingji Li
Metal Pass LLC
Pittsburgh, Pennsylvania

Yuli Liu
Quad Engineering Inc.
Toronto, Ontario, Canada

Hans-Ulrich Löffler
Siemens AG
Erlangen, Germany

Arif S. Malik
Wright State University
Dayton, Ohio

Fabio Miani
University of Udine
Udine, Italy

Daniel V. Miller
Duraloy Technologies, Inc.
Scottdale, Pennsylvania

Alberto Molinari
University of Trento
Trento, Italy

Gert Mücke
VDEh-Betriebsforschungsinstitut GmbH
Düsseldorf, Germany

Per A. Munther
HATCH
Mississauga, Ontario, Canada

John Nauman
Metal Pass LLC
Pittsburgh, Pennsylvania

Eugene Nikitenko
Research and Technology Center
U.S. Steel Corporation
Munhall, Pennsylvania

Kazuhiro Ohara
Toshiba Mitsubishi-Electric Industrial Systems Corporation
Tokyo, Japan

Yuji Ohara
JFE R&D Corporation
Kawasaki, Japan

Roman I. Pankiw
Duraloy Technologies, Inc.
Scottdale, Pennsylvania

Paolo Patrizi
University of Udine
Udine, Italy

Massimo Pellizzari
University of Trento
Trento, Italy

Paul Dieter Pütz
VDEh-Betriebsforschungsinstitut GmbH
Düsseldorf, Germany

Peter Reeve
Converteam Ltd.
Rugby, United Kingdom

François Reizine
American Sensors Corporation
Pittsburgh, Pennsylvania

Robert L. Ricciatti
George Kelk Corporation
Toronto, Ontario, Canada

C. D. Romanauski
ArcelorMittal
Cleveland, Ohio

P. Sopp
Seimens VAI Metals Technologies
Erlangen, Germany

R. A. Stankie
Benchmark Automation
Cleveland, Ohio

John Stubbles
Steel Industry Consultant
Mason, Ohio

Lili Tian
University of Science and Technology of Beijing
Beijing, China

John B. Tiley
HATCH
Mississauga, Ontario, Canada

Alexander Traino
A.A. Baikov Institute of Metallurgy and Materials Science
Moscow, Russia

Alberto Tremea
INNSE Cilindri
Brescia, Italy

Klaus Weinzierl
Siemens AG
Erlangen, Germany

Michael Windhager
Eisenwerk Sulzau-Werfen
Tenneck, Austria

Qiulin Yu
Nucor Steel
Tuscaloosa, Alabama

Jie Zhang
University of Science and Technology of Beijing
Beijing, China

Karl Heinz Ziehenberger
Eisenwerk Sulzau-Werfen
Tenneck, Austria

Mark E. Zipf
Integrated Industrial Systems, Inc.
Yalesville, Connecticut

Section I

New Concepts and Modernization of Rolling Mills

1 A History of Minimills Producing Flat-Rolled Steel

John Stubbles

CONTENTS

1.1 The First Minimill 3
1.2 Ken Iverson 4
1.3 Crisis in Big Steel 4
1.4 Breakthrough 6
1.5 Expansion 6
1.6 Thin Strip Casting 9
1.7 Iron Unit Supply 9
1.8 The International Scene 11
1.9 The Future 12
References 14

1.1 THE FIRST MINIMILL

This is the story of a technological revolution that has occurred within this generation, although the seeds were sown in 1943 [1]. That was the year that the Iron and Steel Division of the American Institute of Mining, Metallurgical, and Petroleum Engineers (AIME) U.S. hosted a conference in Pittsburgh, in conjunction with the government, to stimulate the production of electric furnace steel for the war effort. As a result, a number of integrated mills installed such furnaces to produce carbon steels, although they still played second fiddle to the open hearths (OH) and even the old Bessemer process. In retrospect, however, a more significant event that year was the graduation of a metallurgist named Jerry Heffernan from the University of Toronto (Figure 1.1). He followed up wartime service in Europe with graduate work at the University of British Columbia (UBC), where he worked on some business projects for Professor Frank Forward. Then he entered the steel business in Canada and spent the next 7 years acquiring industrial experience and nurturing a vision.

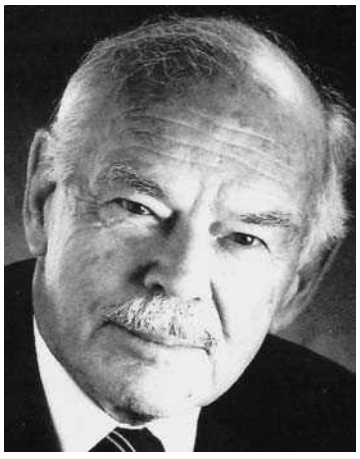


FIGURE 1.1 Jerry Heffernan (1919–).

Heffernan was no ordinary metallurgist; he was, at heart, an entrepreneur. His vision was to continuously cast steel, and he saw a perfect market in oil-rich Alberta—sucker rods. These are long, thin rods that connect the push-pull action of the lever arm at the wellhead to the underground pump that sucks the oil into the tubing. Heffernan's first step was to raise enough capital to build Premier Steel in Alberta. (This became Alta Steel, which was recently purchased by Scaw Industries. It is designated an ASM historical site.) In 1959, he installed a Rossi/Koppers billet caster at Premier with the intent of producing 55,000 tons of billets per year from 17-ton batches of liquid steel tapped from a small electric furnace. At this time, the continuous casting of steel was in its commercial infancy in Europe, but it was clearly a viable process. In North America, interest in continuous casting seemed minimal as the productive blooming and slabbing mills of the integrated companies pounded out millions of tons annually. Yet as far back as 1954, Atlas Steel in Tracy, Canada, had installed a Rossi/Koppers stainless slab caster. The melt shop at Premier still produced primarily ingots, but the sucker rods produced from continuously cast billets sold well enough to worry the giant Steel Company of Canada (Stelco, now owned by U.S. Steel). To avoid losing its Western market, Stelco bought out Premier in 1963 and provided Heffernan with enough capital to build the very first legitimate minimill

in 1965. Lake Ontario Steel (Lasco) was globally unique in that no ingot molds were present in the shop to provide a safety net; the 200,000 annual tons of liquid steel was either continuously cast or returned to the electric arc furnace (EAF) as liquid or scrap. Lasco was built just outside Toronto, where Stelco had its corporate office. To rub salt into the wound, Heffernan persuaded an MIT post-doctoral researcher who was disillusioned with "big steel" to leave Stelco and join him in his new venture. Dr. Gordon Forward was the son of Heffernan's former mentor at UBC and advanced quickly in the less bureaucratic minimill environment. He carved his own entrepreneurial niche a few years later when he managed Chaparral Steel (now Gerdau-Ameristeel) in Midlothian, Texas, as part of Heffernan's Co-Steel empire. With Lasco running well, Heffernan later built the North Star minimill in association with Cargill at Minneapolis/St. Paul, but this venture turned sour when Cargill acquired controlling interest in a rather underhanded way. Heffernan responded by negotiating his shares for a handsome profit and acquired enough capital to build Chaparral Steel.

1.2 KEN IVERSON

It was at North Star, however, that Ken Iverson (Figure 1.2) met Heffernan. Iverson was seeking a source of concrete reinforcing bar or rebar for his Vulcraft fabricating plant in Nebraska because the billets from big steel were getting too pricey. Iverson located a cheaper source that was relatively close by, and after visiting the North Star facility, he saw some potential in building his own minimill and producing steel internally. But his Nuclear Corporation (as it was then called) was near bankruptcy. However, desperate times called for desperate measures, and the price of scrap was so cheap (about $30 per ton) and the capital outlay so modest ($60 per ton), that he decided to take the risk. Iverson commissioned his first minimill at Darlington in 1969 with a planned capacity of 200,000 annual tons. This was considered typical of the annual output of a small EAF shop—a 50-ton furnace tapping one heat every 2 hours. The Nuclear mill was located near another Vulcraft plant and close to corporate headquarters at Charlotte. It took 2 years of frustrating effort to train crews of green farmhands to continuously cast billets for rebar. By 1971, however, Darlington had turned into a goldmine. The company changed its name to Nucor, and in short order, built two more similar minimills: in Norfolk, Nebraska, in 1974 and Jewett, Texas, in 1975.

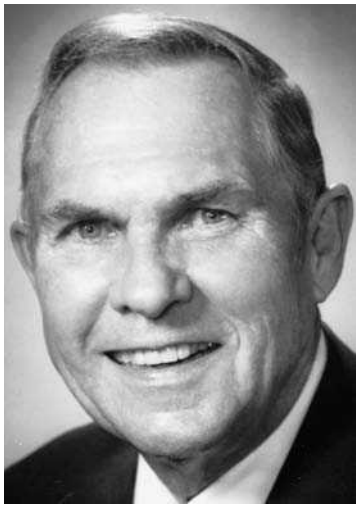


FIGURE 1.2 Ken Iverson (1926–2002).

Iverson introduced some radical human relations policies into the steel industry. His shops were nonunion (Lasco was unionized) and located in rural areas with market potential and no competition for an adequate supply of cheap scrap. They were staffed initially by farmhands who were used to hard work, had mechanical skills, and no bad steelmaking habits to unlearn. They worked in teams under minimal supervision and were paid relatively low wages, but they earned huge weekly bonuses by ensuring good quality and high productivity. The penalties for absenteeism were severe. There were also college tuition benefits and other perks for families of employees. The work was rewarding financially and also psychologically in the sense that a team spirit prevailed, unlike the unproductive "them" and "us" attitudes in the unionized big steel mills.

1.3 CRISIS IN BIG STEEL

In the early 1970s, about 30 small minimills in the United States contributed only about 6 million tons to annual shipments of about 110 million. In fact, EAF production within the integrated sector was much larger (Figure 1.3). Since these small mills produced primarily rebar and junior sections, they seemed to pose no threat to the primary markets of the integrated steel producers, although the erosion of the so-called gravy business was irritating. But big steel was about to be crippled by a succession of mandatory environmental and safety regulations that increased both operating and capital costs significantly. The 1970s saw implementation of the Clean Air Act, the Clean Water Act, the Occupational Safety and Health Act (OSHA), and hazardous waste legislation (Resource Conservation and Recovery Act, RCRA). The minimills were not exempt from these regulations, but they were impacted to a much lesser degree.

Then came the first oil crisis of 1973, which increased the cost of all energy sources. Shipments from the integrated companies started to plummet, which resulted in a number of bankruptcies. The replacement of the workhorse OH process by the basic oxygen process (BOP) had been occurring throughout the 1960s. Since the latter operated with a higher percentage of hot metal, purchased scrap requirements were minimal as long as liquid steel was poured into ingot molds. When these were used, the yield of shipped tons from liquid steel still hovered around an abysmal 70%, a figure that had not changed in over 50 years. Even with the BOP, the integrated mills were noncompetitive on a global basis. Ingots had to go. A few companies had ventured into large-scale slab casting in the late 1960s (McLouth, Weirton, U.S. Steel Gary), but the integrated companies as a whole were reluctant to embrace

the new technology for a number of reasons, including productive written-off slabbing mills and lack of capital for the low-productivity continuous casting (CC) process that could not cope with the overall U.S. product mix. However, with a second oil crisis in 1979, the situation became desperate, and survival for the integrated companies hinged on the infusion of capital and technology from Japanese steel companies, who wanted a share of the U.S. automotive market and had mastered the continuous casting of quality slabs at an acceptable productivity level. The transformation was rapid in the 1980s, and the benefits of increased yield and quality soon paid off (Figure 1.4). The 1980s also heralded the end of the really cheap scrap era, as home scrap supplies dwindled.

A new intermediate process, the ladle refining furnace, had also appeared and was essential to successful casting. This unit was a buffer between the melting furnace and the caster, where both chemistry and temperature could be controlled precisely. It called for the separation of steel and furnace slag at tap, after which the liquid steel was heated by arcs from three alternating current (AC) electrodes under an artificial nonoxidizing slag. Heating under vacuum, a process that was patented in the United States (C. Finkl, March 17, 1970, No. 3501289), also allowed for the removal of carbon and hydrogen, as well as cleaner steels (i.e., fewer nonmetallic inclusions) [2]. The long-product minimills, with experience in electrode handling and the ability to separate steel from slag by tapping from tilting EAFs with specially designed eccentric bottom tapholes (EBTs), pioneered this process in the United States. It also moved them up the product quality chain. The EBT tapholes also enabled the EAFs to operate with a large residual heel of steel in the furnace that accelerated the melting process and increased productivity.

By the late 1980s, the U.S. markets were split between the integrated producers producing flat-rolled steels for automotive, containers, and appliances, as well as plate and heavy sections, and the ever-expanding EAF-based minimills that now monopolized the bar, rod and wire, and light section markets. Bankruptcies had severely diminished the capacity of, and employment within, the integrated sector, but the more efficient integrated mills had survived with new technology and foreign partnerships. The long-product minimills had grown in number and capacity, introduced new technology in

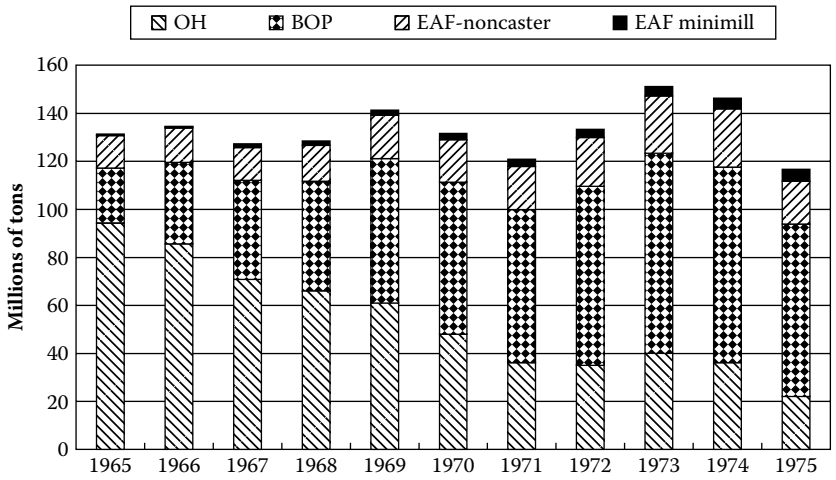


FIGURE 1.3 U.S. raw steel production by process (1965–1975).

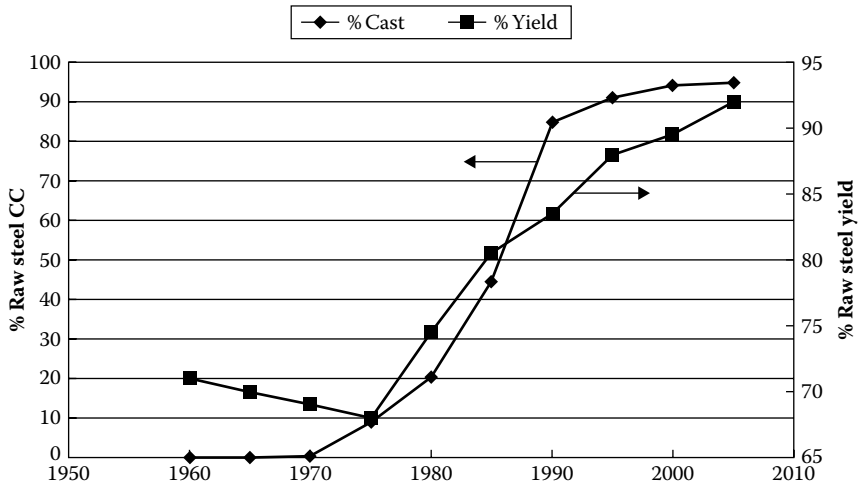


FIGURE 1.4 Impact of continuous casting (CC) on U.S. raw steel yield.

both melting and casting to become very efficient, and were enjoying significant profits due to relatively cheap scrap and low electrical power costs.

1.4 BREAKTHROUGH

Nucor was very profitable in the late 1970s, but facing competition from other minimills. The Vulcraft division still bought steel decking from integrated producers to cover joists, so it seemed a logical step for the company to move into the flat-rolled business. The trouble was that casting a thick slab, which was now relatively easy to do, called for a large and very expensive hot mill to produce hot band. On the other hand, worldwide ventures into the world of thin slab casting had been numerous but very unsuccessful, even when attempted by major research groups in large companies [3]. Nevertheless, in 1986, Nucor opted to explore the Hazelett twin-belt strip caster and installed an experimental unit at Darlington for $5 million. Mark Millett spent a frustrating year trying to coax steel out of the machine and finally did succeed in producing steel "fit for garbage cans." But, earlier that year, David Aycock, a Nucor executive, had traveled to Germany to observe thin slab production on an SMS Schloemann-Siemag AG pilot plant machine, which was equipped with a special funnel-shaped mold invented by Manfred Kolakowski. Aycock's favorable report triggered a series of meetings between Nucor and SMS, culminating in a contract to build a full-scale Compact Steel Plant (CSP) in December 1986. Millett's twin-belt caster was quickly abandoned, and the Crawfordsville, Indiana, project was under way. It is of interest to note that dozens of executives from around the world had visited the SMS pilot machine, but all had dismissed the concept of the CSP for various reasons.

The Crawfordsville plant was designed for 910,000 annual tons of hot band and cold rolled sheet, at a maximum width of 1345 mm (53 in.), well below the width capability of most hot mills at integrated plants. In this CSP, a continuous slab of steel 50 mm (2 in.) thick emerges from a single strand vertical caster at about 5 m/min (16 ft/min). After shearing, when horizontal, the thin slabs continue to move into a long-tunnel furnace for temperature equalization and holding, if necessary. An in-line five-stand rolling mill (originally only four) turns them into coils of hot band. Secondhand cold-rolling and galvanizing mills were also installed in Crawfordsville. The plant was commissioned with considerable difficulty during 1989, creating a colossal cash drain each month, but eventually, the bugs were worked out and the mill became a significant moneymaker [4]. It soon became apparent that the rolling mill could easily outrun the caster, and when a second Nucor CSP mill was commissioned at Hickman, Arkansas, in the summer of 1992, the ultimate plan called for two large direct current (DC) furnaces to feed two casters and two tunnel furnaces. Hot slabs would then be shuttled in a special car from one line to the other to feed the six-stand rolling mill. The ultimate mill capacity was projected to be 2.2 million tons per annum. Crawfordsville has since been similarly upgraded to increase annual capacity from 0.9 to 1.8 million tons. It should be noted that the capacity figures for all minimills are merely targets, which have been surpassed time and time again through innovative practices and additional capital investments.

1.5 EXPANSION

Both Nucor mills reached capacity quickly, with Hickman benefiting from the Crawfordsville experience, but skepticism about quality still remained in the market place. Apart from the width issue, could these products really compete with aluminum killed automotive steels produced by the integrated mills? What about the high residuals from scrap—how could the EAF mills dilute them to meet the stringent automotive specifications? For the integrated producers, the real problem was that there was plenty of hot and cold rolled tonnage of lower quality coils with an average width of about 1346 mm (53 in.), and there would be inevitable erosion of their lower quality tonnage markets, as had happened when the original minimills captured the rebar business. The other intangible factor was the can-do attitude that prevailed in the minimill world where the continuous improvement philosophy was promoted. No one in the minimill business doubted that the quality issues would be addressed and solved as dictated by market opportunities.

While Nucor had a head start in the flat-rolled minimill business, it would not enjoy that advantage for very long. The next few years saw the construction of several competitive mills, both CSP and some variants. The first mill out of the blocks was Gallatin in Kentucky, initially a 50/50 joint venture between Dofasco and Heffernan's Co-Steel empire, which produced commercial steel in May 1995 [5]. As at Hickman, an SMS caster is fed by two large DC Man GHH furnaces, but Gallatin opted for a common power supply for each shell. The commissioning was not easy, but problems have now been solved and, with planned expansion, the mill is expected to produce over 2 million tons annually. Early in 1996, Steel Dynamics (SDI) started up the fourth CSP plant in Butler, Indiana [6]. The twin-shell concept was again used, but this time with AC furnaces designed by Fuchs. The hot mill has six finishing stands, giving it the capability to roll hot band down to 1.0 mm (0.04 in.), as against the normal 1.4 mm (0.055 in.), and close to cold rolled gauges. The successful startup here was not unexpected because the plant was run by Keith Busse, Mark Millet, and Dick Teets, who were involved in starting and then optimizing operations at Crawfordsville. Later that year, BlueScope North Star (then BHP) tapped the first heat from its mill in Delta, Ohio [7]. But this mill installed a Sumitomo (SHI) medium slab caster 90 mm (3.54 in.) as against 50 mm (2 in.) slabs from the casters in the CSP mills, which meant installing a two-stand roughing mill to reduce the slab gauge to 30 mm (1.2 in.) coupled with a preheating table before the bar entered the six-stand finishing mill. This mill also installed the first U.S. double-shaft, twin-shell AC EAF where some of the sensible heat in the hot gas exiting the fourth hole is captured to reduce the electrical energy required. The only product

from this facility is coiled hot band, and production is now approaching about 1.9 million tons annually. In early 1997, LTV (50%), British Steel (25%), and SHI (25%) commissioned a mill for flat-rolled products (Trico) in Decatur, Alabama, with a caster producing 90-mm (3.5 in.) slabs [8]. The two large NKK DC furnaces were unusual in that they each had two electrodes in elliptically shaped furnaces. The mill was supposed to produce 2 million tons annually, but never got beyond 1.65 million and shut down in 2001 after suffering a series of equipment problems. In 2002, Nucor purchased the mill, now known as Nucor, Decatur, and has since run it successfully with few modifications to the original equipment. In 2004, Nucor purchased an adjacent cold mill from Worthington Industries and eventually expects to ship about 2.7 million tons annually [9]. The hot mill can produce band up to 1650 mm (65 in.) in width and down to 1 mm (0.04 in.). While Trico was struggling in Decatur, Nucor built another mill in Berkeley, South Carolina that produces a whole range of flat-rolled products, as well as structurals. In fact, under John Bell, the melt shop became the most productive of all the Nucor mills, topping 2.7 million tons (3 million tons) in 2006, of which about two-thirds was flat-rolled [10]. The twin-shell DC furnaces, each with its own electrode mast but with one power source in the shop, are charged with one bucket of scrap and supplementary alternative iron units (AIU), which include pig iron, directly reduced iron (DRI), and hot briquetted iron (HBI). To satisfy the voracious appetite of the two casters, four ladle furnaces were installed.

The term minimill had clearly become obsolete, not only because of the new greenfield sheetmills, but also because of ventures by EAF shops into plate and structural markets. The original 1988 joint venture in Blytheville between Nucor (51%) and Yamato (49%) producing structural beams has been wildly successful first under John Correnti (with John Bell as melt shop manager), and then under Dan DiMicco, who is now president of Nucor [11]. It now ships over 3 million tons annually, although the original plans called for only 600,000 tons. By 2001, Ipsco (now SSAB) had installed 2.5 million annual tons of plate capacity with mills in Alabama and Iowa, Nucor (Hertford) had the capacity to produce another 1 million tons of plate with a Consteel melting unit [12], while Tuscaloosa Steel, now in the Nucor stable, contributed another 750,000 tons. With other structural mills at Whitley (SDI) and the two former Chaparral mills (now Gerdau-Ameristeel), the so-called minimills monopolized all markets, except sheet and strip and tinplate, and since 2002, have produced more raw steel than the integrated mills [13].

One recent development in EAF flat-rolled steelmaking has an interesting background. In 1999, Ken Iverson and John Correnti, then CEO and president of Nucor, respectively, were surprisingly ousted from Nucor by a hostile board. Iverson was not well and died a few years later. Correnti explored a number of options within the industry and finally surfaced as 20% owner of a new CSP in Columbus, Mississippi, called SeverCorr [14]. The start-up was August 2007 and, needless to say, this mill incorporated all the best features that Correnti had seen in the Nucor mills, with a powerful DC furnace tapping 165 tons and retaining a 90 ton heel. Twin-ladle furnaces (SMS Demag) and a vacuum degasser for producing ultralow carbon grades fed an SMS thin slab caster with a 1880 mm (74 in.) wide funnel mold, the widest in the industry. The six-stand hot mill rolled 915 mm (36 in.) to 1880 mm (74 in.) wide hot band down to 1.4 mm (0.054 in.), and downstream equipment was comparable to that in a modern integrated plant. Current plant capacity of 1.4 million annual tons will be expanded eventually to 3.1 million. However, in early 2008, after commissioning the mill, Correnti and his associates were bought out by Severstal, a Russian company and the majority owner of SeverCorr.

The timeline for the installation and the estimated output of EAF flat-rolled mills, including plate mills, is shown in Figure 1.5. Tables 1.1 and 1.2 include current information on the melting and rolling facilities, but these data will be quickly outdated because of frequent upgrading.

While U.S. shipments of sheet and strip have grown steadily since the mid-1980s, the increase has been taken up primarily by the new EAF mills. At the present time, annual EAF production of carbon sheet and strip is in the range

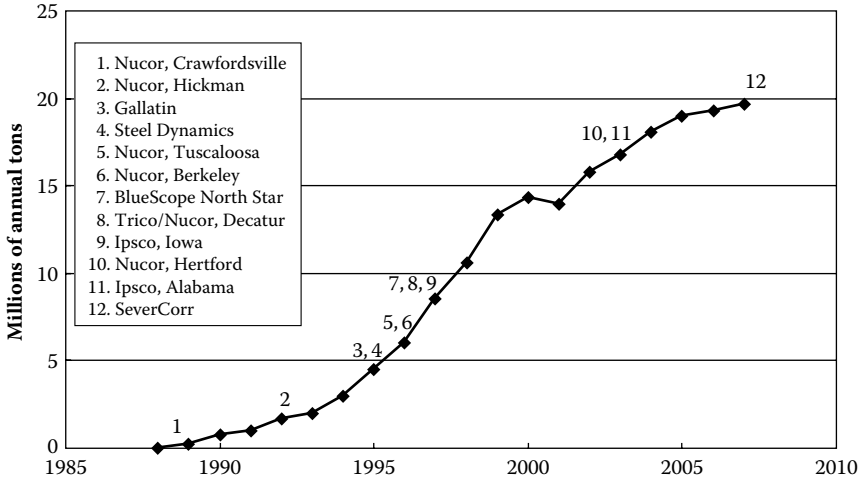


FIGURE 1.5 Cumulative production of U.S. flat-rolled steel minimills.

TABLE 1.1
EAF Facilities in U.S. Flat-Rolled Steel Minimills

Facility (Sheet)	Start	Furnaces	Electrode Diameter (in.)	Transformer Power (MVA)	Tap Tons	Ladle Metallurgy Furnaces	Degas Capability	Melt Shop Capacity (MM tons)
Nucor, Crawfordsville	1989	2 AC	24	65	120	2	Yes	>2
Nucor, Hickman	1992	2 DC	28	100	165	2	No	>2.5
Gallatin	1995	1 Twin-shell DC	28/30	90	185	2	No	>1.9
Steel Dynamics	1995	2 Twin-shells AC	24	120	165	2	No	>2.5
Nucor, Berkeley	1996	2 Twin-shells DC	28	110	165	4	Yes	>3.0
BlueScope North Star	1997	1 Twin-shell shaft AC	24	140	160	2	No	>1.9
Nucor, Decatur	1997	2 Twin electrode DC	24	150	170	2	No	>2.2
SeverCorr	2007	1 DC	30	2×85	165	1	Yes	>1.5
Facility (Plate)								
Nucor, Tuscaloosa	1996	1 Twin-shell DC	28	2×58	150	1	No	>0.75
Ipsco, Iowa	1997	1 Twin-shell DC	28	2×70	125	1	Yes	>1.25
Ipsco, Alabama	2001	1 Twin-shell AC	24	140	125	1	No	>1.25
Nucor, Hertford	2001	1 Consteel DC	30	2×88	165	1	No	>1.0

TABLE 1.2
Casting and Rolling Facilities—EAF Flat-Rolled Steel Minimills

Facility (Sheet)	Start	Slab Thickness (mm)	Slab Width (mm)	Casting Speed (m/min)	Tunnel Furnace Length (m)	Number of Hot Mill Stands	Gauge (mm)	Cold Rolling	Galvanizing
Nucor, Crawfordsville	1989	40/50	900/1350	5–6	164	6	2.5–12.7	Yes	Yes
Nucor, Hickman	1992	40/50	1220/1560	5–6	207	6	1.8–12.7	Yes	Yes
Gallatin	1995	55/65	1080/1625	6–7	207	6	1.4–16	Yes	Yes
Steel Dynamics	1995	40/80	990/1625	4–6	220	6	1–13	Yes	Yes
Nucor, Berkeley	1996	50/55	1220/1676	6–7	206	6	1.3–16	Yes	Yes
BlueScope North Star	1997	90	900/1565	5	27	2 Roughers + 6	1.5–9.5	No	No
Nucor, Decatur	1997	70/90	940/1650	4–5	175	2 Roughers + Coil box + 5	1.0–9.5	Yes	No
SeverCorr	2007	60/65	915/1880	5	261	6	1.4–12.7	Yes	Yes
Facility (Plate)									
Nucor, Tuscaloosa	1996	130	915/2610	?	No	Steckel mill	Coils (?):50 Plate	NA	NA
Ipsco, Iowa	1997	125/150	1220/3050	1.25/2.5	No	Steckel mill	2.3/19 Coil:5/51 Plate	NA	NA
Ipsco, Alabama	2001	150/230	2440/3050	1.2/1.65	No	Steckel mill	4.8/19 Coil:5/76 Plate	NA	NA
Nucor, Hertford	2001	130/160	1830/3125	4	No	Plate mill	9.5–51	NA	NA

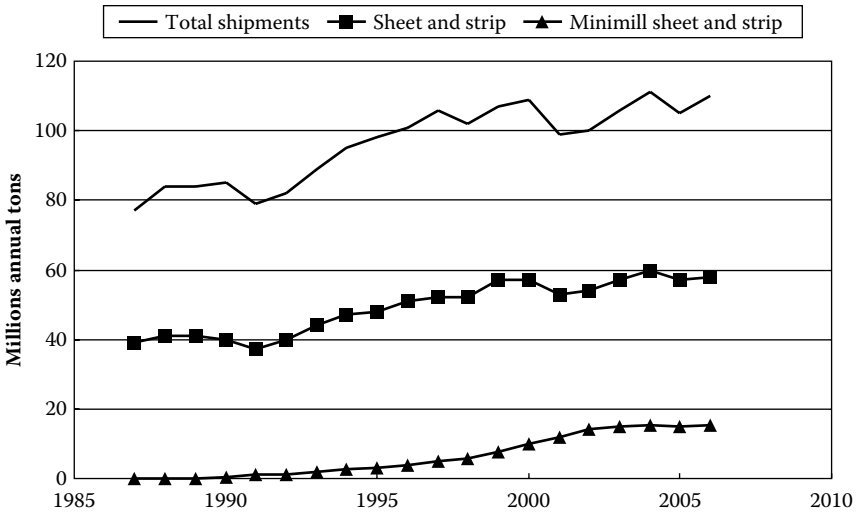


FIGURE 1.6 U.S. total and sheet and strip shipments.

of 14–16 million tons out of 55 million, or about 27%; the growth curve is shown in Figure 1.6. The EAF mills produce no tinplate. However, they dominate all nonflat-rolled markets, as well as stainless steel production. It appears that sheet and strip shipments from the domestic integrated mills have peaked at between 40 and 45 million tons. With the trend toward international control of the U.S. steel industry and the need for about an additional 1 million tons of new domestic capacity annually, the growth of the domestic industry and the sourcing of crude steel remain uncertain. However, most likely, it depends on new capacity in the EAF sector, because it is improbable that new blast furnace capacity will be built in the United States.

1.6 THIN STRIP CASTING

The thin strip concept can be credited to Henry Bessemer, who in 1857, conceived pouring steel between rotating rolls (British Patent September 18, 1857, No. 2432) to produce a ribbon of solid sheet steel akin to casting sheets of glass. The technology he needed to make this a practicable venture was not available then, but in the 1980s and 1990s, a number of global companies pursued this dream. Out of this effort emerged Project M (named for marsupial, an Australian mammal) at Port Kembla, Australia, where BHP (now BlueScope) and IHI collaborated for nearly 10 years to finally produce a commercial low-carbon, silicon-killed product 2 mm (0.08 in.) thick and 1350 mm (53 in.) wide in 1998 [15]. They needed a strong technical partner to go further and, not surprisingly, selected Nucor, who decided to install a commercial unit in Crawfordsville. Groundbreaking for Castrip occurred early in 2001, and the first commercial coil was shipped in mid-2002 [16]. The ultrathin cast strip (UCS) emerges from the rolls 1350 mm (53 in.) wide, and between 1 and 2 mm thick, and an in-line rolling stand can reduce the strip another 30%. At 1.6 mm thickness, the speed is about 80 m/min (260 ft/min), or about 13 times the rate of thin slabs. The annual plant capacity is projected to be 450,000 tons. At 2 mm UCS thickness and a 30% hot reduction, the final product is 1.4 mm (0.055 in.) thick, equivalent to the thinnest economic hot band from a conventional mill. In the last few months of 2007, 24 ladles of steel were cast sequentially, and the process can certainly be considered commercial for non-AK steels. The development trend is obviously toward casting the thinnest possible strip and capturing cold rolled and galvanized steel markets for substantial cost savings. Casting AK steels presents a formidable challenge and may not be worth the effort. The capital cost savings is in the avoidance of constructing a tunnel furnace and a five- or six-stand hot mill, as well as the savings in real estate. There are also operating cost savings associated with energy conservation, such as no soaking in a tunnel furnace. The downside is that the slightest blip in this very fast-moving operation kills yield and productivity. However, it also makes a portable micromill a real possibility in the future for specific markets.

Nucor is planning to install an additional Castrip unit in Blytheville, where there is surplus melting capacity. Expansion into the industry probably depends on the existing balance in any facility between melt and rolling capacity, as well as the cost of licensing and commissioning the process.

1.7 IRON UNIT SUPPLY

One of the incentives to enter the minimill business was inexpensive scrap (~$30 per ton), which constituted 100% of the ferrous raw material charge. The United States is fortunate to have a scrap-handling network administered by the Iron and Steel Recycling Institute that has served the steel industry well for over a century. The recycling of cans, cars, and white goods has been a tremendous success story in itself. Over 66 million tons of steel scrap are converted annually into prime steel in the United States; about 10 million net tons are exported. There has been steady growth in the installation of giant mechanical shredders to provide EAF steelmakers with a source of consistent physical scrap that is easily melted. Over 200 units in the United States now produce

over 25 million tons of this grade, which has displaced No.1 heavy melt as the bell-weather scrap in the industry [17]. Instrumentation to check the metallic residual chemistry of the scrap streams from the shredders has resulted in consistent copper levels between 0.13% and 0.15%, which would have been unthinkable a few decades ago [18]. Shredded scrap can now command premium prices (Figure 1.7).

When the BOP process began to displace OH in the 1960s and 1970s, the integrated companies needed less purchased scrap because the average hot metal in the charge rose significantly to about 70%. The EAF minimill sector became the beneficiary. Although industry yields improved and home scrap declined further in the 1980s due to slab casting, the number of integrated companies also declined due to bankruptcies, so scrap still remained a bargain. But with the growth of both the flat-rolled EAF mills and integrated mills based on 100% continuous casting, the prime scrap supply tightened severely in the 1990s due to high yields, reduced tonnages of home scrap, and high levels of exports. For the flat-rolled EAF plants competing for automotive business, the cost and availability of low residual scrap have become critical. Tight residual specifications are not confined to automotive flat-rolled products either. The transition from cheap scrap at stable prices in the 1960s to costly scrap in today's volatile market is shown clearly in Figure 1.7.

The minimill flat-rolled sector anticipated this situation even in the early 1990s, and explored options for acquiring sources of low-residual AIU. Cold pig iron from domestic sources was more expensive than imported pig iron from either Russia or Brazil, and not readily available. The domestic production of DRI or HBI using natural gas as a reductant was nonviable due to the cost of the natural gas, which was already high and predicted to soar. (Georgetown Steel, now owned by Mittal, operated a Midrex DRI gas-reduction plant in South Carolina as early as 1969, to supply a high-quality wire operation with 50% of the charge as DRI. The melt shop now receives DRI from Trinidad; soaring gas prices eventually forced closure of the DRI plant.) Nucor explored the idea of producing iron carbide offshore in Trinidad where natural gas was cheap [19]. On paper, this was a great idea. The granulated product, Fe_3C, produced from cheap South American ore fines, could be blown into the EAF, thus avoiding the cost of charge carbon and possibly eliminating a bucket charge. The limitation per heat was the carbon level in the melt. A 25% charge of carbide at 6% carbon would have resulted in well over 1% C in the melt, compared to the present aim levels of about 0.4%. With the existing oxygen injection rates and waste gas handling facilities in even the most productive EAF shops, it would have taken too long to remove the carbon, even though it might have been energetically attractive. There was also the problem of handling much more hot waste gas.

In 1995, Nucor, without any pilot plant experience to fall back on, built a full-scale plant in Trinidad. The first carbide shipments reached the United States in the spring of 1996. The facility was cursed with one operating problem after another, and the thermodynamic window for producing Fe_3C and avoiding magnetite (Fe_3O_4) formation involved careful control of both pressure and temperature. The melt shops were enthusiastic about the trial shipments, but an unforeseen issue was the bulk handling; in the presence of moisture, the black sand in a silo turned into rock. The carbide plant was mothballed in 1998. Meanwhile, Nucor has shipped two gas reduction modules from a defunct Air Reduction plant in Louisiana to Trinidad to produce over one million tons of conventional DRI annually.

Qualitech broke ground for its carbide plant in Corpus Christi, Texas, in late 1996, with seed money from SDI, but this plant was never completed due to corporate financial problems.

Undeterred, SDI explored another approach, based on many years of Midrex pilot plant experience. A carbon-iron oxide fines mixture plus binder was made into balls, and these were partially reduced in a rotary hearth furnace (RHF) heated by natural gas. The hot product was fed to a submerged arc furnace (SAF) to melt and desulfurize. The

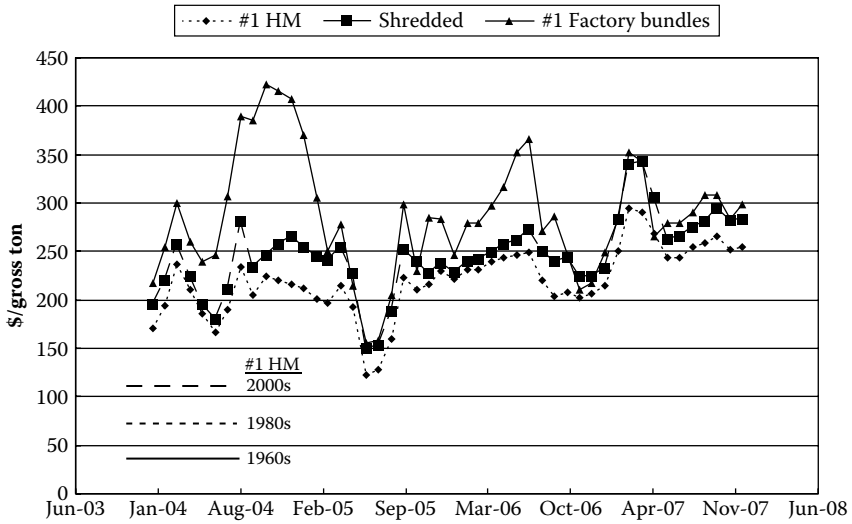


FIGURE 1.7 Recent U.S. scrap prices ($/gross ton).

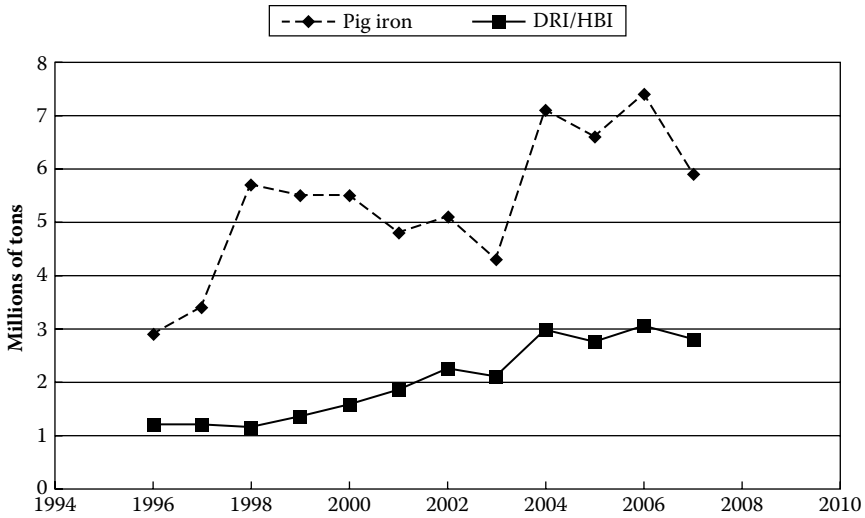


FIGURE 1.8 Imports of AIU.

EAFs were then charged with liquid iron to increase productivity and produce a low, metallic, residual steel using less prime scrap. Iron Dynamics was created to operate the facilities on the site of the Butler CSP, with an aim start-up of late 1998 [20]. Once again, theory was confounded in practice. The balls did not behave well on the hearth, and there were numerous problems with the SAF units. When liquid iron was produced, it worked well in the EAFs as planned, but the costly operation was mothballed in 2000. Again, SDI was not deterred. Midrex (now owned by Kobe Steel) was the premier DRI producer in the world. Midrex recognized that any DRI process in the United States had to be coal based, so had explored the rotary hearth process with various carbon-iron oxide mixtures (e.g., FastMet). But the breakthrough occurred at the Kobe pilot plant of Kakagawa in 1997 and the ITmk3 process (Ironmaking Technology, mark 3) was born. By raising the hearth temperature to about 1350°C (2460°F), which was much higher than with natural gas reduction in shaft furnaces, the iron oxide could be reduced quickly to a barely liquid iron containing less carbon than hot metal. Because of surface tension, the liquid iron formed globules like M and M's that separated easily from the viscous gangue material as it exited the RHF. In mid-2003, a 30,000-ton-per-year ITmk3 pilot plant began operating in Minnesota, funded by state, private, and government money [21]. Mesabi Nugget LLC is licensed by Kobe. A viable process was developed, and environmental permits have now been sought for commercial facilities with capacities of 270,000 tons per annum. The first will be built in Minnesota, with SDI as the primary recipient of the nuggets. Cleveland Cliffs is also negotiating for a facility on the iron range in Silver Lake to produce merchant nuggets. The carbon content of around 2% will allow a higher percentage in the EAF charge than with either hot metal (4% C) or carbide (6% C).

The tight and volatile bundle pricing coupled with the need for EAF flat-rolled mills to produce low metallic residual steel has resulted in a steady rise in DRI/HBI imports from South America and pig iron imports from Russia and Brazil (Figure 1.8). Some of these are purchased by specialty bar companies and even by integrated companies (for enhanced blast furnace production and also BOP tap temperature control) so that only 5–6 million of the 9–10 million total end up in EAF flat-rolled mills. The EAF flat-rolled sector as a whole has settled for AIU levels in the charge of up to 30%, when required, and will probably adopt a wait-and-see attitude relative to further on-shore capital investment until the nugget process has been shown to be truly commercial.

The same can be said for the HIsmelt Direct Iron process that has been in gestation since 1993. An 800,000-tons-per-year plant was finally constructed in 2004 at Kwinana, Australia (Nucor committed 25% of the $200 million capital cost), and is expected to produce hot metal directly from ore fines and coal [22]. Absence of news suggests there are operating problems.

1.8 THE INTERNATIONAL SCENE

It is puzzling that the SMS pilot work in Germany did not inspire at least one European steelmaker to take the lead in the flat-rolled minimill story. There are historic parallels, however, for "stealing" European technological initiatives. The development of the Bessemer process by Holley and Carnegie in the 1870s vaulted the U.S. steel industry into a world leadership role, while the upscaling of the Austrian LD process from 30-ton vessels in the 1950s to the highly productive 250-ton U.S. BOPs in the 1960s followed a similar pattern. In the early 1990s, there were thin slab pilot plant trials by Arvedi in Cremona, Italy, with an in-line strip process developed by Mannesmann Demag Huttentechnik, but the first commercial unit was not commissioned there until 1992. In this process, the 50-mm (2-in.) slab from a regular mold is squeezed down while the core is still molten, and induction units and coil boxes replace the tunnel furnace. The Arvedi plant was designed for only 500,000 annual tons, but by 1994, it was producing close to 700,000 annual tons [23].

Hylsa in Mexico started conventional CSP operations in 1995 and was able to charge hot DRI to its EAF—the innovative Hytemp process—to reduce EAF energy consumption per ton [24]. According to Midrex, there are 28 true CSP plants operating in the world today, with about half of them in Asia. In Europe, only four thin slab casters are operational, and two of those (Corus, Ijmuiden, and TKS, Duisberg) are in BOP shops. None exists in Japan [25]. Yet steel engineering expertise for most new steelmaking developments remains headquartered in Europe and consolidation has been the order of the day. Danieli is still intact, SMS has absorbed Mannesmann-Demag, and Siemens has taken over Voest. In Japan, all the former companies, including IHI, NKK, and SHI, are now known as JP Steel Plantech.

The restructuring of the minimill sector is following the pattern of the integrated sector (i.e., the buyout of several former major U.S. steel companies by Mittal), with ownership by non-U.S. companies growing fast. Nucor has put a brake on this by acquiring a number of domestic mills (Auburn, Marion, Trico, Tuscaloosa, Kankakee, Kingman, Birmingham, Seattle, Connecticut, and Jackson) to add to its homegrown facilities, and it is now the largest domestic steel company with an annual output exceeding 20 million tons. The Gerdau-Ameristeel merger embraces another 15 U.S. mills in the long products sector and is a co-owner with Mittal-Arcelor of Gallatin. The Ipsco plate mills have recently been purchased by SSAB. Oregon Steel and Claymont have been purchased by the Russian Evraz group recently, and there are rumors of more Russian ownership in the Midwest to add to the Severstal acquisition. In a reverse trend, Nucor signed a 50/50 agreement with Duferco in Switzerland for beam production in Italy. This globalization will no doubt continue, and one hopes that the original U.S. minimill continuous improvement philosophy will be retained. The sharing of technical expertise should be positive, along with global access to raw materials.

1.9 THE FUTURE

The focus in this chapter has been on the history of EAF melting facilities associated with the production of steel for plate and sheet mill products. It is fair to say that liquid steel from EAFs can now be continuously cast to meet any chemical and most dimensional specifications. Metallic residuals can be diluted, while carbon and hydrogen can be removed to low parts per million levels by degassing. The ability to roll thin slabs at lower temperatures than on a conventional hot mill will enable metallurgists to exploit recrystallization technology [26,27]. The Castrip UCS process with even less segregation than in thin slabs may open up new possibilities with respect to acceptable residual levels in sheet steels and make available the opportunity to cast cold rolled gauges directly. Without any chemical restraints with respect to specifications, the EAF sector is likely to continue to grow to supply the needs of an expanding U.S. economy. To avoid growth in semifinished steel imports, which are currently at about 30% of U.S. shipments, the domestic industry needs to melt at least an additional one million tons annually. There are restraints with respect to EAF expansion, however.

The first is a raw material issue. Prime scrap has become, and will continue to be, very expensive and scarce as the Asian economies soar. Net scrap exports in 2007 exceeded over 12 million tons, much higher than normal. The growth of the Chinese steel industry has been phenomenal over the last decade, with a 2007 output of over 480 million tons [28]. In 1990, it was only 67 million tons. As China moves toward efficient EAF steelmaking and away from inefficient hot-metal operations, the world scrap market will tighten. There are no trade restrictions on U.S. scrap exports. The Mesabi (ITmk3) nugget process opens up the possibility of a domestic, coal-based AIU product that, if it proves commercially viable, will augment the supply of domestic prime scrap. Either the HIsmelt process or mini-blast furnaces could supply liquid hot metal to EAF shops to augment productivity and substitute for prime scrap, but they have not been commercialized in the United States at this time, and they would increase CO_2 emissions per ton of steel. None of these developments is likely to have a noticeable impact on the scrap supply for at least 5 years.

The second restraint is the power supply and rising power costs. A few years ago, U.S. engineering societies voted the power grid in the United States to be the greatest engineering achievement of the twentieth century (ahead of space exploration and computers), but older power plants are being maxed out, and the direction of future growth is uncertain. The U.S. nuclear program stalled in the 1970s due to unjustified public fears, but the time has come for a nuclear renaissance. The energy from wind and sun can provide only limited and low-intensity local power, and even the U.S. Department of Energy predicts that the contribution of these "green" renewables to the U.S. grid supply will be less than 1% by 2030 [29]. More coal-fired power plants with higher energy conversion efficiencies are needed, along with standardized designs of nuclear reacters to facilitate licensing and construction.

The third potential restraint is the introduction of cap-and-trade programs for CO_2 that are now under consideration in Congress. If implemented, companies that do not meet mandatory targets for CO_2 emissions per ton will be forced to pay a penalty. The problem is that, while the world has talked about reducing CO_2 emissions since Kyoto, the steel industry has actually done something about it. The use of fossil fuel is intrinsic to all steelmaking processes, and in the last 15 years, the energy per ton, which is basically a direct function of CO_2 emissions, in both the integrated and EAF sectors, has been dramatically reduced to asymptotic levels (Figure 1.9). Although the curve dipped sharply in the 1980s and 1990s due to the introduction of slab casting and the displacement of integrated plants by EAF-based mills, the drop even since 1990 has been 29%, far beyond the Kyoto target. There are no proven or even pilot scale processes on the horizon that will reduce current CO_2 emissions per ton significantly. EAF furnaces use electricity as their primary energy source, but over the last two decades, fossil fuels have been used in the process to supplement the electrical energy input, thus increasing

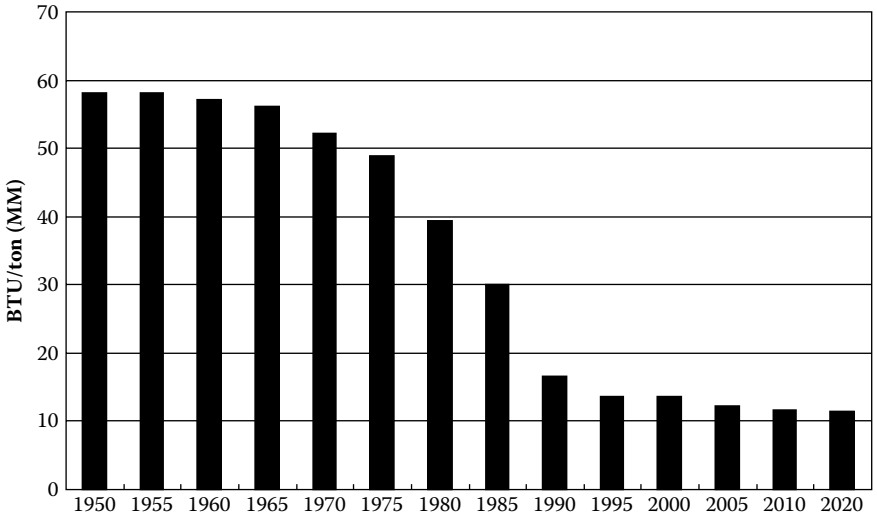


FIGURE 1.9 U.S. steel industry-million BTUs/ton.

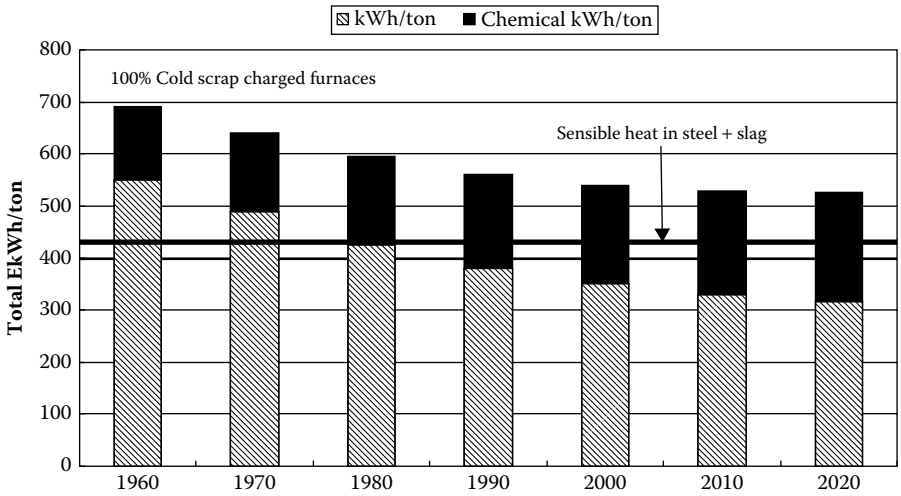


FIGURE 1.10 Reduction in chemical and electrical energy in EAFs.

productivity (Figure 1.10). Over 80% of the total energy consumed in a conventional cold-charged EAF operation can be assigned to the sensible heat in the molten steel and associated slag. The other 20% is used to either cover heat losses to the furnace enclosure, most of which is water cooled above the slag line, or is lost as sensible heat in the off-gases. To reduce these significantly is simply not possible. The one obvious solution, namely charging hot metallics as in Consteel, Shaft, or Hytemp installations, has resulted in less than anticipated net energy savings, and the cost of retrofitting shops for these processes could not be justified on energy cost savings alone, even if the shop design could accommodate such changes.

The financial health of both the U.S. steel industry and the overall economy is directly related to fossil fuel usage. The political posturing on climate change needs to be challenged to avoid catastrophic economic and social consequences for both rich and poor nations.

Technically, thanks to the minimill revolution, the U.S. steel industry has transformed itself since 1990. The U.S. EAF sector is now the largest consumer of recycled scrap in the world (45 million tons annually), the "greenest" steel industry in the world in terms of CO_2 emissions per ton (0.70 tons/ton), has the lowest man hours per ton in the world (about 1), and has an enviable safety record. However, both the EAF and integrated sectors have reached efficiency levels that preclude further significant reductions in energy and CO_2 emissions per ton. Unlike the "old days," process analysis and control through computers now provide the tools to maximize efficiency and minimize operational costs through the optimum selection of energy and raw material sources, whose costs and availability are constantly changing. Steelmaking is no longer an empirical process. Heffernan and Iverson could never in their wildest dreams have envisaged the revolution they initiated.

REFERENCES

1. Stubbles, J. 2002. History of minimills in steelmaking. *CIM Bulletin* 95(1057): 82–88.
2. Finkl, C. 1981. Degassing—Then and now. *Iron and Steel Maker*, December 1981, pp. 26–32.
3. Cramb, A.W. 1988. New steel casting processes for thin slabs and strip. A historical perspective. *Iron and Steel Maker*, July 1988, pp. 45–60.
4. Preston, R. 1991. *American Steel*. New York: Prentice Hall.
5. Pollock, B.A. 1995. Gallatin Steel—Learning to run. *Iron and Steel Maker*, October 1995, pp. 97–98.
6. Samways, N. 1997. Steel dynamics: High quality flat-rolled products at low cost. *Iron and Steel Engineer*, April 1997, p. 15.
7. Dunholter, D. 1997. Design and start-up of the North Star-BHP steel minimill. *Iron and Steel Engineer*, December 1997, p. 49.
8. Samways, N. 1998. Trico Steel: A 2.2 million ton/year joint venture flat rolled minimill. *Iron and Steel Engineer*, March 1998, p. 21.
9. Samways, N. 2004. Nucor Steel-Decatur: A potential 3 million tons/year strip steel facility. *Iron and Steel Engineer*, December 2004, p. 19.
10. Samways, N. 1997. Nucor-Berkeley: A high quality 1.8 million tons/year hot and cold rolled minimill. *Iron and Steel Engineer*, October 1997, p. 15.
11. Bagsarian, T. 1999. DiMicco and his 780 customers: The best in beams. *New Steel*, November 1999, p. 22.
12. Adjei-Sarpong, M., Fox, M., Trumble, B., and Powers, J. 2006. Optimization of Nucor steel-Hertford County's Consteel and DC EAF operations. *Iron and Steel Technology*, February 2006, p. 65.
13. AISI Annual Statistical Reports. Annual reports 2002–2007.
14. Samways, N. 2007. SeverCorr—A unique producer of automotive sheet steels, *AISTech*, October 2007, p. 41.
15. Blejde, W., Mahapatra, R., and Fukase, H. 2000. Development of low carbon thin strip production capability at project "M." *Iron and Steel Maker*, April 2000, p. 29.
16. Campbell, P., Bledje, W., Mahapatra, R., Wechsler, R., and Gillen, G. 2005. The Castrip process: Direct casting of steel sheet at Nucor Crawfordsville. *Iron and Steel Technology*, July 2005, p. 56.
17. SMA Archives (Steelnet.org). 2007. Presentation to SMA Board on 2/16 by K. Grass, David Joseph Co.
18. Pflaum, D. 2002. The end of "visual inspection" for monitoring scrap quality. In *ISS 60th Electric Furnace Conference*, San Antonio, Texas.
19. Scheel, J. and Anderson, K.M. 1997. The production of iron carbide. *Iron and Steel Maker*, July 1997, p. 25.
20. Lehtinen, L., Hansen, J., and Rokop, N. 1999. Iron dynamics process: A new way to make iron. *AISE Steel Technology*, December 1999, p. 97.
21. Hansen, J. 2005. Mesabi Nugget—The new age of iron. *Iron and Steel Technology*, March 2005, p. 149.
22. Aker Kvaerner. 2005. *HIsmelt Kwinana Direct Iron Smelting Project*. http:/www.Akerkvaerner.com, July 8 press release.
23. Schonbeck, J., Kruger, B., Hoppmann, H.D., and Maffini, C. 1997. Current status of the ISP technology and new developments. *MPT International* 1:38.
24. Quintero, R. 1999. The minimill of the new millenium: Streamlining for quality. Presented at the Gorham/Intertech Conference, Atlanta, Georgia.
25. Direct from Midrex. 2007. 4th quarter. In *The Shortest Route from Ore to Hot Strip*. Corporate publication, pp. 7–9.
26. Brimacombe, J. and Samarasekera, I. V. 1994. The challenge of thin slab casting. *Iron and Steel Maker*, November 1994, p. 29.
27. Flemming, G. and Hensger, K.E. 2000. Present and future CSP technology expands product range. *AISE Steel Technology*, January 2000, p. 53.
28. AIST. 2007. Industry statistics. *Iron and Steel Technology*, October 2007, p. 14.
29. Annual Energy Outlook. 2007. Department of Energy/EIA-0383. p. 14.

2 Review of Casting and Rolling Lines with Thin- and Medium-Slab Casters

Vladimir B. Ginzburg

CONTENTS

2.1 Introduction 15
2.2 Optimum Slab Thickness and the Number of Mill Stands 16
2.3 Main Components of the CR lines 17
2.4 The CR Lines of the First Group 20
2.5 The CR Lines of the Second Group 20
2.6 The CR Lines of the Third Group 26
2.7 The CR Lines of the Fourth Group 28
2.8 Supercompact CR Lines 30
2.9 Summary 31
References 32

2.1 INTRODUCTION

The casting and rolling (CR) line is defined in this chapter as a hot-strip production facility that comprises either a thin- or a medium-slab caster, slab-reheating furnace, and a hot rolling mill. The slab casters with the slab thickness range from 40 to 100 mm are defined as the thin-slab casters, while the slab casters with the slab thickness range from 100 to 150 mm are defined as the medium-slab casters. Liquid steel for the CR lines may come either from the electric arc furnaces (EAFs) or from the basic oxygen furnaces (BOFs). The CR lines are the main components of the minimill producing flat steel products that, in addition to the CR lines, also contain melt shops. The most common minimills for flat steel products became known as the compact strip production (CSP) plants [15,21,25,37,44,59,63,71,79,83,84]. The first CSP plant, Nucor Steel, was built in 1969 in Crawfordsville, Indiana [15,63,84]. The original plant installation included a melt shop with two EAF and two ladle metallurgy furnaces, one thin-slab caster, a slab-reheat tunnel furnace, a tandem-finishing mill with four stands, a strip-cooling system, and one downcoiler.

In a combination with a very effective can-do management style, the new technology helped increase significantly the efficiency of strip production. The success of Nucor Steel became even more impressive because it took place during the time when many integrated steel plants in the United States experienced severe problems of competing with foreign suppliers of steel products, and some experts predicted a gloomy future for the integrated steel plants. The future for these plants, however, turned out to be much brighter. Following Nucor Steel's lead, many integrated steel plants adopted production incentive programs along with a more effective management style. A recent consolidation of the steel industry had helped improve the competitive strength of these plants. It also created a much better opportunity for the exchange of technological know-how between the sister plants.

At the same time, the economic advantages of the CR lines were diminished due to an unprecedented increase in the scrap prices, forcing them to seek more expensive alternative sources of raw materials, such as cold and hot direct reduction iron and hot metal [88,92,96,99,102–109]. The other two original advantages of the first CSP plants, the absence of roughing mill stands and the use of tunnel reheat furnaces, had also become less evident. This was due to a noticeable improvement in both the strip quality and productivity made by using the slabs thicker than 50 mm. The increase of slab thickness required a use of roughing mills in addition to the finishing mills. Furthermore, in the CR lines with the medium-slab casters, it became more practical to use conventional walking beam furnaces rather than less sophisticated tunnel furnaces. Thus, from both economic and technological aspects, the minimills for the flat products were getting closer to the conventional integrated steel mills.

In this new environment, two principal capabilities will play a more significant role in the competition between the minimills and the integrated steel mills: (1) The capability to produce a variety of steel products demanded by the steel market and (2) the capability to achieve the required quality level and consistency of produced steel products. The experience gained since the start-up of the first CSP plant stimulated a search for a more efficient way of achieving these two

goals. This chapter reviews several novel configurations of the CR lines that were proposed and implemented to achieve the above two goals. The two most important parameters that affect the capabilities of the CR lines are the slab thickness and the number of mill stands.

2.2 OPTIMUM SLAB THICKNESS AND THE NUMBER OF MILL STANDS

The original CSP plants were designed to cast 50-mm-thin slabs versus 200- to 250-mm thick slabs produced by conventional hot strip mills of integrated steel mills. There are two principal reasons why it is easier to produce a better slab surface quality in a conventional hot strip mill than in the CR line [26]. The first reason is well known. It is a much slower casting speed. For instance, a 200-mm-thick slab can be cast by a conventional thick slab caster with a four times slower speed than a 50-mm-thin slab to achieve the same production rate.

The second reason is less known. It is a longer retention time of the slab in a reheat furnace. As shown in Figure 2.1, it takes as long as 70 minutes to reheat a hot, charged 200-mm thick slab to the desired temperature of 1235°C. At the same time, it usually takes about 30 minutes to reheat a 50-mm thin slab to the desired temperature of 1100°C. Incidentally, in spite of this difference in time and temperature, the scale losses per unit weight of steel for thin and thick slabs are approximately the same. This is because the slab-to-volume ratio decreases as the slab thickness increases. There is a useful side effect to this scaling process, which had probably been underestimated during the design of the original CSP plant. As shown in Figure 2.2, although the unit scale losses are the same, the thickness s of the scale layer is substantially greater in the thick slab (a) than in the thin slab (b). Consequently, as the slab thickness increases, a thicker surface layer with inevitable casting defects will be removed after descaling, improving the slab surface quality.

Another important factor affecting the strip quality is the number of mill stands, or the number of rolling passes used to reduce a slab to a desired strip thickness. In a conventional hot strip mill, a thick slab is first reduced by a roughing mill to a transfer bar, which thickness usually varies from 25 to 35 mm. Then, a tandem-finishing mill with either six or seven mill stands reduces the thickness of the transfer bar to a desired gauge. The first CSP plant, Nucor Steel, Crawfordsville, originally had only four mill stands capable of reducing a 50-mm thick slab to 2.5 mm. This required using excessive reductions at the last stands, consequently producing rough strip surface. Nucor Steel solved this problem by adding first the fifth mill stand and later the sixth mill

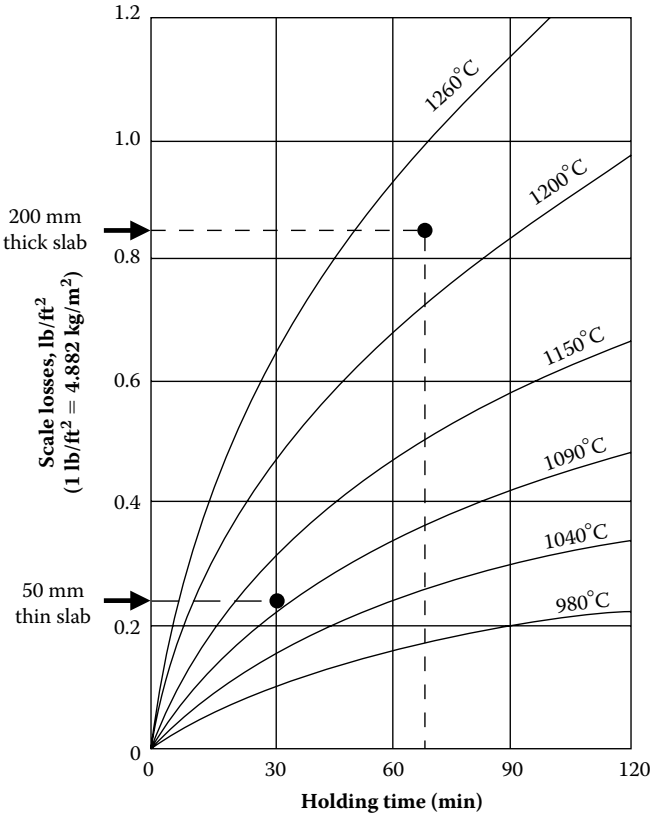


FIGURE 2.1 Scale losses during slab reheating [26].

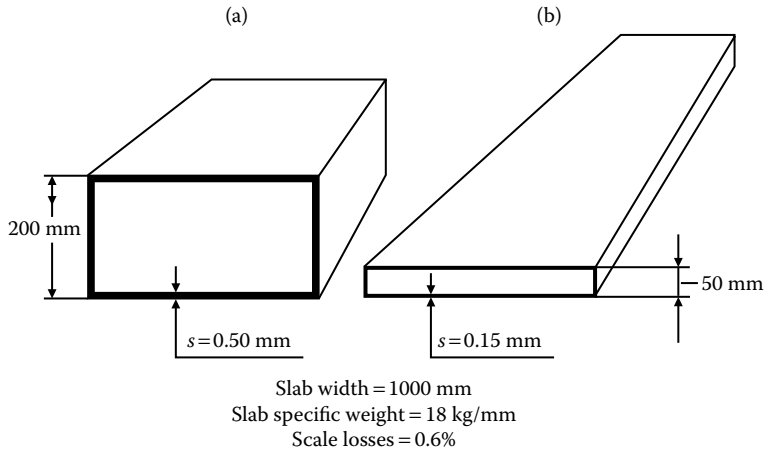


FIGURE 2.2 Slab surface scaling for (a) thick slab and (b) thin slab [26].

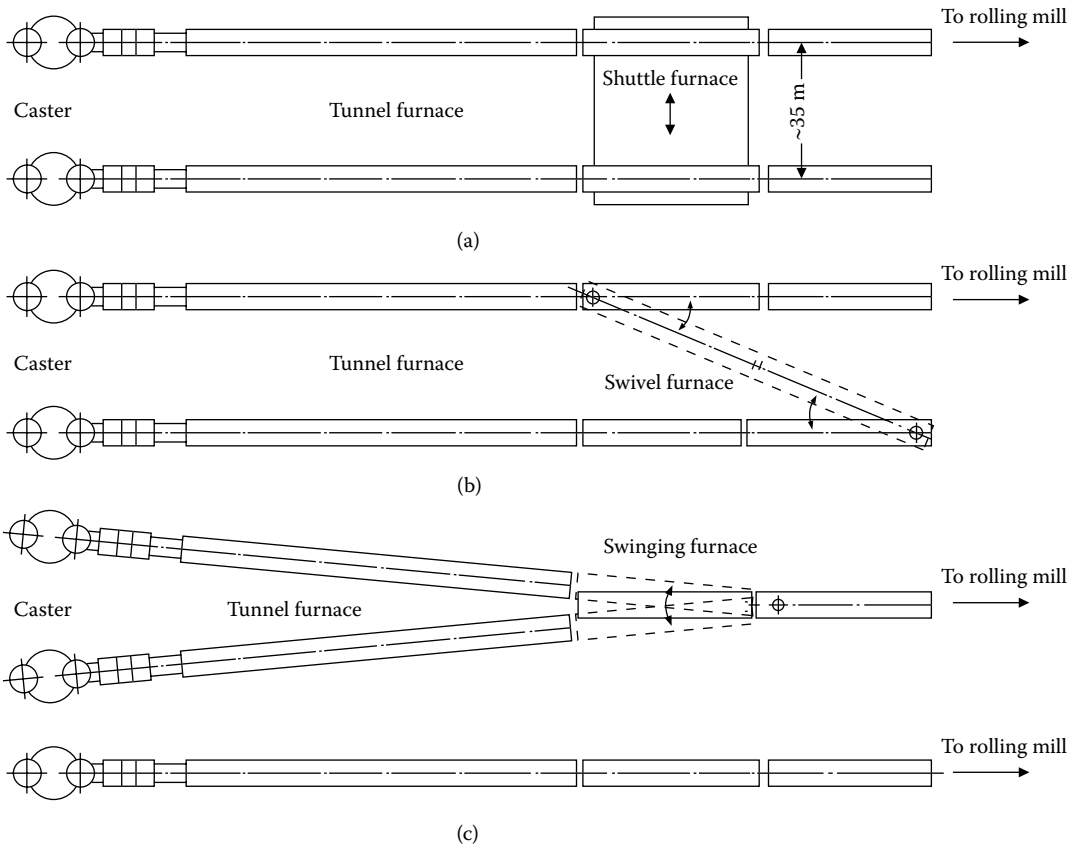


FIGURE 2.3 Three types of slab transfer furnaces: (a) shuttle [31], (b) swivel [44], and (c) swinging furnace [54].

stand. As we show in this chapter, nowadays some CR lines include as many as seven and even eight mill stands. In our review of these lines, we use the original names of the steel companies prior to any changes during a recent consolidation of steel industry.

2.3 MAIN COMPONENTS OF THE CR LINES

The CR lines may include the following main components:

- Continuous slab caster
- Reheat furnace
- Heat conservation devices
- Shears
- Descalers
- Vertical edger
- Roughing mill
- Finishing mill
- Cooling systems
- Coilers

Slab casters—The CR lines have either thin- or medium-slab casters. Some casters have liquid core (soft) reduction capability [16,35], reducing the slab thickness by as much as 20 mm. Both casters include a tundish, a submerged entry nozzle, a mold, a strand guide system, a secondary cooling system, and a dummy bar. The mold cross section of the thin slabs can have either a bomb shape [16] or a funnel shape [19,35], while in the medium-slab casters, the mold cross section is rectangular [52,53,60,62]. The casters are commonly equipped with the devices for the optimization of the casting process, such as the mold oscillators [16,19,53,60] and level control systems [35]. Some casters also have the electromagnetic break designed to reduce turbulence of cast steel [53,60,115].

Shears—The shears are usually installed at two locations of the CR lines, at the exit of the slab caster and at the entry of the finishing mill. The caster shear is usually a pendulum type upcut shear [16,19,60,78], while the mill shear is either a pendulum [19,60] or a rotary drum type [16,78,86]. In the CR lines with the capabilities for either endless or semiendless rolling, an additional high-speed rotary drum shear is installed in front of the downcoilers.

Reheat furnaces—The CR lines with the thin-slab casters use tunnel furnaces heated either by gas [32], oil or induction furnaces [16,34]. When a CR line has more than one thin-slab caster, at least one reheat furnace is located off the mill line. In this case, a reheated slab can be transferred to the mill line by using one of three types of furnaces shown in Figure 2.3. Another possibility is to transfer a bar in a coiled form [42]. The CR lines with the medium-slab casters use conventional walking beam furnaces [52,62,65,75,86,87].

Heat conservation devices—The main purpose of the medium heat conservation devices is to reduce heat losses

in a bar while it is transferred from a roughing mill to a finishing mill. Three types of these devices are used at the CR lines: Coilbox [41], Cremona furnace [49], and heated covers [50,53,56]. It is also possible to use the Steckel coiling furnaces, both singular (Figure 2.4a) and dual (Figure 2.4b) [1,4,38].

Descalers—The descalers use high-pressure water to clean the slab surface from scale. They are usually located at the entry sides of roughing and finishing mills. In some CR lines, the descalers are also installed at the entry side of a reheat tunnel furnace [50,56,57]. The range of the descaling water pressure is commonly from 200 to 280 bars. Another possible purpose of the high-pressure descalers is to remove the excessive layer of oxide scale from the work roll surfaces of the upstream finishing mill stands [39].

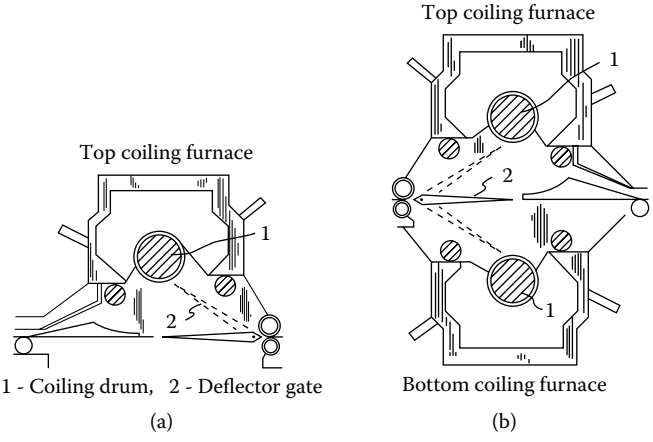


FIGURE 2.4 Two types of Steckel coiling furnace arrangements: (a) singular and (b) dual [1,4,38].

Vertical edgers—The vertical edgers of the CR lines are installed in front of the first roughing mill stand with a close-coupled connection between the mill stand and the edger. The edgers are usually designed to reduce the slab thickness as much as 25 mm [50,56,62,65,75,78].

Roughing mills—The existing roughing mills of the CR lines have one [29], two [51,53], or three stands [11] close-coupled to one another. They may have either two-high or four-high roll stack configuration. The former is used in some CR lines as the first roughing stand [51]. The roughing mill stands can be either nonreversing [49,53,55,56] or reversing [87]. Some of them have a close-coupled arrangement with either a caster [49], Coilbox [60,87], or finishing mill [2,3].

Finishing mills—There are three kinds of arrangements of finishing mills of the CR lines: tandem, reversing, and reversing-tandem. The number of stands of a tandem-finishing mill may vary from four to seven. Unlike conventional hot strip mills in which the diameters of work rolls are usually the same, in the CR lines, the work roll diameters of the finishing mill stands are usually smaller at the downstream stands. Also smaller in some mills are the distances between the downstream stands [7,31,48,60]. The reversing finishing mills, known as the Steckel mills [12,47], usually have either one or two reversing mill stands [62,65,75]. The multi-stand reversing finishing mills contain at least one reversing mill stand close-coupled with either one nonreversing mill stand or several tandem mill stands [4].

Water cooling systems—Three types of water cooling systems are used in the CR lines: a conventional type laminar flow cooling system (Figure 2.5a), an ultrafast cooling system (Figures 2.5b and 2.5c), and an intermediate cooling system [78]. The ultrafast cooling system is installed immediately after the exit of a finishing mill. It is used to enhance

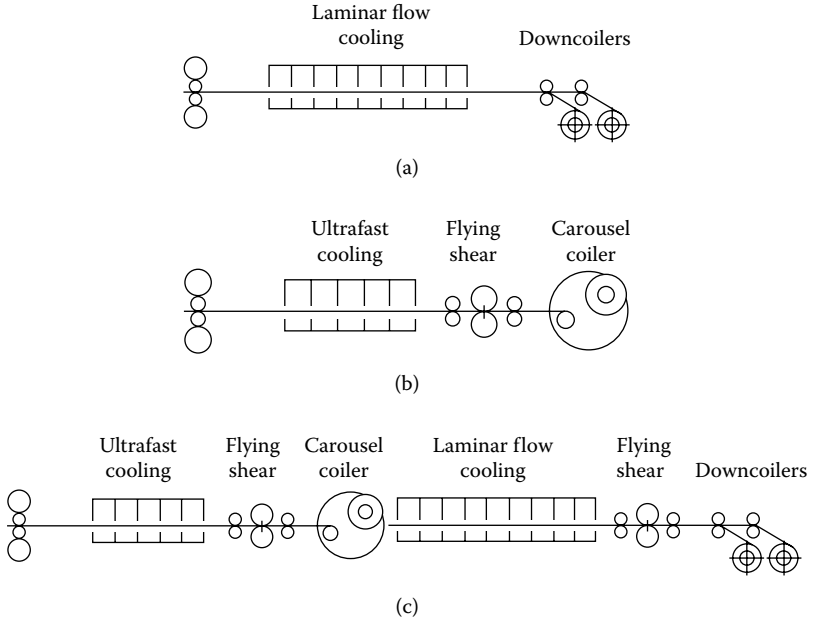


FIGURE 2.5 Three arrangements of the strip water cooling systems: (a) laminar flow, (b) ultra fast, and (c) combined ultra fast and laminar flow [59].

the semi-endless rolling [59]. The intermediate cooling system is located between the roughing and finishing mills. Its purpose is to provide a capability for ferritic rolling [78].

Coilers—Conventional downcoilers and upcoilers with hydraulically operated wrapper rolls are usually used in the CR lines. The carousel coilers are used in the CR lines designed for either endless or semi-endless rolling (Figures 2.5b and 2.5c) [59,74].

The rolling mills are typically equipped with several automatic control systems.

Automatic gauge control—This control includes three major subfunctions: the roll gap control, the mill stand speed control, and the interstand strip tension control [20,70]. The roll gap control commonly employs the long-stroke hydraulic cylinders in combination with the cylinder displacement sensors, cylinder pressure transducers, and load cells. Either hydraulic or electric loopers are used in the tandem-finishing mills to perform the interstand strip tension control, while a looperless tension control is used to control the bar tension between close-coupled roughing mill stands. A feedback signal is provided by the X-ray gauge installed at the exit of the finishing mill.

Strip profile and flatness control—Several devices are employed to perform this function:

- Continuous variable crown (CVC) and CVC Plus technology [10,100]
- Pair-Cross backup roll technology [6,76]
- Roll shifting system of symmetrically crown rolls [14]
- Work roll bending system, both positive and negative [20,70]
- Strip profile tension control [5]
- Roll thermal crown (RTC) control system [24]
- In-line roll grinding system [17,78]

The feedback signal is provided by the strip profile and flatness meters installed at the exit of the finishing mill.

Automatic width control—This control function is performed in the CR lines having vertical edgers that are usually equipped with the hydraulic roll gap position cylinders. In the finishing mills, it is possible to use the width control by modifying the interstand strip tension that was developed for the conventional hot strip mills [20].

Among the other emerging online control functions are the strip surface inspection control [73,81,90,97,98] and the control of mechanical properties [85,95].

The currently installed CR lines can be divided into four main groups, as shown in Table 2.1.

Group 1—This group includes the CR lines with the simplest mill configuration, having no roughing mill stands. The continuously cast thin slabs are reheated in the tunnel furnaces and rolled by tandem-finishing mill stands [70,82].

Group 2—In the CR lines of this group, in addition to a thin-slab caster, a tunnel furnace, and a tandem-finishing mill, there is a nonreversing roughing mill followed either by a heat conservation device, such as a heat cover [50,57] and Coilbox [51], or by an intermediate cooling system [78].

Group 3—The CR lines of this group also use a thin-slab caster and a tandem-finishing mill. Their main two features are a tandem nonreversing roughing mill close-coupled with a thin-slab caster and an induction furnace. These lines may also contain a heat conservation device, such as the Cremona furnace or Coilbox [42].

Group 4—The CR lines of this group use a medium-slab caster. The cast slabs are reheated in a walking beam furnace and then rolled by either a semicontinuous hot strip mill [86,87] or by a Steckel type mill [52,62,65].

TABLE 2.1
Groups of the CR Lines

Group	Typical Plant	Max. Slab Thickness (mm)	Mechanical Equipment Supplier	Main Variable Components
1	Nucor Steel-Hickman, Arkansas, USA	50 (future 65)	SMS	2TSC + 2TF + 6TFM
	Hylsa, Mexico	50	SMS	1TSC + 1TF + 6TFM
	SeverCorr, Mississippi, USA	65	SMS-Demag	2TSC + 2TF + 6TFM
2	Algoma Steel, Canada	90	Danieli	2TSC + 2TF + 1NR + 1HC + 6TFM
	BHP North Star, Ohio, USA	100	Sumitomo, Danieli	1TSC + 1TF + 2NR + 1HC + 6TFM
	Trico Steel, Alabama	90	Sumitomo, INNSE + MHI	2TSC + 2TF + 2NR + 1CB + 5TFM
	Tangshan I&S, China	85	Danieli, MHI Hitachi, IHI	1TSC + 1TF + 2NR + 1IC + 6TFM
3	Arvedi, Italy	55	MDI/Arvedi	2(TSC + 3NR) + 1IF + 1CF + 4TFM
	Posco, Republic of Korea	55	MDI	2(TSC + 2NR) + 2IF + 2CB + 5TFM
	Arvedi, Italy (future)	—	Arvedi, Siemens	1(TSC + 3NR) + 1IF + 5TFM
4	Tangshan, Guofeng, China	135	VAI, Danieli	1MSC + 1WF + 1RR + 1CB + 6TFM
	Tuscaloosa Steel, Alabama, USA	130	SMS Concast, Tippins	1MSC + 1WF + 1SM
	Nova Hut, Czech Republic	127	VAI, Tippins	1MSC + 1WF + 2SM

TSC = Thin-slab caster, MSC = Medium-slab caster, TF = Tunnel furnace, IF = Induction furnace, WF = Walking beam furnace, NR = Nonreversing rougher, RR = Reversing rougher, HC = Heat covers, CB = Coilbox, CF = Cremona furnace, IC = Intermediate cooling, TFM = Tandem-finishing mill, SM = Steckel mill.

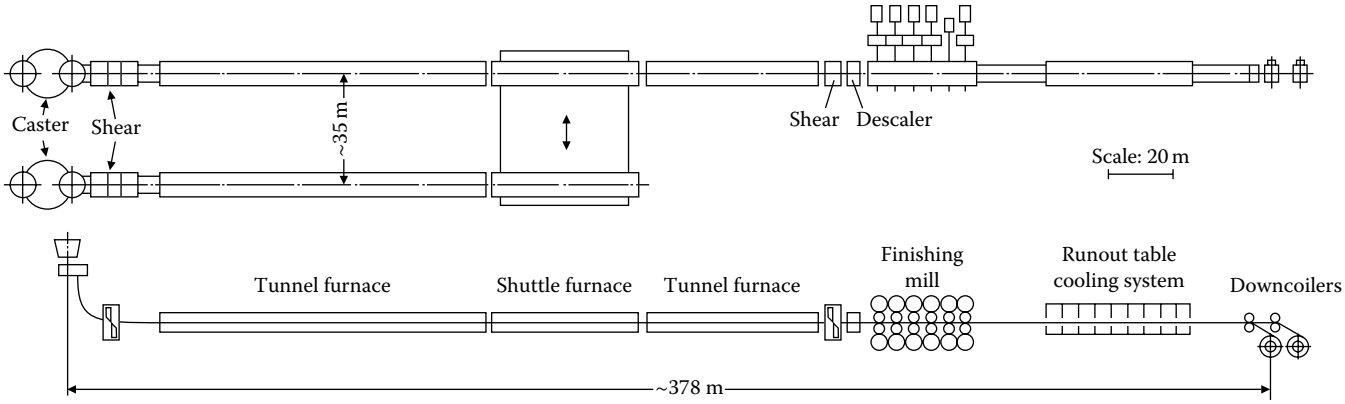


FIGURE 2.6 Schematic layout of the CR line at the Nucor Steel-Hickman, Arkansas CSP plant [31].

2.4 THE CR LINES OF THE FIRST GROUP

Figure 2.6 shows the layout of the CR line at Nucor Steel-Hickman, the Arkansas CSP plant built in 1991 [19,28,31–33,36]. This is a typical example of the CR line of the first group. The casters and rolling mill for this plant was supplied by SMS (Germany), while the reheat tunnel furnace was built by Bricmont (USA). It has two thin-slab casters originally designed to cast 50-mm thick slabs. The casters were recently upgraded to cast the slabs with a maximum thickness of 65 mm. A pendulum-type mechanical shear is installed at the exit of each caster and is followed by a reheat, gas-fired tunnel furnace. The shear cuts the cast steel into the slabs of a required length. One of the casters is installed in line with a finishing mill line. A shuttle furnace is used to transfer the slabs from the adjacent parallel caster line to the mill line. The second pendulum-type mechanical shear is used only for emergency purposes. A high-pressure descaling box is located at the entry of the six-stand tandem-finishing mill. The mill is followed by a laminar flow strip cooling system and two downcoilers. Tables 2.2 and 2.3 show the design parameters of the CR line of this plant.

Besides the CSP plants at Nucor Steel-Crawfordsville and Nucor Steel-Hickman, Arkansas, more than two dozen similar CSP plants have been built since 1989 around the world. Among them are the CSP plants in Hylsa, Mexico, built by SMS in 1995, and in SeverCorr, Mississipi, built by SMS-Demag in 2006. The thin-slab caster of the Hylsa CSP plant [40,45,48,72,80] produces 50-mm thick slabs. The CR line of this plant was designed to produce the strip within a range of widths (790–1350 mm) and thicknesses (1.0–12.7 mm). Table 2.4 shows the design parameters of finishing mill of this plant.

The CR line of Hylsa CSP plant has the following design features that help roll the strip down to 1.0 mm in thickness:

- Stands F4 through F6 have smaller work roll and backup roll diameters to decrease roll, separating forces and heat losses to the rolls.
- The distances between stands F4 through F6 are smaller to facilitate threading.
- Loopers located between stands F4 and F5, and also between stands F5 and F6, have motorized rolls to enhance threading.
- A high-speed blower is installed at the exit of stand F6 to prevent the strip head end from rising and losing contact with roller table.
- Immediately after exiting the last stand, the strip is cooled by the water sprays to stiffen the strip before it is impacted by laminar cooling water.
- Short pitch is used for runout table rolls to create better conditions for transporting the strip between the mill and downcoiler.
- Top laminar cooling water jets are aligned with the runout table rolls to prevent bending of the strip.

By 1998, the strip with the gauge range of 1.0 to 1.3 mm had accounted for almost 30% of Hylsa's output, corresponding to around 20,000 tons per month [55]. Further improvements in the consistency of rolling of thin gauges can be achieved by implementation of the tail-end crashing reduction technique [89] and strip steering control [69,101] developed for conventional hot strip mills. Degner et al. [74] reviewed several alternative techniques for production of ultrathin strips.

At the SeverCorr, Mississippi, CSP plant, the CR line is designed to produce a hot band for high-quality steel grades, including the ultra-low-carbon interstitial-free steel grades for automotive exposed applications [110,116]. This is the first CSP plant designed to produce 1880-mm-wide hot coils. Tables 2.5 and 2.6 show the design parameters of the CR line of this plant.

2.5 THE CR LINES OF THE SECOND GROUP

Figure 2.7 shows the layout of the Direct Strip Production Complex (DSPC) at Algoma Steel, Canada, built by Danieli United (Italy) in 1997. This is a typical example of the CR line of the second group [29,35,50,56,57]. This plant produces liquid steel by BOF [58]. The two-strand caster is fed by 230-ton ladles through a large-capacity tundish. The thickness of the cast slabs is 90 mm. That can further be reduced

TABLE 2.2
Original Design Parameters of the Melt Shop, Caster, and Reheat Tunnel Furnace at Nucor Steel-Hickman, Arkansas CSP Plant

	Parameter	Units	Value/Definition
Slab Dimensions	Slab thickness	mm	50
	Slab width	mm	1250–1560
	Slab length	m	47
Slab Caster	Tundish capacity	t	28
	Tundish metal depth	mm	812
	Maximum production rate per caster	tons/hr	196
	Mold cross-sectional shape	—	Funnel
	Mold length	mm	1100
	Mold oscillator type	—	4-eccentric
	Number of strands	—	1
	Number of roll support segments	—	2
	Number of secondary cooling zones	—	6
	Metallurgical length	m	6.02
	Bending radius	m	3.0
	Casting speed	mpm	2.5–6.0
Shears	Caster shear type	—	Pendulum, upcut
	Mill (emergency) shear type	—	Pendulum, upcut
Reheat Furnace	Furnace type	—	Tunnel, gas-fired
	Typical slab temperature at the mill	°C	1135
Descaling Box	Water flow rate	m^3/hr	220
	Descaling pressure	bar	280
Finishing Mill	Number of mill stands	—	6
	Work roll shifting system type	—	CVC
Runout Table Cooling System	Strip cooling method	—	Laminar flow
	Number of cooling zones	—	20
	Maximum top headers flow rate	L/min	37,850
	Maximum bottom headers flow rate	L/min	43,528
Finish Coil Size	Strip thickness range	mm	1.5–12.7
	Strip width range	mm	1220–1625
	Maximum specific coil weight	kg/mm	18.0

TABLE 2.3
Original Design Parameters of the Finishing Mill at Nucor Steel-Hickman, Arkansas CSP Plant

	Finishing Mill Stands					
Parameter	**F1[a]**	**F2[a]**	**F3**	**F4**	**F5**	**F6**
Maximum work roll diameter (mm)	800	800	800	735	735	735
Work roll body length (mm)	1900	1900	1900	1900	1900	1900
Maximum backup roll diameter	1350	1350	1350	1350	1350	1350
Backup roll body length (mm)	1700	1700	1700	1700	1700	1700
Distance to next stand (m)	5.588	5.588	5.588	5.588	5.588	—
Main drive motor power (kW)	7000	7000	7000	7000	7000	7000
Main drive motor speed (rpm)	0–108	0–108	0–108	0–108	0–108	0–108
Gear ratio	1:4.555	1:4.555	1:2.345	1:1.6	Direct	1:0.8
Maximum roll face speed (m/s)	1.016	2.59	4.91	7.65	10.58	13.23
Maximum rolling force (MN)	35.0	35.0	35.0	35.0	35.0	35.0

[a] Roll diameters and main drives of stands F1 and F2 were modified in 2008 to roll slabs with thickness of up to 65 mm.

TABLE 2.4
Design Parameters of the Finishing Mill of the Hylsa CSP Plant

	Finishing Mill Stands					
Parameter	**F1**	**F2**	**F3**	**F4**	**F5**	**F6**
Maximum work roll diameter (mm)	790	790	790	500	500	500
Maximum backup roll diameter (mm)	1350	1350	1350	1350	1350	1350
Main drive motor power (kW)	6400	6400	6400	6400	6000	6000
Maximum roll face speed (m/s)	—	—	—	—	—	13.61
Maximum roll force (MN)	30.0	30.0	30.0	25.0	25.0	25.0

TABLE 2.5
Design Parameters of the CR Line at the SeverCorr, Mississippi CSP Plant

	Parameter	**Units**	**Value/Definition**
Slab Dimensions	Slab thickness before soft reduction	mm	60, 65
	Slab width	mm	912–1880
Slab Caster	Tundish capacity	t	36.0
	Mold cross-sectional shape	—	Funnel
	Mold oscillator type	—	Hydraulic
	Mold electromagnetic break (EMBR)	—	Installed
	Number of strands	—	1
	Metallurgical length	mm	8065
	Bending radius	mm	3250
	Maximum casting speed	m/min	6.0
	Pendulum shear maximum force	MN	8.5
Reheat Furnace	Furnace type	—	Tunnel, gas-fired
	Furnace length	m	269
Descaler	Mill entry descaler pressure	bar	380
CSP Mill	Number of mill stands	—	6
	Work roll shifting system type	—	CVC Plus
Finish Coil Size	Thickness range	mm	1.4–12.7 mm
	Width range	mm	900–1880
	Maximum specific coil weight	kg/mm	21.4

TABLE 2.6
Design Parameters of the Finishing Mill of the CR Line at the SeverCorr, Mississippi CSP Plant

	Finishing Mill Stands					
Parameter	**F1**	**F2**	**F3**	**F4**	**F5**	**F6**
Maximum work roll diameter (mm)	950	950	750	750	620	620
Maximum backup roll diameter (mm)	1500	1500	1500	1500	1500	1500
Work roll width (mm)	2300	2300	2300	2300	2300	2300
Backup roll width (mm)	2100	2100	2100	2100	2100	2100
Main drive motor power (kW)	8700	8700	10,000	10,000	10,000	8700
Maximum roll force (MN)	46.0	46.0	46.0	46.0	32.0	32.0

down to 70 mm by utilizing the slab dynamic soft reduction. Table 2.7 shows the design parameters of the CR line of this plant.

A pendulum-type mechanical shear is installed at the exit of each caster strand. After shearing, a cut slab is then descaled by a rotary descaler prior to its entry into a reheat gas-fired tunnel furnace. One of the tunnel furnaces is in line with a finishing mill line. A shuttle furnace is used to transfer the slabs from the adjacent parallel tunnel furnace to the mill line. The reheated slab is then descaled by the second descaler installed in front of an edger close-coupled with a single-stand roughing mill. The edger is capable of the recovery of

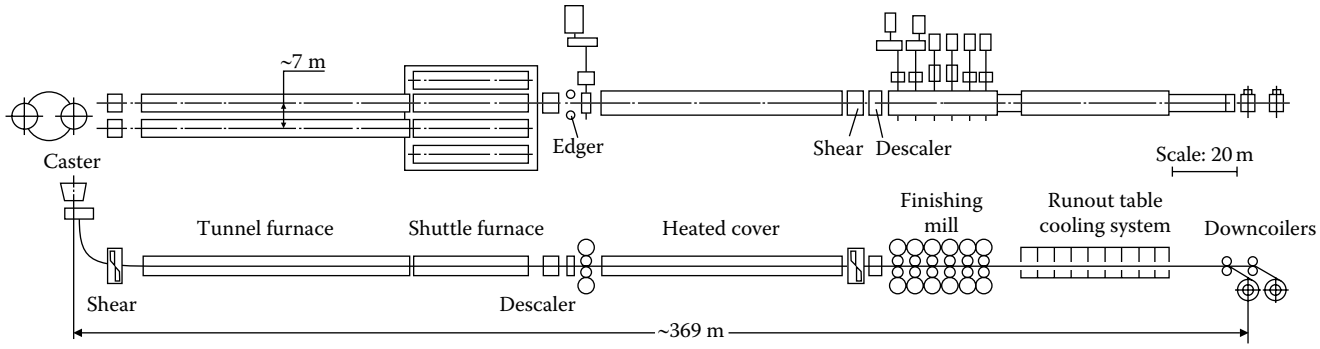


FIGURE 2.7 Schematic layout of the CR line at Algoma Steel Canada Direct Strip Production Complex [56].

TABLE 2.7
Design Parameters of the CR Line at Algoma Steel Direct Strip Production Complex

	Parameter	Units	Value/Definition
Slab Dimensions	Slab thickness before soft reduction	mm	90
	Slab thickness after soft reduction	mm	70
	Slab width	mm	800–1600
Slab Caster	Number of strands	—	2
	Dynamic soft reduction	—	Installed
	Heat size	t	230
	Mold cross-sectional shape	—	Funnel
	Mold length	mm	2200
	Mold level control	—	Hydraulic
	Mold oscillator type	—	Hydraulic
	Breakdown prevention system	—	Installed
	Secondary cooling type	—	Air mist
	Casting speed	mpm	2.8–6.5
Shears	Caster shear type	—	Pendulum upcut
	Mill shear type	—	Rotary drum
Reheat Furnace	Furnace type	—	Tunnel, gas-fired
Heat Cover	Heat cover type	—	Gas-fired
Roughing Mill Area	Vertical edger location	—	In front of R1
	Roughing mill type	—	Nonreversing
	Number of roughing mill stands	—	1
	Mill stand roll stack type	—	Four-high
Descalers	Furnace descaler pressure	bar	240
	Mill descaler pressure	bar	200
Finishing Mill	Number of mill stands	—	6
	Work roll shifting system type	—	Schedule-free rolling
Finish Coil Size	Width range	mm	800–1600
	Maximum specific coil weight	kg/mm	17.86

tapered slabs—up to 25 mm, while the roughing mill reduces the slab to the thickness within the range of 30 to 45 mm. The transfer bar then enters a heated cover. A flying shear located at the exit of the heated cover is designed to cut both the head and tail ends of the transfer bar prior its entry to the third descaler. The six-stand tandem-finishing mill then rolls the transfer bar to a desired strip thickness. Subsequently, the strip is cooled by a laminar flow cooling system and coiled by one of two downcoilers.

The BHP North Star Steel minimill [53] also incorporates the CR line of the second group. It began operation in 1997. Sumitomo Metals Industries (Japan) supplied a single-strand caster. Danieli (Italy) supplied the remaining mechanical equipment. The slab caster was originally designed to cast 90-mm thick slabs. After a recent addition of one segment, the slab thickness was increased to 100 mm. The CR line of BHP North Star Steel is similar to the CR line of Algoma Steel, except for two features: the BHP plant has only one caster, but

TABLE 2.8
Design Parameters of the CR Line at BHP North Star Steel (Delta, Ohio) Minimill

	Parameter	Units	Value/Definition
Slab Dimensions	Slab thickness	mm	90 (currently 100)
	Slab width	mm	900–1565
Slab Caster	Number of strands	—	1
	Bend radius	m	3.5
	Mold cross-sectional shape	—	Rectangular
	Mold length	mm	950
	Mold oscillator type	—	Hydraulic
	Mold EMBR	—	Installed
	Breakout prediction system	—	Installed
	Secondary cooling type	—	Air mist
	Maximum casting speed	mpm	5.0
Shears	Caster shear type	—	Pendulum upcut
	Mill shear type	—	Rotary drum
Reheat Furnace	Furnace type	—	Tunnel, gas-fired
Heat Cover	Heat cover type	—	Gas-fired
Roughing Mill Area	Vertical edger location	—	In front of R1
	Roughing mill type	—	Tandem
	Number of roughing mill stands	—	2
	Mill stand roll stack type	—	Four-high
	Vertical edger	—	Installed
Descalers	Furnace descaler pressure	bar	240
	Mill descaler pressure	bar	200
Finishing Mill	Number of mill stands	—	6
	Work roll shifting system type	—	Schedule-free rolling
Finish Coil Size	Width range	mm	900–1565
	Maximum specific coil weight	kg/mm	17.86

two roughing mill stands. Table 2.8 shows the design parameters of the CR line of this plant.

A different configuration of the CR line of this group is implemented at TRICO Steel-Decatur, Alabama, built in 1997 [51,60,61]. Sumitomo Metals Industries (Japan) supplied two thin-slab casters. Chugai Ro (Japan) built a reheat tunnel furnace. INNSE (Italy) supplied a two-stand roughing mill with a vertical edger, a Coilbox, and two downcoilers, while Mitsubishi Heavy Industries (Japan) supplied a five-stand tandem-finishing mill. As shown in Figure 2.8, the line comprises two slab casters each followed by a pendulum shear and a gas-fired tunnel furnace located parallel but off-center from the mill line. A shuttle furnace transfers the slabs from the tunnel furnaces to the mill line. The hot rolling mill consists of two sections, roughing and finishing. The roughing area includes a vertical edger attached to the first two-high roughing mill. The second four-high roughing mill is located 3 m downstream from the first one. It is followed by the Coilbox. The finishing mill area includes a rotary drum shear, a descaling box, a five-stand finishing mill, a runout

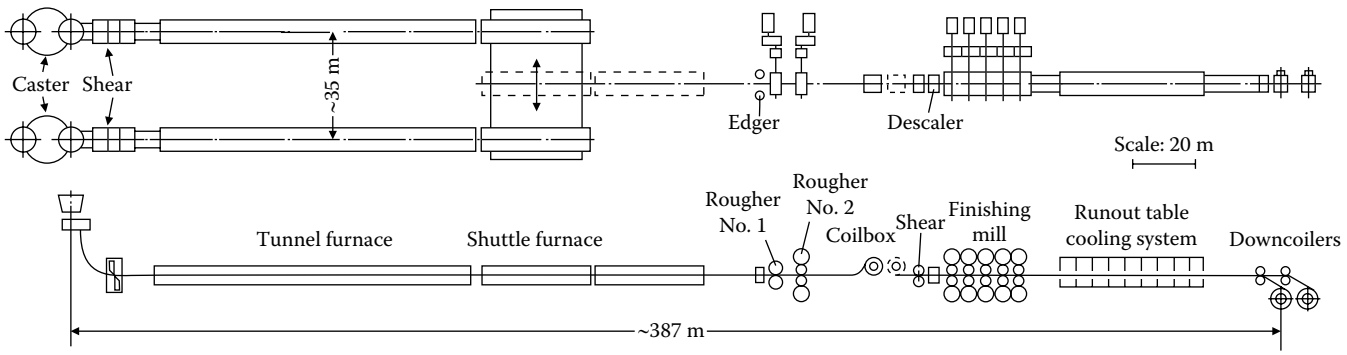


FIGURE 2.8 Schematic layout of the CR line at TRICO Steel-Decatur, Alabama [60].

TABLE 2.9
Design Parameters of the CR Line at Trico Steel Minimill

	Parameter	Units	Value/Definition
Slab Dimensions	Slab thickness	mm	70, 90
	Slab width	mm	940–1650
Slab Caster	Number of strands	—	1
	Caster height	m	5.7
	Bend radius	m	3.5
	Mold cross-sectional shape	—	Rectangular
	Mold length	mm	940
	Mold oscillator type	—	Hydraulic
	Mold EMBR	—	Installed
	Liquid core reduction	—	Installed
	Breakout prediction system	—	Installed
	Secondary cooling type	—	Air mist
	Maximum casting speed	mpm	5.0
Shears	Caster shear type	—	Pendulum upcut
	Mill shear type	—	Rotary drum
Reheat Furnace	Furnace type	—	Tunnel, gas-fired
Descalers	Rougher descaler pressure	bar	240
	Finishing mill descaler pressure	bar	240
Roughing Mill Area	Vertical edger location	—	In front of R1
	Roughing mill type	—	Tandem
	Number of roughing stands	—	2
	R1 roll stack type	—	Two-high
	R2 roll stack type	—	Four-high
Coilbox	Coilbox location	—	After R2
	Coilbox coiled thickness range	mm	17–30
Finishing Mill	Number of mill stands	—	5
	Backup roll control system type	—	Pair-cross
Finish Coil Size	Thickness range	mm	1.0–15.875
	Width range	mm	914–1650
	Maximum specific coil weight	kg/mm	17.86

TABLE 2.10
Design Parameters of Finishing Mill at Trico Steel Minimill

Parameters	R1	R2	F1	F2	F3	F4	F5
Maximum work roll diameter (mm)	1350	1150	825	680	680	680	680
Work roll body length (mm)	1770	1770	1770	1770	1770	1770	1770
Maximum backup roll diameter (mm)	—	1450	1450	1450	1450	1450	1450
Backup roll body length (mm)	—	1770	1770	1770	1770	1770	1770
Distance to next stand (m)	3.0	8.9	45.9	5.8	5.8	5.8	5.8
Main drive motor power (kW)	6800	8000	6000	7500	7500	7500	6000
Main drive motor speed (rpm)	180/300	180/300	200/400	360/720	360/720	360/720	200/400
Gear ratio	1:8.436	1:4.703	1:5.47	1:5.47	1:2.86	1:2.22	Direct
Maximum roll face speed (m/s)	2.5	3.84	3.15	5.69	8.97	11.57	14.25

table laminar flow cooling system, and two downcoilers. Tables 2.9 and 2.10 show the design parameters of the CR line of this plant.

Figure 2.9 shows the layout of the ultrathin strip production (UTSP) line at Tangshan I&S, China [78], built in 2003. This is another example of the CR line of the second group. The mechanical equipment for this line was supplied by Danieli (Italy), Bricmont (USA), Mitsubishi-Hitachi Metals Machinery, and IHHI (Japan). Thin-slab caster produces either 85- or 70-mm thick slabs. The slab thickness of 70 mm is usually used

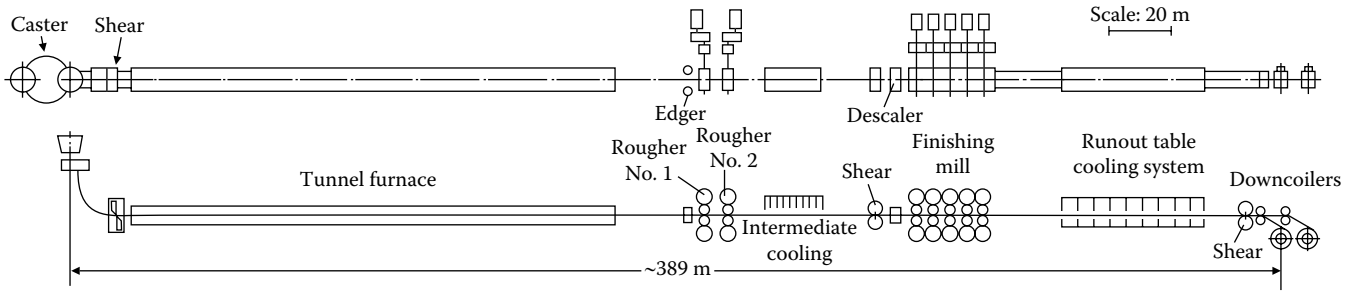


FIGURE 2.9 Schematic layout of the CR line at Tangshan I&S, China [78].

for rolling thinner strip of less than 1.2 mm. After cutting by an upcut pendulum shear, a slab is reheated to a rolling temperature of about 1150°C in the tunnel furnace. The discharged slab is then rolled by a vertical edger and a two-stand tandem-roughing mill. After exiting the roughing mill, the transfer bar thickness is usually between 10 and 30 mm. A finishing mill rolls the transfer bar to a required strip thickness within the range of 0.8 to 12.7 mm. Table 2.11 shows the design parameters of the CR line of this plant.

The CR line provides two special rolling capabilities, ferritic rolling and semi-endless rolling.

Ferritic rolling—To provide this capability, an intermediate cooling system is installed between the roughing and finishing mills. After exiting the roughing mill, the strip is cooled, so it enters the finishing mill below the transformation temperature Ar3. Consequently, the strip is rolled by the finishing mill in the ferritic structure region.

Semi-endless rolling—To provide this capability, a high-speed rotary drum shear is installed at the end of the runout table cooling system in front of two downcoilers. In semi-endless rolling, a thin cast slab is cut into long slabs up to 220 m long. After reheating in the tunnel furnace, the long slabs are rolled in tandem by both the roughing and the finishing mills. To avoid the difficulty of threading and tailing out of the thin strip, both the head end and the tail end of the long transfer bar are rolled by the finishing mill with a greater thickness than the thickness of the middle of the strip. After water cooling, the strip is cut into the required coil lengths by a high-speed strip shear and then coiled alternatively at one of the two downcoilers.

2.6 THE CR LINES OF THE THIRD GROUP

The plants of the fourth group utilize the inline strip production (ISP) technology developed by Mannesmann Demag jointly with Arvedi, Italy [11,16,18,23,27,34,42,45,49,66,68, 114]. This is the shortest CR line built to date of publication of this book. Figure 2.10a shows the layout of the ISP plant

TABLE 2.11
Design Parameters of the Ultrathin Strip Production Line at Tangshan I&S, China

	Parameter	Units	Value/Definition
Slab Dimensions	Slab thickness	mm	70, 85
	Slab width	mm	850–1680
Slab Caster	Number of strands	—	1
	Dynamic soft reduction	—	Installed
Shears	Caster shear type	—	Pendulum upcut
	Finishing mill shear type	—	Rotary drum
	Downcoiler high-speed shear type	—	Rotary drum
Reheat Furnace	Furnace type	—	Tunnel, gas-fired
	Shifting zone	—	Installed
Roughing Mill Area	Vertical edger location	—	In front of R1
	Roughing mill type		Tandem
	Number of roughing stands	—	2
	Mill roll stack type	—	Four-high
	Each mill stand main drive power	kW	6600
Finishing Mill	Number of stands	—	5
	Work roll shifting system type	—	Schedule-free rolling
	Stands F1–F4 main drive power	kW	10,000
	Stand F5 main drive power	kW	7500
Cooling Systems	Intermediate cooling system	—	Two banks
	Runout table cooling system	—	Six banks

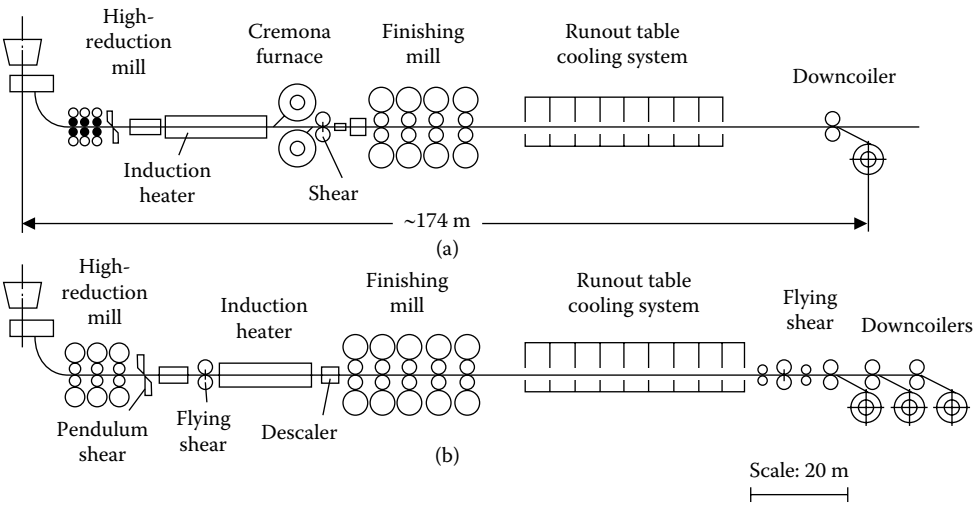


FIGURE 2.10 Two schematic layouts of the CR lines: (a) Arvedi, Italy Inline Strip Production plant [114] and (b) proposed Arvedi Endless Strip Production plant [113].

built in Arvedi, Italy, in 1992. The liquid steel produced by EAF is cast by a thin slab caster. The slab thickness exiting the caster mold is 60 mm. After soft reduction and cooling, the slab thickness is further reduced down to 43 mm. Then a fully solidified slab is strengthened and descaled prior to entering a roughing (high-reduction) three-stand tandem mill that is close-coupled with the caster. The range of the transfer thickness after the roughing mill is from 15 to 25 mm. After reheating by an induction heater, the transfer bar is coiled in the Cremona furnace. The uncoiled bar first passes through a descaling box and then enters a four-stand tandem-finishing mill. Subsequently, the rolled strip is cooled by the runout

TABLE 2.12
Design Parameters of the CR Line at Arvedi Inline Strip Production Minimill

	Parameter	Units	Value/Definition
Slab Dimensions	Slab thickness before soft reduction	mm	60
	Slab thickness after soft reduction	mm	43
	Slab width	mm	650–1330
Slab Caster	Number of strands	—	1
	Bend radius	m	5.2
	Mold type	—	Bow
	Mold cross-sectional shape	—	Bomb-shaped
	Mold oscillator type	—	Hydraulic
	Dynamic soft reduction	—	Installed
	Secondary cooling type	—	Air mist
	Maximum casting speed	mpm	5.0
Descalers	Descaler pressure	bar	220
Roughing Mill	Roughing mill type	—	Tandem
	Number of stands	—	3
	Mill roll stack type	—	Four-high
Shears	Caster shear type	—	Pendulum upcut
	Finishing mill shear type	—	Rotary drum
Reheat Furnace	Furnace type	—	Induction heater
	Furnace length	m	18.0
	Connected load	MVA	20.0
	Furnace temperature	°C	1200
	Maximum bar exit temperature	°C	1150
	Heat conservation device type	—	Cremona furnace
Finishing Mill	Number of mill stands	—	4
	Strip thickness range	mm	1.2–12.0
	Maximum coil specific weight	kg/mm	20.0

TABLE 2.13
Design Parameters of Finishing Mill at Arvedi Inline Strip Production Minimill

Parameters	R1	R2	R3	F1	F2	F3	F4
Maximum work roll diameter (mm)	410	410	410	700	700	600	600
Work roll body length (mm)	1500	1500	1500	1900	1900	1900	1900
Maximum backup roll diameter (mm)	800	800	800	1400	1400	1400	1400
Backup roll body length (mm)	1400	1400	1400	1770	1770	1770	1770
Main drive motor power (kW)	500	500	500	6000	6000	4000	4000
Maximum rolling force (MN)	13.0	13.0	13.0	40.0	40.0	25.0	25.0
Maximum roll face speed (m/s)	—	—	0.23	—	—	—	12.5

table cooling system and coiled. Tables 2.12 and 2.13 show the design parameters of the CR line of the Arvedi plant.

Figure 2.10b shows the proposed layout of the CR line of the future Arvedi endless strip production (ESP) plant [93,113]. Proposed by Siemens and Arvedi, the plant will contain three main sections. The first section includes a thin slab caster followed by a close-coupled three-stand tandem-roughing mill. The second section includes an induction heater. A five-stand tandem-finishing mill and a strip cooling system are the main parts of the third section. The fourth section includes a high-speed rotary drum shear and two downcoilers. The plant will be designed to produce strips with a thickness range of 0.6 to 12 mm, a maximum width of 1570 mm, and a maximum coil weight of 32 tons.

2.7 THE CR LINES OF THE FOURTH GROUP

The CR lines of this group utilize the medium-slab casters with the walking beam furnaces. The strip production plant at Tangshan Guofeng, China [86,87], utilizes the CR line of this group (Table 2.14). It was built in 2005. Two medium-slab casters were supplied by Siemens VAI Technologies (Germany/Austria), while the mechanical equipment was supplied by Danieli (Italy). The line comprises a medium-slab caster with the exit slab thickness of 135 mm, a conventional walking beam reheat furnace, a reversing rougher with an attached vertical edger, a Coilbox, a six-stand tandem-finishing mill, a laminar flow cooling system, and two downcoilers. Table 2.14 shows the design parameters of the CR line of this plant.

Figure 2.11 shows several configurations of Steckel mills that can be used in the CR lines with medium-slab casters [9,11–13,22,30,46,47,67,68]. The mill configuration shown in Figure 2.11a includes a stand-alone reversing roughing mill and a single-stand Steckel finishing mill. The Steckel mill shown in Figure 2.11b provides both roughing and finishing rolling operations. A typical example of a CR line with this type of mill is the Tuscaloosa Steel, Alabama minimill [52].

TABLE 2.14
Design Parameters of the CR Line at Tangshan Guofeng, China Minimill

	Parameter	Units	Value/Definition
Slab Dimensions	Slab thickness	mm	135
	Slab width	mm	600–1300
	Slab length	mm	8000–15,600
Roughing Mill Area	Vertical edger location	—	In front of R1
	Number of roughing mill stands	—	1
	Roughing mill stand type	—	Reversing, four-high
	Main drive mill power	kW	12,000
	Maximum roll separating force	kN	40,000
Finishing Mill	Finishing mill shear type	—	Rotary drum
	Number of mill stands	—	6
	Work roll shifting system type	—	Schedule-free rolling
	Main drive F1–F4 power	kW	6000
	Main drive F5–F6 power	kW	5000
	Maximum roll separating force F1–F4	kN	35,000
	Maximum roll separating force F1–F4	kN	30,000
Finish Coil Size	Strip thickness range	mm	1.2–12.7
	Strip width	mm	600–1300
	Maximum coil specific weight	kg/mm	16.0

Built by Tippins Industries (USA) in the mid-1980s, the mill started operation by using purchased slabs. In 1996, after the installation of a medium-slab caster by SMS Concast (Germany), the plant was converted into a minimill. The CR line of the minimill comprises a medium-slab caster, a walking beam reheat furnace, and a Steckel mill followed by a runout table cooling system and an upcoiler. The design parameters of this line are shown in Table 2.15.

Figure 2.11c shows a double-stand Steckel mill that provides both roughing and finishing rolling operations [9]. A typical example of this type of mill is the Tippins Strip Process (TSP®) mill installed at Nova Hut Steel, Czech Republic [62,65,75]. The mill comprises a medium-slab caster, a walking beam reheat furnace, and a two-stand Steckel mill with a vertical edger installed between the stands. The Steckel mill is followed by a laminar flow cooling system and an upcoiler. The design parameters of this line are shown in Table 2.16.

Figures 2.11d and 2.11e show three close-coupled arrangements of a Steckel mill with a tandem-finishing mill [70]. In the first arrangement (Figure 2.11d), a reversing Steckel mill having singular entry and exit coiling furnaces is close-coupled with a tandem-finishing mill [4]. In the second arrangement (Figure 2.11e), a Steckel mill with a singular entry coiling furnace and a dual exit coiling furnace is close-coupled with a tandem-finishing mill [1,8]. In that case, a strip can be uncoiled from one of the exit coiling furnaces and rolled by the tandem-finishing mill simultaneously with rolling of the next coil at the Steckel mill. In the third arrangement (Figure 2.11f), the first stand of the tandem-finishing mill works as a reversing mill having a Steckel-type coiling furnace only at its entry side. After the first reversing pass at the first stand, the strip is coiled inside the entry coiling furnace. During the next reversing pass, it is uncoiled and rolled by the tandem mill [26,38].

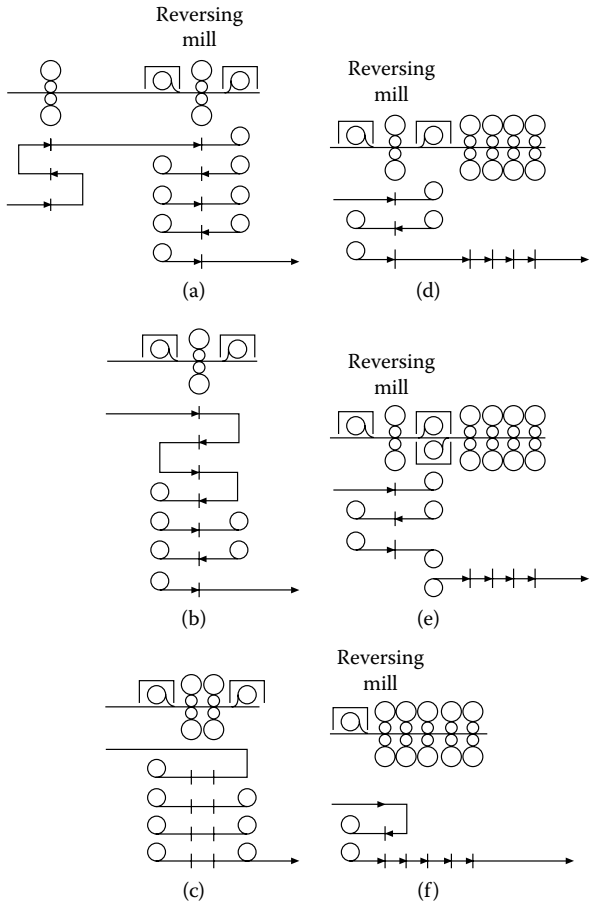


FIGURE 2.11 Six arrangements of hot rolling mills utilizing Steckel mills that can be used in the CR lines with medium-slab casters [9,11–13,22,30,46,52,47,67,68,75].

TABLE 2.15
Design Parameters of the CR Line at Tuscaloosa Steel

	Parameter	Units	Value/Definition
Slab Dimensions	Slab thickness	mm	130
	Slab width	mm	914–2591
Slab Caster	Number of strands	—	1
	Bend radius	m	6.5
	Mold cross-sectional shape	—	Rectangular
	Mold length	mm	900
	Mold oscillator stroke	mm	3–12
	Mold width adjustment	—	Automatic, online
	Sticker detection system	—	Installed
	Secondary cooling type	—	Air mist
	Maximum casting speed	mpm	2.5
	Metallurgical length	m	14.7
Rolling Mill	Mill type	—	Steckel, coil/plate
	Number of stands	—	1
	Mill stand roll stack type	—	Four-high

TABLE 2.16
Design Parameters of the CR Line at Nova Hut Steel

	Parameter	Units	Value/Definition
Slab Dimensions	Slab thickness	mm	127
	Slab width	mm	740–1575
Slab Caster	Number of strands	—	1
	Mold cross-sectional shape	—	Rectangular
	Mold EMBR	—	Installed
	Maximum casting speed	mpm	2.0
Rolling Mill	Mill type	—	Steckel
	Number of stands	—	2
	Mill stand roll stack type	—	Four-high
	Main drive power for each stand	kW	5225
	Maximum mill speed	mpm	792
	Maximum roll separating force	kN	35,630
	Maximum work roll diameter	mm	840
	Maximum backup roll diameter	mm	1730
	Roll barrel length	mm	1725
	Vertical edger location	—	Between mill stands
	Strip thickness range	mm	1.5–13.0
	Strip width range	mm	740–1575
	Maximum coil weight	t	28.5

2.8 SUPERCOMPACT CR LINES

Supercompact CR lines shown in Figures 2.12 and 2.13 include the same main components as the currently installed CR lines, but they are much shorter in length. The supercompact layout of these lines is achieved by splitting them into two sections, upstream and downstream in which the metal flows in opposite directions in respect to one another [111]. In the CR line shown in Figure 2.12, there are two upstream sections, each containing a thin-slab caster and a reheat tunnel furnace. The downstream line contains a tandem-finishing mill, a runout table cooling system, and two downcoilers. The centerlines of the upstream and downstream sections intersect

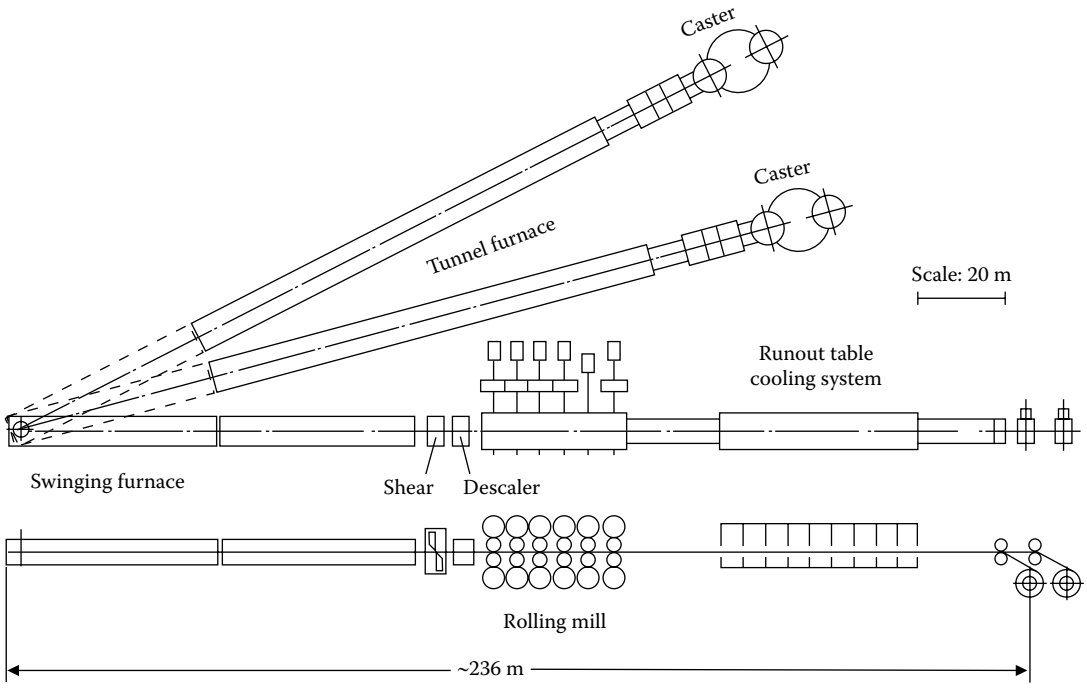


FIGURE 2.12 Schematic layout of a supercompact CR line for hot rolling of discrete coils [111].

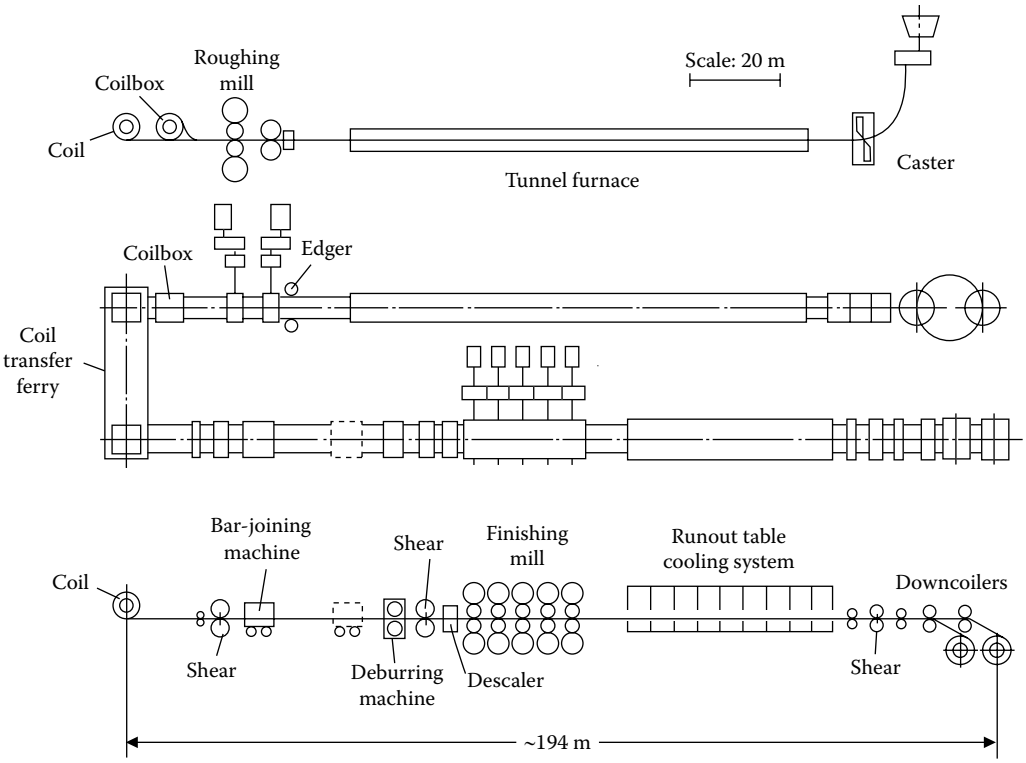


FIGURE 2.13 Schematic layout of a supercompact CR line for endless hot rolling [112].

at the same pivot point. The slabs are transferred from the upstream section to the downstream section by turning a swinging furnace around a pivot point. In this example, all components of the supercompact CR line are the same as the components of the conventional CR line shown in Figure 2.6. In that case, by using a supercompact layout, it is possible to reduce the plant length by 142 m.

The supercompact CR line shown in Figure 2.13 is intended for endless rolling [112]. The upstream section of this line contains a thin-slab caster, a tunnel furnace, a roughing mill, and a Coilbox. The downstream section includes bar-joining equipment, a finishing mill, a high-speed rotary drum shear, and two downcoilers. The reheated slabs are transferred from the upstream section to the downstream section in the coiled form. There are three known methods for joining the bar: induction welding, laser welding, and the solid-state joining process [43,94]. Figure 2.13 shows a joining machine utilizing the induction welding that is similar to the machine installed at Kawasaki Steel Chiba Works No. 3 hot strip mill [43]. The self-propelled bar-joining machine is equipped with an induction heater. The crop shear installed at the entry of the bar-joining machine crops the tail end of a preceding bar and the head end of the following uncoiled bar. The bar-joining machine travels with the transfer bars to be joined. It is capable of completing the bar joining within a 20-m traveling stroke. A deburring machine located at the exit side of the bar joining machine removes the material raised at the joint. After rolling and cooling, the strip is cut in the coil lengths by a high-speed shear installed in front of the downcoilers.

2.9 SUMMARY

1. In the compact CR lines of the original CSP plants, the production of hot-rolled strips was very simple: after casting by a thin-slab caster and reheating in the tunnel furnace, a 50 mm thin slab was rolled by a tandem-finishing mill. This process was distinctly different and more efficient than the process of production of hot-rolled strips by the integrated steel mills that use much more expensive equipment, including the thick-slab casters, walking beam reheat furnaces, and roughing mill stands, in addition to the finishing mills. The economic success of the original CSP plants was further assured due to the use of much less expensive EAF fed with a low-cost scrap.
2. The experience gained during the operation of various designs of the CR lines showed that a 50-mm thick slab is not the optimum slab thickness for achieving the best quality and consistency of rolled products, as well as from the productivity point of view. It was possible to make significant improvements in these areas by increasing the slab thickness into the range of 65 to 100 mm. The increase in the slab thickness, however, came with a price. A thicker slab required using the roughing mills along with conventional heat conservation devices, such as the heat covers and the Coilbox. The design of the CR lines with medium-slab casters became even closer to the design of conventional hot strip

mills. Both of them contain conventional walking beam reheat furnaces instead of much simpler reheat tunnel furnaces.

3. A significant recent increase in scrap prices forced the minimills producing the flat steel products to use much more expensive scrap substitutes. Consequently, from both economical and technological aspects, the minimills for the flat steel products are getting closer to the conventional integrated steel mills. In this new environment, two principal capabilities will play a more significant role in the competition between the minimills and the integrated steel mills: the capability of producing a variety of steel products demanded by the steel market and the capability of achieving the required quality level and consistency of produced steel products. In the course of this competition, both parties will have a great opportunity to continue to learn from each other.

REFERENCES

1. G.W. Tippins, V.B. Ginzburg, and W.G. Potmeyer, U.S. Patent 4,430,874, February 14, 1984.
2. V.B. Ginzburg, U.S. Patent 4,430,876, February 14, 1984.
3. V.B. Ginzburg, U.S. Patent 4,444,038, April 24, 1984.
4. G.W. Tippins and V.B. Ginzburg, U.S. Patent 4,503,697, March 12, 1985.
5. W. Fabian et al. On-line flatness measurement and control of wide strip. *Metallurgical Plant and Technology*, August 1985, (4):68–75.
6. K. Nakajima et al. Basic characteristics of pair cross mill. *Mitsubishi Technical Review*, June 1985, pp. 143–148.
7. V.B. Ginzburg, U.S. Patent 4,599,883, June 15, 1986.
8. V.B. Ginzburg, U.S. Patent 4,630,352, December 23, 1986.
9. H. Wiesinger et al. Hot strip rolling for compact mills: The HSRC mill. *Iron and Steel Engineer*, August 1987, pp. 50–55.
10. W. Bald et al. Continuously variable crown (CVC) rolling. *AISE Book*, 1988, pp. 497–506.
11. H.J. Ehrenberg et al. Casting and cast-rolling of thin slabs at the Mannesmannrohren-Werke AG. *MPT International*, June 1989, (3):52–69.
12. V.B. Ginzburg, *Steel-Rolling Technology—Theory and Practice*, New York: Marcel Dekker, Inc. 1989.
13. P. Meyer and F.P. Pleschiutschnigg. Thin slab caster combined with a Steckel mill. *6th I.S.M.O. Annual Meeting*, September 10–14, 1990. Tornio, Finland.
14. V.B. Ginzburg and R.V. Vidil, U.S. Patent 4,898,014, February 6, 1990.
15. F.K. Iverson and K. Basse. A review of first year CSP operations at Nucor Steel's new thin slab casting facilities. *MPT International*, February 1991, (1):40–51.
16. G. Gosio et al. First minimill in Italy for high-quality inline-strip-production at Arvedi. *MPT International*, October 1991, (5):60–69.
17. K. Hayashi et al. Development of on-line roll grinding system for hot strip mill. *ISIJ International* 31(6):588–593.
18. F.P. Pleschiutschnigg et al. First minimill with I.S.P. technology in comparison with other hot-strip production lines. *MPT International*, April 1992, (4):66–82.
19. P.B. Hendel et al. Concepts and start-up of the Nucor Steel—compact strip production hot strip mill. *AISE Spring Convention*, Nashville, TN, May 1992.
20. V.B. Ginzburg, *High Quality Steel-Rolling—Theory and Practice*. New York: Marcel Dekker, Inc. 1993.
21. G. Flemming et al. The CSP plant technology and its adaptation to an expended production programme. *MPT International*, April 1993, (2):84–96.
22. A. Lederer. State of development of Steckel mills. *MPT International*, June 1993, (3):56–69.
23. F.P. Pleschiutschnigg et al. The I.S.P. process, its potential and first operating results. *MPT International*, August 1993, (4):44–68.
24. V.B. Ginzburg, U.S. Patent 5,212,975, May 25, 1993.
25. F. Hofmann et al. State of the art in CSP technology. *Unarc Family Meeting*, Memphis, TN, September 1993.
26. V.B. Ginzburg et al. Production-quality cost-balanced (PQCB) plant for flat products. Paper presented at *The 1993 AISE Annual Convention*, Pittsburgh, PA, September 20–23, 1993.
27. P. Niles. Quality aspects of near net shape casting. *MPT International*, June 1994, (3):46–56.
28. R. Mott et al. The performance of the Nucor CSP plant in Hickman and its further expansion. *MPT International*, June 1994, (3):98–108.
29. G. Coassin and U. Meroni. Flexible thin slab conticaster. *MPT International*, June 1994, (3):110–120.
30. A. Wilson and J. Pietryka. TSP, a new method of thin slab casting and rolling. *MPT International*, June 1994, (3):122–130.
31. N.L. Samways. Nucor Steel, Hickman—2.2 million ton/year flat rolled minimill. *Iron and Steel Engineer*, April 1994, pp. 77–84.
32. R.C. Skagen and D.C. Gilbert. CSP tunnel furnace—concept through operation. *AISE Spring Convention*, Memphis, TN, April 1994.
33. D. Chase and J. Küper. Performance of Nucor Hickman's CSP plant and the progress of phase II. *AISE Spring Convention*, Memphis, TN, 1994.
34. G. Gosio et al. The technology of thin slab casting, production and product quality at the Arvedi I.S.P. Works, Cremona. *METEC Congress 94 Proceedings*, Vol. 1, June 1994.
35. C. Mantovani et al. Flexible thin slab rolling: A new challenge to improve production mix and quality. *METEC Congress 94 Proceedings*, Vol. 1, June 1994.
36. A. Ritt and B. Berry. What Nucor Hickman learned from Crawfordsville. *New Steel*, August 1994, pp. 28–34.
37. W. Rhode and G. Flemming. Current state, capabilities and further developments of the CSP technology. *MPT International*, August 1995, (4):82–98.
38. B. Di Giusto and V.B. Ginzburg, U.S. Patent 5,435,164, July 25, 1995.
39. V.B. Ginzburg, U.S. Patent 5,460,023, October 24, 1995.
40. A. Fernández et al. First operating results of Hylsa's CSP plant. *MPT International*, February 1996, (1):34–38.
41. T. Korabi. New developments expands coilbox applications. *Iron and Steel Engineer*, December 1996, pp. 13–19.
42. J. Schonbeck et al. Current status of the ISP technology and new developments. *MPT International*, February 1997, (1):38–49.
43. X.T. Takano et al. Endless hot rolling at Kawasaki Steel Chiba Works. *Iron and Steel Engineer*, February 1997, pp. 41–47.
44. G. Flemming et al. CSP—the advanced technology for minimills leading into the next century. *MPT International*, June 1997, (3):64–75.
45. B. Kruger et al. Saldanha Steel—the new minimill process line for high quality thin gauge flat products. *MPT International*, October 1997, (5):68–81.

46. E.D. Carballal Revival and modernization of the Steckel hot strip mill. *Steel World*, 1997, 2(1):41–45.
47. S. Kramer et al. Technology and performance of modern Steckel mills. *Iron and Steel Engineer*, July 1997, pp. 17–26.
48. L.A. LeDuc-Lezama et al. Hot rolling of thin gage strip at Hylsa. *Iron Steel Engineer*, April 1997, pp. 27–31.
49. D. Kothe et al. ISP—thin slab casting and rolling concept for economical processing of quality products. *Iron and Steel Engineer*, June 1997, pp. 31–38.
50. E.A. Donini et al. Flexible thin-slab rolling: Matching the requirements of integrated producers. *Iron and Steel Engineer*, June 1997, pp. 39–44.
51. W.D. Huskonen. Trico take off. *33 Metalproducing*, July 1997, (7):32–38.
52. E.G. Mueller and J. Dzierzawski. Tuscaloosa's conversion to minimill. *MPT International*, June 1997, (3):82–91.
53. D.A. Dunholter. Design and start-up of the North Star BHP Steel minimill. *Iron and Steel Engineer*, December 1997, pp. 49–52.
54. Y. Abe et al. U.S. Patent 5,601,137, February 11, 1997.
55. P. Sudau and O.N. Jepsen. Production of 1 mm thick hot rolled steel strip. *MPT International*, February 1998, (1):50–51.
56. R. Borsi et al. Algoma's direct production plant for quality steel. *MPT International*, February 1998, (1):88–96.
57. R. Borsi and M. Rotti. Algoma's DSP complex. *Metal-Producing*, February 1998, (2):33–36.
58. A. Ritt. Thin slabs from BOF steel in Canada. *New Steel*, February 1998, pp. 20–25.
59. G. Kneppe and D. Rosenthal. Hot strip rolling technology: Tasks for the new century. *MPT International*, June 1998, (3):56–67.
60. N.L. Samways. Trico Steel—A 2.2 million ton/year joint venture flat rolled minimill. *Iron and Steel Engineer*, March 1998, pp. 21–34.
61. M. Mizuno et al. QSP (quality strip production) process in Trico Steel Company. *AISE Specialty Conference Proceedings*, March 15–17, 1998, Birmingham, AL, USA.
62. A. Flick et al. Operational and quality results from thin slab casting/rolling plants at ARMCO and Nova Hut. *AISE Proceedings*, September 21–22, 1998, Pittsburgh, PA, USA.
63. X.S. Bouchillon et al. Nucor Crawfordsville 2000—setting a standard for the world's first CSP mill. *Iron and Steel Engineer*, July 1998, pp. 47–54.
64. W.D. Huskonen. Posco goes "mini" to grow larger. *Metal-Producing*, July 1998, (7):30–36.
65. W.J. Pampiks and H. Scherley. The TSP™ process for high quality flat rolled products. *AISE Proceedings*, September 21–22, 1998, Pittsburgh, PA, USA.
66. W.D. Huskonen. Italian mini-mill designed for quality, flexibility. *MetalProducing*, July 1998, (7):42–46.
67. H. Wehage et al. New trends in flat rolling technologies and pass schedule optimization. *MPT International*, August 1998, (4):60–71.
68. H. Wehage et al. Pass schedule optimization for new hot flat rolling processes. *MPT International*, October 1998, (5):92–104.
69. M.J. Steeper and D.G. Park. Development of steering control system for reversing hot mills, *Iron and Steel Engineer*, November 1998, pp. 21–24.
70. V.B. Ginzburg. *Flat-Rolling Fundamentals*. New York: Marcel Dekker, Inc. 2000.
71. G. Flemming et al. Present and future CSP technology expands product range. *Steel Technology*, January 2000.
72. F.E. Fonner. Hylsa's flat products div.—fully integrated minimill with an annual capacity of 2.5 million tonnes. *Steel Technology*, March 2000.
73. P. Ceracki et al. On-line surface inspection of hot rolled strip. *MPT International*, August 2000, (4):66–71.
74. M. Degner et al. Developments in production of ultra-thin hot strip. *MPT International*, February 2001, (1):92–95.
75. Minimill Flat Products, *NOVÁ HUŤ Technical Report*, March 16, 2001.
76. F. Stella et al. New minimill in Egypt for the production of ultra-thin hot strip coils. *MPT International*, June 2003, (3):38–44.
77. M. Peretic et al. Coordinated application of roll gap lubrication, work roll cooling and antipeeling systems in hot rolling mills. *Iron and Steel Technology*, May 2004, pp. 27–36.
78. N. Shimoda et al. Process control technology for thin strip production in Tangshan, China. *Iron and Steel Technology*, January 2005, pp. 35–42.
79. C.P. Reip et al. Recent developments in the integrated technology of compact strip production. *Iron and Steel Technology*, September 2005, pp. 29–31.
80. M.A. Herrera et al. Improvement in surface quality and internal cleanliness of thin-slab casting at Hylsa. *Iron and Steel Technology*, September 2005, pp. 34–40.
81. V. Tretyakov. Automatic surface inspection at the NLMK hot strip mill. *MPT International*, October 2005, (5):54–60.
82. V.B. Ginzburg. *Metallurgical Design of Flat Rolled Steels*. New York: Marcel Dekker, Inc. 2005.
83. C.P. Reip. Challenges and solutions of compact strip production. *MPT International*, May 2006, (3):66–68.
84. S. McDougal. Reduction of surface defects on 0.25%C hot band at Nucor Steel—Crawfordsville. *AISTech 2006 Proceedings*, May 2006, (2):49–58.
85. A. Jordan. IMPOC®: Online mechanical properties measurement—Reducing processing and material problems. *AIST Proceedings*, May 7–10, 2007, Indianapolis, IN.
86. J. Watzinger et al. Medium-thick-slab casting technology. *AIST Proceedings*, May 7–10, 2007, Indianapolis, IN.
87. R. Borsi et al. Tangshan Guofeng 1450 hot strip mill (P.R. China) start up and first operational results. *AIST Proceedings*, May 7–10, 2007, Indianapolis, IN.
88. R. Cheeley. Gasification and the MIDREX® direct reduction process. *AIST Proceedings*, May 7–10, 2007, Indianapolis, IN.
89. A.F.L. da Costa et al. CST Arcelor Brasil HSM tail-end CRashing reduction using six sigma methodology. *AIST Proceedings*, May 7–10, 2007, Indianapolis, IN.
90. E.M. Dillon and T. MacDougall. Deriving quality improvement using automated surface intelligence system™. *AIST Proceedings*, May 7–10, 2007, Indianapolis, IN.
91. R. Arnken et al. Commissioning and optimization of the roll gap lubrication system at the ANSDK CSP plant. *Iron and Steel Technology*, August 2007, pp. 81–86.
92. J. Kempken et al. Short route—Long-term success: Integrated mini-mill solutions by Midrex and SMS Demag. *Archives of Metallurgy and Materials*, 2008, 53(2):331–336.
93. G. Arvedi et al. The Arvedi endless strip production line (ESP)—From liquid steel to hot-rolled coil in seven minutes. *AIST Proceedings*, May 5–8, 2008, Pittsburgh, PA.
94. J.S. Lee et al. Development of a new solid-state joining process for endless hot rolling. *AIST Proceedings*, May 5–8, 2008, Pittsburgh, PA.
95. A. Mukhopadhyay et al. CQE—controlling mechanical properties of hot rolled coils. *AIST Proceedings*, May 5–8, 2008, Pittsburgh, PA.

96. M. Abel and M. Hein. The use of scrap substitutes like cold/hot DRI and hot metal in electric steelmaking. *AIST Proceedings*, May 5–8, 2008, Pittsburgh, PA.
97. L. Zhang et al. Optimization of surface inspection system performance. *AIST Proceedings*, May 5–8, 2008, Pittsburgh, PA.
98. S.Y. Kim and K.W. Kim. Development of surface quality tracking system of steel flat products. *AIST Proceedings*, May 5–8, 2008, Pittsburgh, PA.
99. R.S. Sampaio et al. Hot metal strategies for the EAF industry. *AIST Proceedings*, May 5–8, 2008, Pittsburgh, PA.
100. S. Berger and Karl Hoen. Latest developments in CVC Plus®. *AIST Proceedings*, May 5–8, 2008, Pittsburgh, PA.
101. J. Daafouz et al. New steering control in a hot strip mill. *AIST Proceedings*, May 5–8, 2008, Pittsburgh, PA.
102. A. Farhadi et al. Direct reduction technology progress in ArcelorMittal. *Scrap Substitutes & Alternative Ironmaking V*, November 2–4, 2008, Baltimore, MD.
103. R. Whipp. Present HBI plant operation at Orinoco iron. *Scrap Substitutes & Alternative Ironmaking V*, November 2–4, 2008, Baltimore, MD.
104. R. Dabideen and S. Heraldo. Nucor's successful relocation and start-up of the AIR plant. *Scrap Substitutes & Alternative Ironmaking V*, November 2–4, 2008, Baltimore, MD.
105. M.T. Guerra et al. DRI—Premium raw material for electric steelmaking. *Scrap Substitutes & Alternative Ironmaking V*, November 2–4, 2008, Baltimore, MD.
106. J. McClelland. Successful development of MIDREX® RHF technologies 40 years from concept to commercial realities. *Scrap Substitutes & Alternative Ironmaking V*, November 2–4, 2008, Baltimore, MD.
107. C.B.V. Varnbüler et al. Ironmaking for Nichse quality products. *Scrap Substitutes & Alternative Ironmaking V*, November 2–4, 2008, Baltimore, MD.
108. K. Siuka et al. Development and current status of the COREX® process with special focus on Corex Baosteel. *Scrap Substitutes & Alternative Ironmaking V*, November 2–4, 2008, Baltimore, MD.
109. S. Joo and H. Lee. An update on FINEX® plant operations. *Scrap Substitutes & Alternative Ironmaking V*, November 2–4, 2008, Baltimore, MD.
110. L.C. Prichard et al. First operational results at the new SeverCorr mini-mill, USA. *MPT International*, September 2008, (4):52–61.
111. V.B. Ginzburg. Provisional U.S. Patent Application No. 61/123,887, April 12, 2008.
112. V.B. Ginzburg. Provisional U.S. Patent Application No. 61/190,903, September 4, 2008.
113. Arvedi ESP—Endless Strip Production. *Siemens—VAI Metals Technologies Report*.
114. Inline Cast Rolling on the World's Shortest Production Line—Market Mill for Flat Products. *Mannesmann Technology Report*.
115. CC-EMS For Flat Products. EMBR, Electromagnetic Brake for Thin Slab Casters. *ABB Automation Technologies AB, ABB Inc. Technical Report*.
116. SeverCorrLLC—A Greenfield Plant for Automotive Sheets. *SMS Demag Technical Report*.

3 Methodology and Results of Major Hot Strip Mill Modernization Projects

Wlodzimierz Boleslaw Filipczyk

CONTENTS

3.1 Introduction 36
3.2 Upgrades of Electrical and Automation Systems 36
3.2.1 The Scope and Justification 36
3.2.2 The Features of the Modern Control System 36
3.2.3 Electrical Drives Upgrade Solutions 36
3.2.4 Sensors and Input/Output Upgrade Solutions 38
3.2.5 Level 1 Equipment Control Upgrade Solutions 38
3.2.6 Operator's Interface Upgrade Solutions 39
3.2.7 Supervisory Process Control (Level 2) Upgrade Solutions 40
3.2.8 The Basic Rules of Electrical and Automation Systems Upgrade 41
3.2.8.1 Identification of Critical Interfaces and Connectivity Solutions 41
3.2.8.2 Detailed Engineering and Factory System Test 41
3.2.8.3 Process and Control Shadowing on Site 41
3.2.8.4 Ghost Bar Rolling and Switchover Trials 42
3.3 China Steel Hot Strip Mill Modernization Project 43
3.3.1 1730-mm Hot Strip Mill #1 History 43
3.3.2 Actual Mill Configuration and Basic Data 43
3.3.3 The Scope of the Mill Modernization 44
3.3.4 The Downcoilers and Strip Cooling Modernization 44
3.3.4.1 Mechanical Equipment 44
3.3.4.2 Electrical Equipment and Control System 45
3.3.5 Slab Sizing Press Installation 47
3.3.5.1 Mechanical Equipment 47
3.3.5.2 Electrical Equipment and Control System 47
3.3.6 Project Implementation 48
3.3.7 General Project Schedule 48
3.3.7.1 Coilers Area 48
3.3.7.2 Slab Sizing Press 49
3.3.7.3 Main Shutdown for Both Projects 50
3.3.8 Mill Start-Up 50
3.3.9 Project Highlights and Milestones 50
3.3.10 Results 50
3.3.10.1 Cast Slab Width Range 50
3.3.10.2 Coil Width Performance 50
3.3.10.3 Material Properties for New Products and CTC Performance 50
3.3.10.4 Coil Presentation 51
3.3.10.5 Coil Shape Defects 52
3.3.10.6 Coil Surface Defects 52
3.3.10.7 Decrease in Mill Delays 52
3.4 Summary 52
Reference 53

3.1 INTRODUCTION

One of the common features of modernization projects in the metal industry has been very noticeable in recent years: multi-phased, multi-year implementation. This is for various reasons, the most important being budgetary restrictions and minimum negative impact (no extra shutdowns, no decrease in production) on current plant operation. Implementation of modernization projects in phases divides the whole scope into smaller chunks, where the amounts of new equipment and new functions are easier to commission, and the risk of production disturbances after the switchover is minimized. The Big Bang approach, where all new equipment is installed and activated at once, requires additional, longer production shutdowns and results in much longer ramp-up curves compared to normal production levels. However, in the case of significant mechanical modification, long production shutdown cannot be avoided, and it has to be planned and coordinated with other activities well in advance.

This description of rolling mill modernization projects is divided into two parts. The first part presents the fundamental strategies of electrical and automation system upgrades. It is based on the cumulative experience acquired from numerous modernization projects in rolling mills worldwide.

The second part describes the major upgrade project (mechanical and electrical) of China Steel Hot Strip Mill #1 in Kaohsiung, Taiwan. The applied modernization strategies, as well as final results, are presented.

3.2 UPGRADES OF ELECTRICAL AND AUTOMATION SYSTEMS

The minimum impact installation and start-up of a new electrical control system on an operating production line, and the frequent necessity to connect to the "remnants" of the old existing control system, make such implementation (or perhaps better called "implantation") very challenging. All stages of the implementation, including intermediate configurations, parallel operation, process shadowing, "ghost rolling," and control switchovers, must be carefully planned and supported in both hardware and especially software design.

3.2.1 The Scope and Justification

There may be many possible excuses to upgrade electrical and automation equipment in the mill, but the real reasons must be clearly justified before commencing such a project. Many potential upgrade projects were never approved due to excessive scope, poor justification, or both. The analysis of return on investment must be conducted showing real benefits of the upgrade.

The most frequent upgrade reasons can be listed as follows:

- Productivity improvements by eliminating frequent downtimes due to existing equipment failures
- Lack of maintainability of old equipment due to its obsolescence (lack of spare parts, lack of knowledge of the old equipment, etc.)
- Improvement of the mill operation: decrease of the cobble rates, decrease of production delays due to better process and equipment diagnostics
- Improvement of the product quality by applying new "state-of-the-art" control technology
- Functional expansion of the process due to the introduction of new equipment and/or technologies

The new electrical and automation system must be designed to meet all of these requirements.

3.2.2 The Features of the Modern Control System

Besides obvious objectives regarding adequacy of the control system for its specific functionality and performance, users specify more general requirements related to the openness, simplicity, and flexibility of system architecture and software concepts.

The systems recently implemented in modernized rolling mills were based both on specific demands of the high-speed and complex metal rolling process and on modern general control solutions.

The following control system features are very important for both user and supplier because they affect cost of system ownership and maintenance as well as cost/productivity of system design and commissioning.

- Open architecture
- Scalability and ease of expansion
- Simple control network communication
- Unified Level 1/Level 2 human–machine interface (HMI)
- Fully structured and configurable software products and distributed computing
- Global system metadata definition
- Tools for process/equipment data analysis
- Level 2 platform independence
- Ease of system maintenance

The application software on all system levels should be designed and programmed to cover all phases of implementation including support for temporary interfaces, intermediate configurations, and equipment operations. This extra engineering effort has to be accounted for during the definition of the scope of the upgraded system.

3.2.3 Electrical Drives Upgrade Solutions

Various progressive solutions are available in the electrical motors and drives field. The most popular (if justified) trend is to replace old DC equipment with new AC motors and drives. This is an ultimate solution and brings long-term savings and operational benefits.

AC technology using variable voltage variable frequency (VVVF) drives is often the only solution in the case of a mill

re-powering project when bigger power motors are required and must be installed in the same footprint as the old, smaller power DC machines.

One very economically justifiable change is the replacement of old fixed-speed AC drives with VVVF drives to adjust the motor speed to the actual process needs. This solution can be applied for auxiliary drives, such as pumps and fans, and it delivers the most beneficial results for mill descale pumps.

In general, new drives (either AC or DC) have extensive diagnostics and user-friendly troubleshooting tools available to assist with quick problem-finding and fixing.

However, unless the drives/motors are nonmaintainable or costly and troublesome to operate and maintain, there is no real reason to replace them in full. Existing DC motors can still be used, and drive solutions vary depending on the upgrade goals. The basic choices are as follows:

- Digitization of the speed regulators—The least expensive solutions that deliver more accurate speed tracking (important for close-coupled stands, such as finishing mills) and better speed regulator response and provide digital network interface to drives.
- Firing circuits' replacement, also known as digital front ends (DFEs)—This is the more expensive but the most advisable solution in the majority of DC drive upgrades. Whole drive regulating modules are replaced with new digital electronics and interfaced directly to the existing thyristor power bridges (gate leads). Since the existing power bridges are re-used, there are substantial savings in both equipment and installation cost. New electronics, however, deliver all the benefits of new drive technology, such as connectivity to standard drive networks such as PROFIBUS and a full range of drive diagnostics and troubleshooting tools. New DFEs can also be connected on the maintenance ethernet network for remote access, which may be an important asset for both drive supplier and maintenance personnel.
- Complete new DC drives—They provide all of the benefits of DFE solution, but they are usually more expensive for bigger-size drives (thyristor bridges and power circuits installation). They are justifiable for small-size auxiliary drives where the cost of full drive is comparable with DFE and for big-size main drives, which are not economically maintainable anymore.

Figure 3.1 shows examples of possible upgrades for electrical motors and drives.

There are various possible solutions regarding new drive connectivity to the existing and new control systems, depending on the "vintage" of the existing controls. Typically, old

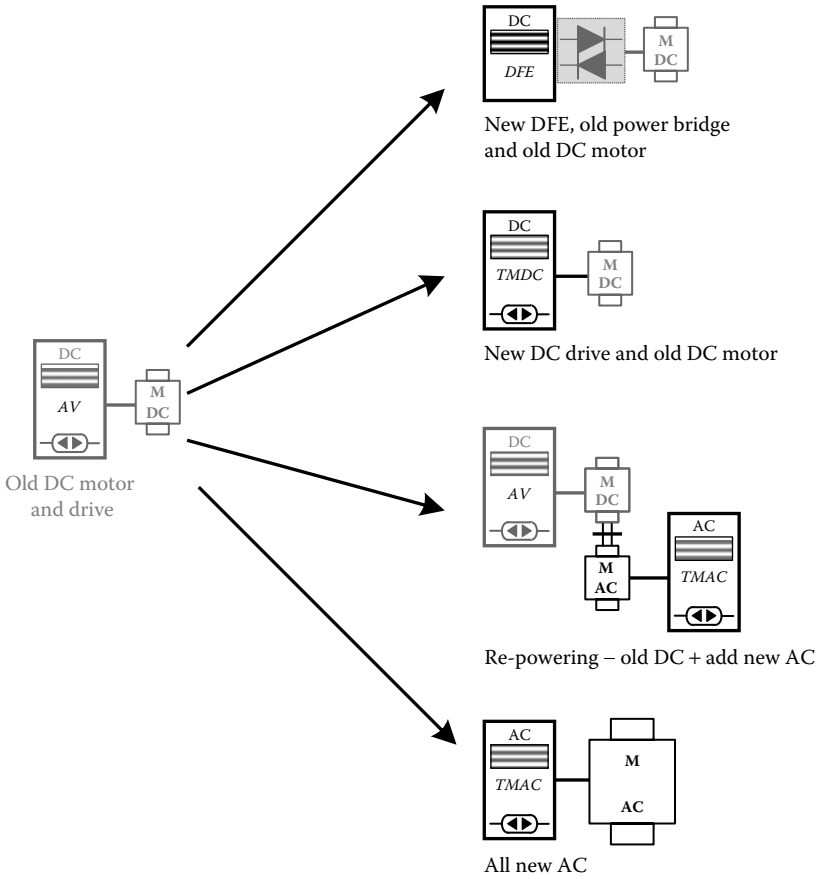


FIGURE 3.1 Examples of electrical motors and drives upgrade scenarios.

drives were connected using hard-wired inputs/outputs (I/O) or some type of proprietary drive bus. If the modernization project is planned to replace or upgrade old drives first, the connectivity to an existing control system must be provided. Fortunately, most of the modern drives have both I/O connectivity and some choice of drive network interfaces, such as PROFIBUS. New drives can then be connected both to the old system (I/O to I/O) and to the new system via the drive bus. This provides an excellent opportunity for drive control shadowing and an easy way to achieve a control switchover.

Other drive connections are also possible through control "bridging," which will be described later.

3.2.4 Sensors and Input/Output Upgrade Solutions

Most of the existing process sensors, like hot metal detectors, pyrometers, width and thickness gauges, etc., can usually be connected in parallel to old and new systems, thus allowing for good process shadowing. However, in the case of sensors mounted on the mechanisms (speed and position sensors), the approach may be different, since many of these sensors use old technology (selsyns) or have to be replaced due to inadequacy for an application, old "age," etc.

To allow thorough checkout and quick changeover trials of a new control system, it is critical that new sensors be installed in parallel with existing ones. Various solutions are possible, such as new digital tachometers with analog converters, new rotary sensors with double-shaft for mounting "in-between," and new linear displacement transducers working in parallel with old rotary sensors.

For I/O equipment, few solutions regarding replacement and implementation are possible as well:

- All of the old I/O is replaced; the new I/O is to be wired in parallel as quickly as possible. Full system shadowing is possible; switchover trials are easy, although some isolation (automatic or manual switch) for the control outputs is required.
- All of the old I/O will eventually be replaced, but a new control system should re-use it for temporary (sometimes as long as several years) operation. The connectivity to old I/O buses is required, preferably with selectable "passive" and "active" modes. In the passive mode, new controller will have access to all I/O space, but it will not transmit any of the outputs—this can be used for very effective shadowing, and switchovers are done very easily by software switch. Such a solution allows for gradual installation of new I/O (that does not require big, concentrated installation effort) and allows for extending the use of old I/O while more and more spare parts for old I/O are available after gradual switchovers to new I/O.
- Re-use of old I/O, which is similar to the case above, requires connectivity of a new control to old I/O buses.

See Figure 3.2 for various I/O upgrade examples.

3.2.5 Level 1 Equipment Control Upgrade Solutions

The existing control system usually consists of a mixture of various vendors' drives, controllers, and computers. The old system control networks (if they exist) are usually closed and use proprietary communication protocols. The key to the successful, gradual, noninvasive implementation of new Level 1 controllers is, again, connectivity. The best solution is the direct connection onto the old control system network (passively and then actively). After shadowing and verification of the new control logic, old controllers can be switched off one by one, while new controller(s) take over their functions. Such partial switchovers can be fully transparent to the old system, and thus will cause no disturbance to the production process.

Direct connection to the control network is not always possible. The alternative solution could be the direct interface

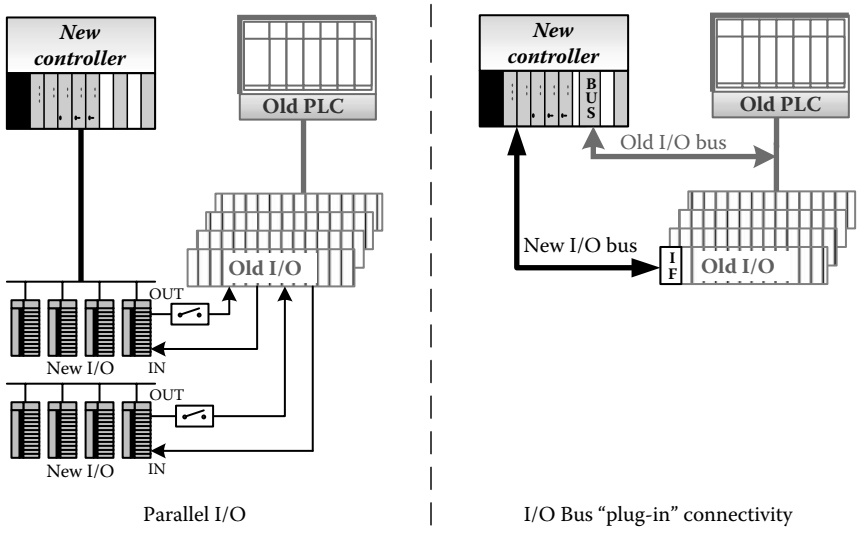


FIGURE 3.2 Input/output systems upgrade possibilities.

between old and new controllers via fast data link. In this case, various scenarios can be implemented:

- Some of the old controllers will remain functioning in a new system and will exchange data via new (fast) direct interface to new controller(s).
- New controllers will temporarily act as a bridge to new drives, new HMI, or new supervisory process control (Level 2). Initially, new controllers will only "pass-through" the control commands and feedbacks between old controllers and new system parts. Gradually, the functionality is migrated from an old to a new controller until the old one is finally shut down.
- A somewhat opposite solution to the above is a controller temporarily acting as a bridge to old drives, old I/O, old operators' interface, and old Level 2, etc. This allows for new controllers to function with old control system parts, as needed. Such a connection can be especially important to old I/O where the old controller is stripped of control functions (which are moved to a new controller) and acts merely as an I/O station.

Figure 3.3 shows new and old controllers bridging configurations.

Thanks to some unification in controller hardware, most of the contemporary controllers are based on world standard backplanes, the most popular being the Versa Module Europa (VME) or the compact peripheral component interconnect (PCI). A wide spectrum of interface boards is available for these standards from numerous hardware manufacturers, allowing implementation of various controllers' interfaces.

3.2.6 Operator's Interface Upgrade Solutions

Old control systems were typically equipped with operator's desks containing numerous discrete control devices, such as pushbuttons, lights, digital displays, lever-type controllers, etc. The cathode ray tube (CRT) displays and keyboards were also used for process status display and less frequent operator entries and interventions. Most of the earlier man–machine interface (MMI; the name HMI came later) systems were custom programmed, often with proprietary interfaces to a control system.

New HMI systems applied today are based on standard "off-the shelf" software, such as Wonderware® (registered name of Invensys Co.), typically in a client–server configuration. These new systems include of course interfaces to all modern control networks and support new communication standards, such as OLE for process control (OPC) and ActiveX. The ideal scenario would be if the new HMI system could be also connected to the old system. Again, connectivity is extremely important since new HMI could be implemented in the first phase of a modernization project so operator entries can be received in both old and new systems. Switchover is easy on the HMI display, and control signal attributes are changed from old to new definitions.

The implementation of a new HMI system should consider the application requirements of a particular operator's control devices. It is very common now to replace most discrete

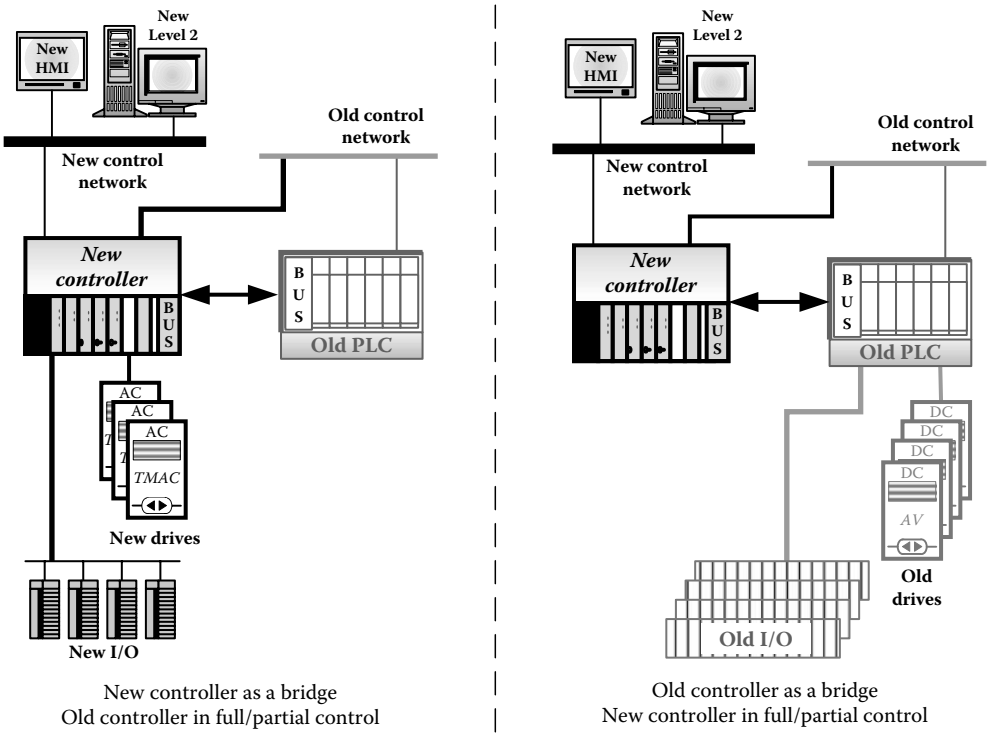


FIGURE 3.3 Examples of Level 1 controllers bridging functionality.

control devices with new HMI terminal "touch screens." These terminals can replace hundreds of traditional devices with virtual ones. However, only one device on the screen can be activated at a time, the latency between the operator's action (touch or un-touch) and the actuator can be as long as 0.5 s, and the operator has to look carefully at the screen while selecting a virtual control device, rather than looking at controlled machinery. Therefore, other solutions must be considered, including traditional "pistol-grip" and "joystick" switches for fast and safe manual interventions and control.

3.2.7 Supervisory Process Control (Level 2) Upgrade Solutions

Old Level 2 computers and networks were somehow less diverse (except European systems) than other parts of a control system, since many companies in the steel industry decided to standardize on Digital Equipment Corporation (DEC—nonexistent anymore) hardware and the virtual memory system (VMS) operating system. The Level 2 computers were connected using ethernet and serial links. There was either direct connection to Level 1 via the control system network or some type of "gateway" device for such interface.

Due to the obsolescence of the old platform (lack of spare parts), the Level 2 subsystem was one of the most frequently upgraded parts of old control systems. The various upgrades possible are as follows:

- Porting the entire existing application software to new computers. This requires the same operating system (OS) platform (e.g., VMS) to be retained. Some of the applications, such as communication drivers, must be replaced with new versions for newer computer hardware.
- Porting a (expensive) part of the existing applications, such as process models. All other Level 2 software infrastructure is changed to the newest versions, allowing for easy communication with new controllers, new HMI, etc.
- Porting the existing application software into the new operating system (OS) platform, such as Windows® (registered name of Microsoft Co.). This requires "virtualization" of the software environment for old applications. All existing applications are recompiled under the new system. Some parts of the old applications must be changed for communication interfaces in the new system.
- Replacing the entire Level 2 hardware and software with the newest standards. In this case, a new operating system platform can be chosen, such as Windows or Linux.

See Figure 3.4 for Level 2 hardware and software upgrade solutions.

Regardless of the chosen solution, a very important factor for successful switchover is again connectivity. New Level 2 systems must be connected to all other control levels for full

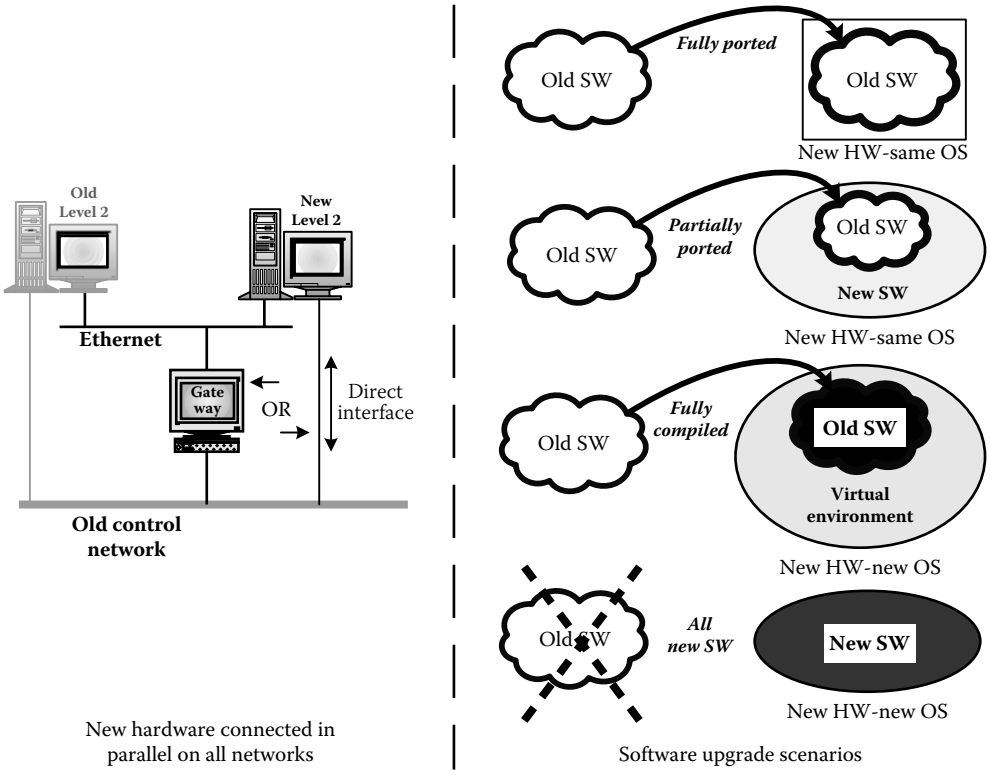


FIGURE 3.4 Supervisory process control upgrade solutions.

process shadowing and bumpless switchover. The production data sent from the enterprise level planning system should be sent to both the old and the new systems. Connectivity to Level 1 can be either direct via interface boards (switching from passive to active modes) or through some type of "gateway" or "proxy" computer.

In some cases, modifications to an old Level 2 may be required to pass critical data from old MMI terminals (e.g., DEC VT screens) to the new system to allow for reliable process shadowing.

3.2.8 The Basic Rules of Electrical and Automation Systems Upgrade

Based on experience gleaned from numerous modernization projects the following points should be emphasized as critical to a successful "no-impact-on-production" implementation.

3.2.8.1 Identification of Critical Interfaces and Connectivity Solutions

The existing system topology and interfaces should be studied and identified on all system levels. The amount and required frequency of each data exchange should be identified as well. The research should be performed to find adequate interface hardware, which allows for required *connectivity* to old system. Direct connectivity to old system buses and local area networks (LANs) allows for easy, noninvasive interface to all I/O control signals without the need for duplicating each I/O point, as well as provides an access to "virtual I/O," which is available only on system networks. Direct connectivity also allows for fast and easy switchovers between old and new controls, so short routine maintenance shutdowns can be utilized for new system verification and tune-up.

3.2.8.2 Detailed Engineering and Factory System Test

The following items are important for consideration during new system engineering and factory tests:

- Detailed definition of all I/O and interfaces to the remaining control during interim and final operation.
- Identify switchover needs for new drives with old controls and provide necessary hardware and software for interim operation.
- Proper definition of bumpless switchover schemes and procedures for "old" to "new" and back, identification and design of required hardware and "software" switches. Switchover schemes should be designed to achieve switching times of less than 30 minutes.
- Design of parallel installation of the new sensors.
- Design of parallel (at least partial) installation of new HMI in the pulpits for switchover trials.
- Definition of a user's involvement in all stages of the project, help with hardware and software modifications of existing controllers, proper planning and coordination of on-site activities, usage of any unscheduled shutdowns.
- Thorough verification of all "foreign interfaces" and communication links during factory system testing. Old controllers need to be brought into the integrated system test, connected to the new system, and their interfaces fully tested.
- Wherever possible, the integrated system test should include the verification of the system functionality corresponding to the various stages of implementation on site. This includes process shadowing, "ghost bar" rolling, partial switchovers, and final configuration.

3.2.8.3 Process and Control Shadowing on Site

Process shadowing is performed (wherever possible) on all system levels. Shadowing is performed on individual sections of the process, as the equipment and software of the new system is installed. Full shadowing and verification can be achieved after all system components are connected both to the process and together.

New systems should be designed to maximize the use of shadowing by implementing the correct algorithms and procedures, which will keep both old and new systems in synchronization. This especially applies to

- Tracking (handling all tracking scenarios, such as rejects, etc.)
- Critical data entered by the operators (e.g., roll diameters)

The goals of shadowing are different for different control levels.

3.2.8.3.1 Level 1 Control

The goals of shadowing for Level 1 control are as follows:

1. Verification of the correctness of all process inputs (signal timing, noise, and correlations of the process parameters).
2. Verification of Level 1 physical tracking based on the real sensor signals from the process: find and fix possible areas of tracking problems.
3. Verification of the new control actions as a response to the process status, such as "What would new controls do?" This is a very powerful and effective way to verify new control algorithms and logic. Since all required process and operator inputs are available to new controllers, control software should follow the process status on-line and respond to it by sending the references to the mill actuators. The actual outputs from the new control are disabled during the shadowing (either by hardware or by software switches). These control outputs are, however, continuously monitored (through the data historian) and then can be compared with real actuator/process responses (feedbacks). The actuators are responding, of course, to the references from the old control, so such shadowing comparisons and analysis

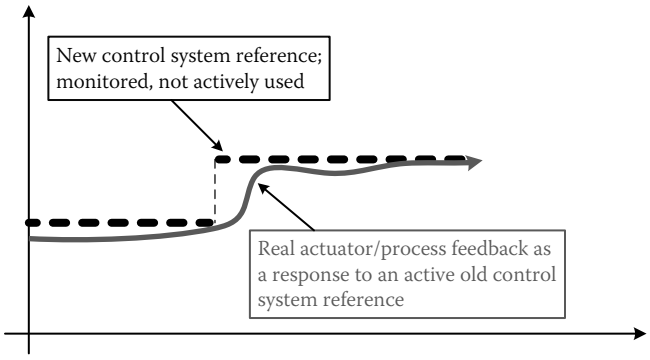


FIGURE 3.5 The example of Level 1 control shadowing functionality.

will expose the possible timing and logic problems. It is the most complete control software verification possible before active switchover.

See Figure 3.5 for a Level 1 shadowing example.

3.2.8.3.2 Level 2 Control and HMI System

The goals of shadowing for Level 2 control and the HMI system are

1. Verification of the control network (and other) interfaces data integrity: all data received and transmitted correctly
2. Verification of the Level 2 zone tracking, including operator tracking adjustments (rejects, etc.)
3. Verification of the correct data flow, from primary data to models to reference sendouts
4. Verification of process scans timing
5. Verification of data logging and reports
6. Verification of ALL data displays and operator inputs

3.2.8.3.3 Process Models

Process models have the biggest potential benefits to obtain from shadowing by learning the process and various steel product behavior under the real rolling conditions.

1. Verification of the correct data send/receive via the model records
2. Verification of correct model data logging
3. Verification of model scans (process feedbacks) and adaptation logic
4. Analysis of engineering log data (for the whole spectrum of rolled products), comparison of model references and calculated parameters with real feedbacks, and correlation analysis of rolling parameters
5. Tune up model tables as a result of the above analysis and repeat procedures until satisfactory results are achieved. In other words, until calculated model parameters are close to the measured process quantities.

3.2.8.3.4 Integrated System

Shadowing allows the verification of the integration of the whole new system. The interfaces on all levels are verified; the global tracking and data flow through the entire system are verified. The potential problems with network traffic, computer, and controller loads, etc. can be discovered and fixed.

3.2.8.3.5 Shadowing Verification Tools

New HMI wherever available is used for all system level verification since it is the most convenient window both to the process and to the system.

The basic shadowing tool for Level 1 is the data historian function, where the required process data and control signals are collected continuously in the background and then presented in the graphical form. Live, high and medium speed, and historical time-based collections are used.

Level 2 tools include the diagnostic logs and various utilities.

Model tools include the engineering logs and specialized reports accessing the process data from database servers and presenting them in the desired (graphical and textual) form.

3.2.8.4 Ghost Bar Rolling and Switchover Trials

Whenever a new system is switched to active control, the ghost bar rolling is always tried first as a last verification test before attempting to roll real steel.

Ghost bar rolling provides a convenient method for verifying readiness of mechanical and electrical equipments, as well as the automation system itself. The phantom ("ghost") bar is created on the process entry, then it is tracked throughout the entire process. The technological process inputs (normally generated by real metal), such as tracking sensors, pyrometers, load cells, etc., are simulated by a process simulator using physical tracking integrations for realistic timing behavior. Since simulated inputs are acting in parallel to real ones, the real control logic can be verified on all system levels. References are distributed to transport drives and position regulators, descale sprays, etc. Real mill equipment responds as if real bar were moving through the process. Ghost bar functionality built into modern control systems contributes to shorter start-up periods, saves possible material losses, and aids in the regular system and mill maintenance procedures.

The intermediate switchover trials are performed during regularly scheduled maintenance shutdowns. After ghost bar rolling, some test slabs will be rolled. Besides normal situation rolling, other possible abnormal scenarios, including manual interventions, should be tested. This will minimize the production ramp-up period after the final switchover and give the operators adequate familiarization with new controls.

After a few test slabs are rolled under new system, the mill is then switched back to the old control. The test results are evaluated and any control errors are fixed. It is expected that due to the parallel paths of communication, either by

double-wiring of I/O or by control networks interfaces, the switching between two control systems should be rather short (not exceeding 30 minutes). Most of the switching should be done in software using control arbitration logic; however, some hardware switches may be required.

The usage of unscheduled mill delays, such as major cobbles, mechanical breakdowns, etc., should be maximized. This can be achieved by close coordination of the installation activities and mill operations.

When process shadowing and switchover trials are successfully completed, the new system is put into permanent operation.

3.3 CHINA STEEL HOT STRIP MILL MODERNIZATION PROJECT

A good example of the complex modernization project should include both mechanical and electrical/automation portions. The upgrade methods described earlier were applied to the electrical/automation part of this project. Significant planning and management efforts were also needed to coordinate the whole project. The project has been implemented in China Steel Hot Strip Mill #1. The 1730-mm high-production Hot Strip Mill #1 is part of the China Steel Corporation (CSC) steel complex located in Kaohsiung, in the southern part of Taiwan. This mill has been expanded and modernized several times during the last two decades.

3.3.1 1730-mm Hot Strip Mill #1 History

The China Steel HSM #1 began production in 1982 with basic mechanical equipment supplied by Mitsubishi Heavy Industry and electrical equipment from General Electric. The mill started with two reheating furnaces (250 t/hr each), a stand-alone vertical edger (VE1), one reversing roughing mill (R2) with front and back edger (VE2 and VE3), a six-stand finishing mill (F1–F6), and two downcoilers (#1 and #2).

Production reached 2 Mt/yr within one year after start-up. The maximum thickness was 12.7 mm, and stainless steel grades were introduced into the product mix.

The first mill expansion to increase production capacity was conducted in 1987. The mill additions included the following:

- Two reheating furnaces (250 t/hr each)
- New reversing stand (R1) in front of the existing R2
- Two closed-coupled roughing stands (R3 and R4) with front edgers (VE4 and VE5)
- New finishing mill (FM) stand (F7)
- New downcoiler #3 with hydraulic actuators
- Edger VE5 was equipped with hydraulic automatic width control, all FM stands had roll bending, stands F4–F7 roll shifting, stands F6 and F7 short-stroke hydraulic automatic gauge control (AGC)

The mill production quickly reached the design capacity of 3.7 Mt/yr. The maximum strip thickness was increased to 25 mm, and new alloy steel grades were introduced.

The constant increase of product quality requirements by steel customers, as well as obsolescence of electrical and automation systems, justified the next upgrade almost 10 years later.

The mill upgrade from 1995 to 1997 included the following:

- Augmentation of work roll bending on all FM stands from 90 to 200 tons per chock
- Widening of work roll shifting range (F4–F7) from ±75 to ±150 mm
- Addition of the short-stroke hydraulic AGC on stands F4 and F5
- New DFEs for DC drives (ca. 200 drives)
- New Level 1, Level 2, HMI, and process technology control system

The latest modernization project was undertaken in the mid-2000s. Major modifications to the mechanical and electrical equipment were implemented on both the entry and exit sides of the rolling mill. A slab sizing press (SSP) was installed in front of the roughing mill, and on the FM exit, all new runout tables (ROTs), laminar cooling system, downcoilers, and coil handling equipment were installed.

The mechanical equipment was supplied by IHI (SSP) and MH (coilers and ROT cooling) from Japan. The electrical equipment and automation were supplied by TMEIC GE Automation Systems from the United States. This latest mill modernization project is described in detail below.

3.3.2 Actual Mill Configuration and Basic Data

The basic mill equipment included the following:

- Four walking beam reheating furnaces
- SSP (new; original vertical scalebreaker was removed)
- Reversing roughing mill #1
- Reversing roughing mill #2 with front and back edgers
- Closed-coupled RM #3 and RM #4 with front edgers
- Intermediate (delay) tables with thermal covers
- Crop shear
- Seven-stand finishing mill with interstand cooling
- ROTs (new)
- Laminar cooling system (new)
- Three downcoilers (new)
- Coil conveyors with banders, coil shape meters, scales, and markers (new)
- Automatic surface inspection system (new)

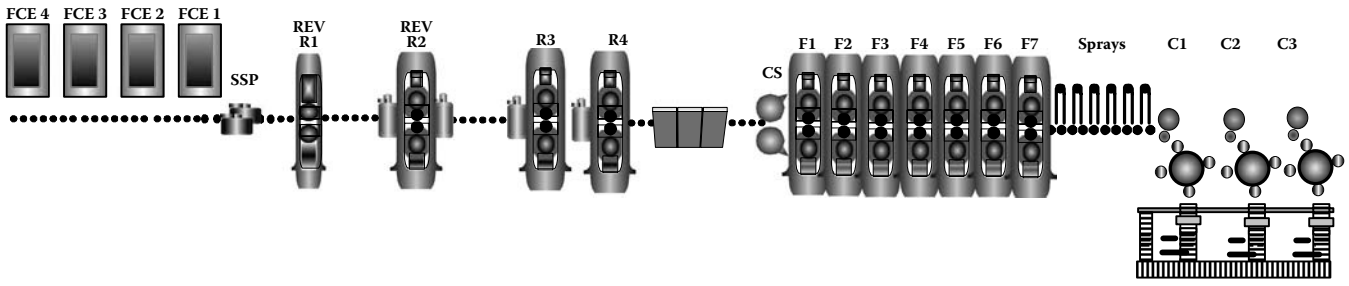


FIGURE 3.6 CSC HSM#1 mill configuration.

The basic mill data were as follows:

- Slab dimensions range: thickness: 150–270 mm; width: 700–1575 mm; length: max. 9000 mm
- Strip dimensions range: thickness: 1.2–25.4 mm; width: 700–1575 mm
- Types of steel grades rolled: ultralow, medium, and high carbon; HSLA; stainless; DP; API X80; TRIP

Figure 3.6 shows simplified mill configuration.

3.3.3 The Scope of the Mill Modernization

Two separate projects were closely coordinated and executed in parallel to optimize the utilization of the production shutdowns and manpower resources.

- Downcoilers and strip cooling system installation
- SSP installation

3.3.4 The Downcoilers and Strip Cooling Modernization

The main objectives are as follows:

- To increase final strip thickness from 20 to 25.4 mm
- To produce special steel grades, which meet specific structural requirements such as DP, API, TRIP grades
- To achieve better coil presentation and quality (telescopicity, head marks, etc.)
- To improve the operation of the coil handling area

In order to achieve these goals, the following equipment and functionality were implemented.

3.3.4.1 Mechanical Equipment

The mill was originally equipped with three downcoilers, two identical and a third one with higher power and hydraulic actuators dedicated to coil heavy products. They were replaced by three new identical, universal wide-range coilers. Each new coiler is equipped with four unit rolls and variable expanding mandrels. The sideguides, pinch rolls, and unit rolls have hydraulic gap/force actuators.

To provide the ability of coiling heavier and much harder products, the mandrel power was increased by 35% to 1100 kW per coiler. The coil diameter ranges from 1140 to 2200 mm with a coil weight of up to 37 tons.

The coil handling area was completely reconstructed. Three walking beam conveyors were installed to transport coils from the individual coilers to chain-driven cross conveyors. At the end of the chain conveyors, the coils are picked up by an overhead crane and transported to the coil storage bay. A new shuttle car provides the coil handling between individual conveyors and a new coil inspection station. A banding machine, weigh scale, and paint marker (actuated by robotic-driven arms) are installed at each individual conveyor. In addition, at each conveyor, a laser coil shapemeter was installed to measure the straightness of coil sidewalls. Figure 3.7 shows the coiler exit and coiler handling area.

To provide better thin-gauge strip transport and to fit the tables' geometry into the new cooling system, the FM ROTs were modified to decrease the roller pitch to 360 mm. The total number of rollers, including new carryover tables, was increased to 435 rollers. The existing 295 rollers were re-used in the new ROT arrangement.

The requirement for producing new steel grades with specific metallurgical properties resulted in the implementation of a new laminar cooling system on the ROT. The water capacity remained the same as in the original system; however, the characteristics of the cooling system were significantly changed. The number of individually controlled valves was increased to provide better cooling controllability. Each header is fed directly from the overhead tank through an individual pipe, thus eliminating the interaction between sprays (known as "cross-talk") during turn on/off actions. The ROT spray system characteristics are as follows:

- 432 spray controllable units (240 top and 192 bottom) in 15 banks
  - Banks 1–4 and 13–14 are intensive banks
    - 16 controllable units top, each 1700 lpm flow
    - Eight controllable units bottom, each 1700/2380 lpm at low/high flow

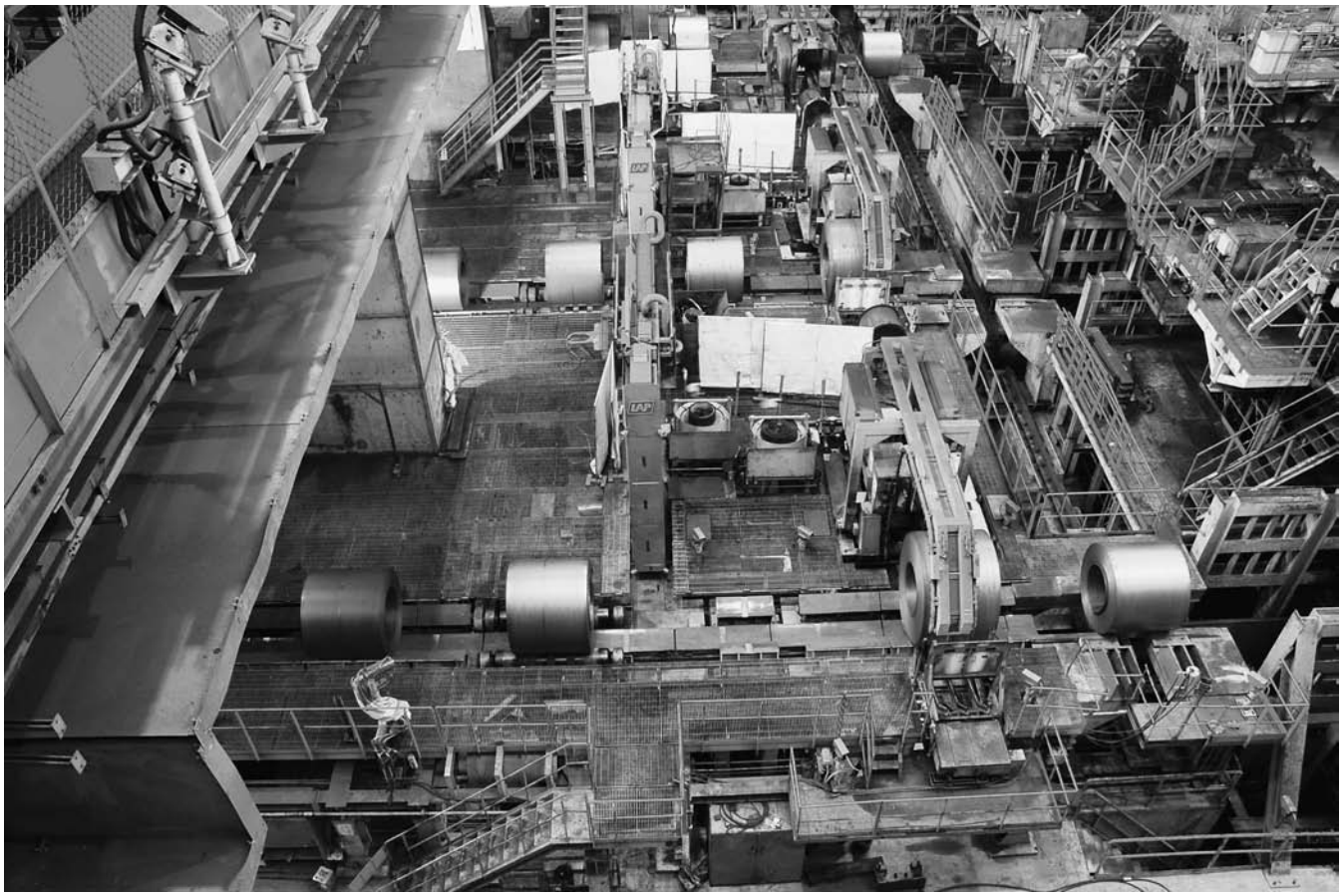


FIGURE 3.7 New coiler area. (From W. Filipczyk, C.H. Lin. *Iron & Steel Technology*, May 2007. With permission.)

- Banks 5–12 and 15 are fine banks
  - 16 controllable units top, each 850 lpm flow
  - 16 controllable units bottom, each 850 lpm flow
- Total available flow
  - Four-pump operation: 256 m^3/min (256,000 lpm)
  - Five-pump operation: 320 m^3/min (320,000 lpm)

Figure 3.8 presents new ROTs and a laminar cooling system. Please note the piping from the overhead tank to the cooling headers.

3.3.4.2 Electrical Equipment and Control System

A new electrical building for the downcoilers was constructed on the drive side of the mill. The new control rooms house the switchgear, transformers, drives, and Level 1 controllers. All new motors and drives are based on variable frequency, state-of-the-art AC technology.

The new control system was based on the following platforms:

- LEVEL 1—GE Innovation Series Controllers (registered name of General Electric Co.)
- HMI—Wonderware ArchestrA system
- LEVEL 2—PC Windows based with database server

The Level 1 controller for laminar cooling directly controls all ROT cooling spray valves. This controller, called a spray director, is responsible for executing coiling temperature control (CTC) model references in a timely manner, as well as performing sample tracking, and provides feedback information to the model.

The Level 1 soiler controllers perform the standard functions of strip tracking, reference distribution, and sequencing from FM exit to coil conveyor exit. Most important for coil quality are, however, the regulating functions implemented in individual coiler controllers. These include

- Various coiler sideguides operating/coiling modes:
  - For head and tail of the coil: short stroke (head and tail, head only, off)
  - For body of the coil: constant force, constant gap, oscillation (zigzag)
  - Symmetry selections: symmetrical, asymmetric drive side, asymmetric operator side



FIGURE 3.8 New ROT laminar cooling system. (From W. Filipczyk, C.H. Lin. *Iron & Steel Technology*, May 2007. With permission.)

- Various coiler pinch roll gap operating/coiling modes:
  - For tail/head and body: constant gap, constant force (total or independent)
  - For tail approach: tail fanning (unipolar vs. bipolar force regulator)
- Continuous (step-less) coiler mandrel expansion
- Various unit roll gap operating/coiling modes:
  - For head end of the coil: constant force mode
  - For head end of the coil: quick opening control (QOC) a.k.a. automatic jump control—gap/force mode
  - For head end of the coil: QOC—gap/gap mode
  - For body of the coil: thin/thick strip mode

The existing HSM #1 Level 2 system is based on Alpha VMS HW and includes the functionality to control and set up the entire mill. The functionality of the CTC model, as well as spray control (spray director) has been removed from this computer.

The new CTC model was implemented in a new PC Windows-based computer, while laminar and interstand spray controls were implemented in a new innovation controller (spray director).

The communication between the new Level 2 computer and new Level 1 is done via industrial ethernet control network using the global memory concept.

The communication path using interprocess service messaging was established between "old" existing Level 2 and new CTC computer. The required reference data, such as bar data, time–velocity–distance profile, etc. from existing Level 2, and required feedbacks (such as CTC interlocks, logging data, etc.) to the existing Level 2 are transmitted via this path.

Besides "standard" functionality to achieve desired coiling temperature, the CTC model supports strategies using various spray patterns including interrupted cooling ("dual phase"). Some of the most important features of the CTC model include:

- Flexibility in applying spray patterns:
  1. The activation sequence order of each top and bottom spray can be specified in each pattern database table.
  2. CTC will calculate the order in which sprays are used so as to achieve a target cooling rate, target air cooling time, forward or reverse activation, and differential cooling rates

for top and bottom surfaces of the piece. Target rates, times, and forward or reverse order are specified in each pattern database table. Calculated patterns can be used for both interrupted cooling, where early and late quench zones are separated by an air cooling region, and for noninterrupted cooling. In the case of noninterrupted cooling, a target air cooling time is applied as a dry zone at the beginning of the spray pattern sequence.

- Flexibility in prioritization of the control targets for interrupted cooling is based on the specific requirements for particular steel structures, for example, bainitic versus martensitic. The basic priority is as follows:
  1. Coiling temperature
  2. Intermediate temperature
  3. Early zone cooling rate
  4. Dry zone time
- Variable control sample length as a function of strip thickness.
- Comprehensive recording of the strip status along the whole length of the ROT. In addition to temperatures, mass flow and water flow, such parameters like heat losses, ferrite content, etc. are logged at the exit of each cooling bank.

New pyrometers were installed in the intermediate and final control locations. Both top and bottom surface temperatures were measured. The measuring range had to be expanded in the low temperature range down to 200°C. A laser velocimeter was installed at the coiler entry location to provide more accurate strip speed measurements, which are especially important for "short bars" where strip tails out of the FM before entering coilers.

The HMI system is based on the latest Wonderware ArchestrA architecture. This is an innovative approach to application integration and data interfaces in the HMI system. The centralized repository contains the definitions of process data objects (roller table, servo valve, electrical drive, etc.). These can be simply instanced and then deployed for the specific application. This provides centralized management of data interfaces, which allows for easy and quick modifications and additions in the HMI system.

Two sets of the control desks with HMI terminals were installed: one in the coiler pulpit and one in the FM pulpit (for future remote operation).

3.3.5 Slab Sizing Press Installation

The main objectives of slab sizing press installation are

- To improve caster efficiency by minimizing the number different slab widths
- To increase the width reduction capability of the mill resulting in faster order execution for customers
- To increase the capability of slab head/tail tapering (preforming) for yield increase and better final width uniformity

3.3.5.1 Mechanical Equipment

The SSP was installed in front of the first RM stand (R1) in the place of old vertical scalebreaker. This is a "flying" type of the press, which means that the slab is continuously moving while pressing is performed. Besides SSP, other mechanical devices in the RM area were added or replaced. The new mechanical equipment, shown in Figure 3.9, includes:

- RM entry descale box
- SSP main core with feed and hold down rolls
- SSP entry table (with Table Lift) and SSP exit table
- SSP entry, R1 entry, R2 entry/exit sideguides (hydraulic)
- R2 entry centering devices (2)

The basic characteristics of SSP are as follows:

- Maximum draft = 350 mm
- Pressing transport speed = 0.3 m/s
- Maximum force = 2200 tons
- Main motor power = 3400 kW

3.3.5.2 Electrical Equipment and Control System

The SSP is equipped with all AC motors and drives. The main motor was installed in the RM motor room on an elevated foundation since the main shaft is connected to gears mounted on the top of the press. SSP drives were located in the new control room inside the RM motor room. The main drive is based on the most advanced semiconductor technology utilizing IEGT elements.

A Level 1 controller (Innovation Series) was connected to the existing RM control network. The complete control functionality for SSP—microtracking, position and pressure regulators, die synchronization, sequencing, and auxiliary systems control—is performed by this controller. Due to the SSP mechanical capability of "on-line" dies reversal, several pressing modes were possible to implement:

- Forward press
- Reverse press
- Head/tail running preforming
- Head/tail stopped preforming

Level 2 control for the SSP involves RM setup (RSU) model. Existing RSU model functionality was augmented by the addition of SSP module to calculate the setup for the press and scan-associated process feedbacks. RSU allocates total width reduction required among SSP and RM edgers, and then calculates the SSP setup. The references and auxiliary calculated values include die gap opening, press draft, head/body/tail deformation forces, hold down roll force,



FIGURE 3.9 Slab sizing press. (From W. Filipczyk, C.H. Lin. *Iron & Steel Technology*, May 2007. With permission.)

head/body/tail width reduction ratios, head and tail preforming lengths, exit head/body/tail thicknesses, elongation ratio, and travel time.

Some of the process feedbacks, such as measured gap, force, temperature, etc., are used for model analysis and off-line tuning. The adaptive loop is based on the width feedback measured on the exit of R1 stand.

New width gauges with thermal profile measurement capability were installed in front of SSP and at the exit of the R1 stand. At the entry to SSP, the slab width is scanned and is used to generate the final RSU setup. The R1 stand exit gauge is used for model feedbacks and the "feedforward" setup. The thermal profile is used for off-line analysis of furnace heating practices and correlation with bar camber.

3.3.6 Project Implementation

The two projects described above were led separately during the bidding and contractual phase. However, the implementation in the mill was fully coordinated to take full advantage of the planned mill downtime. The two projects had different mechanical suppliers but the same electrical/automation supplier. The coordination of both products also resulted in optimum use of electrical supplier resources, thus minimizing the installation and commissioning cost.

The major execution steps for each project are presented in Figure 3.10.

3.3.7 General Project Schedule

3.3.7.1 Coilers Area

The first step in the project was to erect foundations for new coilers and new coil handling area, as well as build new coiler electrical building. The new foundations were located behind any of the active mill equipment, thus not interfering with mill operation.

After new mechanical and electrical equipment for oilers was delivered to the site, the mounting and installation of new Coilers #4 and #5 was done while the mill was in full operation.

The start-up of the electrical and automation equipment followed. The coiler area fluid systems were commissioned first to make sure existing coiler operation was supported by the new control system. The new HMI system was implemented from the very beginning since it could be used to control both old and new equipment. The new Coilers #4 and #5 were started, checked, and tuned under no-load conditions while the mill was running with the existing #3 coilers. Having the new equipment and control logic thoroughly checked out before putting it to rolling operation contributed

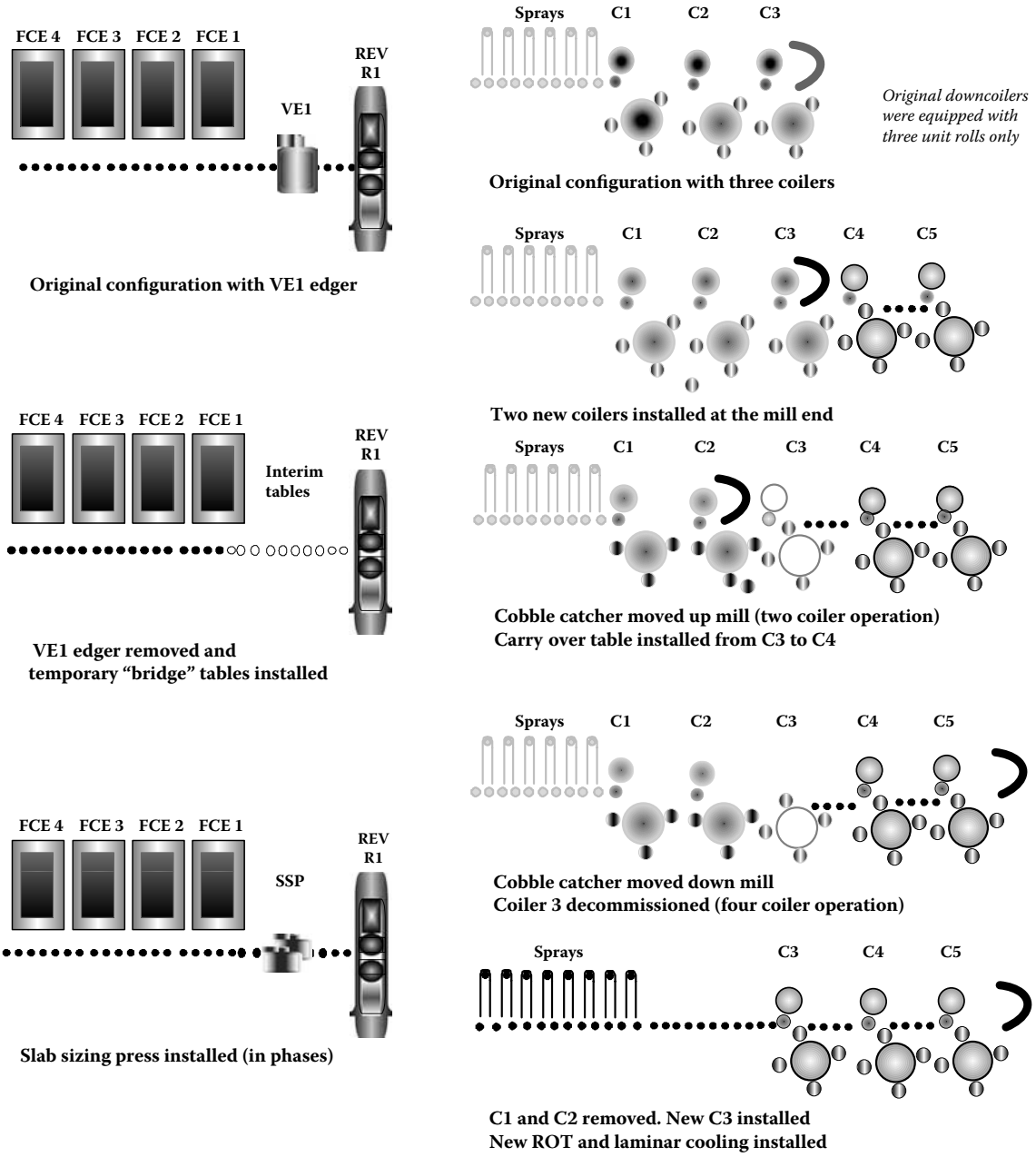


FIGURE 3.10 Project implementation concepts. (From W. Filipczyk, C.H. Lin. *Iron & Steel Technology*, May 2007. With permission.)

to a very smooth switchover. Thorough shadowing was conducted to verify the new coiler master and sequencing functions, so that future addition of new coilers will be bumpless and have no impact on production. New controllers were connected to the existing system via network bridging.

A 1-day shutdown for Coiler #3 stoppage (Coilers #1 and #2 remained in operation) was used to prepare for the installation of the carryover table between existing Coiler #3 and new Coiler #4. The cobble catcher was moved from behind Coiler #3 to Coiler #2. For the next 2 weeks, the mill was operating with two existing coilers while the carryover table installation was completed. After this, the mill was shut down for 1 day for electrical tests, and the cobble catcher was moved behind Coiler #5; thus, two new coilers were added to the mill operation. Due to the mechanical obstruction, the existing Coiler #3 had to be put out of service, so the mill was then running with four active coilers. This operation continued until the main shutdown. During this time, the old Coiler #3 was being decommissioned and new mechanical and electrical equipment installed to the greatest extent possible during mill operation and regular maintenance shutdowns.

3.3.7.2 Slab Sizing Press

The first step of SSP installation was removal of the vertical scalebreaker between Furnace #1 and RM Stand #1. The edger

had to be removed since the short distance from the furnace to the first stand did not allow for adding the SSP in the space available without doing so. This was done partly during rolling operation. When the mill went into a scheduled 14-day shutdown, the removal of the vertical scalebreaker was completed, the new foundation for SSP was erected, and a temporary "bridge" table section was installed. The mill then operated without a vertical scalebreaker for almost a year until the main shutdown near the end of the project. During this time, the civil engineering and mechanical work continued, and SSP equipment was partially put into place. The electrical and control equipments for SSP and RM sideguides were also installed during that period.

3.3.7.3 Main Shutdown for Both Projects

The main shutdown was scheduled initially for 40 days, then planned for 35 days, and finally, due to the excellent execution of the mechanical and electrical work, was shortened to 30 days. This shutdown combined the activities for both projects. The major tasks included

- Removal of temporary SSP "bridge" tables and existing RM sideguides
- Installation of new SSP and RM mechanical equipment, piping, and wiring
- SSP start-up, cold test, and then hot load test
- Removal of old ROTs, laminar cooling system, Coiler #1, Coiler #2, conveyor area equipment
- Civil engineering, mounting and installation of new ROT and laminar cooling system
- Completion of mounting and installation of Coiler #3
- Mounting and installation of conveyor equipment, scales, banders, and markers
- Start-up of all new equipment and no load tests
- Coordinated "ghost bar" rolling

3.3.8 Mill Start-Up

The mill started regular production 5 days ahead of the original schedule.

The mill ramp-up to production was very rapid, since within just a few hours after start-up, the mill was up to the normal level of production. Taking into account the scope of the new equipment and supporting control functions, which had to perform flawlessly within such a short time, this was an enormous accomplishment.

The quality ramp-up was very quick as well since within the first week, new CTC performance was at the level (or better) of the old system. The number of coils out of tolerance or coils requiring reclassification (due to coiling temperature) was extremely low and far below expectations. Within the first 5 weeks of rolling, only 40 coils needed to be diverted because of quality, but they were still saleable products.

The initial tune-up work was completed within 1 month. Final tuning was performed 3 months later when new products were scheduled for production.

The tune-up, which required special attention, included specialty steels where single coils are rolled, results are tested, and changes made as necessary with the goal of achieving the target material properties. CTC pattern and rate calculations were being configured to meet the bainitic and martensitic control priorities.

The SSP was put into operation within the first week after the main shutdown. Within 3 days of operation, the drafts taken were increased to a maximum of 350 mm.

3.3.9 Project Highlights and Milestones

- The delivery of mechanical equipment: 16 months for coilers, 16 months for SSP
- The delivery of electrical equipment: 14 months for coilers, 14 months for SSP
- The mill began operation with all new equipment 24 months after the contract was finalized
- The final acceptance test was performed in 5 months after switchover
- Three production shutdowns were dedicated to project execution
- Total extra days of shutdowns (beyond routine maintenance shutdowns) = 24 days

3.3.10 Results

The final results can be presented using the process measurements and production data, comparing them with the objectives specified or expected for each project.

3.3.10.1 Cast Slab Width Range

The number of different slab widths ordered from the caster was reduced from 19 to 7 due to the increase in width reduction capability by SSP. The caster efficiency was significantly increased.

For the HSM #1, 85% of cast slab widths are 1050, 1270/1280, and 1420 mm, thus the mold change frequency is extremely reduced. The financial gain for the caster department results in annual savings of about $2 million.

3.3.10.2 Coil Width Performance

After implementation of SSP and retune FM width spread model, the width performance (as measured on FM exit) increased from 90% to 95%, ±4 mm of all rolled length for all rolled coils.

3.3.10.3 Material Properties for New Products and CTC Performance

The primary goal with respect to material property was to be able to use dual phase cooling to produce bainitic and martensitic steel.

For bainitic products, the goals were

- To quench to an intermediate temperature
- To provide an air-cooling region (fixed and narrowly constrained) to allow ferrite formation in an approximately isothermal setting
- To quench to a final temperature in the range of 400°C

For martensitic products, the goals were

- To quench to an intermediate temperature
- To provide the maximum amount of air cooling (the intermediate temperature can be sacrificed to provide max. air time)
- To quench as rapidly as possible to a final temperature in the range of 200°C

These goals were fully achieved with the new ROT cooling system and CTC model functionality.

CTC performance was improved to achieve ±15°C for 97% of all rolled and evaluated products.

Additionally, shortening of the ROT roller pitch has resulted in the possibility of reducing the "hot head end" of the very thin strip from a minimum of 100 m to 0 with stable coiler thread.

3.3.10.4 Coil Presentation

New measuring devices (laser shapemeter) were installed at the exit from each coiler for automatic, no-contact measurements of coil telescopicity (side wall).

The example of a coil side-wall measuring report is presented in Figure 3.11.

The coil parameters related to its coiling process and coiler equipment and control performance were achieved at the following levels:

- Telescopicity and wrap protrusion within ±15 mm
- Head end marks (indentations):
- First wrap ≤ 0.050 mm
- Second wrap ≤ 0.030 mm
- Third wrap ≤ 0.020 mm
- Fourth wrap = None

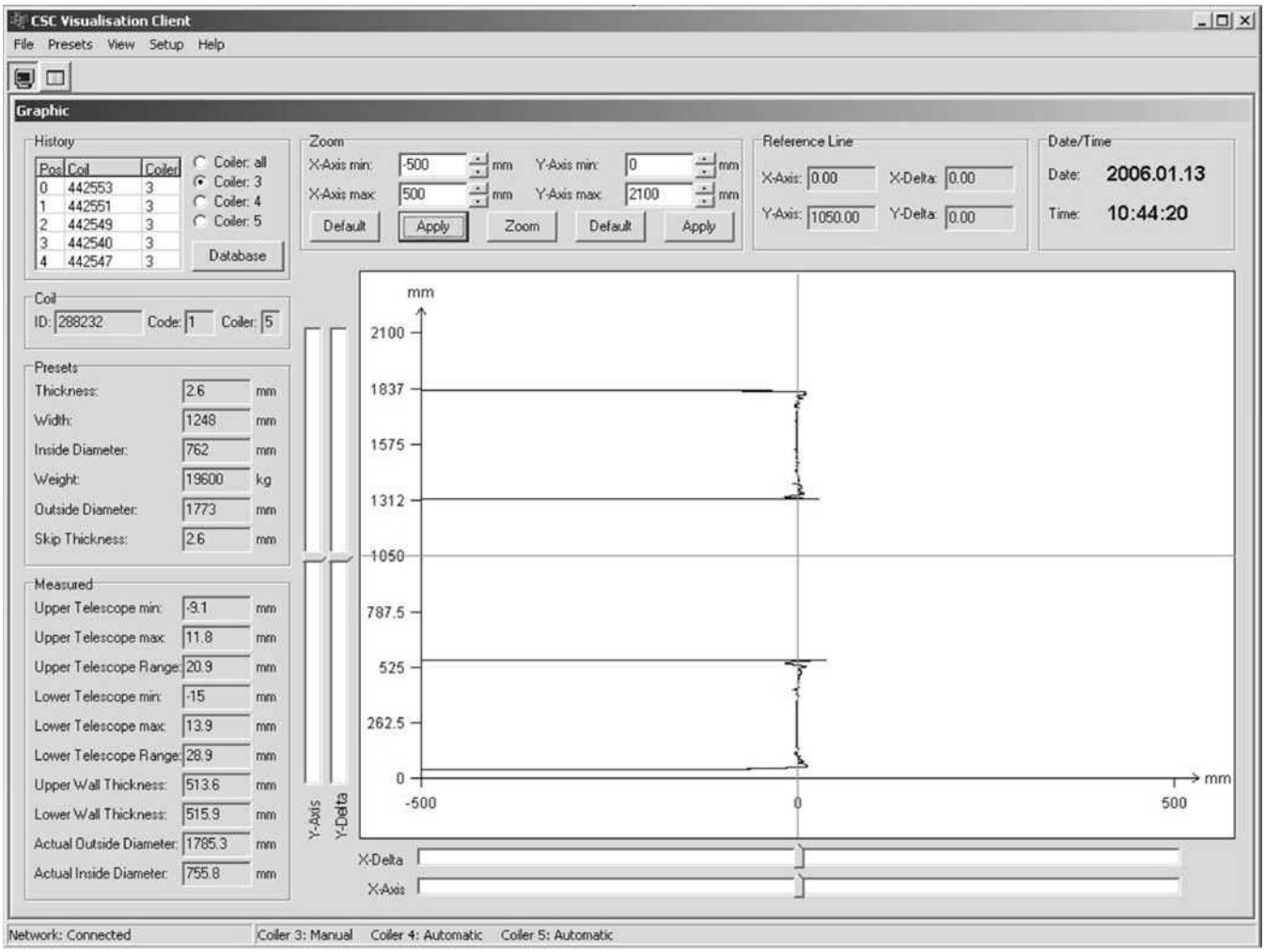
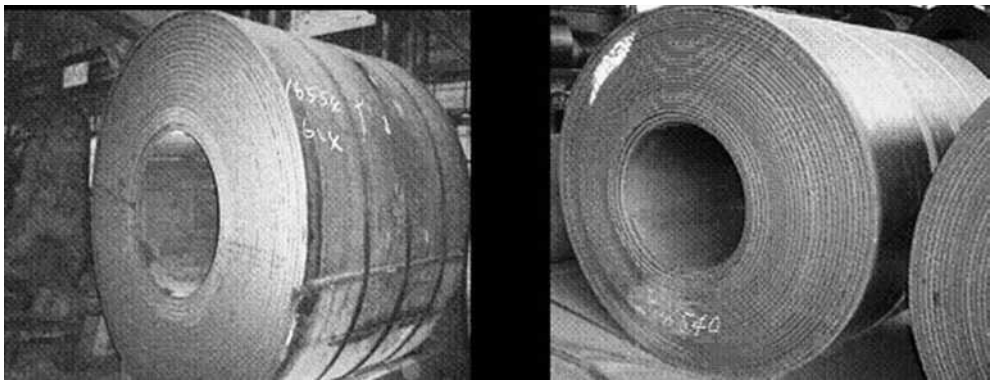


FIGURE 3.11 Coil telescopicity report. (From W. Filipczyk, C.H. Lin. *Iron & Steel Technology*, May 2007. With permission.)



Thickness 25.4 mm SS400C Thickness 20.0 mm API X80

FIGURE 3.12 Examples of heavy thickness coils presentation. (From W. Filipczyk, C.H. Lin. *Iron & Steel Technology*, May 2007. With permission.)

The thickness of the products was increased to 25.4 mm with excellent coil presentation results; see Figure 3.12.

3.3.10.5 Coil Shape Defects

All coil shape defects (including telescope, protrusion, loosely wrapped coil, oval coil, and nonmatching diameter) were reduced, as shown in Table 3.1.

3.3.10.6 Coil Surface Defects

Coil surface defects (include gouge, pinch roll mark, pincher, rolled-in object, head mark) were reduced from 23.6% to 15.4% due to the improvement in the coil shape. The pincher defect increased initially from 3.6% to 36.2% because of changing the pinch roll gap control to hydraulic actuators. After tuning the control of pinch roll and sideguides, the cut length weight percentage due to the pincher was reduced (annually) from 0.28% to 0.16%.

In order to improve the coils quality even more, the optical surface inspection system was installed at the entry to the coiler area.

The benefit of automatic surface inspection systems are summarized in Table 3.2.

All surface defects are flagged from the system, thus they can be handled much more quickly than before.

3.3.10.7 Decrease in Mill Delays

The production delays due to failure of the electrical equipment before and after revamp of down coiler area were dramatically reduced. There were outages totaling 4851 min during the year before switchover, and *zero outages* during the year after switchover. Only a ROT motors tripped twice and was replaced due to a frozen bearing.

Table 3.3 presents a comparison of delays with instances of failure/total time lost (minutes).

TABLE 3.1
Coil Defects Comparison

Defect	Before (1 year) (%)	After (1 year) (%)
Telescope	16.9	0
Protrusion	17.6	4.6
Loosely wrapped coil	50.9	0.5
Oval coil	20.8	0
Nonmatching diameter	22.6	0

TABLE 3.2
Surface Inspection Benefits

Quality	Before	After
Coil inspected due to defect (times/per month)	39.5	6
Coil rejected because of roll mark defect (ton/per month)	496.73	275.5
Coil rejected owing to rolled in scale (percentage of production)	0.121%	0.077%

Source: W. Filipczyk, C.H. Lin. *Iron & Steel Technology*, May 2007. With permission.

TABLE 3.3
Mill Delays Comparison

Reason	Before (1 year)	After (1 year)
Mandrel	14/747	0
Pinch roll	3/85	0
Wrapper roll	4/57	0
Run out table	18/3962	2/127

Source: W. Filipczyk, C.H. Lin. *Iron & Steel Technology*, May 2007. With permission.

3.4 SUMMARY

The SSP laminar cooling and coilers were large-size projects providing significantly positive results on mill production in both productivity and in quality. Scheduled shutdowns were necessary for such a large amount of mechanical and electrical

equipment to be installed but were reduced to minimum durations. Besides the major configuration change at the front of the mill (SSP addition), the entire mill exit area (from the last FM stand to coil storage) was replaced with new equipment and control.

The proven methodology of control system modernization was applied, including control networks bridging, parallel operation of HMI, shadowing, and ghost bar rolling. This contributed to bumpless control switchover and virtually eliminated negative impact on mill operation.

This careful and coordinated approach to phased implementation resulted in minimum production disturbances during start-up periods after shutdowns. The ramp-ups to normal production levels were almost nonexistent, while quality also quickly improved to levels higher than before modernization.

The mill production has remained steadily above 4 Mt/yr level during the last several years.

REFERENCE

Filipczyk, W., and Lin, C.H. Pressing, cooling and coiling—China Steel HSM #1 Major Upgrade Project. *Iron & Steel Technology*, May 2007, 4(5): 301–311.

4 Plate Mill Upgrades for High-Strength Products

J. F. Evans and P. Sopp

CONTENTS

4.1 Overview 55
4.2 Introduction 55
4.3 Aspects of the Marketplace for High-Strength Plate 55
4.3.1 Linepipe 55
4.3.2 Ship Plate 56
4.4 Key Features of the Upgraded Mill 56
4.5 Upgrading of Motors and Drives 60
4.6 Conclusion 60
References 61

4.1 OVERVIEW

Due in large part to investment in China and India, the first decade of the 21st century has added twice as much plate producing capacity to the overall world steel output than did the preceding 30 years. The many application sectors driving this expansion are in infrastructural construction, including pipeline for oil and gas, and shipbuilding. The product mix of new mills is moving upward in width and thickness and toward higher tensile strength. This chapter reviews the resulting changes in the mills themselves and focuses particularly on the ways in which existing mills operated by established plate manufacturers are being upgraded.

4.2 INTRODUCTION

There is nothing new about the steel industry's pursuit of higher-strength plate products. That was the objective that drove the original development of micro-alloyed steels some 40 years ago. Neither is there anything novel about the need to maintain, or better still to improve, the plate's other properties in these high-strength variants. Toughness and weldability, as well as a whole range of application-specific quality attributes, remain as important as ever.

In recent years, the thing that has really changed is the pace of development. The economic benefits of light-weighting are becoming ever more significant in the shipbuilding and pipeline industries. The traditional methods of increasing product strength, such as increasing alloy content or using more extreme rolling schedules, are no longer guaranteed ways for the plate mill to maintain its competitive advantage. Application and process development, in turn, drive plant development, and the emergence of a range of technologies allows platemakers to upgrade their manufacturing facilities and to establish and keep a market-leading position.

4.3 ASPECTS OF THE MARKETPLACE FOR HIGH-STRENGTH PLATE

Two high-volume applications of steel plate dominate today's technical advances in the sector. These are linepipe and ship plate. The powerful and sophisticated business organizations that make up these application sectors dictate the quality standards and accreditation criteria for these products.

The strongest plate products of all, though, have different applications. They include wear-resisting steels and military armor and belong to a class of steels that develop their properties through postrolling heat treatment. Both these product groups influence the technology of the mill and its upgrades.

4.3.1 Linepipe

This technically demanding product is also the one that is exhibiting the greatest demand growth. It's a truly global demand, too, since developing and established economies alike need to extract oil and gas from increasingly remote and inaccessible reserves. A new pipeline infrastructure is spanning the earth, reaching into polar wastes and ocean depths, exploiting ever-higher line pressures and pipe diameters. Its growth will continue for another 50 years, and the enterprise of the energy sector is going to dominate the design of plate mills for the foreseeable future.

4.3.2 Ship Plate

The rise of the economies of Eastern and Southern Asia is driving unprecedented increases in ocean freight capacity, bringing tankers, bulk carriers, and container vessels to the fore. One double-hulled crude carrier may use up to 40,000 tons of plate in its construction. Technical advances in shipbuilding, such as the advent of laser cutting and welding, are also imposing new demands on plate quality. Wider plates are sought, thus reducing the number of welds per hull. Thinner hulls (to the point of tolerating a measure of plastic yield in service) are increasingly permitted, and topside structures are being aggressively lightened compared with traditional designs (Figure 4.1). Developments in fabrication technology make complex bulkhead structures economically feasible, and the old notion of structural strength founded in plate thickness is disappearing into history.

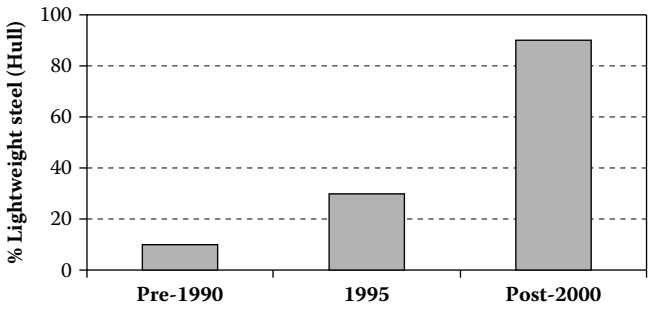


FIGURE 4.1 Increase in the proportion of thin steel plate (less than or equal to 10 mm) being used in U.S. Navy vessel construction. (Adapted from McPherson, N. A. 2006. *Iron and Steelmaking* 33(3): 190–192.)

It's clear why both of these dominant application sectors require higher-strength steel. There are other common attributes of the two markets—the strength must be won without degrading weldability and wider plates are also sought. The main difference is that shipbuilding is tending toward a thinner product, whereas large-diameter linepipe is, if anything, getting thicker (the thin, low-pressure end of the pipe market is seeing increasing penetration by plate-coil route product and spiral welding). Linepipe alloy design is also more diverse because of the variety of application environments, both inside and outside the pipe.

There is, of course, no easy and economically attractive way to substantially widen an existing plate mill. Everything else that's needed for the developing steel plate markets, however, is achievable through a well-planned upgrade with selected technology. It's now time to look at how the product requirements translate into mill design attributes.

4.4 KEY FEATURES OF THE UPGRADED MILL

Certain parameters of an existing mill stand are difficult and expensive to alter. The width has already been mentioned, but the maximum roll separating force is almost as resistant to significant increase. The torque and the power are a little easier (via remotoring, which we discuss later), but are still at the costly end of the upgrade spectrum. Taking all this into consideration, we can see that an ideal solution is an ability to roll the new product in a way that doesn't require an increased mill duty. At the same time, of course, we must ensure that throughput is also maintained: an upgraded mill that needs a lot more passes to roll a given product than does a rival's brand new mill has a weak competitive position.

The only way to do this is to substantially develop the strength of the steel after rolling is completed. The central technology, therefore, is going to be the accelerated cooling system.

In fact, it's not only the upgraded mill that relies heavily on the accelerated cooling system to make the linepipe and ship plate products described. A new mill (with its generally higher power and load capacity) is scarcely less dependent. This is because the strengthening mechanisms that most increase rolling forces and torques (solid solution mechanisms) are constrained in their use by their effect on weldability. Microalloying, in combination with thermomechanical controlled rolling (TMCR), develops strength through two additional mechanisms: grain refinement and precipitation. Both become effective only at lower temperatures, and both are enhanced by postrolling cooling at high rates. Used assiduously, the TMCR process enhances strength and toughness together, and throughput can also be maintained by exploiting multipiece rolling techniques (Figure 4.2) [1].

TMCR products exhibit high deformation resistance in the late passes, once recrystallization has ceased. To maintain flatness, wide and thin plates need a schedule with a long **tail**, a sequence of finishing passes at descending loads, and coupled with elevated hot strength, this can extend the rolling time to uneconomic levels. Profile actuators based on axial roll-shifting provide a means to alleviate this effect, allowing the finishing loads to be maintained near to mill capacity by progressively increasing the effective roll gap crown.

The microstructural development of high-strength plate is now sufficiently understood to be incorporated in model-based process control systems. Variants developed specifically for the plate mill and its products are now in use and cover both rolling and cooling phases, allowing maximum asset utilization to be achieved within product metallurgical constraints [2].

Accelerated cooling systems are probably the most active field of upgrade investment in plate mills today (Figure 4.3). These systems first appeared in Japan in the 1980s, and for many years, the only technology available elsewhere was laminar cooling devices adapted from the hot strip mill application. Operational experience has proved, however, that exploitation of high cooling rates requires specialized design. High cooling rates (Figure 4.4) mean that products that used to be made exclusively in an off-line roller, quench-and-temper operation can now be made in-line by exploiting the rolling heat—a true direct quench duty. The same systems can be used in a more conventional accelerated cooling mode

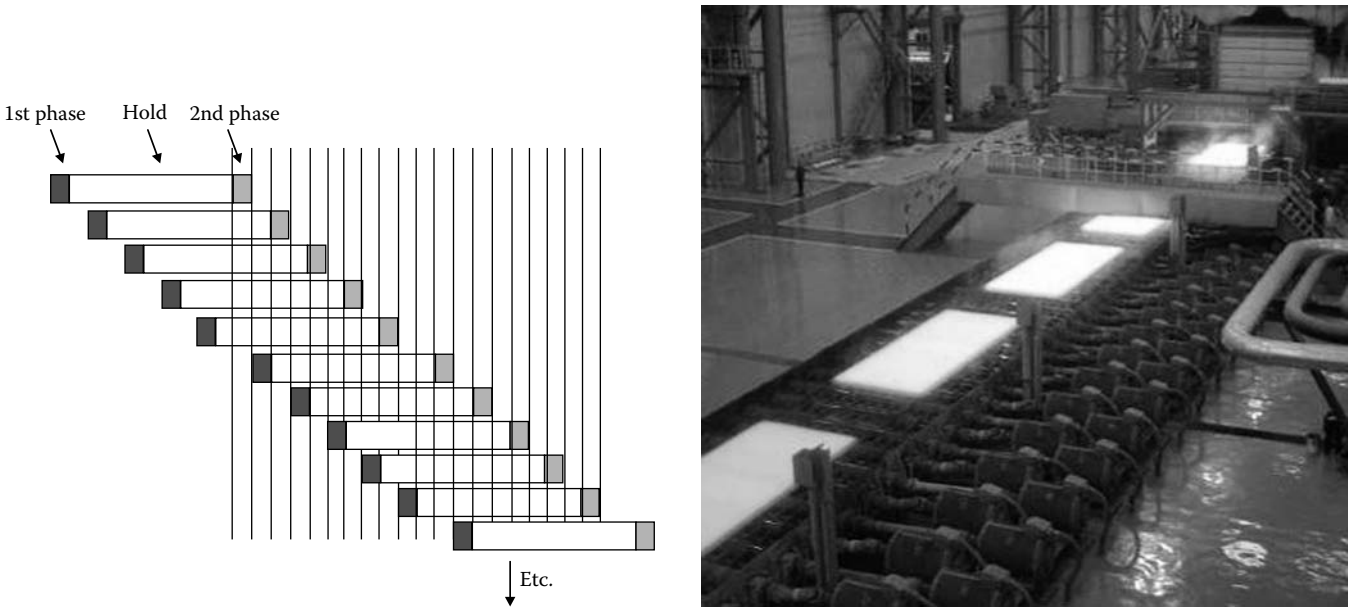


FIGURE 4.2 Schematic of the interleaving of TMCR plates, maximizing asset utilization, and pacing uniformity.

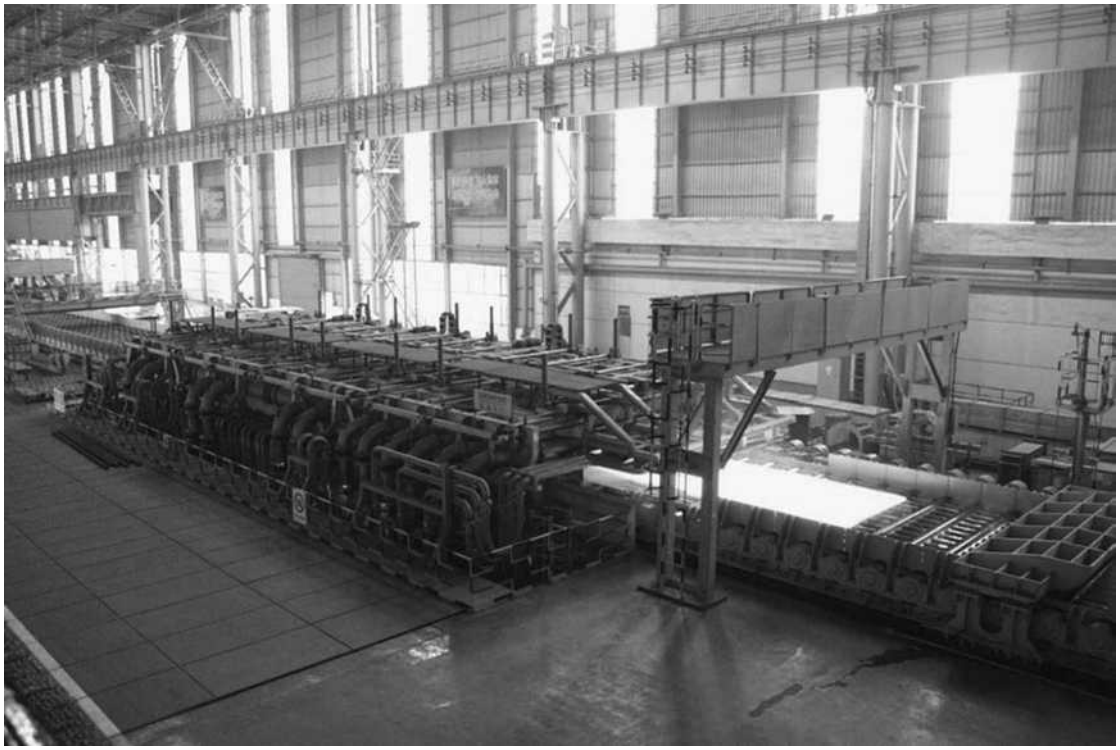


FIGURE 4.3 MULPIC (Multi-Purpose Interrupted Cooling) accelerated cooling system in operation.

for developing the properties of controlled-rolled products including linepipe and high-specification ship plate. Further down the specification range, the system can provide internal business return for the user by allowing equivalent properties to be achieved at lower alloying levels and/or elevated finishing temperatures.

Strength and toughness are maximized together by the finest possible grain size, which, in turn, demands the highest achievable cooling rates. To characterize the most advanced accelerated cooling systems simply as fast-cooling technologies is to underestimate their potential, though. In conjunction with a suitable control system, they become precision metallurgical tools. They can take the plate though a complex time-temperature path, so that the metallurgical mechanisms designed into the alloying practice are exploited with optimum efficiency and accuracy.

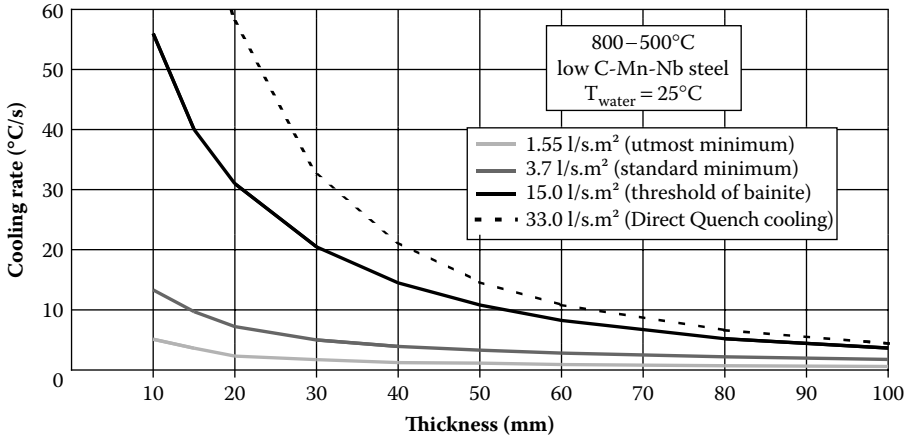


FIGURE 4.4 MULPIC system—typical cooling rates.

As has already been observed, TMCR rolling invokes a complex interplay of different microstructural processes in multiphase regimes—the cooling system is the instrument to control them.

Full-surface uniformity is the practical prerequisite in cooling systems, and the design feature that ensures plate mill accelerated cooling technology is set apart from simpler strip mill variants. The plate has to stay flat, not just to avoid costly downstream rectification, but more fundamentally, to apply uniform microstructural control. Full-surface uniformity ultimately underwrites the dual-product attribute of well-controlled mechanical properties and maximized yield. There are ancillary asset benefits to such uniformity, too—a relatively small preleveler with a full set of frame and roll bending modes can suffice for hot leveling, which might otherwise demand a much bigger machine downstream of the accelerated cooling (AC) and direct quench (DQ) units.

Levelers, both hot and cold, are themselves an area where relatively modest investment can generate high return in terms of improved operational efficiency and increased prime yield [3]. The performance of a leveler varies significantly with the products it processes, so that the optimum roll arrangement is characteristic of the mill's product mix. As has already been noted, the migration to higher-strength products usually also entails a reduction in average thickness, and the two effects in combination can shift the critical operating conditions of a leveler a long way. In upgrade terms, this means that the adaptation of an existing leveler for a changed mix can deliver major performance improvement. Process control upgrading is effective, too, with modern hydraulic gap adjustment systems maximizing process flexibility and overload protection. The fast response of such systems allows dynamic compensation of stretch variation through the length of the plate (Figure 4.5).

In the shearline itself, higher strength means increased machine duty since the product strength is fully manifest by this stage of the process. Recent equipment development recognizes that maintenance of a correct blade gap is a prerequisite for cut edge quality (Figure 4.6) [4]. A stiff assembly is

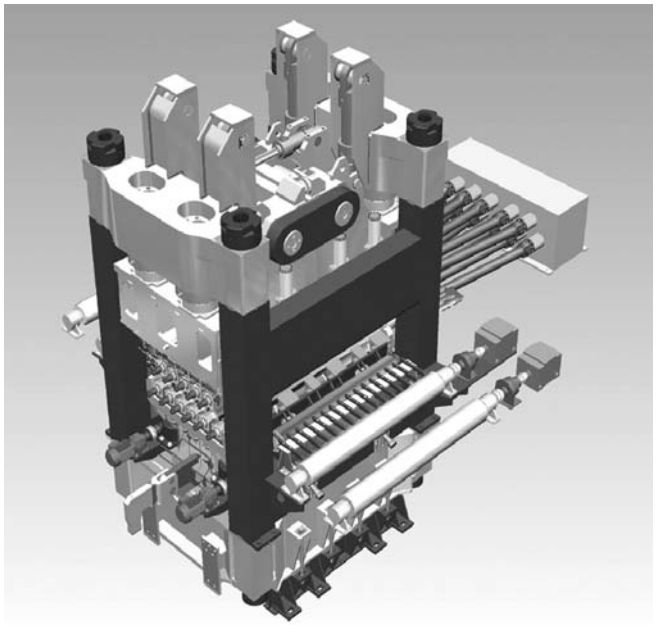


FIGURE 4.5 Three-dimensional computer-aided engineering model of leveler.

the key. The group of steels under discussion retain relatively good ductility in spite of their strength, so mechanical shearing is quite possible even at very full thickness (order 40 mm or higher), provided the blade deflection is constrained.

A particular challenge of the plate mill upgrade that is often overlooked is product-flow logistics. Linepipe, in particular, is characterized by large order-sizes, so a mill that is successful in this market can often be required to process similar product for days on end. Consistency of mill pacing becomes the critical guarantor of product quality, and maximized asset utilization through multipiece rolling is fundamental to this. Holding in-line may be sufficient in some cases, but some mills rolling fuller thickness pipe-plate for extreme low temperature duty will need off-line holding stations.

Even beyond the mill, a TMCR operation has a complex inventory. There is usually a greatly increased need for

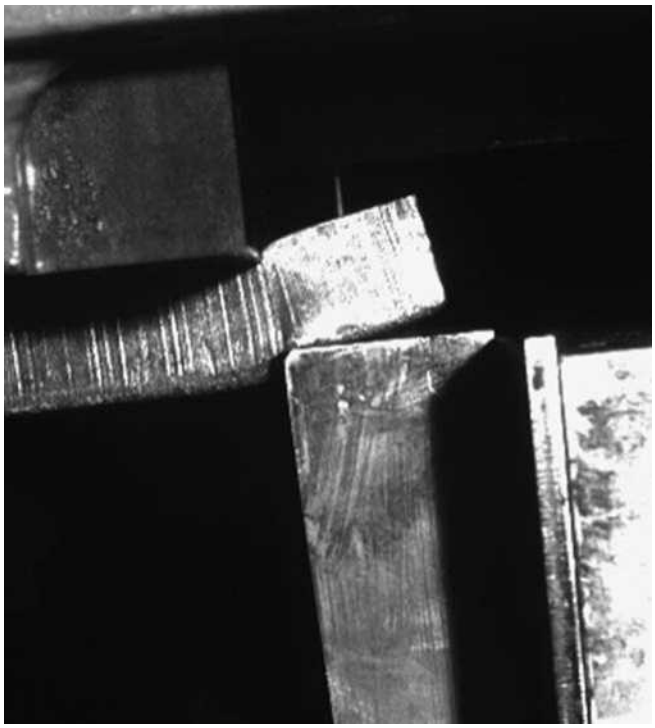


FIGURE 4.6 Still from high-speed video of heavy shearing trials (cut quality investigation).

plate stacking for dehydrogenation. Careful design of the downstream process flow is very desirable, and investment in marking and tracking systems is likely to be rewarded. The inspection instrumentation requirements (including on-line ultrasonic testing) and the testing regime will also need review (Figure 4.7).

The extreme end of the plate mill upgrade spectrum is the replacement of an existing stand with a stronger one and/or the addition of a second stand to an original single-stand mill. This option should not be discounted, particularly in cases where a mill capacity increase, as well as a product strength increase, is sought, and there are many precedents. When done well, a stand-replacement upgrade can fully match the operational performance of an entirely new mill at significantly lower capital cost. The minimization of outage in a working asset is often the deciding factor in the feasibility of the upgrade approach.

In the case of the addition of a second stand, the availability of space in the mill line may become critical. Some of the concepts mentioned above now acquire a secondary advantage. When the new stand must occupy space previously used for in-line TMCR, holding stations can recover the lost utilization. Additional in-line, stock-cooling systems can also be considered, to compress holding times and to enhance strain penetration in thicker product.

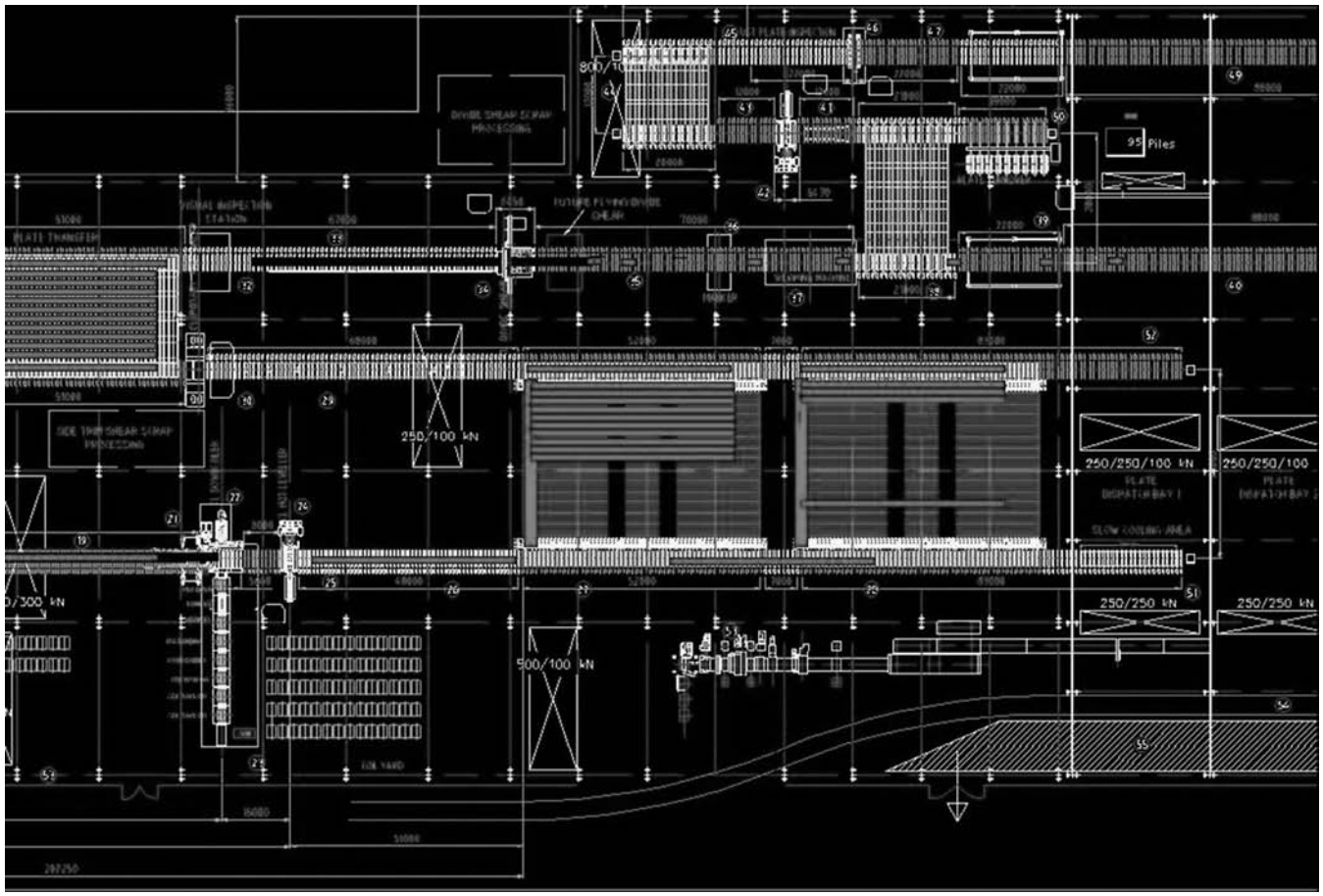


FIGURE 4.7 Still from discrete event simulation of plate mill process flow (logistical evaluation using animated plant layout).

A final and special variant is the conversion of the mill to a plate-Steckel configuration. This allows a considerable increase in piece-weight, because the extra run-out length and consequent temperature loss is contained by coiling in Steckel furnaces added on either side of the finishing mill. The final product can be either coiled or hot sheared, and then finished as conventional reversing mill plate. When rolling in Steckel mode at full, developed length, the mill must forego broadsiding, though the alternative original mode of rolling may usually be retained.

4.5 UPGRADING OF MOTORS AND DRIVES

Most plate mills being considered for an upgrade are equipped with direct current (DC) main motors, since their construction predates modern AC technology. A requirement for higher torque, better control, and increased operating efficiency leads naturally to a synchronous motor solution. The virtuous circle of market need driving technical development means that the steel industry can now call on motor configurations that can be adjusted to fit existing foundations, installed quickly, and require a minimum of maintenance [5].

Compared to DC machines, AC machines deliver more than simply increased torque at low speed. Because the limitations of commutation are eliminated, the cutoff at field weakening range can be increased by up to 50%. For heavy reversing duty, the cylindrical or nonsalient-pole configuration is ideal, being both compact and robust, as well as maximizing dimensioning torque through the use of the greatest number of poles possible (Figure 4.8).

It may not be sufficient, of course, to upgrade only the motors and drives. The transmission as a whole must be capable of delivering the increased torque. Spindle design and selection need consideration, and a simple size increase in the joints is seldom straightforward, because the roll-neck size and separation are usually constrained. It is common for electrical and mechanical engineering design issues to be closely combined in mill upgrade projects, and the drive/spindle example typifies this.

4.6 CONCLUSION

Profitable plate-making is one of the special challenges of the world of rolling. The markets served by plate mills are exceptionally diverse and demanding, and the processing requirements of the more lucrative products lead to fragmented utilization. Few metals industry products exhibit such complex and process-sensitive metallurgical behavior, and few have such exacting accreditation standards or such mighty commercial organizations as their principal customers.

These characteristics can be seen as a problem, or they can be seen as an opportunity. Because of the market factors described in this chapter, plate mills arguably have the most reliable long-term customer demand profile in all of steel processing. Existing plate mills are, therefore, fertile ground for targeted investment, and technology is available that allows older and less powerful mills to compete with new plants. In a sector where product quality and operational flexibility will always count for more than sheer tonnage, the well-focused upgrade is an effective competitive strategy.

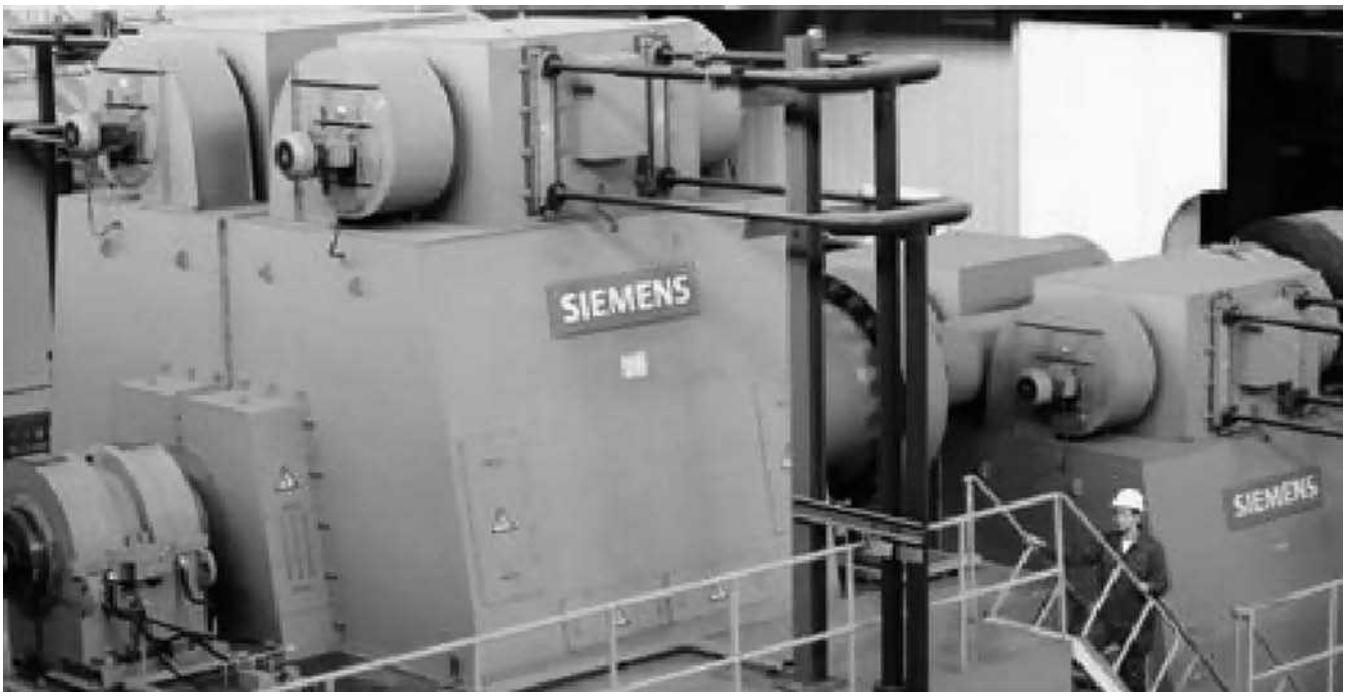


FIGURE 4.8 Main drive motors of modern 5-m plate mill.

REFERENCES

1. Brammer, M. P. 2006. Plate mills for higher-strength products. *Ironmaking and Steelmaking* 353–356.
2. Evans, J. F. and Flick, A. J. 2002. *Efficient Casting and Rolling for Quality Plate Production.* Paper presented at the 2002 CISA International Steel Congress, Beijing, China.
3. Maillard, S. 2005. *Technological Advances in Leveller Performance*. Paper presented at the 2005 Plate Mill Symposium, Linz, Austria.
4. McPherson, N. A. 2006. Quality criteria in plate production: Customer competitive advantage from upstream process control. *Iron and Steelmaking* 33(3): 190–192.
5. Paisley, P., Steeper, M. J., Egan, J., and Howard, I. C. 2006. *Numerical and Physical Modelling of the Plate Shearing Process*. Paper presented at the 9th International and 4th European Rolling Conference, Paris, France.
6. Wiechmann, H., Sopp, P., and Bhooplapur, P. 2006. *Drive Systems on One Common System Platform for Rolling Mill Applications*. Paper presented at the 2006 CISA International Steel, Congress, Beijing, China.

5 Roughing Mill Work Rolls for Hot Strip Production

Michael Windhager and Karl Heinz Ziehenberger

CONTENTS

5.1 Evolution of Roll Materials 63
5.1.1 Early Developments 63
5.1.2 From Chrome Steel to High-Speed Steel 64
5.2 Roll Performance 65
5.2.1 Operational Safety 66
5.2.2 Residual Stress 66
5.2.3 Microstructural Integrity 67
5.2.4 Core Material 67
5.2.5 Testing of Large-Sized Compound Rolls 68
5.3 Basic Requirements for the Safe and Cost-Efficient Use of Semi-HSS and HSS Rolls 68
5.3.1 Mill Practices 68
5.3.2 Roll Shop Practices 69
5.4 Conclusions 69
References 69

5.1 EVOLUTION OF ROLL MATERIALS

5.1.1 Early Developments

In roughing mills, slabs have to be reduced from 200 to 300 mm thickness down to transfer bar thicknesses between 15 and 50 mm. In continuous roughing mills, each stand reduces the slab thickness in one pass. In reversing roughing stands, usually between five and seven passes are applied.

Initially, low-carbon, adamite mono-cast work rolls were used as standard work rolls. The low carbon content did not allow any major carbide formation in the working zone of these rolls (Figure 5.1). The lack of carbide in the working zone resulted in low wear resistance and high surface roughness, thus giving short rolling campaigns, although the high roughness had the advantage of reduced slippage.

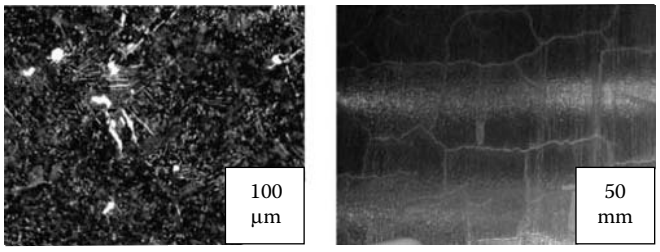


FIGURE 5.1 Microstructure of low-carbon, adamite mono-cast steel roll and fire crack pattern of adamite work roll diameter × barrel length = Ø1200 × 1700 mm after rolling 10,000 tons in a reversing roughing mill (top roll, middle of the barrel).

The adamite rolls did not allow long rolling campaigns, mainly for two reasons:

- Mono-cast rolls show only limited compressive stress in the surface. This leads to rapid heat crack formation and propagation during rolling. Heavy fire cracking finally results in the destruction of the roll surface and requires immediate roll change and redressing [1].
- The low total alloying content, lack of carbides, and low surface hardness limits the wear resistance of the rolls. The result is heavy wear after only short rolling campaigns.

The introduction of spun-cast, double-poured, high-chrome steel rolls resulted in tremendous improvement in roll performance and campaign length. The rolls consist of a high alloy, high carbide, high hardness, martensitic shell of 40–120 mm radial thickness and a low alloy pearlitic nodular iron core; Figure 5.2 gives an idea of the spun-cast compound roll.

Complex heat treatment during production defines not only the hardness of the working zone, but also the stress level of the roll itself. The roll surface will show considerable compressive stress in longitudinal and circumferential direction, whereas the core is under tensile stress (Figure 5.3) [2].

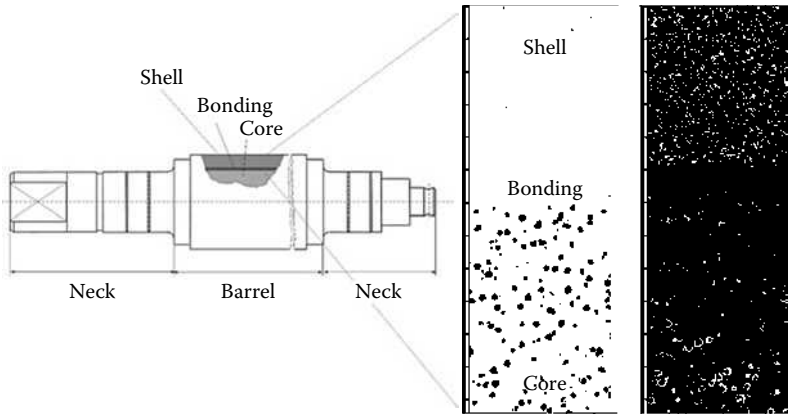


FIGURE 5.2 Principle of spun-cast compound roll.

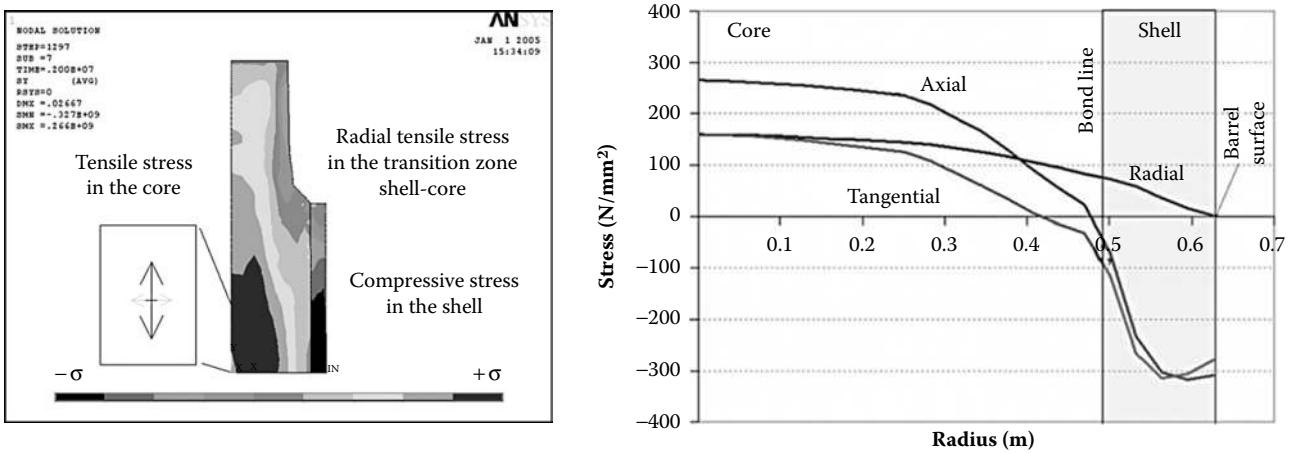


FIGURE 5.3 Residual stress FEM calculation of chrome steel roughing mill work roll Ø1250 mm; right: stress field in middle of barrel length.

This new concept of work rolls proved to be superior to the old mono-cast rolls for the following reasons:

- The compressive stress in the roll surface helps limit the formation of heat cracking during rolling (Figure 5.4).
- The high-hardness chromium carbides embedded in a high alloy martensitic shell provide excellent wear resistance.
- As a consequence, the rolls were able to run longer campaigns, the shape and surface quality of the transfer bar were improved, and the total tonnage rolled during a work roll's lifetime increased significantly.

All further developments in roughing mill work rolls merely focused on increasing shell hardness and changes in the alloying system of the shell. The principle of spin casting and double pouring, as well as the use of a nodular iron core, are still valid.

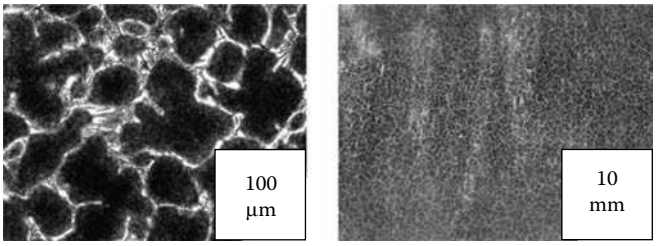


FIGURE 5.4 Microstructure of chrome steel and fire crack pattern of chrome steel work roll Ø1200 × 1700 mm after rolling 10,000 tons in a reversing roughing mill (top roll, middle of the barrel).

5.1.2 From Chrome Steel to High-Speed Steel

The first chrome steel rolls were available in a hardness range of 65–75 ShC. Within certain limits, variations in the chemical composition made it possible to adapt the carbide content to the requirements of the rolling mill. Carbide enhancement, which means introducing carbides

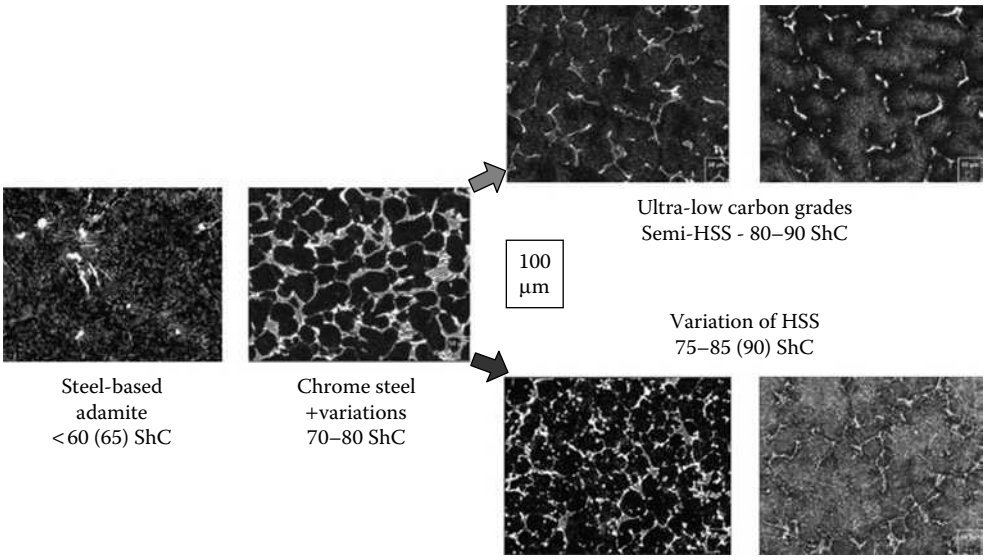


FIGURE 5.5 Development of shell microstructures of roughing mill work rolls.

with higher hardness than the usual chromium carbides, helped further increase the hardness and wear resistance of the rolls.

The final stage of chrome steel development resulted in carbide-enhanced rolls with a surface hardness of more than 80 ShC and a medium level of compressive stress in the shell [3]. Any further increase in wear resistance, surface quality, and performance could only be reached by a fundamental change in the shell microstructure. At this point, two completely different developments began: semi-high-speed steel (HSS) and HSS. Figure 5.5 shows the development of roll microstructures from conventional chrome steel to carbide-enhanced chrome steel and then semi-HSS and HSS. Semi-HSS is an ultra-low carbon shell material (C < 0.9%) consisting mainly of martensite and a small amount of high-hardness carbides. The uniformity of the microstructure makes it very resistant against thermal fatigue during the rolling process. The low carbide content of the shell material makes it necessary to produce these rolls with high surface hardness to achieve best wear resistance [4,5].

HSS is a medium carbon shell material with a higher content of special carbide-forming elements when compared to semi-HSS. This results in a greater percentage of high hardness carbides. Therefore, wear resistance is very high even at lower hardness levels, but the microstructure is less uniform due to the higher amount of carbides and, therefore, in principle is more prone to thermal fatigue.

Both roll concepts have been developed and introduced to the market and, together with carbide-enhanced HiCr steel, these two roll types represent the current state-of-the-art top performance solution for roughing mill work rolls.

5.2 ROLL PERFORMANCE

Over the years, the performance of roughing mill work rolls has increased dramatically. This is partly due to general improvements in the mill and roll shops, but is also a consequence of major changes in roll manufacturing.

The first big improvement was the change from mono-cast adamite to spun-cast double-poured chrome steel rolls, which improved not only wear resistance but also the heat cracking resistance of the rolls. Over the years, the high chrome rolls have been optimized and have reached a performance level regarded as acceptable for most hot rolling operations.

The introduction of highly sophisticated shell materials, like semi-HSS and HSS, brought another major improvement in both wear resistance and campaign length. The total performance per set of rolls now can exceed 4 million tons, and it would be possible to extend the campaign length to more than 70,000 tons in the case of reversing roughers and 300,000 tons in the case of continuous roughing stands [6].

Figure 5.6 shows the performance increase obtained in a 1250-mm diameter reversing rougher. The campaign length could be extended to almost 70,000 tons, and the wear per 100,000 tons decreased significantly. Figure 5.7 gives an idea of the microstructure and the excellent surface condition of an HSS roughing mill work roll after having rolled a campaign of 60,000 tons. Compared to the high chrome steel roll surface given in Figure 5.4, the heat cracking of the HSS roll is negligible.

When analyzing these figures, it is important to point out that they can only be obtained in the case of favorable rolling programs, optimized rolling and cooling conditions, the perfect adjustment of the backup roll and work roll geometry, etc. Experience in many mills has shown that carbide-enhanced high chrome steel work rolls with barrel hardness around 80 ShC can be used in most mills without any restrictions regarding the rolling program, roll cooling, and roll shop practice.

The situation changes drastically as soon as the roll user wants to take further steps toward increasing the campaign

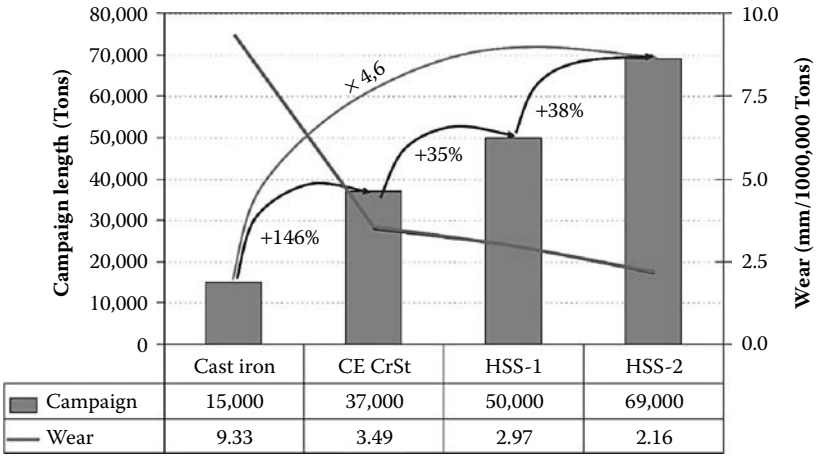


FIGURE 5.6 Development of roughing mill work roll performance levels (reverse rougher of a semi-conti HSM, Ø1250 × 2050 mm).

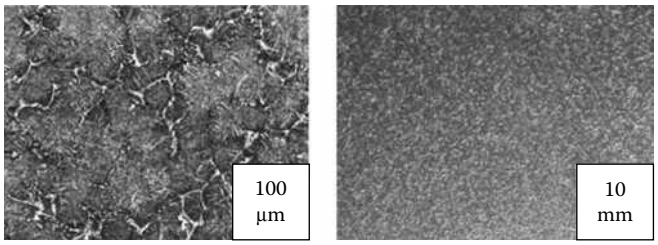


FIGURE 5.7 Microstructure of HSS and fire crack pattern of HSS work roll Ø1250 × 2050 mm after rolling 60,000 tons in a reversing roughing mill (top roll, middle of the barrel).

length and minimizing roll wear. To ensure the safe and cost-efficient use of high performance roll grades like semi-HSS and HSS, certain basic requirements concerning mill and roll shop practices have to be observed, which deserve a closer description.

5.2.1 Operational Safety

The work rolls have to operate safely, which means without internal cracks forming that lead to the development of spalls or even roll breakage. This applies to normal rolling conditions, as well as moderate overload situations, which can happen in everyday rolling mill practice. Severe overloads (e.g., rolling several slabs without water and then switching on roll cooling) will destroy any roll, but this should be regarded as bad rolling practice and will not be discussed further (for examples, see Figure 5.8, also [7]).

To secure the operational safety of roughing mill work rolls, general requirements concerning the quality of compound rolls have to be fulfilled, such as defect-free bond, sufficient roll core strength, etc. [8]. The large dimensions of the roughing rolls and the highly sophisticated shell materials in use create risks many users of small size compound rolls might not be aware of.

5.2.2 Residual Stress

Roughing rolls are usually large-sized rolls with high usable shell thickness. This leads to high residual stresses in the roll, that is, compression stress in the shell and, as a consequence, tensile stress in the core. The trend toward high hardness levels (80–85 ShC) also plays its part in increasing the overall stress level in these high performance rolls.

In radial direction, the shell and interface are under tensile load. As a consequence, each defect that might act as a crack

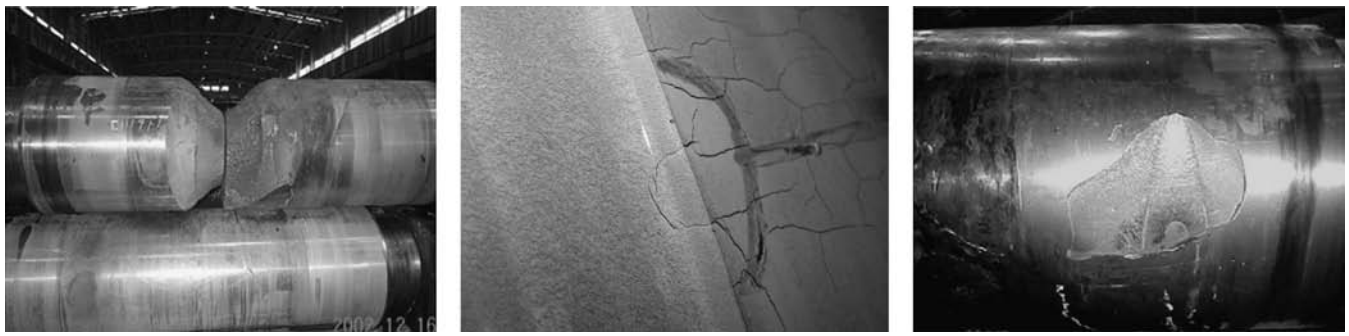


FIGURE 5.8 Catastrophic roll failures.

initiator is preloaded by tensile stress even without applying any load by the rolling operation. During the long life of such a high performance roll, these potential crack initiators in the inner part of the shell or in the bond zone are under high cyclic loads, which may ultimately lead to fatigue crack formation and, finally, spalling [9].

5.2.3 Microstructural Integrity

Utmost resistance against thermal fatigue of the roll surface can only be secured with highly uniform shell materials. In cast-iron-based material, this can only be provided by using a high amount of martensite and low amounts of carbides.

Looking at the solidification of large iron-base castings, it is evident that by using chemical compositions that create a low amount of eutectic carbides, the risk that microporosities will form will automatically be increased, especially at the end of the solidification process. In the case of rolls, this means in the inner part of the spun-cast shell. These microporosities, if undetected or not constantly surveyed and controlled during roll life, may act as a starting point of fatigue crack formation (as an example, see Figure 5.9) and roll spalling [10]. In particular, in the production of semi-HSS, the big difference between shell and core material may lead to unfavorable microstructures in the bond area that will either increase the scrap rate or lead to potential risks in operation [11].

5.2.4 Core Material

The pearlitic nodular core material used in roll making cannot be compared to standardized nodular iron materials used in mechanical engineering. During the production process, the roll core material has to re-melt a small layer of the inner part of the spun-cast shell in order to secure good bonding. Although special techniques like triple-layer technology are in use, a certain amount of shell material containing carbide-forming elements will always be diluted in the core material. This leads to the formation of carbides and the suppression of ferrite formation in the nodular core of the rolls.

The mechanical properties are, therefore, quite different from standardized nodular iron grades. Figure 5.10 shows the difference in the stress-strain curve between standard grades GJS 400 and GJS 600 and nodular roll core material extracted from a 1200-mm HiCr steel roll.

In nodular roll core material, the difference between ultimate tensile strength (UTS or R_m) and yield strength (YST or $R_{p0.2}$) is small, and the elongation (A_5) is usually <1%. But, although the ultimate tensile strength is only approximately 400 N/mm^2, the yield strength (even though hardly measur-

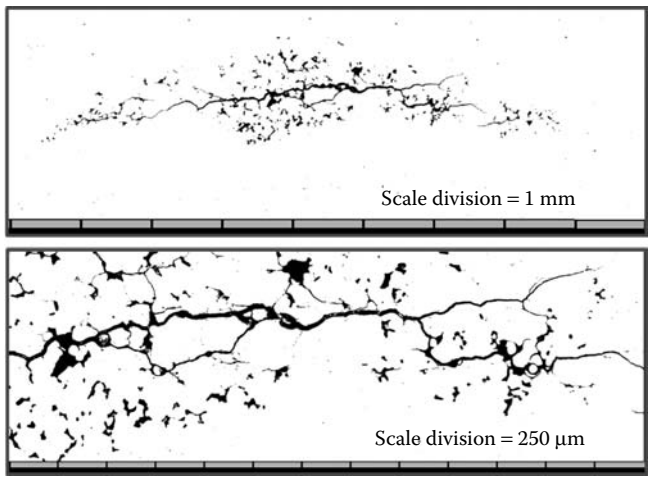


FIGURE 5.9 Shell porosities in low carbon shell material linked by fatigue crack formation.

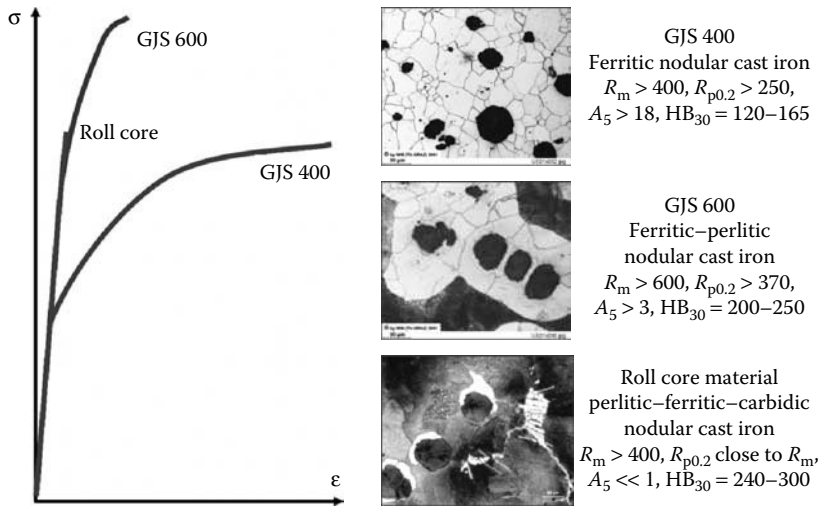


FIGURE 5.10 Comparison of mechanical properties of roll core versus standard nodular iron. R_m = ultimate tensile strength, $R_{p0.2}$ = yield strength, A_5 = elongation, HB_{30} = Blineu hardness.

able) is close to the yield strength of high strength standard nodular iron grades like GJS 600.

These values are being achieved in the neck and outer parts of the roll core. In large size rolls with a diameter >1000 mm, it is almost impossible to avoid segregations and the formation of coarse graphite and microporosities in the inner part of the core, especially in the center line where solidification ends.

The quality of this inner part of the roll core cannot be checked by nondestructive testing methods. This fact clearly limits the maximum stress level the roll is able to bear. In particular, the combination of high residual stress and thermal stress at the beginning of the rolling campaign (when the roll shell is heating up rapidly and the roll core is still cold) may lead to catastrophic barrel breakages starting at the center of the roll body (see Figure 5.8, left) [12].

5.2.5 Testing of Large-Sized Compound Rolls

In everyday roll shop practice, bond zone defects as well as porosities can usually only be found by ultrasonic testing [13–17].

When testing new rolls, the fact that roughing mill work rolls have high shell thicknesses makes it impossible to find small-sized defects in the inner part of the shell or in the bond zone. This is due to physical constraints of this testing method [18].

The decreasing shell thickness during roll life gives us the opportunity to detect smaller and smaller defects, because the distance between ultrasonic test head and defect becomes smaller while the roll diameter decreases step by step (see Figure 5.11) [19]. In general, this is positive because it gives the roll user the opportunity to find defects before they create big spalls with a loss of roll life and maybe huge consequential damage. On the other hand, the correct interpretation of Ultrasonic Test (UT) signals from the bond zone requires a lot of practical experience, and it is not easy to make a decision whether to stop a roll or to continue to use it.

5.3 BASIC REQUIREMENTS FOR THE SAFE AND COST-EFFICIENT USE OF SEMI-HSS AND HSS ROLLS

5.3.1 Mill Practices

Experience with highly sophisticated roughing mill work rolls has shown that, in many mills, the percentage of roll stock lost due to heat cracking after mill stalls and microspalls due to undetected subsurface cracks is quite high. In many cases, this prevents the use of these rolls with acceptable cost/performance ratio.

It is evident that avoiding mill stalls and mechanical overload of the rolls should have first priority, although other facts have to be taken into consideration. Sophisticated roll grades like semi-HSS and HSS have high alloy shells, high barrel hardness, and high levels of residual stress.

High wear resistance makes it possible to run very long campaigns. At the beginning of such a long campaign, any mill incident that creates a surface or subsurface crack in the roll barrel can be regarded as highly dangerous because of possible crack growth and even spalling within the same campaign. It is, therefore, highly recommended to ensure that such rolling incidents are reported and that, in such cases, the rolls are changed and checked for cracks.

Longer campaigns may increase the wear difference between barrel center and barrel edge area. This may lead to unfavorable load distribution between work roll and backup roll and, as a consequence, to fatigue damage in the barrel edge area of the backups. Even edge spalling may occur both on backup and work rolls (see Figure 5.12).

It is, therefore, necessary to optimize the rolling schedule (if possible) to achieve a more even wear distribution on the work roll. It is also necessary to adjust the crown of the work roll and the geometry of the backup (edge relief strategy) to ensure that the high performance potential of semi-HSS and HSS can be used without major risk. Concerning the geometry of backups, the major backup roll suppliers can help

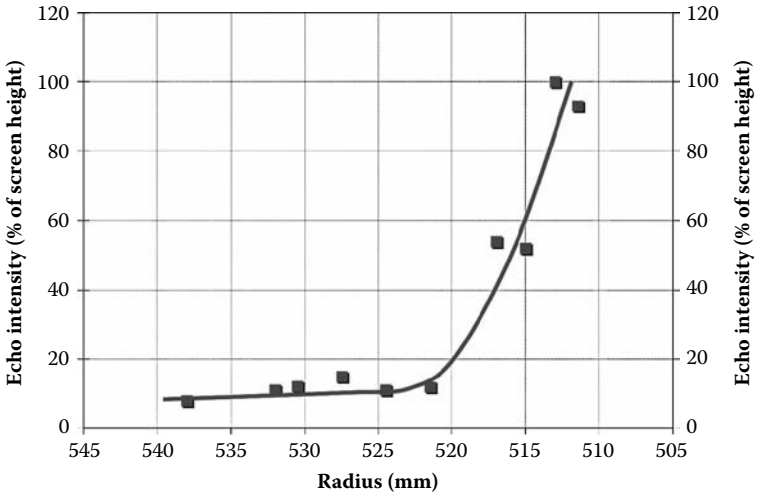


FIGURE 5.11 Increase in ultrasonic response with decreasing distance between test head and failure.

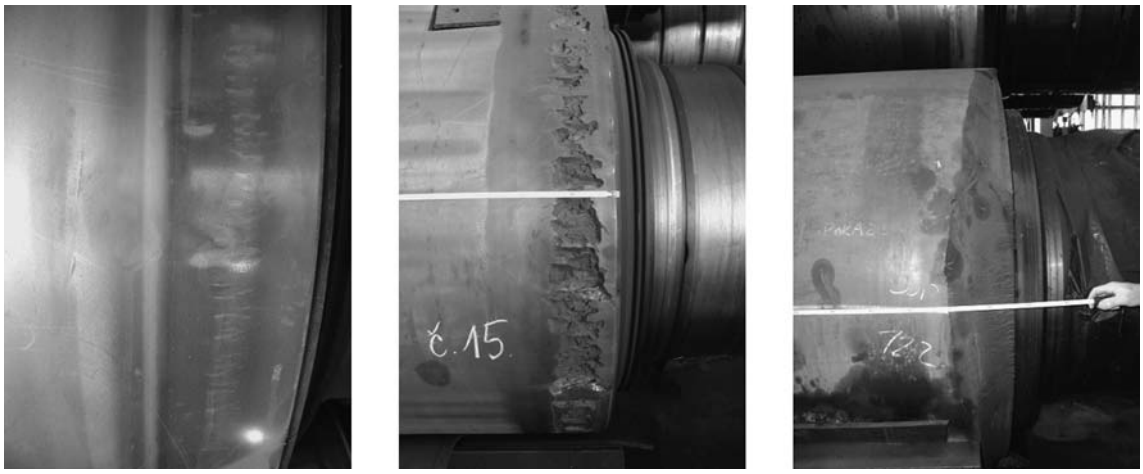


FIGURE 5.12 Typical backup roll and work roll failures as a result of high campaign lengths and lack of work roll–backup roll geometry adjustment.

[20,21]. When rolling mainly stainless steel grades, the low amount of carbides in the shell of semi-HSS leads to unfavorable wear characteristics [5,11,22,23], which are not superior when compared to conventional high chrome material.

5.3.2 Roll Shop Practices

High alloy rolls need more care than conventional rolls. State-of-the-art roll shop practice nowadays includes online crack detection (either by eddy current or surface wave ultrasonic testing) during or after every grinding operation. Periodical testing of the bond zone by ultrasound and documenting the individual test results have proven to be very helpful in detecting any changes in the bond zone area during roll life [24,25].

The interpretation of the changing UT response from the bond zone during roll life may be difficult. The intensity of the UT response increases as the roll diameter decreases, and areas with a coarser microstructure that had not been detected when testing the new roll will sooner or later give an echo above the threshold limits. In general, an increase in intensity does not necessarily indicate the formation or growth of a dangerous bond zone defect. An increase in area of such a zone with higher UT response has to be regarded as being more critical.

Sophisticated UT crack detection systems are in use because of their ability to detect subsurface cracks close to the roll surface, which cannot be detected by conventional eddy current testing systems [26]. The elimination of subsurface cracks induced by local mechanical overload during rolling is vital to ensure that such cracks do not start to grow into the roll during the subsequent campaign. This is of utmost importance, especially in the case of continuous roughing mills where campaign lengths may even exceed 300,000 tons.

5.4 CONCLUSIONS

Carbide-enhanced high chrome steel, semi-HSS and HSS rolls represent the state-of-the-art work roll grades for roughing stands in hot strip mills. In some cases, outstandingly high campaign length and tonnage performance have been achieved.

Carbide-enhanced roll grades can nowadays be used by most mills without taking special measures; they simply replace the standard roll grades. To ensure the successful use of more sophisticated roll grades like semi-HSS and HSS with good cost/performance ratio, rolling conditions and roll shop practices need to be revised and optimized.

REFERENCES

1. Schröder K. H. 2003. A basic understanding of mechanics of rolling mill rolls. http://www.esw.co.at/downloads/
2. Ziehenberger K. H., Windhager M. 2006. Recent developments in HSM rougher rolls—Risks and chances. *Iron & Steel Technology*, Joann Cantrell (ed.), September 2006, pp. 38–41.
3. Ziehenberger K. H., Windhager M. 2003. Carbide enhanced high chrome iron and steel work rolls for rolling flat products. *2003 Materials Science and Technology Conference Proceedings*, ISS, Vol. 41, pp. 133–142, Chicago, IL.
4. Lewis J., Prenni, L. J. Jr., McGregor J. 2000. Technology enhanced work rolls for the roughing mill application. *42nd MWSP Conference Proceedings*, ISS, Vol. 38, pp. 675–684, Toronto, Ontario, Canada.
5. Martiny F., Sinnaeve M. 2001. Improved roughing work rolls for the hot rolling of low carbon and stainless steel. *43rd MWSP Conference Proceedings*, ISS, Vol. 39, pp. 683–692, Charlotte, NC.
6. Ziehenberger K. H., Windhager M. 2007. State of the art work rolls for hot rolling flat products. *CONAC 2007—3rd Steel Industry Conference and Exposition*, AIST, November 2007, Monterrey, México.
7. CAEF. 2002. *Roll Failures Manual—Hot Mill Cast Work Rolls*, 1st edition. Düsseldorf, Germany: CAEF.
8. Brandner M., Ziehenberger K. H., Windhager M. 2007. How to increase performance and operational safety of work rolls. *44th Rolling Seminar—Processes*, *Rolled and Coated Products*, ABM, October 2007, pp. 871–879, Campos do Jordão, Brazil.

9. Kapadia B. M., Marsden K. W. 1996. Safe minimum operating diameter of duplex cast roll with shell/core. *37th MWSP Conference Proceedings*, ISS, Vol. 33, pp. 221–242, Warrendale, PA.
10. Kapadia B. M., Marsden K. W. 1998. Fracture analysis of hot mill work rolls. *40th MWSP Conference Proceedings*, ISS, Vol. 36, pp. 395–405, Pittsburgh, PA.
11. Lyckström B., Nylen T., Prenni L., Heisterkamp P. 2007. The use of high tech work roll materials in the roughing stands of various hot strip mill applications. *2007 IOM Rolls Conference Proceedings*, IOM, Session ID 1.3, Birmingham, U.K.
12. Schleiden R. F. 1995. Association of roll manufacturers roll failures—Why? *36th MWSP Conference Proceedings*, ISS, Vol. 32, pp. 11–20, Warrendale, PA.
13. van Kollenburg R. J. W. M., Tensen J. P. M. 2007. Developments in roll inspection. *2007 IOM Rolls Conference Proceedings*, IOM, Session ID 7.2, Birmingham, U.K.
14. Justice D. 2007. The evolution of roll inspection systems and their use in today's roll shops. *2007 JSW Rolls Conference*, pp. 39–52, Vijayanagar Works, Bellary, India.
15. Bavestrelli G. 2007. Roll shop management system. *AISTech 2007 Conference Proceedings*, AIST, Session ID PR-351–198, Indianapolis, IN.
16. Takada H., Torao A., et al. 2000. Development of roll surface testing technique by use of broad bandwidth surface waves. *15th World Conference on Nondestructive Testing*, WCNDT, Session ID 16, Roma, Italy.
17. Kerr E. 2002. Roll inspection practice in use. In *Rolls for the Metalworking Industries*, *Section V—Roll Inspection and User Preparations*, ed. Gene E. Lee, pp. 397–421.
18. Guo-hua D. 2001. Compound roll inspection by using longitudinal wave, dual crystal straight probe. *43rd MWSP Conference Proceedings*, ISS, Vol. 39, pp. 695–705, Charlotte, NC.
19. Brandner M. van Kollenburg R. 2008. Interpretation of UT and EC results in roll testing. *45th Rolling Seminar: Processes, Rolled and Coated Products*, Ipojuca-Porto Galinhas, Brazil, pp. 36–45.
20. Decultieux F., Hoffman M., Adams T. 2004. Back up roll chamfer design, profile and maintenance. *2004 Materials Science and Technology Conference Proceedings*, TMS/AIST, pp. 311–321, New Orleans, LA.
21. Ji W., Schumacher M. 2005. Influence of roll profiles and linear load distribution and barrel edge damages of backup rolls. *2005 Materials Science and Technology Conference Proceedings*, pp. 37–47, Pittsburgh, PA.
22. Sinnaeve M., Ji W. 2003. HSS work rolls for the roughing stands in HSM and the first finishing stands of CSP mill. *ASIA Steel International Conference 2003*, pp. 3.i.5.1–3.i.5.9, Jamshedpur, Jharkhand, India.
23. Tremea A., Biggi A., Grespi M. 2007. Choice and performance of work roll materials through the stand in the hot strip mill. *2007 JSW Rolls Conference Proceedings*, pp. 35–49, Vijayanagar Works, Bellary, India.
24. Schönfeld M., van Kollenburg R. J. W. M. 2003. Case at EKO Stahl where combined eddy current (ET)/ultrasonic (UT) roll inspection minimized the number of major mill accidents. *45th MWSP Conference Proceedings*, ISS, Vol. 41, pp. 317–324, Chicago, IL.
25. Cubakovic P. A., Nagy P. B. 2001. The limitations and capabilities of ultrasonic testing of bimetallic work rolls and steel back-up rolls. *43rd MWSP Conference Proceedings*, ISS, Vol. 39, pp. 719–728, Charlotte, NC.
26. Stork F. G., Tensen J. P. M., van den Elzen C. M. J. 2001. Combined roll inspection. *43rd MWSP Conference Proceedings*, ISS, Vol. 39, pp. 707–718, Charlotte, NC.

6 High-Speed Steel Rolls: The Last Frontier in Hot Steel Rolling

Alberto Tremea, Angelo Biggi, Massimo Pellizzari, and Alberto Molinari

CONTENTS

6.1 Introduction 71
6.2 High-Speed Steels for Rolls 71
6.3 Roll Surface Deterioration 73
6.4 HSS Behavior in Lab Test 73
6.4.1 Wear Tests 73
6.4.2 Thermal Fatigue Test 75
6.5 Results and Considerations from the Mills 76
6.5.1 Roughing Stands in a Continuous HSM 76
6.5.2 Roughing Stands in a Minimill 77
6.5.3 Reversing Roughing Stands 78
6.5.4 General Considerations about Roughing Stands 78
6.5.5 Early Finishing Stands 78
6.6 Conclusions 80
References 81

6.1 INTRODUCTION

Hot rolling of steel represents one of the most important manufacturing processes because of the large volume of steel worked. The behavior of work rolls is a key factor in rolling technologies that influences the quality of the rolled products and even the operating rates (and costs) of the mill. During the last 10 years, different applications of high-speed steel (HSS) rolls started covering different stands of the mill, aimed at a progressive replacement of more conventional grades like high chromium irons (early finishing stands) and high chromium steel (roughing stands). Despite the potential of these high-strength materials, there are only a few instances that indicate the advantage of using HSS rolls. It is the opinion of the authors that the operating practice in the mills and in the roll shops can be held responsible, at least in part, for the lack of evidence of their role in improved performance. The following sections provide a general overview of the behavior of this class of rolls based on both industrial experience and laboratory tests carried out under more reliable conditions than those usually encountered during rolling.

6.2 HIGH-SPEED STEELS FOR ROLLS

HSS groups include many different alloyed steels; the specific balancing among carbon and several strong carbide-forming elements produces different microstructure types. In the case of centrifugal casting bimetallic rolls (core of the roll in nodular cast iron), the external working layer is a ledeburitic steel. The presence of this microstructural constituent characterizes the mechanical and technological properties of the steel. The volume fraction, type, size, and distribution of carbides directly influence hardness, strength, toughness, and, therefore, the wear resistance of material. The ferrous martensitic matrix surrounding the carbides gives an important contribution to sustain mechanical and thermal stresses of rolls by helping secondary carbides spread in. Table 6.1 shows the wide range of chemical composition of the HSS rolls. The influence of alloying elements on the solidification structure is well known [1,2]. Figure 6.1 shows the typical microstructure of these steels resulting from solidification sequences, as illustrated in Figure 6.2. Figure 6.3 summarizes the main characteristics of carbides in HSS rolls, while Figure 6.4 outlines roughly the effect of important elements in the steel chemistry with respect to carbide typologies formed.

TABLE 6.1
Main Elements in HSS for Rolls (wt%)

%C	%Cr	%Mo	%W	%V	%Nb
1.5–2.5	2.0–8.0	2.0–6.0	0.0–6.0	2.0–6.0	0.0–2.0

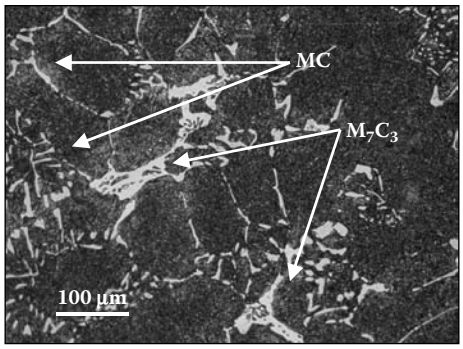


FIGURE 6.1 Typical microstructure of HSS for rolls.

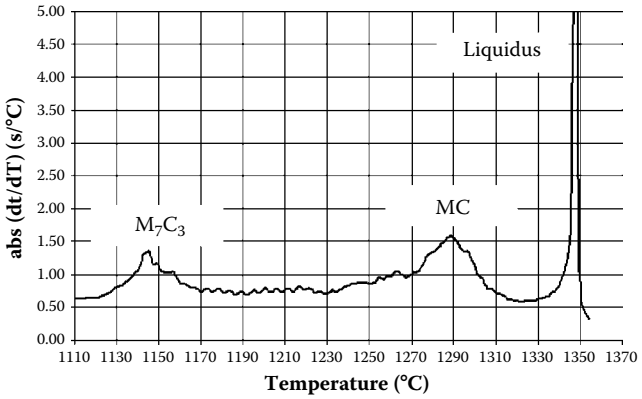


FIGURE 6.2 Thermal analysis of HSS in Figure 6.1 (%C = 1.65).

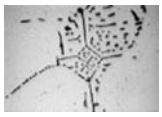
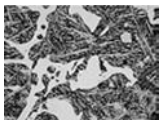
Name	Elements	Density (g/cm³)	HV	Aspect	Size (mm)
MC	V, Nb, Mo (W)	6–8	2500–3000		10–50
M_7C_3	Cr, Fe	7	1400–1800		50–250
M_2C	Cr, Mo (W), V	9–18	1900–2100		50–250
M_6C	Fe, V, Mo (W), Cr	7–14	1200–1500		50–250
M_3C	Fe, Cr	7–8	1000–1100		50–250

FIGURE 6.3 Carbides in HSS for rolls.

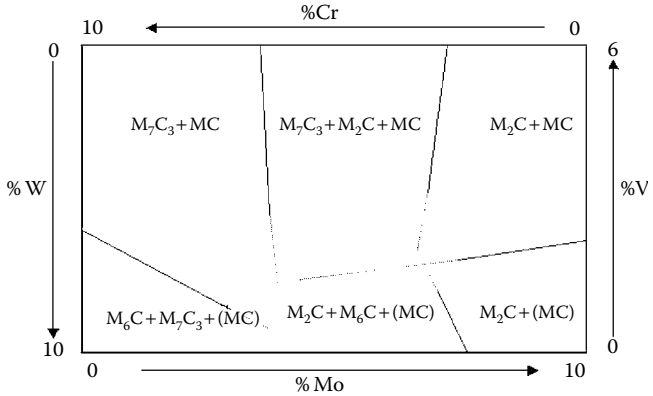


FIGURE 6.4 Effect of elements on carbide typology.

6.3 ROLL SURFACE DETERIORATION

During normal service in the mill (i.e., no accidental events), roll life is determined by proper consumption during rolling, which also establishes the campaign length. In many cases, damages to the surface roll lead to fixes in the roll change to avoid quality problems on the rolled strip. A large amount of roll consumption is due to regrinding wear not always optimized with respect to real surface damaging of the roll. The complex tribological situations encountered by the work rolls are

- Surface fatigue (thermal and mechanical)
- Normal and tangential stress needed for rolling
- Hertzian stress developing during contact with the back-up roll
- Stress corrosion phenomena due to cooling and lubrication system

In all stands of the mill, work rolls must guarantee sufficient hot strength. The dominant mode of roll wear is the abrasion, which assumes more and more weight moving from roughing to finishing stands. The scale of the rolled steel is the main cause of the abrasion of the roll surface; the abrasion effect of this scale depends strongly on rolling parameters, and a general discussion does not cover specific mill (and/or stand) situations. The level of damage due to thermal fatigue establishes not only the surface aspect of the roll, but also the weight of abrasion phenomena concerning roll material loss. Existing theories also involve adhesive wear mechanisms, where the roll surface plastically deformed, but there is a lack of consensus. So the HSS-specific microstructure with its mechanical properties is of great importance, because it can limit surface damage with only positive consequences for reducing roll consumption. The correlation between microstructural features and rolling stresses is still actual valid matter for discussion because, in many cases, laboratory test results are not confirmed during mill trials. What are the reasons? Many times, there isn't the goodwill to clarify thoroughly the situation concerning roll consumption, and then confusion reigns supreme.

6.4 HSS BEHAVIOR IN LAB TEST

Next to standard ways to analyze mechanical properties of steels (hardness, phase analysis, etc.), many laboratories have set particular tests to simulate rolling conditions. Given the complex and overlapping types of stress that rolls encounter in a revolution, the study of surface deterioration in laboratory moves through specific tests focused on specific problems [3].

For many years, Innse Cilindri has cooperated with the Department of Materials and Technology of Trento University in the characterization and testing of materials for hot rolls. Regarding HSS, a lot of work has been done to identify the criteria for the choice of the best grade based on the specific requirements of the singular mill.

6.4.1 Wear Tests

The wear resistance of roll materials was studied by means of a customary test rig providing the rolling-sliding contact between the disc simulating the roll material and a C40 plain carbon steel disc, induction-heated up to 700°C simulating the strip [4]. The disc was left to rotate for 5 minutes at this temperature, allowing the formation of the oxide scale before the coupling with the sample, to better reproduce the condition during hot strip rolling. The surface temperature was monitored by means of an infrared pyrometer. The rotating speed of the C40 was 200 rpm, while that of the sample was 180 rpm, thus realizing 28% sliding between the mating surfaces. A load of 300 N was applied, corresponding to a maximum contact pressure, calculated by the Hertz formula and considering a reduced elastic modulus at 700°C (170 GPa) for C40 [5] was of 300 MPa. The sample was periodically weighted to determine the curve of the cumulative mass losses and the wear rate. The surface roughness of the discs was also measured by means of a profilometer before and after each test interval on four different positions at angular distance of 90°. The profiles were then mathematically averaged. The conditions selected for the present wear test were largely determined by the limits of the laboratory experimental apparatus. These are different from those used in the real rolling practice, particularly due to the relatively low temperature used and also to the absence of lubrication. Assume, then, that the test conditions thus realized are noticeably different from those in actual rolling practice; the present wear test reproduces the wear mechanism of work rolls quite satisfactory. As evidenced by optical microscopy, damage results from abrasion in combination with triboxidation. The hard oxide layer developing on the surface of the C40 steel (Figure 6.5a) causes the abrasion of the roll surface [6]. The consequent oxidation of the roll then occurs (Figure 6.5b), due to the transfer from the counterpart and promoted by the adhesion occurring at high temperature.

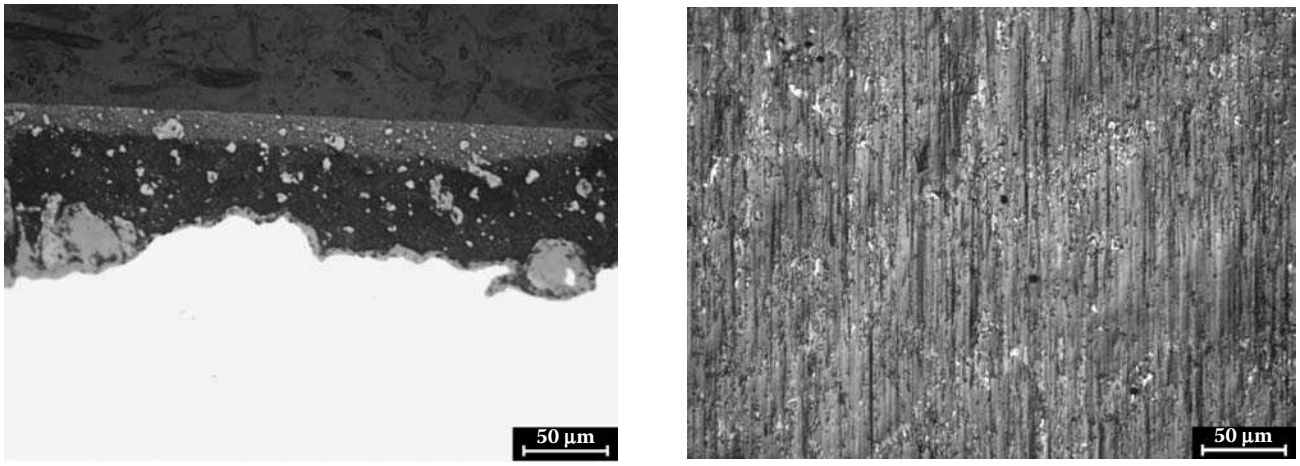
The tribological contact realized is quite complex, involving material transfer from the roll to the C40, and vice versa. The mechanism has been verified by the presence of chromium oxide on the surface of C40 mating against HiCr irons.

As a general observation, HiCr irons are more oxidized than HSS at the end of the test. This was ascribed to the higher tendency to oxidation of the martensitic matrix [4,7,8] depleted in chromium because of the high volume of Cr-rich M_7C_3 carbides. However, in light of recent investigations, it is believed that the formation of the oxide layer on the roll is aided by the transfer from the C40. The lower matrix microhardness of HiCr irons compared to HSS causes a more pronounced wear of the matrix than eutectic carbides, which favor an easier entrapment of oxide debris and their following compacting and sintering to form uniform and protecting oxide layers (*glazes*). The exposed mechanism well agrees with the theory of triboxidation wear proposed in the literature [9,10] and also with a model proposed by the authors [4,21,22] (Figure 6.6).

A key important question regards the transfer of lab tests to real rolls. Present results seem to confirm the better surface finishing claimed for HiCr compared to HSS due to the higher tendency toward oxidation and the better frictional properties in the mills. As long as a continuous and stable oxide layer is able to form, this will generally lower the rolling force [11].

Furthermore, in Figure 6.7, the influence of the carbide volume percentage on wear resistance is shown for HSSs and other materials typically used in different stands of the hot strip mill.

According to the higher abrasion resistance imparted by hard eutectic carbides, a lower wear rate is observed by increasing volume percentage (carbide volume percentage) of this phase. With respect to the general trend, higher rates were displayed by HiCr irons and indefinite chill (IC) irons. This has to be ascribed to the lower hardness of M_7C_3 and M_3C carbides, predominant in HiCr and IC irons, respectively, if compared to MC carbides in HSSs. This result is confirmed by the evidence shown in Figure 6.7, where the lowest wear rates pertain to steels with the highest MC content [12].



(a) (b)

FIGURE 6.5 Surface aspects after wear tests: (a) composite oxide scale developing on the C40 counterpart during the hot wear test; (b) oxide scale (gray region) developing on the steel roll during the hot wear test. Non-oxidized eutectic carbides (white region) are still visible on the roll surface.

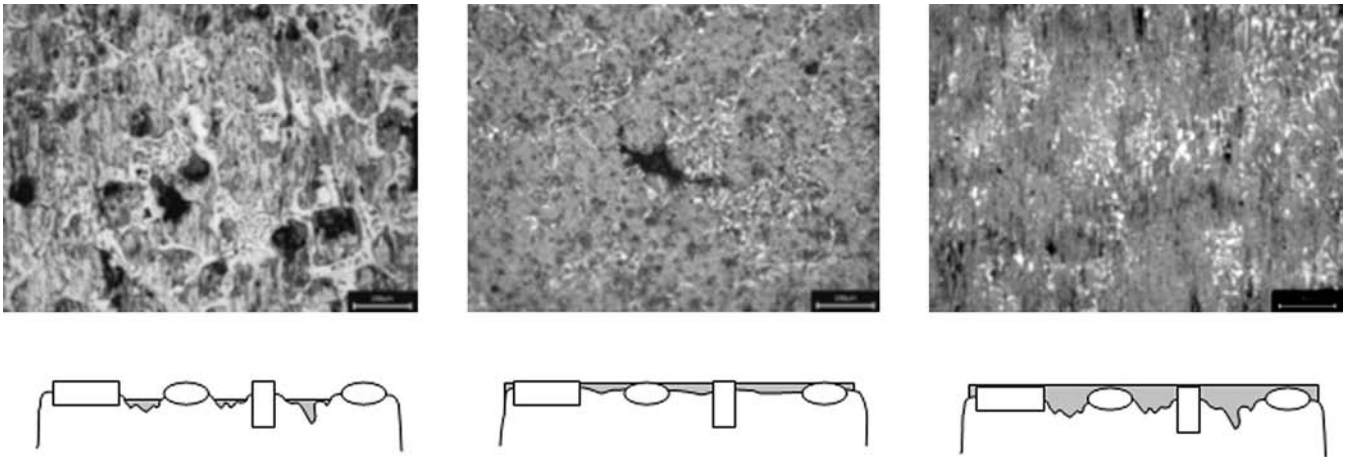


FIGURE 6.6 Schematic model of the influence of the oxide layer extension and matrix microhardness on the surface quality of work roll materials. (Reprinted from M. Pellizzari, A. Molinari, G. Straffelini. *Wear* 259: 1281–1289, Copyright Elsevier 2005. With permission.)

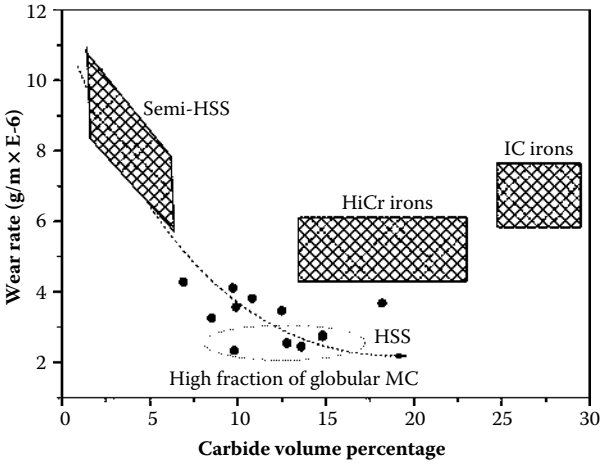


FIGURE 6.7 Wear rate of high-speed steels compared to other work roll materials.

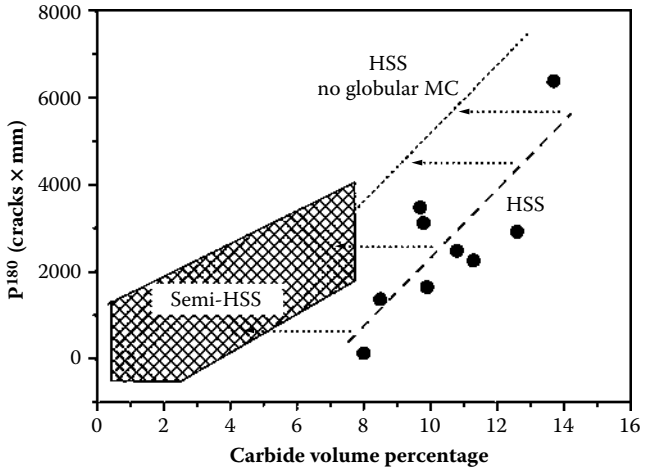


FIGURE 6.8 Pyrocracking factor versus carbide volume percentage in semi-HSS and HSS.

6.4.2 Thermal Fatigue Test

Thermal fatigue tests were carried out using a rig based on induction heating and water cooling of a specimen disc. A portion of the surface is cyclically heated up to 670°C and rapidly water-cooled to 80°C. Because of the constraint exerted by the core, at a temperature different from that at the surface, thermomechanical stresses are present, causing the formation of thermal cracks, also known as heat checks or firecracks. Cracks form on the surface and propagate in a radial direction. Because of the relative low width of the sample, a biaxial state of stress is generated during the test and only cracks parallel to the disc axis are detected. This situation slightly differs from that occurring in real rolls, by which the higher width/diameter ratio establish a triaxial state of stress and the formation of a crack network (Figures 6.14, 6.16, 6.20, and 6.21).

Mean (l_m) and maximum (l_{max}) crack length and crack density (ρ) were used to evaluate the thermal fatigue (TF) damage. A fourth parameter, the so-called pyrocracking factor P, given by the product of the three aforementioned values, represents a measure of the global damage to which the material is subjected during service. Thermal softening occurs during periodic thermal cycling [13].

As far as the test conditions realized in the laboratory test are concerned, the thermal fatigue (TF) resistance of hot roll materials mostly depends on the amount of eutectic carbides. More specifically, the damage is correlated to the interconnection of carbides, representing a preferential propagation path for cracks. In Figure 6.8, the resistance to thermal cracking is shown to increase by decreasing carbide volume percentage (CVP) for semi-HSS and HSS. Due to the lower carbide fraction, semi-HSSs show a lower pyrocracking factor P. However, despite the higher CVP, some HSS grades show behavior comparable to that of semi-HSS. Beneath the carbides volume percentage, their degree of interconnection also plays a crucial role. It is demonstrated that given a certain CVP, a high content in globular MC carbides lowers the degree of interconnection, resulting in a higher thermal fatigue resistance [14]. This is well illustrated in Figure 6.9, where a thermal crack is shown to deviate along the boundary of a eutectic cell containing so-called dissociated MC carbides.

As a consequence, it was deduced that these carbides do not really influence TF resistance and should not be taken into account for the determination of the pyrocracking factor. The dashed line in Figure 6.8 represents the correlation between P and CVP after removal of the MC contribution, by means of image analysis (Figure 6.10). The difference between semi-HSS could also be explained. In the present tests, the influence of the martensitic matrix has been proved to be less crucial than that of carbides [15].

Figure 6.11 highlights the well-known inverse relationship between mean crack length and crack density. In other words, the higher the rate of crack nucleation, the lower their rate of propagation [16]. Materials showing high values of l_m are

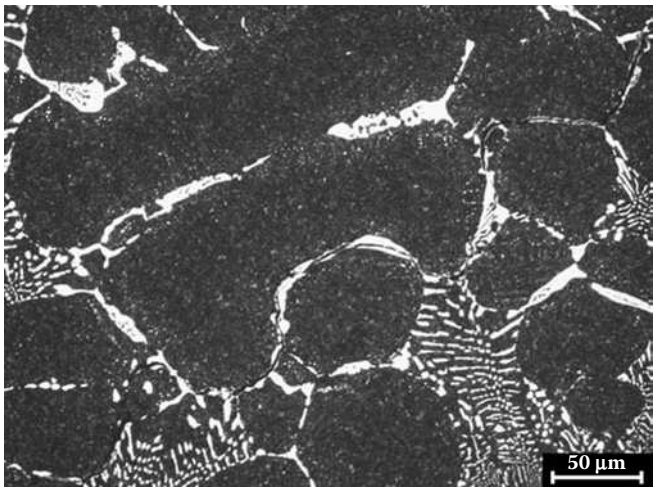


FIGURE 6.9 Thermal crack deviating along the boundary of a eutectic cell containing dissociated MC carbides in globular form.

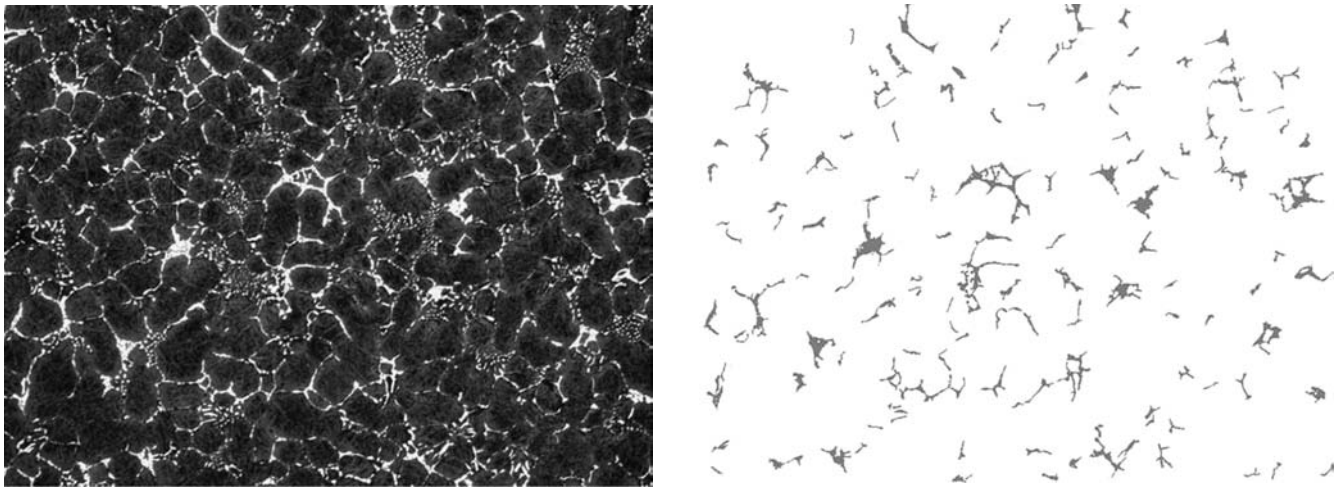


FIGURE 6.10 Schematic representation of the image analysis procedure used to remove globular MC carbides not influencing thermal cracking. The CVP thus obtained is used to determine the new relationship between P and CVP (see Figure 6.8).

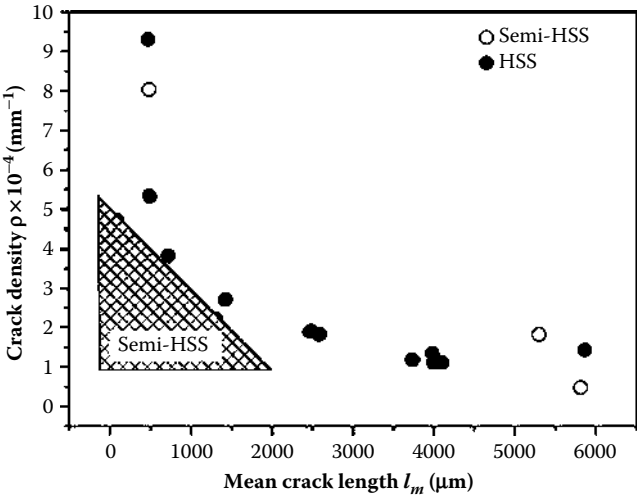


FIGURE 6.11 Crack density versus crack length in semi-HSS and HSS.

those with the highest amount of carbides with high interconnection. The propagation of long cracks occurs very easily in such steels because of their low crack arrest fracture toughness. A high amount of globular MC carbides, with low interconnection, improves crack nucleation at expense of propagation. The crack density after 180 cycles is thus very high (almost 10 cracks per mm) and l_m is very low. The experimental points pertaining to the best semi-HSSs are closer to the origin in the graph of Figure 6.11, confirming their better resistance to thermal cracking than HSS. This result can be explained by the very low degree of interconnection displayed by semi-HSSs.

6.5 RESULTS AND CONSIDERATIONS FROM THE MILLS

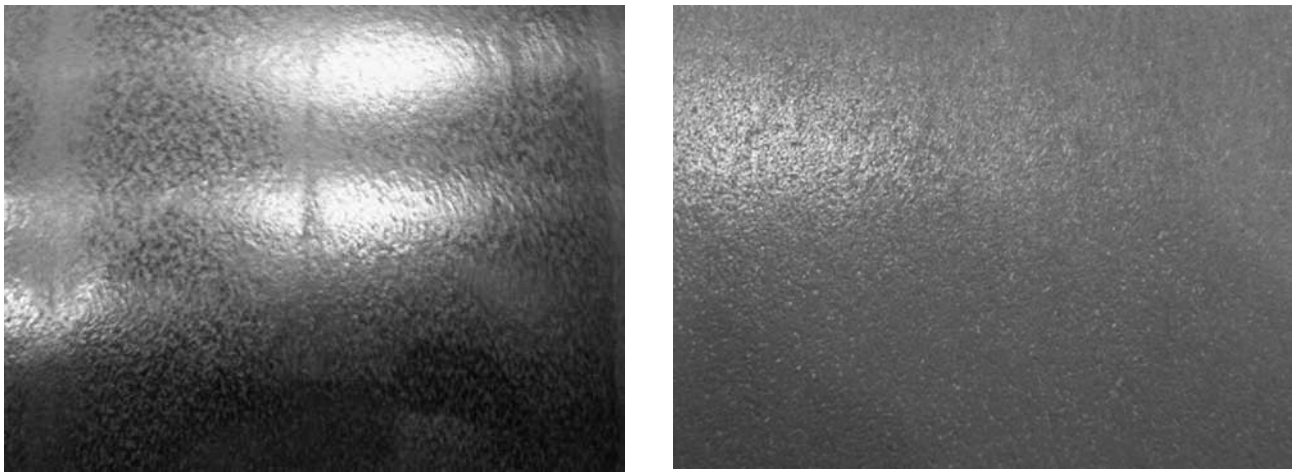
This section outlines some typical aspects of the type and the level of damage to HSS rolls in different rolling situations.

6.5.1 Roughing Stands in a Continuous HSM

The optimal properties at high temperatures of HSS allow the withstanding of very long campaigns. It's possible to reach more than 300,000 tons with rolls working for periods longer than three weeks (Table 6.2). The roll wear in stands R4 and R5 is two times greater than in stands R2 and R3 and normally the roll surface appears in worst condition (Figures 6.12 and 6.13).

TABLE 6.2
Results of HSS Rolls in Continuous Roughing Stands

Stand	R2–R3	R4–R5
Ton per campaign	250,000–300,000	
Campaign length (days)	20–25	
Wear (mm)	1–2	2–4
Roughness R_a (μm)	3–6	



(a) (b)

FIGURE 6.12 Aspect of HSS surfaces: (a) stand R3 $R_a = 3$ µm; (b) stand R4 $R_a = 5$ µm.

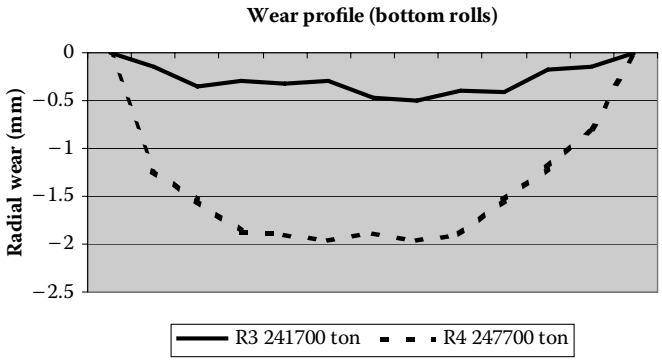


FIGURE 6.13 Radial wear profiles.

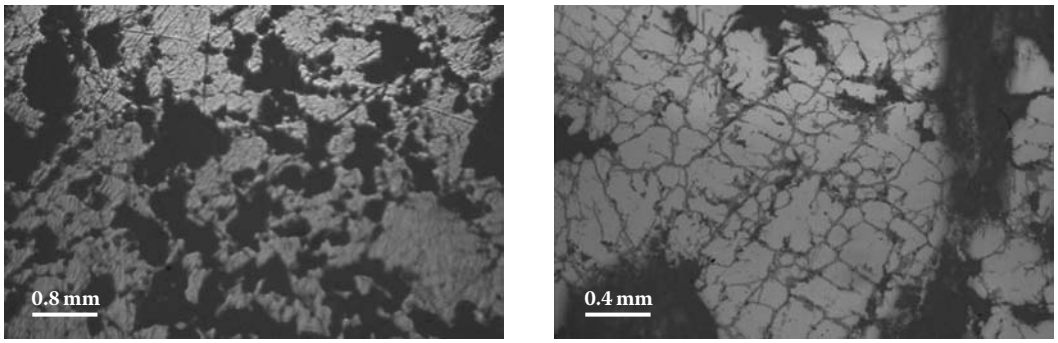


FIGURE 6.14 Damaging in stand R4 (surface after a very light polishing).

Figure 6.14 underlines the level of damaging in stand R4: the pits affect the entire dendrite arms and the firecracks follow perfectly the pattern of eutectic carbides.

6.5.2 Roughing Stands in a Minimill

In a continuous roughing group composed of three stands, it's possible to reach campaign of 6000–6500 tons without important wear. The medium stock removal is 0.5 mm: this level of regrinding allows first, the rebuild of roll profile and second, the reduction in the level of pitting (stand R1; Figure 6.15).

The visible cracks due to thermal fatigue are a maximum of 1 mm deep; the firecrazing of the surface affects a layer of 0.15 mm (Figure 6.16).



FIGURE 6.15 Roll surface in stand R1.



FIGURE 6.17 Aspect of the surface after 50,000 tons (R_a = 4.5 μm).

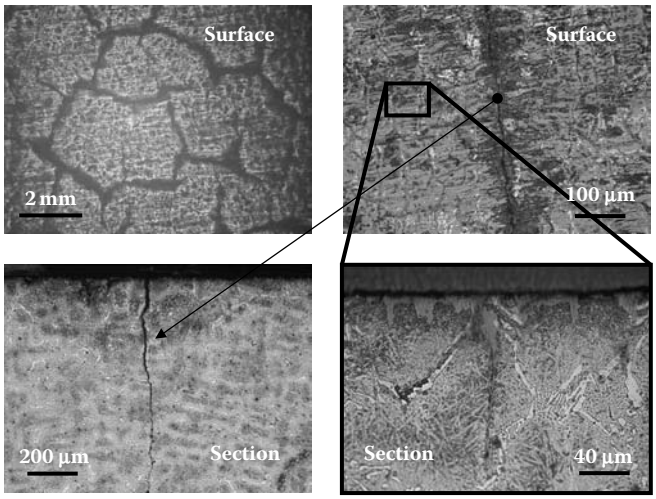


FIGURE 6.16 Damaging of the surface in stand R1.

6.5.3 Reversing Roughing Stands

In this type of stand, the use of HSS rolls provides long campaigns maintaining a good surface and a regular wear profile (Table 6.3). In an attempt to reduce the frequency of slippage events, HSS proposed for this application has a particular chemistry to limit the presence of eutectic carbides. Figure 6.17 shows the roll surface after 50,000 tons (Mill B).

6.5.4 General Considerations about Roughing Stands

The use of HSS rolls gave satisfactory results in terms of wear and surface quality. The main problem with these rolls is their relative low resistance to thermal fatigue and thermal shock if compared to more conventional grades, such as high chromium steels. On the other hand, because of the very complex state of stress during rolling, it was quite difficult to obtain useful information from the mills about the microstructural properties required for the rolls. In this way, thermal fatigue tests on a laboratory scale suggest the need for a reduced eutectic carbide network looking at improved resistance versus thermal cycling. Another crucial aspect contributing to the definition of HSS performance is the establishment of a suitable amount of extra grinding in relation to surface damage. In many cases, a fixed ratio between wear and extra grinding is adopted in roll shops, without any correlation to damage. It is the authors' opinion that this approach did not help maximize the real benefits of HSS rolls or define the comparative performance of different rolls.

6.5.5 Early Finishing Stands

The examples that follow represent typical situations of wear and damaging of HSS rolls used in the early stands of finishing mills.

Comparison F2–F3

After a campaign of about 5000 tons, the HSS rolls don't show appreciable wear. In both stands, the bottom rolls appear in worse condition. Figures 6.18 and 6.19 show the roll surface after the campaign: moving from F2 to F3, the firecracking diminishes while abrasion causes heavier scratches on bottom rolls of both stands. The F3 roll surface is less covered by oxide scale.

Comparison F0–F1–F2

Table 6.4 summarizes the wear situation of HSS rolls in this mill.

The firecracks due to thermal fatigue are obvious in stand F0, accompanied by micropitting of less than 0.1 × 0.1 mm (Figure 6.20). The pattern of firecracks appears lighter in stand F1, and in this case, only the carbides are cracked. Figure 6.21 shows also the matrix damage.

The scratches of the oxide scale on rolls can generate bands with high values of R_a (Figure 6.22): in these areas, the level of damage (and wear) is the same as in other parts of the roll where the oxide scale is still present (Figure 6.23).

TABLE 6.3
Results of HSS Rolls in Reversing Roughing Stands

Mill	A	B	C	D (Stainless Steel)
Ton per campaign	45,000–55,000	40,000–50,000	70,000–80,000	150,00–20,000
Wear (mm)	1 (T)–1.5 (B)	~0.6	1.5–2.0	1.0–1.5
Roughness R_a (μm)		2–6 μm		

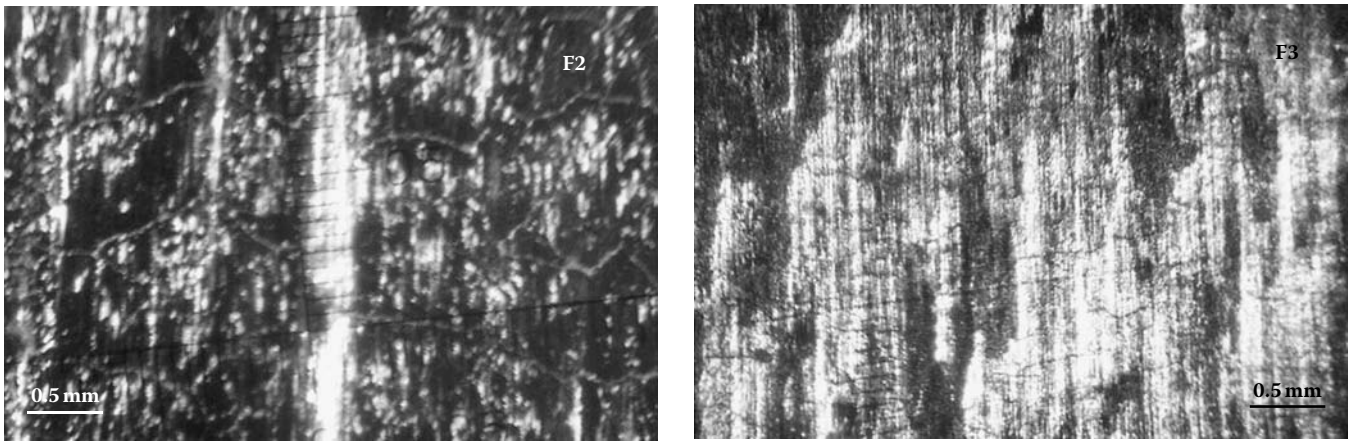


FIGURE 6.18 Aspect of the roll surface for bottom rolls: R_a = 3.5–4.0 μm.

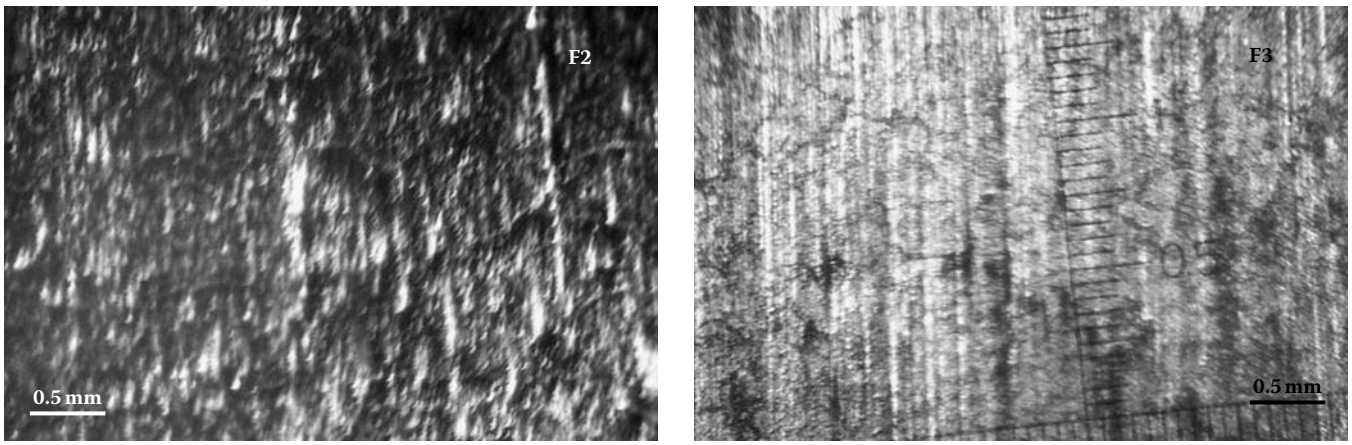


FIGURE 6.19 Aspect of the roll surface for top rolls: R_a = 1.2–1.6 μm.

TABLE 6.4
Results of HSS Rolls in Early Finishing Stands

Stand	Wear (λm/Km)	Max Wear (λm/campaign)	Delta Bot/Top (%)
F0		No data but impalpable wear	
F1	4.4	130	38
F2	4	230	40

Note: Roll wear can be expressed as roll consumption (microns) per rolling distance (km) (column 1) or per rolling campaign (column 2).

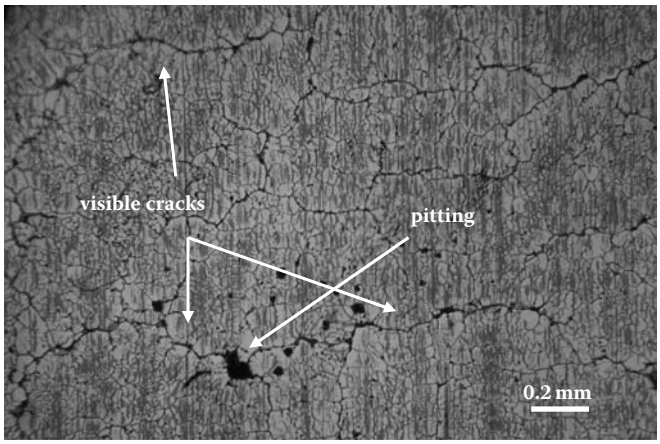


FIGURE 6.20 Details of roll surface in stand F0.

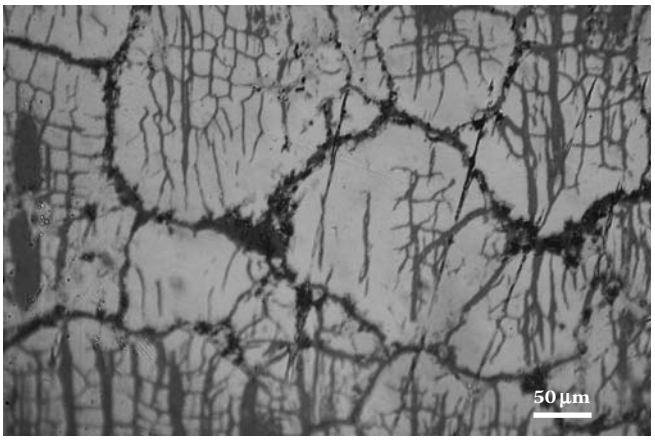


FIGURE 6.21 Damage due to thermal fatigue (stand F1).

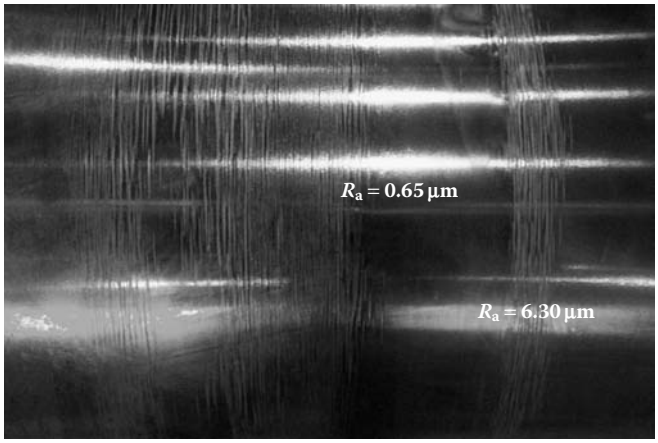


FIGURE 6.22 Aspect of roll surface in stand F1.



FIGURE 6.23 Roll surface damage with scratches.

6.6 CONCLUSIONS

This chapter has reviewed the service performance of rolls in the roughing and finishing stands. Despite the large number of test results collected (also those not included in this work), it is the authors' opinion that it is quite difficult to establish a well-defined correlation between roll performance and material properties (amount, type, morphology of eutectic carbides, hardness, matrix microhardness, and so on). More defined results (wear and thermal fatigue) come from laboratory tests aimed at reproducing the damage mechanism observed during actual rolling, even if they often could not be confirmed in field tests, because of the very complex state of solicitations acting during service. If possible, an even more chaotic situation is observed in the proper definition of the correct regrinding procedure as a function of the roll damage. This explains the uncertainty of the method to measure the real yield of roll materials.

In the recent past, many efforts were spent searching for new grades that showed improved properties in different stands. Less work was done regarding the manufacturing process, particularly in Europe, while in Japan considerable improvements were introduced with the CPC process. In most cases, wear is not a real problem, since impalpable wear is measured on certain stands. Indeed, abrasion deteriorates surface finishing together with pitting, causing the need to redress the roll. Hence, currently it is widely accepted that good surface quality of the rolls is more important than their high wear resistance (i.e., high hardness). More and more studies are aimed at defining the optimum chemical analysis to form a shiny and compact oxide layer. For example, it was proposed that hard MC carbides in HSS strongly improve wear resistance, but are deleterious for surface finishing because of the preferential wear of the adjacent metallic matrix. Hence, a proper compromise has to be found in order to obtain acceptable levels of both these properties. Following these guidelines, many grades also were developed by the authors [17–20].

The content of carbon and carbide-forming elements (Cr, Mo, W, V, Nb) was changed in order to achieve rolls having the proper amount of eutectic carbides combined with adequate matrix secondary hardness.

In this framework, the influence of the rolling process was completely and deliberately disregarded. To the authors' best knowledge, however, factors like roll cooling and lubrication, or the temperature of the strip (oxide scale), can significantly alter the working conditions, partially or totally covering any possible influence of roll chemistry. In any case, the development of new HSS roll materials should be tailored considering the whole tribological system.

In light of the results presented here and the current state of the art, the replacement of conventional grades by means of HSS rolls still remains a frontier for the 21st century.

REFERENCES

1. H.F. Fischmeister, R. Riedl, S. Karagöz. (1989). *Metallurgical Transactions A*, 20: 2133.
2. J.A. Golczewsky, H.F. Fischmeister. (1993). Solidification of high speed steels: Thermodynamic and kinetic aspects. *Zeitschrift fur Metallkunde*, 84: 860–866.
3. A. Tremea, A. Biggi, G. Corbo, D. Cescato, M. Pellizzari, A. Molinari. Performances evaluation of high-speed steels for hot rolling by wear and thermal fatigue tests. In *Proceedings of the AISTech 2006*, Cleveland, OH, May 1–4, 2006.
4. M. Pellizzari, A. Molinari, G. Straffelini. (2005). Tribological behaviour of hot rolling rolls. *Wear*, 259: 1281–1289.
5. M. Fukuhara, A. Sanpei. (1993). Elastic moduli and internal friction of low carbon and stainless steels as a function of temperature. *ISIJ International*, 33: 508–512.
6. J.H. Ryu, O. Kwon, P.J. Lee, Y.M. Kim. (1992). Evaluation of the finishing roll surface deterioration at hot strip mills. *ISIJ International*, 32(11): 1221–1223.
7. A. Molinari, M. Pellizzari, A. Biggi, G. Corbo, A. Tremea. Primary carbides in spincast HSS for hot rolls and their effect on the oxidation resistance behaviour. In *Proceedings of the 6th International Tooling Conference*, pp. 365–377, Karlstadt, Sweden, September 10–13, 2002.
8. G. Savage, R. Boelen, A. Horti, H. Morikawa, Y. Tsujimoto. (1996). Hot wear testing of roll alloys. In *Proceedings of the 37th MWSP Conference*, Vol. 33, pp. 333–337. Warrendale, PA: ISS.
9. F.H. Stott, G.C. Wood. (1978). The influence of oxides on the friction and wear of alloys. *Tribology International*, 11: 211.
10. F.H. Stott, M.P. Jordan. (2001). The effect of load and substrate hardness on the development and maintenance of wear-protective layers during sliding at elevated temperature. *Wear*, 250: 391–400.
11. D. Steiner, D. Liquet, G. Nicoloudis, H. Uijtdebroeks, A. De Paepe, J.C. Herman. (2001). Optimisation de la lubrification des cylindres de travail au train à chaud. *La Revue de Métallurgie*, 11: 1045–1053.
12. J.W. Park, H.C. Lee, S. Lee. (1999). Composition, microstructure, hardness, and wear properties of high-speed steel rolls. *Metallurgical Transactions A*, 30: 399–409.
13. M. Pellizzari, D. Cescato, A. Molinari, A. Tremea, G. Corbo, A. Biggi. Laboratory testing aimed at the development of materials for hot rolls. In *Proceedings of the Steel Rolling 2006, 9th International & 4th European Conferences*. Paris La Defense, France, June 19–21, 2006.
14. A. Molinari, A. Tremea, M. Pellizzari, A. Biggi, G. Corbo. (2002). High speed steels for hot rolls with improved impact and thermal fatigue resistance. *Materials Science and Technology*, 18: 1574–1580.
15. A. Molinari, M. Pellizzari, A. Tremea, A. Biggi, G. Corbo. (2005). Effect of the matrix microhardness on thermal fatigue behaviour of spincast high-speed steels for hot rolls. *Materials Science and Technology*, 21(3): 352–356.
16. M. Pellizzari, A. Molinari, A. Biggi, G. Corbo, A. Trema. (2005). Semi-high-speed steels for roughing rolls with improved thermal fatigue resistance. *La Metallurgia Italiana*, 9: 57–61.
17. A. Molinari, M. Pellizzari, A. Biggi, G. Corbo, A. Tremea. Development of spincast hot rolls through microstructural tailoring. In *Proceedings of the 44th Mechanical Working and Steel Processing*, Vol. 60, pp. 1233–1244, Orlando, Florida, September 8–11, 2002. Warrendale, PA: ISS.
18. A. Molinari, M. Pellizzari, A. Biggi, G. Corbo, A. Tremea. Metallurgical development of hot rolls with improved rolling performances. In *Proceedings of the SARUC2002*, p. 37, Gauteng (RSA), October 17–18, 2002.
19. M. Pellizzari, A. Molinari, A. Biggi, G. Corbo, A. Tremea. New semi high-speed steel with low carbon content for the production of spincast roughing rolls with improved thermal fatigue resistance. In *Proceedings of the SARUC2004*, Gauteng, RSA, May 14–15, 2004.
20. M. Pellizzari, A. Molinari, D. Cescato, A. Tremea, G. Corbo, A. Biggi. Wear and friction behaviour of high chromium iron and high-speed steels for hot rolls. In A. Sinatora, M. Boccalini Jr., M.E. Hara, (eds.), *Proceedings of the International Conference on Abrasion 2005*, pp. 189–198, Sao Paolo, Brazil, August 14–17, 2005.
21. M. Pellizzari, D. Cescato, M.G. De Flora, A. Tremea, A. Biggi, G. Corbo. Tribological properties of high chromium white cast irons in rolling of plain carbon steel. In *Proceedings of the International Conference on Abrasion 2008*, pp. 90–101, Trento, Italy, August 24–27, 2008.
22. M. Pellizzari, D. Cescato, M.G. De Flora. Hot friction and wear behavior of high-speed steel and high chromium iron for rolls. To be published in *Wear*, 2009 special issue.

7 Tunnel Furnace Roll Options and Energy Considerations

Robert J. Echlin, Daniel V. Miller, and Roman I. Pankiw

CONTENTS

7.1 Introduction 83
7.2 Tunnel Furnace Rolls—Energy Use Overview 84
7.3 Tunnel Furnace Roll Options 84
7.4 Water-Cooled Roll Heat Loss 86
7.5 Dry Roll Heat Losses 87
7.6 Dry Roll Conversion—Natural Gas Savings 88
7.7 Conclusions 88
Appendix—Heat Transfer Calculations and Heat 89
References 90

7.1 INTRODUCTION

The compact strip production (CSP) process for making strip steel became a reality in 1989 when Nucor Steel began production at its mill in Crawfordsville, Indiana. At its inception, the plant in Crawfordsville consisted of a single continuous caster with one tunnel furnace feeding slabs to a grossly underutilized hot strip mill. Annual output of the mill at that time was limited to less than 1 million tons, yet it ushered in a new era in strip steel production.

In the CSP process, tunnel furnaces link one or two continuous casters with a rolling mill, and in doing so, make the minimill approach to strip steel making practical. About twice as long as a football field, these furnaces utilize a series of motor-driven rolls, typically spaced at intervals of about 1 m, to transport steel slabs ranging from 55 to 90 mm in thickness to the rolling mill for gauge reduction. They can each handle about 1 million tons annually serving (1) to provide limited reheating of the slab, (2) to equalize slab temperature for rolling, and (3) to hold the freshly cast slab until the mill is ready to receive it.

Initially, the Crawfordsville tunnel furnace was outfitted entirely with water-cooled rolls. However, by early 1991, Nucor had begun trial use of non-water-cooled, or dry, rolls in some sections of its furnace. The success of these trials was important in that it allowed dry rolls to be incorporated in the design of the second phase of construction of Crawfordsville's hot mill, which included a second tunnel furnace and continuous caster. This additional equipment could provide twice the quantity of slabs to the hot mill, increasing output to about 2 million tons annually.

By necessity, the new furnace included a moveable slab transfer section, or shuttle, to allow transportation of slabs from the new second furnace into the entry section of the mill that was aligned with the original tunnel furnace. A shuttle also had to be added to the original furnace so that section of the furnace could be moved out of the way to allow access of the new shuttle to the mill entry.

The shuttles proved to be ideal locations for dry rolls since they eliminated the need for cumbersome and expensive water distribution systems that would have been required with water-cooled rolls. For the next 10+ years, until the early 2000s, dry rolls were used almost exclusively in the shuttles and water-cooled rolls in the stationary sections of tunnel furnaces. A few plants with heavier slabs, over 70 mm thick and/or operating with higher furnace temperatures, were the exceptions and utilized only water-cooled rolls. Often the extensive use of water-cooled rolls was justified because of their perceived economy, considering only their lower initial purchase price. This thinking did not recognize the energy costs associated with tunnel furnace operation and, in particular, the considerable heat loss involved in the use of water-cooled rolls. Moreover, it tended to retard development of improved dry rolls that could replace water-cooled ones in the hotter sections of tunnel furnaces.

Recently, the use of higher creep-strength alloys, roll designs incorporating larger diameter barrels, and improved means of insulating roll ends to reduce heat flow to the journals have paved the way for more extensive use of dry rolls. Just as important, the energy cost associated with the use of water-cooled rolls is now being recognized and has become

the primary justification for replacing water-cooled rolls with dry rolls, whenever possible.

7.2 TUNNEL FURNACE ROLLS—ENERGY USE OVERVIEW

Tunnel furnaces use natural gas and operate at temperatures in the range of 2050–2250°F (1120–1230°C). Because of their tremendous throughput, high operating temperatures, and considerable length, tunnel furnaces consume considerable quantities of natural gas. A typical furnace with about 100 water-cooled rolls in the stationary heating sections and another 50 dry rolls in the moveable shuttle will consume the amount of natural gas needed to produce about a trillion Btu annually—about 1 billion cubic feet in a year when the plant is running near capacity [1]. A single furnace containing only water-cooled rolls will use up to 15–20% more natural gas, and plants with two casters and twin parallel furnaces will consume twice that amount or more.

Tunnel furnaces are not only large consumers of energy, but they also waste a considerable portion of the heat produced by their burners. Like all large, fuel-fired industrial furnaces, tunnel furnaces have lower fuel efficiency due to heat losses out the stack, through the insulation lining the roof and furnace walls, through cracks and openings, into the excess air passing through the burners, and the like. Additionally, tunnel furnaces lose significant amounts of heat through the 80 to 100 water-cooled rolls that would typically be found in a new installation. With water-cooled rolls, heat conducted to the center shaft raises the temperature of the cooling water circulating through it and is lost—wasted—as the heated water is discharged from the roll [2]. Rolls of this type have traditionally been used in the heating zones, but are sometimes used in the holding zones and transfer sections as well, where dry rolls may have been thought impractical for various reasons, including excessively high temperatures or extreme slab loads, as previously noted.

In CSP tunnel furnaces, heat lost through water-cooled rolls is second only to stack losses. It has been determined that a single water-cooled roll will lose on average 175,000–250,000 Btu or more each hour, and the 100 water-cooled rolls in a typical tunnel furnace can waste 170 billion or more Btus annually. When process thermal efficiency is considered, the burners must put out almost twice as many Btus to compensate for the heat, which is lost through the water-cooled rolls. For a single tunnel furnace, this equates to upward of 300 million cubic feet or 310,000 mmBtu of natural gas being wasted annually due to heat lost by the water-cooled rolls alone [4].

Dry rolls also lose some heat by convection and radiation from the exposed sections of the roll journals, which protrude from the furnace. However, these losses are less than 7% of the heat wasted by water-cooled rolls—that is, about 5,000 to fewer than 15,000 Btu/hr/roll. Obviously, the use of dry rolls wherever possible can result in major energy savings in a tunnel furnace operation.

7.3 TUNNEL FURNACE ROLL OPTIONS

As previously noted, tunnel furnace rolls are generally of two distinct types—water-cooled and dry. Water-cooled rolls have traditionally been used in the heating zones of the furnace. They consist of a refractory-covered hollow steel shaft with four to six cast heat-resisting alloy tires affixed to it. The tires are normally 12-in. outside diameter (OD), and their outer face is the only part of the roll in contact with the slab. However, it is the carbon steel shaft, which is usually 5–6 in. in diameter, that basically carries the slab load (see Figure 7.1). The maximum bending stress acting on the roll shaft is about 3000 psi, which is six to eight times greater than the stress acting on the barrel of a dry roll. Since carbon steel has extremely poor elevated temperature strength, the water-cooled roll shaft must be maintained at a relatively low temperature to resist the bending stresses acting upon it. This is accomplished by circulating rather large volumes of cold water through the roll. Severe overheating of a carbon steel shaft due to loss of cooling water will result in roll failure in a matter of minutes. A properly cooled roll with refractory intact may last several years.

Traditionally, dry rolls have been designed with 12-in.OD barrels—the same diameter as the tires on the water-cooled rolls (see Figure 7.2). For many years, rolls of this design had been confined mainly to the moveable transfer sections, that is, shuttles or shifters, where furnace temperatures are usually in the 2050–2100°F (1120–1150°C) range as compared with 2100–2200°F (1150–1200°C) or higher in the heating zones. Until recently, available roll manufacturing practices, particularly welding of component sections, and

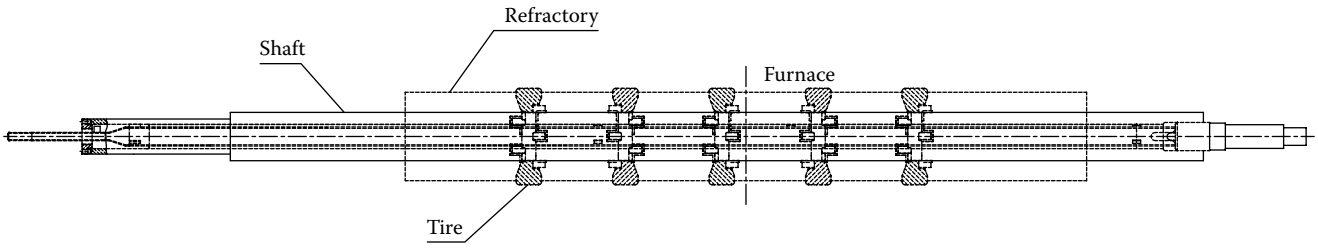


FIGURE 7.1 Typical water-cooled roll.

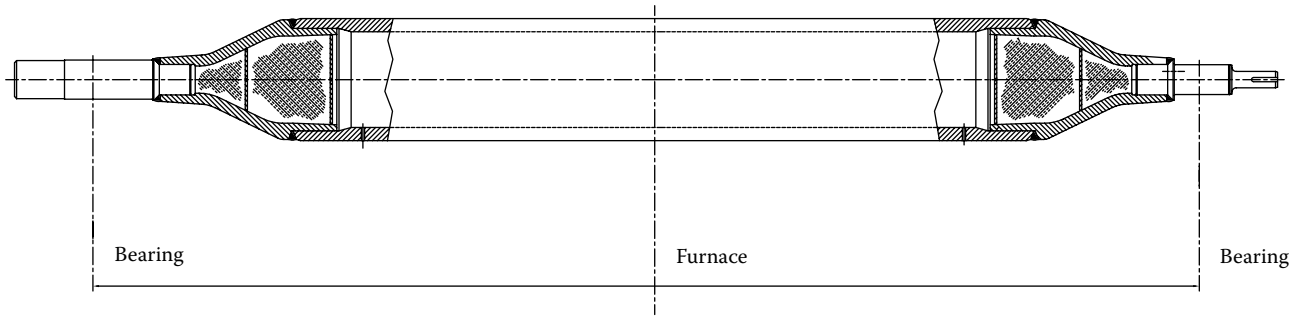


FIGURE 7.2 Typical dry roll.

alloy limitations often precluded the introduction of dry rolls into the heating sections of tunnel furnaces. However, more recently, improved weld procedures, weld joint designs, and casting geometries, along with new higher creep strength alloys, have been introduced, making it possible to produce dry rolls suitable for the heating zones and other locations where dry rolls had previously been deemed unsuitable.

In the area of alloy development, new alloys for dry rolls such as MO-RE®-2150 have been introduced with considerably higher creep properties than the 28Cr–48Ni–5W–3Co (Super 22H®* or 30–50–W+Co) type alloy, which has been used successfully since the early 1990s in the moveable shuttles. Table 7.1 provides stress-to-rupture data from the respective Larson–Miller diagrams for the aforementioned two dry roll alloys. This information was used to make lifetime predictions for rolls subjected to the operating conditions (stress and temperature) expected in actual service [3]. The authors have successfully used this method in the design and evaluation of several thousand dry rolls that have been installed in dozens of tunnel furnaces worldwide. Table 7.1 shows that, for 12-in.OD dry rolls engineered for use in the heating zones in one customer's furnace, dry roll life was determined to increase by 50% or more using newer high temperature alloys with improved creep properties such as MO-RE®-2150. It should be noted that for this particular application, the slab load and roll dimensions are such that relatively low bending stresses can be achieved even with 12-in.OD rolls. This is generally not the case with most plants, which typically run heavier slabs in wider furnaces that require longer rolls (i.e., with greater spacing between roll bearings)—all of which increase the bending stresses acting on the roll barrel. Table 7.2 shows stress and lifetime calculations for more typical installations with higher bending stress. The authors have detailed the method for calculating roll bending stresses in their earlier paper, "Advances in Tunnel Furnace Rolls" [5].

It is noteworthy that the Super 22H® roll evaluated in Table 7.1 would provide well over 6 years' service if used in the shuttle section of the furnace. In contrast, a "standard" Super 22H® type dry roll engineered to provide approximately 4 years' service in the shuttles where furnace temperature is typically about 2080°F (1140°C) is projected to survive only 10–11 months in the heating sections of the furnace where the temperature is 2150°F (1175°C). This illustrates the dramatic effect furnace temperature has on the creep properties of the roll material and, more importantly, on roll life.

In addition to material differences, one of the key differences between older type dry rolls manufactured for shuttle applications and newer rolls to be used in the heating zones is that the latter are engineered so that the bending stresses acting on them are significantly lower [5]. To lower bending stresses and to enhance the use of dry rolls, some furnaces

TABLE 7.1
Creep Test Data and Roll Lifetime as Affected by Roll Alloy for Heating Zone Rolls Operating at 2150°F (1175°C)

Alloy	Hours to Failure in Standard Creep Rupture Test[a]	Projected Roll Life[b]
Super 22H®	4710	1.6–1.8 years
MO-RE®-2150	7190	2.5–2.7 years (+50%)

[a] Data for standard creep test specimens tested at 460 psi and 2150°F (1175°C).

[b] Roll has 12-in.OD, with cast components engineered for heating zone use.

TABLE 7.2
Effect of Roll Diameter on Bending Stress and Lifetime for Rolls Specifically Engineered for Use in Tunnel Furnace Heating Zones

Roll OD (in.)	Maximum Bending Stress (psi)	Projected Roll Life (years)	Relative Roll Cost
12	515	1.9–2.4	1
13	455	2.8–3.4	1.2
14	405	4.1–4.7	1.4

* Duraloy®, Super 22H®, and MO-RE® are registered trademarks of Duraloy Technologies, Inc. in the United States, Canada, the European Community, and many other countries. All rights reserved.

have been modified to accept larger diameter rolls. One furnace was recently altered so that 13⅛-in.OD rolls could be used, and several others to use 14-in.OD rolls. The effects of roll diameter on bending stress and roll lifetime are shown in Table 7.2. These calculations were made for rolls that were specifically engineered to carry 55- to 65-mm thick slabs in heating zone applications where the furnace temperature is 2125–2150°F.

While dry rolls have a higher purchase price than water-cooled rolls, they become quite cost-effective when energy losses are taken into consideration, as the following sections will further demonstrate. As an example, installation of the aforementioned 13⅛-in.OD rolls provided sufficient savings in natural gas charges to pay for themselves in less than 6 months.

7.4 WATER-COOLED ROLL HEAT LOSS

Heat balances constructed using the appropriate heat-transfer mechanisms allow calculation of heat losses that occur with water-cooled rolls. Simply put, heat from the furnace atmosphere and hot furnace walls is transferred to the exposed surface of the roll largely by radiation. It is then conducted through the tires, and the roll refractory to the center shaft, and finally through the shaft to the cooling water circulating within it. An even greater quantity of heat is transferred to the shaft directly by radiation in areas where the refractory has spalled off and is missing. The heat arriving at the inside surface of the shaft heats the cooling water and is carried out of the furnace as in the discharge water—it is wasted heat.

Appendix 7.1 shows the heat balances that are involved, the solutions of which provide the heat loss information shown in Table 7.3.

Using the figures contained in Table 7.3, it can be determined that a water-cooled roll with four tires operating in a furnace having an interior width of 67 in. would experience a heat loss of approximately 145,000 Btu/hr if all of the refractory was intact and undamaged. However, partial refractory loss is the norm rather than the exception. In fact, the writers would estimate that considering all rolls in a typical furnace, the average roll exhibits 10–15% refractory loss. Recognizing this, and taking the added heat loss for missing/damaged refractory into account, the calculated heat loss for the example roll increases to about 225,000 Btu/hr.

It is a rather simple matter to determine just how much heat is actually wasted in this manner. Measurements of flow rate and inlet and outlet water temperatures are all that are needed. Once these quantities are known, the heat loss can be calculated as follows:

$$\text{Heat loss (Btu/hr)} = (T_{\text{outlet}} - T_{\text{inlet}}) \times \text{FR}_{(\text{gpm})} \times 8.33_{(\text{lb/gal})} \times 60_{(\text{min/hr})} \quad (7.1)$$

where T is the water temperature in degrees Fahrenheit, and FR is the rate of flow of the cooling water in gallons per minute.

Using this approach, the furnaces at one CSP plant were monitored to determine water-cooled roll heat losses. Cooling water flow rates, and water inlet and outlet temperatures for 14 cooling circuits (42 rolls) in the heating zones of its furnaces, were measured. Each cooling circuit consists of three rolls in series served by a common water inlet and outlet [4]. The rolls have four 12-in.OD tires on a 5-in.OD carbon steel shaft and are insulated with a castable refractory with a thermal conductivity of about 0.8–1.0 Btu/ft-ft-°F-hr. The furnace set point is 2110–2120°F. The data accumulated are shown in Table 7.4.

TABLE 7.3
Calculated Heat Losses for Water-Cooled Rolls

Heat Transferred to Cooling Water Via	Heat Loss (Btu/hr)
Conduction through tires	17,000–25,000 per tire[a]
Conduction through roll refractory	75,000–85,000[b]
Conduction through shaft with complete loss of refractory	650,000–900,000[c]

[a] Actual loss depends on tire design and geometry of tire-shaft weld.
[b] Actual loss depends on length of shaft within furnace (i.e., furnace interior width) and the type of refractory applied. Above figures are for typical "hard" castable.
[c] Actual loss depends on furnace width, and inside and outside diameters of the shaft.

TABLE 7.4
Water Temperature and Flow Rate Data for 42 Water-Cooled Rolls in Twin, Parallel Furnaces

Water flow rate:	30–41 gpm	Average = 36.4 gpm
Inlet temperature:	70–74°F	Average = 71°F
Outlet temperature:	95–120°F	Average = 105°F

Source: Bennett et al., private communication.

Using the above formula for heat loss and the data in Table 7.4, the average heat loss for an individual roll in this particular plant was found to be 205,900 Btu/hr. Note that this figure is in reasonably good agreement with the calculated heat loss in the above example (i.e., 235,000 Btu/hr). For the full 193 water-cooled rolls in that plant's two furnaces, this equates to a loss of 39,740,000 Btu/hr. Furnaces that are wider (width > 67 in.) and/or that operate at higher temperature (T > 2120°F) will experience even greater heat losses through their water-cooled rolls than those shown above. Rolls evidencing more or less refractory loss will also show variances from the 205,900 Btu/hr average heat loss determined for these rolls.

Individual rolls in the foregoing heat loss study showed a fairly wide variance in heat loss, ranging from about 160,000 to 260,000 Btu/hr. Variation inherent in measurement technique and devices undoubtedly accounts for some of this deviation from average. For example, a ±1°F variance in

water temperature results in a variation of ±19,000 Btu/hr in the heat loss calculation. Additionally, some of the observed variance is attributable to differences in location of individual rolls within the furnace and to variations in actual roll temperature. Finally, there are undoubtedly differences in the amount of refractory insulating the shafts of the various rolls studied—this factor probably being the most significant source of variance in the individual measurements.

The importance of maintaining refractory protection on the center shafts of water-cooled rolls cannot be overemphasized. As Table 7.3 shows, in the worst case scenario, complete loss of refractory is calculated to increase the heat lost in the rolls included in this study from an average value of 205,900 Btu/hr to over 650,000 Btu/hr/roll.

The use of a lower-conductivity, heat-resisting alloy shaft can help reduce heat loss in water-cooled rolls. Heat-resisting alloys typically have thermal conductivities of one-third to one-half that of carbon steel. As a result, the use of an alloy shaft can reduce heat loss by about 7% as compared with rolls with carbon steel shafts. The alloy shafts also have the benefit of improved oxidation resistance, which increases roll life when refractory loss occurs. The alloy shaft also allows rolls to survive brief periods of water loss when those with carbon steel shafts would be ruined.

7.5 DRY ROLL HEAT LOSSES

As previously noted, the use of dry rolls also results in some heat loss, but these are usually less than 5% of the losses for water-cooled rolls. Losses from dry rolls occur when heat is conducted from the furnace interior through the end bells to the journals, which are situated outside of the furnace. Heat thus conducted to the journals is transferred by convection and radiation to the furnace surroundings, and the amount of heat lost depends on how hot the journals are running. Properly constructed dry rolls incorporate a system of internal insulation and alloy radiation shields to minimize heat transfer to the journals and maintain lower journal temperature.

Heat lost from the journals of dry tunnel furnace rolls can be determined as follows:

$$\begin{aligned}\text{Heat loss } (Q) &= \text{Convective loss} + \text{Radiation loss},\\ Q &= \mathrm{h}A(T_{\text{journal}} - T_{\text{surroundings}}) +\\ &\quad \varepsilon\sigma A(T^4_{\text{journal}} - T^4_{\text{surroundings}}),\end{aligned} \tag{7.2}$$

where the constants are $\mathrm{h} = 1.5$, $\varepsilon = 0.5$, and $\sigma = 0.1714 \times 10^{-8}$. A is the area (ft^2), and T is the temperature (in °R).

As an adjunct to the water-cooled roll study cited above, a temperature survey of the journal sections of a typical dry roll was also made. The results of this survey are shown in Figure 7.3 [4].

To calculate the heat loss using these data, the individual heat losses for each section of the journal, those labeled 1, 2, and 3 in the figure, are calculated independently using the above formula and then added together to arrive at the total. With this approach, the heat loss (Q) from a single journal

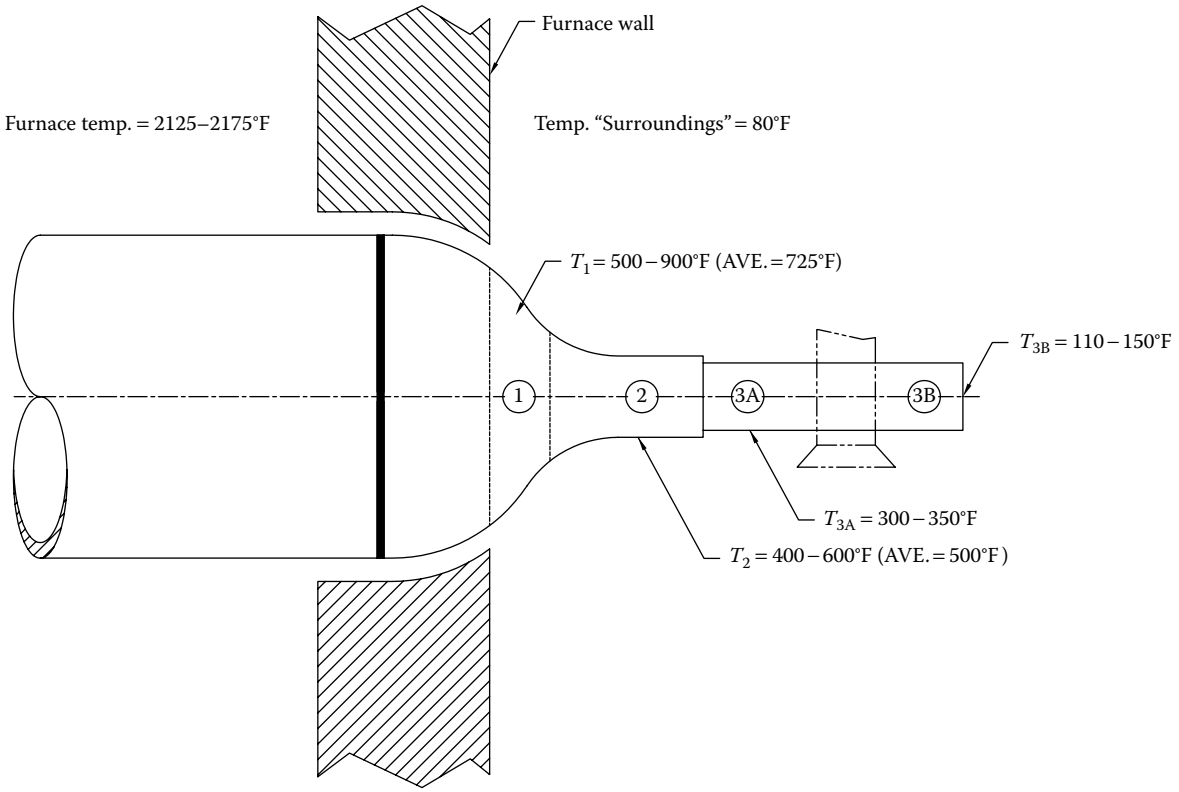


FIGURE 7.3 Typical end and journal temperatures for dry tunnel furnace rolls.

was calculated to be about 4500 Btu/hr and for the entire dry roll (two journals) the heat loss is 9000 Btu/hr, which is about 4% of the heat loss for the water-cooled rolls in the same furnace.

7.6 DRY ROLL CONVERSION—NATURAL GAS SAVINGS

For the plant that conducted the study summarized in Table 7.3, the net energy savings determined to be attainable by replacing water-cooled rolls with dry rolls is about 197,000 Btu/hr/roll or for the full 193 rolls in the two furnaces there—a staggering 38 mmBtu/hr. Using a thermal efficiency of about 55% [4], and assuming reasonably full production levels, the calculated energy savings translate to annual natural gas savings for that plant of about 580,000 mmBtu or $3.5 million for gas at $6 per mmBtu to $5.2 million at $9 per mmBtu. Of course, actual savings depend on the plant's operating level and the prevailing cost of natural gas. Based on this study, that plant began installing using 12-in.-diameter dry rolls specifically engineered for the heating zones of their furnaces.

A second plant investigating replacement of its 12-in.OD water-cooled rolls presented a somewhat different challenge. In this furnace, slab loads were unusually high due to the casting of 90-mm slabs and because of the greater than usual spacing between individual rolls. This resulted in roll bending stresses as much as two times greater than those experienced for 12-in.OD rolls at other CSP plants. Because of this, the entire furnace, including the shuttle sections, had been designed and equipped with water-cooled rolls. Lifetime calculations for 12-in.OD rolls indicated that even in the coldest sections of these furnaces, a 12-in.OD roll could not be expected to provide more than one year's service. However, with recent advances in dry roll technology and the plant's willingness to modify its furnaces, larger-diameter, 13⅛-in.OD, MO-RE® 2150 dry rolls were installed in one of that plant's shuttles in May 2006. This successful introduction of dry rolls has resulted in natural gas savings reported to be on the order of 500,000 Btu/hr/roll, or about 15 mmBtu/hr for the 30 rolls in that section of the furnace. The actual savings experienced are about 20% greater than anticipated, making the dry roll substitution very cost-effective. In fact, the cost savings generated were sufficient to pay back the expenditure for these rolls in less than 6 months [6].

Subsequent to the installation of the aforementioned 13⅛-in.OD rolls, it was found that the furnaces in that plant could be successfully modified to accept 14-in.OD rolls. In November 2006, the second shuttle was outfitted with 14-in.OD rolls and current plans call for replacing the 13⅛-in.OD rolls when they reach the end of their useful lives with 14-in.OD rolls.

Several other furnaces have been modified to accept 14-in.OD dry rolls to take advantage of the extended life offered by these larger diameter rolls. In those installations, preliminary reports indicate natural gas savings in line with projections. Additionally, in several cases where it had been impossible to maintain set point temperatures prior to the introduction of dry rolls, it has been found that once the water-cooled rolls were replaced, it was a simple matter to hold the desired temperature and even to increase it. One plant reported that with water-cooled rolls in the furnace, set point temperature could not be reached even with the burners firing at 100% output. Once dry rolls were substituted, the furnace had only to be fired at 18% to achieve set point temperature.

More recently, yet another plant embarked on a program to totally replace its 200 water-cooled heating zone rolls with 14-in.OD dry rolls. While the energy savings to be realized are important here, the driving force for this changeover is the need to achieve higher slab temperatures, which has not been possible when running water-cooled rolls.

In summary, dry rolls specifically engineered to replace water-cooled rolls in CSP tunnel furnaces have been demonstrated to result in considerable energy savings and dramatically reduced natural gas costs (Table 7.5). Additionally, further savings result due to reduction of peripheral costs associated with water-cooling—such as hoses, water treatment chemicals, pumping costs, etc. In total, these savings more than pay for the added cost of the dry rolls, and return substantial savings dollars to the CSP plant's bottom line.

TABLE 7.5
Substitution of Dry Rolls for Water-Cooled Rolls—Projected Net Energy and Natural Gas Savings

Number of Water-Cooled Rolls Replaced		1	100	200
Typical Net Reduction in Annual Natural Gas Usage (mmBtu):		3350	335,000	670,000
Net reduction in annual natural gas expenditure ($/mmBtu):	@ $6	$20,000	$2.0 million	$4.0 million
	@ $7	$23,500	$2.3 million	$4.6 million
	@ $8	$27,000	$2.7 million	$5.4 million
	@ $9	$30,000	$3.0 million	$6.0 million

7.7 CONCLUSIONS

1. Water-cooled tunnel furnace rolls lose large quantities of heat that is discharged with the water circulating through them. Data from actual furnaces show that losses ranging upward of 200,000 Btu/hr/roll are typical.
2. Loss of insulating refractory has the adverse effect of increasing heat loss in water-cooled rolls. Complete loss of refractory can more than triple the amount of heat lost per roll to over 650,000 Btu/hr/roll.
3. Dry rolls also lose some heat to the outside of the furnace through the journals. However, losses

calculated for dry rolls were found to be typically less than 10,000 Btu/hr/roll for rolls with well-insulated end bells. This is less than 5% of the losses for water-cooled rolls in the same furnaces.

4. Dry rolls specifically engineered to lower the bending stress acting on them and made of higher creep strength alloys can replace water-cooled rolls in tunnel furnace heating sections, where the water-cooled rolls are commonly used. Larger diameter dry rolls of this type can provide up to 5 years continuous service in heating zone applications.
5. Substituting dry rolls for water-cooled rolls in the heating zones of a tunnel furnace can conserve 150 billion Btu annually in a single furnace—300 billion in a plant with two furnaces. In plants with two casters and parallel tunnel furnaces, natural gas costs can be cut by $4–$5 million or more depending on furnace size, number of rolls, and the prevailing cost of natural gas.
6. Several plants have begun using advanced dry rolls, including larger 13-in.- and 14-in.OD rolls, in applications where water-cooled rolls had once been used exclusively. Feedback from these facilities indicates that actual energy savings in line with, or even exceeding, expectations are being achieved, with the added benefit that furnace set point temperatures are readily maintained at reduced firing rates.

APPENDIX—HEAT TRANSFER CALCULATIONS AND HEAT

Balances for Water-Cooled Rolls

Section 2.2.1 of this chapter, Water-Cooled Roll Heat Loss, notes that heat balances can be established using formulae for the appropriate heat transfer mechanisms that are in play during the operation of water-cooled rolls.

In rather simple terms, heat radiated from the hot furnace interior and atmosphere is transferred to the exposed portions of the roll—the outside surfaces of the refractory and the tires—and in cases where refractory is damaged or missing, directly to the roll shaft. Ignoring for the time heat losses due to missing refractory, the heat path continues through the mass of the refractory and the tires by conduction. Heat energy reaching the shaft is finally conducted through it to its inside surface where it heats the cooling water circulating therein. Ultimately, this heat is removed from the system—lost or wasted—when the heated cooling water is discharged from the roll. The following heat balance can be established to represent the foregoing,

$$q_{\text{radiation}} = (q_{\text{conduction-refractory}} + q_{\text{conduction-tires}}) = q_{\text{conduction (shaft)}} = \text{heat loss} \quad (7.3)$$

and this can be defined by the following heat transfer equation,

$$\varepsilon\sigma A(T_F^4 - T_1^4) = \left[\frac{2\pi L_r k_r (T_1 - T_2)}{\ln(r_r \div r_{so})} + \frac{2\pi L_t k_t (T_1 - T_3)}{\ln(r_t \div r_{so})}\right] = \frac{2\pi L_s k_s (T_2 - T_4)}{\ln(r_{so} \div r_{si})} = \text{heat loss} \quad (7.4)$$

where in the above equations (see Figure 7.4 as well)

- ε = emissivity (approximately 0.85)
- σ = (constant) = 0.1714×10^{-8}
- A = area of surface exposed to radiant heat source (ft^2)
- T_F = furnace temperature (atmosphere °R) (usually 2150–2250°F or 2610–2710°R)
- T_1 = surface temperature of tires/refractory (°R for radiation, °F for conduction)
- T_2 = temperature of shaft (at outside; °F) (also = Temp of refractory inside)
- T_3 = temperature of tires (inside; °F)
- T_4 = temperature of shaft (inside; °F)
- L = length in ft (L_r = length-total-of refractory section, L_T = combined width of tires, L_s = length of shaft within furnace)
- k_r = thermal conductivity of refractory = 1 (typical for "hard" castable refractory)
- k_t = thermal conductivity of tires = 12, for heat resisting alloy at average T = 1400°F
- k_s = thermal conductivity of shaft = 26, for carbon steel
- r_r = radius of refractory
- r_t = radius of outside of tire
- r_{so} = radius of outside of shaft
- r_{si} = radius of inside of shaft

A few simplifying assumptions have been made to arrive at Equation 7.4 that are reasonable when making approximations of heat losses as shown in Table 7.3 of this chapter. For example, it is assumed that the temperature of the outside surface (rim) of the tire, T_1, is the same as the outside surface of the refractory. Also, the temperatures of the inside surface of the refractory, T_2, and the outside surface of the shaft being in contact are the same. However, solution of similar heat balances shows this is not the case with the inside (bore) of the tire and the outside of the shaft—the tire being substantially hotter, such as, $T_3 > T_2$. Also, the radiant heat transfer portion of the heat balance is simplified, using A as the combined surface area of the refractory and the rims of the tires, and using a single value for emissivity, ε, which is approximately the same for each of these materials at the temperature of interest.

A similar heat balance can be constructed to calculate the heat loss, which occurs when the water-cooled shaft is exposed directly to radiation from the furnace interior due to loss of refractory. The results of this calculation are also given in Table 7.3. The range in values shown in that table is for differences in shaft length and diameter.

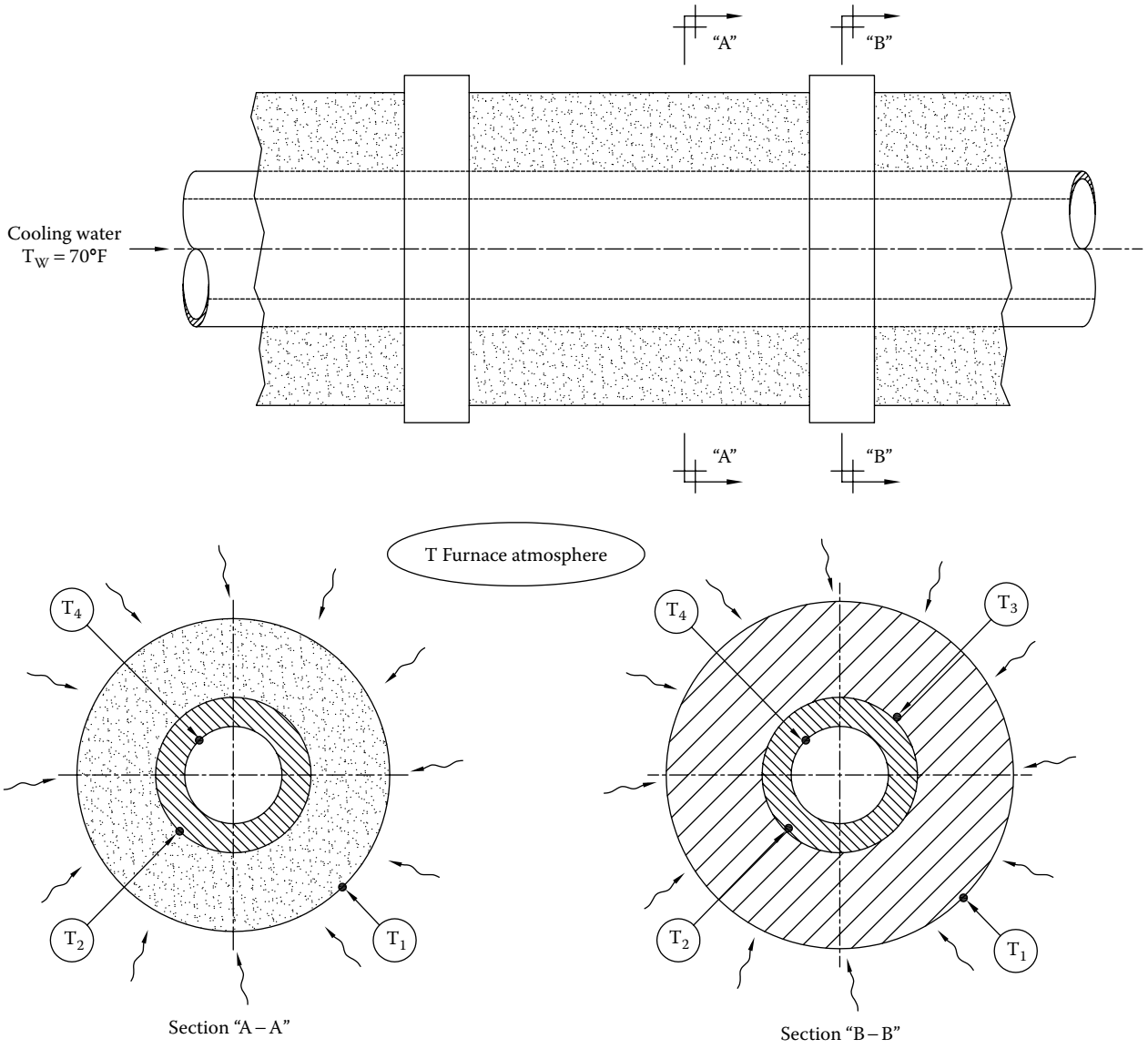


FIGURE 7.4 Water-cooled roll sections—surface temperatures for journal temperatures heat balances and heat-transfer calculations.

REFERENCES

1. N.A. Lagios. Thin-slab reheating with tunnel furnaces. *Industrial Heating,* June 2006.
2. A. Thedki. Identifying waste heat reduction opportunities. *Energy Matters*, Summer 2005.
3. E. Dieter. *Mechanical Metallurgy*, 3rd ed., McGraw-Hill, New York, 1986.
4. Bennett et al., private communication.
5. D. Miller, R. Pankiw, and R.J. Echlin. Advances in tunnel furnace rolls. *41st MWSP Conference Proceedings,* ISS, Vol. 37, pp. 765–772, 1999.
6. Radke et al., private communication.

8 Descaling of Hot-Rolled Strip

John B. Tiley and Per A. Munther

CONTENTS

8.1 Introduction 91
8.2 Formation of Scale 91
8.3 Impingement Pressure 92
8.3.1 Sample Calculation for Maximum Entry Temperature to Avoid Critical Tertiary Scale Thickness 94
8.4 Descale Spray Nozzle Interference 94
8.5 System Design 95
References 95

8.1 INTRODUCTION

Rolled in scale has been a continual problem in the hot rolling of steels. The descale systems developed in the 1960s have evolved very slowly. The first major upgrade was to install self-aligning nozzles, followed by decreasing the distance between the nozzle tips and the bar surface from about 350 mm to less than 125 mm. In recent upgrades (late 20th century), the descale system pressure has been raised from ~140 bar into the 170–210 bar range and, at the same time, flow has been minimized to limit cooling of the bar. Pressures have been raised to the exceed the 350 bar range with the advent of thin slab casting and thick sticky tunnel furnace scales.

8.2 FORMATION OF SCALE

The oxidation of iron has been carefully studied in laboratories and is well described in many texts [1,2]. Oxidation of iron, or steel, begins with initial growth of an iron oxide (scale) layer on the surface of the steel. This reaction is controlled by the gas phase transport of oxygen to the surface of the steel. This leads to a linear growth rate of oxide, given by

$$X_{\text{scale}} = K_{\text{L}} t \tag{8.1}$$

Typically, the thickness, X_{scale}, is measured in micrometers and time, t, in seconds. This linear growth continues until an oxide layer has formed, which prevents direct contact of the oxygen with the steel surface. The scale thickness required to do this varies with temperature, but has been found to be 1.3 μm at 850°C, and 7 μm at 900°C, at times around 20 s [3]. A similar behavior was found by Basabe and Spunar [4] in flowing air and this fits well with the theoretical relationship developed by Munther and Lenard [5] shown in Equation 8.2 and Figure 8.1,

$$X_{\text{FeO}} = \frac{1 + M_{\text{Fe}}/M_{\text{O}}}{\rho_{\text{FeO}}} k_{\text{e}} \exp\left(-\frac{Q_{\text{scale}}}{RT}\right)\sqrt{t} \tag{8.2}$$

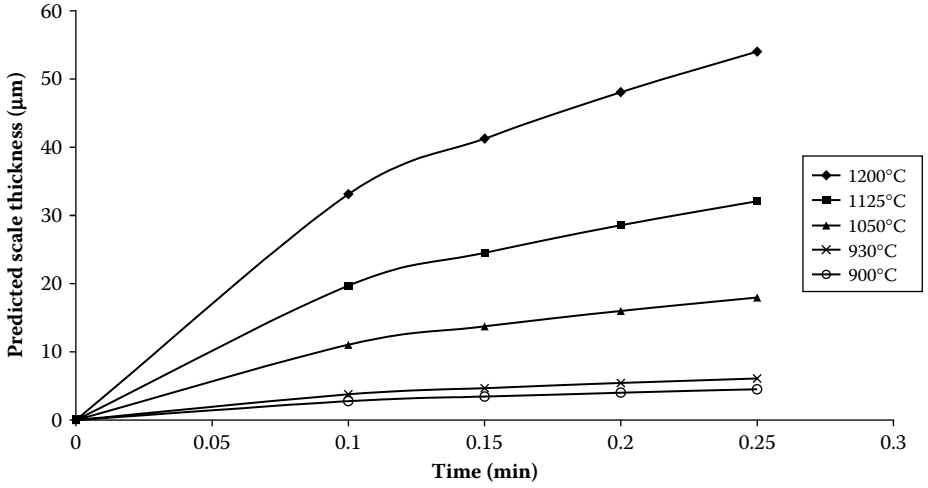


FIGURE 8.1 Predicted scale thickness X_{FeO} versus time, t from Equation 8.2. (From P.A. Munther, J.N. Tiley, V. So. Unpublished proceedings of AISTech 2006, Cleveland, Ohio. With permission.)

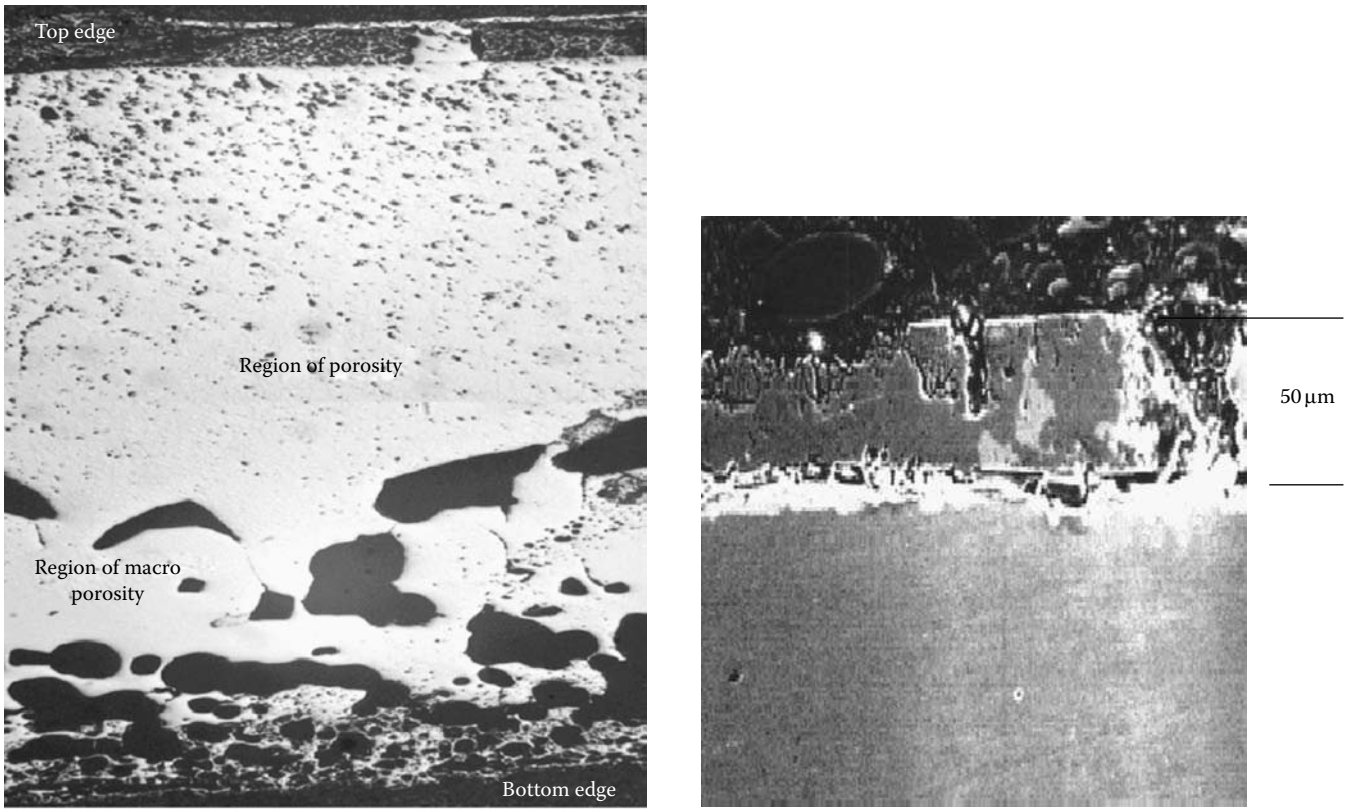


FIGURE 8.2 (a) Primary scale 5.7 mm thick; (b) secondary scale and scale metal interface.

In Equation 8.2, X represents the FeO thickness in micrometers, M_{Fe} and M_O are the molar masses of iron and oxygen respectively, k_e is a material constant, Q_{scale} is the activation energy of the scale, T is the temperature, and t is time in minutes.

The linear growth rate continues for up to ~20 s and then changes to a parabolic growth rate. This time period is quite relevant when considering the secondary and tertiary scaling of steel during rolling in a hot mill. Once an initial layer of iron oxide (scale) on steel is present, the rate of the scale growth is controlled by diffusion of iron through the existing scale layer to the gas-scale interface. Growth rates of oxide are parabolic, as given by

$$X^2_{scale} = K_p t \tag{8.3}$$

This reaction continues until stresses in the scale layer build up enough to cause voids and cracks between the scale and steel. These cracks prevent further diffusion of iron through the scale layer, and oxidation must take place through oxygen transport down the cracks and voids in the scale layer. This causes a reduced parabolic growth rate of form similar to Equation 8.3. The formation of minor voids and blisters can be seen on scale layers with thicknesses over 30 µm. Major porosity, which cracks easily at the scale-steel interface, is typically only seen on primary scales (Figure 8.2a—5.7 mm thick), with oxide layers larger than 1 mm. However, cracks are also present in secondary scales, typically less than 0.1 mm thick (Figure 8.2b). Adhesion of primary scales can be strongly dependent on the chemistry of the steel [6].

Small additions of Ni and Cu and higher levels of C led to greatly increased adherence of scale. Incomplete removal of a primary scale or secondary scale layer may lead to defects on the finished steel surface. One such defect is shown in Figure 8.3. The source of this defect is incomplete removal of secondary scale at the rougher and finishing mill descalers.

8.3 IMPINGEMENT PRESSURE

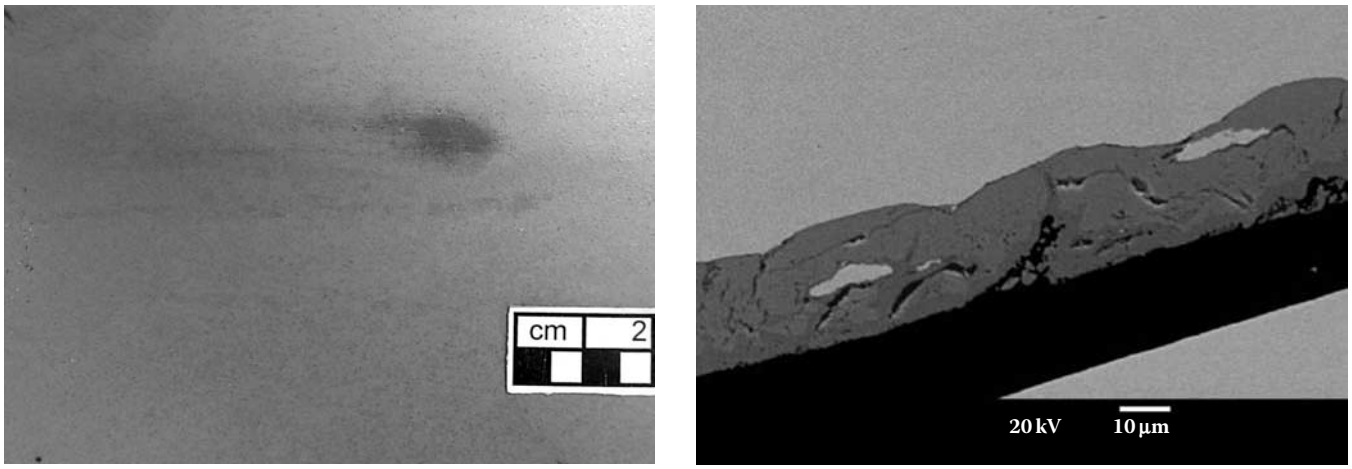
Descale nozzle suppliers provide impingement pressure calculations in their literature [7].

A review of Bernoulli's conservation of energy criteria leads to an understanding of these equations. From Bernoulli:

$$P/\gamma + V^2/2g + z = \text{the head, a constant} \tag{8.4}$$

where

P = pressure
γ = specific weight
V = velocity
g = gravity
z = elevation



(a) (b)

FIGURE 8.3 (a) Linear scale defect caused by incomplete removal of secondary scale; (b) cross-section showing scale flap. (From B.D. Nelson, G. Gebara, J. Tiley. *AISTech 2005 Proceedings* 2: 437–447. With permission.)

Applying Bernoulli's equation at the tip of the spray nozzle exit at the descaling header:

$$P_1/\gamma_{water} + V_1^2/2g + z_1 = P_2/\gamma_{water} + V_2^2/2g + z_2 \quad (8.5)$$

Equation 8.5 can be simplified knowing that z_1 equals z_2 and that P_2 equals zero (gauge pressure), and since V_1 is small then,

$$P_1 = \gamma_{water}(V_2^2/2g) \quad (8.6)$$

The spray force, F, over the area of contact of the bar surface is equal to flow, Q, multiplied by velocity, V_2, multiplied by density, ρ.

$$F = QV_2\rho \quad (8.7)$$

After substituting for V_2 from Equation 8.6, we obtain that the spray force over the area of the nozzle footprint is

$$F = \rho Q(2gP_1/\gamma_{water})^{1/2} \quad (8.8)$$

Spray pressure, P, is the force divided by the nozzle footprint area (available from nozzle supplier charts), where L is the spray width and W is the spray thickness,

$$P = F/L \times W \quad (8.9)$$

Impact pressure equations are modified by nozzle suppliers, based on measured data from their laboratories. Figure 8.4 compares the effect of impact pressure and header height.

From the Bernoulli equation, the impact force is proportional to flow rate and to the square root of the pressure. A specific flow rate, U, is obtained by dividing flow rate by cross-sectional area per unit time (spray width × speed of stock). Typically, U is measured in liters per square meter.

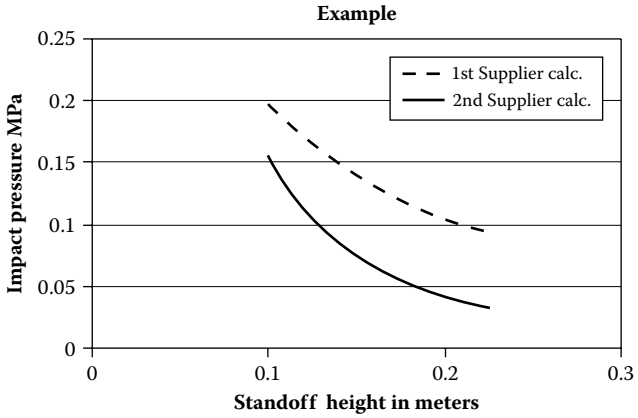


FIGURE 8.4 Comparison of nozzle impact pressure and standoff height. (From B.D. Nelson, G. Gebara, J. Tiley. *AISTech 2005 Proceedings* 2: 437–447. With permission.)

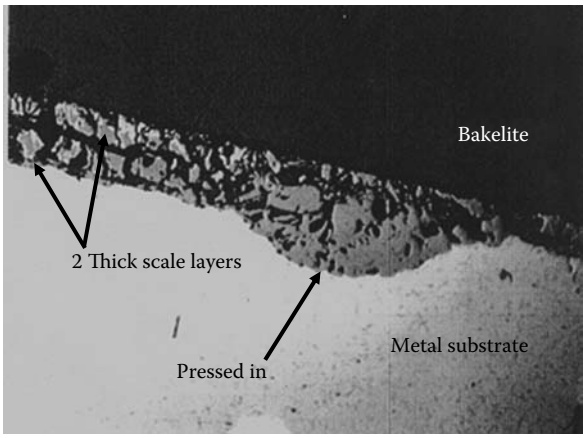
Knowledge of both impact pressure and specific flow rate is required to compare systems with high flow and low pressure (or vice versa) for benchmarking purposes.

Ludwig [8] developed a graphic representation of descaling effectiveness, as shown in Figure 8.5. The impact pressure required to remove the various types of scales is based on furnace operating strategy (low or rich in oxygen) alloying agents for primary scale, scale growth rate and alloying agents for secondary scale (formed after furnace scale is removed).

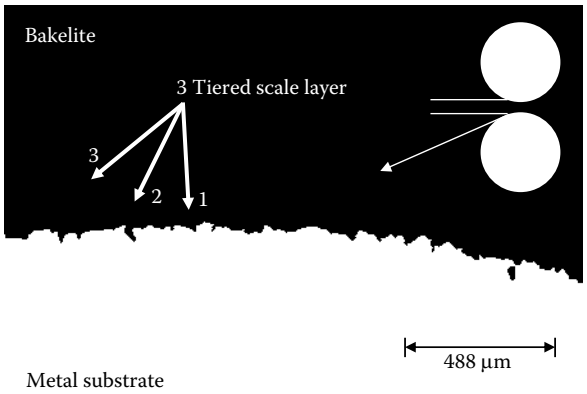
From Figure 8.5, and as also reported by Sheridan and Simon [10], low carbon steel can be descaled at impact pressures of 0.1 Mpa and low specific flow rates (U more than 2 l/m^2). This is critical when descaling secondary and tertiary scales formed after the roughing operation on a semicontinuous generation of hot strip mill. The effectiveness of the finishing mill entry descaler is affected by the time and temperature for re-scaling before the bar reaches the first

2 MPa	Adhering scales all according to mode of furnace operation and/or nickel alloy steels	
1 MPa		
	Dry furnace scales	Secondary scales
0.5 MPa	Secondary scales all according to extent of scale and type of alloy	
0.1 MPa		

FIGURE 8.5 Required impact pressures to successfully remove oxide scales. (From B.D. Nelson, G. Gebara, J. Tiley. *AISTech 2005 Proceedings* 2: 437–447. With permission.)



(a)



(b)

FIGURE 8.6 (a) Rolled in secondary scale; (b) multilayered scale. (From J. Tiley, J. Lenard, Y. Yu. *42nd Mechanical Working and Steel Processing Conference*, Toronto, Ontario, Canada, October 2000; pp. 215–222. With permission.)

finishing stands. Once the scale layer has cracks and blisters (Figure 8.6), it can be rolled into the surface.

The initial thin scale layer is metallurgically bonded to the steel substrate. The thickness of this scale layer must grow to greater than ~30 µm for it to crack and blister [10] and be rolled into the metal substrate.

8.3.1 Sample Calculation for Maximum Entry Temperature to Avoid Critical Tertiary Scale Thickness

Inputs

- Product exit strip thickness of 2.5 mm rolling at a speed of 600 mpm
- 25-mm transfer bar and distance from the descaler to first finishing stand is 4.0 m

Calculations

- Elongation = $\text{thickness}_{in}/\text{thickness}_{out}$ = 25 mm/2.5 mm = 10 times
- Entry speed to stand 1 = 600 mpm/10 = 60 mpm or 1 mps
- Time for 25-mm bar to traverse 4.0 m = 4 s

The growth rate of the oxide to 30 µm is dependent on temperature and has been shown to take approximately 10 s at 1050°C and 6 seconds at 1100°C [11].

Since the calculated time is less than 6 s, the entry temperature can be ~1100°C. This is an important criterion when rolling products are close to mill power and force limits since higher entry temperature reduces the deformation energy required.

8.4 DESCALE SPRAY NOZZLE INTERFERENCE

Descale nozzles are often shown to have a footprint with overlaps that lead to inadequate coverage or interference (Figure 8.7a). This leads to standard overlaps from 10 mm up to 50% of nozzle footprint, as is practiced in the industry. When a redesign is contemplated, it is important to understand the process in three dimensions. The rebounding water fans out from the nozzle as flow increases for the same nozzle (Figure 8.7b). This leads to interference, especially inside a descaling hood designed for lower flow or pressure. In these cases, it is advisable to evaluate three different overlap strategies on hand for testing the new pressure/flow

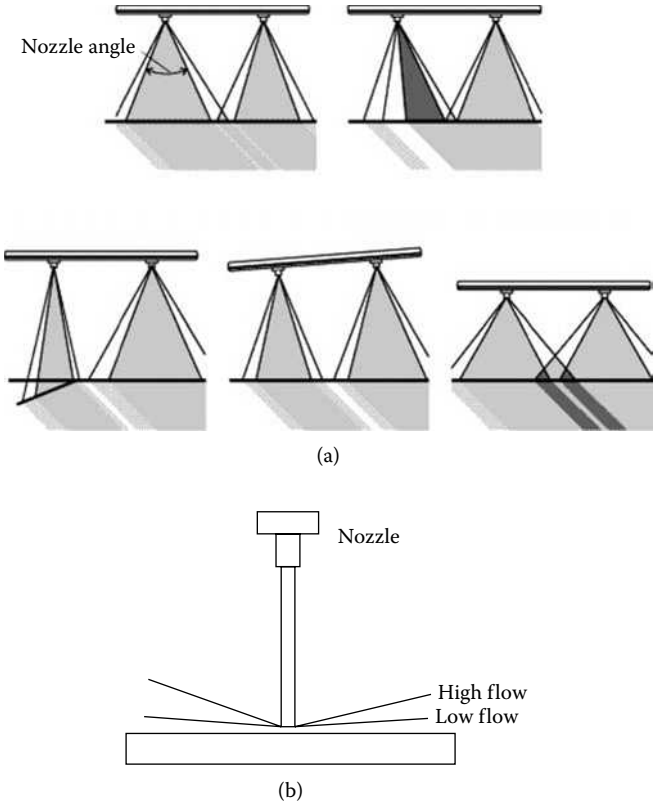


FIGURE 8.7 (a) Nozzle overlaps; (b) effect of flow on rebounding water.

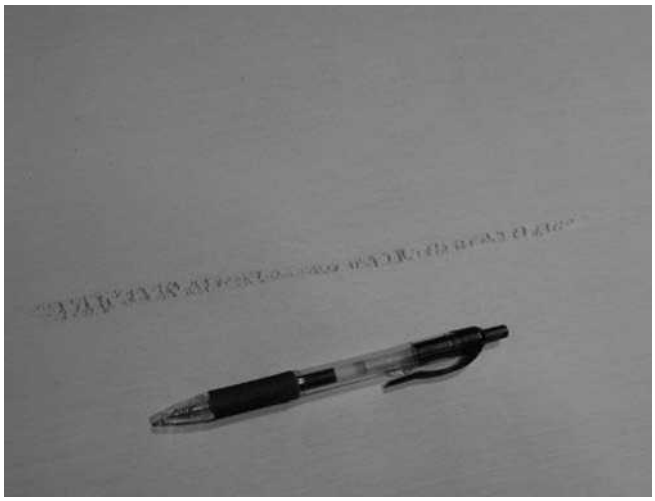


FIGURE 8.8 Scale streak from nozzle interference issues.

rate. A typical defect from interference issues is shown in Figure 8.8.

8.5 SYSTEM DESIGN

In a conventional hot strip mill rolling thick slabs, a typical descale system consisted of six or seven fixed speed pumps, equipped with 1100 kW motors with accumulators. Descale header stations were installed at the following locations: a) the exit of the slab reheat furnace, b) the entry and exit of the reversing rough mill, and c) the entry of the finishing mill (two pairs of headers). In addition, two interstand descale headers were installed at the finishing mill, one of them between stands 1 and 2 and the other one between stands 2 and 3. The descale system was capable of delivering 15,000 l/min at 145 bar. During simultaneous descaling at the various stations, significant pressure losses up to ~14 bar would be experienced at the descale headers.

Throughout most of the 1980s and 1990s, improvements were made to descaling capability. The following is a listing of the significant process changes made:

- Increase in system available flow and pressure through conversion of the finishing mill interstand descale headers to low pressure strip surface cooling headers to minimize scale growth
- Finishing mill descale practice changed to operate both entry header sets on all product to avoid inadequate descaling
- Increased descale spray impingement pressure through nozzle redesign, and physically moving the headers as close to mill pass-line as possible
- Improved descale hood designs for better water removal and reduced spray interference
- Reduced descale nozzle plugging by replacing carbon steel piping with stainless steel and installing in-line high pressure strainers
- Installing independent process descale systems and bring system pressures to the 200-bar level for integrated mills that do not need to descale the heavy tunnel furnace primary scale

REFERENCES

1. K. Hauffe. *Oxidation of Metals*, New York: Plenum Press, 1965.
2. P. Kofstad. *High-Temperature Oxidation of Metals*, New York: Wiley, 1966.
3. J. Benard, O. Coquelle. Nouvelles recherches par la methode micrographique sur l'oxidation du fer aux temperatures elevees, *Comptes Rendus* 222: 796–797, 1946.
4. V. Basabe, J. Spunar. Growth rate and phase composition of oxide scales during hot rolling of low carbon steel. *ISIJ International* 44(9): 1554–1559, 2004.
5. P.A. Munther, J.G. Lenard. The effect of scaling on interfacial friction in hot rolling of steels. *Journal of Materials Processing Technology* 88: 105–113, 1999.
6. D. Poirer, E.W. Grandmaison, M.D. Matovic, K.R. Barnes, B.D. Nelson. High temperature oxidation of steel in an oxygen-enriched low NO_x furnace environment. *IFRF Combustion Journal* article no. 200602, September 2006.
7. T. Kuyurita et al. Effect of high pressure descaling condition on red scale defect in hot strip mill. In *Hydraulic Descaling in Rolling Mills*, IOM, London, U.K.: Painters Hall, 1995.
8. B. Ludwig. Working pressure of hydro-mechanical decaling systems in hot strip mills. *Metallurgical Plant and Technology* 9(1): 55–61, 1986.

9. J. Tiley, J. Lenard, Y. Yu. Roll bite deformation of the thin scale layer on a plain carbon steel during hot rolling. *42nd Mechanical Working and Steel Processing Conference*, pp. 215–222, Toronto, Ontario, Canada, October 22–25, 2000.
10. A.T. Sheridan, P. Simon. Descaling of steels in rolling mills. *Proceedings of the Forum on European Steelmaking Developments and Perspectives,* pp. 233–244, Luxembourg, February 1–2, 1995.
11. M. Lalik, R. Webber. Scale growth in the hot mill, December 11, 1995. Dofasco Research Report (unpublished), 1995.
12. B.D. Nelson, G. Gebara, J. Tiley. Design criteria for descaling at Dofasco's No. 2 hot mill. *AISTech 2005 Proceedings* 2: 437–447.
13. P.A. Munther, J.N. Tiley, V. So. Rolled-in-scale—Defects in hot mills and their counter measures. Unpublished proceedings of AISTech 2006, Cleveland, Ohio.
14. J. Tiley, J. Lenard, Y. Yu. Roll bite deformation of the thin scale layer on a planin carbon steel during hot rolling. *42nd Mechanical Working and Steel Processing Conference*, Toronto, Ontario, Canada, October 2000; pp. 215–222.

Section II

Modeling of Flat Rolling Processes

9 Modeling for Reheat Furnace Practices

Shaojie Chen

CONTENTS

9.1 Introduction 99
9.1.1 Background 99
9.1.2 Categories of Reheat Furnace Modeling 100
9.2 Slab Target Furnace Exit Temperature Determination 101
9.2.1 Background 101
9.2.2 Mechanical Requirements 101
9.2.3 Metallurgical Requirements 103
9.2.3.1 Dissolution of the Relevant Microalloy Precipitates 103
9.2.3.2 Avoidance of Excessive Austenite Grain Coarsening 104
9.2.3.3 Consideration of No-Crystallization Temperature and Finishing Rolling Temperature 104
9.3 Slab Temperature Modeling 105
9.3.1 Calculation Domain 105
9.3.2 Numerical Formulation 106
9.3.3 Heating Criteria for Skid Marks 107
9.3.4 Impact of Curved Skid Riders on Skid Marks 108
9.4 Slab Thermal Stress Modeling 108
9.5 Residence Time Determination 110
9.6 A Case Application of Practice Modeling 110
9.6.1 Background 110
9.6.2 Modeling Package and Calibration 111
9.6.3 Heating Practice Modifications 112
9.6.4 Model Implementation Results 112
9.7 Summary 112
Acknowledgments 113
References 113

9.1 INTRODUCTION

9.1.1 Background

Hot rolling of steel requires an initial high material temperature of up to 1320°C. Reheat furnaces are commonly employed to meet this basic requirement, although there exist a few routines where a reheat furnace can be eliminated, such as DR (direct rolling) and Castrip® (Castrip LLC, USA) processes. In most of the steel flat manufacturing works, reheat furnaces serve as the essential link between the casting and rolling operations [1], as illustrated in Figure 9.1.

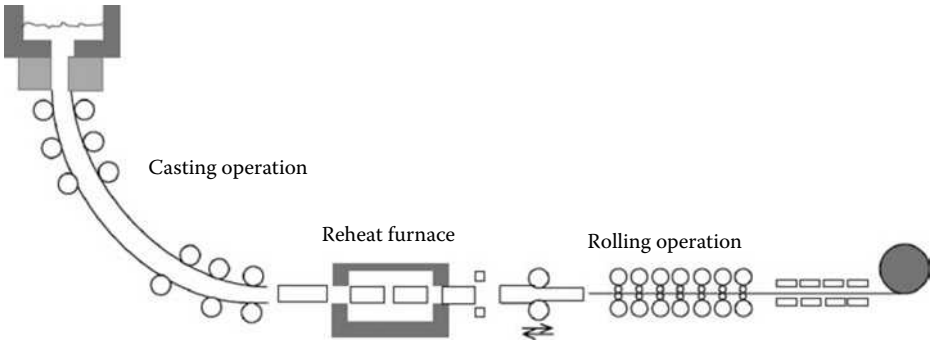


FIGURE 9.1 Reheat furnace as the link between the caster and rolling operations.

There are two major types of reheat furnaces that are widely used to continuously heat the slabs for flat-rolled products. A pusher-type furnace transports all the slabs in the furnace by means of a pusher, such that when a new slab is introduced into the furnace, the slab closest to the exit door is pushed out. A walking-beam-type furnace transports the slabs forward using a cyclical sequence of vertical and horizontal movements of walking-beams [2]. Figure 9.2 schematically shows a typical three-zone reheat furnace. The preheat zone is usually unfired to recover the sensible heat contained in the combustion products leaving the furnace. The heat zone is designed to heat the slabs close to the desired discharge temperature, while the soak zone homogenizes the temperature within a slab.

In today's competitive marketplace, steelmakers expect increased throughput, enhanced product quality, and reduced specific fuel consumption while simultaneously complying with ultra-low nitrogen oxide (NO_x) emission [3]. These expectations involve satisfaction of mechanical, metallurgical, environmental, and economic requirements and can only be fulfilled with a well-designed furnace and optimized operational heating practices.

During the past few decades, numerous new furnace design technologies have been introduced [4–6]. Any further improvement requires a better understanding of combustion engineering, which involves chemistry, mathematics, thermodynamics, heat transfer, and fluid dynamics [7]. Attempts to modify furnace designs or heating practices by empirical investigations are fraught with pitfalls due to the large number of furnace variables, the extensive and time-consuming analysis required, and the expenses and difficulties associated with implementing even minor changes in furnace design [8]. Moreover, with currently available measurement techniques, the temperature distribution within the slabs cannot be obtained directly. In a reheat furnace, only the slab surface temperature can be measured by radiation pyrometers. The reflected radiation can interfere with the readings so that the reliability of the measurements could be affected [9].

Computer modeling is essential because it offers an efficient tool with which to predict the internal temperature of the slab at any instant, to isolate the actual causes of the specific furnace problems, to examine the impacts of various influential factors, and to assess the effectiveness of the various possible remedies [8]. The advance of computer capacities allows the development of more and more complex simulation models.

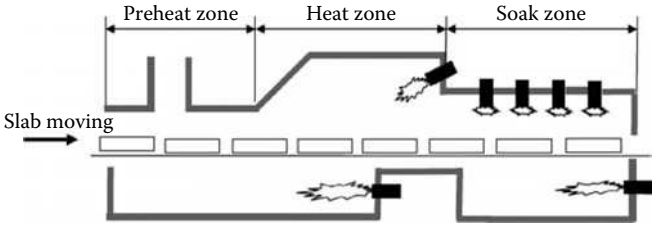


FIGURE 9.2 Schematic of a typical continuous reheat furnace.

9.1.2 Categories of Reheat Furnace Modeling

Depending on the application, reheat furnace computer modeling can be roughly classified into three major categories:

1. Furnace design models
2. Furnace heating practice models
3. Furnace dynamic control models

Furnace design models are intended to help the furnace suppliers/designers better design a new furnace or make innovations to an existing furnace. Computational fluid dynamics (CFD) software, such as FLUENT® (Fluent Inc., USA) or PHOENICS® (Concentration Heat & Momentum Ltd., USA), are the most appropriate approach for this purpose [3,10–13]. A complete modeling package involves building and meshing the 3D geometry of the burners, the furnace enclosure, and the working loads. Fluid dynamics, momentum, combustion, turbulence, and heat transfer equations are then solved on the mesh in the steady-state state or transient working conditions. By predicting the gas flow pattern, the atmosphere temperature distribution, and the composition of gas in the furnace, the model will provide recommendations for the furnace geometries and burners arrangements [12,13]. It also helps modify the burner designs to achieve desired flame shapes and to reduce pollutant emissions, such as NO_x, to an ultralow level [3].

Furnace heating practice models are developed to help steel manufacturers generate optimal operational heating practices to maximize the efficiency of a given reheat furnace. A proper heating practice should guarantee the satisfaction of thermal and metallurgical requirements. In particular, a heating practice will define the target furnace discharge temperature, heating speed, heating curves, and residence time, while it takes fuel consumption, scale formation, and decarburization into account. The thermal and metallurgical requirements are strongly related to the grade and dimensions of the final products. Especially in the last several decades, the production of the high strength low alloy (HSLA) grades with thermo-mechanical control process (TMCP) with stringent thermal and metallurgical requirements has been rapidly increasing. The reheat furnace has indeed extended its role as a *heating tool* to a combination of heating tool and *metallurgical tool*. Similar to the *controlled rolling* and *controlled cooling*, the concept of *controlled heating* has attracted considerable attention. A comprehensive model to address all these issues is needed. Although many good models have been developed to deal with some individual aspects of the reheating process [1,14–18], few have been developed to integrate all aspects to form a complete package for reheat furnace practice optimization [19].

Furnace dynamic control models are used for online control purposes, usually as part of the Level 2 control system of a rolling mill. Although manual operation can give a reasonable heating quality when the furnace is in a steady state, there usually are changes in the slab grades and in the charge temperature; there are also downstream events that lead to

delays in the line. All these situations dynamically generate variations in the slab temperatures, and it is difficult for the operators to achieve consistency [8]. The online control model will track each individual slab in the furnace in real-time and, based on instantaneous situations, it determines the best heating parameters to achieve the required heating qualities [3,20,21].

It should be noted that the three types of models are not separate from one another but work together to achieve the same goals. Furnace design models provide the best-designed furnace, and the furnace heating practice models and dynamic control models make the best use of a given furnace. The heating practice models provide guidance and set-ups for the dynamic control models, and the dynamic control models try to achieve those setups. For instance, the heating practice models predetermine a target discharge temperature for a certain product, and this information will be set up in the dynamic model. Then, the dynamic model manipulates the heating parameters to achieve that target based on the real-time furnace conditions.

In the following sections, discussions will focus on the furnace heating practice models.

9.2 SLAB TARGET FURNACE EXIT TEMPERATURE DETERMINATION

9.2.1 Background

The primary function of the reheat furnace is to raise the slab temperature high enough for the downstream rolling operation. The question is: "How high is enough at the exit of a reheat furnace?"

Traditionally, the lower limit of the furnace discharge temperature is constrained by the rolling mill load capacity. If the slab temperature at the exit from the reheat furnace is too low, it does not provide sufficient plasticity and it leads to increased flow stresses and rolling forces. As a consequence, the maximum rolling force, motor torque, and power limits may be exceeded, therefore, and the rolling process cannot be performed. On the other hand, if the discharge temperature is too high, it may overheat or burn the slab and cause excess scale formation, surface layer decarburization, and unnecessary fuel consumption [7]. To simplify this issue, some manufacturers just specify a universal target discharge temperature (for example, 1290°C or 2350°F) for all their products, regardless of the slab grades and dimensions, which is obviously not optimal. As mentioned earlier, with the exponential increase of the development of the HSLA steels and the requirements of controlled rolling, the traditional way to determine the discharge temperature is insufficient. The metallurgical requirements may become the predominant factor to determine the desired discharge temperature.

9.2.2 Mechanical Requirements

As illustrated in Figure 9.3, a slab is discharged from the reheat furnace at a temperature of $T_{\text{rh-exit}}$. The temperature starts to decrease once it leaves the reheat furnace. It travels through the descale box, where it has a significant surface temperature loss due to the high-pressure water spray. At the entry of the roughing mill, the slab has a temperature of $T_{\text{r-entry}}$, which drops to $T_{\text{r-exit}}$ after a number of roughing passes. The slab passes through the transfer table with the temperature decreasing to $T_{\text{f-entry}}$ at the entry of the finishing stand(s) and $T_{\text{f-exit}}$ at the delivery side of the finishing mill.

Ideally, a model is needed that is capable of performing the following calculations:

1. Predicting temperature losses throughout rolling due to radiation, convection, descale spraying, film boiling, contact with mill and table rolls, and inter-stand water cooling, as well as the temperature gain due to plastic deformation and friction during each pass.
2. Calculating the minimal allowable temperature for each stand (pass), provided that the mill limits, the slab dimensions, material flow stresses, the pass scheduling, and the mill configuration are given. The lowest minimal allowable temperature of all the stands will be defined as the critical temperature, T_{critical}.
3. Based on these calculations, the model back calculates the required reheat furnace exit temperature as

$$T_{\text{rh-exit}} = T_{\text{critical}} + \sum \Delta T_i^{\text{pass}} + \sum \Delta T^{\text{transf}} + \sum \Delta T_{\text{DS}} - \sum \Delta T_i^{\text{gain}} + \Delta T_{\text{safety}} \tag{9.1}$$

where

$T_{\text{rh-exit}}$ = required reheat furnace exit temperature
T_{critical} = critical temperature
ΔT_i^{pass} = temperature loss of pass i (up to the pass with T_{critical})
ΔT^{transf} = temperature loss due to transfer between stations

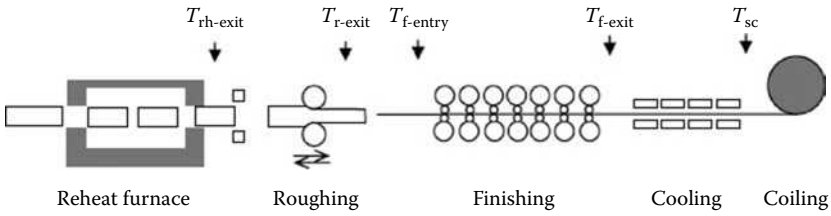


FIGURE 9.3 Slab temperature history through the rolling-line.

ΔT_{DS} = temperature loss due to descaling
ΔT_i^{gain} = temperature gain of pass i due to plastic deformation and friction
ΔT_{safety} = safety factor

To the author's knowledge, there is no such model reported in the literature that was designed to perform the calculations described above. However, some other models [22,23] may be used to achieve this objective. One of them is the commercial software Hot Strip Mill Model (HSMM®, AISI and Integ Process Group, USA). The HSMM model is an integrated PC-based, off-line model that allows the user to simulate the hot rolling process from the reheat furnace dropout to the up/down coiler to predict the thermal history, deformation, roll forces, microstructural evolution, and mechanical properties of steel strip in a hot strip mill [22]. The theoretical details of the model will not be revisited here. Instead, a trial-and-error modeling technique is used to demonstrate how to determine the minimum reheat discharge temperature by using this model.

To start, one could guess a furnace exit temperature, and then run the model to obtain the temperatures and rolling forces for every stand/pass. If the rolling forces for all the stands are well below the allowable maximum forces, one may decrease the initial trial furnace exit temperature; otherwise, increase the initial guess. Several runs of this type of what–if studies will help the user determine a proper furnace exit temperature to meet the mechanical requirements.

As an example, Figures 9.4 and 9.5 depict the slab temperatures and rolling forces for all the seven roughing passes and seven finishing passes for various reheat exit temperatures of 1100, 1200, and 1300°C, respectively. As can be seen, a reheat exit temperature of 1100°C will result in overloading in the third roughing pass, R3 (assuming that a change of the pass schedule is not favorable). Increasing the reheat exit temperature to 1200°C will meet the rolling force requirements. It should be noted that similar exercises should be also performed to ensure a safety margin for the rolling torque and motor power capacity. Moreover, the model should be properly calibrated before application.

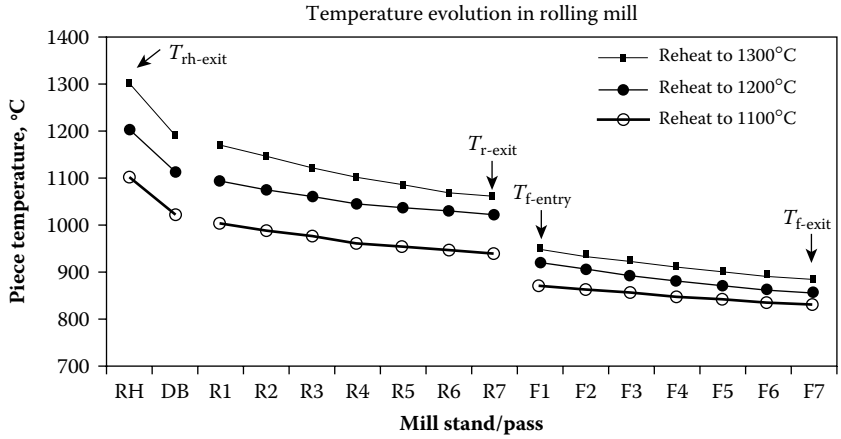


FIGURE 9.4 Slab temperatures at each stand/pass.

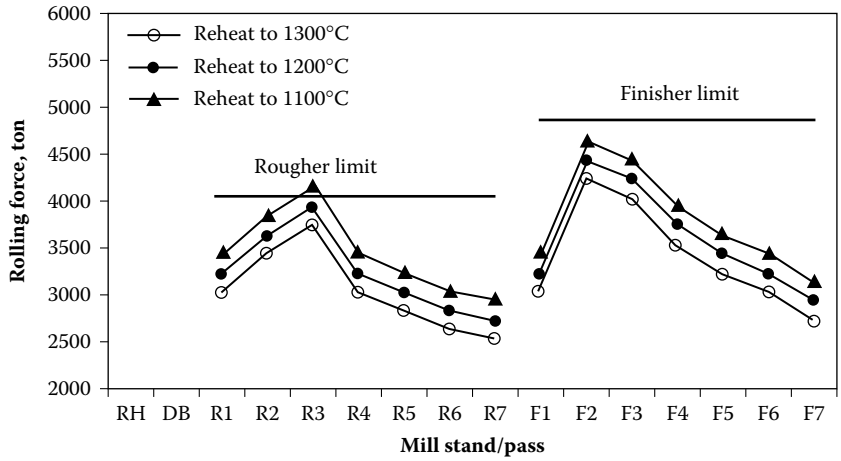


FIGURE 9.5 Rolling forces at each stand/pass.

9.2.3 Metallurgical Requirements

To determine the reheat furnace discharge temperature, three metallurgical aspects that relate to this process will be discussed in this section:

1. Dissolution of the relevant microalloy precipitates
2. Avoidance of excessive grain growth
3. Consideration of no-crystallization temperature and finishing rolling temperature

9.2.3.1 Dissolution of the Relevant Microalloy Precipitates

To maximize the effectiveness of the microalloy elements, it is essential to dissolve the relevant precipitates [such as Nb(C, N), VN, VC, and TiC] during reheating such that they can precipitate in the subsequent rolling to effectively retard the recrystallization and strengthen the material [24].

For the dissolution temperatures of various microalloy particles, the traditional Irvine's equations [25] are widely accepted. Those equations take a simple form as follows:

$$\log[A][B] = C_1 - C_2/T \tag{9.2}$$

where

$[A]$ = concentration of microalloy element, Nb, V, or Ti
$[B]$ = concentration of carbon, nitrogen, or combination
C_1, C_2 = constants
T = dissolution temperature

However, for the steels containing complex multiple microalloy elements with mixed carbonitrides, such as $Nb_xV_{1-x}C_yN_{1-y}$, Speer's theory may be more suitable [26]. Speer's theory consists of a system of nonlinear thermodynamic models that is capable of predicting the amount and composition of precipitates in a given Nb/V steel, which is at equilibrium at any particular temperature within the austenite (plus carbonitride) phase field.

Based on the thermodynamics, the molar free energy of the precipitate of $Nb_xV_{1-x}C_yN_{1-y}$ may be written as [26]

$$\begin{aligned} G_{Nb_xV_{1-x}C_yN_{1-y}} &= xyG^{\circ}_{NbC} + x(1-y)G^{\circ}_{NbN} + (1-x)yG^{\circ}_{VC} \\ &\quad + (1-x)(1-y)G^{\circ}_{VN} - T{}^{I}S^{m} + {}^{E}G^{m} \end{aligned} \tag{9.3}$$

where

$G^{\circ}_{NbC}, G^{\circ}_{NbN}, G^{\circ}_{VC}$, and G°_{VN} = the molar free energies of the pure binary compounds
${}^{I}S^{m}$ = the integral ideal molar entropy of mixing
${}^{E}G^{m}$ = the integral excess molar free energy of mixing
x, y = the precipitate fraction

The austenite/carbonitride equilibrium condition is identified by requiring the partial molar free energy of each atomic species to be identical in both phases. A system of equations was then derived [26]. A numerical procedure was developed to solve these equations to determine the dissolution temperature of the complex particles [19].

Figures 9.6 and 9.7 demonstrate the effects of C and Nb on the dissolution temperatures of Nb(C, N) and (Nb, V)(C, N), as calculated by Irvine's equation and Speer's theory, respectively. As indicated in the figures, Speer's theory gives higher dissolution temperatures than Irvine's, which implies that Speer's theory will be more conservative when applied to determine the reheat discharge temperatures. Also shown in the figures is that the calculated dissolution temperature differences between the two theories diminish with the increased the carbon content.

The dissolution temperatures for all the mentioned particles should be calculated. The greatest of these values is defined as the final dissolution temperature, which will ensure all the related particles dissolve into the solution [19]. It is worth mentioning that dissolution of the particles also involves the kinetics of the dissolution, which requires sufficient time for the particles to dissolve. However, the kinetics of dissolution has not been well established so far and a systematic study is needed.

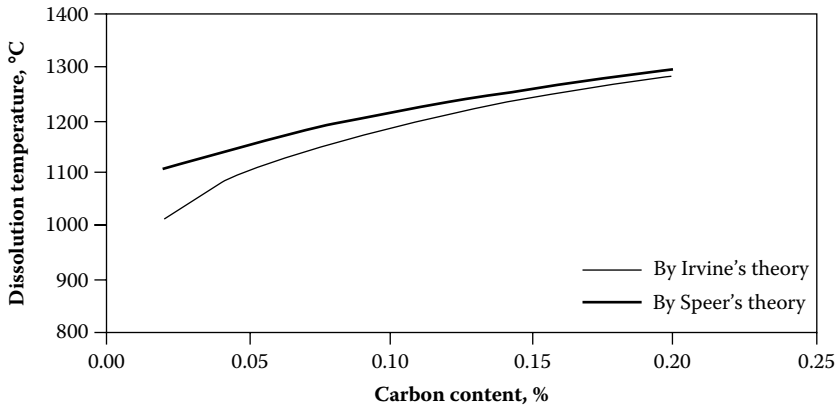


FIGURE 9.6 Effect of C% on dissolution temperatures of Nb(C, N) and (Nb, V)(C, N).

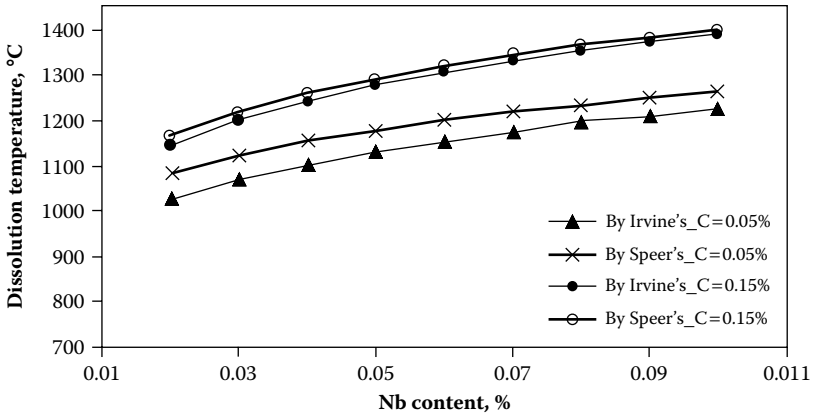


FIGURE 9.7 Effect of Nb% on dissolution temperatures of Nb(C, N) and (Nb, V)(C, N).

9.2.3.2 Avoidance of Excessive Austenite Grain Coarsening

It is well known that fine-grained materials have a combination of high strength and toughness. Although some studies have demonstrated that grain size after reheating has limited effects on the final microstructure [27], many still believe that control of austenite grain size after reheating is an important factor in achieving fine-grained final products [28–30].

The grain growth process is very complicated and depends on many factors, such as steel composition, reheat temperature and time, size and distribution of the microalloy precipitates, grain boundary structure, segregation of solute atom or impurities, oxide film on the surface, and reheating atmosphere [28,29]. Figure 9.8 compares the grain coarsening behavior of plain C steel and Nb bearing steel as functions of reheating temperature. As can be seen, the addition of Nb retards the grain growth significantly. The plain C steel exhibits normal grain coarsening characteristics in that the grain size systematically increases with increasing reheat temperature. However, the steel that contains Nb indicates abnormal grain coarsening starting at a temperature called the grain coarsening temperature, T_{GC} [30]. When the reheat temperature is above T_{GC}, some grains grow rapidly, and the steel exhibits a mixed microstructure of small and large grains until all of the precipitates are dissolved in austenite.

Many modeling works have been published to predict the grain coarsening behavior, ranging from simple empirical equations to the complex cell automata model [28] and neural network model [29]. However, currently available information is inconclusive and additional investigations are required [31].

9.2.3.3 Consideration of No-Crystallization Temperature and Finishing Rolling Temperature

The use of Nb in HSLA steels is well known because of its ability to retard recrystallization, both by solute drag and by strain-induced precipitation, which leads to pancaked austenite after hot rolling and after transformation and provides fine microstructures with improved properties [32,33]. In this context, the critical temperature, known as the no-crystallization temperature (T_{nr}), below which the pancaking of austenite grains can take place, is important in controlled rolling of those microalloyed steels. To achieve a sufficient amount of pancaking to maximize the refinement of the final microstructure, it is essential to perform a certain amount of deformation in temperatures below T_{nr} [32]. Usually, the amount of deformation for pancaking is carried out in finishing stands/passes, and it is required that the roughing exit temperature, $T_{r\text{-}exit}$, be above T_{nr}. In some cases, T_{nr} can be very high (over 1100°C), which in turn demands a high $T_{r\text{-}exit}$ and hence high reheat exit

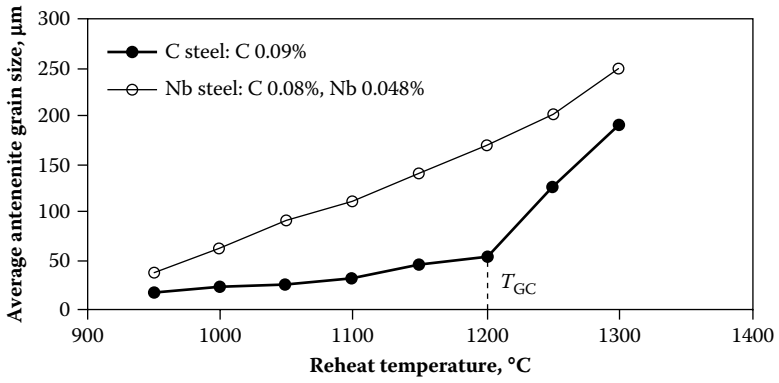


FIGURE 9.8 Grain coarsening behavior during reheating.

temperature, considering the temperature losses during the roughing passes, descaling, and transportation.

T_{nr} is related to the chemical composition of the steel and process parameters, and it can be calculated as [32]:

$$T_{nr} = \begin{cases} (88.1 \cdot \log(\mathrm{Nb} + 0.31\mathrm{Ti} \\ \quad + 0.15\mathrm{Al}) + 1156) \cdot \varepsilon^{-0.012} \cdot \dot{\varepsilon}^{-0.01} t^{-0.1} \ldots\ldots (t \le 12.5\,\mathrm{s}) \\ (63.5 \cdot \log(\mathrm{C} \cdot \mathrm{Nb} \\ \quad + 885) \cdot \varepsilon^{-0.012} \cdot \dot{\varepsilon}^{-0.01} t^{-0.1} \ldots\ldots\ldots\ldots (12.5\,\mathrm{s} < t \le 30\,\mathrm{s}) \end{cases} \tag{9.4}$$

where

Nb, Ti, Al, C = wt% of the element
ε and $\dot{\varepsilon}$ = strain and strain rate, respectively
t = interstand/interpass time

Figure 9.9 demonstrates the effect of Nb and C content on the T_{nr}. Obviously, T_{nr} increases with the increase of Nb and C content in the steel. Once T_{nr} is determined, replace $T_{critical}$ with it in Equation 9.1 to determine the required reheat exit temperature. It should be noted that accurate determination of T_{nr} for various steel compositions with various rolling parameters is still a popular area for many researchers.

Moreover, in many cases, specific ranges of finishing rolling temperature (start cooling temperature), $T_{f\text{-}exit}$, and stop cooling temperature, T_{sc}, are required to achieve desired cooling rates in the run-out table cooling and final microstructures. The finishing rolling temperature could also become the critical temperature. In these cases, the same approach can be used to take this requirement into consideration, as for T_{nr}. A final examination of the obtained results to satisfy both mechanical and metallurgical requirements should lead to an appropriate furnace target exit temperature.

9.3 SLAB TEMPERATURE MODELING

Slab temperature prediction is the most important component of the reheat furnace modeling. It provides fundamental information (such as bulk temperature, temperature gradient, etc.) for establishing heating practices, modifying furnace design, and controlling the furnace dynamically.

9.3.1 Calculation Domain

In top and bottom fired furnaces, the slabs rest on the riders connected to a water-cooled skid system. Physical contact between the riders and the slabs, as well as radiation shadowing caused by the presence of the skid system, leads to cold spots, or skid marks, on the bottom surface of the slabs. In order to take the skid effects into account, a 2-D longitudinal section of a slab was modeled, as shown in Figure 9.10 [19]. This full-thickness representative section can accommodate different characteristics of the top and bottom surfaces, the end of a slab, the skid area, and the cross-section plane

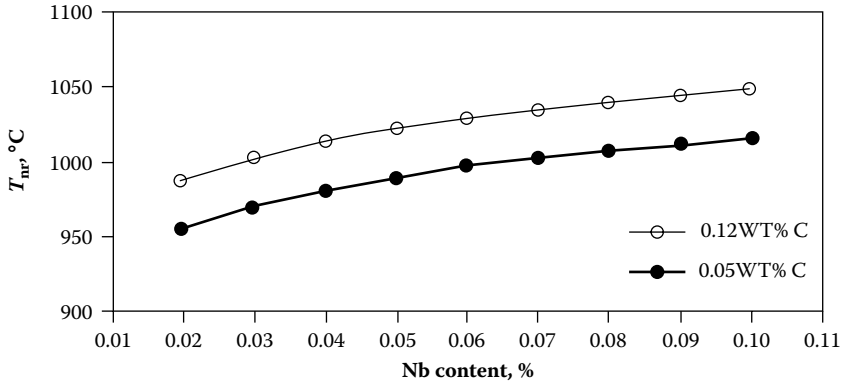


FIGURE 9.9 Effects of Nb and C content on T_{nr}.

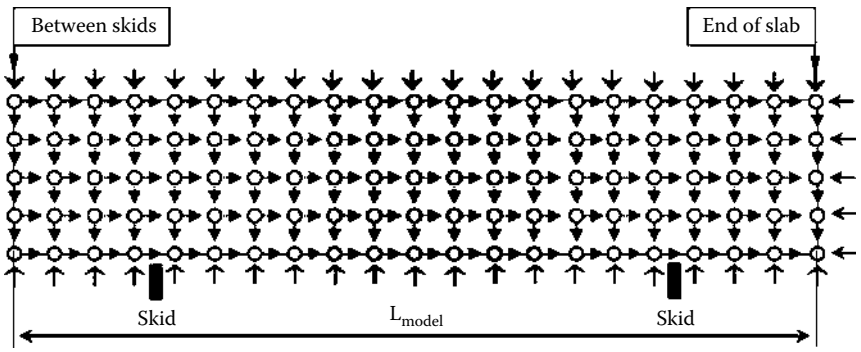


FIGURE 9.10 Modeled domain with FDM mesh. (From S. Chen, D. Poshard, and S. Abraham. 2007. *Iron & Steel Technology* 5(8): 66–79. With permission.)

between two skids. The modeled section results could be expanded to reflect the full-length slab. A 1-D model, which only considers the heat conduction through slab thickness, is insufficient to determine an optimal heating practice to maintain the thermal integrity of the slab due to its inability to predicting the skid-induced temperature gradient.

9.3.2 Numerical Formulation

When a slab travels through the furnace, the transient heat conduction can be expressed by the following partial differential equation [19]:

$$C_s(t)\rho_s \frac{\partial T(x,\, y,\, t)}{\partial t} = \frac{\partial}{\partial x}\left(K_s(t)\frac{\partial T(x,\, y,\, t)}{\partial x}\right) + \frac{\partial}{\partial y}\left(K_s(t)\frac{\partial T(x,\, y,\, t)}{\partial y}\right) \quad (9.5)$$

where

$T(x, y, t)$ = temperature at time step t
x = slab longitudinal direction coordinate
y = slab gauge direction coordinate
$C_s(t)$ = specific heat of the slab
ρ_s = density of the slab
$K_s(t)$ = thermal conductivity of the slab

To solve this unsteady nonlinear heat transfer problem, a finite difference method (FDM) utilizing explicit methods was used by dividing the section being modeled into a grid of nodes. As shown in Figure 9.10, the heat flow pattern and the boundary condition for each surface are different. The heat flux into the slab's bottom surface is reduced due to the shadow effects of the skids. There is no heat flow across the cross section of the "between skids" plane.

In view of the various boundary conditions and different locations within the slab, there exist various types of nodes, such as corner nodes, edge nodes, internal nodes, etc. Energy equilibrium equations are derived for each type of node. For example, for an internal node, the finite difference equation representing the instantaneous heat balance is expressed as [19]:

$$\rho_s C_s(t)\Delta x\Delta y\frac{T_{i,j}^{t+\Delta t} - T_{i,j}^{t}}{\Delta t} = -K_s(t)\Delta x\left[\frac{2T_{i,j}^{t} - T_{i,j+1}^{t} - T_{i,j-1}^{t}}{\Delta y}\right] - K_s(t)\Delta y\left[\frac{2T_{i,j}^{t} - T_{i+1,j}^{t} - T_{i-1,j}^{t}}{\Delta x}\right] \quad (9.6)$$

where

x, y, and t = increment of x coordinate, y coordinate, and time, respectively
$T_{i,j}^{t}$ = node temperature at time step t
$T_{i,j}^{t+\Delta t}$ = node temperature at time step $t + 1$

The boundary conditions are complicated due to the complex heat transfer behavior in a furnace. Heat flows from the flame and products of combustion to the slabs via six routes [7]:

Route 1: Direct from triatomic gas radiation (mainly CO_2 and H_2O) to surfaces of slabs and walls
Route 2: Direct from soot particles radiation to surfaces of slabs and the walls
Route 3: Direct convection from flue gases that flow across the surfaces of slabs and walls
Routes 4 to 6: Indirect reradiation from walls (already heated by routes 1, 2, or 3) to the surfaces of slabs

The radiation heat flux, q_r, between the slab and the gases, and the slab and the furnace walls can be combined as [17]:

$$q_r = \frac{\sigma\varepsilon_s}{[1-(1-\varepsilon_s)(1-A_{gs})]}(\varepsilon_g T_g^4 - A_{gs}T_s^4) + \sigma\left[\varepsilon_s\varepsilon_w\left(1-\frac{A_{gs}+A_{gw}}{2}\right)F_{sw} + \Delta\varepsilon_f\right](T_w^4 - T_s^4) \quad (9.7)$$

where

T_g and T_s = temperature of the furnace gas and the slab, respectively
F_{sw} = view factor
σ = Stefan–Boltzmann constant
ε_g, ε_w, and ε_s = emissivity of furnace gas, wall, and slab, respectively
$\Delta\varepsilon_f$ = correction factor for flame radiation
A_{gs} and A_{gw} = gas absorptivity from the slab and wall, respectively

In furnaces that operate at high temperatures (>1000°C), the convection heat flux only accounts for 10–15% of the total heat flux, while for a low furnace temperature (<650°C), heat transfer by convection is of major importance because radiation decreases dramatically. The convection heat flux, q_c, can be calculated as [18]:

$$q_c = h_c(T_g - T_s) = 0.175\left(\frac{m_g D_{eq}}{A\mu_g}\right)^{0.75}\left(\frac{k_g}{D_{eq}}\right)(T_g - T_s) \quad (9.8)$$

where

A = the surface area of the roof
μ_g and k_g = the viscosity and conductivity of the gas, respectively
m_g = mass flow velocity
D_{eq} = the equivalent diameter

For simplicity, some researchers have used a constant convection file coefficient of 7.8 W/(m^{2}K) [15,16].

On the bottom side of the slab, the heat transfer modeling becomes more complicated by the appearance of a skid pipe system. For a point on the slab bottom surface, the view factor can be determined from the expression [17]:

$$F_{sw}^{bottom} = \frac{1}{2}\{[1-\sin(90-B_1)] + [\sin(90-B_1-B_2) + \sin(90-B_3-B_4)] + [1-\sin(90-B_4)]\} \quad (9.9)$$

where B_1 through B_4 are the angles defined in Figure 9.11 [17].

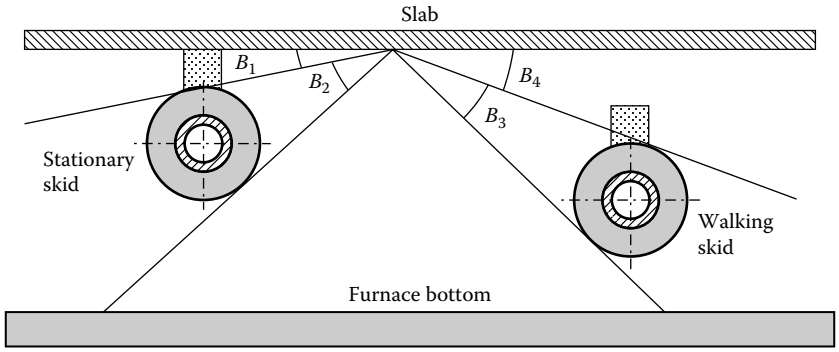


FIGURE 9.11 Skid shadow effects.

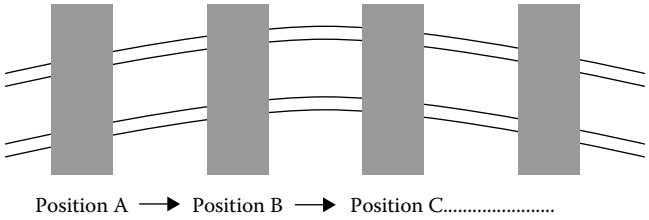


FIGURE 9.12 Curved skid riders and varying contact boundary conditions.

To alleviate the skid marks, some furnaces employ curved skid riders (Figure 9.12), which further complicate the boundary conditions. The contact boundaries between the slab and the curved skid riders vary when the slab travels through the furnace. A moving boundary module was developed to accommodate this feature [19].

9.3.3 Heating Criteria for Skid Marks

Figure 9.13 plots a temperature contour of the modeled slab section after being heated for certain time. It can be seen that the skid marks are distinctive areas where the slab temperatures are much lower than those areas located between the skids and at the ends of the slab. Two issues associated with the lower temperature skid marks need to be properly addressed [19].

The first issue is the unfavorable rolling load and product gauge/width fluctuation caused by the skid marks. Usually, a point-to-point approach is used to quantify the temperature difference of the over-skid point and the between-skid point (point P and Q in Figure 9.13, respectively). As seen from Figure 9.13, not only a single point of the slab bottom surface, but also a through-thickness slice is affected by the skid effect. The combined result of the lower temperatures of the affected slice, instead of a single point, will lead to a rolling load variation. Therefore, a slice-to-slice method was created to establish a heating criterion in this regard. With the new criterion, the average temperature difference of the over-skid slice and the between-skid slice (the areas defined by the dashed lines in Figure 9.13) was used as the index of the skid-induced temperature gradient. This index has to be within a certain limit to avoid rolling load and gauge fluctuation.

The second issue is the possibility of failing to dissolve the microalloy particles in the lower temperature areas, the worst case within the slab. This issue has not received wide attention due to two reasons: (1) for the traditional steels without microalloy elements, there is no issue with the dissolution of microalloy particles; (2) one tends to apply the bulk temperature to evaluate particle dissolution without recognizing the significantly lower temperatures at the skid marks. With regard to this issue, another heating criterion is generated that requires that the lowest temperature spot within the slab be heated above the dissolution temperature and maintained for a certain time.

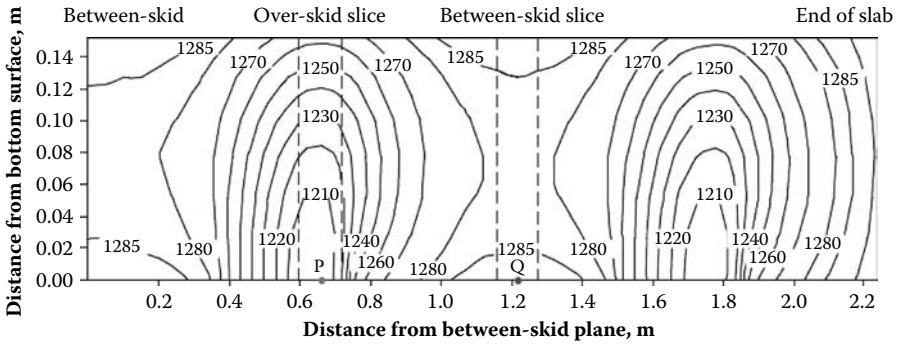


FIGURE 9.13 Temperature contour and concept of slice-to-slice method for skid mark criterion.

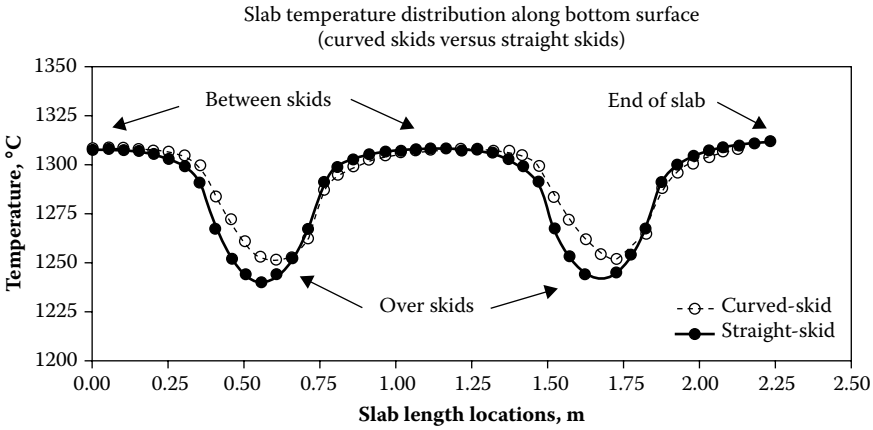


FIGURE 9.14 Temperature comparison between curved and straight skid riders. (From S. Chen, D. Poshard, and S. Abraham. 2007. *Iron & Steel Technology* 5(8): 66–79. With permission.)

9.3.4 Impact of Curved Skid Riders on Skid Marks

Figure 9.14 compares the modeling results obtained from straight and curved skid riders along the length direction of the slab bottom surface. It was revealed that compared to the straight skid riders, the curved skid riders are beneficial in alleviating skid marks by spreading out the lower temperature areas and reducing the magnitude of skid cooling. As a result, the time required to achieve a target discharge temperature of 1290°C can be reduced by approximately 2 min for the studied case. It should be realized that an optimal design and layout of the curved riders could lead to more favorable results.

9.4 SLAB THERMAL STRESS MODELING

Figure 9.15 illustrates two types of heating curves: fast heating and slow heating. A slow heating curve may help increase the fuel efficiency due to less sensible heat loss to the stack. On the other hand, fast heating with a higher heating curve can reduce residence time and hence improve the productivity of a reheat furnace. However, very high heating speeds may result in cracking for some steels. To address the concern that rapid heating of a slab may cause cracking due to the induced thermal stresses within the slab and to help properly specify the heating speeds and heating curves, a thermal stress model was developed to determine the thermal stress level and the likelihood of cracking.

Thermal stress determination is basically a coupled analysis of thermal calculation and mechanical stress calculation. To perform such calculation, the temperature field has to be determined and the results are input as "load" to a stress calculation model.

To derive the FEA equations for the temperature calculation, the variational form of the heat transfer equation was used [19].

$$\int_{\text{vol}} (C_s \rho_s \delta T \left(\left(\frac{\partial T}{\partial t} + \{v\}^T \{L\} T \right) + \{L\}^T (\delta T)([D_t]\{L\}T) \right) d(\text{vol}) = \int_{S_2} \delta T_q^* d(S_2) + \int_{S_3} \delta T h_f (T_f - T) d(S_3) + \int_{\text{vol}} \delta T q_g d(\text{vol}) \quad (9.10)$$

where

$[D_t]$ = thermal conductivity matrix of the slab

$\{L\}$ = vector operator $= \left\{ \frac{\partial}{\partial x}, \frac{\partial}{\partial y}, \frac{\partial}{\partial z} \right\}^T$

$\{v\}$ = velocity vector for mass transport of heat = $\{v_x, v_y, v_z\}^T$

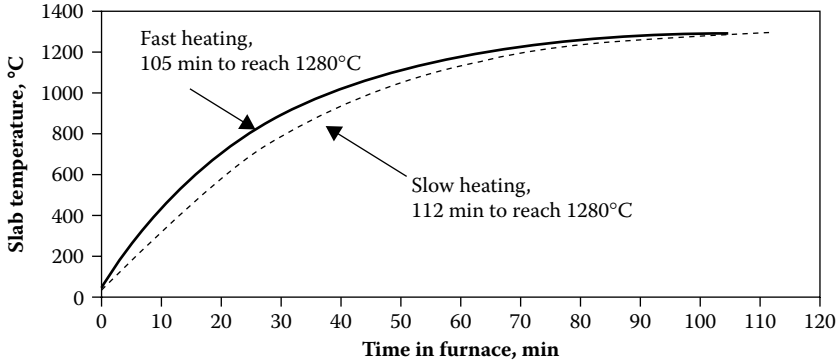


FIGURE 9.15 Fast heating curve compared to slow heating curve.

S_2, q^* = the second boundary condition with specified heat flow of q^*
S_3, h_f = the third boundary condition with heat transfer coefficient of h_f
T_f = bulk temperature of the adjacent atmosphere
δT = an allowable virtual temperature
vol = volume of an element
q_g = heat generation rate per unit volume

A quarter of a slab was considered and meshed into 41 × 21 nodes with 1600 triangle elements. When the temperature in an element is expressed as a function of the node temperatures by an element shape function, Equation 9.10 is converted to

$$[C_e^t]\cdot\{\dot{T}\}+([K_e^{tm}]+[K_e^{tb}]+[K_e^{tc}])\cdot\{T_e\}=\{Q_e^f\}+\{Q_e^c\}+\{Q_e^g\} \tag{9.11}$$

where
$[C_e^t]$ = element specific heat matrix
$[K_e^{tm}]$ = element mass transport conductivity matrix
$[K_e^{tb}]$ = element diffusion conductivity matrix
$[K_e^{tc}]$ = element convection surface conductivity matrix
$[Q_e^f]$ = element mass flux vector
$[Q_e^c]$ = element convection surface heat flow vector
$[Q_e^g]$ = element heat generation vector

The total strain consists of two parts: a mechanical strain and a thermal strain. The strain–displacement relationship is expressed in terms of the nodal displacements

$$\{\varepsilon_{total}\}=\{\varepsilon_{me}\}+\{\varepsilon_{th}\} \tag{9.12}$$

where $\varepsilon_{total}, \varepsilon_{me}, \text{and } \varepsilon_{th}$ are the total strain, mechanical strain, and thermal strain, respectively.

By applying the constitutive equations, the strain energy stored in an element is derived:

$$\begin{aligned}U_e &= \frac{1}{2}\int_{vol}\{\varepsilon_{me}\}^T[D]\{\varepsilon_{me}\}d(\text{vol})\\ &= \frac{1}{2}\int_{vol}\left([B]\{\delta^e\}\right)^T[D]\left([B]\{\delta^e\}\right)d(\text{vol})\\ &\quad -\int_{vol}\left([B]\{\delta^e\}\right)^T[D]\{\varepsilon_{th}\}d(\text{vol})\\ &\quad +\frac{1}{2}\int_{vol}\left(\left(\{\varepsilon_{th}\}\right)^T[D]\{\varepsilon_{th}\}\right)d(\text{vol})\end{aligned} \tag{9.13}$$

where
$[B]$ = the strain matrix
$[D]$ = stress–strain matrix
$\{\delta^e\}$ = an allowable virtual displacement vector

Equation 9.13 can be rewritten as

$$U_e=\frac{1}{2}\{\delta^e\}^T[K^e]\{\delta^e\}-\{\delta^e\}^T\{Q_{th}^e\}+c \tag{9.14}$$

where
$[K^e]$ = element stiffness matrix,

$$\{K^e\}=\int_{vol}[B]^T[D][B]d(\text{vol}) \tag{9.15}$$

$\{Q_{th}^e\}$ = equivalent element thermal "load" vector

$$\{Q_{th}^e\}=\int_{vol}[B]^T[D]\{\varepsilon_{th}\}d(\text{vol}) \tag{9.16}$$

The last term in Equation 9.14, c, equals the last term of Equation 9.13. It can be ignored because it is not explicitly a function of the virtual displacement, $\{\delta^e\}$. The above matrix equations are solved and the displacements, strains, and stresses are calculated.

Figure 9.16 compares the thermal stress evolution with time for the fast heating and slow heating curves for a 152-mm (6-in.) thick cold charged slab, and Figure 9.17 compares 152-mm and 254-mm (10 in.) slabs at fast heating. It was found that:

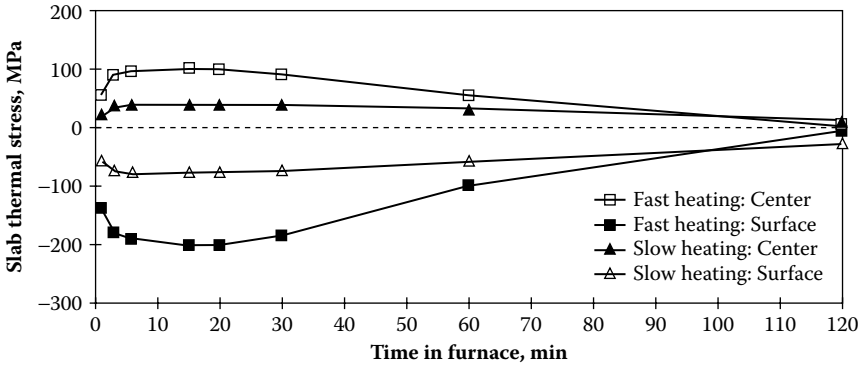


FIGURE 9.16 Comparison of thermal stress evolution during fast heating and slow heating of 152-mm slabs.

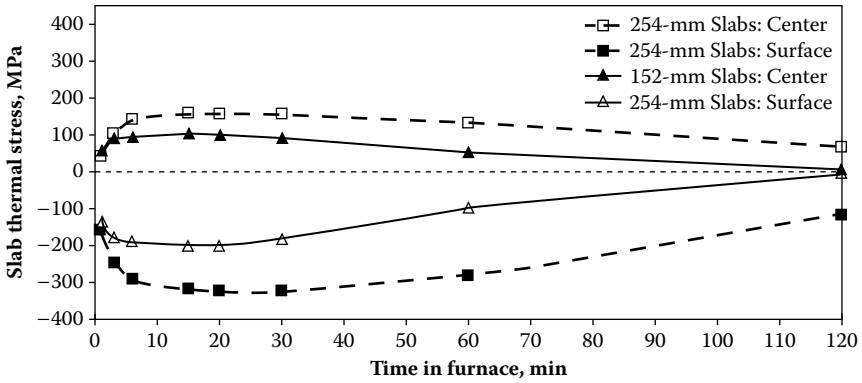


FIGURE 9.17 Comparison of thermal stress evolution of a 152-mm (6 in.) and a 254-mm (10 in.)-thick slab.

1. For both fast and slow heating curves, the stresses increase first and then begin to decrease with the peak thermal stresses occur after about 15–20 min of heating in the preheat zone. It is expected that, unless there is a sharp temperature increase, the stresses in heat and soak zones will be reduced.
2. The slab surfaces exhibited compressive stresses, while the slab center (middle thickness) area is in tension.
3. Rapidly heated and heavy gauge slabs experienced larger thermal stresses than slow heated and light gauge slabs.
4. Therefore, for heavy gauge slabs (especially high alloyed steels), attention needs to be paid at the early stage of the reheating where the stresses are at maximum to avoid center cracking caused by fast heating.

9.5 RESIDENCE TIME DETERMINATION

Under given furnace settings, there exists an optimum residence time to achieve the desired discharge slab temperature. The target function of this optimization problem is [19]

$$Abs(T_{\text{Calculated}} - T_{\text{Target}}) \le \varepsilon \tag{9.17}$$

where

$T_{\text{Calculated}}$ = calculated slab temperature
T_{Target} = desired target slab temperature
ε = temperature tolerance

The optimum design variable is the residence time (or average walking or push speed). The design constraints are the dissolution temperature, length of each zone of the furnace, temperature setpoints for the furnace zones, slab dimension, slab chemistry, the limit of the through-thickness temperature gradient, the limit of the skid-induced temperature gradient, and the maximum reheat time limit.

To perform the optimization, a *guessed* residence time is initially assumed, and then the slab temperature is calculated. Depending on the difference between the calculated temperature and the target temperature, an intelligent algorithm was developed to properly adjust the residence time and search for the optimum value until the difference of the calculated temperature and the target is within the tolerance.

As is well known, warm and hot charging of slabs will improve production and save energy. Figure 9.18 quantitatively demonstrates the required residence time as a function of charge temperature. It is obvious that a hotter charged slab will need less time. In the studied case for 152-mm (6 in.)-thick slabs targeting an exit temperature of 1290°C, a slab charged at 1000°C can save 13 min or 10% as compared to slab cold charged at room temperature. The time savings will vary with different slab dimensions, chemistries, target exit temperatures, furnace designs and settings, etc.

9.6 A CASE APPLICATION OF PRACTICE MODELING [19]

9.6.1 Background

The study was conducted on a mill with a nominal production capacity of 1.25 million tons per year. Shortly after the commission of the mill, it was recognized that the reheat furnace was the bottle neck, and must be corrected to increase the productivity of the rolling mill. Driven by the market demand, a decision was made to modify the existing heating practices of the reheat furnace with the aim of increasing the

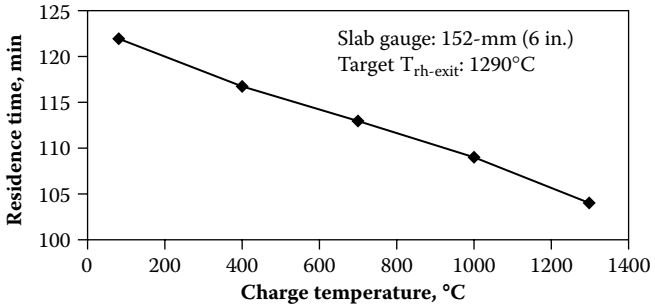


FIGURE 9.18 Required residence time decreasing with charge temperature.

throughput. However, proper reheating of a slab may require a minimum residence time to achieve the desired final product qualities. Therefore, before any educated and practical modifications can be made, the following questions need to be answered:

- How large are the thermal stresses in the slab?
- How severe are the skid marks (or skid-induced temperature inhomogeneity)?
- How do the curved skid riders affect the skid marks?
- How fast can the slab travel?
- How can a target discharge temperature be properly specified?
- How can a proper residence time be determined?
- How severe is the through-thickness temperature gradient within a slab?
- How can the dissolution of the microalloy particles be ensured?

9.6.2 Modeling Package and Calibration

In order to answer these questions, a comprehensive reheat furnace model was developed, along with a complete definition of the heating criteria. An integrated, user-friendly, and comprehensive reheat furnace optimization package, the reheat model, was developed. This package consists of six submodels: an FEA thermal stress model, a slab temperature model, a furnace temperature profile model, a microalloy dissolution temperature model, a heating speed model, and a residence time optimization model. The program was coded by using Visual Basic V6.0® (Microsoft Corp., USA), except the FEA-based, thermal stress submodel, which was coded in Compaq® (Compaq Computer Corp., USA) Visual Fortran V6.0. Figure 9.19 is a snapshot of one of the modeling results display screens.

The calibration of the slab temperature model was conducted by comparing the model predictions to extensive plant operational data and by instrumented slab measurements

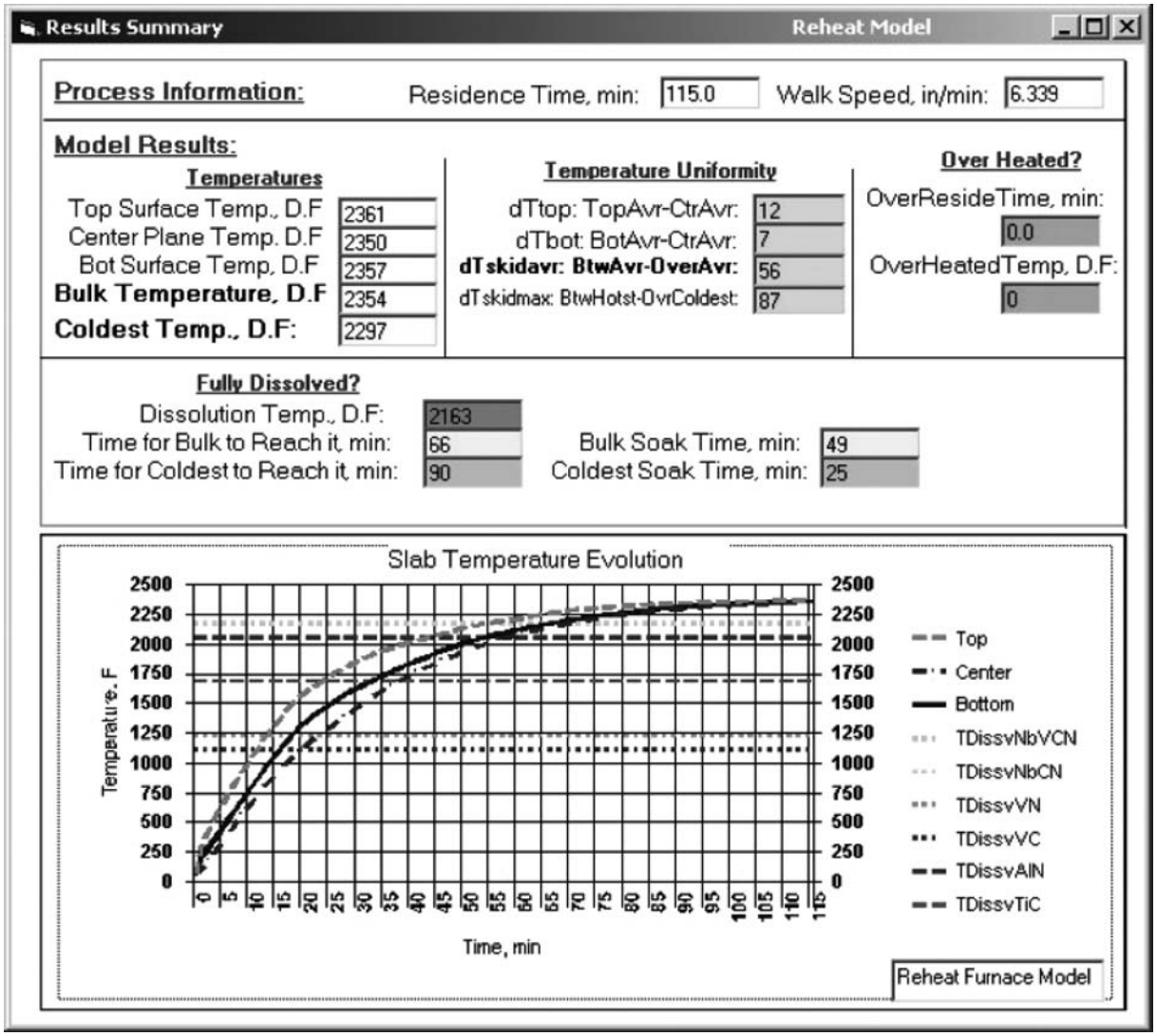


FIGURE 9.19 Snapshot of the model summary results screen. (From S. Chen, D. Poshard, and S. Abraham. 2007. *Iron & Steel Technology* 5(8): 66–79. With permission.)

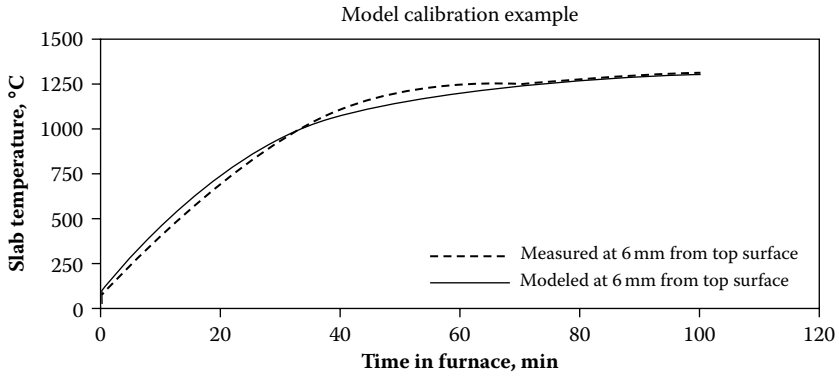


FIGURE 9.20 Heating curves comparison between the model calculated and the instrumented slab measurements.

using Datapaq's Furnace Tracker® (Datapaq Inc., USA) in which nine thermocouples were embedded in various locations in the interior of a slab to measure the temperature profiles and one thermocouple to measure the furnace atmosphere temperature. The model was tuned in such a way that the calculated heating curves (center thickness, top surface, bottom surface, and bulk average temperatures) match the ones obtained from the instrumented slab measurements. Figure 9.20 provides an example comparing the heating curves from the model with the instrumented slab measurements for a point close to the slab surface. It can be seen that very good agreement was achieved between the model predictions and the measurements.

9.6.3 Heating Practice Modifications

Based on the modeling analysis, a thorough review of the existing heating practices was conducted, and the following modifications were made:

- All the products were regrouped by merging, splitting, and eliminating the existing heating families (groups) according to the dissolution temperature calculations.
- The target discharge temperatures were decreased or increased depending on the product gauge and heating family. For instance, the discharge temperatures were decreased by up to 30°C for the heavy gauge products of the steels containing less microalloy elements, but increased by up to 40°C for the heavy gauge plain C steels, which had very low discharge temperatures.
- New heating practices were developed for warm charged slabs to take the advantage of warm temperatures, in lieu of sharing the same practices for both cold and warm charged slabs as specified by the old practices.
- The minimum residence times were reduced by 5–25 min for cold charged slabs, 5–25 min for warm charged slabs, and up to 35 min for hot charged slabs, depending on the heating family and the gauge group.

With these modifications, a production increase of over 7.0% was expected. It is worth mentioning that the increase of the discharge temperatures for some heavy gauge products will result in reduced residence time. This is opposite to what has been commonly believed, in other words, that a lower discharge temperature will save time. This is true when one considers only the bulk temperature. If one considers the extra time needed to achieve acceptable temperature uniformity, a higher discharge temperature may, in some cases, be more favorable in terms of time saving.

9.6.4 Model Implementation Results

The modified heating practices were put into operation on July 17, 2006. Significant residence time savings were achieved as compared to the old heating practices. As an example, Figure 9.21 compares the actual residence times before and after the modifications for vanadium bearing grades. As seen, the residence time was reduced by 8.7 min to 21.2 min, depending on the gauge group. An average time saving of 13 min (from 133.7 to 120.7 min) was attained, which would translate to a production increase of 9.72% for this heating family.

Figure 9.22 provides the results for all the products. Overall, the actual residence time was reduced by 12.3 min, corresponding to a throughput increase of 8.8%. The before modification practices had an average residence time of 139.8 min for 6462 slabs produced during a period of about 3 months. The after modification practices had an average residence time of 127.5 min for 13,055 slabs produced over a 5-month period. It is obvious that this production increase will result in substantial financial benefits.

9.7 SUMMARY

In today's competitive marketplace, steelmakers expect increased productivity, enhanced product quality, reduced specific fuel consumption, and ultra-low NO_x emission from a reheat furnace. These expectations involve satisfaction of mechanical, metallurgical, environmental, and economic requirements and can only be fulfilled with a well-designed furnace and optimized operational heating practices. In

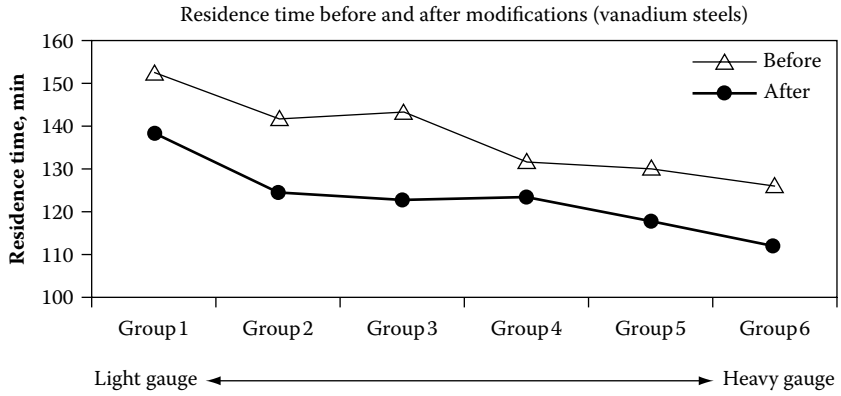


FIGURE 9.21 Model implementation results for vanadium bearing products. (From S. Chen, D. Poshard, and S. Abraham. 2007. *Iron & Steel Technology* 5(8): 66–79. With permission.)

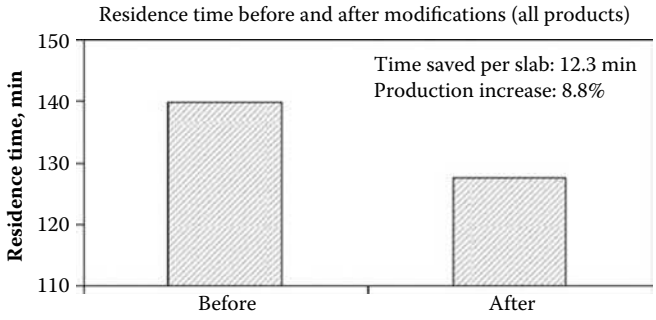


FIGURE 9.22 Overall model implementation results for all products.

particularly, with the rapidly increased production of HSLA steels, the controlled heating concept has received considerable attention. Comprehensive computer modeling has offered an effective tool for the furnace designers and users to accomplish these objectives.

Depending on the application, reheat furnace computer modeling can be roughly classified into three major categories: furnace design models furnace, heating practice models, and furnace dynamic control models. This chapter focused on the heating practice models.

The first step to establishing a heating practice is to properly specify a target reheat exit temperature. In addition to the traditionally considered slab plasticity and fuel consumption, the metallurgical requirements may become the predominant factor to determine the desired exit temperature. A proper furnace exit temperature should ensure dissolution of the relevant microalloy precipitates, avoid excessive grain coarsening, and guarantee the no-crystallization temperature and finishing rolling temperature.

Slab temperature prediction and thermal stress modeling were discussed. These models will help determine the optimal heating speed, heating curves, and furnace residence time to improve productivity, enhance product quality, and reduce fuel consumption.

A case application of furnace practice modeling to an industrial reheat furnace has demonstrated a significant furnace production increase of 8.8% as a result of comprehensive heating practice modifications, which will result in substantial financial benefits.

ACKNOWLEDGMENTS

The author would like to thank S. Hansen, J. Dorricott, J. Thomas, R. Boccardo, V. Clark, D. Poshard, A. Bruner, D. Bai, S. Abraham, L. Collins, and F. Hamad of IPSCO division of SSAB for their support. Special thanks go to J. Asante, who originated the reheat modeling project at IPSCO.

REFERENCES

1. P. Barr. 1995. The development, verification, and application of a steady-state thermal model for the push-type reheat furnace. *Metallurgical and Materials Transactions* 26B: 851–869.
2. P. Marino, A. Pignotti, and D. Solis. 2004. Control of pusher furnaces for steel slab reheating using a numerical model. *Latin American Applied Research* 34: 249–255.
3. J. Feese and F. Lisin. 2005. Pusher reheat furnace: technology advancement. In proceedings of *AISTech2005* II: 1071–1079.
4. P. Vesterberg and G. Moroz. 2006. Flameless oxyfuel for highly visible results. In *Proceedings of AISTech2006* II: 1101–1109.
5. S. O'Connor, J. Qin, and L. Deng. 2006. Performance of the regenerative burners in Baosteel 2050 hot strip mill furnace. In *Proceedings of AISTech2006* II: 1077–1090.
6. L. Ballarino, M. Fantuzzi, and M. Senarega. 2007. Industrial application of flameless low NO_x burners. *Metallurgical Plant and Technology International* 30(4): 64–71.
7. W. Trinks, M. Mawhinney, R. Shannon, R. Reed, and J. Garvey. 2004. *Industrial Furnaces*. Hoboken, NJ: John Wiley & Sons.
8. P.V. Barr and A.W. Burgess. 1990. Computer models for pusher-type and walking beam reheating furnaces. In *Proceedings of the International Symposium on Steel Reheat Furnace Technology*, CIM/ICM, ed. F. Mucciardi, pp. 85–102.
9. Y. Yang, J. Kroeze, and M. Reuter. 2004. Simulation of slab movement and transient heating in a continuous steel reheat furnace. *Progress in Computational Fluid Dynamics* 4: 46–58.
10. L. Ferrand, P. Reynes, and F. Duigou. 2006. Simulation tools make new furnace technology. *Revue de Metallurgie* 103: 67–75.

11. N. Stockwell, C. Zhang, T. Ishii, and Y. Hino. 2001. Numerical simulation of turbulent non-premixed combustion in a regenerative furnace. *ISIJ International* 41(10): 1272–1281.
12. M.Y. Kim. 2007. A heat transfer model for the analysis of transient heating of the slab in a direct-fired walking beam type reheating furnace. *International Journal of Heat and Mass Transfer* 50: 3740–3748.
13. Y. Tang, J. Laine, T. Fabritius, and J. Harkki. 2003. The modeling of gas flow and its influence on the scale accumulation in the steel slab pusher-type reheating furnace. *ISIJ International* 43(9): 1333–1341.
14. W. Yan and F. Zhang. 2000. Mathematical model study on billet heating furnace. *Industrial Furnace* 22(2): 54–58.
15. B. Yang, C. Wu, and C. Ho. 1995. A heat transfer model for skid mark formation on slabs in a reheating furnace. *Journal of Materials Processing and Manufacturing Science* 3: 277–295.
16. Z. Li, P. Barr and J. Brimacombe. 1988. Computer simulation of the slab reheating furnace. *Canadian Metallurgical Quarterly* 27(3): 187–196.
17. D. Lindholm and B. Leden. 1999. A finite element method for solution of the 3-D time dependent heat-conduction equation with application for heating of steels in reheating furnaces. *Numerical Heat Transfer* 35 (A): 155–172.
18. J. Harish and P. Dutta. 2005. Heat transfer analysis of pusher type reheat furnace. *Ironmaking and Steekmaking* 32: 151–158.
19. S. Chen, D. Poshard, and S. Abraham. 2007. Modification of reheat furnace practices through comprehensive process modeling. *Iron & Steel Technology* 5(8): 66–79.
20. S. Hori, S. Nishitomo, and S. Tanifuji. 1983. Reheating furnace combustion control system for hot charge rolling. *Hitachi Review* 32(2): 89–93.
21. E. Kihlburg. 1992. Optimization of reheat furnace operation. *ABB Review* 3: 13–18.
22. R. Shulkosky, D. Rosburg, J. Chapman, and K. Barnes. 2003. A microstructure evolution model used for hot strip rolling. In *Proceedings of the 2003 Modeling, Control and Optimization in Ferrous and Nonferrous Industry Symposium*, pp. 509–527.
23. Y. Lan, D. Li, X. Sha, and Y. Li. 2004. Prediction of microstructure and mechanical properties of hot rolled steel strip: Part I—Description of models. *Steel Research International* 75(7): 462–467.
24. P. Hodgson and R. Gibbs. 1992. A mathematical model to predict the mechanical properties of hot rolled C-Mn and microalloyed steels. *ISIJ International* 32(12): 1329–1338.
25. K. Irvine, F. Pickering, and T. Gladman. 1967. Grain-refined C-Mn steels. *Journal of the Iron and Steel Institute* 205(2): 161–182.
26. J. Speer, J. Michael, and S. Hansen. 1987. Carbonitride precipitation in niobium/vanadium microalloyed steels. *Metallurgical Transactions* 18A(2): 211–222.
27. T. Siwecki. 1992. Modeling of microstructure evolution during recrystallization controlled rolling. *ISIJ International* 32(3): 368–376.
28. W. Yu, E. Palmiere, S. Banks, and J. Han. 2005. Cellular automate modeling of grain coarsening during reheating and validation with the experimental results. *Acta Metallurgical Sinica* 18(2): 113–120.
29. Y. Yang, D. Linkens, M. Mahkouf, and A. Rose. 2003. Grain growth modeling for continuous reheating process—A neural network-based approach. *ISIJ International* 43(7): 1040–1049.
30. E. Palmiere, C. Garcia, and A. DeArdo. 1994. Compositional and microstructural changes which attend reheating and grain coarsening in steel containing niobium. *Metallurgical and Materials Transactions* 25A: 277–286.
31. M. Militzer. 2007. Computer simulation of microstructure evolution in low carbon sheet steels. *ISIJ International* 47(1):1–15.
32. D. Bai, S. Yue, T. Maccagno, and J. Jonas. 1996. Static recrystallization of Nb and Nb-B steels under continuous cooling conditions. *ISIJ International* 36(8): 1084–1093.
33. B. Pereda, B. Lopez, and J. Rodriguez. 2007. Increasing the non-recrystallization temperature of Nb microalloyed steels by Mo addition. In *International Conference on Microalloyed Steels: Processing, Microstructure, Properties and Performance*, Pittsburgh, PA: 151–159.

10 Improvement of Schedules for Hot Rolling of Thin Wide Strips

Eduard Garber, Alexander Traino, and Irina Kozhevnikova

CONTENTS

10.1 Introduction 115
10.2 Formulation of the Problem and Assumptions 115
10.3 Main Points of the Calculation Procedure 118
10.4 Application of the Calculation Procedure to Analyze Contact Stresses in the Working Stands of Wide-Strip Mills 121
10.5 Calculation of Main Drive Power and Moment for Wide-Strip Mills 122
10.5.1 Calculation of Rolling Power 122
10.5.2 Calculation of Moment and Power of Working Stand Main Drive 122
10.6 Conclusion 125
References 125

10.1 INTRODUCTION

Modern flat rolling process tends to produce hot-rolled steel strips 0.8–1.5 mm thick, which had been previously attributed to the range of cold-rolling mills.

Most operating wide-strip, hot-rolling mills were designed to produce strips as thin as 1.8–2.0 mm, and their energy–force parameters (the roll force and the main drive engine power) are not intended for the rolling of thinner strips, which is characterized by higher reductions and contact stresses acting on rolls, complicated thermal conditions for the rolls because of an increase in the machine time in a rolling cycle, and (as a consequence) more intense roll wear.

To design effective technological regimes and to ensure reliable (without overload) operation of the equipment of wide-strip mills during the production of strips 0.8–1.5 mm thick, it is necessary to improve the methods of their energy–force calculation, since existing calculation methods do not take into account the state of stress in a metal subjected to hot rolling.

10.2 FORMULATION OF THE PROBLEM AND ASSUMPTIONS

It is important that the major portion of the deformation zone of a working stand in a wide hot-strip mill be occupied by a stick zone, which is characterized by the absence of relative slip of the strip-roll contact surfaces:

$$v_{x\text{surf}} = v_r$$

where $v_{x\text{surf}}$ is the velocity of the strip surface layer in contact with a roll and $v_{x\text{surf}}$ is the peripheral velocity of the roll body.

Sticking appears in the portion of the deformation zone where tangential contact stresses τ_x are maximal, $\tau_{x\max} = \tau_s$, where τ_s is the pure shear resistance of the strip material. These stresses are proportional to the normal contact stresses, ρ_x, $\tau_x = \mu\rho_x$, where μ is the friction coefficient in the deformation zone. The structure of a deformation zone containing a stick zone was analyzed in Tselikov's work [1]. This analysis has a predominantly qualitative character and predicts many dependences for the state of stress in a strip in the stick zone that can be supported and refined by calculations performed using modern, state-of-the-art mathematical simulation. In particular, Tselikov [1] was the first to show that the variation of the tangential stresses with the stick-zone length does not obey the friction law given above and that these stresses are independent of the friction coefficient between the strip and rolls.

According to Tselikov [1], the stick zone can occupy the entire deformation zone, provided $l/h_{\text{av}} \le 2$, where l is the deformation-zone length and h_{av} is the average strip thickness. However, our detailed analysis of the state of stress in a strip in the deformation zones of the working stands of finishing groups in wide-strip, hot-rolling mills shows that deformation zones consisting mainly of stick zones are characterized by the range $l/h_{\text{av}} \le 0.5$–15. The ratios of the stick-zone length to the entire deformation zone under these conditions are as follows (%):

98%–99% in the first stands of the finishing groups ($l/h_{av} \le 0.5$–3.0) and
83%–90% in the last stands of the finishing groups ($l/h_{av} \le 10$–15)

Table 10.1 gives the ranges of the average values of p_x, μ, τ_x, and τ_s characteristic of the hot rolling of steel strips in wide hot-strip mills.

As follows from Table 10.1, even the average tangential stresses in the deformation zone calculated by the friction law $\tau_{av} = {}_{\mu}p_{av}$ exceed the pure shear resistance of the strip material by a factor of 1.5–2.5. This means that this friction law holds true only in very short regions (near the entrance and exit sections of the strip) and that, over the major portion of the deformation zone, the tangential stresses depend on the pure shear resistance of the strip material (which is characteristic of the stick zone) rather than on the friction coefficient.

The problem of the variation of the tangential stresses with the stick-zone length, that is, the form of the $\tau_x(x)$ dependence, is also disputable. Tselikov [1] gave several hypothetical versions for this dependence and did not estimate their reliability. It should be taken into account that the absence of strip slip with respect to rolls, which is characteristic of the stick zone, means that the tangential stresses $\tau_x(x)$ in this zone represent static-friction stresses. The alternating character of these stresses is determined by their opposite directions in the backward and forward slip zones and their zero value in the neutral section. Although the strip and roll velocities on the contact surface are the same, the strip velocity averaged over the strip cross section v_{xav} increases when the strip moves through the deformation zone (Figure 10.1a). As a result, the velocity difference $v_r - v_{xav}$ changes according to the curve shown in Figure 10.1b.

It is natural to assume that the static-friction stresses $\tau_x(x)$ are related to this velocity difference, which is a specific velocity head acting on the strip-roll contact surface.

Another substantial specific feature of the deformation zone in a wide-strip, hot-rolling mill belongs to the last stands of its finishing group and includes a significant length of the elastic regions of this zone, especially of the second elastic region (where part of the strip thickness is recovered). In the first stands of the finishing group, the length of these regions accounts for 1%–2% of the total deformation-zone length; in the last stands, this fraction increases to 15%–17%.

Therefore, the simulation of the state of stress in thin strips subjected to hot rolling in wide-strip mills can give reliable results only in the case of an elastoplastic model for the deformation zone.

All well-known methods of energy–force calculations for these mills neglect stresses in the elastic regions, which result in high errors in the calculation of the hot-rolling forces and power for strips 0.8–1.5 mm thick.

TABLE 10.1
Parameter Ranges for the State of Stress in a Still Strip Subjected to Hot Rolling in a Wide-Strip Mill

Parameter	Parameter Range
Average normal contact stresses $p_x(p_{av})$, MPa	300[a]–1050[b]
Friction coefficient in the deformation zone, μm	0.56[a]–0.2[b]
Average tangential stresses $\tau_x(\tau_{av})$ calculated by the formula $\tau_{av} = \mu\rho_{av}$, MPa	170–210
Pure shear resistance of the strip material, τ_s	70–160

[a] In the first stands of the finishing group.
[b] In the last stands of the finishing group.

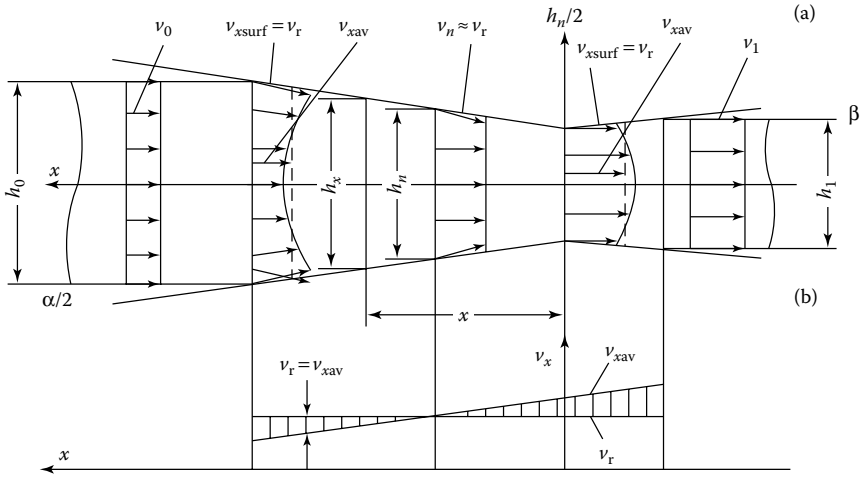


FIGURE 10.1 Schematic diagrams for (a) velocities in strip cross sections and (b) the velocity difference $v_r - v_{xav}$ along the deformation zone of a working stand in a wide-strip, hot-rolling mill. v_0 and v_1 are the strip velocity at the entrance and exit at the deformation zone, respectively; v_{xsurf} is the strip velocity on the contact surface with a roll; v_r is the peripheral velocity of the roll body; v_n is the strip velocity in the neutral section; v_{xav} is the strip velocity averaged over thickness h_x in the section with coordinate x; and h_0, h_1, and h_n are the strip thicknesses at the entrance and exit of the deformation zone and the neutral section, respectively.

Allowing for these specific features of the state of stress in a strip, we have developed a procedure for contact-stress calculation and propose the following friction stress model (Figure 10.2) [2]:

1. In elastic regions of lengths x_{1el} and x_2, the friction law is

$$\tau_x = \mu\rho_x \tag{10.1}$$

2. In the plastic region, which is the stick zone, the tangential stresses change linearly from the maximum ($\tau_{x\max} = \tau_s$) to the minimum ($\tau_x \geq -\tau_s$) value and pass through a value $\tau_x = 0$ in the neutral section according to the expression:

$$\tau_x = \tau_s \left(\frac{h_x - h_n}{h_{1el} - h_n} \right) \tag{10.2}$$

where h_n is the strip thickness in the neutral section, $h_{1el} = h_{i-1} - \Delta h_{1el}$ is the strip thickness at the boundary between the first elastic and the plastic regions, h_{i-1} is the strip thickness at the entrance of the ith working stand, $\Delta h_{1el} = h_{i-1}\sigma_{sr.pl}/E_s$ is the maximum elastic strip deformation at the end of the first elastic region, $\sigma_{sr.pl}$ is the average strain resistance of the strip in the plastic region of the deformation zone, and E_s is the elastic modulus of the strip material.

The linear character of the $\tau_x(h_x)$ dependence is specified by Equation 10.2 as an assumption, since it is impossible to establish the real shape of the $\tau_x(h_x)$ curve in the stick zone using existing methods of investigation.

Note that, although the strip-surface layer velocity is constant in the plastic region because of sticking, the velocity averaged over the strip thickness is as follows:

$$\text{at } h_x > h_n,\ v_{xav} < v_r$$
$$\text{at } h_x < h_n,\ v_{xav} > v_r$$

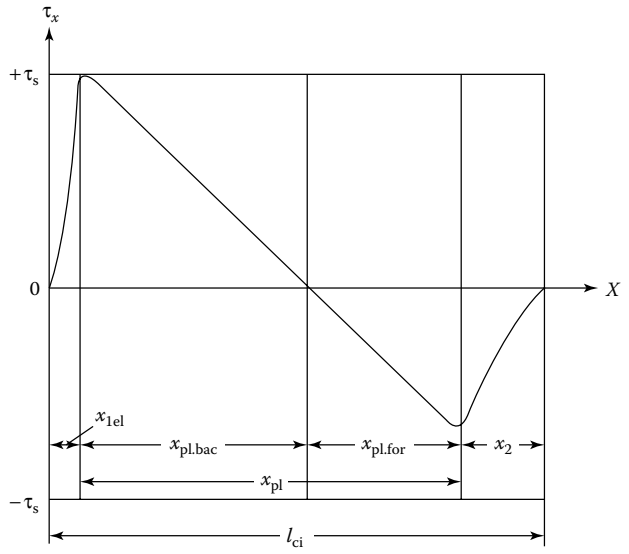


FIGURE 10.2 Tangential contact stresses in the deformation zone.

Therefore, with respect to the velocity averaged over the strip thickness, the plastic region consists of two zones, namely, backward and forward slip zones.

The calculation of contact stresses depends on both a tangential stress model and a strip-strain resistance model.

Our strain resistance model is based on the curve shown in Figure 10.3.

According to this curve, the strain resistance varies linearly (according to Hooke's law) in the elastic regions and is taken to be approximately constant ($\sigma_{sr.pl}$) in the plastic region, since recrystallization occurs along with hardening during hot rolling. After analyzing the well-known formulas used to calculate $\sigma_{sr.pl}$, we chose the Andreyuk formula [3]:

$$\sigma_{sr.pl} = S\sigma_{bsr}u^a(10\varepsilon_{\Sigma i})^b(t_i/1000)^c$$

as the most reliable one. Here, S, a, b, and c are constants to be determined for every steel grade from tests on a plastometer; σ_{bsr} is the base strain resistance; u is the strain rate (s^{-1}); $\varepsilon_{\Sigma i}$ is the total relative reduction in i passes; and t_i is the strip temperature at the exit of the ith stand,

$$t_i = t_0 - \Gamma\left(\frac{h_0}{h_i} - 1\right)$$

Here, t_0 and h_0 are the semifinished rolled product temperature and thickness, respectively; h_i is the strip thickness at the exit of the ith stand; and Γ is the temperature gradient:

$$\Gamma = \frac{t_0 - t_f}{h_0 - h_f} h_f$$

where t_f and h_f are the temperature and thickness of the ready semifinished rolled product, respectively.

The determination of the strain resistance from the curve shown in Figure 10.3 distinguishes our procedure from the classical procedures in [1,3,4], in which $\sigma_{sr.pl}$ is taken to be

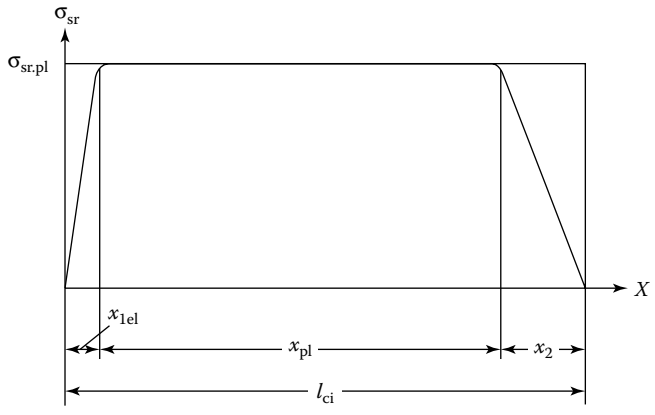


FIGURE 10.3 Schematic diagram for the variation in the strain resistance along the contact arc in the ith stand of a wide-strip, hot-rolling mill.

constant over the entire deformation zone during hot rolling and the effect of the elastic regions (where the average strain resistance is $\sigma_{sr.pl}/2$) is not taken into account.

As follows from Equation 10.2, the tangential stresses in the stick zone are explicitly independent of the friction coefficient μ; according to Equation 10.1, this coefficient is only used for the elastic regions. Based on an analysis of the well-known empirical formulas for the friction coefficient, we use the formula [3]:

$$\mu_i = k_1 k_2 k_3 (1.05 - 0.0005 t_i)$$

where k_1 is a coefficient that takes into account the surface state and the roll material, k_2 is a coefficient that takes into account the rolling speed, and k_3 is a coefficient that takes into account the carbon content in the steel.

10.3 MAIN POINTS OF THE CALCULATION PROCEDURE

Allowing for the accepted initial data and assumptions, we calculate contact stresses separately for two elastic regions and one plastic region. To this end, we use a plain state of stress, which is valid for a thin wide strip, and set up a system of the following three equations in variable stresses $p_x(h_x)$, $\tau_x(h_x)$, and $\sigma_x(h_x)$ (where $\sigma_x(h_x)$ stands for the compressive normal stresses parallel to the rolling axis) for each region (see Tables 10.2 and 10.3):

1. A differential equation of strip equilibrium.
2. An equation of elasticity (for the elastic regions) or plasticity (for the stick zone).
3. An equation that reflects the variation of the friction stresses: Equation 10.1 for the elastic regions, Equation 10.2 for the plastic region, and the same equation for the backward and forward slip zones.

The contour of the deformation zone is approximated by two straight-line segments with allowance for elastic flattening: the first segment extends from the entrance section to the vertical axial plane of the rolls (which corresponds to the angle of nip α and, hence, makes an angle α/2 with the rolling axis), and the second segment covers the region of elastic recovery of part of the strip thickness (which is tilted at an angle β to the rolling axis in the opposite direction). To calculate α and

TABLE 10.2
Basic Expressions for the Elastic Regions of the Deformation Zone

Elastic Compression Region of Length x_{1el}	Elastic Recovery Region of Length x_2
1. Equilibrium Differential Equations	
$d\sigma_x - (p_x - \sigma_x)\frac{dh_x}{h_x} + \frac{\mu p_x}{\tan\alpha/2}\cdot\frac{dh_x}{h_x} = 0,$	$d\sigma_x - (p_x - \sigma_x)\frac{dh_x}{h_x} + \frac{\mu p_x}{\tan\beta}\cdot\frac{dh_x}{h_x} = 0,$
where $\tan\alpha/2 = \frac{\Delta h_1 + \Delta h_{2el}}{2x_1}$	where $\tan\beta = \frac{\Delta h_{2el}}{2x_2}$
2. Elasticity Equations	
$p_x - \sigma_x = 1.15E_s\frac{h_x - h_{i-1}}{h_{i-1}}$	$p_x - \sigma_x = 1.15E_s\frac{h_x - h_i}{h_i}$
3. Friction Law	
$\tau_x = \mu_i p_x$	
4. Formulas for $p_x(hx)$	
$p_x = 1.15E_s\left\{\frac{1}{\delta_{i-1}} - \frac{2}{\delta_{i-1}+1}\cdot\frac{h_x}{h_{i-1}} + \left(\frac{h_{i-1}}{h_x}\right)^{\delta_{i-1}} \times\left[\frac{\delta_{i-1}-1}{(d_{i-1}+1)\delta_{i-1}} - \frac{\sigma_{i-1}}{1.15E_s}\right]\right\},$	$p_x = 1.15E_s\left\{\frac{1}{\delta_i} - \frac{2}{\delta_i+1}\cdot\frac{h_x}{h_i} + \left(\frac{h_i}{h_x}\right)^{\delta_i} \times\left[\frac{\delta_i-1}{(d_i+1)\delta_i} - \frac{\sigma_i}{1.15E_s}\right]\right\},$
where $\delta_{i-1} = \frac{\mu_i}{\tan\alpha/2}$.	where $\delta_i = \frac{\mu_i}{\tan\beta}$.

Note: h_{i-1} is the strip thickness at the entrance of the ith stand; σ_{i-1} and σ_i are the backward and forward specific pulls, respectively.

TABLE 10.3
Basic Expressions for the Plastic Region of the Deformation Zone

Equation	Formula
1. Equilibrium differential equation	$d\sigma_x - (p_x - \sigma_x)\frac{dh_x}{h_x} + \frac{\tau_x}{\tan\alpha/2}\cdot\frac{dh_x}{h_x} = 0$
2. Plasticity equation	$p_x - \sigma_x = 1.15\sigma_{sr.pl}$
3. Friction law	$\tau_x = \tau_s\left(\frac{h_x - h_n}{h_{1el} - h_n}\right)$
4. Formula for $p_x(h_x)$	$p_x = 1.15\sigma_{sr}\left[\frac{0.5}{\tan\alpha/2}\cdot\frac{h_{1el}-h_x}{h_{1el}-h_n} + \left(1+\frac{0.5}{\tan\alpha/2}\cdot\frac{h_n}{h_{1el}-h_n}\right) + (\ln h_x - \ln h_{1el}) + \frac{p_{1el}}{1.15\sigma_{sr}}\right]$

β, we use the formulas obtained in [5] for the deformation zones of cold-rolling mills.

Each of the systems given in Tables 10.2 and 10.3 (lines 1–3) is reduced to one first-order differential equation in normal contact stresses $p_x(h_x)$.

We then solve this equation under real boundary conditions for each region in the deformation zone and obtain a calculation formula for $p_x(h_x)$ (Tables 10.2 and 10.3; line 4).

As the boundary conditions at the entrance and exit of the deformation zone, we use given specific strip pulls σ_{i-1} and σ_i. As the boundary conditions for the stick zone, we use the values of $p_x(h_x)$ calculated for the first elastic region in the section where $h_x = h_{1el}$.

To obtain an expression for the calculation of the strip thickness in the neutral section, we put the expressions obtained for the stick zone and the second elastic region [$p_x(h_x = h_{2el})$] equal to each other and, thus, obtain an equation in $h_x = h_n$. Its solution gives a new refined formula for the strip thickness in the neutral section that takes into account all of the specific features of the deformation zone discussed above:

$$h_n = \{2h_{1el}\tan\alpha/2[(p_{2el} - p_{1el})/1.15\sigma_{sr} - \ln h_{2el} + \ln h_{1el}] - h_{1el} + h_{2el}\} \times \{2\tan\alpha/2[(p_{2el} - p_{1el})/1.15\sigma_{sr} - \ln h_{2el} + \ln h_{1el}] - \ln h_{1el} + \ln h_{2el}\}^{-1}$$

where p_{2el} is the normal contact stress calculated from the equation for $p_x(h_x)$ for the second elastic region in the section $h_x = h_{2el} = h_1 - \Delta h_{2el}$.

Table 10.4 lists the formulas for the calculation of the average normal contact stresses in each region that were obtained by integrating the $p_x(h_x)$ expressions.

TABLE 10.4
Formulas for the Average Normal Contact Stresses

Rgion	Formula
Elastic region of length (x_{1el})	$p_1 = 1.15E_s\left\{\frac{1}{\delta_{i-1}} + \frac{L}{\delta_{i-1}+1}\left[\left(\frac{\delta_{i-1}-1}{(\delta_{i-1}+1)\delta_{i-1}} - \frac{\sigma_{i-1}}{1.15E_s}\right)(D^{\delta_{i-1}+1} - 1) - 2\ln D\right]\right\}$ where, $L = \frac{E_s - \sigma_{sr.pl}}{\sigma_{sr.pl}}$, $D = \frac{E_s}{E_s - \sigma_{sr.pl}}$
Stick zone of length (x_{pl})	$p_2 = \frac{1.15\sigma_{sr}}{h_{2el}-h_{1el}}\left\{\left[1+\frac{0.5}{\tan\alpha/2}\cdot\frac{h_n}{h_{1el}-h_n}\right][h_{2el}(\ln h_{2el}-1) - h_{1el}(\ln h_{1el}-1)] - \frac{0.25(h_{2el}^2 - h_{1el}^2)}{\tan\alpha/2(h_{1el}^2 - h_n)} + \frac{p_{1el}}{1.15\sigma_{sr}} + \frac{0.5}{\tan\alpha/2}\cdot\frac{h_{1el}}{h_{1el}-h_n} - \left[1+\frac{0.5}{\tan\alpha/2}\cdot\frac{h_n}{h_{1el}-h_n}\right] - \ln h_{1el}(\ln h_{2el} - \ln h_{1el})\right\}$
Elastic region of length (x_2)	$p_1 = 1.15E_s\left\{\frac{1}{\delta_i} + \frac{L}{\delta_i+1}\left[\left(\frac{\delta_i - 1}{(\delta_i+1)\delta_i} - \frac{\sigma_i}{1.15E_s}\right)(D^{\delta_{i-1}+1} - 1) - 2\ln D\right]\right\}$

Note: h_{2el} is the strip thickness at the boundary between the second elastic and plastic regions: $h_{2el} = h_1 - \Delta h_{2el}$, where $\Delta h_{2el} = h_i\sigma_{sr}/E_s$.

Knowing the average stresses in each of the three regions, we can calculate the average (for the entire deformation zone) normal contact stress and the rolling force by the formulas:

$$p_{avi} = \frac{1}{l_{ci}}(p_1 x_{1el} + p_2 x_{pl} + p_3 x_2)$$

$$P_i = p_{avi} l_{ci} b$$

where l_{ci} is the deformation-zone length and b is the strip width (without regard for strip widening).

We realized this procedure using an iteration algorithm in which the first approximation of p_{avi} was taken to be $p_{avi} = \sigma_{sr.pl}$.

To check the adequacy of this procedure, we compare the rolling forces calculated for and measured in the working stands of the six-stand 1700 mill. The comparison indicates that the average error in the rolling-force calculation is 5% and that the maximum error does not exceed 10%. The maximum calculation error for the classical procedures in [1,3,4] under the same rolling conditions is 23%, and the average error is 12%.

As an example of our procedure, we present the energy–force and technological rolling parameters for 0.9 × 1000 mm St1PS steel strips and 1.2 × 1000 mm S235JR steel strips (Tables 10.5 and 10.6).

Tables 10.5 and 10.6 indicate that, under the conditions used in experiments, the maximum difference between the calculated and measured forces are 8.80 and 3.96%, respectively, and that the minimum difference is less than 1%.

Such a high accuracy in determining the rolling force indicates the adequacy of our calculation procedure and the related assumptions, in particular, the assumed law of friction stress distribution over the stick-zone length (Equation 10.2, the curve in Figure 10.2). Therefore, we may use the expressions given in Tables 10.1–10.4 to construct a mathematical

TABLE 10.5
Energy–Force and Technological Hot-Rolling Parameters for a 0.9 × 1000 mm St1PS Steel Strip

(Chemical Composition of St1PS Steel [%])

C	Si	Mn	S	P	Cr	Ni	Cu	N
0.06–0.10	0.05	0.25–0.50	0.02	0.025	0.06	0.06	0.06	0.01

Stand №	v_i (m/s)	h_{i-1} (mm)	h_i (mm)	μ_i	σ_{i-1} (MPa)	σ_i (MPa)	ε_i (%)	$\varepsilon_{\Sigma i}$, %	l_{ci} (mm)	p_{avi} (MPa)	p_i (MN)		ΔP_i (%)
											meas.	calc.	
1	1.03	24.90	10.15	0.560	0	0.48	59.20	59.20	71	306	21.5	21.71	1.00
2	2.37	10.15	3.95	0.375	0.48	0.81	61.08	84.14	46	432	20.9	19.86	5.00
3	4.42	3.95	2.18	0.333	0.81	1.83	44.81	91.25	26	708	19.8	18.1	8.80
4	6.82	2.18	1.71	0.373	1.83	1.97	21.56	93.13	14	712	10.5	9.82	6.46
5	9.81	1.71	1.04	0.200	1.97	2.43	39.18	95.82	17	1017	15.6	16.7	7.00
6	11.74	1.04	0.87	0.300	2.43	32.3	16.35	96.51	9	904	8.5	8.26	2.80

Note: Meas. means measured and calc. means calculated.

TABLE 10.6
Energy–Force and Technological Hot-Rolling Parameters for a 1.2 × 1000 mm S235JR Steel Strip (Chemical Composition of S235JR Steel [%])

C	Si	Mn	S	P	Cr	Ni	Cu	Al	N
0.06–0.10	0.05	0.25–0.50	0.02	0.025	0.06	0.06	0.06	0.02–0.07	0.01

Stand №	v_i (m/s)	h_{i-1} (mm)	h_i (mm)	μ_i	σ_{i-1} (MPa)	σ_i (MPa)	ε_i (%)	$\varepsilon_{\Sigma i}$ (%)	l_{ci} (mm)	p_{avi} (MPa)	p_i (MN)		ΔP_i (%)
											meas.	calc.	
1	1.22	24.72	11.40	0.646	0	0.40	53.76	53.76	67	301	21.10	20.26	3.96
2	2.51	11.40	5.17	0.465	0.40	0.57	54.77	79.09	46	447	20.90	20.70	0.92
3	4.25	5.17	3.14	0.426	0.57	1.74	39.27	87.30	27	607	17.70	16.28	8.00
4	6.61	3.14	2.01	0.331	1.74	2.49	35.99	91.87	20	726	14.42	14.63	1.47
5	9.31	2.01	1.43	0.272	2.49	2.15	28.86	94.22	15	902	13.98	13.83	1.07
6	11.32	1.43	1.22	0.335	2.15	28.69	11.49	95.06	10	751	6.94	7.04	1.47

Note: Meas. means measured and calc. means calculated.

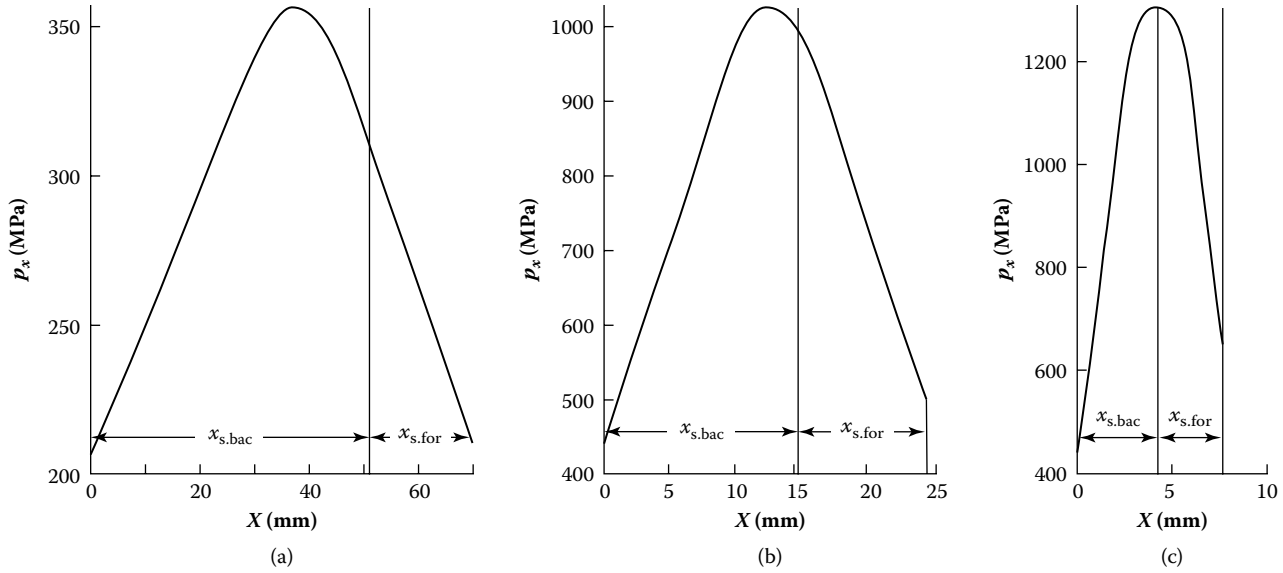


FIGURE 10.4 $p_x(h_x)$ curves in the stick zones of the deformation zones in stands (a) 1, (b) 3, and (c) 6.

model for the contact stresses and forces during hot rolling of thin wide strips and to apply this model to analyze the state of stress in the deformation zones in the working stands of finishing groups in wide-strip mills.

10.4 APPLICATION OF THE CALCULATION PROCEDURE TO ANALYZE CONTACT STRESSES IN THE WORKING STANDS OF WIDE-STRIP MILLS

For analysis, we chose real conditions for hot rolling of a strip 0.9 mm thick and 1000 mm wide made of a semifinished rolled product 25 mm thick in the six-stand 1700 mill, whose parameters are given in Table 10.5. Figure 10.4 shows the variation of the normal contact stresses p_x with the plastic-region length for the deformation zones of stands 1, 3, and 6 that were calculated using the formulas given in Tables 10.2 and 10.3 (line 4).

Figure 10.5 shows the $p_x(x)$ curve (which is scaled up along the rolling axis) in the region of the elastic recovery of part of the strip thickness in stand 6, and Table 10.7 gives the structural parameters of the deformation zones of all working stands.

Analyzing these simulation results, we can draw the following conclusions.

1. The ratio of the elastic regions to the total deformation-zone length increases from 1%–2% in the first stands to 10%–17% in the last stands of the finishing group. This increase means that these regions should be taken into account in the energy–force calculation of hot-rolling, wide-strip mills. Although the effect of the elastic regions on the rolling force in the first stands of the finishing group is insignificant, the calculation of contact stresses in these regions can reliably determine the stresses in the main (plastic) region of the deformation zone.
2. The maximum normal contact stresses increase from 350–500 MPa in the first stand to 1300–1450 MPa in the last stands, where they correspond to the stresses induced by cold rolling and exert a strong effect on the wear of work rolls. However, the strip temperature in the first stands is much higher, which leads to the burning of the roll body surface. Therefore, the problem of increasing the wear resistance of work rolls for rolling thin strips is important for all stands of the finishing groups of wide-strip mills.
3. The neutral section does not coincide with the section of the maximum contact stresses, especially in the first stands of the finishing group, where the distance between these sections is 11 mm. As the strip

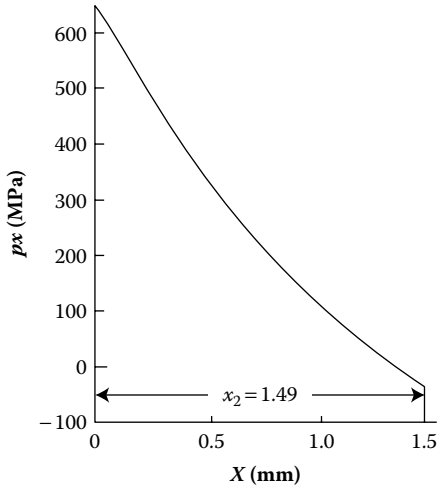


FIGURE 10.5 $p_x(h_x)$ curve for the elastic recovery region of the deformation zone in stand 6.

TABLE 10.7
Structural Parameters of the Deformation Zones of Working Stands during Hot Rolling of a 0.9 × 1000 mm St1PS Steel Strip

Stand №	l_{sri} (mm)	x_{1el} (mm)	x_{p1} (mm)	x_2 (mm)	$\frac{x_{1el}+x_2}{l_{sri}}$ (%)	$\frac{x_2}{x_{1el}+x_2}$ (%)	X_i	p_{max} (MPa)	p_n (MPa)	x_n (mm)
1	71	0.10	70.3	0.51	0.86	84	0.76	358.0	308.0	11.00
2	46	0.07	45.2	0.71	1.70	91	0.68	537.0	526.0	4.00
3	26	0.07	24.4	1.18	4.90	94	0.61	917.0	915.0	2.00
4	14	0.09	12.5	1.19	9.20	93	0.57	920.5	919.6	0.50
5	17	0.06	14.8	1.65	10.40	96	0.59	1140.0	1437.0	0.36
6	9	0.08	7.6	1.49	17.00	95	0.56	1293.7	1293.5	0.02

Note: X_i is the parameter characterizing the position of the neutral section, $X_i = x_{pl.back}/x_{pl}$; p_{max} is the maximum contact stress in the deformation zone; p_n is the contact stress in the neutral section; and x_n is the distance from the neutral section to the section with the maximum normal stress.

thickness decreases, this distance also decreases, and, in the last stands, the neutral section almost coincides with the section of the maximum contact stresses. Tselikov [1] was the first to note that these sections do not coincide in the stick zone. Our calculation procedure supports this specific feature of the deformation zone and can reliably calculate the positions of both sections.

4. In contrast to cold rolling, where the backward slip zone accounts for 80%–100% of the total length of plastic regions, this fraction for hot rolling is 56%–76%. In other words, both the neutral section and the forward slip zone take place in the deformation zones of all working stands.
5. The variation in the friction coefficient in the deformation zone shows that, even if μ increases twofold, the rolling force increases by, at most, 2%–4%. This behavior is explained by the fact that, in the main (plastic) portion of the deformation zone, the contact stresses are virtually independent of the friction coefficient.

10.5 CALCULATION OF MAIN DRIVE POWER AND MOMENT FOR WIDE-STRIP MILLS

10.5.1 Calculation of Rolling Power

In order to calculate the rolling power for each area in the deformation zone, specific rolling values were obtained. Normal and tangent forces in the directions parallel and perpendicular to the rolling axis were summarized.

These specific rolling values obtained in this way are given in Table 10.8.

Specific value of strip rolling obtained when moving through rolls of *i*-stand presents itself a sum of specific values given in Table 10.8:

$$a_{roli} = a_1 + a_2 + a_3 + a_4$$

Power of strip rolling in *i*-stand is calculated using the following formula:

$$N_{roli} = a_{roli} V_1$$

where V_1 is the volume of strip rolled at a unit of time, m^3/s.

The analysis of values given in Table 10.8 gives grounds for two conclusions.

1. That rolling work and power depend exclusively upon tangent forces caused by tangent tensions.
2. That the rolls perform useful work only in the first elastic area and in the backward slip zone. In the forward slip zone and in the second elastic area, the strip returns part of the used energy to the rolls (values a_3 and a_4 are negative).

10.5.2 Calculation of Moment and Power of Working Stand Main Drive

Because of the fact that four-high (quarto) mill stands of hot and cold-rolling mills are identical in design one can use technique [6] to calculate the parameters of the main drive of continuous wide-strip mill used for hot rolling.

According to this technique, the power of the main drives of working stand when the rolling speed is steady equals

$$N_{dr} = \frac{N_w}{\eta}$$

where η is the coefficient of main drive efficiency; N_w is the power necessary to cause plastic deformation and to overcome all kinds of friction, including rolling friction between working and backup rolls:

$$N_w = M_w \cdot \omega_w$$

TABLE 10.8
Calculation Formulas for Specific Values of Strip Rolling Made by Rolls in Each Area of the Deformation Zone

Area	Formula
Elastic area, length x_{1el}	$a_1 = \tau_1\left(\frac{1}{\tan(\alpha/2)} + \tan\frac{\alpha}{2}\right)\ln\frac{h_{i-1}}{h_{1el}}$, where $\tau_1 = \mu p_1$
Backward slip zone, length $x_{pl.bac}$	$a_2 = \frac{\tau_s}{2}\left(\frac{1}{\tan(\alpha/2)} + \tan\frac{\alpha}{2}\right)\ln\frac{h_{1el}}{h_n}$
Forward slip zone, length $x_{pl.for}$	$a_3 = -\frac{\tau_s}{2}\left(\frac{h_n - h_{2el}}{h_{1el} - h_n}\right)\left(\frac{1}{\tan(\alpha/2)} + \tan\frac{\alpha}{2}\right)\ln\frac{h_n}{h_{2el}}$
Elastic area, length x_2	$a_4 = -\tau_3\left(\frac{1}{\tan\beta} + \tan\beta\right)\ln\frac{h_1}{h_{2el}}$, where $\tau_3 = \mu p_3$

(Angles α/2 and β— see Figure 10.1)

where ω_w is angle velocity of working roll rotation; M_w is moment necessary to drive the working rolls (without taking into consideration the moment of inertia during acceleration and deceleration):

$$M_w = M_{rol} + M_{ten} + M_{fr.b} + M_b$$

where M_{rol} is rolling moment; M_{ten} is moment of strip tension forces; $M_{fr.b}$ is moment of the working rolls bearings force; M_b is moment necessary to rotate drag backup rolls.

Values of the given moments are as follows:

$$M_{rol} = \frac{N_{roli}}{\omega_w} \qquad M_{ten} = \Delta N_i \frac{D_w}{2}$$

where $\Delta N = N_{i-1} - N_i$ is difference of forces of rear and front tension of the strip.

$$M_{fr.b} = \mu_{b.w}\frac{d_{b.w}}{2}[\Delta N - 2P\tan(\theta + \gamma)]$$

where $\mu_{b.w}$ is friction coefficient in working rolls bearings; $d_{b.w}$ is working diameter of these bearings; P is rolling force; θ is the angle between flat surface of inner rolls force and flat surface in which rolls axes are situated; γ is the angle between the vertical axis of the flat surface of backup roll and the flat surface that goes through the axes of working rolls (see Figure 10.6).

The given angles can be calculated with the help of the following formulas:

$$\tan\theta = \frac{2\left(cb_b + \mu_{b.b}\frac{d_{b.b}}{2}\right)}{D_b}$$

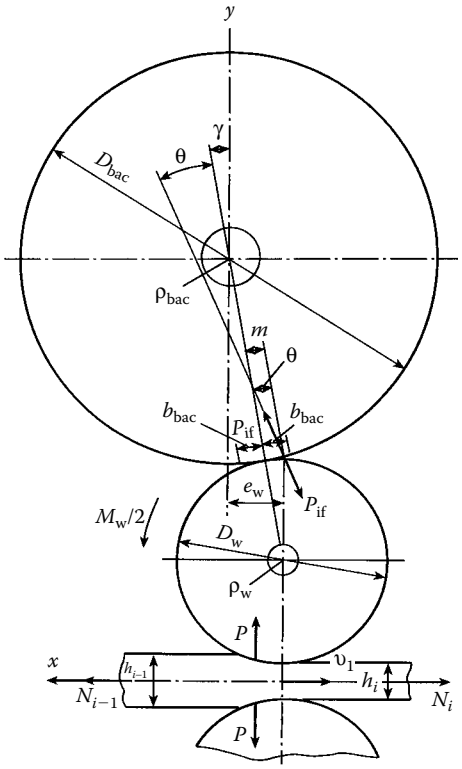


FIGURE 10.6 Force and moment calculation scheme for a four-high stand.

where c is coefficient of rolling friction arm; b_b is half of the width of contact area calculated according to the Hertz–Belyaev formula:

$$b_b = 0.798\sqrt{\eta\cdot\frac{P_{IR}}{L}\cdot\frac{D_w\cdot D_b}{D_w + D_b}}$$

where D_w, D_b are barrel diameters of working and backup rolls; η is coefficient of elasticity (given module of elasticity for their materials); L is length of contact area of their barrels; P_{IR} is inner rolls force ($P_{IR} \approx P$);

$$\tan\gamma = \frac{2e_w}{D_w + D_b}$$

$\mu_{b.b}$ is the friction coefficient in backup rolls bearings; $d_{b.b}$ is the working diameter of these bearings; and e_w is the horizontal shift of working roll axis relative to the vertical axial flat surface of the backup roll.

The moment necessary to drive drag backup rolls is equal to:

$$M_b = \frac{2P}{\cos(\theta+\gamma)} \cdot \left[\frac{D_w}{2}\sin\theta + cb_b \cdot \cos\theta\right]$$

As can be seen from the given expressions, there is a direct impact of rolling friction on the main drive power through rolling friction arm equal to cb_b. There is also an indirect impact through the angle θ.

To define the arm coefficient of rolling friction c, regression equation used in the processes of cold rolling and the technique of making this equation are given in the chapter [4]. There were no formulas to define coefficient c in the processes of hot rolling in special literature.

In order to receive them, a set of investigations was made. As a result, a regression equation was received in the form of dependence of rolling friction arm coefficient upon the following factors:

p_0 is the maximum normal tension in inter-roll contact, taking into account a set of parameters of rolling mode (reduction, tension, mechanical properties of the strip);

ω_{dr} is the angular velocity of drive roll rotation:

$$c = 1.256938 - 0.000409\, p_0 - 0.047173\, \omega_{dr}$$

For the expression given multiple determination coefficient R^2 turned out to be equal 82% which testifies to the high degree of reliability of the relation received.

Usage of the above-mentioned technique showed that the maximum difference between calculated and measured powers of the main drives was not more than 10%, the average difference being 5%.

The analysis of the results of power calculation made for a number of mills showed the following:

1. During hot rolling values of nondimensional coefficient c are between 0.27 and 0.85. The power, used for rolling friction, in inter-roll contact is between 29% and 68% of the total power of working stands drives.
2. The share of moment used for plastic deformation relative to the total moment is 38%–70% and is being reduced from the first to the last stand; the share of moment necessary to drive the drag backup roll is 30%–80%, and it is being increased up to the last stand; the rest part (less than 1%) is the sum of moments of friction in working roll bearings and forces of strip tension.
3. Between 83% and 93% of moment necessary to drive drag backup rolls is used to overcome rolling friction, and only 7%–17% of this moment does not depend upon rolling friction.

To define the possibility of reducing the level of contact stresses acting on the rolls and energy saving during rolling of the thinnest strips, technological modes and force energy parameters were analyzed for the acting six-stand continuous wide-strip, hot-rolling mill "1700."

For analysis, a working mode was chosen to roll the strip made of St1PS with dimensions 0.9 × 1000 mm. It is given in Table 10.9. Reductions of cross-sectional area varied in the following actual ranges: in stand № 1, 40%–60%, in the run-down mill, 20%–50%, in the stand № 6, 10%–20%. Inter-stand tensions varied in the range of 0 to 15% as to the resistance of metal to deformation. The temperature at the beginning of the rolling process was varied in the range of 1040°C–1080°C, which provided for necessary microstructure and mechanical properties of the metal.

The results of varying of the parameters given showed the following:

1. Reduction of cross-sectional area in the first stands during most of actual rolling modes make up

TABLE 10.9
Mode of Hot Rolling of the Strip Made of St1PS with Dimensions 0.9 × 1000 mm (see the Chemical Composition of Steel in Table 10.5)

Stand №	v_i (m/s)	h_{i-1} (mm)	h_i (mm)	μ_i	σ_{i-1} (MPa)	σ_i (Mpa)	ε_i (%)	$\varepsilon\Sigma_i$ (%)
1	1.03	24.9	10.15	0.56	0	0.48	59.2	59.2
2	2.37	10.15	3.95	0.375	0.48	0.81	61.08	84.14
3	4.42	3.95	2.18	0.333	0.81	1.83	44.81	91.25
4	6.82	2.18	1.71	0.373	1.83	1.97	21.56	93.13
5	9.81	1.71	1.04	0.2	1.97	2.43	39.18	95.82
6	11.74	1.04	0.87	0.3	2.43	32.3	16.35	96.51

50%–55% which corresponds to values of normal contact stresses of 300–500 MPa and in the last 6th stand maximum contact stresses p_{max} make up 1300–1950 MPa in spite of the small reduction of 15%–20%. Increase of reduction in stand № 1 from 50%–60% causes increase of contact stresses in it by 10%–15% and possible decrease of reduction in the sixth stand due to this fact up to 10% make it possible to reduce stresses by 20%–60%, that is, up to the level of 800–1200 MPa. Increase in reduction in intermediate-stands by 10% leads to an increase of contact stresses up to 20%–30%.

2. Two times an increase of intermediate-stand tensions (from 5%–10% from yield stress) leads to the decrease of maximum contact stresses only by 1%–2%, which means that this factor of influence on roll durability does not give substantial results.
3. An increase in temperature at the beginning of rolling up to the maximum tolerable limit of 1080°C makes it possible to reduce contact stresses up to 5%–15%. Thus it is possible to reduce dangerous contact stresses in the last stand of a continuous wide-strip, hot-rolling mill by 25%–80% by varying technological parameters of hot rolling and redistribution of reductions between stands and it is also possible to increase durability of working rolls.
4. The two factors that most influence the power of electric engines of the main line of the working stand drive are the relation between lengths of zones of backward and forward slip and the resistance of metal to deformation.

   It is possible to influence these factors by changing the redistribution of reductions and tensions between stands and by changing rolling temperature.

   For example, when increasing the reduction in the first stand from 40% to 60% the length of the backward slip zone increases by 5%–6%, and resistance to deformation rises up to 7%–8%. As a result, the power of electric drive increases by 19%–20%. This creates the possibility of decreasing the reduction in the last stand from 15% to 10%, thus allowing for the power to decrease 2.3–3.7 times, a considerable savings for the mill in general.

   When the front tension increases the length of backward slip zone decreases, and the forward slip zone in which part of the rolling work is returned from the strip to the rolls is increased. As a result, a two times increase in the front tension (from 5% to 10% from the yield limit) leads to a decrease in rolling power up to 4%–22%, an increase in the power of rolling friction up to 0.9%–2.5%, and an increase in the power of the electric engine of the working stand main drive of up to 6%–17%.

   On the other hand, with the increase in the rear tension the backward slip zone increases and the forward slip zone decreases. The two times rear tension increase leads to an increase in the rolling power of up to 4%–21%, with the power of the electric engine increasing up to 4%–15%.

   Thus, inter-stand tensions influence considerably the power consumption practically without influencing the level of contact stresses.
5. The increase in rolling temperature does not influence the correlation of lengths of backward and forward slip zones but leads to a decrease in deformation resistance, which is why the hot rolling power is reduced. For example, a temperature increase from 1040°C to 1080°C leads to a reduction in power of electric engines of the working stand main drive by 5%–20%.

Based on the results of the research conducted, it is possible to carry out optimization of hot-rolling modes according to two criteria: maximum durability of rolls and minimum energy consumption.

10.6 CONCLUSION

A new procedure has been developed and tested for the calculation of contact stresses, hot-rolling forces and power for wide strips 0.8–1.5 mm thick. This procedure takes into account the presence of a stick zone in the deformation zone and stress distributions in both elastic and plastic regions in the deformation zone.

The average error in calculating the forces according to the new procedure is 5%, which is more than two times smaller than the calculation error for other well-known calculation procedures.

Using our procedure, we simulated the contact stresses in the deformation zones of the working stands of wide-strip mills and revealed a number of new relations for the state of stress in a strip.

Our calculation procedure can be used to optimize the technological regimes of wide-strip mills by equalizing the loads on work rolls and to save energy.

REFERENCES

1. Tselikov, A. I. 1962. *Theory of Force Calculations in Rolling Mills*. Moscow: Metallurgiya [in Russian].
2. Garber, E. A., Kozhevnikova, I. A., Tarasov, P. A., Zavrazhnov, A. A. and Traino, A. I. 2007. Simulation of contact stresses and forces during hot rolling. *Russian Metallurgy* 2: 112–119.
3. Konovalov, Yu. V., Ostapenko, A. L. and Ponomarev, V. I. 1986. *Calculation of Sheet-Rolling Parameters: Handbook*. Moscow: Metallurgiya [in Russian].
4. Tselikov, A. I., Nikitin, G. S. and Rokotyan, S. E. 1980. *Theory of Lengthwise Rolling.* Moscow: Metallurgiya [in Russian].
5. Garber, E. A., Shadrunova, I. A., Traino, A. I. and Yusupov, V. S. 2002. Analysis of a deformation zone and the refined calculation of the forces for cold-rolling of strips thinner than 0.5 mm in a continuous mill. *Russian Metallurgy* 4: 340–345.
6. Garber, E. A., Samarin, S. N., Traino, A. I. and Ermilov, V. V. 2007. Simulation of rolling friction in the working stands of wide-strip mills. *Russian Metallurgy* 2: 120–126.

11 Width Variation Behavior during Hot Rolling

Qiulin Yu

CONTENTS

11.1 Introduction 127
11.2 Mechanical Model 128
11.3 Transverse Distribution of Tensile Stresses of Strip 129
11.4 Measurement of Lateral and Longitudinal Displacements 130
11.5 Rolling Parameters 133
11.6 Simulation of Width Necking Using FEM 136
11.7 Discussion 137
11.8 Summary 138
Acknowledgments 139
References 139

11.1 INTRODUCTION

Width variation plays an important role in determining product width tolerance. It is difficult to predict and to control width variation in a portion of strip length in hot-rolling processes. As noted, these variations include width spreading or necking at strip heads and tails, as well as midwraps in an unstable rolling state. Most hot band users specify minimum widths in the orders. Coil producers provide extra widths to meet the specifications for compensation of potential width necking, which does not only cause the loss of process yield, but also create a series of problems to the downstream processes, such as side trimming and spiral welding, etc.

Currently, most studies on width variation focus on the transverse flow of materials in the roll bite. A computational model was developed to describe the lateral variations of the magnitude and direction of the plastic deformation of strip (Dixon and Yuen 2004). The result contained the residual stresses and lateral spreading. By means of coupling analysis of the plastic deformation of the rolled material with a rigid-plastic, finite-element method, and the roll elastic deformation with the axially partitioned computation method (Ishii and Takamachi 2003), it was found that the strip width variation in the vicinity of the roll bite was principally governed by the stresses acting in the rolling direction near the strip width edge. The width variation depends mainly upon the tensions at the entry and exit, and the change of strip crown ratio during rolling. To clarify the influence of rolling conditions and material characteristics on width variation, a three-dimensional, transient rigid-plastic finite element method (FEM) was employed to evaluate the width variation in an unstable rolling deformation (Higo et al. 2002). In addition, a finite-element package called "Deform" is able to perform simulation of the rolling process of thick slabs, strips, and plates. By utilizing the package, it was found that the lateral material flow was negligible for thickness less than 6 mm, but predominant in heavy gauge plates greater than 12 mm (Kainz and Zeman 2004).

In production, strip necking is encountered frequently in rolling wide thin-thickness strips with gauge less than 6 mm and width greater than 2200 mm. This phenomenon contradicts the previous conclusion, that is, the lighter the gauge, the less lateral material flow the strips possess. After comparing both edge contours, we found that one edge had more necking than the other. Meanwhile, several other defects might appear, such as stretching marks, strip oscillation, and quarter buckles.

This chapter introduces the most recent study on width variation that was presented at the 2007 *Iron and Steel Technology* conference (Yu 2007). To understand the mechanism of the local width necking, this chapter establishes a mechanical model to combine the residual stresses of strip with the back tensile stresses generated by the Steckel drums. The lateral displacements of strip are obtained by measuring the positions of a series of stainless pins buried in a slab. The residual stresses are derived from the gauge profiles

and length extensions, as well as lateral displacements of the strip. Strip camber is measured from a width meter. The tensile stresses generated by the drums are converted from the motor current and rolling speed.

In this chapter, the effect of rolling parameters, material characteristics, strip shape, and camber on the width variation is investigated. The rolling parameters include rolling temperature, strip tension, and rolling speed. The loading condition of strip and the deforming characteristics of the rolled materials at the entry vary with the changes of the rolling parameters. Meanwhile, an elastic–plastic finite-element method is used to validate the analytical result. The theoretical and experimental results are useful for identifying the root cause of the local width variation and establishing a properly corrective procedure. The obtained results could be applied to other types of strip mills.

11.2 MECHANICAL MODEL

According to the recent survey of the 14th International Association of Steckel Mill Operators (IASMO) conference, there are four configurations of Steckel mills in operation: single stand, twin stand, single finishing stand, and three finishing stands with one rougher (Kapoor 2006). The mill configuration at Nucor Steel Tuscaloosa is a single-stand, four-high reversing Steckel mill.

For a single-stand Steckel mill, roughing and finishing passes are carried out on the same stand. In roughing passes, the Steckel mill performs the same function as other roughing mills. After slabs are rolled under 25.4 mm thick, the mill automatically switches into a finishing mode. The transfer bars are coiled on the Steckel drums during intermediate finishing passes.

In production, the width necking could occur in either roughing passes or finishing passes, or both. To analyze the width necking, two mechanical models are established, as shown in Figures 11.1 and 11.2.

To simplify calculations, all friction forces are ignored. For forward roughing passes, the bending moment generated by the edger and centering guides near the entry of the roll bite is written as

$$M_0(x) = F_0 x + G_0\left(x - W_2 + W_1 + \frac{1}{2}W_0\right) - G_1\left(x - W_2 + W_1 - \frac{1}{2}W_0\right) \quad \left(W_2 - W_1 + \frac{1}{2}W_0 < x \le W_2\right) \tag{11.1}$$

where

F_0 = load acted by the edger roll
G_0 = load acted by the centering guide on the operator side
G_1 = load acted by the centering guide on the drive side
W_0, W_1, and W_2 = geometric dimensions
x = coordinate in the X-axis

For forward roughing passes, the first term of Equation 11.1 can be ignored. For forward finishing passes, the bending moment generated by the back drum and centering guides at the entry of the roll bite is described as follows:

$$M_0(x) = T_0(\delta(x) - \delta_0) + G_0\left(x - W_3 + W_1 + \frac{1}{2}W_0\right) - G_1\left(x - W_3 + W_1 - \frac{1}{2}W_0\right) \quad \left(W_3 - W_1 + \frac{1}{2}W_0 < x \le W_3\right) \tag{11.2}$$

where T_0 is the back tension and W_0 is the geometric dimension.

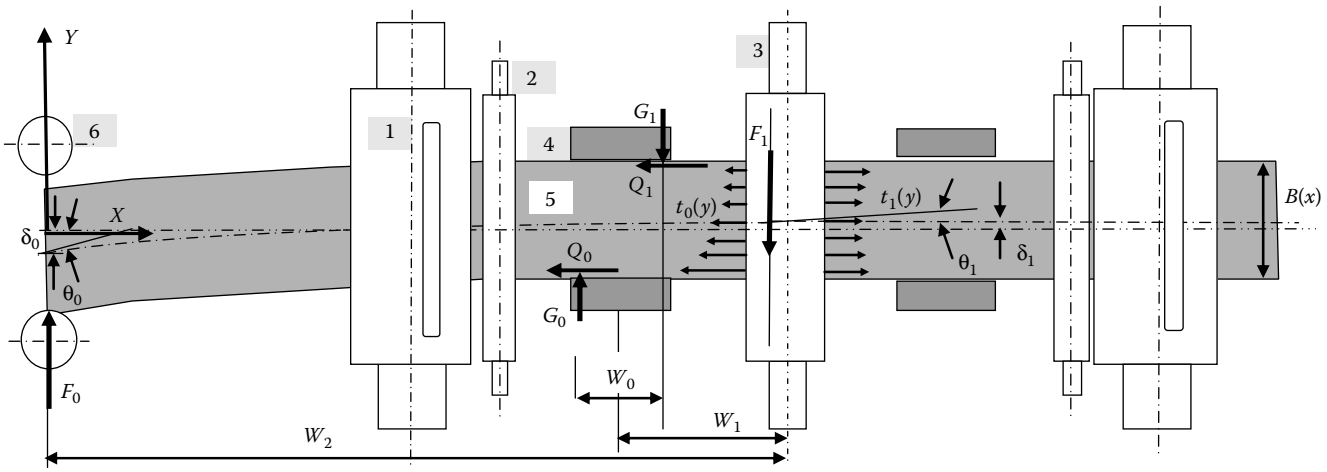


FIGURE 11.1 Mechanical model in the reverse roughing passes. 1-Steckel drum, 2-Vertical pinch roll, 3-Work roll, 4-Centering guide, 5-Strip, and 6-Edger. (From Yu, Q. *Iron and Steel Technology* 2: E186. With permission.)

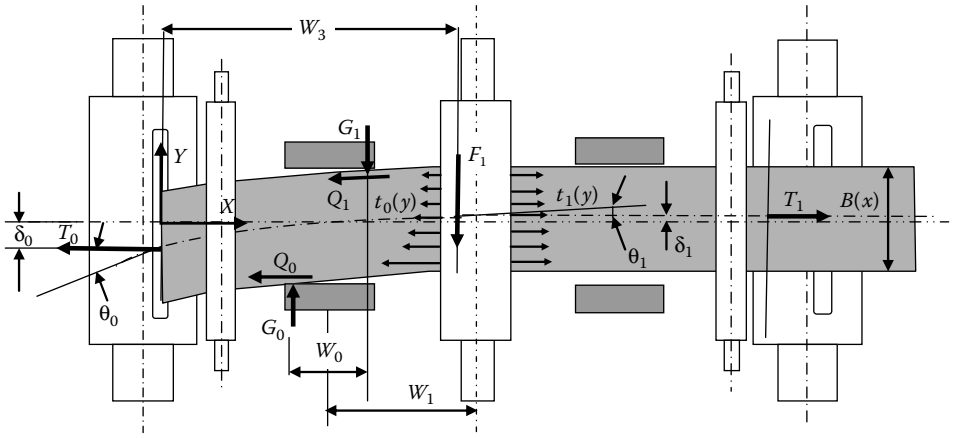


FIGURE 11.2 Mechanical model in the forward finishing passes. (From Yu, Q. *Iron and Steel Technology* 2: E186. With permission.)

The bending moment generated by the front drum at the exit of the roll bite is given as

$$M_1(x) = -T_1\delta_1 \qquad (x > W_3) \tag{11.3}$$

where $\delta(x)$ = curvilinear function of the strip centerline, $\delta_0 = \delta(0)$ and $\delta_1 = \delta(W_3)$, and T_1 = front tension.

11.3 TRANSVERSE DISTRIBUTION OF TENSILE STRESSES OF STRIP

Occasionally, the strip is torn between the drum and roll bite when one edge of the strip is much tighter than another. The looser edge suffers compressive stress and then starts buckling deformation. The tensile stress on the tighter edge exceeds the rupture strength of the material. Accompanied by the breakage, stretching marks appear on the strip surface at the exit of the roll bite.

It is well known that there is a neutral point in the roll bite. At the neutral point, there is no slippage between the strip and work roll. The position of the neutral point is related to the reduction, work roll diameter, friction coefficient, separating force, and front and back tensions. The higher the back tension, the closer the neutral point is to the exit of the roll bite. In the transverse direction, a series of neutral points form a neutral line in the roll bite. While the neutral line is curved sharply due to uneven distribution of the back tensile stress, stretching marks on the strip surface will appear. Typically, the back tension ensures that no part of the strip in front of the roll bite suffers the compressive stress that yields buckling deformation longitudinally.

Figure 11.3 shows that the front and back tensile stresses are distributed uniformly across thickness. The tensile stresses at the entry and exit of the roll bite are composed of the tensile stresses of the drums, the bending stresses, and the residual stresses of the strip. The tensile stresses of the drums are usually controlled by tension regulators with input of strip dimension, mechanical

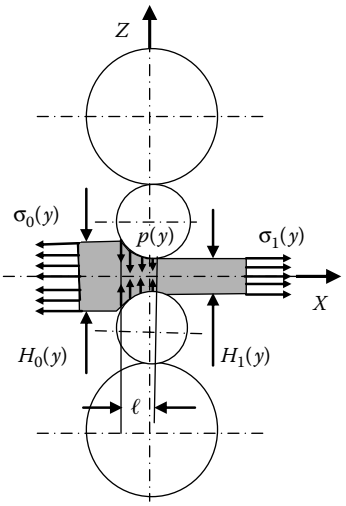


FIGURE 11.3 Pressure distribution in the roll bite. (From Yu, Q. *Iron and Steel Technology* 2: E186. With permission.)

property, and rolling speed. The bending stresses are determined by the bending moments from Equations 11.1 through 11.3. The residual stresses are determined by the gauge profiles, length extensions, and lateral displacements of the strip.

To obtain the residual stresses, it is important to know the transverse distribution of the relative length difference. By means of the law of conservation of mass, the laterally relative length difference at the exit of the *i*th pass is written as:

$$\frac{\Delta L_i(y)}{L_i} = \frac{\Delta H_0(y)}{H_0} + \frac{\Delta L_0(y)}{L_0} - \frac{\Delta H_i(y)}{H_i} - \Delta u_i'(y) \tag{11.4}$$

where $u'(y) = \dfrac{\partial u(y)}{\partial y}$

$u(y)$ = the function of the lateral displacement accumulated from i passes

$\Delta u'(y)$ = the increment of the derivative of lateral displacement function between a reference strip and a given strip located at y

$\Delta L(y)$ = the lateral length difference that is defined as the length difference between a reference strip and a given strip

$\Delta H(y)$ = the lateral thickness difference that is defined as the gauge difference between a reference strip and a given strip

L and H = the average length and thickness across width, and subscripts: i = the exit of the ith pass; 0 = the coming slab

By means of Hooke's law, the front residual stress difference between the reference strip and the given strip can be expressed as:

$$\Delta\sigma_{1i}(y) = -\frac{E}{1-\mu^2}\frac{\Delta L_i(y)}{L_i} \tag{11.5}$$

where E and μ are the elastic modulus and Poisson's ratio of the strip at the exit, respectively.

Substituting subscript i with $i - 1$ into Equation 11.4 produces the back residual stress difference. When a reference strip is located at the centerline, utilizing the known tensions of the strip, the tensile stress at the centerline is obtained by integrating Equation 11.5 across the width. The front and back tensile stresses are derived as follows:

$$\sigma_{1i}(y) = \frac{T_{1i}}{B(x)H_i} - \frac{M_1(x)}{I}y + \frac{E}{1-\mu^2}\left[1 + \frac{H_i(y)}{H_i} - \frac{H_0(y)}{H_0} - \frac{L_0(y)}{L_0} + u_i'(y) - \frac{\Delta B_i(x)}{B_i(x)}\right] \tag{11.6}$$

$$\sigma_{0i}(y) = \frac{T_{0i}}{B(x)H_{i-1}} - \frac{M_0(x)}{I}y + \frac{E}{1-\mu^2}\left[1 + \frac{H_{i-1}(y)}{H_{i-1}} - \frac{H_0(y)}{H_0} - \frac{L_0(y)}{L_0} + u_{i-1}'(y) - \frac{\Delta B_{i-1}(x)}{B_{i-1}(x)}\right] \tag{11.7}$$

where

T = the tension of the strip

$B(x)$ and $\Delta B(x)$ = the strip width and its increment, respectively

I = the moment of inertia of the cross section in the y–z plane of the strip with respect to the z-axis

subscripts: 0 = the entry of the roll bite, 1 = the exit of the roll bite

In Equations 11.6 and 11.7, the first term on the right side of the equal sign represents the tensile stresses generated by the drums. The second term reflects the bending stresses caused by the bending moments. The last long term stands for the residual stresses. Equations 11.6 and 11.7 can be applied to calculate the tensions of the drums. The criterion is that the maximum tensile stress must be less than the yield strength of the material under an elevated temperature. In addition, a more broad conclusion is that the residual stress measured by a shape roll (shape meter) could be affected by the bending moment.

11.4 MEASUREMENT OF LATERAL AND LONGITUDINAL DISPLACEMENTS

It is well known that plastic deformation in hot rolling results in extension of length and spreading (or necking) of width. The length extension and width spreading (or necking) could be evaluated by means of the longitudinal and lateral displacements accumulated in all previous passes.

To measure the longitudinal and lateral displacements, stainless pins were used for reference points. A 9271-mm-long slab 129 mm thick and 2465 mm wide was selected for an experiment. Since the accurate location of the narrowest width at the head and tail of a wide thin-thickness coil is unpredictable, it is necessary to use multiple rows of stainless pins for measuring the displacements of the pins. The experiment design is explained in the following paragraphs.

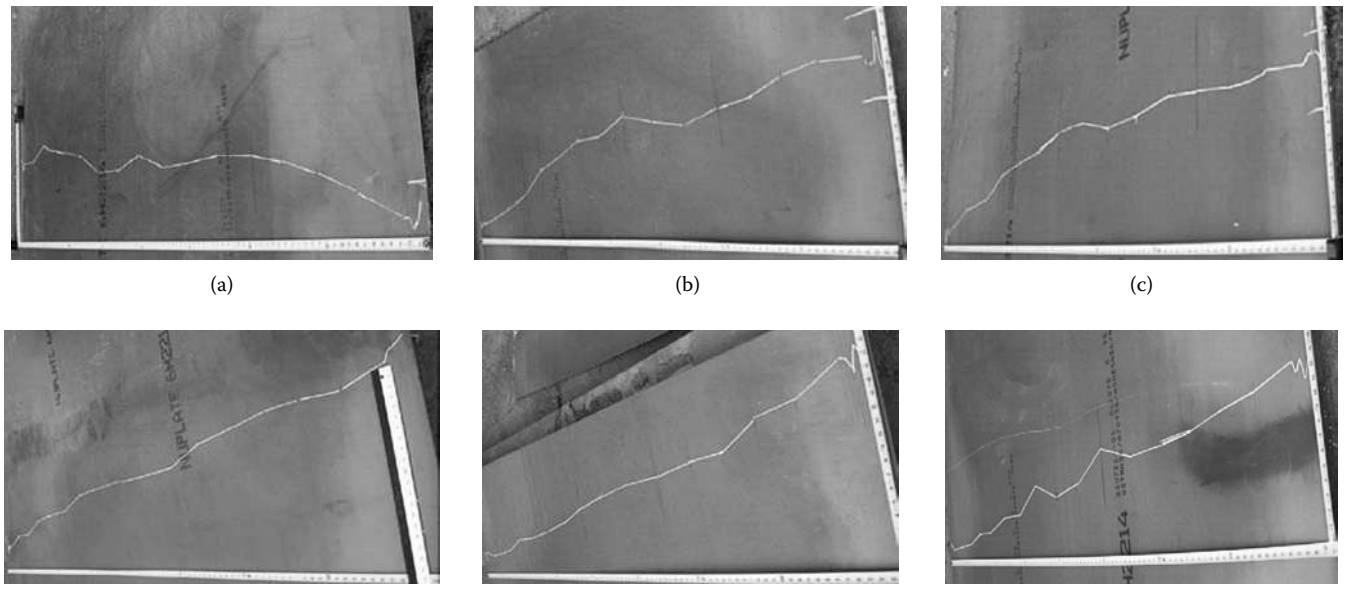
- Six rows of pinholes were drilled from the slab head (coil head) at longitudinal intervals 305, 610, 762, 914, 1067, and 1219 mm, respectively.
- There were 25 pinholes drilled on each row. The pinholes divided the entire width into 26 spaces, i.e., eight equal 165-mm spaces in the center area, eight equal 127-mm spaces in both quarter areas, and ten equal 12.7-mm spaces near both edges.
- The diameter and depth of the pinholes are 4 and 19 mm, respectively. The diameter and length of the pins are 3.6 and 12.7 mm, respectively. The assembly of the pins is shown in Figure 11.4a.
- After the pins were placed into the holes, the entries of the pinholes were welded and ground. The pins faced upward while the slab was charged into the equalizing furnace, as shown in Figure 11.4b.

The slab was cold charged with other slabs in one rolling schedule. After rolling, the coil was cut into plates at 3048 mm long. Consequently, the third, sixth, seventh, eighth, tenth, and eleventh plates counted from the coil head contained the pins rolled in, as shown in Figure 11.5a through f. Comparing row 1 with row 2, the patterns of the pins distributed from the drive side to the operator side are opposite, which means that the rolling process was unstable and that the mill steering was performed for correction of camber between row 1 and row 2. From Figure 11.5b through f, the similar distribution patterns



(a) (b) (c)

FIGURE 11.4 Location and dimension of the stainless pins buried in the slab. (a) Dimension of stainless pin and hole; (b) distribution of pins; (c) pins rolled in. (From Yu, Q. *Iron and Steel Technology* 2: E186. With permission.)



(a) (b) (c)

(d) (e) (f)

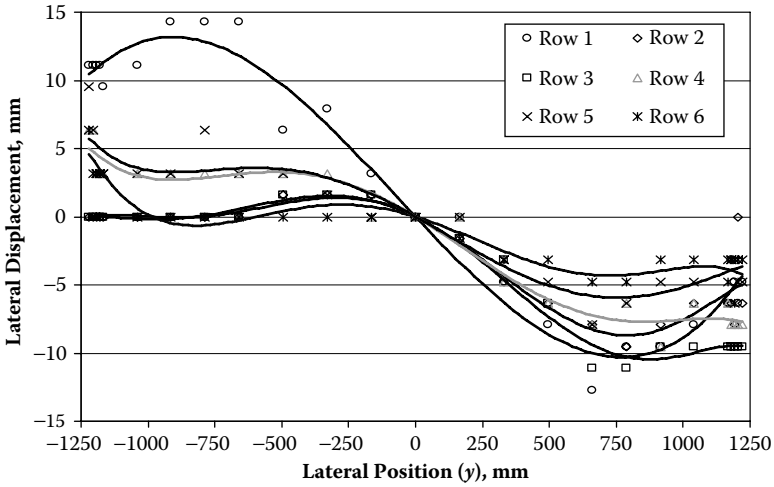
FIGURE 11.5 Transverse distribution patterns of the pins rolled in (left bottom corner: operator side toward the coil head). (a) Pins on row 1; (b) pins on row 2; (c) pins on row 3; (d) pins on row 4; (e) pins on row 5; (f) pins on row 6. (From Yu, Q. *Iron and Steel Technology* 2: E186. With permission.)

of the pins indicate that the rolling process has entered a stable state.

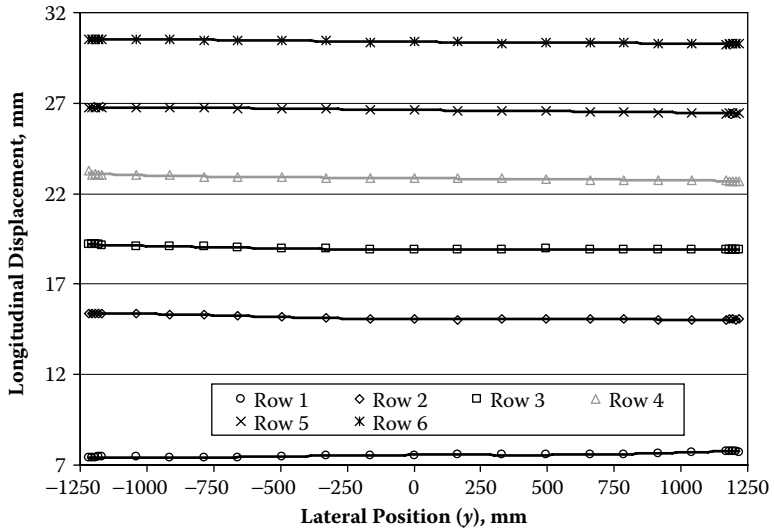
To demonstrate the displacements quantitatively, the lateral and longitudinal displacements were measured from the operator side to the drive side, as shown in Figure 11.6a and b. The entire strip can be divided into three segments in width; the operator edge segment from the first pin on the operator side to the strip edge, the center segment from the first pin to the last pin on the drive side, and the drive edge segment from the last pin to the strip edge. The width changes of the segments are listed in Table 11.1. The total width spreading of the edge segments is from 5.56 to 13.49 mm. The width necking of the center segment is from 6.35 to 15.88 mm. Comparing the width variations, the highest necking is located at row 1. The strip was necked 7.15 mm.

The plastic deformation in the edge segments is more complicated than that in the center segment. The earlier slab experiment found that the pins buried on the slab sidewall were moved to the broad faces after rolling. Therefore, transfer of the pins from the narrow faces to the broad faces is one of the reasons for the width spreading in the edge segments. On the other hand, both edge segments possess lower back tensile stress than that in the center segment due to a 0.05-mm edge drop.

From the polynomial trend lines in Figure 11.6a, it can be seen that the lateral displacements vary with the *y*-coordinate. The width variation is determined by the derivative of the



(a)



(b)

FIGURE 11.6 Transverse distribution of the lateral and longitudinal displacements. (a) Lateral displacement; (b) longitudinal displacement. (From Yu, Q. *Iron and Steel Technology* 2: E186. With permission.)

TABLE 11.1
Average Gauge, Length, and Width Variation (in mm)

Row	Average Gauge	Average Fiber Length	Total Width Variation	Width Variation of the Edge Segments	Width Variation of the Center Segment
1	4.881	7865.7	–7.15	8.73	–15.88
2	4.883	7911.7	–0.79	5.56	–6.35
3	4.876	3984.4	–0.80	8.73	–9.53
4	4.843	4029.1	–0.80	13.49	–14.29
5	4.938	3892.3	–0.80	13.49	–14.29
6	4.857	3938.5	2.38	11.91	–9.53

Source: Yu, Q. *Iron and Steel Technology* 2: E186. With permission.
Note: In column four, Negative values = necking; Positive values = spreading.

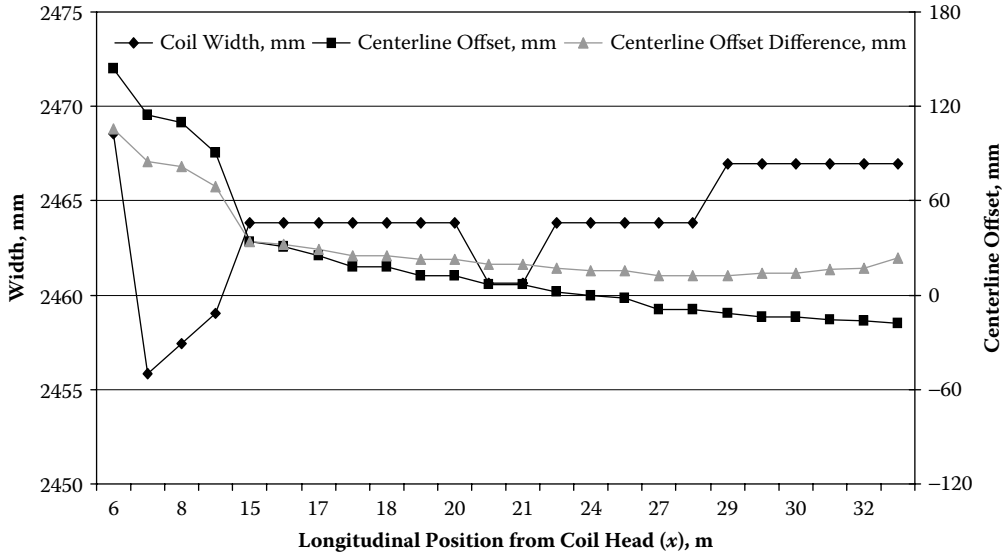


FIGURE 11.7 Longitudinal distribution of coil width, centerline offset and its difference between the drum and roll bite. (From Yu, Q. *Iron and Steel Technology* 2: E186. With permission.)

lateral displacement with respect to *y*-coordinate. When the derivative is positive, strip width is spreading; when the derivative is negative, the strip is necking. On row 1, the strip width was necked 26.99 mm between two *y*-coordinates (–914.4 and 660.4 mm), and spread 11.12 mm outside the range. The difference of the lateral displacements between the first pin and last pin is 4.76 mm. At the middle of the segment, the higher back tensile stress drew the metal toward the strip center. As a result, it is inevitable that the width necking occurred.

The centerline offset of a strip is a key parameter for determining the bending moments. It is used not only to estimate strip camber, but also to reflect the alignment of the centering guides. The centerline offset of strip was measured using a width meter, as shown in Figure 11.7. The difference of the centerline offsets between the drum and roll bite is used to calculate the bending moments in Equations 11.2 and 11.3. From Figure 11.7, it can be seen that the width variation is closely related to the difference of the centerline offset. The maximum difference of the centerline offsets is 82 mm on row 1.

For the sake of convenience, the relative thickness difference and the relative length difference are defined as the ratios of the thickness and length differences between the center and any transverse location to the average thickness and length. The thickness of the strip corresponding to each pin was measured using a micrometer. The measured data are plotted in Figure 11.8.

The relative thickness difference is another type of dimensionless variable for describing the gauge profile. Figure 11.8a shows a comparison of the gauge profiles of the strip on the different rows with that of the original slab. The relative thickness difference of the slab is less than 1.5%. It is also noted that the slope of the relative thickness difference on the operator side of row 1 is greater than that on the drive side, which means that the strip was cambered to the drive side. The strip fiber length on the operator side is much longer than that on the drive side, as shown in Figure 11.8b. After the roll stack was steered properly on row 2, the relative thickness difference on rows 3–6 is less than 4%.

11.5 ROLLING PARAMETERS

Some rolling parameters can be obtained directly from the mill level II database, and other parameters can be calculated from the known parameters. To determine the strip speeds, drum tensions, and material mechanical properties at the entry and exit of the roll bite, it is necessary to know the rolling parameters, such as roll speed, strip temperature, separating force, reduction, and drum motor current.

Several intermediate rolling parameters are related to the dimensions of the roll stack, such as the projected length and the coefficient of the slip in the roll bite. The dimensions of the roll stack are given in Table 11.2.

In hot rolling, the rolling parameters were recorded at 610-mm-long intervals. To simplify the analysis, the transient rolling parameters corresponding to rows 1–6 are selected in turn for all passes, as shown in Figure 11.9.

Since either drum is equipped with any tensiometer and tension regulator, the average tensile stresses generated by the drums are converted from the motor current, strip speed, and dimension, assuming 80% efficiency of the drum motors. Each drum is driven by two 415-volt DC motors. The frictional coefficient in the roll bite is approximately 0.32. The strip speeds are calculated based on the roll speeds and the coefficients of the forward and backward slip in the roll

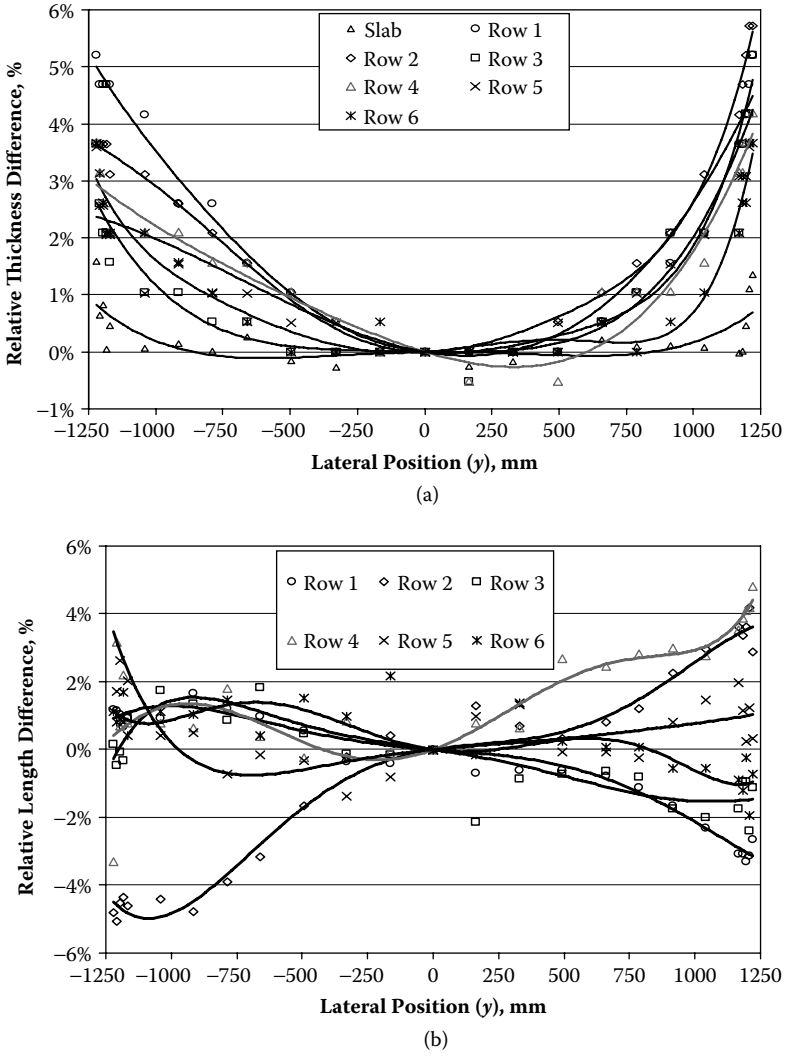


FIGURE 11.8 Transverse distribution of the relative thickness and length differences. (a) Relative thickness difference; (b) relative length difference. (From Yu, Q. *Iron and Steel Technology* 2: E186. With permission.)

TABLE 11.2
Dimensions of the Roll Stack (in mm)

Effective Contact Barrel Length	Diameter of the Top Backup Roll	Diameter of the Bottom Backup Roll	Diameter of the Top Work Roll	Diameter of the Bottom Work Roll
2642	1327	1380	708.56	708.53

Source: Yu, Q. *Iron and Steel Technology* 2: E186. With permission.

bite. The average front and back tensile stresses are compared with the yield strength of the material, as shown in Figure 11.10.

In the hot-rolling process of the Steckel mill, the material goes through four stages: grain deformation, recovery, recrystallization, and growth. The yield strength of the material depends on temperature, strain, and strain rate. By means of a nonlinear regression method and Tselikov's separating force formula (Wusatowski 1969), the yield strength of the mild-carbon steel is obtained:

$$\sigma_m = \sigma_0 e^{-0.001872S} \varepsilon^{0.007297} \dot{\varepsilon}^{0.511516} \tag{11.8}$$

where

σ_0 = yield strength under a room temperature, 290 MPa
ε = average reduction in the roll bite or strain
$\dot{\varepsilon}$ = average strain rate in the roll bite, 1/s
S = temperature of the strip

Equation 11.8 is valid within the range of the strip temperature between 870°C and 1120°C. Equation 11.8 without the last term produces the yield strength of the material at the entry of the roll bite. When strip deformation is in an elastic range, the last two terms are negligible.

Figure 11.10 shows that the average front tensile stress generated by the drum is much lower than the yield

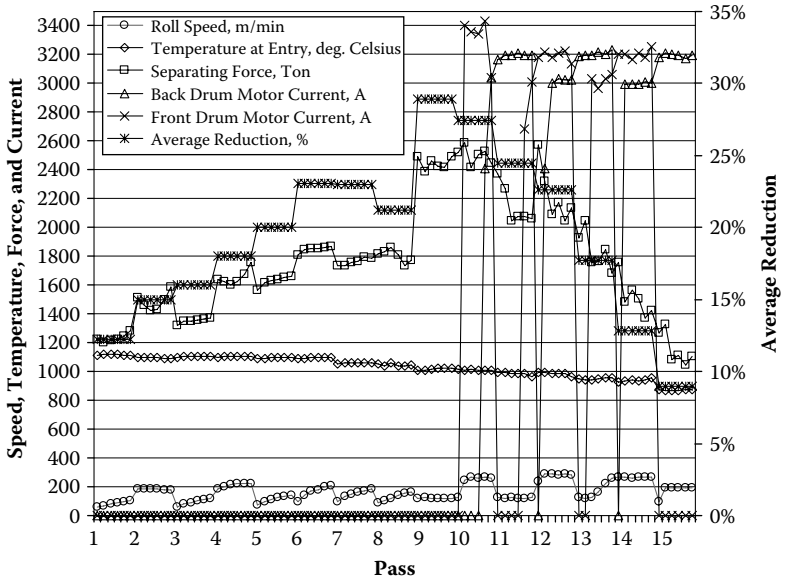


FIGURE 11.9 Rolling parameters. (From Yu, Q. *Iron and Steel Technology* 2: E186. With permission.)

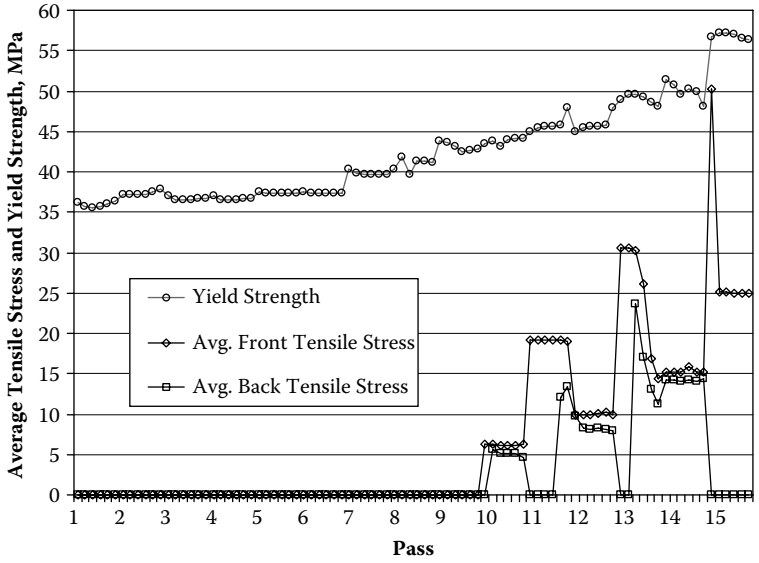


FIGURE 11.10 Comparison of the average tensile stresses with the yield strength at the entry. (From Yu, Q. *Iron and Steel Technology* 2: E186. With permission.)

strength. As a result, the strip has little plastic deformation. For the first row in the fifteenth pass, the minimum difference between the yield strength and the average back tensile stress is only 11.2%. Plastic deformation could occur if either the residual stresses or the bending stresses are over a certain value. The reason is that the low thread speed (94.71 m/min) created a great tension at the entry under the condition of the constant motor drive power. Therefore, strip speed plays an important role in determining the tensile stresses of the drums.

Since the strip width corresponding to row 1 is narrowest, the transverse distribution of the back tensile stress on row 1 is of great interest. To calculate the residual stress by using Equation 11.7, it is assumed that the strip shape in pass 15 is similar to that in pass 14. The strip temperature at the entry is 870°C. From the previous study (Yu and Muncie 2003), the corresponding elastic modulus and Poisson's ratio are 144.52 GPa and 0.387, respectively. Combination of the residual stress and bending stress with the average back tensile stress yields the tensile stress at the entry of the roll bite, as shown in Figure 11.11.

When strip departs the drum, it does not have any bending stress. The back tensile stress is less than the yield strength. The strip is in an elastic deformation state. The average

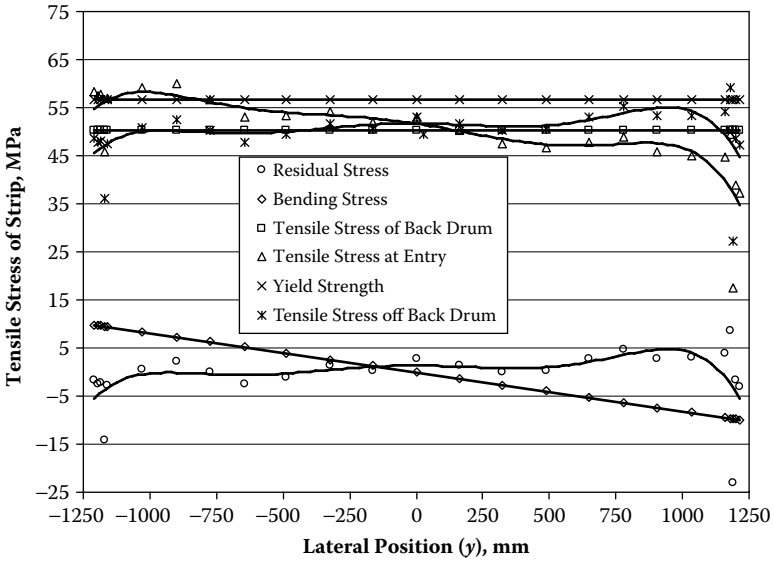


FIGURE 11.11 Transverse distribution of the tensile stresses at the entry. (From Yu, Q. *Iron and Steel Technology* 2: E186. With permission.)

back tensile stress is calculated to be 50.32 MPa. When the *y*-coordinate of a selected position is between −1160 and −836 mm, the tensile stress at the entry of the roll bite exceeds the yield strength. The partial width of the strip enters a plastic deformation state prior to the roll bite. This also explains why the strip edge on the operator side was necked more than that on the drive side, as shown in Figure 11.6a. The difference between the operator side and the drive side of the bending stresses is about 20 MPa. The maximum difference of the residual stresses on the trend line shown on the chart is approximately 10 MPa. Therefore, the bending stress is a major reason to cause the strip necking. The effective way to minimize the bending stress is to reduce the drum tension and strip camber.

The plastic deformation of the strip near the entry of the roll bite will change the transverse distribution of the tensile stress since the tensile stress in Equation 11.7 is based on the theory of elasticity. Therefore, the tensile stress and width necking near the entry of the roll bite should be analyzed via other numerical methods.

11.6 SIMULATION OF WIDTH NECKING USING FEM

An elastic–plastic FEM is employed to simulate the transverse distributions of the tensile stress and lateral displacement at the entry. The strip between the back drum and roll bite is selected for the analysis. The strip length, width, and camber are 8.433 m, 2.463 m, and 82 mm, respectively. The strip is discretized using 800 plane-stress elements, with 40 elements in the longitudinal direction and 20 elements in the transverse direction. A linear isotropic and multilinear-kinematical hardening material is selected for the material model.

While the first row of the pins enters the mill bite, the average back tensile stress and residual stress of the strip in Figure 11.11 can be treated as static loads. The residual stress at each node is transferred to Gauss points by interpolation and applied to all elements first. However, the bending stress caused by the drum tension and the difference of the centerline offsets vary with *x*-coordinate. Since the partial width of the cross section corresponding to row 1 produces plastic deformation gradually while the cross section approaches the roll bite, the average tensile stress is loaded to the left end of the strip by ten substeps. The nodes at the right end are constrained in the *x*-direction, and the central node in the *y*-direction. The result simulated by the static nonlinear elastic–plastic finite-element method is shown in Figures 11.12 through 11.15.

The yield strength at the elevated temperature is 56.67 MPa. Figure 11.12 shows the maximum tensile stress of 56.95 MPa at the entry of the roll bite on the operator side. A very small plastic deformation occurs at the right bottom corner in Figure 11.15. The minimum tensile stress is 25.46 MPa at the entry of the roll bite on the drive side. If the average back tensile stress of the drum reduces by 50%, the strip on the drive side is in a critical state from stretch to compression. Therefore, the back tensile stress must be greater than 50% of the current setting.

The width variation at the entry relies on the displacements in the *y*-axis. From Figure 11.13, it is noted that all isopleths of the displacements in the *y*-axis are diagonal, which is similar to the pattern of the stretching marks. Since the plastic deformation area is very small and close to the roll bite, the displacements in the *y*-axis near the roll bite only provide a reference. The maximum displacement in the *y*-axis on the drum is about 1.4 mm. On the other hand, this result states that the centering guides could not control the strip tracking instantly by a big margin besides generation of the plastic deformation at the entry and change of the strip feed angle. The change of the feed angle could lead to

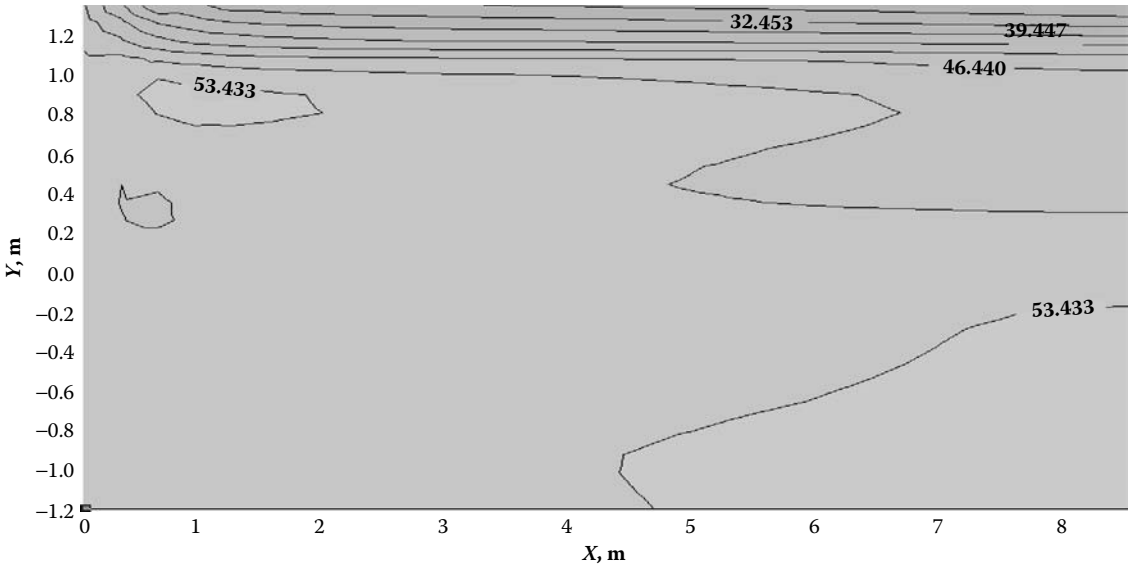


FIGURE 11.12 Distribution of the back tensile stress. (From Yu, Q. *Iron and Steel Technology* 2: E186. With permission.)

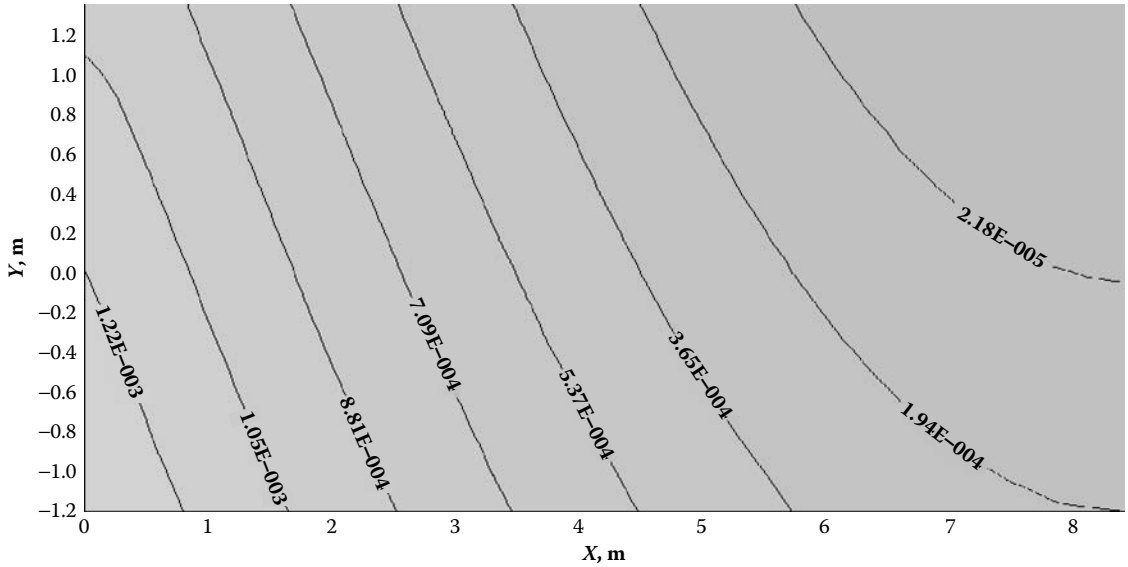


FIGURE 11.13 Distribution of the displacements in the *Y*-axis. (From Yu, Q. *Iron and Steel Technology* 2: E186. With permission.)

the coil oscillation. To achieve more accurate results, fine meshes should be adopted in the plastic deformation area. Figure 11.14 shows that the contours of the von Mises stress are similar to those of the back tensile stress, which states that the back tensile stress dominates the deformation status at the entry.

11.7 DISCUSSION

In the FEM model, it is assumed that the back tensile stress generated by the drum acts on the left edge of the strip uniformly. In the hot-rolling process of the Steckel mill, other factors may affect the transverse distribution of the back tensile stress, such as cold ends of strip, leveling of pinch rolls, alignment of centering guides, etc.

When a cold end of strip enters the mouth of a drum, the bent cold end may not be tightened against the drum surface, which results in either tension spikes in circumference or change of the transverse distribution of the tensile stress, or both. While the drum coils up the strip with heavy edge waves or buckles, the strip vibrates on the roll table vertically. The vibration produces a shock load to the strip. Furthermore, pinch roll leveling could affect the transverse distribution of the back tensile stress significantly. In the finishing passes, it is possible that the centering guides contact the strip edges. The additional bending stress could be generated by the strip

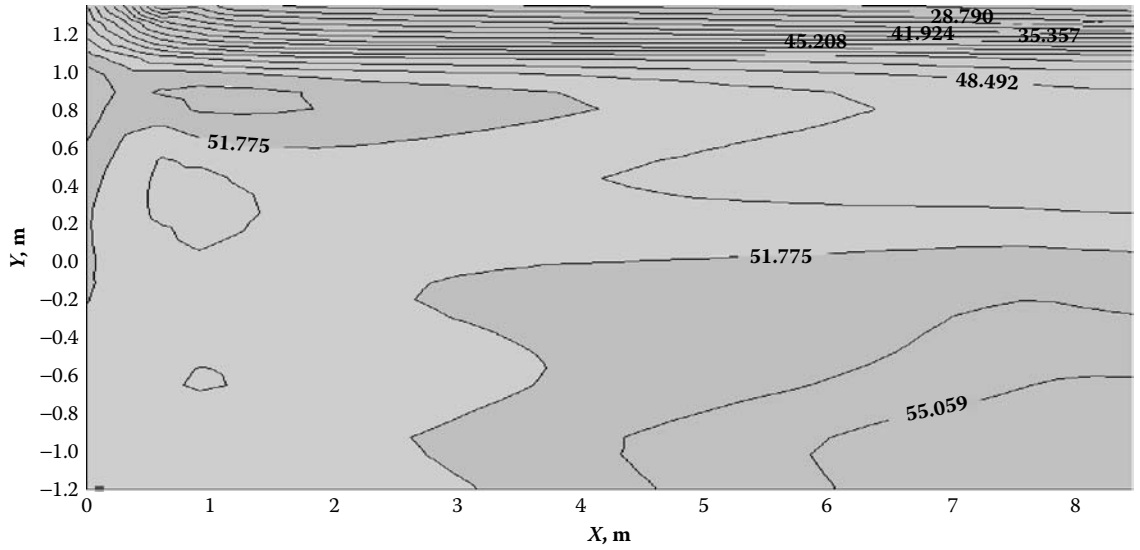


FIGURE 11.14 Distribution of the von Mises stress. (From Yu, Q. *Iron and Steel Technology* 2: E186. With permission.)

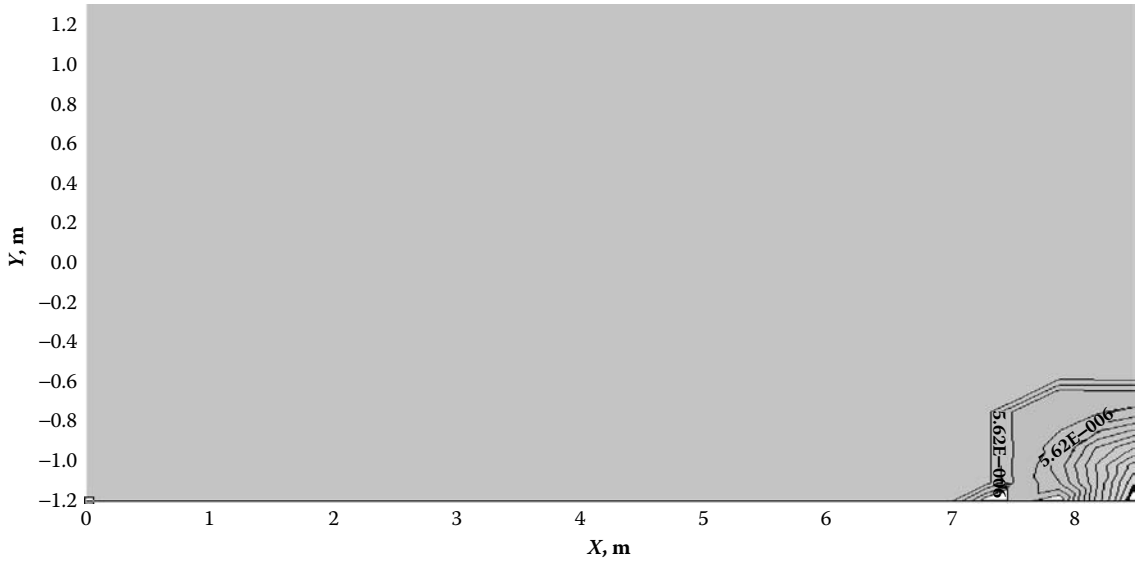


FIGURE 11.15 Distribution of plastic strain. (From Yu, Q. *Iron and Steel Technology* 2: E186. With permission.)

contacts with external mill equipment. In addition, a transfer bar could hit the edger rolls and contact the centering guides in the roughing passes. The factors should be considered when setting the back drum tension.

From Figure 11.12, it can be seen that the strip track-out changes the transverse distribution of the tensile stress at the entry of the roll bite. The transverse flow of the material in the roll bite is certainly impacted by the boundary condition. Incorporating the boundary condition with the transverse flow in the roll bite is of great interest in the future study.

Furthermore, big buckles and edge waves hide width and affect the accuracy of width measurement. After the strip is leveled, the residual stress will be released and the hidden width will be recovered at a certain extent.

11.8 SUMMARY

Width variation in a portion of strip length is investigated by incorporating the back tensile stress with the residual stress and the bending stress of the strip. By means of the stainless pins buried in the slab, the lateral and longitudinal displacements of the pins are measured. The residual stress is derived from the displacements and the gauge profile. A comprehensive model is proposed to evaluate the tensile stress near the roll bite. The model is validated by the width measurement and the elastic–plastic finite-element simulation. The width variation behavior is summarized as follows:

The back tensile stress near the roll bite has a significant effect on the local width necking. The back tensile stress could

cause the strip to enter the plastic deformation state in front of the roll bite due to addition of the bending stress and the residual stress. The residual stress and the bending stress should be evaluated and considered when setting the back tension. The criteria to set the tension of the drum are that the tensile stress must be less than the yield strength of materials and that no part of the strip suffers compression across width.

In the hot-rolling process, the yield strength of materials under elevated temperatures is mainly dependent upon the yield strength at room temperature, rolling temperature, strain, and strain rate. Due to material hardening, the front tensile stress may be higher than the back tensile stress because of shape control due to increase of the yield strength.

The difference in the centerline offsets of the strip is a major reason to generate the bending stress. It is necessary to control the end condition of the strip, such as camber, wedge and single-edge wave, etc. Alignment of the drums, pinch rolls, table rolls, and centering guides plays an important role in minimizing the track-out issue of strip. In addition, regular inspections of the liners of the mill windows and the work roll chocks are also useful to prevent the track-out.

Residual stress is another factor that causes the width necking. It is essential to control strip shape prior to last couple of finishing passes, such as center buckles and quarter buckles.

Strip tensiometers and tension regulators could be adopted in the Steckel mill for monitoring tensile stresses and reducing the width necking. Strip dimensions, rolling parameters and material mechanical properties should be used as the additional input parameters to the tension regulators.

ACKNOWLEDGMENTS

The author thanks the hot-rolling and plate-finishing teams of Nucor Steel Tuscaloosa for their support of this study.

REFERENCES

Dixon, A. and Yuen, W. 2004. A matched solution method for the prediction of residual stresses for flat rolling. *ANZIAM* 45(E): C435–C447.

Higo, T. and Yamada, K. et al. 2002. 3D transient FEM analysis of width variation during hot rolling. *44th MWSP Conference Proceedings* 60: 335.

Ishii, A. and Takamachi, Y. 2003. Strip width variation behavior and its mathematical model in hot strip finishing mills. *Journal of the Japan Society for Technology of Plasticity* 44(509): 645–650.

Kainz, A. and Zeman, K. 2004. Selected rolling and smart material simulations by utilizing the finite-element package deform. *The Third European Deform User's Meeting 2004*, Manchester, England.

Kapoor, P. N. 2006. Survey on descaling: *The 14th conference of the International Association of Steckel Mill Operators*, hosted by Nucor Steel Tuscaloosa. Tuscaloosa, AL.

Wusatowski, Z. 1969. Roll pressure, torque, work, and power in rolling. *Fundamentals of Rolling*. New York: Pergamon Press Inc. Chapter 4: 229.

Yu, Q. 2007. Width variation behavior during hot rolling - 2007 AIST Proceedings. *Iron and Steel Technology*, Indianapolis, IN. 2: E186.

Yu, Q. and Muncie, M. 2003. Effect of cooling and stacking on buckling of plates. *AISE Steel Technology* 23(6): 35–44.

12 Parameter Optimization and Uncertainty Quantification in Rolling

Arif S. Malik and Ramana V. Grandhi

CONTENTS

12.1 Introduction 141
12.2 Optimization 141
12.2.1 Traditional versus Modern Approach to Optimization 142
12.2.2 Formulation of Mathematical Optimization Statements 142
12.2.2.1 Design Variables and Cost Function 142
12.2.2.2 Optimization Constraints 144
12.3 Uncertainty Quantification and Reliability Analysis 144
12.3.1 Random Variables 144
12.3.2 Probability Calculation for Reliability Analysis 145
12.3.3 The Role of Uncertainty Quantification in Optimization 146
12.4 Application 1: Productivity Optimization on a Four-High Temper Mill 147
12.4.1 Objective for Temper Mill Optimization 147
12.4.2 Formulating an Optimization Problem for Temper Mill Productivity 147
12.4.2.1 Design Variables 147
12.4.2.2 Cost Function 148
12.4.2.3 Constraints 148
12.4.2.4 Side Bounds 148
12.4.3 Results and Discussion for Temper Mill Productivity Optimization 148
12.4.3.1 Optimization Case 1 (Unassigned Roll Crowns) 148
12.4.3.2 Optimization Case 2 (Fixed-Roll Crowns) 149
12.5 Application 2: Estimating the Probability of Achieving Target Strip Crown and Flatness in Rolling (Uncertainty Quantification) 150
12.5.1 Objective in Determining Strip Flatness Probability 150
12.5.2 Formulating the Strip Flatness Probability Problem 151
12.5.3 Limit State Functions for Flatness Reliability 152
12.5.4 Results and Discussion for Strip Flatness Probability 152
12.5.4.1 Reliabilities of $g1$ and $g2$ 152
12.5.4.2 System Reliability 152
12.6 Summary 153
Acknowledgments 153
References 153

12.1 INTRODUCTION

This chapter provides an introduction to the basics of formulating mathematical optimization statements that can be applied to improve rolling processes. The optimization formulations introduced can accommodate probabilistic constraints using uncertainty quantification (UQ), which accounts for stochastic variations in material properties and mill operating conditions. The combination of UQ with mathematical optimization methods leads to process-improvement tools collectively known as reliability-based design optimization (RBDO). Following an introduction to the formulation of mathematical optimization statements and a discussion of the benefits of UQ, the two steel-rolling applications in Table 12.1 are presented and discussed.

12.2 OPTIMIZATION

The word *optimization* is used frequently to imply that something—usually a product or a process—will perform such that the best outcome is achieved for a group of desired

TABLE 12.1
Optimization and Uncertainty Quantification Examples

Example	Application	Subject
1	Maximizing yield on a four-high temper mill equipped with work roll and backup roll bending	Optimization
2	Calculating the probability of achieving target flatness in rolled strip	Uncertainty quantification

metrics. Optimization of a steel-rolling process, therefore, suggests that the best outcome is obtained for those productivity and quality criteria that are important in steel rolling. Usually, the best outcome involves maximizing or minimizing a primary metric (or group of metrics), while ensuring that minimum standards for all the other important metrics are simultaneously met. For example, an optimization effort in the rolling of type 301 stainless steel on a four-high reversing mill might involve maximizing the mill productivity, while ensuring that requirements for material yield strength, hardness, gauge, flatness, and surface quality are all concurrently met. Traditionally, optimization tasks like this have been carried out mostly by trial and error, with the amount of error reduced through the insight and skill of experienced individuals. As performance requirements for industrial processes become greater, however, and the processes themselves become increasingly complex, it becomes more difficult to advance the optimized state using intuition and experiment alone. In addition, when using a heuristics approach, there is no systematic way to identify whether a process is, in fact, really optimized or whether it is simply operating better than its previous state. Fortunately, the last two decades have brought about simultaneous advances in mathematical optimization tools, computing power, and process simulation capabilities that address these issues and facilitate the attainment of truly optimized processes. These advances have also made it easier to implement the findings of more ambitious optimization projects into complex processes such as steel rolling. Indeed, many of today's computerized rolling parameter setup models are being commissioned with sophisticated mathematical optimization routines.

12.2.1 Traditional versus Modern Approach to Optimization

Figure 12.1 shows two flowcharts that illustrate the difference between the traditional optimization process (based on experience and trial and error) and the modern optimization process, which includes mathematical techniques to perform complex optimization tasks. As shown by the shaded flowchart boxes, the modern optimization process includes identification of the design variables, formulation of a cost (or objective) function to be optimized, and the establishment of limiting constraints. As the modern optimization procedure progresses from an initial baseline design, mathematical methods, rather than human guidance, are used to improve the design until convergence at the optimum is reached.

12.2.2 Formulation of Mathematical Optimization Statements

12.2.2.1 Design Variables and Cost Function

To facilitate understanding of the rolling applications in Table 12.1 (discussed later), an introduction to the basics of mathematical optimization is necessary.

Consider the simple example of optimizing the beer can as shown in Figure 12.2 [1]. In the high-volume manufacture of beer cans, it may be desirable to minimize the amount of sheet metal used, given that certain volume and dimensional requirements are met. If the diameter, D, and the height, H, of the can are allowed to vary within certain bounds, then one can minimize a surface area cost function, f, expressed in terms of design variables, D and H, as indicated in Equation 12.1.

$$\text{Minimize: } f(D,H) = \pi DH + \frac{\pi}{2}D^2 \ (\text{cm}^2) \qquad (12.1)$$

It should be clear that the values of the design variables, D and H, should be positive—otherwise the beer can would have no physical surface area and would be incapable of holding any beer! In addition, the can's size should be practical (not too large and not unusually shaped). To accommodate these basic requirements, design variable *side bounds* limiting the upper and lower values of the diameter, D, and height, H, are imposed. The side bounds for diameter and height can be assigned, as in Equation 12.2, which states that the diameter can vary between 3.5 and 8 cm, while the height can vary between 8 and 18 cm.

$$3.5 \le D \le 8; \qquad 8 \le H \le 18 \ (\text{cm}) \qquad (12.2)$$

Using only these side bounds for design variables D and H, one could infer (without calculation) that the minimum surface area for the beer can, governed by $f(D, H)$, is attained simply by using the minimum allowable values of D and H. Hence, a trivial solution exists and optimization is not really necessary. In contrast to this, real optimization problems require calculation because their solutions are not so straightforward. This is because there are always competing factors

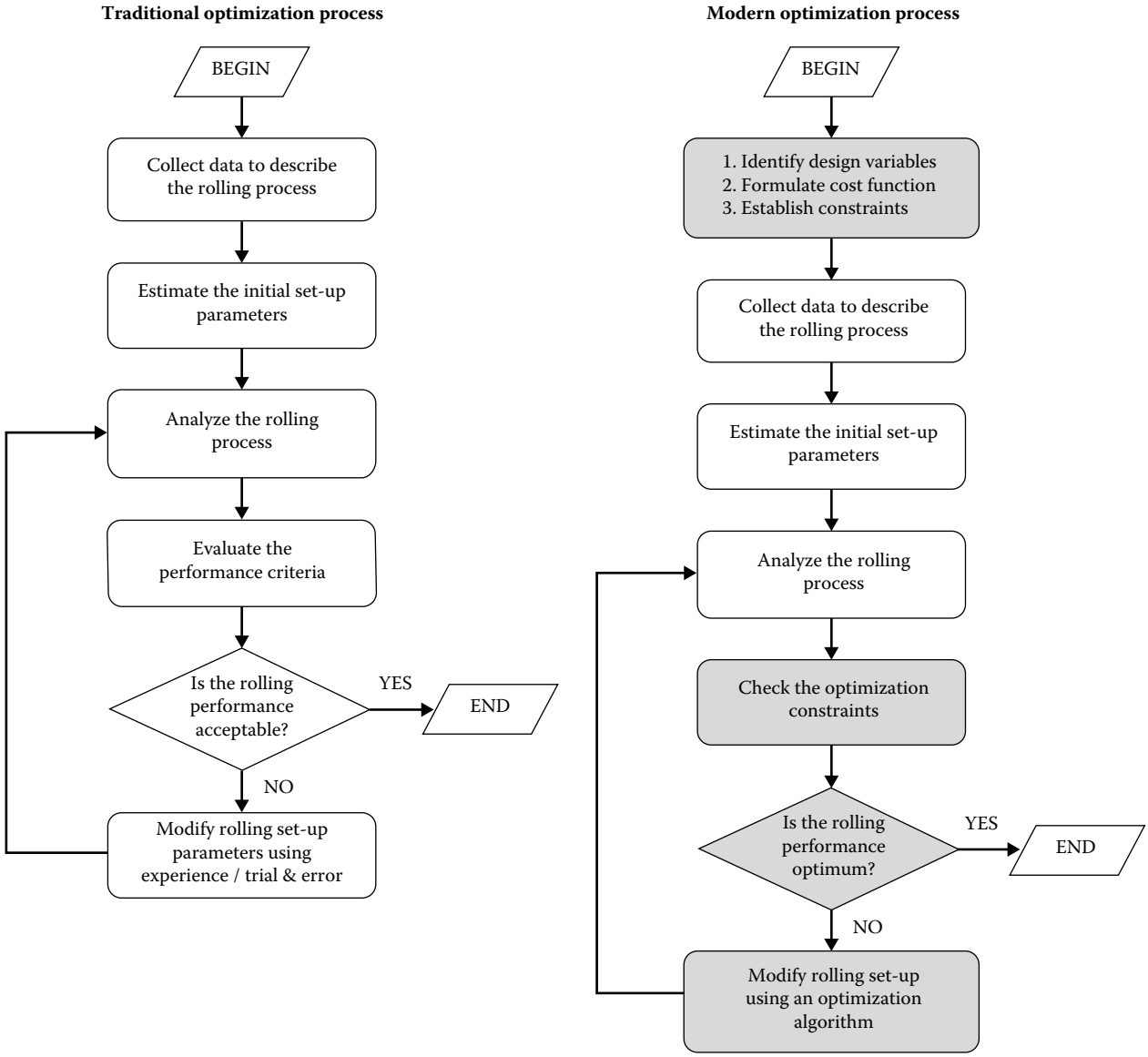


FIGURE 12.1 Comparison of traditional optimization process with modern mathematical optimization process.

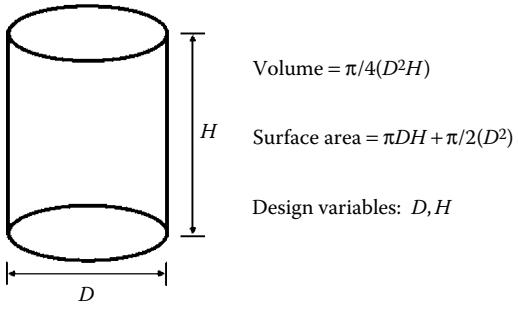


FIGURE 12.2 Beer can optimization example. (From Arora, J. S. 1989. *Introduction to Optimum Design*. New York: McGraw-Hill. With permission.)

that force the design variables to reach a compromise, preventing them from collectively assuming side bound values. In this example, if the can is now required to hold a minimum specified volume of beer, then the solution for the optimum values of design variables D and H is not trivial and requires mathematical optimization. The minimum volume requirement is addressed by adding a constraint to the optimization problem, as discussed in the next section.

An analogous (simple) rolling-related problem can be conceived from the earlier example of maximizing a reversing mill's productivity during the rolling of type 301 stainless steel. If the productivity design variables are chosen as rolling speed, V, and number of passes, N, then one could minimize the cost function, $f(V, N)$, shown in Equation 12.3, where w_N and w_V are positive weighting coefficients. Side bounds on the rolling speed and the number of passes can be assigned as in Equation 12.4.

$$f(V,N) = w_N N - w_V V \tag{12.3}$$

$$100 \le V \le 1000; \qquad 1 \le N \le 11 \tag{12.4}$$

Note that the cost function $f(V, N)$ is decreased by reducing the number of passes, N, and increasing the rolling speed, V. According to Equations 12.3 and 12.4, the cost f will be minimized (and productivity maximized) for side bound values $V = 1000$ and $N = 1$. This, again, is not yet a real optimization problem because the solution is trivial and perhaps even unrealistic—it suggests rolling the material in only one pass at 1000 m/min. In practice, the constraints of material yield strength, hardness, gauge, flatness, and surface quality (in addition to side bounds on rolling force, torque, etc.) will invoke a compromise among the design variable values. The optimum solution will then also require calculation using a mathematical procedure.

12.2.2.2 Optimization Constraints

As mentioned earlier, in practice, every optimization problem has constraints that prevent all of the design variables from assuming trivial values based on their side bounds. Returning to the beer can example, if the volume of the can is required to be at least 400 cm^3, then a complete optimization problem with the volume constraint can be written as follows in Equation 12.5.

Minimize the surface area:

$$f(D,H) = \pi DH + \frac{\pi}{2} D^2 \ (\text{cm}^2) \tag{12.5}$$

Subject to the volume constraint:

$$\frac{\pi}{4} D^2 H \ge 400 \ (\text{cm}^3)$$

With design variable side bounds:

$$3.5 \le D \le 8; \qquad 8 \le H \le 18 \ (\text{cm})$$

Equation 12.5 now represents a real optimization problem requiring a systematic procedure to find the optimum values for the diameter, D, and height, H. It should be noted that excessive or ill-posed constraints in an optimization problem may preclude the existence of any feasible optimum solution. This occurs when not all constraints and side bounds can be satisfied by a single set of design variable values.

Computer packages for solving such problems are widely available. The burden on the design engineer, instead, is manifested in two other major tasks. The first major task is to formulate the mathematical optimization problem. In other words, write the equations that, when solved, will enable improvements in the rolling process. Since the mathematical formulation will likely contain expressions involving complex rolling phenomena, the second major task is to identify appropriate simulation models and integrate them into the optimization problem. For instance, if a constraint on strip flatness were included in the previous rolling mill optimization example, then one would need a strip-flatness calculation model that can be expressed either explicitly or implicitly in terms of the selected design variables, N and V (number of passes and rolling speed, respectively).

The foregoing discussion has provided only a brief introduction to the formal design optimization procedure. To gain a better understanding of mathematical optimization methods, the text *Introduction to Optimum Design* (McGraw-Hill, 1989) is suggested as further reading.

12.3 UNCERTAINTY QUANTIFICATION AND RELIABILITY ANALYSIS

Uncertainty quantification is an active field of study that attempts to characterize the uncertainties of input and output parameters in practical applications [2,3]. Industrial operations, such as rolling, have an abundance of parameter uncertainty that can lead to serious process failures. The natural response for reducing such risks is for process engineers and operators to employ conservative operating practices that lessen the chances of process failure. The trade-off, however, is that the potentially better performance—achievable when failure does not occur—is lost.

To appreciate this circumstance, consider the conventional *factor-of-safety* design concept. In the design of a metal component, such as a work roll chock, the engineer might execute the design using a specific factor-of-safety to protect against failure due to material yielding. For instance, if the yield strength of the chock material were 300 MPa, and the nominal loading condition (due to work roll bending) produced an equivalent stress of 100 MPa, then the factor-of-safety would be (300 MPa)/(100 MPa) or 3. In this approach, a gamble is made that the applied stress does not exceed the material yield strength. But what is the probability that the applied stress does in fact exceed the yield strength and the chock fails? Conventional design methods do not answer this question. If a new, cost-effective chock with a factor-of-safety of 2 could be designed, would this be better?

Uncertainty quantification helps answer these types of questions by analyzing the variability in parameters such as yield strength, applied stress, and others. Reliability analysis techniques are then used to efficiently predict a *probability of failure* that can be evaluated and considered by the designer. When multiple parameter uncertainties exist, reliability analysis also provides insight as to which ones contribute most to specific modes of failure. Figure 12.3 summarizes the benefits of UQ and reliability analysis over the conventional factor-of-safety concept.

12.3.1 Random Variables

Uncertainties can result from natural variations, process/system variations, lack of data, or lack of knowledge. An uncertain or nondeterministic parameter that varies at any

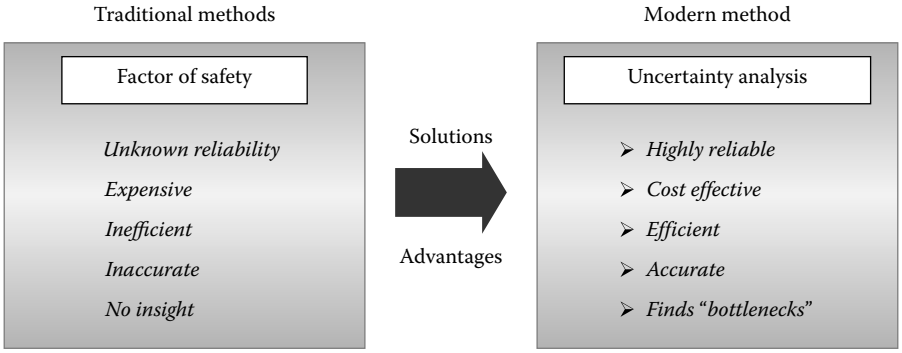


FIGURE 12.3 Benefits of uncertainty quantification and reliability analysis over factor-of-safety approach.

given point in time or space is called a *random variable*. The yield strength of rolled steel within a coil, for example, will vary due to other inherent process deviations and can, therefore, be considered a random variable. Likewise, the strip crown throughout a coil may be considered a random variable, unless it is measured precisely by profile gauges at every instant during rolling. If the measurement is not precise, then the measured strip crown may still be considered a random variable, albeit to a lesser degree.

As stated earlier, the general response to uncertainties in all processes (including rolling) is that a conservative approach is taken to minimize the detrimental impact that results in the rare cases when one or more random variables take on values away from their average or expected values. The vast majority of random variables relating to products and processes conform to the well-known Normal (Gaussian) distribution. The Normal distribution is depicted in Figure 12.4 along with other sample random variable distributions. These distribution curves represent continuous histograms, known formally as probability density functions (PDF). They indicate the frequency at which random variables take on particular values. Hence, the tail portions of these PDF curves reflect the relatively rare cases when extreme values of the random parameters occur.

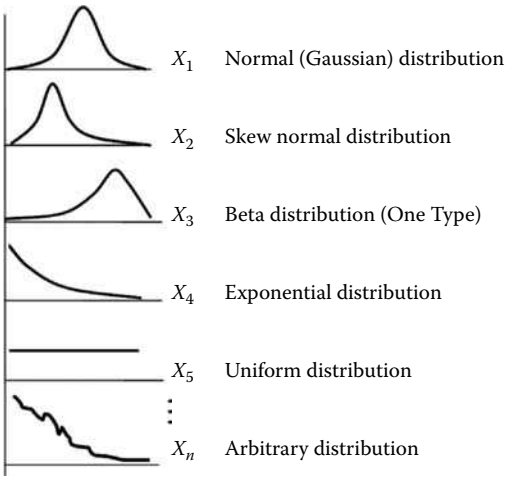
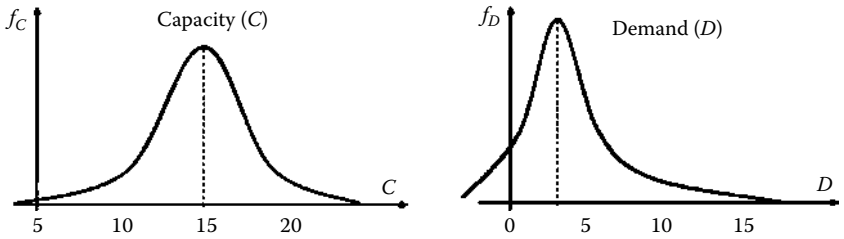


FIGURE 12.4 Sample random variable distributions.

12.3.2 Probability Calculation for Reliability Analysis

To gain insight into how parameter variations lead to process failure and understand why it is beneficial to predict the probability of failure, consider the distributions of two generic random variables, named Capacity and Demand, as shown in Figure 12.5. The random variable Capacity, *C*, represents the strength or capability of a given system, while the Demand, *D*, reflects the stress or load on the system. Referring to the earlier work roll chock example, Capacity is analogous to the yield strength of the chock material, while Demand is analogous to the applied stress due to work roll bending. Using a traditional factor-of-safety approach with the mean values of Capacity and Demand, one can infer that failure in the system is unlikely—because the factor-of-safety is 15/3 or 5. However, when the random variable distribution plots are superposed, as in Figure 12.6, it is easy to see that there are circumstances when the Demand exceeds the Capacity. This is illustrated by the overlapping portions in the respective PDFs. In fact, the probability that Demand exceeds Capacity (probability of failure) is equivalent to the area of the overlapping region (note that the area under each curve is equal to 1 or 100%). Clearly, if there is less variation in either Capacity or Demand, the probability of failure is reduced—this has been the motivation for the six-sigma concept. (Six-sigma, however, does not address the probability of process failures.) Knowledge of the distribution characteristics of the influential random variables in a process can provide insight into the likelihood of success or failure of the system. Modern reliability analysis methods include tools for calculating probabilities of failure (or success) for multiple random variables according to their distribution type and degree of statistical correlation with one another. The methods can also effectively identify bottleneck random parameters that contribute most to process failure.

As will be shown later in Application 2—*Calculating the probability of achieving target flatness in rolled strip*—reliability analysis methods can also eliminate the need to conduct computationally expensive Monte Carlo simulations in calculating probabilities of success or failure. In the Monte Carlo approach, the random variables are sampled a total of



- If *C* and *D* are *correlated* random variables (not independent), the PDF of *C* depends on each specific value of *D* (vice versa)
- For correlated random variables, a 3D surface plot, f_{CD}, describes the *Joint* PDF of *C* and *D*

FIGURE 12.5 Probability density functions for two random variables "Capacity" and "Demand."

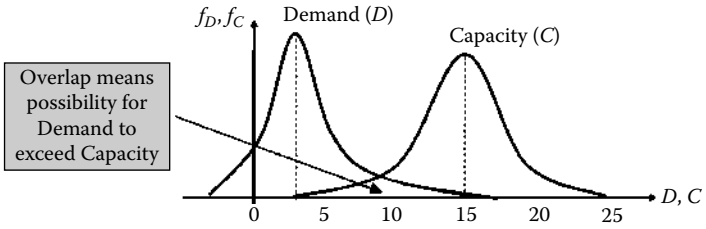


FIGURE 12.6 Failure results from PDF overlap and "Demand" exceeds "Capacity."

M times, and a simulation of the process is performed for each sampling to check whether the process will succeed or fail based on the sampled values. The probability of failure, P_f, is calculated by dividing the number of failures, N_f, by the total number of samplings:

$$P_f = \frac{N_f}{M} \tag{12.6}$$

The major drawback to the standard Monte Carlo approach is that for low probabilities of failure, a large number of simulations are required. For instance, if the probability of failure is .01%, then 10,000 simulations can be expected before a single failure is recorded. If the simulations were to involve nonlinear finite element analysis of the elastic–plastic interaction between a rolled strip and an adjacent work roll, each one could require hours of computing time. The modern reliability analysis methods discussed for Application 2 employ techniques that calculate probabilities of failure more efficiently.

12.3.3 The Role of Uncertainty Quantification in Optimization

Once the probability of failure or success of an output parameter for a given process is available using UQ and reliability analysis methods, the information can be used very effectively in cost functions and/or constraints for mathematical optimization problems. As an example, a reliability-based constraint on strip flatness, *S*, can be added to the earlier rolling productivity optimization, in which the design variables include the number of passes (*N*) and the rolling speed (*V*):

Minimize the cost function:

$$f(V,N) = w_N N - w_V V \tag{12.7}$$

Subject to a flatness probability constraint:

$$P_f\left[S(N,V)\right] \le 0.01$$

With side bounds: $100 \le V \le 1000; \qquad 1 \le N \le 11$

Equation 12.7 states that the rolling productivity is to be maximized (by minimizing *f*), while ensuring that the probability of failure, P_f, of the strip flatness, *S*(*N*, *V*), is less than 1%. This is equivalent to stating the *reliability* of achieving target strip flatness is constrained to be at least 99%. Note that the strip flatness is shown here as a function of the design variables, *N* and *V*. Like the cost function, constraint equations must be either explicit or implicit functions of at least one design variable. Since the strip flatness is probabilistic in nature, it is a *random* constraint, which depends on one or more random input variables. The random input variables do not have to be associated with the optimization design variables, although the mean values of random parameters (and other statistics) can be used as design variables.

The integration of probabilistic reliability information into mathematical optimization leads to a powerful process improvement tool known as RBDO, an overview of which is illustrated graphically for rolling processes in Figure 12.7.

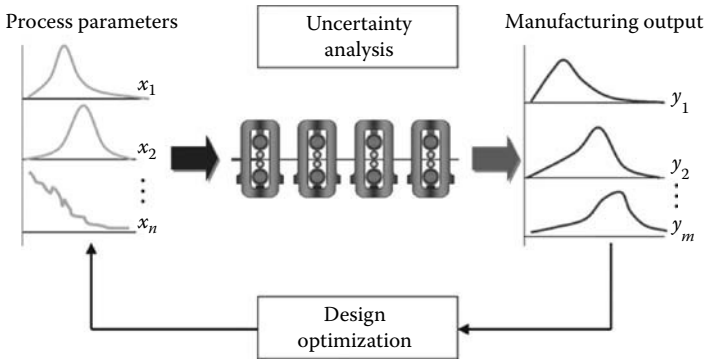


FIGURE 12.7 Overview of reliability-based design optimization.

12.4 APPLICATION 1: PRODUCTIVITY OPTIMIZATION ON A FOUR-HIGH TEMPER MILL

12.4.1 Objective for Temper Mill Optimization

The objective for this application of the mathematical optimization method is to maximize the productivity on a single-stand, four-high cold mill used to temper-roll carbon plate. The mill is equipped with both work roll bending (WRB) and backup roll bending (BUB) to provide online strip flatness control. Work roll bending and backup roll bending on a four-high mill is shown in Figure 12.8. In addition, ground crowns on the work rolls and backup rolls and edge taper on the backup rolls are considered.

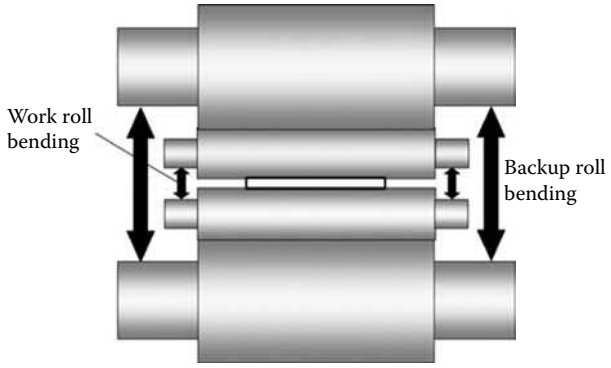


FIGURE 12.8 Four-high temper mill with work roll bending and backup roll bending.

The main job of the temper mill is to impart a small thickness reduction (or elongation) of at least 2%, but no more than 4%, in order to impart desirable yield strength and hardness properties while meeting gauge and flatness requirements. The product mix for this mill includes carbon steels with nominal yield strength ranging from 48 to 100 ksi, strip width ranging from 48 in. to 96 in., and gauge ranging from 3⁄16 in. to ¾ in. Even with the installed WRB and BUB systems, such diversity in the product mix makes it very difficult to satisfy customer requirements for yield strength, hardness, and gauge, while simultaneously delivering plate with adequate flatness. The conventional approach when operating this type of mill is to "roll for flatness" and anticipate a temper somewhere between 2% and 4% elongation. Since productivity can be increased by rolling longer plate with tempers closer to 4%, an optimization of the rolling process can be performed to establish the best setup values to strive for this.

12.4.2 Formulating an Optimization Problem for Temper Mill Productivity

The formulation of the four-high temper mill optimization problem involves establishing design variables, creating a cost function to be minimized or maximized, identifying constraints, and assigning side bounds for the design variables.

12.4.2.1 Design Variables

The design variables imply the parameters that can be adjusted to meet the objective of maximum productivity while satisfying necessary constraints. The following six design variables are selected according to this rationale:

t_2	Exit gauge (mils)
P_{WRB}	Work roll bending force (tons/side)
P_{BUB}	Backup roll bending force (tons/side)
C_{WR}	Work roll parabolic crown (mils)
C_{BUR}	Backup roll parabolic crown (mils)
T_{BUR}	Backup roll taper or chamfer (mils/in.)

This application of the mathematical optimization method for this mill will include the two cases identified in Table 12.2. The first case will represent that situation in which the roll profile parameters (C_{WR}, C_{BUR}, and T_{BUR}) are sought; hence, these are not fixed and will thus be allowed to vary between their respective side bounds. This circumstance might represent a rolling schedule investigation prior to mill commissioning. In the second case, the roll profile design variables C_{WR}, C_{BUR}, and T_{BUR} are fixed, implying that the roll crowns will have already been established.

TABLE 12.2
Optimization Parameters and Side Bounds for Two Cases Involving a Four-High Temper Mill

Case No.	Plate Width (in.)	Plate Min. Gauge (mils)	Work Roll Crown Range (mils)	Backup Roll Crown Range (mils)	Backup Roll Taper Range (mils/in.)	Work Roll Bending Range (tons/side)	Backup Roll Bending Range (tons/side)
1	48	177.0	3–10	3–5	0–4	0–25	0–250
2	96	590.0	Fixed at 5	Fixed at 3	Fixed at 3	0–50	20–500

12.4.2.2 Cost Function

Since the objective is to maximize productivity (for a fixed rolling speed), a cost function for the percent elongation can be maximized as follows:

$$\text{Maximize: } f = \left(1 - \frac{t_2}{t_1}\right) \times 100\% \text{ percent elongation} \qquad (12.7)$$

where t_1 is the plate's entry gauge (assumed constant). Note that although f is only an explicit function of one design variable, t_2, the other design variables are necessary because they will appear in the constraint equations.

12.4.2.3 Constraints

The optimization of productivity will include various constraints on the strip flatness, exit gauge, percent elongation, rolling force, and roll contact stress. The flatness is tied directly to the change in strip crown ratio during rolling (refer to Chapter 30, *Recent Developments in Strip Profile Calculation*); therefore, strip crown calculation and flatness deadband information are needed to establish flatness-related constraints. A rolling-force calculation is also needed in the calculation of a maximum force constraint. A complete set of constraint equations for this problem can be written as follows:

$g1$: $\text{CR}_{\text{exit}} \le \text{CR}_{\text{entry}} + \text{CR}_{\max}$ — Exit crown ratio upper limit

$g2$: $\text{CR}_{\text{exit}} \ge \text{CR}_{\text{entry}} - \text{CR}_{\max}$ — Exit crown ratio lower limit

$g3$: $t_2 \ge t_{2,\min}$ — Exit gauge lower limit

$g4$: $\left(1 - \frac{t_2}{t_1}\right) \ge e_{\min}$ — Elongation lower limit

$g5$: $\left(1 - \frac{t_2}{t_1}\right) \le e_{\max}$ — Elongation upper limit

$g6$: $P + 2\left(P_{\text{BUB}} + P_{\text{WRB}}\right) \le P_{\max}$ — Total mill force limit

$g7$: $\sigma_{c,\max} \ge 0.418\sqrt{\left(\frac{(P + 2P_{\text{WRB}})E}{L}\frac{(R_1 + R_2)}{R_1 R_2}\right)}$ — Roll contact stress limit

where CR is the strip crown, e is the elongation, P is the total mill force, E is the roll elastic modulus, R_1 and R_2 are the roll radii, L is the roll length, and σ_c is the contact stress between the rolls.

12.4.2.4 Side Bounds

The side bounds are implemented to restrict the values of the design variables, according to specific practical limitations, as follows. Note that no side bounds are needed for the exit gauge design variable since it is already bounded by the exit gauge lower limit constraint ($g3$) and the elongation lower limit constraint ($g4$).

$P_{\text{WRB},\min} \le P_{\text{WRB}} \le P_{\text{WRB},\max}$ — Work roll bending limits

$P_{\text{BUB},\min} \le P_{\text{BUB}} \le P_{\text{BUB},\max}$ — Backup roll bending limits

$C_{\text{WR},\min} \le C_{\text{WR}} \le C_{\text{WR},\max}$ — Work roll crown limits

$C_{\text{BUR},\min} \le C_{\text{BUR}} \le C_{\text{BUR},\max}$ — Backup roll crown limits

$T_{\text{BUR},\min} \le T_{\text{BUR}} \le T_{\text{BUR},\max}$ — Backup roll taper limits

12.4.3 Results and Discussion for Temper Mill Productivity Optimization

12.4.3.1 Optimization Case 1 (Unassigned Roll Crowns)

As stated previously, computer packages are widely available for solving optimization problems, once care is taken in formulating them correctly. The results for the first case of this application are obtained using an optimization add-on module for a common spreadsheet application. The required strip crown and rolling-force calculations were also incorporated into the simple spreadsheet using surrogate (approximate) modeling techniques.

The parameters shown in Table 12.2 for case 1 of the optimization indicate the selection of a plate with narrow width (48 in.) and low nominal gauge (3⁄16 in.) relative to the overall product mix. The side bounds for the roll crowns indicate an allowable work roll crown range from 3 to 10 mils, a backup roll crown range from 3 to 5 mils, and a backup roll taper (chamfer) range from 0 to 4 mils/in. Note that the upper limits on the WRB and BUB forces are set to 25 tons/side and 250 tons/side, respectively. These values represent the midpoints of the actual roll bending control ranges. The rationale for doing this is to identify the roll crowns that will allow for maximum elongation at 50% of the total roll bending range.

This provides the mill operator with some flexibility in modifying the elongation and strip crown as needed for specific rolling conditions.

Following execution of the optimization program for the formulated problem with the side bounds assigned for case 1, the maximized cost function and the optimum design variable values are calculated, as shown in Table 12.3. As indicated, the cost function reflecting the percent elongation achieves a desirable 4%. Only the exit gauge and work roll crown design variables are optimized at values away from their side bound limits. The details of all assigned and calculated parameters for case 1, including constraint values, are indicated in Table 12.4.

12.4.3.2 Optimization Case 2 (Fixed-Roll Crowns)

Referring again to Table 12.2, the side bound values assigned to the design variables for the second case represent a much more difficult but typical task to assign mill setup parameters after roll crowns and tapers have already been established. For this second case, the plate width and entry gauge values reflect the maximum allowable for this mill (96 and ⅝ in., respectively). Side bounds on the work roll crown and backup roll crown design variables are fixed at 5 mils and 3 mils, respectively, and the backup roll taper is fixed at 3 mils/in. To reflect normal rolling conditions, the side bounds for the roll bending design variables are assigned to their physical limits.

TABLE 12.3
Cost Function and Design Variable Results for Temper Mill Cases 1 and 2

Case No.	Cost Function Elongation (%)	Exit Gauge (mils)	Work Roll Crown (mils)	Backup Roll Crown (mils)	Backup Roll Taper (mils/in.)	Work Roll Bending (tons/side)	Backup Roll Bending (tons/side)
1	4.00	181.9	5.1	3.0	4.0	25	250
2	3.81	600.2	Fixed at 5	Fixed at 3	Fixed at 3	50	500

TABLE 12.4
Temper Mill Productivity Optimization Details (Case 1)

Objective Function		Design Variables	
% Elongation (reduction)	4.00	Exit Gauge (mils)	181.9
		Work Roll Diameter Crown (mils)	5.1
		Backup Roll Diameter Crown (mils)	3.0
		Backup Roll Chamfer (mils/in)	4.0
		Work Roll Bending (tons/side)	25.0
		Backup Roll Bending (tons/side)	250.0
Parameters and Calculations Used for Constraints and Side Bounds			
Strip Width (in.)	48.00	Roll Width (in.)	106.00
Minimum AJSI Gauge (mils)	177.00	Work Roll Radius (in.)	9.50
Entry Gauge (mils)	189.50	Backup Roll Radius (in.)	22.00
Strip Exit Crown (mils)[a]	5.11	Maximum Work Roll Crown (mils)	10.00
Strip Exit Crown Ratio (%)	2.81	Minimum Work Roll Crown (mils)	3.00
Incoming Crown (mils)	1.50	Maximum Backup Roll Crown (mils)	5.00
Incoming Crown Ratio (%)	0.79	Minimum Backup Roll Crown (mils)	3.00
Elongation (%)	4.00	Maximum Backup Roll Chamfer (mils/in.)	4.00
Minimum Elongation (%)	2.00	Minimum Backup Roll Chamfer (mils/in.)	0.00
Maximum Elongation (%)	4.00	Maximum WR Bending (tons/side)	25.00
Strip Modulus (Mpsi)	4.04	Minimum WR Bending (tons/side)	0.00
Rolling Force (tons)[a]	735.54	Maximum BU Bending (tons/side)	250.00
Total Rolling Load (tons)	1285.54	Minimum BU Bending (tons/side)	0.00
Maximum Total Rolling Load (tons)	3750.00	Crown Ration Change Deadband (%)	3.00
Peak Roll Contact Stress (ksi)	108.21		
Allowable Roll Contact Stress (ksi)	200.00		

[a] Calculated using strip crown and rolling force models.

Following execution of the optimization problem, the maximized cost function and optimum design variable values reflected in Table 12.3 are generated for case 2. We can see that the percent elongation (cost function) cannot exceed 3.81% since both the work roll and backup roll bending forces assume their upper side bounds. Increasing the elongation further would mean that the strip-exit, crown ratio constraint would be violated because there is no way to prevent an enlargement of the strip crown due to increased mill deflection. Details of the parameter assignments and constraint values for case 2 are provided in Table 12.5.

This second case represents a much more common, but challenging, circumstance in which mill operators are unable to achieve target rolling productivities. Troubleshooting these types of problems and identifying maximum possible performance, however, cannot be done effectively by trial and error due to the difficulty, high production cost, and excessive time involved. Optimization applications, on the other hand, are limited only by the creativity of the designer and the needs of the product or process. Another important and useful optimization problem regarding temper mills is the prediction of optimum work roll crowns, backup roll crowns, and backup roll chamfers to suit a diverse product mix. A formulation for this particular optimization problem, using an efficient linear programming method, was published by Malik and Guo [4].

12.5 APPLICATION 2: ESTIMATING THE PROBABILITY OF ACHIEVING TARGET STRIP CROWN AND FLATNESS IN ROLLING (UNCERTAINTY QUANTIFICATION)

12.5.1 Objective in Determining Strip Flatness Probability

In the earlier discussion of UQ, it was mentioned that probabilistic constraints can be incorporated into mathematical optimization routines to create a powerful tool known as RBDO. The application discussed next provides an example of how to calculate the probability of achieving flat strip. The intention is for the reader to gain insight into how to create reliability-based optimization constraints and cost functions.

The Monte Carlo sampling technique was discussed previously as the standard tool for establishing the probability of a random event. In contrast, this application example uses an

TABLE 12.5
Temper Mill Productivity Optimization Details (Case 2)

Objective Function		Design Variables	
% Elongation (reduction)	3.81	Exit Gauge (mils)	600.2
		Work Roll Diameter Crown (mils)	5.0
		Backup Roll Diameter Crown (mils)	3.0
		Backup Roll Chamfer (mils/in.)	3.0
		Work Roll Bending (tons/side)	50.0
		Backup Roll Bending (tons/side)	500.0
Parameters and Calculations Used for Constraints and Side Bounds			
Strip Width (in.)	96.00	Roll Width (in.)	106.00
Minimum AISI Gauge (mils)	590.00	Work Roll Radius (in.)	9.50
Entry Gauge (mils)	624.00	Backup Roll Radius (in.)	22.00
Strip Exit Crown $(mils)_a$	0.70	Maximum Work Roll Crown (mils)	5.00
Strip Exit Crown Ratio (%)	0.12	Minimum Work Roll Crown (mils)	5.00
Incoming Crown (mils)	0.10	Maximum Backup Roll Crown (mils)	3.00
Incoming Crown Ratio (%)	0.02	Minimum Backup Roll Crown (mils)	3.00
Elongation (%)	3.81	Maximum Backup Roll Chamfer (mil/in.)	3.00
Minimum Elongation (%)	2.00	Minimum Backup Roll Chamfer (mil/in.)	3.00
Maximum Elongation (%)	4.00	Maximum WR Bending (tons/side)	50.00
Strip Modulus (Mpsi)	1.0049	Maximum WR Bending (tons/side)	0.00
Rolling Force (tons)[a]	1147.69	Maximum BU Bending (tons/side)	500.00
Total Rolling Load (tons)	2247.69	Minimum BU Bending (tons/side)	20.00
Maximum Total Rolling Load (tons)	3750.00	Crown Ration Change Deadband (%)	0.10
Peak Roll Contact Stress (ksi)	136.37		
Allowable Roll Contact Stress (ksi)	200.00		

[a] Calculated using strip crown and rolling force models.

TABLE 12.6
Random Variables Used in Calculating Probability of Achieving Strip Flatness

Random Variable	Description	Distribution	Type	Mean	Variance
X_1	Strip entry crown	Normal	Independent	0.0 mils	4.0×10^{-3} mils^2
X_2	Work roll diameter crown	Normal	Independent	10.0 mils	0.09 mils^2
X_3	Compressive yield strength	Normal	Independent	0.159 Mpsi	2.5×10^{-3} Mpsi^2
X_4	Work roll elastic modulus	Normal	Independent	30.0 Mpsi	0.25 Mpsi^2

approximate but more efficient method to calculate the probability of achieving target strip flatness on a single-stand, four-high mill. Since the strip flatness is directly related to the change in the crown ratio during rolling, the strip crown is the random output parameter that is to be quantified and used in the reliability analysis. The flatness reliability (probability of success) is related to the probability that the change in the strip crown ratio during rolling will not exceed certain limits that would produce edge-wave or center-buckle flatness defects.

12.5.2 Formulating the Strip Flatness Probability Problem

For the purpose of this example, the following four parameters are selected as random input variables. All other parameters, including those that significantly influence the strip crown and flatness, are assumed to be deterministic (known precisely) and are not discussed.

X_1: Strip entry crown (mils)
X_2: Work roll parabolic crown (mils)
X_3: Compressive yield strength of strip (Mpsi)
X_4: Work roll elastic modulus (Mpsi)

Each of these four random input variables is assumed to have a Normal (Gaussian) distribution, with estimated statistics as shown in Table 12.6. The variables are also assumed to be independent, since their evolutionary processes are considered to be unrelated. Random variables that are not independent, and are correlated, require additional treatment not considered here.

To aid in explaining how the probability of achieving strip flatness is calculated based on the four random input variables, it is useful to first return to the earlier discussion involving two generic random variables, Capacity, C and Demand, D. If one again thinks of Capacity as representing "strength" and Demand as representing "stress," then a *performance function*, $g(C, D)$, can be written as follows:

$$g(C, D) = C - D \tag{12.8}$$

Whenever $g(C, D)$ is negative, the Demand exceeds the Capacity and the process fails. This concept is illustrated in Figure 12.9, where $g(C, D)$ is indicated as a *limit state* threshold between the safe and failure random variable regions. The probability of failure, P_f, is calculated as the probability that $g(C, D)$ is less than zero, indicated symbolically as Prob $[g(C, D) < 0]$. Conversely, the probability of success (or the reliability) is $P = (1 - P_f)$. For linear limit state functions of normally distributed independent random variables, the reliability calculation is straightforward [5]:

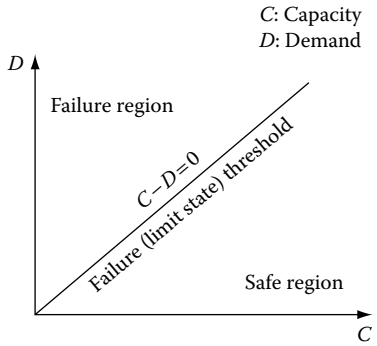


FIGURE 12.9 Limit state threshold separating failure region and safe region. (From Grandhi, R. 2003. *Reliability Analysis and Optimization Engineering*. Dayton, OH: Wright State University. With permission.)

$$P = \text{Prob}\,[g(C, D) > 0] = \Phi(\beta) \tag{12.9}$$

In Equation 12.9, Φ is the standard normal cumulative distribution function, for which computation tables are widely available [6]. The cumulative distribution function is the integral, or area under the curve, of the normal (Gaussian) probability density function. The term β in Equation 12.9 is known as a *reliability index* and is calculated as the ratio of the mean value of g to the standard deviation of g. Since $g(C, D)$ is linear, β is calculated directly from the mean and variance of the random variables C and D as follows.

$$\beta = \frac{\mu_g}{\sigma_g} = \frac{\mu_C - \mu_D}{\sqrt{\sigma_C^2 + \sigma_D^2}} \tag{12.10}$$

Although $\Phi(\beta)$ in Equation 12.9 determines the actual reliability, β itself provides a direct indication of reliability. A larger reliability index, β, implies a lower probability of failure.

When a nonlinear limit state function exists, a linear approximation to the actual nonlinear failure threshold is created, as illustrated in Figure 12.10. Note that in Figure 12.10, Capacity is represented as *R* (resistance), and Demand is represented by *S* (stress). The reliability index, β, for the nonlinear limit state function in Figure 12.10, is calculated as the shortest distance between the failure threshold and an origin created by normalizing the random variables to have zero mean and unit variance. In this nonlinear limit state function case, an iterative procedure, such as the Hasofer-Lind method, is used to calculate the reliability index [7]. The same approach applies when more than two random variables are considered, such as the four identified in Table 12.6 for this rolling application.

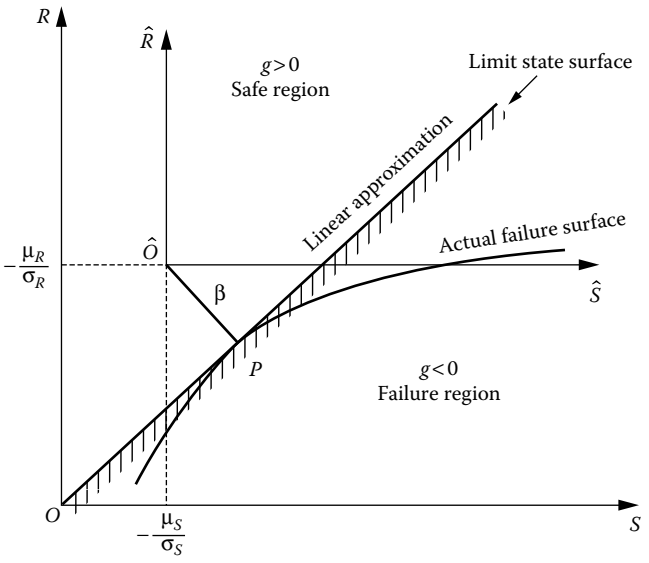


FIGURE 12.10 Linear approximation of nonlinear limit state threshold. (From Grandhi, R. 2003 *Reliability Analysis and Optimization Engineering*. Dayton, OH: Wright State University. With permission.)

12.5.3 Limit State Functions for Flatness Reliability

Based on the preceding discussion, two limit state performance functions for the flatness reliability analysis can be generated by imposing upper and lower limits on the strip exit crown ratios. A lower crown ratio limit, CR_{min}, is imposed to avoid center-buckle flatness problems, while an upper limit, CR_{max}, is imposed to prevent wavy-edge flatness problems and avoid excessive material yield loss (due to large strip crown). It should be noted that CR_{max}. is actually the smaller of the two upper limit crown ratios that represent thresholds for wavy-edge and yield-loss, respectively. The two performance functions can be written as follows:

$$g_1 = CR_{max} - CR \tag{12.11}$$

$$g_2 = CR - CR_{min} \tag{12.12}$$

In Equations 12.11 and 12.12, CR is the predicted strip exit crown ratio calculated using an available strip crown model that can accommodate the random input variables. Note that the performance functions are nonlinear in terms of the random input variables of Table 12.6. A positive value for both of the performance functions indicates that the strip exit crown ratio is in the safe random variable domain. If either performance function is negative, the strip exit crown ratio is in the failed random variable domain, due to a limit imposed by either CR_{max} or CR_{min}. These performance functions, together with the distribution information for the random variables in Table 12.6, can be used to perform a reliability analysis of the strip exit crown using the Hasofer-Lind method.

12.5.4 Results and Discussion for Strip Flatness Probability

12.5.4.1 Reliabilities of *g*1 and *g*2

Using the Hasofer-Lind method to calculate the probability of satisfying the performance functions *g*1 and *g*2 in Equations 12.11 and 12.12, the respective reliability indices, β_{HL1} and β_{HL2}, can be calculated as 1.3534 and 0.7677. Using a cumulative density distribution table for standard normal random variables, estimates of the reliabilities of *g*1 and *g*2 are then obtained as 91.1% and 77.9%, respectively. These statistics indicate that the probability of achieving flat strip because wavy edge *does not* occur is 91.1%, while the probability of achieving flat strip because center-buckle *does not* occur is 77.9%. Failure due to the random input parameters, therefore, would most likely be manifested in a center-buckle strip flatness defect.

12.5.4.2 System Reliability

The next task is to calculate the overall *system reliability*, or the total probability that neither wavy-edge nor center-buckle flatness defects occur. Several techniques are available to calculate the system reliability, but the most straightforward method here is to use set theory [8].

The overall system reliability is calculated using Equation 12.13. It represents the probability of not realizing wavy-edge *and* not realizing center-buckling condition. If event *A* represents failure due to wavy-edge condition and event *B* represents failure due to center-buckling, then using set theory and the fact that events *A* and *B* are mutually exclusive, the overall system reliability (of achieving flat strip) is calculated as follows:

$$\begin{aligned} \text{System reliability} &= P(\overline{A} \cap \overline{B}) = P(\overline{A \cup B}) \\ &= 1 - P(A \cup B) = 1 - [P(A) + P(B)] \\ &= 1 - (0.089 + 0.221) = 0.69 \text{ or } 69\%, \end{aligned} \tag{12.13}$$

where

$P(A)$ = Probability of event *A*, or the probability of wavy-edge = 1 − 0.911 = 0.089;

$P(B)$ = Probability of event *B*, or the probability of center-buckle = 1 − 0.779 = 0.221;

and

$P(\overline{X})$ = Complement of probability of event X, or probability of not achieving event X.

As a result, the probability that the strip meets flatness requirements on this particular mill, given the variability of the rolling parameters in Table 12.6, is only 69%. Needless to say, measures to reduce parameter variability or implement improve flatness control devices would be needed. The Hasofer–Lind algorithm to calculate the reliability of specific performance functions, such as those used here for strip-crown ratio, can provide insight into the sensitivity of the reliability with respect to each random variable. Information regarding which operating parameters need to be addressed in the rolling process is then obtained. Further reading on this subject is recommended (see [2,3]).

12.6 SUMMARY

This chapter has introduced the benefits of the mathematical optimization procedure and demonstrated its application to maximize the productivity of a four-high mill used for temper-rolling carbon steel plate. The subjects of UQ and reliability analysis have been introduced to facilitate understanding of the detrimental effects that random variations pose in rolling operations. Application of these reliability-based methods was demonstrated by estimating the probability of achieving adequate strip flatness on a four-high mill. By integrating reliability-based constraint formulations into mathematical optimization routines, users can exploit the effective process improvement tool RBDO.

ACKNOWLEDGMENTS

The National Science Foundation is acknowledged for supporting this work (Award No. 0758539).

REFERENCES

1. Arora, J. S. 1989. Optimum design problem formulation. In *Introduction to Optimum Design*, J. Holman (ed.), pp. 32–33. New York: McGraw-Hill.
2. Choi, S., Grandhi, R., and Canfield, R. 2006. *Reliability-Based Structural Design*. London: Springer-Verlag.
3. Halder, A., and Mahadevan, S. 2000. *Reliability Assessment Using the Stochastic Finite Element Method*. New York: John Wiley & Sons.
4. Malik, A. S., and Guo, R. M. 2003. Roll profile optimization using the linear programming method. *AISE Steel Technology* 80(4): 46–52.
5. Grandhi, R. 2003. *Reliability Analysis and Optimization in Engineering*. Dayton, OH: Wright State University.
6. Box, G. E. et al. 1978. *Statistics for Experimenters*. New York: John Wiley & Sons.
7. Hasofer, A. M., and Lind, N. C. 1974. Exact and invariant second-moment code format. *Journal of the Engineering Mechanics Division, ASCE* 100(1): 111–121.
8. Christensen, P. T., and Murotsu, Y. 1986. *Application of Structural Systems Reliability Theory*. Heidelberg: Springer-Verlag.
9. Malik, A. and Grandhi, R. 2007. A computational method to predict strip profile in rolling mills. *Journal of Materials Processing Technology* 206: 263–274.

13 Simulation for the Dynamic Behavior of Strips Running on Hot Run-Out Tables

Yuji Ohara, Shin-ichiro Aoe, Hiromasa Hayashi, and Kazushige Ishino

CONTENTS

13.1 Introduction 155
13.2 Theory 156
13.2.1 Theoretical Derivation of Maximum Stable Threading Speed on ROT 156
13.2.1.1 Steady-State Equation of Motion for Strip Traveling on ROT 156
13.2.2 Theorem of Equivalence Between Dynamic Characteristics of Strip on ROT and Buckling Phenomenon (Theory of Maximum Stable Threading Speed for ROT) 156
13.3 Experiments 157
13.3.1 Experimental Verification of Maximum Stable Threading Speed Using Run-Out Simulator 157
13.3.1.1 Run-Out Simulator and Similarity Law 157
13.3.1.2 Experimental Conditions and Experimental Results 157
13.4 Numerical Simulation 158
13.4.1 ROT Strip Travel Simulation 158
13.5 Discussion 159
13.5.1 Current Status of Maximum Threading Speed at Actual ROT and Discussion 159
13.6 Conclusions 159
References 159

13.1 INTRODUCTION

In the hot-rolling process, comparatively thin strips travel at high speed on the run-out table (ROT). The strip is run without tension during its threading and tailing out. Various defects—termed folded defect in head (Figure 13.1) and folded defect in middle (Figure 13.2)—caused by treading instability in this process have become a chronic problem. When a folded defect occurs in the head end or middle of a strip and is folded under by the coiler pinch roll, the affected part must be cut and discarded in the next process, which reduces product yield. If threading becomes extremely unstable, there are cases where the head end fails to reach the coiler, resulting in serious trouble and long downtime.

Therefore, on the operational side, the maximum threading and rolling speeds are commonly established based on operating practice. However, this impedes higher productivity. In addition, the slab heating temperature is set high to compensate for temperature drop at the head end due to the threading speed restriction, and this increases energy unit consumption. On the other hand, on the equipment/control side, much labor is devoted to maintenance to ensure that the level and wear condition of ROT rollers and guides, speed deviations in the respective zones, and other conditions are kept within the control range, which is also set based on experience. Although a variety of countermeasures to

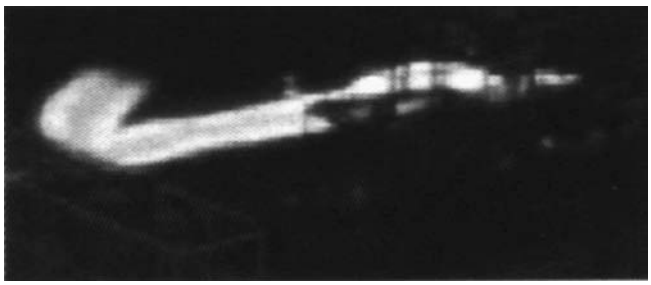


FIGURE 13.1 Folded defect in head.

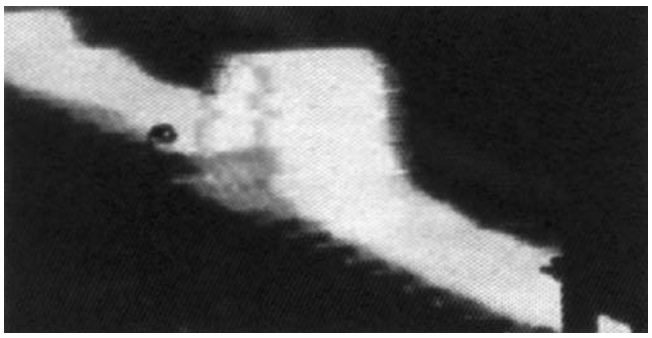


FIGURE 13.2 Folded defect in middle.

stabilize threading have been proposed since an early date, complete stabilization has not been achieved. Moreover, the various kinds of operational and equipment/control restrictions mentioned above, which were established empirically, are not clearly justified.

Among the reasons for this are (1) no guiding principle that enables a clear-cut, rational explanation of unstable strip travel behavior on the ROT has been proposed, and (2) verification and optimization of countermeasures for unstable threading phenomena, which occur under high-speed, unsteady conditions using actual equipment is difficult. Thus, it would seem that the root cause of this problem is the lack of experimental and numerical simulation techniques for reproducing the dynamic characteristics of strip travel on the ROT.

Kinematic model of traveling strips on the ROT is well expressed in a principle for the dynamic characteristics of belt or chain, and some has been reported [1–3]. But these have not provided practical ways to stabilize threading yet, because of complicated mechanical and operational conditions in real ROT strip mills.

In this chapter, first, the maximum stable threading speed on the ROT is derived theoretically by considering the dynamic characteristics of strips traveling on the ROT in hot strip mills. Next, the theoretical results are verified experimentally using a run-out simulator (ROS), which is capable of reproducing experimentally the dynamic characteristics of strip travel on the ROT. Also, an ROT strip travel simulation model capable of reproducing threading phenomena on a computer is described. Based on these results, the maximum stable threading speed at actual ROT equipment is discussed.

13.2 THEORY

13.2.1 Theoretical Derivation of Maximum Stable Threading Speed on ROT

13.2.1.1 Steady-State Equation of Motion for Strip Traveling on ROT

When the equation of motion for a strip traveling steadily on an ROT is formulated assuming very slight deformation, the result is expressed by Equation 13.1:

$$\frac{\partial^2}{\partial x^2} EI \frac{\partial^2 w}{\partial x^2} + \frac{D}{Dt} \rho A \frac{Dw}{Dt} = F, \quad \frac{D}{Dt} = \frac{\partial}{\partial t} + v \frac{\partial}{\partial x} \tag{13.1}$$

where

w = deformation of strip in vertical direction
E = Young's modulus
I = second moment of area
ρ = density of strip
A = cross-sectional area of strip
F = distributed load in vertical direction
D/Dt = material differentiation
v = strip velocity

Considering the case where the cross section is uniform in the line direction, the equation of motion for strip shown in Equation 13.2 can be obtained from Equation 13.1:

$$EI \frac{\partial^4 w}{\partial x^4} + \rho A \frac{\partial^2 w}{\partial t^2} + 2\rho A v \frac{\partial^2 w}{\partial t \partial x} + \rho A v^2 \frac{\partial^2 w}{\partial x^2} = F \tag{13.2}$$

In Equation 13.2, the first term on the left-hand side is a bending stiffness term, the second term is inertia force in the vertical direction, the third term is the Coriolis force, and the fourth term is a centrifugal force term. Considering the steady state (time derivative term = 0), the equation of motion for the steady state of a strip obtained from Equation 13.2 is expressed by Equation 13.3:

$$EI \frac{d^4 w}{dx^4} + \rho A v^2 \frac{d^2 w}{dx^2} = F \tag{13.3}$$

13.2.2 Theorem of Equivalence Between Dynamic Characteristics of Strip on ROT and Buckling Phenomenon (Theory of Maximum Stable Threading Speed for ROT)

The equation for the deformation of a beam compressed by compressive load P is expressed by Equation 13.4 [4]:

$$EI \frac{d^4 w}{dx^4} + P \frac{d^2 w}{dx^2} = F \tag{13.4}$$

Equation 13.4 expresses the buckling phenomenon (elastic instability phenomenon). Comparing Equations 13.3 and 13.4, if the second term in Equation 13.3, $\rho A v^2$, can be considered to be the compressive load P in Equation 13.4, the two equations become completely identical. In other words, the unstable phenomena (dynamic characteristics) occurring in a strip traveling on the ROT can be considered to be a buckling phenomenon in which a compressive load, $\rho A v^2$, acts on the strip. This is the theorem of equivalence between the dynamic characteristics of strip on the ROT and the buckling phenomenon. The concept of this theorem is shown in Figure 13.3. The compressive force, $\rho A v^2$, is termed the apparent compressive force due to centrifugal force (inertia pressure force).

According to the buckling theory based on Equation 13.4, a specific compressive load, called the Euler buckling load, P_c, exists, and if the compressive load, P, exceeds the buckling load, P_c, a buckling phenomenon will occur and the

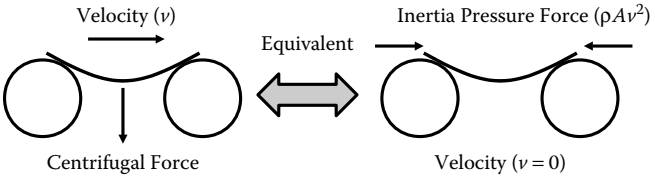


FIGURE 13.3 Equivalent theorem.

beam will display large deformation. Assuming this is also applicable to the process of running the strips on the ROT based on Equation 13.3, the process will be stable when the inertia pressure force, $\rho A v^2$, is smaller than the specific inertia pressure force, $\rho A v_c^2$, and conversely, when the inertia pressure force, $\rho A v^2$, is larger than the specific inertial pressure force, $\rho A v_c^2$, a loop or loops will be generated in the strip, and strip travel will become unstable. Here, v_c is the specific strip velocity obtained from Equation 13.3 for the buckling load, P_c, in Equation 13.4 and will be termed the critical strip velocity in the following. Using the equivalence theorem for the dynamic characteristics of strips on the ROT and the buckling phenomenon, the relation between the buckling load, P_c, and the critical strip velocity, v_c, is expressed by Equation 13.5:

$$P_c = \rho A v_c^2 \tag{13.5}$$

Equation 13.5 expresses the guiding principle for the dynamic characteristics of strips on the ROT.

Using Equation 13.5, we will now attempt to calculate the critical strip velocity for the problem of an ROT in which the table rolls are arranged at an equal pitch interval, L, which represents the simplest form of ROT. The buckling load in this problem is the same as the buckling load when a beam of length, L, is simply supported at its two ends and is expressed by Equation 13.6 [4]:

$$P_c = EI\left(\frac{\pi}{L}\right)^2 \tag{13.6}$$

When Equation 13.6 is substituted into Equation 13.5, the critical strip velocity for an ROT with an equal roll pitch is obtained, as expressed by Equation 13.7:

$$v_c = \frac{\pi}{L}\sqrt{\frac{EI}{\rho A}} \tag{13.7}$$

Actual ROT strip travel problems are not as simple as the problem described above; for example, the roll pitch may not be uniform, guides are used, the second moment of the area is not uniform, and the object is not a two-dimensional beam, but a three-dimensional strip. Nevertheless, if the buckling load can be obtained experimentally or by applying a general structural analysis code, it is possible to obtain the critical strip velocity by using the equivalence theorem expressed by Equation 13.5.

13.3 EXPERIMENTS

13.3.1 Experimental Verification of Maximum Stable Threading Speed Using Run-Out Simulator

13.3.1.1 Run-Out Simulator and Similarity Law

Figure 13.4 shows the ROS. The ROS is an experimental device with a scale of one-tenth that of the actual ROT, in which sheets are discharged from the work rolls and travel

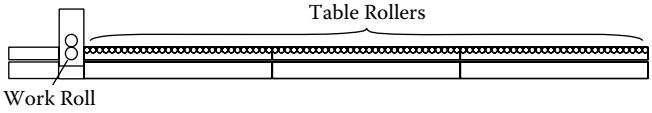


FIGURE 13.4 Run-out simulator.

over groups of transport rolls simulating table rolls, in the same manner as the actual machine. Because the ROS has a scale of one-tenth that of the actual machine, it is necessary to introduce a similarity law for ROT threading phenomena to ensure consistency with actual machines. Assuming that the distributed load, F, in the equation of motion shown in Equation 13.1 comprises the friction force of the table rolls, the aerodynamic force acting on the strip, and the weight of the strip, the equation of motion for the strip shown in Equation 13.8 is derived:

$$\rho A\frac{D^2 w}{Dt^2} + EI\frac{\partial^4 w}{\partial x^4} - \mu\rho A g\frac{\partial}{\partial x}x\frac{\partial w}{\partial x} + \frac{1}{2}C_L\rho_a W v^2\frac{\partial w}{\partial x} - \rho A g = 0 \tag{13.8}$$

where

μ = coefficient of friction
g = acceleration due to gravity
C_L = coefficient of lift
ρ_a = density of air
W = strip width

When Equation 13.8 is nondimensionalized, the nondimensional equation of motion for strip shown in Equation 13.9 is obtained:

$$\frac{D^2\omega}{D\tau^2} + \alpha\frac{\partial^4\omega}{\partial\xi^4} - \beta\frac{\partial}{\partial\xi}\xi\frac{\partial\omega}{\partial\xi} + \frac{1}{2}C_L\gamma\frac{\partial\omega}{\partial\xi} - \delta = 0 \tag{13.9}$$

where

$$\alpha = \frac{EI}{\rho A v^2 L^2},\ \beta = \frac{\mu g L}{v^2},\ \gamma = \frac{\rho_a W L}{\rho A},\ \delta = \frac{gL}{v^2},$$
$$\xi = \frac{x}{L},\ \tau = \frac{v}{L}t,\ \omega = \frac{w}{L}. \tag{13.10}$$

L is a representative length (e.g., roll pitch). The nondimensional parameters α, β, γ, and δ mean (stiffness)/(inertia force), (force of friction)/(inertia force), (aerodynamic force)/(inertia force), and (gravity)/(inertia force), respectively. On the assumption that all of these nondimensional parameters are the same in the actual ROT and the ROS, the dynamic characteristics of the strip in the two are also the same (law of similarity).

13.3.1.2 Experimental Conditions and Experimental Results

The purpose of this experiment is to verify experimentally the theory of the maximum stable threading speed of ROT. This means that parameter, α, is the most important parameter. In this experiment, the critical strip velocity, v_c, for the ROT

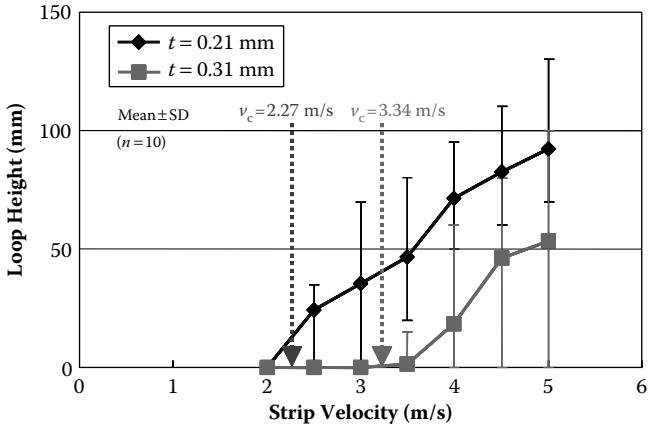


FIGURE 13.5 Experiment results.

was obtained experimentally by selecting two levels of strip thickness, considering the law of similarity with the operating range in the actual machine, and varying the strip velocity. Figure 13.5 shows the experimental results. The *x*-axis is the strip velocity, and the *y*-axis is the maximum value of loop height. The critical strip velocity for the respective strip thicknesses obtained from Equation 13.7 is used as a boundary value. From Figure 13.5, it can be understood that threading is stable when the strip velocity is smaller than this critical velocity, and a loop(s) occurs and threading becomes unstable when the strip velocity is larger than this value. The height of the loop also tends to increase with strip velocity. Thus, the theoretical values obtained using Equation 13.7 and the experimental results are in good agreement, demonstrating that the theoretically derived maximum stable threading speed is practically valid.

13.4 NUMERICAL SIMULATION

13.4.1 ROT Strip Travel Simulation

The authors developed the ROT strip travel simulation model shown in Figure 13.6 based on multibody dynamics. The strip model is a discrete model comprising multiple rigid bodies and springs corresponding to bending. It is possible to consider the force of impact and force of friction between the strip and the table rolls, aerodynamic force, and other external forces acting on the strip. With the conventional methodology, these forces could only be evaluated by actual-machine experiments. In contrast, this model makes it possible to optimize

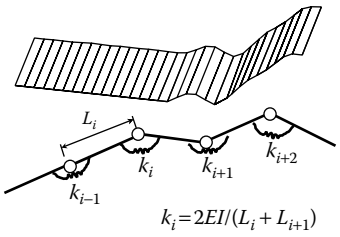


FIGURE 13.6 ROT strip running simulation model.

design specifications on the computer to some extent and thus enables a broad reduction in the development period.

Figure 13.7 shows the strip travel behavior in a numerical simulation using the ROT simulation model described above. Under these conditions, the strip length in the ROT conditions is expressed by conjoining multiple rigid bodies having lengths of 10-mm. Because the radii of curvature of the generated loops are sufficiently large in comparison with the 10-mm length of the rigid bodies, the strip shape can be expressed naturally, as can be understood from its appearance here. The arrows in the figure show the calculated results of external forces acting on the strip as vector expressions.

In order to verify the theory of maximum stable threading speed of ROT in an ROT simulation, the effect of strip velocity on the maximum value of loop height was evaluated. The results are shown in Figure 13.8. The critical strip velocity was approximately the same as the theoretical value given by Equation 13.7. It can also be understood that the size of the loop height in the unstable threading region shows relatively good agreement when compared with the experimental results in Figure 13.5. Thus, using the ROT simulation, it is possible to obtain the critical strip velocity, and the behavior in the unstable threading region, which is not possible to analyze theoretically, can also be calculated.

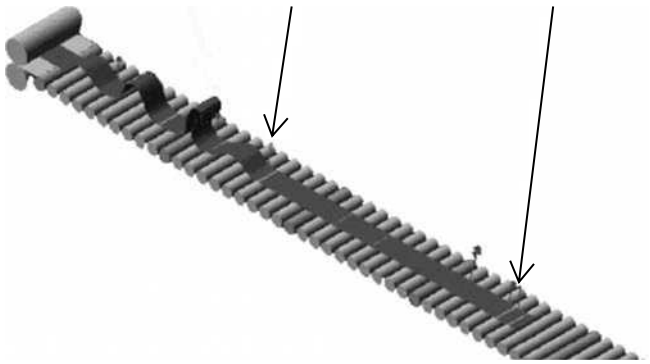


FIGURE 13.7 Appearance of multibody dynamics simulation ($t = 0.21$ mm, $v = 4.0$ m/s).

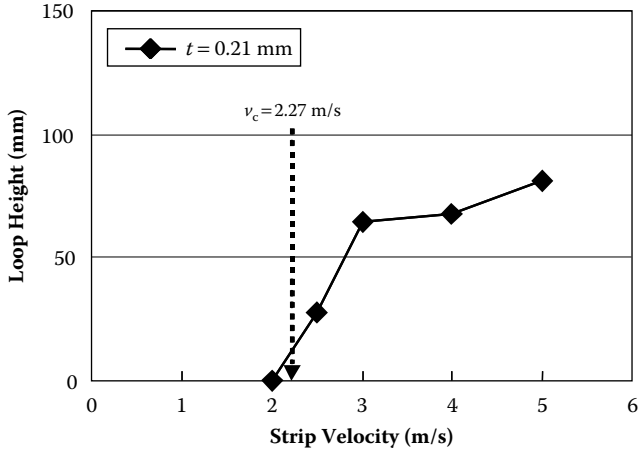


FIGURE 13.8 Simulation results.

13.5 DISCUSSION

13.5.1 Current Status of Maximum Threading Speed at Actual ROT

As described above, the maximum stable threading speed was clarified by theoretical, experimental, and numerical analyses. This chapter summarized the relationship between the thin product threading velocity and equipment conditions at commercial hot strip mills at JFE Steel Corporation under the current condition. Figure 13.9 shows the head end threading speed of thin products relative to the table roll pitch of ROT at the commercial lines and the theoretical maximum critical strip velocity according to Equation 13.7. These results have been normalized with mill A as a standard (=1.0). The head end threading speed in the actual mills decreases as the table-roll pitch increases. In some cases when increasing the mill speed is important for achieving a higher production rate, it is possible to exceed the theoretical critical speed by allowing some light fluttering of the strip. On the other hand there are also some mills (mills B and C) where the threading speed is somewhat lower than the theoretical critical velocity. Where these mills are concerned, it is possible that the threading speed is affected by equipment-related problems such as table-roll level control, the existence of sensor zones where the roll pitch is partially larger, or similar factors.

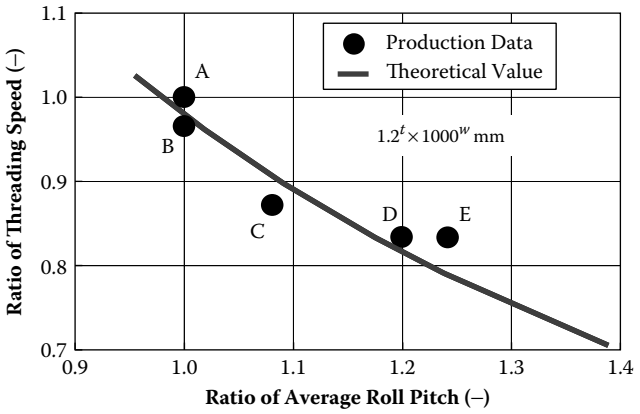


FIGURE 13.9 Relationships between roll pitch and threading speed.

Using the ROT strip travel simulation model introduced in "ROT Strip Travel Simulation," the effect of differences in the table-roll level on threading instability and the effect of partially changing the roll pitch, have been quantified and are being used as guidelines for equipment improvement and maintenance standards for actual equipment.

13.6 CONCLUSIONS

The dynamic characteristics of strips traveling on ROTs in hot strip mills were studied by theoretical, experimental, and by numerical analyses. The following conclusions were obtained.

1. A theory of the maximum stable threading speed on ROT, which explains the dynamic characteristics (threading instability) of strips traveling on the ROT, was developed, and the critical strip velocity for ROT was calculated.
2. The validity of the maximum stable threading speed theory was confirmed using an ROS, which reproduces experimentally the dynamic characteristics of strip travel on the ROT, and good agreement with a newly developed numerical simulation model of strip travel was confirmed.
3. The head end threading speed at commercial hot strip mills at JFE Steel Corporation and the theoretical critical velocity were compared and discussed.
4. The results of this research are being actively used in studies of equipment improvement at hot strip mill ROTs and as maintenance guidelines.

REFERENCES

1. C.D. Mote, Jr. 2005. A study of band saw vibrations. *Journal of the Franklin Institute* 279(6): 430–445.
2. A.G. Ulsoy. 1986. Coupling between spans in the vibration of axially moving materials. *Journal of Vibration, Acoustic, Stress, and Reliability in Design* 108: 207–212.
3. K. Nishinari. 1998. Discrete modeling of a string and analysis of a loop solution. *Transactions of ASME: Journal of Applied Mechanics* 65: 737–747.
4. S.P. Timoshenko and J.M. Gere. 1961. *Theory of Elastic Stability*. New York: McGraw-Hill.

14 Laminar Flow-Cooling of Wide Heavy-Thickness Strip in a Hot Rolling Mill

Qiulin Yu

CONTENTS

14.1 Introduction 161
14.2 Background 162
14.3 Mill Layout and Equipment 162
14.3.1 Laminar Cooling System 162
14.3.2 Modification of Hardware 163
14.4 Formulation of Energy Balance 163
14.4.1 Increment of Internal Energy 164
14.4.2 Heat of Phase Transformation 164
14.4.3 Heat Loss by Radiation 164
14.4.4 Heat Loss by Convection 165
14.5 Temperature Model 165
14.5.1 Two-Dimensional Analytical Model 165
14.5.2 Boundary Conditions 165
14.5.3 Solutions 165
14.6 Mechanical Properties 166
14.7 Critical Temperature Differences of Strip Canoeing 166
14.8 Laminar Flow Distribution 167
14.8.1 Crossbow at Cut-to-Length Line 167
14.8.2 Strip Dimension versus Crossbow 168
14.8.3 Ratio of Bottom Flow to Top Flow 168
14.8.4 Yield Strength 169
14.9 Examination of Heat Removal 169
14.10 Discussion 170
14.11 Summary 170
Acknowledgments 170
References 170

14.1 INTRODUCTION

In recent years, the demand for wide heavy-thickness coils has increased dramatically. The demand comes mainly from projects of spiral-seam and straight-seam steel pipes used for piles, water, and natural gas lines. The most common sizes are 15.5–25.4 mm thick and 1220–2440 mm wide. Generally, carbon steel and low grades of high strength, low alloy (HSLA) steel are employed for piles and water lines. Medium and high grades of HSLA steel are adopted for natural gas lines.

This chapter is a revised version of the article published in Iron and Steel Technology (Yu et al. 2005) with permission. In this chapter, the laminar flow-cooling behavior of wide heavy-thickness is introduced. The intent is to provide a comprehensive description in minimizing transverse canoe (or crossbow) and improving longitudinal uniformity of mechanical properties, which includes modification of a laminar flow-cooling system, analyses of cooling processes, and prediction of mechanical properties of materials.

The present study found that the ratio of the bottom laminar flow rate to the top laminar flow rate has a significant influence on canoe (or crossbow). To understand its mechanism, a control model with proper ratios of the bottom flow rate to the top flow rate is developed. Three basic laminar flow patterns are introduced. Combining the heat-transfer

formulation with phase transformation, mechanical properties of wide heavy-thickness coils are predicted.

To help prevent canoe, bottom-cooling headers with double-set nozzles have been invented and mounted on the run-out table (ROT) of the 4-h reversing Steckel mill at Tuscaloosa. The effectiveness of the model to minimize transverse canoe (or crossbow) and to improve longitudinal uniformity of mechanical properties was validated with the mill database.

14.2 BACKGROUND

Most hot mill laminar flow-cooling systems, upcoilers/downcoilers, and other pieces of equipment are constrained to a maximum coil thickness of 15.5 mm. For wide coils, heat removal per unit width is approximately proportional to the thickness under the same finishing and coiling temperatures. The cooling headers and their flow rates are designed with respect to a maximum thickness. When the finished gauge is greater than the maximum gauge capability of the laminar flow system, finishing speed must be reduced to achieve the required coiling temperature. This results in a decreased cooling rate and, therefore, a reduction in mechanical properties relative to the change in cooling rate. On the other hand, the torque of coilers is composed of three components: bending moment, tension moment, and lifting moment (for upcoilers). It is well known that the bending moment and tension moment are directly proportional to the square of the thickness and increase linearly with respect to width. For wide heavy-thickness coils, the torque of coilers increases dramatically.

Two outstanding problems occur frequently during rolling wide heavy-thickness coils. They are canoe (or crossbow) in the transverse direction and nonuniformity of mechanical properties in the longitudinal direction.

It is commonly observed that wide heavy-thickness coils experience poor cooling temperature performance. The main factors are:

- The strip is tailed out of the mill before coiling. Coil length is shorter than the length of the ROT.
- When the strip starts to be coiled, the speed of the strip on the ROT will increase due to the lead speed of the coiler.
- For wide coils, side sweeps take longer to blow laminar flow water off the top surface.
- There is a significant difference in temperature between the strip surface and middle thickness. The internal heat flux diffuses to the surface and leads to surface temperature rebound.

Nonuniform cooling across the width of the strip on the ROT affects strip flatness significantly (Nakata and Yoshida 1995). From the laminar flow trials; it was found that the ratio of the bottom laminar flow rate to the top laminar flow rate had a significant influence on canoe (or crossbow) of wide heavy-thickness coils. The result is different from light-thickness coils where canoe (or crossbow) is caused by tension and crown (Kaseda and Masui 1994).

In addition, nonuniform cooling will result in variation of mechanical properties through the coils. Nonuniformity of mechanical properties may cause coilers to exceed their torque limits. Consequently, coil cobble is inevitable due to overload trip or loss of cinch.

14.3 MILL LAYOUT AND EQUIPMENT

The four-high reversing Steckel mill at Tuscaloosa is capable of producing coils with dimensions of 4.0–25.4 mm and discrete plate with dimensions of 19–64 mm thick by 914–2590 mm wide. The associated equipment of the mill includes an equalizing furnace, vertical edger, main and inter-pass descaling headers, Steckel furnaces, crop shear, laminar flow cooling, upcoiler, and hot leveler. The layout of the laminar flow-cooling system is shown in Figure 14.1.

14.3.1 Laminar Cooling System

The laminar flow-cooling system is composed of seven banks. Each bank has six top headers over 4572 mm long and eight bottom headers over 6400 mm long. The space between all banks is 2743 mm, except for the space between banks 4 and 5, which are spaced 5486 mm apart. Side sweeps were mounted in the spaces between the banks to blow hot water and bubbles off the strip.

The top headers of each bank are controlled individually via rotating diverters. The diverters are designed in step mouths for fitting various widths and are rotated by air cylinders and chains. There are 38 nozzles rated at 75.7 l/min

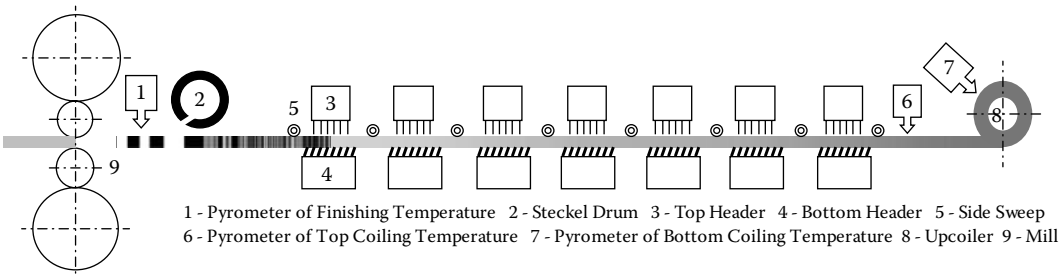


FIGURE 14.1 Layout of laminar flow-cooling system. (From Yu, Q. *Iron and Steel Technology* 2(8): 72–81. With permission.)

distributed along each top header 70 mm apart. The spray coverage is 2660 mm. The bottom headers of each bank are divided into three groups in a 3-2-3 configuration. Each group is controlled via a single valve. There are 30 nozzles rated for 36 l/min at 103,421 Pa. They are distributed along each bottom header at 90-mm intervals. To minimize overcooling the strips caused by the water streams, the nozzles on adjacent headers are offset by half of the distance between the nozzles for both top and bottom headers.

Seven pumps supply water to the laminar flow system. Water flow is rated at 26,498 l/min per bank. The top flow rate is 17,261 l/min per bank and 2877 l/min per header, and the bottom flow rate is 8631 l/min per bank and 1079 l/min per header.

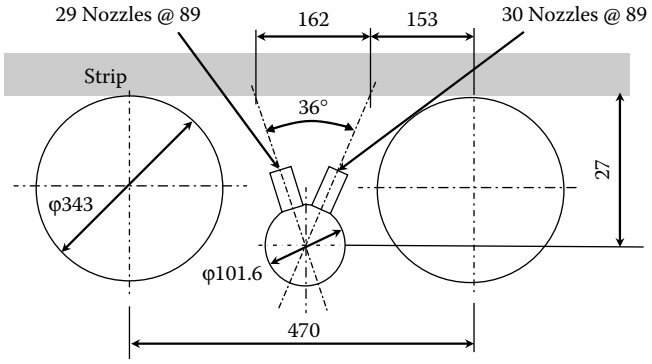


FIGURE 14.2 Modified bottom headers with double set of nozzles (dimension unit: mm). (From Yu, Q. *Iron and Steel Technology* 2(8): 72–81. With permission.)

14.3.2 Modification of Hardware

Since the Tuscaloosa plant added the melt shop and casting facilities in 1996, the capacity of production has doubled. The original laminar flow system did not have sufficient cooling capacity to support the entire product range. A second water-cooling tower was immediately installed after the startup of the melt shop and caster.

It was recognized that canoe in the strip was generated after laminar flow cooling, and test failure rate increased significantly. After technical review, it was concluded that the bottom flow rate was insufficient for producing wide heavy-thickness coils. Four major factors directly contributed to the defects and failures:

1. ROT temperature increased significantly due to increased production.
2. Rolling speed was increased to meet slab pace.
3. The top spray nozzles were melted, clogged, or missing. The bottom headers were filled with debris and scale, which produced a disrupted water jet pattern.
4. Water quality was poor due to shorter cycle time.

The last issue was resolved quickly by refilling industrial water frequently and adding two sand filters. The first three factors required engineering solutions. To clean the headers, all headers had caps machined and mounted on the operation side. The headers could then be flushed regularly with laminar flow water. The nozzles were replaced and flushed during down days.

Originally, side sweeps were installed on the operator side of the ROT. This caused edge waves on the operator side due to thermal shrinkage on the drive side. To eliminate the thermal edge waves, the side sweeps were reinstalled alternatively from the operator side to drive side, bank by bank.

A review of the original design showed that the top total flow rate was twice that of the bottom total flow rate. The top and bottom headers share the same main pipe, and the water pressure of the top headers must be set at a certain level to prevent saturation. It was not possible to increase the bottom flow rate via pressure adjustment. The height of the bottom water stream is restricted to 150–200 mm for minimizing cold edges that are caused by the outside water stream. The remaining option was to increase the cooling efficiency of the bottom water by increasing the wet length. To achieve this, a double set of nozzles was installed on the bottom headers as shown in Figure 14.2.

After modification of the bottom headers in the first three banks, the Corus R&D team performed an audit. It was found that the difference in flow rates between banks with a double set of nozzles per header and a single set of nozzles per header varied from 17%–38%. It was also recognized that the pattern of six inlets was more uniform than the pattern of four inlets. The reason was that the bottom headers were fed from the drive side, which produced a distinctive wedge-shaped spray pattern across the width of the roller table. The required modification was to change four inlets to six inlets for all bottom headers.

The cooling efficiency of the bottom headers was examined by cooling the same size coils with dimensions 19 mm × 2438 mm under the same finishing temperature and the same rolling speed. The same header pattern was also selected for all coils. The result indicated that the bottom surface temperature of the strip with the double set of nozzles was 27°C–55°C colder than that with a single set of nozzles. The efficiency was increased by 10%–22%.

In addition, a trim header with half the flow rate of the top header was installed for trimming cooling temperature at position 5 of bank 7. This header is more suitable to light gauge coils.

14.4 FORMULATION OF ENERGY BALANCE

Other than heat conduction between the bottom strip surface and table rolls, the major types of heat diffusion are radiation of the strip surface and convection of air and water. According to the first law of thermodynamics, mathematical formulation of the energy balance from finishing to coiling can be written as

$$\Delta E = -Q_L + Q_W + Q_A + Q_R \quad (14.1)$$

where

ΔE = increment of internal energy between finishing and coiling
Q_L = heat of phase transformation
Q_R = heat loss caused by radiation
Q_W and Q_A = heat loss caused by water and air convection, respectively

14.4.1 Increment of Internal Energy

Although heat loss continues at finishing and coiling due to radiation and convection, transient enthalpy of the strip may be described by temperature, density, specific heat capacity, and volume, respectively. The increment of internal energy is written as

$$\Delta E = \int_V \rho c \Delta T_0 dV \quad (14.2)$$

where

$\Delta T_0 = T_0 - T_{l6}$
c = specific heat capacity (J/kg · K)
ρ = density (kg/m^3)
V = volume (m^3)
T_0 and T_{l6} = finishing and coiling temperatures (K)

Figure 14.3 shows specific heat capacity under various temperatures for two different grades of plain carbon steel, SAE1008 and 1025. Their difference is negligible, except for the phase transformation zone (line A_1). By means of separation of the data in the transformation zone, two different regression expressions can be obtained.

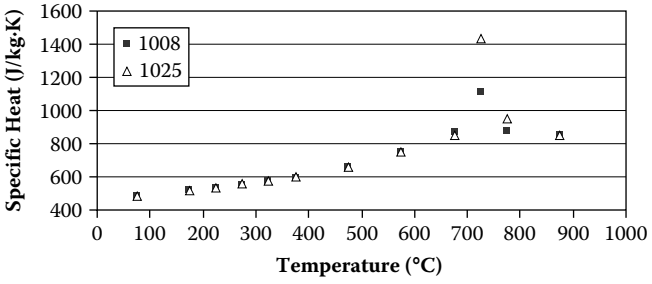


FIGURE 14.3 Specific heat capacity for SAE 1008 and 1025 under various temperatures. (From Yu, Q. *Iron and Steel Technology* 2(8): 72–81. With permission.)

Generally, finishing temperature is above A_3 and coiling temperature is below A_1. Phase transformation occurs between lines A_1 and A_3. Because phase transformation gradually appears from the surface to the centerline and generates greater heat for forming ferrite and pearlite phases, specific heat capacity shows a peak around A_1, as shown in Figure 14.3.

14.4.2 Heat of Phase Transformation

Under laminar flow cooling, austenite can transfer to ferrite, pearlite, and martensite phases. The heat of phase transformation is composed of the individual contribution from each transformation as (Sarmiento et al. 2000),

$$Q_L = \rho \int_V \left[H_F(T)\frac{dX_F}{d\tau} + H_P(T)\frac{dX_P}{d\tau} + H_M(T)\frac{dX_M}{d\tau} \right] dV \quad (14.3)$$

where

τ = time (s)
T = temperature (°C)
$H_F(T)$, $H_P(T)$ and $H_M(T)$ = heat of transformation from austenite to ferrite, pearlite, and martensite
X_F, X_P, and X_M = volume fraction austenite transformed to ferrite, pearlite, and martensite

For low-carbon and mild-carbon steels, the majority of microstructures are in the ferrite phase. When temperature falls to the range between 550°C and 600°C, the value of $H_F(T)$ is 5.71×10^4 J/kg. The heat generation of phase transformation can be simplified as

$$Q_L = \rho V H_F \quad (14.4)$$

14.4.3 Heat Loss by Radiation

Heat from the strip can be transferred not only via direct contact or flow convection, but also by radiation. Thermal radiation consists of a wide spectrum of electromagnetic waves between 0.76 and 360 μm. As long as the strip is finished at a temperature above environmental temperature, heat loss of radiation occurs.

According to the Stefan–Boltzmann law, heat loss due to radiation is given as follows:

$$Q_R = \int_{\tau_0}^{\tau_{l6}} A\varepsilon\eta(T_s(\tau)^4 - T_e^4)d\tau \quad (14.5)$$

where

A = area (m^2)
ε = emissivity
η = Stefan–Boltzman's constant, 5.67×10^{-8} (W/m^2 · K)
T_e = environmental temperature (K)
$T_s(\tau)$ = temperature of strip surface (K)
τ_0 and τ_{l6} = finishing and coiling time (s)

It is well known that emissivity is dependent on the temperature of the strip surface. When the temperature is between 593°C and 870°C, the emissivity is approximated as

$$\varepsilon = 0.205 + 2.277 \times 10^{-3} T_s - 1.755 \times 10^{-6} T_s^2 \quad (14.6)$$

where T_s = temperature of strip surface in °C.

If finishing and coiling temperatures are assumed to be 870°C and 593°C, respectively, the value for emissivity is averaged at 0.92.

14.4.4 Heat Loss by Convection

It is hard to distinguish heat losses caused by either air convection or laminar flow on the ROT. An experience model is given as follows:

$$Q_{\mathrm{A}} + Q_{\mathrm{W}} = \left(\sum_{i=1}^{7} \varphi_i A_i \Phi_i + Q \right) \tag{14.7}$$

where

Q = constant
φ_i = coefficient of regression
Φ_i = flow rate of the ith bank (l/min)

Coefficient A_i is related to the lateral circumference of the strip, time under cooling, strip width, and spray width of the header:

$$A_i = 2\frac{(h+w)}{1000}\frac{w}{w_{\mathrm{h}}}\Delta\tau_i \tag{14.8}$$

where

h = gauge (mm)
w = strip width (mm)
w_{h} = spray width of header
$\Delta\tau_i$ = time of strip passing the ith bank

Substituting Equations 14.2 and 14.4 through 14.7 into Equation 14.1 yields a linear equation with seven unknown coefficients, φ_i. Theoretically, the coefficients can be derived by using the rolling data for seven coils. When more than seven coils are rolled, the coefficients can be determined by a linear regression method.

Because Equation 14.7 does not consider any nonlinear items, the evaluation of model accuracy finds that the error is related to gauge and speed. To eliminate the error, the predicted value of heat loss caused by convection is modified as follows:

$$(Q_{\mathrm{A}} + Q_{\mathrm{W}})_{\mathrm{modified}} = f(h,s)\left(\sum_{i=1}^{7} \varphi_i A_i \Phi_i + Q \right) \tag{14.9}$$

where

$$f(h,s) = \left(0.2246 - 0.06566 \ln\frac{h}{s} \right)^{-1}$$

s = speed (m/min).

14.5 TEMPERATURE MODEL

For production of coils, the longitudinal distribution of temperature through the coils can be treated as uniform. Therefore, a two-dimensional temperature model is enough to simulate the thermal field in the transverse cross section. Of course, the temperatures at the head and tail are not uniform and not simulated by the model.

14.5.1 Two-Dimensional Analytical Model

Hot bands are considered to be homogeneous and isotropic. The two-dimensional unsteady heat transfer governing equation is written as

$$\frac{\partial T}{\partial \tau} = a\left(\frac{\partial^2 T}{\partial x^2} + \frac{\partial^2 T}{\partial y^2} \right) + \frac{q_v}{c\rho} \ (K/s) \tag{14.10}$$

where

x = coordinates in strip width direction (m)
y = coordinates in strip thickness direction (m)
$a = \dfrac{\lambda}{c\rho}$, thermal conductivity (m^2/s)
q_v = internal heat generated by phase transformation, (J/s)
λ = heat conductivity (W/m · K)

Thermal conductivity displays a discontinuous point at magnetic transformation temperature. Heat conductivity is divided into three regions: magnetic, nonmagnetic, and austenitic regions (Browne 1995). Heat conductivity can also be derived from thermal conductivity and specific heat capacity.

14.5.2 Boundary Conditions

Radiation and convection are the major modes of heat transfer on the strip surfaces. For a specific temperature range, boundary conditions can be expressed by the following formula:

$$\alpha(T_{\mathrm{k}} - T_{\mathrm{e}}) = -\lambda\left(\frac{\partial T}{\partial x_j} \right)_{\mathrm{k}} \tag{14.11}$$

where the subscripts are defined as follows;

k = strip side walls and surfaces
j = x- and y-coordinates

α is the heat transmission coefficient between the strip surface and ambient medium. The coefficient is a function of surface temperature. Determination of its value was introduced in detail in the previous study (Yu and Muncie 2003).

14.5.3 Solutions

From Equation 14.10, it can be seen that heat generation from phase transformation generally occurs through the thickness. The heat can be assumed to distribute uniformly everywhere. Utilizing the method of separation of variables and the method of composition, relative temperature to ambient temperature may be described as:

$$\theta(x,y,\tau) = \theta_0\left(\frac{\theta_{x\tau}}{\theta_0} \right)\left(\frac{\theta_{y\tau}}{\theta_0} \right) + \frac{q_v}{c\rho}\tau \tag{14.12}$$

where

$\theta = T - T_e$

$\theta_0 = T_0 - T_e$

$$\theta_{x\tau} = \sum_{i=1}^{\infty} \theta_0 \frac{2\sin\beta_{xi}}{\beta_{xi} + \sin\beta_{xi}\cos\beta_{xi}} \left(\cos\beta_{xi}\frac{2x}{w}\right) e^{-\beta_{xi}^2 F_{ox}}$$

$$\theta_{y\tau} = \sum_{i=1}^{\infty} \theta_0 \frac{2\sin\beta_{yi}}{\beta_{yi} + \sin\beta_{yi}\cos\beta_{yi}} \left(\cos\beta_{yi}\frac{2x}{h}\right) e^{-\beta_{yi}^2 F_{oy}}$$

$$\tan\beta_x = \frac{B_x}{\beta_x}$$

$$\tan\beta_y = \frac{B_y}{\beta_y}$$

T_0 = finishing temperature of strip

T_e = ambient temperature

Calculations of Biot indexes B_x and B_y and Fourier indexes F_{ox} and F_{oy} can be found from the previous study (Yu and Muncie 2003).

14.6 MECHANICAL PROPERTIES

Strength in steels arises from several mechanisms that usually contribute collectively to the observed mechanical properties. In fact, the gamma/alpha phase change allows for great variations in microstructures to be produced, so a wide range of mechanical properties can be obtained even in plain carbon steels. The additional use of metallic alloying elements, primarily as a result of their influence on the transformation, provides even greater control over microstructures, as well as benefits in mechanical properties.

The Steckel mill at Tuscaloosa produces products across a wide range of the strength spectrum, from low-yield strength (250 MPa) to a very high level (585 MPa). These mechanical properties are usually achieved by the combined use of several strengthening mechanisms. The five most important mechanisms are

1. Refinement of grain size
2. Solid solution strengthening by interstitial atoms
3. Solid solution strengthening by substitutional atoms
4. Dispersion strengthening, including lamellar and random dispersed structures (precipitates, etc.)
5. Work hardening

To establish a general model to cover the absolute contributions for yield strength from all mechanisms, the following extended Hall-Petch relationship (Bowker et al. 1993) is adopted:

$$\sigma_y = \sigma_0 + kd^{-1/2} + \sigma_s + \sigma_p + \sigma_d + \sigma_t \qquad (14.13)$$

where

σ_0 = the lattice resistance, or friction stress that opposes dislocation motion, and includes interstitial solid solution strengthening contributed by carbon and nitrogen remaining in solution; the suggested value is 70 N/mm^2

k = constant; for controlled rolled steel, the suggested value is 18.1 N/mm$^{3/2}$

d = the ferrite grain size, mm

σ_s = substitutional solid solution hardening; it has been suggested to equal 32(%Mn) + 84(%Si) + 38(%Cu) + 43(%Ni)

σ_p = dispersion hardening, which includes space between lamellar cementite and precipitates, etc.

σ_d = hardening due to the presence of dislocations that are generated from the rolling schedule below the Ar_3 or lower transformation temperature

σ_t = texture hardening

In Equation 14.13, laminar flow has a direct influence on grain size. Finer grain size results in a material with higher yield strength.

In practical application, the grain size can be determined approximately by cross points of the cooling curve calculated from Equation 14.12, with either the time–temperature transformation curves or continuous cooling transformation diagrams. The grain size can be measured using a microscope. Alternatively, the grain size can be calculated inversely using mechanical test results. As a result, the microstructures in hot rolling are predictable.

14.7 CRITICAL TEMPERATURE DIFFERENCES OF STRIP CANOEING

In normal production, it is undesirable for strip coiled by the upcoiler to exhibit canoe shape across the width. The first reason is that contact between the center of strip and ROT will generate scratches on the bottom surface. The second is that a canoe shape will accumulate water on the top surface and result in even worse shape. The third is that the canoe will become crossbow at the cut-to-length (CTL) line when decoiling upward. Light crossbow shape on the ROT is favorable. Therefore, the establishment of an analytical model to predict the critical temperature difference of transverse buckling is important to production.

By means of strength of materials, the critical temperature difference of transverse buckling is derived as follows:

$$\Delta T = \frac{4(1-\mu_b^2)\sigma_b}{E_b(\omega_b + \omega_t)} \qquad (14.14)$$

where

$\Delta T = T_b - T_t$

σ_b = yield strength of the bottom surface (Pa)

E_b = elastic modulus of the bottom surface (Pa)

μ_b = Poisson's ratio of the bottom surface

T_b and T_t = temperatures of the bottom and top surfaces (°C)

ω_b and ω_t = thermal expansion coefficients of the bottom and top surfaces (m/m · K)

Introducing thermal and mechanical properties of conversion coils made of American Society for Testing Materials (ASTM) 36 steel into Equation 14.14, the critical surface temperature difference is plotted in Figure 14.4.

From Figure 14.4, it can be seen that the critical surface temperature difference decreases with the increase of surface temperature. When finishing and coiling temperatures are 871°C and 593°C, respectively, their corresponding critical surface temperature differences are 37°C and 90°C, respectively.

The critical surface temperature difference is based on the yield point of the material. However, the strip canoe appears in the elastic deformation stage, which leads to a more rapid increase in strip canoe. Therefore, the temperature of the top surface is expected to be hotter than that of the bottom surface, but not over the limit with respect to the surface temperature. The closer the cooling headers are to the mill, the smaller the temperature difference is through the thickness. Generally, it is expected to aim for the bottom surface to be 25°C–50°C colder than the top surface. Sometimes, even if the bottom surface is colder than the top surface, canoe still occurs. This is because the canoe generated at the earlier banks could not be corrected by the later banks.

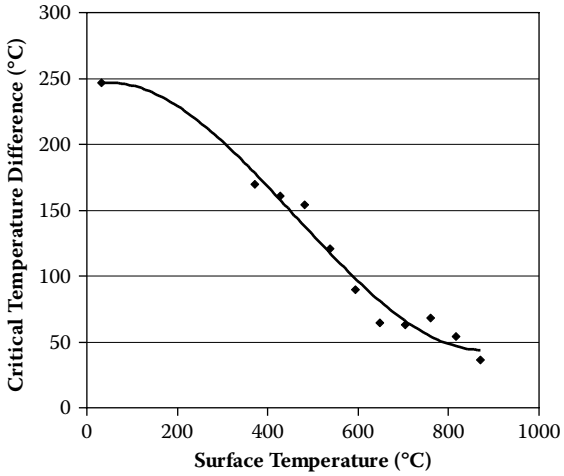


FIGURE 14.4 Critical surface temperature difference of ASTM A36 conversion coils. (From Yu, Q. *Iron and Steel Technology* 2(8): 72–81. With permission.)

14.8 LAMINAR FLOW DISTRIBUTION

Strip size, speed, finishing, and coiling temperatures mainly determine laminar flow requirements. The parameters are either known or pre-designed. Application of laminar flow not only achieves the desirable coiling temperature, but also controls the cooling rate for mechanical properties and minimizes shape defects. To achieve these goals, total laminar flow rate, distribution patterns, and ratios of bottom flow to top flow should be predicted or designed properly.

14.8.1 Crossbow at Cut-to-Length Line

In contrast to canoe shape, it is hard to correct crossbow at the CTL due to deflection of the roll stack of the leveler or processor for wide heavy-thickness coils. Elimination of crossbow is critical for plates used in laser-burning processes. The larger the crossbow is, the worse the warpage of the mults becomes.

Measurement of canoe can be performed on the ROT using a straight bar and wedge. Because the top and bottom surfaces are reversed at the CTL for coils coiled by the upcoiler, measurement of crossbow can be done by a similar method.

The benefit of measurement at the CTL is to consider the effect of Poisson's effectiveness caused by longitudinal bending stress during coiling, de-coiling, and leveling. After straightening by a processor, crossbow measured before and after leveling is shown in Figures 14.5 through 14.7.

Figure 14.5 shows the effect of the ratio of total bottom flow to total top flow on crossbow. When the ratio was over 1.4, no crossbow appeared before and after leveling. Some coils did not display crossbow when the ratio was less than 1.4. The reason is that the banks close to the mill applied a high ratio and the banks far from the mill applied a low ratio, which resulted in a ratio of total flow less than 1.4.

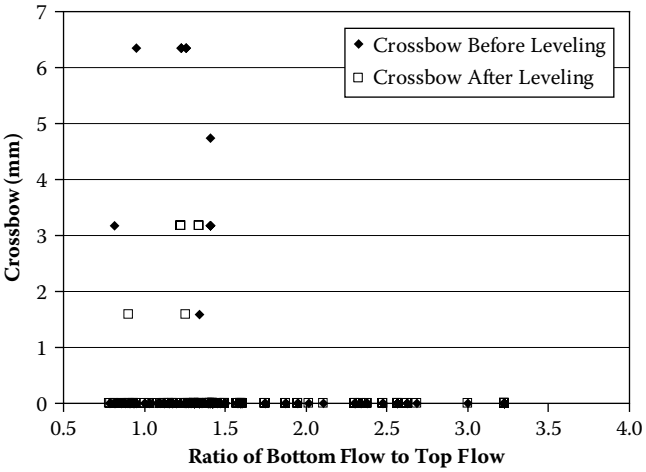


FIGURE 14.5 Effect of the ratio of total bottom flow to total top flow on crossbow. (From Yu, Q. *Iron and Steel Technology* 2(8): 72–81. With permission.)

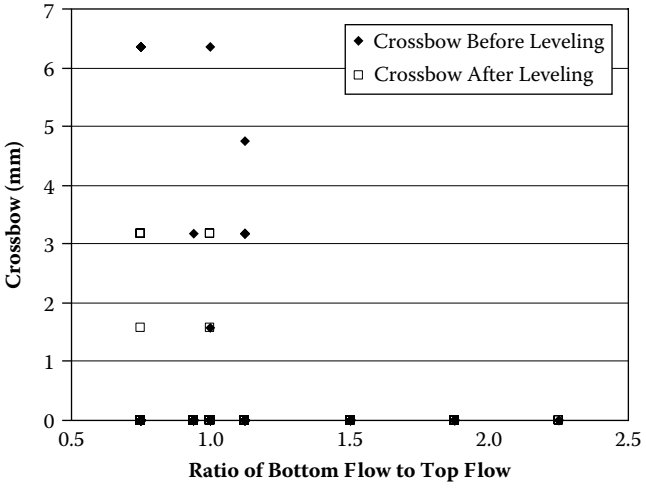


FIGURE 14.6 Effect of the ratio of Bank 1 bottom flow to top flow on crossbow. (From Yu, Q. *Iron and Steel Technology* 2(8): 72–81. With permission.)

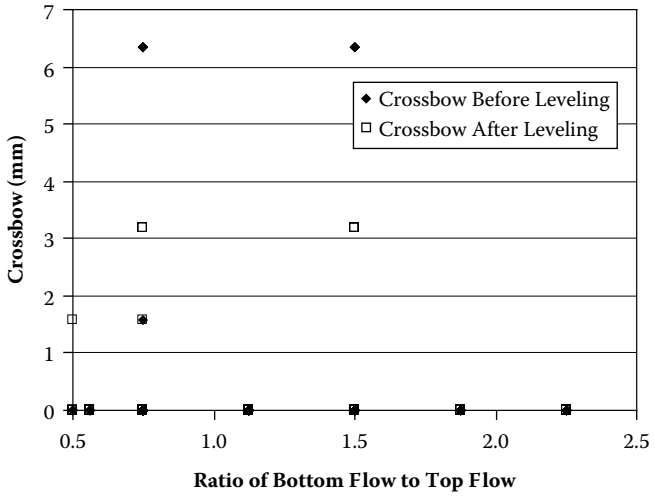


FIGURE 14.7 Effect of the ratio of Bank 4 bottom flow to top flow on crossbow. (From Yu, Q. *Iron and Steel Technology* 2(8): 72–81. With permission.)

Figure 14.6 indicates the effect of the ratio of bottom to top flow at Bank 1 on crossbow. When the ratio is over 1.125, there is no crossbow observed at the CTL. In Figure 14.7, crossbow is not observed when the ratio is greater than 1.5. This phenomenon is agreeable with the result calculated from Equation 14.14. This means that the cold surface needs a great ratio to minimize crossbow.

14.8.2 Strip Dimension versus Crossbow

To demonstrate that wide heavy-thickness coils have greater crossbow than narrow light-gauge strips, the effect of strip dimensions on crossbow is explained using Figures 14.8 and 14.9. When gauge is over 9 mm, crossbow is visible at the CTL. When width is over 1800 mm, crossbow can reach 6–14 mm. It is more critical to control the ratio on wide heavy-gauge coils than on narrow light-gauge coils. This conclusion is agreeable with the fact that narrow light-gauge coils have a smaller temperature difference between the top and bottom surfaces than wide heavy-thickness coils.

14.8.3 Ratio of Bottom Flow to Top Flow

It is practically impossible to have the ratio of bottom flow to top flow changed continuously. Otherwise, tremendous headers would be required.

According to the current layout and control scheme of the laminar flow headers, the availability of the ratios is listed in Table 14.1. When header flow rate is equal to zero, the header is turned off. The most favorable ratios are shown in Table 14.1. Their values fall into the range between 0.75 and 3.0. When the top headers are turned off and only the bottom headers are used, the ratio is infinite.

Each bank has its own laminar flow ratio limit to achieve good shape due to decreasing surface temperature as the strip moves down the ROT. On the other hand, cooling efficiency of each bank might have differences. The greater the ratio, the less top water is applied when maximum bottom water flow is used, reducing the total laminar flow. Consequently, the strip cooling is soft. The cooling pattern is soft. Otherwise, the cooling pattern is hard. The cooling rate of the hard pattern is greater than that of the soft pattern.

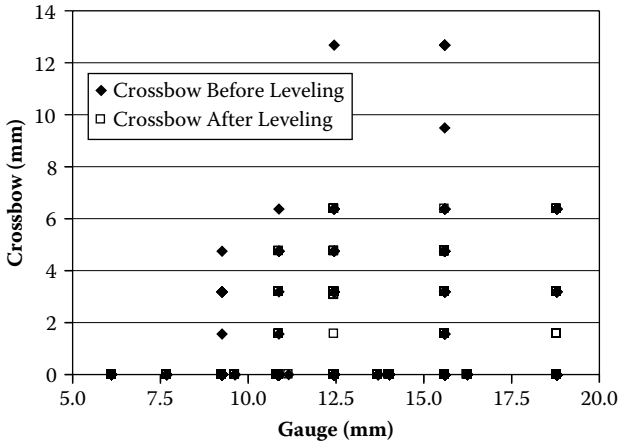


FIGURE 14.8 Effect of strip gauge on crossbow. (From Yu, Q. *Iron and Steel Technology* 2(8): 72–81. With permission.)

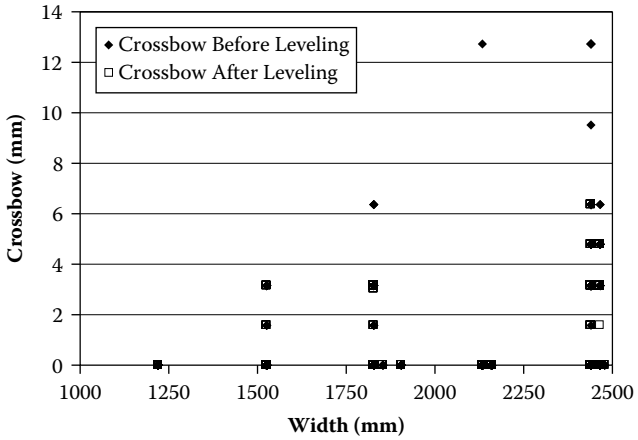


FIGURE 14.9 Effect of strip width on crossbow. (From Yu, Q. *Iron and Steel Technology* 2(8): 72–81. With permission.)

TABLE 14.1
Available Laminar Flow Ratios

	Bottom Flow Rate (l/min)			
Top Flow Rate (l/min)	**0**	**3,237**	**5,394**	**8,631**
0	Off	Infinite	Infinite	Infinite
2,877	0	1.125	1.875	3.000
5,754	0	0.563	0.938	1.500
8,631	0	0.375	0.625	1.000
11,508	0	0.281	0.469	0.750
14,385	0	0.225	0.375	0.600
17,261	0	0.188	0.313	0.500

Source: Yu, Q. *Iron and Steel Technology* 2(8): 72–81. With permission.

TABLE 14.2
Reference Flow Ratios of Each Individual Bank

Bank	Laminar Flow Ratio		
	Hard	Medium	Soft
	$\Delta T_0 - 222$	$166 < \Delta T_0 < 222$	$\Delta T_0 - 166$
1	0.750–1.000	1.000–1.500	1.500–3.000
2	1.000–1.500	1.000–1.500	1.500–3.000
3	1.000–1.500	1.000–1.500	1.500–3.000
4	1.000–1.500	1.500–3.000	1.500–3.000
5	1.000–1.500	1.500–3.000	1.500–3.000
6	0.750–1.500	1.500–3.000	1.500–3.000
7	0.750–1.500	0.750–1.500	0.750–1.500

Source: Yu, Q. *Iron and Steel Technology* 2(8): 72–81. With permission.

The ratio distribution among the banks is also determined by the temperature difference between finishing and coiling. For heavy-gauge coils, most of the bottom headers are needed due to the high required heat removal. Three basic cooling patterns are specified in the control system: hard, medium, and soft cooling patterns. The medium cooling temperature difference is defined within 166°C and 222°C. The hard cooling pattern is defined above that range and the soft cooling pattern below that range. Based on the available laminar flow ratios and statistical report, the reference flow ratios of the each bank are shown in Table 14.2.

14.8.4 Yield Strength

To demonstrate the effect of laminar flow pattern, cooling rate, and temperature difference on mechanical properties, laminar flow ratios of a hard cooling pattern are employed and set between 0.75 and 1.50. The trend lines of A36 plate yield strength are shown in Figure 14.10.

Figure 14.10 shows that yield strength increases with the increase of average cooling rate and the temperature difference between finishing and coiling. It is also observed that the temperature difference range covered by the trend lines is the same as that of a medium cooling pattern. Yield strength values fall between 260 and 360 Mpa. For A36 plates, the values are in the normal distribution although the hard cooling pattern is adopted.

Application of laminar flow patterns depends on the product specification. Strength, formability, and toughness are considered major factors. Typically, HSLA grades require the hard cooling pattern for strengthening. Plain carbon grades require the medium cooling pattern for both strengthening and forming. Low carbon grades use the soft cooling pattern to improve formability. For high X-grades of the American Petroleum Institute (API), the ratios of the first four banks should be selected as low as possible. The later banks can select the high ratio value for correction of canoe generated by the earlier banks. Sometimes, only the bottom headers are turned on at the later banks.

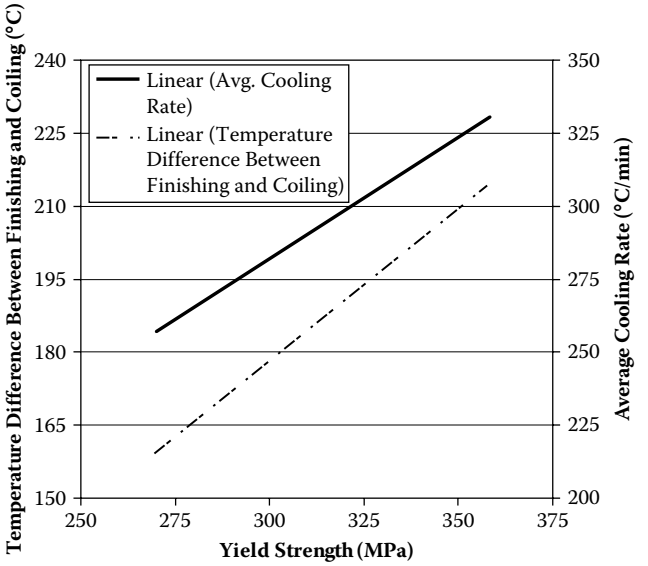


FIGURE 14.10 Effect of average cooling rate and temperature difference on yield strength. (From Yu, Q. *Iron and Steel Technology* 2(8): 72–81. With permission.)

14.9 EXAMINATION OF HEAT REMOVAL

Heat removal by laminar flow and air can be calculated with Equation 14.9 when the ratios of each individual bank are specified. Also, the actual heat removal can be calculated inversely from Equation 14.1. To compare the accuracy of Equation 14.9, typical conversion coils made of ASTM 36 steel are selected. To display the result explicitly, a multiplication factor is introduced, that is, gauge times width, finishing speed, and cooling temperature difference. From Figure 14.11, it can be seen that the actual heat removal and the result predicted by the model are agreeable.

In addition, Figure 14.11 can be used to check the efficiency of laminar flow cooling. When the model heat removal is achieved but coiling temperature is not reached, the laminar flow headers need to be flushed and nozzles inspected.

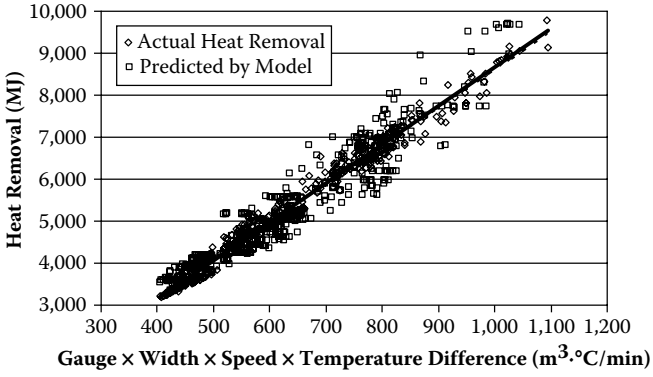


FIGURE 14.11 Comparison of the actual heat removal with the result predicted by the model. (From Yu, Q. *Iron and Steel Technology* 2(8): 72–81. With permission.)

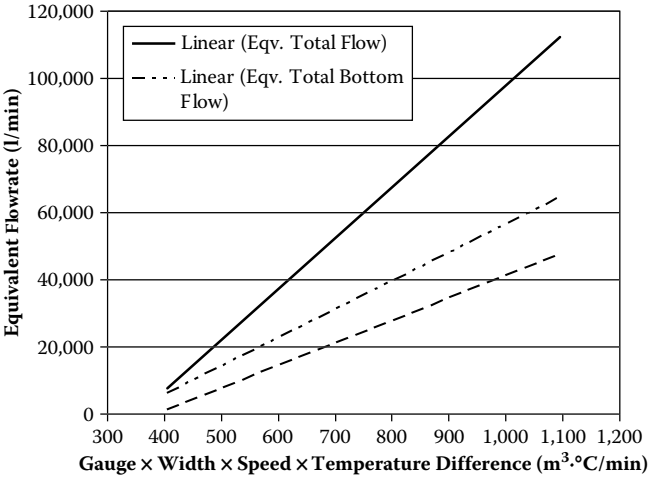


FIGURE 14.12 Equivalent laminar flow rate. (From Yu, Q. *Iron and Steel Technology* 2(8): 72–81. With permission.)

For convenience, an equivalent flow rate is introduced against the multiplication factor. The equivalent flow rate times a factor (2660 mm/strip width in mm) is equal to the header flow rate.

The total laminar flow versus the multiplication factor is plotted in Figure 14.12. The total top and bottom flow rates are also found in this figure. As a result, when feedback or feedforward control of coiling temperature is used, headers to be added can be determined.

14.10 DISCUSSION

Canoe shape at the ROT is not always harmful to downstream processes. For example, pipe mills with upwind decoilers favor using these coils. The benefit is that the wide heavy-gauge coils can reduce forming resistance when the strip is coiled by a downcoiler.

In hot rolling, multipass descaling leads to nonuniform cooling from the top surface to the bottom surface. The cooling length on the top surface is much longer than that on the bottom. Canoe may appear in front of the laminar flow banks. Strip crown and edge drop also affect canoe or crossbow indirectly. When the rolling schedule is lined up for rolling from narrow to wide, coil length at the coil edges is much longer than at other locations. The edge waves will accumulate water at the center of strip.

Under laminar flow banks, the edges of the coil shrink faster than other positions due to water outside the strip width. This will generate canoe on the ROT. Therefore, water height of the bottom headers has to be adjusted properly.

14.11 SUMMARY

The modification of the bottom headers increases the capacity of the laminar flow system to cool wide heavy-gauge coils without inducing a canoe shape. Installation of sand filters and header caps helps maintain cooling efficiency.

The ratio of the bottom flow to the top laminar flow has a significant impact on the transverse shape, canoe, and crossbow. For a mill with an upcoiler, increasing the flow ratio can reduce canoe. The calculated result displays:

Control of canoe or crossbow is very sensitive to adjustment of the laminar flow ratio for the early banks, because the critical temperature differences are smaller.

1. Canoe shape will disappear when the ratio of laminar flow is over 1.5. However, even if its value is much greater than 1.5 and crossbow appears at the ROT, the CTL processor has the capability to correct it.
2. Mechanical properties of wide heavy-gauge coils can be adjusted through selection of proper laminar flow pattern, cooling rate, and temperature difference between finishing and cooling.

ACKNOWLEDGMENTS

The author would like to thank the Department of Hot Rolling at Nucor Steel Tuscaloosa, Inc. (formerly Corus Tuscaloosa) for assistance with tests, trials, and analyses.

REFERENCES

Bowker, J. T., Orr, R. F., et al. 1994. The effect of vanadium on the parent plate and weldment properties of API 5LX-80 linepipe steels. *35th Mechanical Working & Steel Processing Conference*, pp. 403–412, AIME, Warrendale, PA.

Browne, K. M. 1995. The thermal conductivity of carbon steels. *ASME*, 67: 105–115.

Kaseda, Y., and Masui, T. 1994. Control of buckling and crossbow in strip process lines. *Iron and Steel Engineer*, 71(9): pp. 14–20.

Nakata, N., and Yoshida, H. 1995. Influence of cooling uniformity at runout table on strip flatness. *ASME*, 67: 67–77.

Sarmiento, G. S., Chen, X., et al. 2000. A comparison of cooling curve analysis using Inc-Phatran and WinProbe. In *Heat Treating—Proceedings of the 20th Conference*, Vol. 2, pp. 659–665, Materials Park, OH: ASM International.

Yu, Q., and Muncie, M. 2003. Effect of cooling and stacking on buckling of plates. *AISE Steel Technology*, 23(6): 35–44.

Yu, Q., Dickinson, D., et al. 2005. Laminar flow cooling behavior of wide heavy-thickness coils. *Iron and Steel Technology*, 2(8): 72–81.

15 Consideration of Microstructure Evolution in Hot Strip Mill Automation

Hans-Ulrich Löffler, Klaus Weinzierl, and Rüdiger Döll

CONTENTS

15.1 Introduction 171
15.2 A Brief History of Microstructure Modeling and Cooling Section Control 171
15.3 Microstructure Model 172
15.4 From Microstructure to Material Properties 174
15.5 Model Predictive Control to Keep Material Properties Constant over Strip Length 175
15.6 Different Strategies for Different Steel Grades 176
15.7 Conclusions 177
References 178

15.1 INTRODUCTION

Driven by competition from other materials, steel production has experienced major changes in the previous decades. New steel grades have been created, making use of new hardening mechanisms and new microstructure mixtures. This has led to even lighter weight steel and/or steel with new properties.

The automotive industry is only one example for an industrial branch that benefits from these developments. Thinner and lighter, but still very strong, types of steel make vehicles more efficient and more environmentally compatible. Other branches of industry can profit from the use of strength-relevant, load-bearing structures and energy-absorbing components made of dual-phase, multiphase, or high-strength steels such as twinning-induced plasticity (TWIP) and transformation-induced plasticity (TRIP) steels.

For example, the oil and gas industry has an enormous demand for thermomechanically rolled steel for pipelines, where high strength at low temperatures is essential to avoid cracks through geological tensions (pipelines in permafrost or undersea environment).

Two factors are most effective for successful high-quality steel production: the choice of appropriate alloying elements and constant and reproducible production conditions. If production parameters, such as temperature values or more precisely enthalpies, are violated by just a few percent, the mechanical properties of the end product can change in such a way that only lower-quality strip or even scrap is produced. An illustrative example is the manufacture of dual-phase steel: in the cooling section, the steel is typically cooled from 900°C to around 660°C in a few seconds. Then water cooling is stopped for several seconds so that phase transformation proceeds slowly. Finally, when the residual austenite content is at around 20%, the steel is quenched, thus initiating a phase transformation of the remaining austenite into martensite. If the holding time is only a little too long, the residual austenite content may just be below 5%. Instead of dual-phase steel, the result is structural steel, for example, ST37. Its properties would be far from the desired strength and properties of a dual-phase steel. In the reverse case of too short a holding time, we would get far too high a martensite content and thus a hard but brittle material—in the worst case, impossible to be coiled. It is obvious that production conditions need to be well defined and kept constant for such materials in particular.

After a brief history of microstructure modeling and cooling section control, this chapter describes components of a state-of-the-art treatment of microstructure issues in a hot strip mill: a (at least for the decisive issue of phase transformation) physically based microstructure model; a microstructure monitor to compute material properties; and model predictive control to (in combination with the models) keep material properties constant over strip length. Finally, different strategies are discussed for different steel grades.

15.2 A BRIEF HISTORY OF MICROSTRUCTURE MODELING AND COOLING SECTION CONTROL

In addition to the physical dimensions like thickness, profile, or flatness, the quality of hot-rolled strip also depends on its intrinsic properties, like the mechanical properties (tensile strength, yield strength, elongation to fracture, etc.). With increasing requirements of the end user of automotive sheets, pipeline, boiler, bridge, or ship steel, the tolerance range for

mechanical properties has become continuously smaller. Therefore, research laboratories have been developing microstructure models to better understand and even design steels (Sellars and Whiteman 1979; Hodgson and Gibbs 1992; Gladman 1997; Ginzburg 2005). The models then were semiempirical models based on results from laboratory experiments. It was only in the late 1990s when both computing power and degree of mill automation allowed for online application of microstructure models (Löffler et al. 2000; 2001; Andorfer et al. 2002). This opened a new dimension as the available data increased dramatically. Hence, precision of calculations also could be improved so that nowadays quantitatively reliable results are state of the art (Löffler 2004; Löffler et al. 2005). Also, the step from semiempirical models toward physically based descriptions of microstructure behavior has been taken (Vandermeer 2001; Weinzierl et al. 2006; Lissel and Engberg 2007). Meanwhile, both microstructure modeling and calculation of mechanical properties are at a high level so that properties over strip length can be kept constant in a way that was not possible only a few years ago.

Cooling temperature control was identified early as being important for material properties. In the first automation systems, the cooling section was typically divided into two parts. As described in Xie et al. (2006) this approach is still widely used. Feed forward control has been applied within the part close to the finishing mill. Within the so-called trim zone—the part close to the coiler—feedback control has been used. Typically, a classical PI controller combined with a Smith predictor keeps the coiling temperature constant. Shortcomings of this procedure include imprecise control of material properties and inflexible reaction to events such as unforeseen finishing temperature deviations or speed changes.

Especially for high carbon steels, a significant amount of transformation energy influences the strip temperature considerably (e.g., by up to 150 K). In some cases, adding cooling water thus even results in increasing coiling temperature because the place of phase transformation is moved from the coiler to the cooling section. This results in major nonlinearities of the system, destabilizing classical control. Another challenge is that the solutions are not always well defined: up to three different amounts of water may lead to the same coiling temperature, depending on the resulting phase fraction under the pyrometer. These challenges can be properly met only through introduction of phase transformation models.

Phenomenological transformation models like that of Johnson–Mehl–Avrami (Avrami 1941) have been applied worldwide to compute phase fractions after cooling of steel. However, this approach is only valid for constant cooling rates when CCT diagrams are used as data basis. An additional assumption is necessary to make it applicable for varying cooling rates, for example, the Scheil rule or a state-variable approach (Tzitzelkow 1972). Practical applications of the latter are described in Nikula et al. (1996), Lotter et al. (2002), and McNutt et al. (2006). Another problem concerning the computation of latent heat was solved only recently by a thermodynamic phase transformation model based on Gibbs' free enthalpy (Weinzierl et al. 2006). This approach had been used previously for equilibrium computations and diffusion models within material simulation tools, e.g., ThermoCalc, Pandant, Chemsage, Dictra (Sundman et al. 1985; Gustafson 1985; Miettinen 1998; Schneider and Inden 2004; Borgenstam et al. 2000). Its application in cooling automation systems can be regarded as a paradigm shift. The next section deals with this approach in more detail.

Besides the physical model, control itself could be significantly enhanced. Classical cooling control as explained above employs heuristic switching strategies. Therefore, it is, in many cases, not capable of producing new enhanced steel grades with constant material properties along the strip. The modern approach today uses model predictive control for cooling automation. A survey of model predictive control can be found in Carlos et al. (1989) and Qin and Badgwell (2003), and application to hot strip mill automation is shown in Kurz et al. 2006. Control within cooling automation is explained in more detail in the section on model predictive control.

15.3 MICROSTRUCTURE MODEL

Microstructure modeling in hot strip mills began in the late 1970s (Sellars and Whiteman 1979; Sellars 1980) and has been further developed with respect to mechanical properties (Hodgson and Gibbs 1992; Gladman 1997; Linkens et al. 2000; Ginzburg 2005). The steel works already had the foundation of the final properties because of the chemical composition. The addition of microalloying elements, such as niobium, titanium, or vanadium, leads to precipitations of carbonitrides in the cooling section, which in turn, then leads to both high-yield strength and high tensile strength. Another effect is that recrystalization is hindered during deformation in the roughing and finishing mill. This ultimately results in fine ferrite grains, which also increases the strength of the material. During decades of research, those qualitative phenomena have been quantified in semiempirical equations, describing static and dynamic recrystalization and grain growth; see, e.g., Zener 1949 and Sellars and Whiteman 1979. Further refinements and considered excellent theoretical and experimental work have made the processes during hot rolling qualitatively well understood. The evolution of the microstructure model can be well described: beginning in the reheating furnace, where the material becomes austenitic and potential precipitations dissolve; over the roughing and finishing mill with its recrystalization, grain growth, precipitation, and strain hardening; to the cooling section where the hot rolled structure is formed. Based on these works, commercial automation systems are offered to smooth the production of modern steel grades (Andorfer et al. 2002; Löffler et al. 2005). Some large steel companies still do their own research on new steel grades, where the above-mentioned algorithms still play an important role (Lissel and Engberg 2007).

However, it turns out that the major actuator on final microstructure remains in the cooling section.

Here, the final microstructure is created and depending on the mixture and arrangement of different types of microstructure phases (ferrite, cementite, pearlite, bainite, martensite, and even remaining austenite), precipitates, and final grain size, the material properties will result.

Therefore, microstructure evolution until end of the finishing mill can be described with well-known semiempirical models without significant loss of precision—this holds at least for online applications. It is also beneficial to model precisely what happens in the cooling section because the evolution of phases is not only of interest for material properties, but, due to the transformation heat produced, also affects the accuracy of the cooling temperature control.

High carbon steel grades are an example where problems resulting from the transformation heat become obvious. Here, the question "Which water amount is necessary for a desired target coiling temperature?" can have more than one answer, as shown in Figure 15.1. Adding cooling water before the transformation can even lead to an increased coiling temperature.

In the existing literature, the typical approach used to compute the evolution of phase fractions within the cooling section (Nikula et al. 1996; Lotter et al. 2002; McNutt et al. 2006) is the Johnson–Mehl–Avrami approach. In this approach phase, the speed of the phase transformation is parameterized as a function of chemical composition and temperature. It is completely independent of the parameterization of heat capacity and transformation heat. Unfortunately, there is no way to consider the respective relationships within this approach (Weinzierl et al. 2006). This eventually leads to inaccurate results on temperature evolution, violating the energy balance in general, even though the evolution of phases might be modeled accurately enough. This is a major drawback especially for high carbon steels, where the temperature can increase by as much as 150 K depending on chemical composition of the steel, phase evolution, and steel temperature while austenite is decomposed.

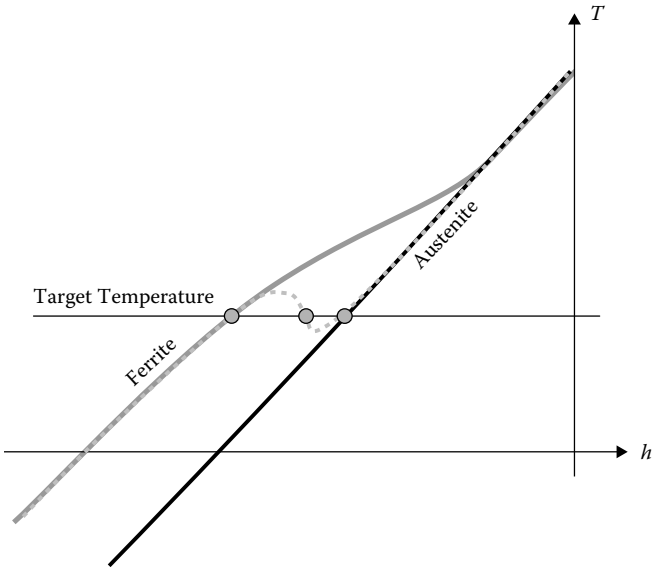


FIGURE 15.1 The dashed line shows a sample path a high-carbon steel grade could follow while cooled. Loss of enthalpy is roughly proportional to the amount of water switched within a cooling section. The example shows that three different values of enthalpy exist where steel temperature equals target temperature. In a similar manner, the material behaves while cooled in a cooling section. There are often situations where three different amounts of water result in the same coiling temperature. Hence, for many carbon steel grades, specifying coiling temperature and cooling strategy is not sufficient to specify material properties.

The dilemma with the Johnson–Mehl–Avrami approach can be shown in more detail using a simple example.

Consider two phases with molar chemical composition $x \in [0,1]^N$, and for simplicity assume that both phases have the same chemical composition. The content of phase 1 is $p \in [0,1]$; the content of phase 2 is $1 - p$. The Gibbs' free enthalpy is given as a function of temperature and dissolved chemical elements:

$$G(T,x) = pG_1(T,x) + (1-p)G_2(T,x)$$

The enthalpy as a function of temperature and chemical composition is given by

$$H(T,x) = pH_1(T,x) + (1-p)H_2(T,x)$$

where for each phase $k = \{1,2\}$ holds:

$$H_k(T,x) = G_k(T,x) - T\frac{\partial G_k(T,x)}{\partial T}$$

Hence, if the Gibbs' free enthalpy is known, enthalpy follows directly. If the enthalpy is known, the Gibbs' free enthalpy can be computed by solving an initial value problem.

Partial differentiation of H with respect to temperature T gives the heat capacity as function of temperature and chemical composition:

$$c(T,x) = -T\frac{\partial^2 G(T,x)}{\partial T^2}$$

On the other hand, the latent heat can be derived by differentiating H with respect to p,

$$L(T,x) = H_1(T,x) - H_2(T,x)$$

Hence, if heat capacities and latent heat are parameterized directly as a function of temperature, it must be ensured that the Cauchy–Schwartz conditions are fulfilled, that is,

$$\frac{\partial^2 H(T,x)}{\partial p \partial T} = \frac{\partial L(T,x)}{\partial T} = \frac{\partial c(T,x)}{\partial p} = \frac{\partial^2 H(T,x)}{\partial T \partial p}$$

Otherwise, H does not exist. Hence, the Cauchy–Schwartz conditions read as:

$$\frac{\partial L(T,x)}{\partial T} = c_1(T,x) - c_2(T,x)$$

This condition can be automatically fulfilled, if $H(T, x)$ is parameterized directly instead of parameterizing the heat capacities and the latent heat. However, there is yet another problem. The following equilibrium must be ensured:

$$\frac{dp}{dt}\frac{\partial G(T,x)}{\partial p} = \frac{dp}{dt}[G_1(T,x) - G_2(T,x)] \leq 0$$

(second law of thermodynamics)

This equilibrium must be maintained at any time t and for each chemical composition, with $G_1(T_e, x) - G_2(T_e, x) = 0$ at phase equilibrium temperature T_e. If the transformation rate dp/dt is not computed based on the Gibbs free enthalpy (but, instead, by the Johnson–Mehl–Avrami or another approach), the problem is to find $H(T, x)$ such that the above equations for $G(T, x)$ directly derived from H are fulfilled. Already for the simple case of two phases with equal chemical composition, finding adequate heat capacities and latent heat as functions of temperature and chemical composition or H consistent with the parameterization of the transformation speed derived from any separate model is a theoretically difficult problem. In practice, this would be impossible, resulting in inaccurate temperature computations.

A clear improvement is achieved by a phase transformation model, which directly uses Gibbs' free enthalpy to calculate the driving force for transformation. The model is completed by a diffusion model to calculate transformation speed. Such a model is explained in more detail in Weinzierl (2006). The main advantage is that the evolution of phases, as well as the transformation heat produced, is computed with one holistic approach. Thus, only consistent results are computed, which always fulfill the balance of energy. The principle behind the model is depicted in Figure 15.2.

Pearlite growth starts at some nucleation site within a grain and continues, while carbon diffuses within austenite. The transformation speed is mainly driven by carbon diffusion. Diffusion of other chemical elements is neglected (quasi-equilibrium). Growth of pure ferrite and pure cementite both can be treated as special cases of pearlite growth. From the Gibbs' free enthalpy, quasi-equilibriums are computed. It is assumed that phase quasi-equilibrium is fulfilled at the phase boundary between ferrite and austenite and between ferrite and cementite, respectively. This determines the carbon concentration in austenite at the phase boundaries and the rather small carbon concentration at the phase boundary within ferrite. Two functions are introduced to describe the carbon concentration within austenite in front of ferrite and in front of cementite, respectively. Within austenite, a coupled Stefan problem is formulated and solved. The speed of the common phase boundary, the cementite content within pearlite, the lamella spacing of pearlite, and the distribution of carbon concentration within austenite are computed. The total latent heat due to phase transformation includes the latent heat produced directly at the phase boundary (cementite and ferrite), the produced heat within austenite due to carbon diffusion,

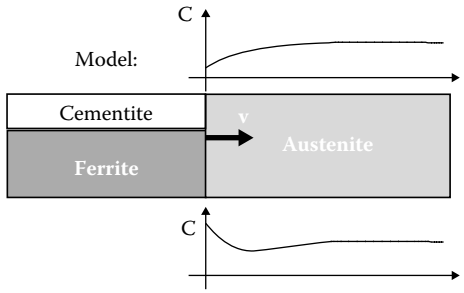


FIGURE 15.2 This figure illustrates the phase transformation model. On the left-hand side, pearlite is assumed. Its cementite content $q \in [0,1]$ is a free parameter, which contains the special cases $q = 0$ (ferrite) and $q = 1$ (cementite). At the phase boundary, carbon concentration is fixed by thermodynamic quasi-equilibrium. Within austenite, carbon concentration varies. In front of cementite and in front of ferrite, there might be a carbon concentration, as depicted. Transformation speed can be computed by modeling the diffusion of carbon within austenite. Within the model, this diffusion problem is approximated by two coupled one-dimensional diffusion problems.

the heat produced in austenite when carbon content changes, and the energy stored in the surface of the lamellas of pearlite. With this approach, temperature and phase fractions are computed consistently and with high accuracy. Even adaptation of the phase transformation model based on temperature measurements during steel production is possible. The model was applied successfully at Hoesch Hohenlimburg GmbH and ThyssenKrupp Steel Beeckerwerth in 2007. Both companies produce a considerable amount of carbon steel grades and stainless steel.

15.4 FROM MICROSTRUCTURE TO MATERIAL PROPERTIES

Although phases, precipitates, grain sizes, and other microstructural information are the key to understanding the physical properties of the final product, it must not be forgotten that the quantitative link between microstructure and strength still lacks accuracy. This is because comparatively few data are available due to a costly sample preparation procedure.

For example, the well-known Hall–Petch equation (Hall 1951; Petch 1953) linking grain size with tensile strength for low-carbon steel grades strongly depends on the accuracy of the grain size measurement, which is on the order of ±15% (Gladman 1997).

Accurate prediction of mechanical properties for automation purposes is vital to the steel industry, and artificial neural networks are perfectly suited for this task (Löffler et al. 2000; Linkens et al. 2000; Yang et al. 2000; Löffler et al. 2001). Thanks to online application, chemical composition, process data, and measured material properties are readily available in large numbers.

Figure 15.3 shows the agreement of calculated data with measured values for mechanical properties (yield strength and

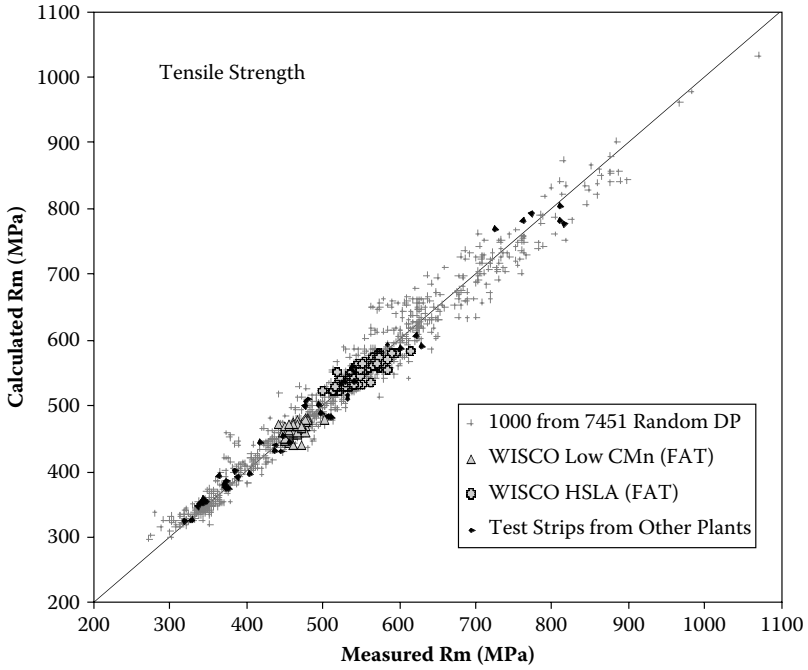


FIGURE 15.3 The figure shows 1000 randomly selected data (+) from Hoesch Hohenlimburg, TKS Beeckerwerth, and Salzgitter AG. Data from several other plants (EKO, Rautaruukki, SW Bremen, and SSAB) are displayed as black diamonds (◆). Data from the final acceptance test at WISCO (Δ for low CMn, and ○ for HSLA), are shown as well.

tensile strength). Results obtained at the medium strip rolling mill of Hoesch Hohenlimburg and at the 2250-mm-wide strip rolling mill of Wuhan Iron & Steel (Group) Corporation (WISCO) are presented, where the system has been running online and stable since 1998 (Hohenlimburg) and 2003 (WISCO), respectively. The Microstructure Monitor system also works successfully at TKS Beeckerwerth since 2001. In addition, the model has been successfully applied offline to several other plants, which proves the algorithms to be transferable.

Online availability of the system allows for continuous quality assurance of the produced strip with respect to mechanical properties. In conventional operation, a major expense is taking the random test amount of samples, which is needed to write certificates. The expense originates from loss of sample material and from the delay in shipping and delivery. This was the initial starting point for the development of an online system to calculate the required quality parameters rather than measure them. Additionally, the model even allows for optimization of process parameters with regard to target mechanical properties (Löffler 2004).

15.5 MODEL PREDICTIVE CONTROL TO KEEP MATERIAL PROPERTIES CONSTANT OVER STRIP LENGTH

To ensure a constant product quality over the complete strip length, equipment operators and control systems try to keep the production conditions as constant as possible. However, the properties of the material are influenced by numerous factors, not all of which can be kept constant at the same time if we look at changing strip speed. Actually, to keep material properties constant over strip length, the temporal cooling trajectory of each strip point should be equal. Classical cooling control is not effective here. It only tries to keep the coiling temperature constant. Cooling course is taken into account only by a switching heuristic, which maps the scalar controller output value to the numerous valve settings of the plant.

The core idea of an enhanced cooling control is to compute deviations from target, not only at a single point at the location of the coiling pyrometer, but along the entire cooling section. The entire temporal cooling course from the last finishing mill stand to the coiler will be influenced by exploiting the full capability of machine construction to switch valves wherever needed to minimize all deviations. If no plant limits would exist, it would be possible to compute perfect valve states based on the knowledge of actual deviations (Latzel 2001).

Plant limits indeed are a major challenge. Each valve of the cooling section has a maximum amount of switchable water, and of course, it is not possible to switch a negative amount of water to compensate for too low temperatures.

The situation can be compared to driving a car. Without limitations on braking power, driving a car would be easy: based on current deviations and current centripetal acceleration, speed could be adjusted to ensure that the car follows its desired trajectory. Knowledge about the street ahead would be unnecessary.

The problem shows its real face as soon as constraints such as limited braking power come into play. Then it is crucial to adjust speed in time, such as in front of a curve. It would not be reasonable to steer the car based on information from the rear view mirror only; see also Figure 15.4. The improved situation of looking ahead translates into model predictive control for the cooling automation. Using a nonlinear model, future control variables are computed up to a given horizon. The entire course of control variables is compared to their desired values, and a deviation functional is derived. The actuator signals are modified within a mathematical optimization algorithm in a way that the functional is minimized. With an adequate solution (e.g., an adequate local minimum), the values of actuator signals are known and can be implemented for the present time step. This procedure is repeated for each of the following time steps, thus working as online control. Constraints are automatically handled by an adequate mathematical optimization algorithm, for example, an SQP method.

For cooling control, model predictive control works, as shown in Figure 15.5.

A real-time cooling observer computes the effective state variables of the strip and the plant along the cooling section. Temperature and enthalpy distribution, as well as the phase fractions of austenite, ferrite, pearlite, and cementite, are the state variables, which are computed in real time along the strip. The model can be adapted in real time by comparing measured temperatures to calculated ones. The observer is the foundation for model predictive control.

Using model calculations, many strip points are introduced along the cooling section. Each strip point is initialized by the effective state derived from the observer. For each strip point, a predictive computation of the future temporal cooling course is performed, until this point reaches the coiler. The entire temporal cooling trajectory can be compared to its desired cooling trajectory. The deviation is minimized taking into account the plant limits. The respective valve states are computed as actuator signals.

By means of model-predictive control, the stipulated time enthalpy curve of cooling in the cooling section is optimally adhered to for the whole steel strip, within the limits of the respective plant. Material properties are kept close to their target in spite of changing production conditions. Hence, model predictive control cyclically results in an optimal set of valve set-point changes, exploiting the full capability of machine construction without any restriction on the switching location, which is the major drawback of classical cooling control.

15.6 DIFFERENT STRATEGIES FOR DIFFERENT STEEL GRADES

The described combination of Microstructure Monitor, accurate phase transformation model, and model predictive control aims directly at the targets of the steel producer: the microstructure properties of the strip. The Microstructure Monitor provides microstructure data from the roughing and finishing mills, direct data about mechanical properties, such as tensile strength and elongation to fracture, and optimizes process parameters like the coiling temperature with regard to those mechanical values. The model predictive control concept enables a temperature course calculation at a point in time before this strip point even enters the mill, thereby providing the enthalpy course for each strip point traveling through the cooling section to the coiler.

The adaptation with the pyrometers in the mill allows for close monitoring and adjustment of the model computations. It includes adaptation of heat transfer, as well as adaptation of the phase transformation rate to achieve the best results for both.

Flexible target definitions (temperature, phase fractions, mechanical properties) give the mill operator more flexibility

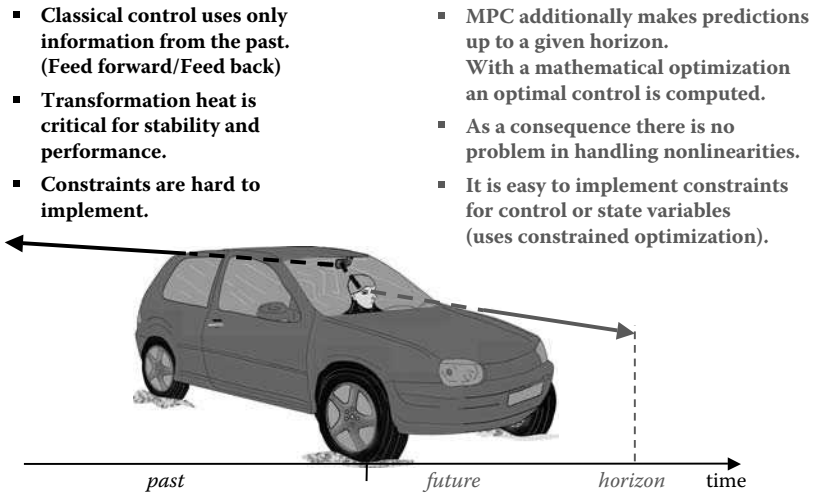


FIGURE 15.4 The main idea of model predictive control can be explained with the example of driving a car. The driver looks toward the future shape of the street up to some given horizon. Classical control only uses information from past and present. That is similar to driving in deep fog. It is clear in which case more dynamics can be achieved.

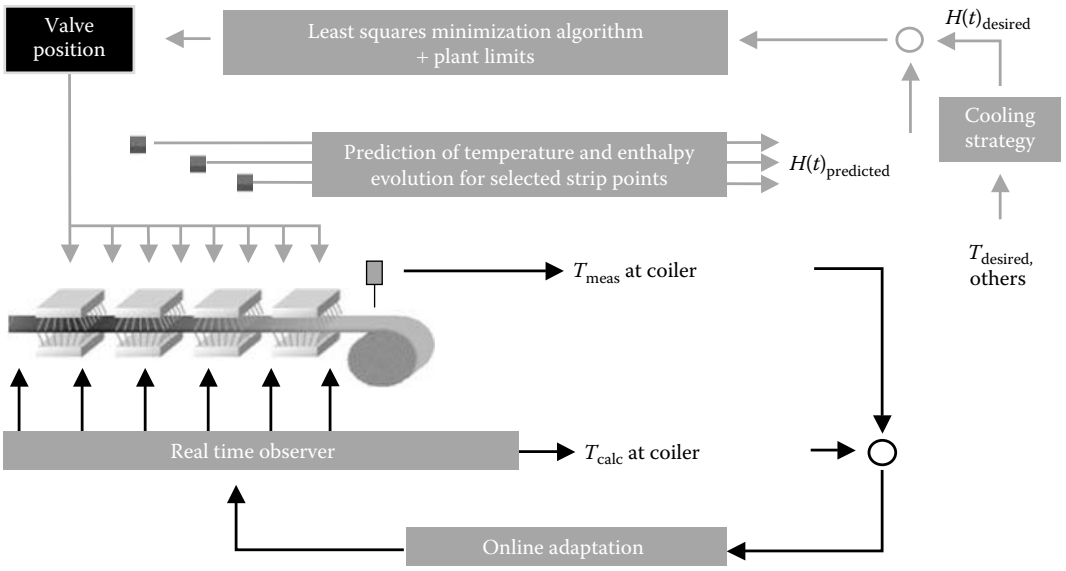


FIGURE 15.5 The structure of model predictive control for cooling steel is shown. A real-time observer computes all state variables in real time. Future estimations are computed by making predictions for several initial strip points of the observer. The predicted temporal enthalpy courses are compared to the desired ones. Optimal valve states are computed employing a mathematical minimization algorithm. Furthermore, the observer computations can be adapted to measurements.

and easier handling. A strip observer applies powerful models in real time. With a time resolution of 200 ms or faster, it updates the enthalpy course and the course of phase fractions along the entire cooling section, taking into account actual measurements and distortions within the plant. Temperature is consistently derived from enthalpy and phase fractions.

Depending on the quality requirements for the steel product, different strategies can be applied; for instance, aiming at a certain tensile strength for one grade (e.g., an HSLA steel), keeping phase fractions constant for a second grade (e.g., a DP or a TRIP steel), and making sure that phase transformation takes place on the run-out table rather than on the coiler for a third grade (e.g., a high carbon grade). Only a consistent model for transformation and temperature ensures the greatest accuracy and allows controlling the sensitive high carbon steels by keeping the transformed fraction constant rather than the coiling temperature.

At the participating pilot plant at Hoesch Hohenlimburg, these models of the SIROLL^{CIS} Microstructure Target Cooling package were tested and verified using mobile pyrometer devices to compare the temperature course over the length of the cooling section. The results show a very close match between the calculated results and the measured values, thus proving the high accuracy of the models.

15.7 CONCLUSIONS

Models to compute microstructural and mechanical properties of steel are becoming more and more important and useful for practical application in industrial processes. Increasing demands for the accuracy of automation solutions also require the use of sophisticated physical models. The current state of microstructural models for hot-rolling applications has been described; semiempirical models are used for the calculation of recrystalization, grain growth, and precipitations in roughing and finishing mills.

A new model based on the Gibbs' free enthalpy is used for consistent calculation of the temperature and transformation course in the cooling section. A model-predictive cooling-section control system keeps the material properties constant over the strip length. This flexible automation system not only has decisive advantages when it comes to the production of highly carbonized steels, where the temperature control is particularly difficult due to the role of transformation energy, but production of multiphase steels also benefits as the desired amount of the different phases can be kept constant over length. Especially for older plants with many restrictions and limitations, the novel cooling-section automation system enables flexible manufacture of modern steel grades.

Finally, neural networks are used to calculate mechanical steel properties close to the precision of measurement for a wide range of steels (low-CMn, HSLA).

These models were applied successfully at TKS Beeckerwerth and at Hoesch Hohenlimburg in 2007 with excellent results. The next installation of the system will be at Bhushan Steel & Strips Ltd., India. Several other projects will be commissioned within the next few years. To summarize, this model and this control can be regarded as a valuable tool with which the steel producer can easily make adjustments to meet customer needs for new steel grades with defined properties in close tolerance to the target, not limited only to coiling temperature.

REFERENCES

Andorfer, J., Auzinger, D., Hriberning, G., Hubmer, G., Luger, A., Schwab, P. 2002. Full metallurgical control of the mechanical properties of hot-rolled strip—A summary of more than two years operational experience. In *International Conference on Thermomechanical Processing: Mechanics, Microstructure & Control*, E. Palmiere et al. (eds.), pp. 164–168, Sheffield, U.K.

Avrami, M. 1941. Kinetics of phase change III—Granulation, phase change, and microstructure. *Journal of Chemical Physics* 9: 177–184.

Borgenstam, A., Engström, A., Höglund, L., Agren, L. 2000. DICTRA, a tool for simulation of diffusional transformations in alloys. *Journal of Phase Equilibria* 21: 269–280.

Carlos, E., Prett, D.M., Morari, M. 1989. Model predictive control: Theory and practice—A survey. *Automatica* 25(3): 335–348.

Düfert, K.-P., Zouhar, G., Kost, R., Donath, A., Donat, B. 1992. Berechnung der gefügeentwicklung und der mechanischen eigenschaften beim warmwalzen. *Stahl and Eisen* 112(10): 93–98.

Ginzburg, V.B. 2005. *Metallurgical Design of Flat Rolled Steels.* New York: Marcel Dekker.

Gladman, T. 1997. *The Physical Metallurgy of Microalloyed Steels*. London: The Institute of Materials.

Gustafson, P. 1985. A thermodynamic evaluation of the Fe-C System. *Scandinavian Journal of Metallurgy* 14: 259–267.

Hall, E.O. 1951. The deformation and aging of mild steel: Discussion of results. *Proceedings Physics Society Series B* 64: 747.

Hodgson, P.D., Gibbs, R.K. 1992. A mathematical model to predict the mechanical properties of hot rolled C-Mn and microalloyed steels. *ISIJ International* 32(12): 1329–1338.

Kurz, M., Metzger, M., Weinzierl, K., 2006. An advanced strip temperature controller for hot rolling mills. *Proceedings of the First IFAC Workshop on Model Predictive Control for Fast Systems* pp. 141–146. October 9–11 2006, Grenoble, France.

Latzel, S. 2001. Advanced automation concept of runout table strip cooling for hot strip and plate mills. *IEEE Transactions on Industry Applications* 37(4): 1088–1097.

Linkens, P.A., Yang, Y.Y., Chen, M., Abbod, M.F. 2000. A comparative study of neural and fuzzy algorithms for prediction of properties in steel processing. In *Proceedings of the IFAC-Symposium, Automation in Mining, Mineral and Metal Processing*, Jämsä-Jounela, S.-L., Vapaavuori, E. (eds.), Helsinki, International Federation of Automation Control, pp. 296–301.

Lissel, L., Engberg, G. 2007. Prediction of the microstructural evolution during hot strip rolling of Nb microalloyed steels. *Materials Science Forum* 558–559: 1127–1132.

Löffler, H.U., Döll, R., Lang, B., Sörgel, G., Holtheuer, U., Zouhar, G. 2000. Control of mechanical properties by monitoring microstructure. In *Proceedings of EUROMAT 99, Steels and Materials for Power Plants*, Neumann, P. et al. (eds.), Weinheim: Wiley-VCH, pp. 57–61.

Löffler, H.U., Döll, R., Poppe, T., Sörgel, G., Holtheuer, U., Zouhar, G. 2001. Control of mechanical properties by monitoring microstructure. *AISE Steel Technology* 1: 44–47.

Löffler, H.U. 2004. Microstructure modeling using artificial neural networks. In *Continuum Scale Simulation of Engineering Materials*, Raabe, D. et al. (eds.), Weinheim: Wiley-VCH, pp. 829–843.

Löffler, H.U., Döll, R., Wen, D. 2005. Microstructure prediction and control in hot strip mills. *Millennium Steel* 1: 182–186.

Lotter, U., Schmitz, H.-P., Zhang, L. 2002. Application of the Metallurgical oriented simulation system TKS StripCam to predict the properties of hot strip steels from rolling conditions. *Advanced Engineering Materials*, 4(4): 207–313.

McNutt, P., Lawrence, W.J., Fryer, C.A. 2006. Run-out table cooling models for high cooling rate products. *9th International Steel Rolling ATS*, June 19–21, Paris, France.

Miettinen, Z. 1998. Approximate thermodynamic solution phase data for steels. *CALPHAD* 22(2): 275–300.

Nikula, A., Ranta, H., Paavola, J. 1996. Effect of alloying elements and cooling rate on thermal properties during γ->α phase transformation. *2nd International Conference on Modelling of Metal Rolling Processes*, London, U.K., pp. 355–363.

Petch, N.J. 1953. The cleavage strength of polycrystals. *Journal of Iron Steel Institute* 174: 25.

Qin, J.S. Badgwell, T.A. 2003. A survey of industrial model predictive control technology. *Control Engineering Practice* 11(7): 733–764.

Schneider, A., Inden, G. 2004. Computer simulation of diffusion controlled phase transformations. In *Continuum Scale Simulation of Engineering Materials*, Raabe, D. et al. (eds.), Weinhem: Wiley-VCH, pp. 3–36.

Sellars, C.M., Whiteman, J.A. 1979. Recrystallization and grain growth in hot rolling. *Metal Science* 13: 187–194.

Sellars, C.M. 1980. The physical metallurgy of hot working. In *Hot Working and Forming Processes*, Sellars, C.M. and Davies, G.J. (eds.) London: Inst. of Metals, pp. 3–15.

Sundman, B., Jansson, B., Andersson, J.O. 1985. The Thermo-Calc Databank system. *CALPHAD* 9(2): 153–190.

Tzitzelkow, T. 1972. *Eine mathematische Methode zur Beschreibung des Umwandlungsverhaltens eutektoidischer Stähle*. Hochschule Aachen: Dissertation Techn.

Vandermeer, R.A. 2001. Advances in the study of recrystallization kinetics. In *Recrystallization and Grain Growth*, Gottstein, G. and Molodov, D.A. (eds.) New York: Springer-Verlag, pp. 645–657.

Weinzierl, K., Franz, K., Schmors, S. 2006. A novel phase transformation model based on Gibbs' free enthalpy and the Stefan equation improves material properties of hot rolled products. *ATS Steel Rolling 2006*, Paris, France.

Xie, H., Liu, X., Wang, G., Zhang, Z. 2006. Optimization and model of Laminar cooling control system for hot strip mills. *Journal of Iron and Steel Research* 13(1): 18–22.

Yang, Y.Y., Linkens, P.A., Trowsdale, A.J., Tenner, J. 2000. Ensemble neural network model for steel properties prediction. In *Proceedings of the IFAC-Symposium, Automation in Mining, Mineral and Metal Processing*, Jämsä-Jounela, S.L. and Vapaavuori, E. (eds.) Helsinki: IFAC, pp. 415–420.

Zener, C. 1949. Theory of growth of spherical precipitates from solid solution. *Journal of Applied Physics* 20: 950–952.

16 Novel Mathematical Models for Cold-Rolling Process

Eduard Garber, Alexander Traino, and Irina Kozhevnikova

CONTENTS

16.1 Introduction 179
16.2 New Cold-Rolling Theory Basics 180
16.3 Practical Implementation of New Theory for Cold-Rolling Technology Improvement 188
16.4 Conclusion 189
References 189

16.1 INTRODUCTION

There are several tendencies in the global development of flat steel rolling that are characteristic of the late 20th and early 21st centuries: increased quality requirements imposed on cold-rolled sheets, increased demand for ultra-thin cold-rolled sheets (structural grades with thickness of 0.3 mm and under, food quality tin sheet with thickness of up to 0.1 mm), and desire to decrease energy consumption at all stages of cold-rolled sheet production.

These tendencies have stimulated the development of various methods for cold-rolling process modeling because recognized mathematical models used in steel mill control systems did not permit calculation of rational and cost-effective technological modes, which would make it possible to turn out high-quality products meeting new, more stringent requirements.

A number of theoretical issues, which were supposedly well explored and described in the works of rolling theory founders in the 1950–1980s [1,2], had to undergo revision.

This was prompted by improvements in both equipment and technology of cold-rolling mills, which have changed deformation zone structure in the working stands and contact stress distribution along the arc of roll contact. For example, application of new lubricant-coolant fluids at cold-rolling mills producing structural and automotive products caused two to three times reduction of strip-on-roll friction coefficient (from 0.02 to 0.07 and 0.07 to 0.12), thus approaching the friction coefficient values achieved during tin plate rolling with palm oil.

Combined with reduced strip thickness, this process has influenced the entire set of rolling process energy and power parameters, and caused an increase in the length of deformation zone's elastic sections where plasticity condition is not effective. In the case of rolling 0.2–0.5 mm thick strips, the length of elastic sections has achieved 50%–70% of total deformation zone length [3].

The structure of plastic areas in deformation zones has changed as well: in the case of friction coefficient reduction to 0.02–0.03, the length of backward slip zone has increased up to 80%–95% of total plastic area length. Conventional cold-rolling models lack the body of mathematics that accounts for the above changes during contact stress, rolling force, and rolling power calculation. Therefore, old model implementation in automatic process control systems of rolling mills under new operating conditions created energy and power parameters calculation error up to 20%–50%, or higher. This inhibits the production of high-quality cold-rolled sheets, wastes energy, and prevents process running at high rolling speeds. In order to overcome the above difficulties, some rolling equipment producers base their automatic process control software not on physical models but on statistical and/or regression models, which does not necessarily lead to positive results.

In view of the above, the authors conducted extensive research from 2000 through 2006 to create up-to-date physical models of the cold-rolling process based on elasticity and plasticity laws, taking into consideration the above-mentioned changes in technology. The models created were verified in practical production environment. They provided high calculation accuracy of power and energy parameters of the rolling mill and were used for raising production efficiency and upgrading cold-rolled sheet quality [3–6].

16.2 NEW COLD-ROLLING THEORY BASICS

It has been determined that, to control rolling process effectively, the determination of neutral section exact position in the deformation zone of the working stands is of vital importance. For that purpose, we have found a solution of contact interaction between strip and roll based on an elastic-plastic model of the deformation zone. This solution, with a full set of its mathematical expressions, is given in the monograph [3]. Its main principles can be summarized as follows.

Deformation area outline with consideration for elastic flattening is approximated by two straight-line segments (see Figure 16.1): first, from entering cross section to vertical axial plane of rolls (it corresponds to bite angle α and, therefore, leans toward the rolling axis at $\alpha/2$ angle), and second, at the section of elastic partial restoration of strip thickness (it leans toward the rolling axis in the reverse direction at β angle).

The deformation zone of i-working stand is divided into j sections: an elastic strip compression section with length of x_{1el}; ($j = 1$); a plastic deformation section with length of $x_{pl.}$, consisting of two zones, a backward slip zone with a length of $x_{pl.bac}$ ($j = 2$) and a forward slip zone with a length of $x_{pl.for}$ ($j = 3$); and an elastic strip thickness partial restoration section with length of x_2 ($j = 4$) at the exit from deformation zone.

Formulas provided for calculation of α and β angles, and the length of each section are given further in the text.

Calculation of contact stress is done for each section separately by solving a system of three equations: a differential equation of strip balance, an elasticity equation for elastic sections, and a plasticity equation for backward and forward slip zones. The law of friction is expressed as:

$$\tau_x = \mu p_x, \quad \tau_j = \mu p_j \tag{16.1}$$

where

τ_x, p_x = tangential and normal contact stresses variable by axial coordinate «x» directed along the rolling axis

τ_j, p_j = average stress values τ_x and p_x for each section numbered «j»

μ = the friction coefficient in the deformation zone

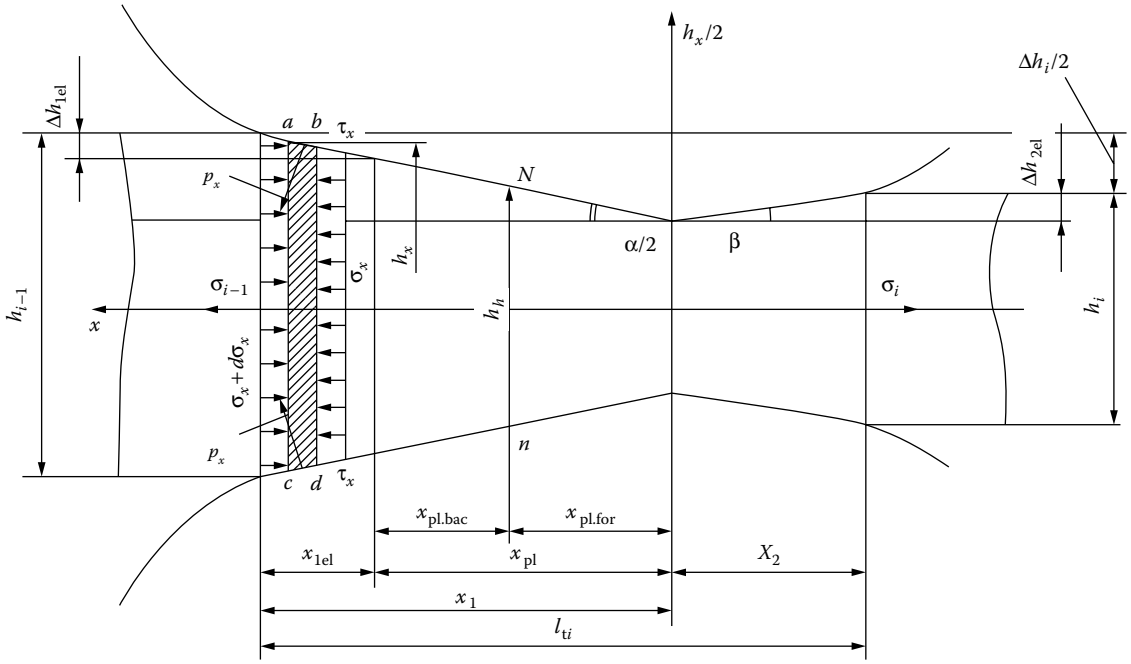


FIGURE 16.1 Elastoplastic model of a deformation zone: l_{ti} is the length of the deformation zone in the ith work stand with allowance for the elastic flattening of the strip and the rolls; x_{1el} is the length of the region of elastic compression of the strip; x_{pl} is the length of the plastic region; $x_{pl.bac}$ is the length of the backward slip zone in the plastic region; $x_{pl.for}$ is the length of the forward slip zone in the plastic region; x_2 is the length of the region of elastic recovery of part of the strip thickness at the end of the deformation zone; h_x is the variable strip thickness in the section with the coordinate X (the origin of coordinates is in the section where the strip thickness is minimum); h_n is the strip thickness in the neutral section n; α is the angle of nip; β is the angle in the region of elastic recovery of the strip thickness; Δh_i is the absolute reduction in the ith stand; Δh_{1el} and Δh_{2el} are the changes in the strip thickness in the regions of lengths x_{1el} and x_{2el}, respectively; σ_{i-1} and σ_i are the forward pull and backward pull of the strip, respectively; p_x and τ_x are the contact stresses (normal and tangential stresses, respectively) in the arcs ab and cd, respectively; $\sigma_x + d\sigma_x$ and σ_x are the compression stresses operating in the section ab and cd, respectively.

We used realistic empirical expressions for determination of μ to consider roll roughness, lubrication properties, and level of contact pressure.

As a result, we obtained the final form of the formulas for p_x, p_j, τ_x, and τ_j values calculations as a function of strip yield strength, reduction, stress, rolling speed, friction coefficient, strip and α, β angles elasticity parameters, characterizing the deformation zone. Integration of expressions for p_j allowed us to get an expression for its average value for the entire deformation zone ($p_{\text{av.}}$), and, after multiplication by contact area, rolling force calculation formulas. Formulas for the calculation of the average normal contact stresses in the regions of deformation zone are given in Table 16.1.

Here, $E_{\text{str.}}$ is the elastic modulus of the strip material, μ_i is the friction coefficient in the deformation zone of the ith stand, and σ_{f2} is the average strain resistance in the plastic region of the deformation zone:

$$\delta_{i-1} = \mu_i/\tan(\alpha/2); \quad \delta_i = \mu_i/\tan\beta$$

$$D = E_{\text{str.}}/(E_{\text{str.}} - \sigma_{\text{f2}}); \quad L = (E_{\text{str.}} - \sigma_{\text{f2}})/\sigma_{\text{f2}}$$

(The other designations are given in Figure 16.1 and Table 16.1.)

The strip thickness in the neutral section, which enters into the calculation formulas for p_2 and p_3 in Table 16.1, is calculated as follows:

TABLE 16.1
Formulas for the Calculation of the Average Normal Contact Stresses in the Regions of the Elastoplastic Deformation Zone

Zone Regions		Designation of the Average Normal Contact Stresses	Formula to Calculate the Average Contact Stress
Code	Force Model		
1	Region of elastic compression of the strip at the beginning of the deformation zone	P_1	$p_1 = 1.15E_{\text{str.}}\left\{\left(\frac{1}{\delta_{i-1}} + \frac{L}{\delta_{i-1}+1}\right)\left[\left(\frac{\delta_{i-1}-1}{(\delta_{i-1}+1)\delta_{i-1}} - \frac{\sigma_{i-1}}{1.15E_{\text{str.}}}\right)\times(D^{\delta_{i-1}+1}-1) - 2\ln D\right]\right\}$
2	Backward slip zone of the plastic region	P_2	$p_2 = \frac{1.15\sigma_{\text{f2}}}{\delta_{i-1}}\times\frac{h_{\text{n}}}{h_{i-1}-h_{\text{n}}D}\left\{\left[\frac{E_{\text{str.}}}{\sigma_{\text{f2}}}\times\frac{1+\delta_{i-1}(1-2D^{-1})-D^{\delta_{i-1}}(\delta_{i-1}+1)}{\delta_{i-1}+1} - \frac{\sigma_{i-1}}{1.15\sigma_{\text{f2}}}D^{\delta_{i-1}}\delta_{i-1}-1\right]\frac{D^{-\delta_{i-1}}}{\delta_{i-1}+1}\left[\left(\frac{h_{i-1}}{h_{\text{n}}}\right)-D^{\delta_{i-1}+1}\right]+\left(\frac{h_{i-1}}{h_{\text{n}}}-D\right)\right\}$
3	Forward slip zone of the plastic region	P_3	$p_3 = \frac{1.15\sigma_{\text{f2}}}{\delta_{i-1}}\times\frac{h_i}{h_{\text{n}}-h_i/D}\left\{\left[\frac{E_{\text{str.}}\delta_{i-1}}{\sigma_{\text{f2}}\delta_i}\times\frac{1+\delta_i(1-2D^{-1})-D^{\delta_i}(\delta_i+1)}{\delta_i+1} - \frac{\sigma_i}{1.15\sigma_{\text{f2}}}D^{\delta_i}\delta_{i-1}+1\right]\frac{D^{\delta_{i-1}}}{\delta_{i-1}+1}\left[\left(\frac{h_{\text{n}}}{h_i}\right)^{\delta_{i-1}+1}-\left(\frac{1}{D}\right)^{\delta_{i-1}+1}\right]+\left(\frac{h_{\text{n}}}{h_i}-\frac{1}{D}\right)\right\}$
2–3	Plastic region consisting of only the backward slip zone (a forward slip zone is absent)	P_{2-3}	$p_{2-3} = \frac{1.15\sigma_{\text{f2}}}{\delta_{i-1}}\left\{\left[\frac{E_{\text{str.}}}{\sigma_{\text{f2}}}\times\frac{1+\delta_{i-1}(1-2D^{-1})-D^{\delta_{i-1}}(\delta_{i-1}+1)}{\delta_{i-1}+1} - \frac{\sigma_{i-1}}{1.15\sigma_{\text{f2}}}D^{\delta_{i-1}}\delta_{i-1}-1\right]\frac{h_i}{\Delta h_i(\delta_{i-1}+1)}\left[\left(\frac{h_{i-1}}{h_i}\right)^{\delta_{i-1}+1}-1\right]+1\right\}$
4	The second elastic region (elastic recovery of part of the strip thickness)	$P_{4(a)}$	(a) In the presence of a forward slip zone $p_{4(a)} = 1.15E_{\text{str.}}\left\{\frac{1}{\delta_i}+\frac{L}{\delta_i+1}\left[\left(\frac{\delta_i-1}{(\delta_i+1)\delta_i}-\frac{\sigma_i}{1.15E_{\text{str.}}}\right)(D^{\delta_i+1}-1)-2\ln D\right]\right\}$
		$P_{4(b)}$	(b) In the absence of a forward slip zone $p_{4(b)} = 1.15E_{\text{str.}}\left\{-\frac{1}{\delta_i}+\frac{L}{1-\delta_i}\left[\left(\frac{1+\delta_i}{(1-\delta_i)\delta_i}-\frac{\sigma_i}{1.15E_{\text{str.}}}\right)(D^{1-\delta_i}-1)-2\ln D\right]\right\}$

$$h_n = \left\{1+\left\{\frac{\delta_{i-1}}{1.15\sigma_{f2}}\left[1+\frac{E_{str.}}{\sigma_{f2}}\left[\frac{1+\delta_{i-1}\left(1-2D^{-1}\right)-D^{\delta_{i-1}}\left(\delta_{i-1}+1\right)}{\delta_{i-1}+1}\right.\right.\right.\right.$$
$$\left.-\frac{\sigma_{i-1}}{1.15E_{str.}}D^{\delta_{i-1}}\delta_{i-1}-\frac{E_{str.}}{\sigma_{f2}}\right]$$
$$\times\left[\frac{\delta_{i-1}}{\delta_i}\times\frac{1+\delta_i\left(1-2D^{-1}\right)-D^{\delta_i}\left(\delta_i+1\right)}{\delta_i+1}\right.$$
$$\left.\left.-\frac{\sigma_i}{1.15E_{str.}}D^{\delta_i}\delta_{i-1}+\frac{E_{str.}}{\sigma_{f2}}\right]\left(\frac{h_{i-1}}{h_i}\right)^{\delta_{i-1}}\right]\Bigg\}^{1/2}$$
$$\times\left[D^{\delta_{i-1}}\left[\frac{E_{str.}}{\sigma_{f2}}\times\frac{\delta_{i-1}}{\delta_i}\times\frac{1+\delta_i\left(1-2D^{-1}\right)-D^{\delta_i}\left(\delta_i+1\right)}{\delta_i+1}\right.\right.$$
$$\left.\left.-\frac{\sigma_i}{1.15\sigma_{f2}}D^{\delta_i}\delta_{i-1}+1\right]\Big/h_i^{\delta_{i-1}}\right]^{-1}\Bigg\}^{1/\delta_{i-1}} \qquad (16.2)$$

If $h_n < h_i$ in the calculation by Equation 16.2, a forward slip zone is absent in the deformation zone; that is, the whole zone is represented by a backward slip zone. In this case, one average normal contact stress p_{2-3} is calculated for the plastic region, rather than the stresses p_2 and p_3. For the second elastic region, the average normal contact stress $p_{4(b)}$ is calculated, rather than the average value $p_{4(a)}$ (Table 16.1).

The tangents of angles $\alpha/2$ and β characterizing the geometry of the deformation zone, which are required for calculation by the procedure in [1–3], are determined from the expressions:

$$\tan\frac{\alpha}{2}=\frac{\Delta h_i+\Delta h_{2el}}{2X_1} \qquad \tan\beta=\frac{\Delta h_{2el}}{2X_2}$$

where

$\Delta h_i = h_{i-1} - h_i$ is the absolute reduction in the ith stand

$\Delta h_{2el} = h_i\sigma_{f2}/E_{str.}$ is the change in the thickness in the second elastic region

$X_1 = (R\Delta h_i + X_2^2)^{1/2}$

R is the radius of the work-roll body

X_2 is the length of the second elastic region, which is determined by the Hertz formula,

$$X_2 = 8p_{avi}R\left(\frac{1-\nu_r^2}{\pi E_r}+\frac{1-\nu_{str.}^2}{\pi E_{str.}}\right) \qquad (16.3)$$

where ν_r^2 and $\nu_{str.}^2$ are the Poisson ratios for the roll and strip materials, respectively, and E_r is the elastic modulus of the roll material.

The average normal contact stress p_{avi} and the rolling force P_i for the deformation zone in the ith stand can be calculated by the formulas:

$$p_{avi}=\frac{(p_1x_{1el}+p_2x_{pl.bac}+p_3x_{pl.for}+p_{4(a)}x_2)}{l_{ti}} \qquad (16.4)$$

or (if the plastic region consists of only the backward slip zone, look at Table 16.1):

$$p_{avi}=\frac{(p_1x_{1el}+p_{2-3}x_{pl}+p_{4(b)}x_2)}{l_{ti}}$$
$$P_i = p_{avi}l_{ti}b, \qquad (16.5)$$

where $x_{1.....}x_2$ are the lengths of the regions shown in Figure 16.1, l_{ti} is the total deformation zone length (the sum of the regions lengths), and b is the strip width.

Since the Hertz formula for length x_2 contains the unknown p_{avi}, this calculation procedure is realized using iterations: as the first approximation, p_{avi} is put equal to, e.g., 1.15 $\sigma_{str.}$, and this value is refined during iterations with Equations 16.4 or 16.5.

According to Table 16.1, the normal contact stresses in the regions depend on the resistance of deformation σ_{f2}. Therefore, average normal contact stress p_{avi} and rolling force P_i depend on σ_{f2}. However, our method calculates these dependencies more accurately than classical methods [1,2].

By using the above model of contact stress, we have created a novel model for rolling work and rolling power calculation. According to this model, the rolling power in the ith stand $N_{rol.i}$ Megawatt (MW) can be calculated by the formula:

$$N_{rol.i} = a_{roli}V_i = a_{roli}bh_iv_i$$

where

V_i is the volume of the strip rolled in unit time, m^3/s

b is the strip width, m

and v_i is the strip speed at the end of the ith stand, m/s

a_{roli} is the specific work of rolling in the ith stand of a continuous mill, MJ/m^3 (the work necessary for rolling of the strip with the volume 1 m^3).

According to our calculation scheme (Figure 16.2), in this model specific rolling works a_j are calculated primarily for each of j deformation area sections, separately along the axis of rolling and across it, taking into consideration energy spent by both normal and tangential forces. While doing so, it is important to keep in mind that tangential forces appearing due to action of stress τ_j on the strip in the backward slip zone are directed toward strip movement, while those appearing in the forward slip zone have opposite direction.

Table 16.2 shows the derived formulas for a_j. Table symbols are: h_0 and h_1—strip thickness at rolls entrance and exit, respectively, including h_{1el} —strip thickness at the end of first elastic section, h_n—strip thickness in neutral cross section, h_{2el}—strip thickness at the beginning of second elastic section.

As seen from the table, rolling work in the forward slip zone (sections $j = 3$, $j = 4$, (a)) is negative, therefore, rolls are not doing any work in this zone; on the contrary, strip returns to rolls a part of the energy obtained in the backward slip zone. Under no circumstances could this result be obtained by well-known, especially classical, methods of rolling power calculation. This was an original result we obtained in our research.

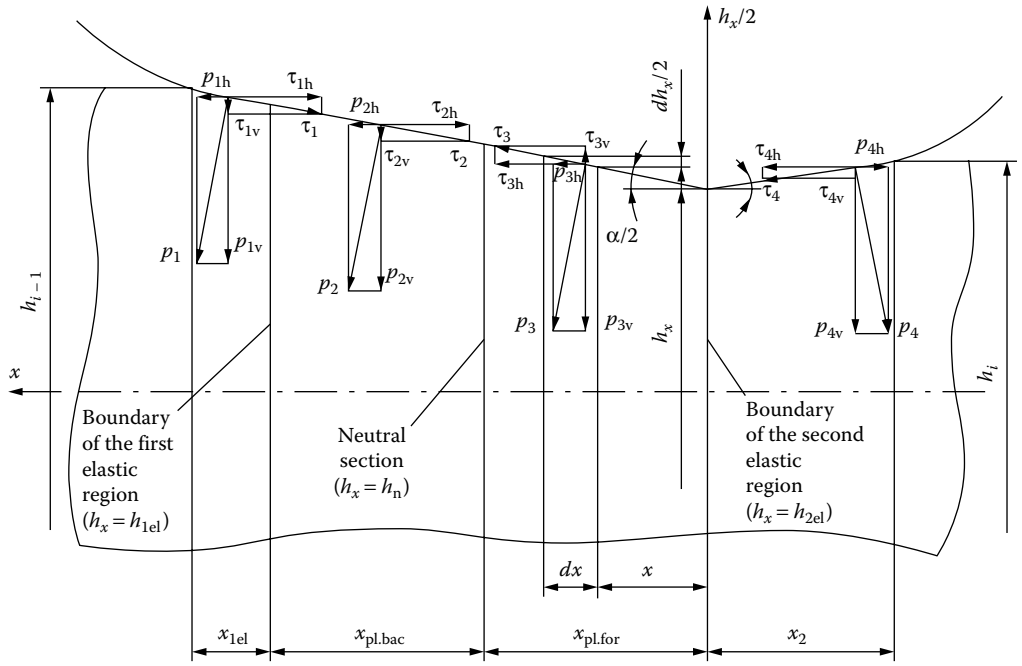


FIGURE 16.2 Calculation scheme for the determination of the rolling power with allowance for the friction work and the elastoplastic scheme of the deformation zone.

TABLE 16.2
Specific Rolling Works on Various Sections of Deformation Zone (a_j)

j	Calculation Formula a_j
1	$+\tau_1\left(\frac{1}{\tan\alpha/2}+\tan\alpha/2\right)\ln\frac{h_0}{h_{1el}}$
2	$+\tau_2\left(\frac{1}{\tan\alpha/2}+\tan\alpha/2\right)\ln\frac{h_{1el}}{h_n}$
3	$-\tau_3\left(\frac{1}{\tan\alpha/2}+\tan\alpha/2\right)\ln\frac{h_n}{h_{2el}}$
2–3[a]	$+\tau_{2-3}\left(\frac{1}{\tan\alpha/2}+\tan\alpha/2\right)\ln\frac{h_{1el}}{h_{2el}}$ ($\tau_{2-3}=\mu\rho_{2-3}$[a])
	In case of forward slip zone existence:
4,(a)	$-\tau_4\left(\frac{1}{\tan\beta}+\tan\beta\right)\ln\frac{h_1}{h_{2el}}$
	In case of forward slip zone absence:
4.(b)[a]	$+\tau_4\left(\frac{1}{\tan\beta}+\tan\beta\right)\ln\frac{h_1}{h_{2el}}$

[a] For deformation area containing backward slip zone only.

Confidence test of the methods stated above has been conducted by means of calculated and measured values comparison for rolling power and rolling forces at the existing continuous cold-rolling mills equipped by automatic process control systems and stationary means of measurement for all major parameters (technological, power and energy). A database containing information on 101 rolling schedules for strips of various steel grades and sizes was built at the five-stand mill 1700. The same was done for 52 rolling schedules of similar strips at the four-stand mill 1700. A statistical divergent series of measured and calculated force and power values contained more than 700 entries each (number of rolling schedules multiplied by number of stands). The result is that average errors of power and force calculation are 4%–6%, respectively, and maximum deviations are 8%–10%, respectively, which is six to eight times less than in the case of calculation according to known (classical) methods.

Cold-rolling process analysis by means of our newly developed methods brought several previously unknown mechanisms to the forefront:

1. We determined that in the backward slip zone the deformation area is self-cleaning of its mechanical and fat contaminants, while in the forward slip zone such self-cleaning is difficult.
2. We determined that, in cases when the length of the backward slip zone changes in relation to that of the forward slip zone in favor of the backward slip zone, the rolling energy consumption increases. If this relation changes in favor of the forward slip zone, the energy consumption decreases.
3. We determined that we can influence the above-mentioned zone length relationship by redistribution of single pass reductions and interstand strip tensions at the continuous rolling mill. In so doing,

it is possible to create a deformation zone in which the neutral cross section and forward slip zone are absent, while contact stresses along the deformation zone are practically constant.

4. We determined that adhesion areas in deformation zones of modem cold-rolling mills are, in fact, absent, regardless of steel grade, reduction schedules, and tensions.

Therefore, smoothing of peaks (extreme values) of contact stresses, appearing close to the neutral cross section, does not take place during cold rolling.

Figure 16.3 shows, as an example, a curve of normal contact stress p_x deviation along the length of deformation zone in the fifth stand of the five-stand mill 1700 during rolling of 0.3-mm-thick strip.

The curve shows that the maximum p_x value in the neutral cross section area $p_{x\max}$ = 1850 MPa, while average strip plastic deformation resistance in this stand is σ_{f2} = 770 MPa. This means that maximum contact stress has exceeded yield strength point more than twice, which may cause a risk of surface defect appearance at both strip and roll (scratches, cuts, collar marks). Such defects may result in strip breakage between stands and lead to undesirable roll changes. Our calculations show that production programs of continuous cold-rolling mills contain steel grades and strip thicknesses during rolling of which maximum contact stress can reach even greater values: 2400–2500 MPa. They can as well be reduced by redistribution of reduction and strip interstand tension values.

From this point of view, the curve shown in Figure 16.4 is of interest; it represents $p_x(x)$ in the third stand of the same mill during rolling of 1.5-mm-thick strip. Deformation area there contains the backward slip zone only, while the neutral cross section is totally absent.

On this graph curve $p_x(x)$ has a radically different character as compared with Figure 16.3: contact stresses remain practically constant throughout the entire length of the plastic

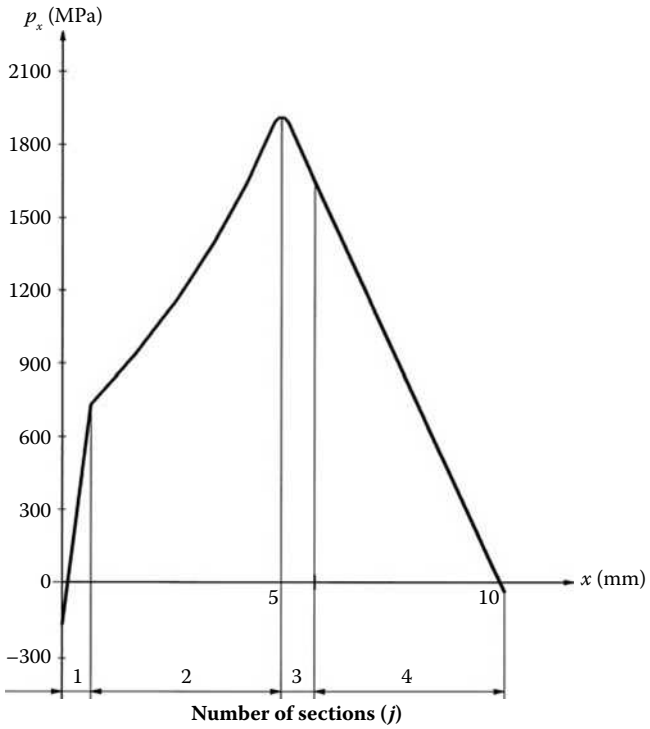


FIGURE 16.3 Deviation of p_x along the length of deformation zone in the fifth stand of five-stand mill 1700 during rolling of 0.3-mm-thick strip.

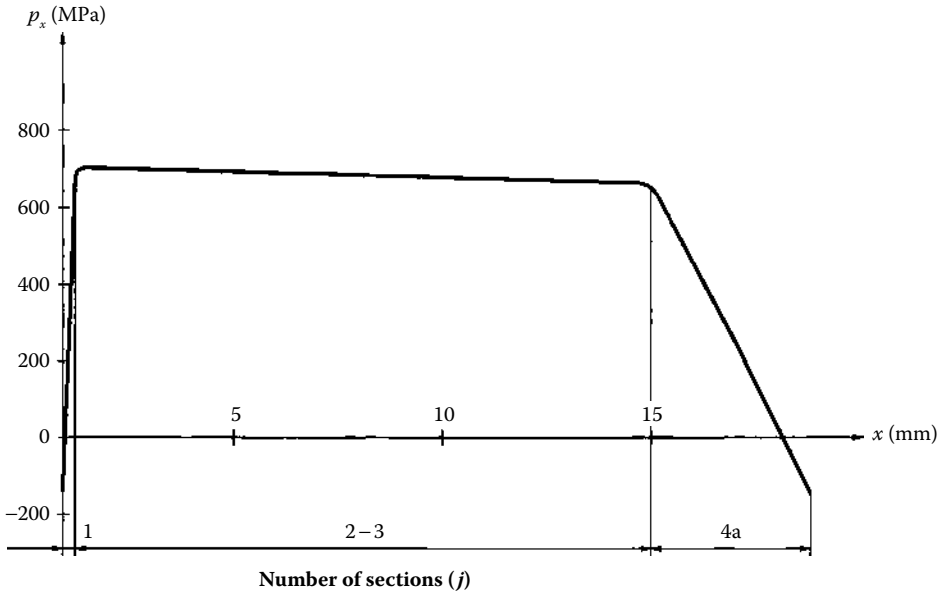


FIGURE 16.4 Deviation of p_x along the length of the deformation zone in the third stand of the five-stand mill 1700 during rolling of 1.5-mm-thick strip.

section of the deformation zone. This significantly reduces the risk of damage to the roll and strip surface.

Consequently, the rolling schedules in which an entire deformation zone is, in fact, a backward slip zone, are much more favorable from the point of view of contact stress risk. This assumption is made upon comparison with the schedules where both the neutral cross section and forward slip zone are present in the deformation area.

However, product range and rolling schedule changes mentioned in the introductory part of this chapter have caused some negative consequences despite significant positive effects. One of them is known to experts around the world. It is the development of roll slippage and vibration of roll stands (especially during rolling of strips with 0.3- to 0.4-mm thickness). In order to determine reasons for these phenomena, we conducted an analysis of directions of forces and moment acting between work rolls and backup rolls. In doing so, the following was taken into consideration: friction forces of type I (sliding and static friction) as well as type II (rolling friction) appearing between rolls; friction and clearance in roll bearings, between roll chocks and support pad surfaces of stand housings, as well as rolling mill accelerations and decelerations, and deviation of rolling force and strip tension.

As a result, we have developed new models of energy and power parameters for a four-high stand (for the calculation scheme see Figure 16.5).

In mechanics, the energy consumed for rolling friction is determined using the coefficient of rolling friction in the arm of the roll force, in other words, the distance m from the center of the area of elastic contact between two parallel cylinders pressed to each other to the point of application of the roll force P_{if}. The arm of the interroll force m was determined by the formula

$$m = cb_{bac} \tag{16.6}$$

where c is an empirical coefficient (coefficient of the arm of the roll force) that depends on the properties of the cylinder materials, their surface roughness, and the force and kinematic conditions that appear in the contact area during the rotation of the cylinders, and b_{bac} is half the contact area width calculated by the Hertz–Belyaev formula. As applied to the contact between the work and backup rolls of a four-high stand (Figure 16.5), this formula has the form

$$b_{bac} = 0.789\left(\eta \frac{P_{if}}{L} \times \frac{D_w D_{bac}}{D_w + D_{bac}}\right)^{1/2} \tag{16.7}$$

where D_w and D_{bac} are the body diameters of the work and backup rolls, respectively; η is the elastic constant (i.e., the reduced elastic modulus of the roll materials); L is the contact length of the roll bodies; and P_{if} is the roll force.

The accuracy of calculating the arm of rolling friction using Equation 16.6 depends on the reliability of coefficient c. However, the values of c recommended in the literature fall in a very wide (0.002–0.4) range [5,6], and no recommendations exist about the effects of the roll force, the roll surface roughness, the speed of roll rotation, and other factors on this coefficient.

Therefore, we aimed to determine the real energy consumption for rolling friction in the working stands of rolling and pinch-pass mills during the production of cold-rolled steel sheets using the databases of the process control systems of these mills, which contain measured technological and energy–force parameters.

The procedure designed to solve the formulated problem is based on the dependence of the moment M_w required to drive the work rolls of a four-high stand, on its design, technological, and energy–force parameters (including m) and was grounded in [3]. This dependence takes into account the following factors:

$$M_w = M_{rol} + M_{pull} + M_{fr.b} + M_{bac} \tag{16.8}$$

where M_{rol} is the rolling moment, M_{pull} is the moment of the strip pull force, $M_{fr.b}$ is the moment of friction in the bearings of work rolls, and M_{bac} is the moment required to drive idle backup rolls.

These moments are as follows:

1. The rolling moment is

$$M_{rol} = N_{rol}/\omega_w \tag{16.9}$$

where N_{rol} is the rolling power and ω_w is the angular velocity of the work-roll rotation.

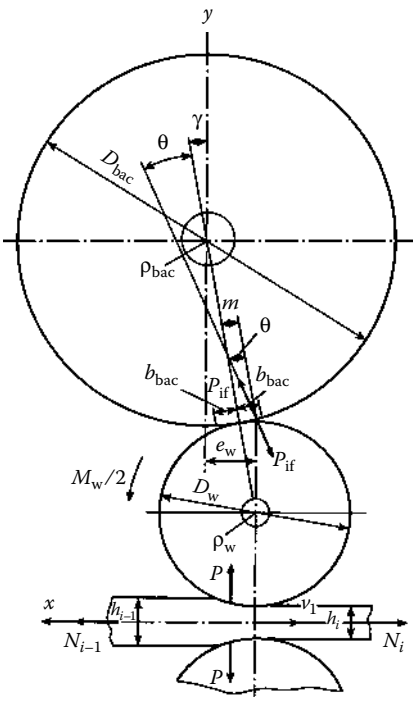


FIGURE 16.5 Force and moment calculation scheme for a four-high stand.

2. The moment of the strip pull force is

$$M_{\text{pull}} = \Delta N_i D_{\text{w}}/2 \tag{16.10}$$

where $\Delta N_i = N_{i-1} - N_i$ is the difference in the forces of the backward (N_{i-1}) and forward (N_i) pulls of the strip.

3. The moment of friction in the bearings of work rolls is

$$M_{\text{fr.b}} = \mu_{\text{b.w}} \frac{d_{\text{b.w}}}{2} [\Delta N_i - 2P_i \tan(\theta + \gamma)] \tag{16.11}$$

where $\mu_{\text{b.w}}$ is the friction coefficient in the bearings of the work rolls, $d_{\text{b.w}}$ is the working diameter of these bearings, P_i is the rolling force, θ is the angle between the plane of the interroll force and the plane of the roll axes, and γ is the angle the vertical axial plane of the backup roll makes with the plane passing through the roll axes (see Figure 16.5). These angles can be calculated using the following expressions:

$$\tan\theta = \frac{2(cb_{\text{bac}} + \mu_{\text{b.bac}} d_{\text{b.bac}}/2)}{D_{\text{bac}}} \tag{16.12}$$

$$\sin\gamma = \frac{2e_{\text{w}}}{D_{\text{w}} + D_{\text{bac}}} \tag{16.13}$$

where $\mu_{\text{b.bac}}$ is the friction coefficient in the bearings of the backup rolls, $d_{\text{b.bac}}$ is the working diameter of these bearings, and e_{w} is the horizontal shift in the work-roll axis with respect to the vertical axial plane of the backup roll (which is one of the design parameters of a four-high stand).

4. The moment required to drive idle backup rolls is

$$M_{\text{bac}} = \frac{2P}{\cos(\theta + \gamma)} \left[\frac{D_{\text{w}}}{2} \sin\theta + cb_{\text{bac}} \cos\theta \right] \tag{16.14}$$

For a driven moment M_{w} to be created according to Equation 16.8, the power

$$N_{\text{w}} = M_{\text{w}} \omega_{\text{w}} \tag{16.15}$$

should be supplied to work rolls from the main drive. Hence, the power of the main drive engines should be:

$$N_{\text{eng.w}} = \frac{N_{\text{w}}}{\eta} = \frac{M_{\text{w}} \omega_{\text{w}}}{\eta} \tag{16.16}$$

where η is the efficiency of the main drive line of the stand.

As follows from Equations 16.8 through 16.16, the effect of rolling friction on the main drive power of the stand manifests itself both explicitly (through arm m, which is equal to the product cb_{bac} (Equation 16.14)) and implicitly (through angle θ, which depends on the same arm (Equations 16.11, 16.12, and 16.14)).

To find the values of m and c, we calculated the engine powers and determined the total actual engine power:

$$N_{\text{eng.a}} = \sum_{i=1}^{k} I_i U_i \tag{16.17}$$

where I_i and U_i are the armature current and the voltage across the terminals of the ith engine, respectively, measured under operating conditions, and k is the number of engines in the main drive line.

We determine the refined value of c as the root of the equation:

$$\Delta N_{\text{eng}} = N_{\text{eng.a}} - N_{\text{eng.w}} = 0 \tag{16.18}$$

in which $N_{\text{eng.w}}$ is expressed through Equation 16.16 and moment M_{w} entering into this equation is expressed in Equations 16.8 through 16.15.

To solve Equation 16.18, we use an iteration method: we change coefficient c at a given step and choose its value so that the calculated and actual powers of the working stand engines are equal to each other. We used the equations described above for the analysis of stands work and have determined some dependencies as follows:

1. Roll slippage will occur should the following inequality not be met:

$$tg\theta < f_{\text{st}} \tag{16.19}$$

where θ = angle of inclination of the force, acting between work roll and backup roll, against the plane, connecting the axes of the rolls (the model provides a method for calculation of this angle); f_{st}, static friction coefficient in contact area between these rolls (we are the first who developed a regression equation in order to determine friction coefficient value, taking into consideration roughness and hardness of rolls, lubricating properties of emulsion, rotational speed of rolls and other factors).

2. The reason for sudden vibration development in one or another work stand is in unstable horizontal balance of working rolls. Variation of rolling speed, deviations of rolling force, and strip tension result in change of equilibrium of forces acting on the rolls and their bearings. In the case of unfavorable balance of these forces, rolls may take an unstable position and begin sliding back and forth within the gaps allowed by theft chocks and support pad surfaces of stand housings. This shifting is accompanied by impacts of chocks on internal surfaces of stand housings, where resonance oscillations appear.

Many specialists have chosen the working stand model as a vibratory system to study vibration processes.

We have developed a different approach in our research: we attempted to develop a combination of technological and power parameters, which could guarantee the exclusion of any vibrations in a working stand.

Rather than simulate vibrations, we have simulated a condition, which totally excludes vibrations:

$$p_i(1-K_p)(1-\delta)\tan(\theta+\gamma) - 0.5[N_{i-1}(1+K_N) - N_i(1-K_N)]\Delta F_{\text{hor}} > 0 \quad (16.20)$$

where

p_i = rolling force
δ = its calculation error
K_p = its instability coefficient (vibration level)
γ = angle between vertical and axial planes of work rolls and backup rolls (Figure 16.5)
N_{i-1}, N_i = strip front and rear tension forces
K_N = their instability coefficient
ΔF_{hor} = maximum possible oscillation of horizontal force acting on the work roll

This model provides for realistic determination of all variables contained in the expression shown in Equation 16.20.

We determined that one of the reasons for strip tension deviations between working stands of a continuous cold-rolling mill is poor adjustment of mill speed settings. The task of such adjustment is the ability to determine radial speed of roll barrel $V_{\text{rol}i}$ with maximum accuracy via strip speed V_i (where i is a stand number) preset for each stand. The value of forward slip coefficient S_i is used for that purpose:

$$V_{\text{rol}i} = \frac{V_i}{S_i + 1} \quad (16.21)$$

However, known methods of S_i determination give significant errors as they do not consider elastic sections of the deformation zone at modern mills.

By using the elastic-plastic model of the deformation zone, we obtained new, more exacting formulas:

1. For deformation zone with neutral cross section:

$$S_i = \frac{h_{\text{n}}}{h_i\left[1+\tan^2\left(\frac{\alpha}{2}\right)\right]^{0.5}} - 1 \quad (16.22)$$

where

h_{n} = strip thickness in neutral cross section;
α = roll-to-strip contact angle.

2. For deformation zone, containing backward slip zone only:

$$S_i = -\frac{\sigma_{\text{f}2}}{E_{\text{str.}}} \quad (16.23)$$

where

$\sigma_{\text{f}2}$ = yield strength of strip (average value in i-stand); $E_{\text{str.}}$ = modulus of elasticity of its material.

The minus (–) sign in Equation 16.23 means that strip exits from such deformation zones at a speed less than that of rolls. Once again, this result could not be achieved by classic methods; our research result was the first ever obtained.

In order to exactly evaluate energy losses on rolling friction between rolls, we have conducted comprehensive industrial and laboratory testing of rolling friction coefficients. As a result, we were able to obtain a regression equation allowing us to calculate this coefficient as a function of substantial factors of real cold-rolling and skinpassing processes. We determined that the energy portion spent on rolling friction during cold rolling may reach as much as 30%–60% of total energy consumed by mill motors, while that spent during skinpassing may reach as much as 60%–80% of the same. The friction coefficient increases as the rolling speed increases.

We found that a deformation zone with two neutral sections can exist in a strip during cold rolling in certain working stands in continuous rolling mills.

Figure 16.6 shows three versions of deformation zones and strip-velocity distributions along their lengths.

The deformation zone in Figure 16.6a has a neutral section and consists of four regions: two elastic regions of lengths x_1 and x_4 and two plastic regions, namely, a backward slip zone and a forward slip zone, of lengths $x_2 = x_{\text{bac}}$ and $x_3 = x_{\text{for}}$ respectively. The strip velocity v_i at the exit of the rolls is higher than the peripheral roll velocity $v_{\text{rol}i}$ (i is the working stand number); that is, the forward-slip coefficient in this deformation zone is positive:

$$S_i = \frac{v_i}{v_{\text{rol}i}} - 1 > 0$$

The parameters $X_i = x_{\text{bac}}/(x_{\text{bac}} + x_{\text{for}})$, which characterize the positions of neutral sections in such deformation zones in modern cold-rolling mills, fall in the range $0.7 \le X_i < 1$.

The deformation zone in Figure 16.6b has neither a neutral section nor a forward slip zone; that is, it consists of only three regions. Two of them are identical to those in the version of Figure 16.6a (namely, two elastic regions of lengths x_1 and x_4), and the third is a plastic region of length $x_{2-3} = x_{\text{pl}}$. All of these regions are in the backward slip zone, and the strip velocity v_i at the exit is lower than the peripheral roll velocity. Therefore, the forward-slip coefficient in this deformation zone is negative

$$S_i = \frac{v_i}{v_{\text{rol}i}} - 1 < 0$$

and X_i is maximal ($X_i = 1$).

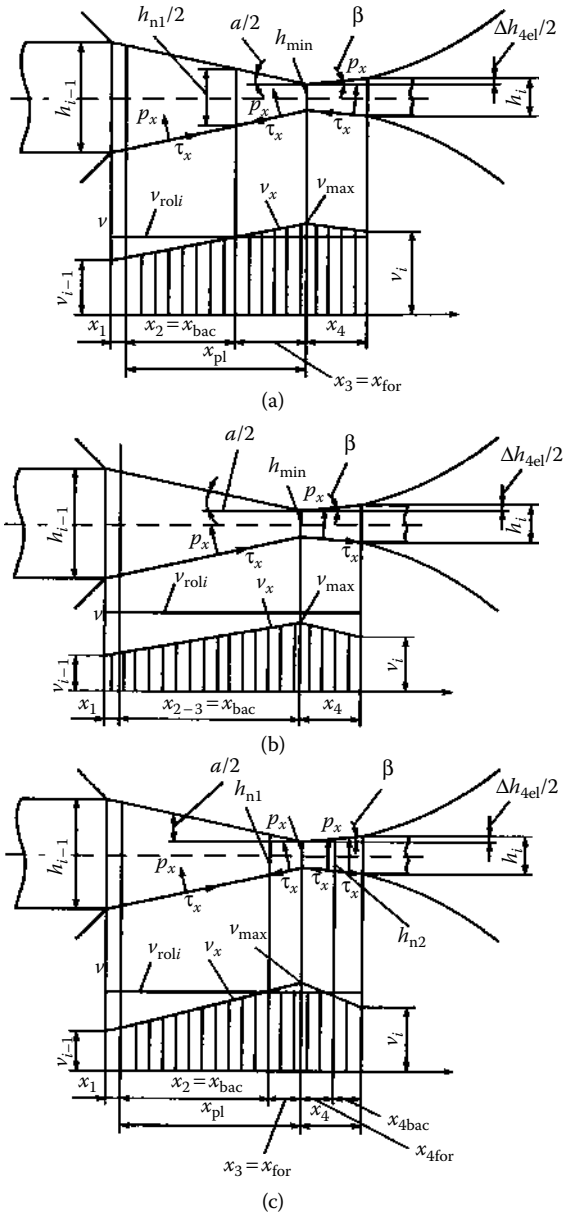


FIGURE 16.6 Versions of structural schemes for deformation zones and strip-velocity profiles in these zones.

The use of the energy–force calculations of cold-rolling mills demonstrates the presence of a third version of a deformation zone, where, apart from the neutral section located in the plastic region, another neutral section appears in the second elastic region (Figure 16.6c). This appearance is caused by the fact that, according to the law of constant instantaneous volumes, the strip has the maximum velocity v_{max} in the section coinciding with the vertical axial plane of the rolls, in which the strip thickness is minimal ($h_x = h_{min}$), at the boundary between the plastic and second elastic regions (see Figure 16.3c).

As the strip moves further, its velocity decreases because of an elastic increase in its thickness from h_{min} to h_i. The first neutral section of thickness h_{n1} is located close to the section of thickness h_{min} (i.e., the forward slip zone length x_3 is much smaller than the backward slip zone length x_2). As the strip velocity decreases in the second elastic region, this strip velocity v_x can become lower than the peripheral roll velocity v_{ri}. In this case (Figure 16.6c), the second neutral section of thickness h_{n2} appears at the site where the v_x and v_{ri} curves intersect each other. As a result, the second elastic region is divided into two zones, namely, a forward slip zone of length x_{4for} and a backward slip zone of length x_{4bac}, and the entire deformation zone consists of five rather than three or four regions (Figure 16.6c).

This deformation-zone version has not yet been considered, and methods for the calculation of the energy–force parameters for this version are absent. We filled this gap and developed a mathematical model for a deformation zone with two neutral sections that should include procedures for the calculation of the contact stresses, the rolling force, the h_{n1} and h_{n2} thicknesses, and the forward-slip coefficient [6]. The application of this method decreases the error of force calculation for rolling mills.

16.3 PRACTICAL IMPLEMENTATION OF NEW THEORY FOR COLD-ROLLING TECHNOLOGY IMPROVEMENT

We have developed and implemented in practice some continuous mill algorithms for adjustment of rolling schedules, allowing such distribution of single reduction and strip tension values among stands that increases the length of forward slip zones in the most energy-consuming intermediate stands and decreases the length of the same zones in the last (finishing) stands.

This provided electric energy saving of 4%–8% and reduction of cold-rolled strip surface contamination by 30%–50%.

We applied this technology to the fourth stand of five-stand mill 1700, which had a tendency to vibrate, which substantially increases while rolling strips of less than 0.4-mm thickness at a speed of 10–12 m/s. We changed technological process parameters so that inequality (Equation 16.20) is eliminated. This allowed us to exclude vibrations and increase rolling speed up to 18–20 m/s. As a result, the condition (Equation 16.20) is included in the algorithm of automatic process control system for this rolling mill.

For five-stand mill 1700, we performed testing of the improved modes of working stand roll speed adjustment based on refined values of forward slip coefficients, calculated by Equations 16.21 and 16.22. As a result, deviations of strip tension between stands were reduced by 20%–30%, which significantly contributed to average rolling speed growth.

We have created improved methods of calculating the installed power of working stand motors with consideration for energy consumed on rolling friction, and with the use of all the above-mentioned new methods of power–energy calculations for the mill. This allows us to reduce capital spending by eliminating unreasonable power reserves at the stage of designing the main drives for continuous cold-rolling and skinpassing mills.

Based on heat mode model discussed earlier, we improved the design of roll cooling system. As a result, the difference in temperature of top and bottom rolls reduced from 6°C to 8°C and 1°C to 2°C; their combined temperature level did not exceed 60°C–70°C as the rolling speed increased up to 20–25 m/s.

16.4 CONCLUSION

We highly recommend the new methods of cold-rolling process modeling presented here for development of rolling mill control systems. They will ensure increased rolling speed, upgrade the quality of cold-rolled sheets, and save energy in production.

The limited scope of the paper did not allow us to explain in detail all theoretical and practical aspects of our research.

Should representatives of metallurgical and machine-building companies be interested, the authors are prepared to share any details they may find important or useful.

REFERENCES

1. Tselikov, A.I., Tomlenov, A.D., Zyuzin, V.I., et al. 1982. *Teoriya Prokatki: Spravochnik* (Theory of Rolling: Handbook). Moscow: Metallurgiya.
2. Tselikov, A.I., Nikitin, G.S., Rokotyan, S.E., et al. 1980. *Teoriya Prodolnoi Prokatki: Spravochnik* (Theory of Lengthwise Rolling: Handbook). Moscow: Metallurgiya.
3. Garber, E.A. 2004. *Cold-Rolling Mills (Theory, Equipment, Technology).* Cherepovets: Chermetinformatsion [in Russian].
4. Garber, E.A., Shadrunova, I.A., Traino, A.I., Yusupov, V.S. 2002. Analysis of a deformation zone and the refined calculation of the forces for cold-rolling of strips thinner than 0.5 mm in a continuous mill. *Russian Metallurgy* 4: 340–345.
5. Garber, E.A., Nikitin, D.I., Shadrunova, I.A., Traino, A.I. 2003. Calculation of the cold-rolling power with allowance for the variable work of friction along a deformation zone. *Russian Metallurgy* 4: 340–346.
6. Garber, E.A., Nikitin, D.I., Shadrunova, I.A., Traino, A.I. 2007. Simulation of the state of stress in a strip in a deformation zone with two neutral sections during cold rolling. *Russian Metallurgy* 4: 293–303.

17 Elastohydrodynamic Lubrication of Cold-Rolling Lubricants and Its Mechanism in Nonconformal Rolling Contacts

Ian Burton

CONTENTS

17.1 Introduction 191
17.2 Discussion 192
17.2.1 Tribocontact Geometries in Cold Rolling and Their Influence upon Film Thickness *h* 192
17.2.2 Cold-Rolling Lubricants 193
17.2.3 Elastohydrodynamic Interferometry 193
17.2.4 Determination of Film Thickness *h* of Fully Formulated Cold-Rolling Lubricants 195
17.2.5 Nonlinear Film Growth 198
17.2.6 Modeling the Boundary and Elastohydrodynamic Films 199
17.2.7 Pressure–Viscosity Coefficients α 200
17.2.8 Mill Validation Testing 202
17.3 Conclusion 204
17.4 Experimental Protocol 204
17.4.1 Determination of Film Thickness *h* by Elastohydrodynamic Interferometry 204
17.4.2 Determination of the Pressure–Viscosity Coefficient α 204
17.4.3 Determination of the Temperature–Viscosity Coefficient β 204
Acknowledgments 205
References 205

17.1 INTRODUCTION

The cold rolling of steel in multistand tandem mills experiences transitions in roll speed, roll force, roll roughness, and tension during production. A lubricant has to accommodate these variables and while the lubricant itself does not change from the first to the last mill stand, its lubrication mode traverses the lubrication spectrum from a boundary condition to one that is more hydrodynamic in character.

The mechanism of boundary lubrication is well understood (Bowden and Tabor 1950; Spikes 1987; Sutcliffe and Johnson 1990) and occurs when speeds are low and roll forces are moderate. At the work roll-strip interface, asperities on the roll make contact with asperities from the strip surface, producing a high coefficient of friction (Figure 17.1a). A lubricant is applied to reduce the friction but under the moderate roll forces the asperities continue to pierce the lubricant film and make contact. Under these conditions, the lubricant is squeezed out of the contact zone leaving only a very thin oil film with a thickness *h* that is almost negligible.

To reduce asperity contact in this thin film, the lubricant relies on polar molecules, particularly ester base oils, organic carboxylic acids, phosphorus, and sulphur derivatives to physisorb on the steel surface through bond anisotropy or induced anisotropy (Figure 17.1b).

The physisorbed film shears sacrificially, under slide/roll friction forces, thus maintaining the integrity of the steel surface through the reduction of friction and wear (Spikes 1987; Najman et al. 2002). If sufficient energy is available, such as from triboelectrons (Nakayama and Fujimoto 2004), and high thermal friction, the activation energy (ΔE_{act}) for chemical bond formation can be exceeded and certain active molecules in the lubricant can chemically bond (chemisorption) to the steel surface. Chemisorbed films are more resistant to shear than those formed by physisorption and offer greater protection to the steel surface. Regardless of the adsorbing mechanism, lubricant films in the boundary condition are thin with *h* typically of 5–15 nm and asperity contact remains high.

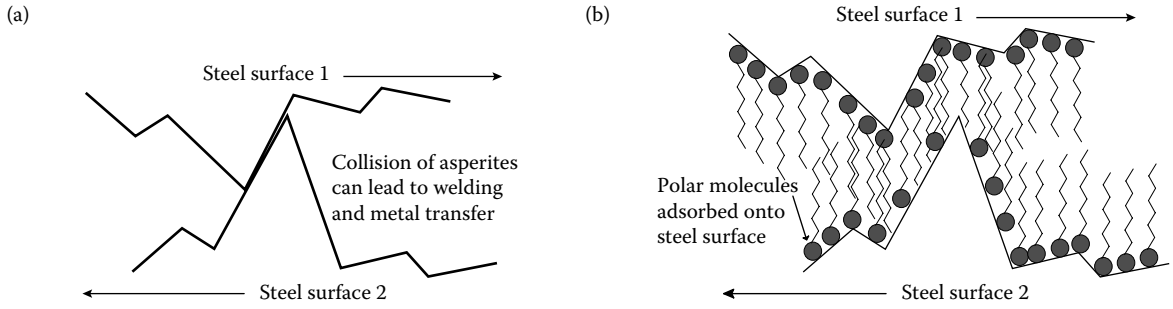


FIGURE 17.1 Boundary lubrication: (a) without lubricant, (b) with lubricant; polar molecules adsorb on the steel surface to form a tribochemical shear film.

The lubrication mechanism at high speeds and high loads has not been extensively researched; however, in ball bearing contacts under these conditions, lubricant film thickness h increased with speed producing an elastic deformation of point contacts (Hamrock and Dowson 1977). This is known as elastohydrodynamic (EHD) lubrication and relies on the properties of the bulk lubricant film, rather than individual polar molecules.

In a recent study (Burton 2007), the EHD properties of base esters and mineral oil were evaluated for the purpose of developing cold-rolling lubricants for the steel industry. Film thicknesses h of up to 1000 nm were reported for some base oils and were a function of entrainment speed into the tribological contact, pressure, and chemical structure of the film forming material. This study concentrated on single component base oils (ester or mineral), and this is far removed from the reality of fully formulated, multicomponent, cold-rolling lubricants. It is envisaged that these may not behave in a similar way. The purpose of this current research is to evaluate the EHD properties of fully formulated rolling lubricants and to determine whether these are influenced by additive components. This will be discussed with regard to nonconformal line contacts, found in rolling geometries.

17.2 DISCUSSION

17.2.1 Tribocontact Geometries in Cold Rolling and Their Influence upon Film Thickness *h*

The work roll makes a contact that is orthogonal to the strip direction to produce a line contact at the work roll-strip interface (Figure 17.2a).

A disparity exists between the shape and geometries of the work roll and strip and the tribocontact is described as nonconformal. A tangent to the roll radius makes a contact with the strip and produces a convergence zone. This is a precontact zone that precedes the tribocontact zone (Figure 17.2b).

The volume of lubricant and its chemical composition within the convergence zone will influence the lubricant film thickness h in the tribocontact zone at the work roll-strip interface. The corollary of this is that the lubrication mode in the cold rolling of steel is dependent upon h, and this can be

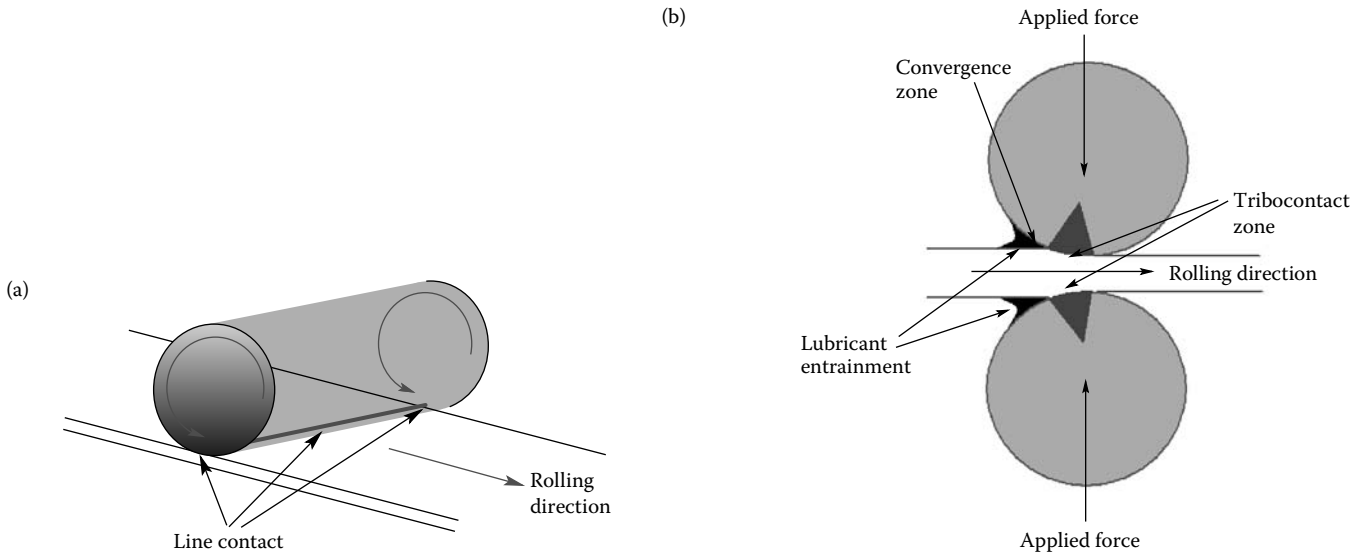


FIGURE 17.2 Contact geometries in steel rolling: (a) nonconformal line contact between the work roll and strip; (b) convergence and tribocontact zones. (From Burton, I., *Proceedings of Iron and Steel Conference*, 2007, 2: 307–319. With permission.)

calculated from the Wilson–Walowit Model, Equation 17.1 (Wilson and Walowit 1971):

$$h = \left[\frac{3\eta_o \alpha \rho \left(v_\sigma + v_\rho \right)}{X_1 \left[1 - e^{-\alpha(\psi - \sigma)} \right]} \right] \tag{17.1}$$

and

$$X_1 = \sqrt{\rho(\gamma_1 - \gamma_2)}$$

where

h = film thickness (nm)
η = kinematic viscosity
α = pressure–viscosity coefficient
v_σ = entry velocity of strip
v_ρ = roll surface velocity
ψ = entry yield stress
σ = unwind tension
ρ = corrected roll radius
γ_1 = entry gauge
γ_2 = exit gauge

Substitution of x_1 into Equation 17.1 gives Equation 17.2:

$$h = \left[\frac{3\eta_o \alpha \rho \left(v_\sigma + v_\rho \right)}{\sqrt{\rho(\gamma_1 - \gamma_2)} \left[1 - e^{-\alpha(\psi - \sigma)} \right]} \right] \tag{17.2}$$

Further rearrangement of Equation 17.2 produces the more useful form of the Wilson-Walowit model in Equation 17.3:

$$h = \left[\frac{3\eta_o \alpha \left(v_\sigma + v_\rho \right)}{1 - e^{-\alpha(\psi - \sigma)}} \right] \left[\frac{\rho}{\gamma_1 - \gamma_2} \right]^{0.5} \tag{17.3}$$

As velocity ($v_\sigma + v_\rho$) increases significantly, as in stand five of a rolling mill, more lubricant is entrained into the contact zones where it experiences high Hertzian asperity contact pressures of 1–2 GPa (Timoshenko and Goodier 1951). This compresses the lubricant and produces a large increase in viscosity, resulting in a rigid oil film that is more rigid than the metal surfaces and applies a force opposite to the normal load that acts to separate the work roll and strip, resulting in a significant increase in film thickness h. The normal load (roll forces) is sufficiently high, however, to resist total separation of the work rolls and strip, and consequently, the work rolls deform elastically (Hertz 1882). This flattens the work rolls (Figure 17.3), increasing the width of the line contact in the rolling direction, and effectively reduces the point contacts, spreads the normal force over a greater surface area, and the flattening action releases more oil in the contact zone. Consequently, roll forces and friction are reduced. Total separation of the two metal surfaces, known as hydrodynamic lubrication, is not normally seen in cold rolling due to the very high roll forces encountered. Indeed, full film separation would be detrimental to the rolling process, as complete loss of friction would result in severe slippage (Yuen et al. 1996).

17.2.2 Cold-Rolling Lubricants

A cold-rolling lubricant is a complex mixture of typically 7–15 different chemical components that are blended together to impart specific properties to the lubricant, as shown in Table 17.1.

It is evident from Table 17.1 that esters and mineral oils are the major constituents, by proportion, of a lubricant designed for the cold rolling of steel. Consequently, these base oils form the major component of the bulk lubricant film, and it is their chemical structure (Figure 17.4) that will strongly influence the lubricant's ability to produce an EHD effect in the Hertzian contact geometry. There are a plethora of esters and mineral oils available, from natural or synthetic sources, each with its own unique bulk film-forming properties.

17.2.3 Elastohydrodynamic Interferometry

To design lubricants with suitable EHD properties, it is necessary to determine their film thickness and correlate it with the rolling process, and this requires modeling of the contact

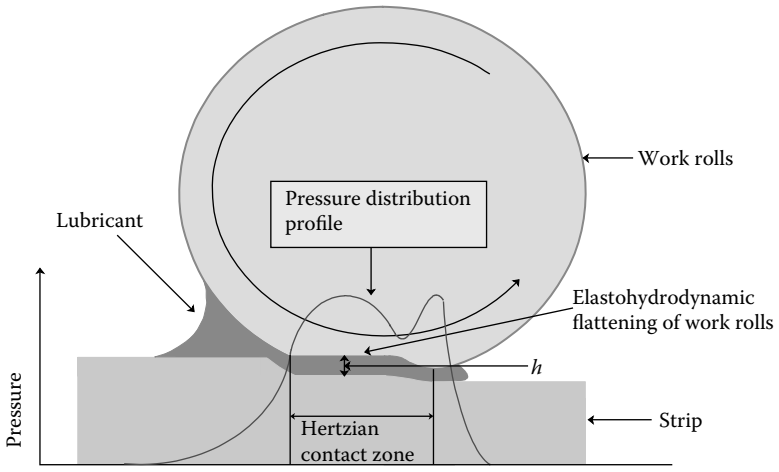


FIGURE 17.3 Exaggerated elastic deformation of work rolls during EHD lubrication.

TABLE 17.1
Typical Components of a Lubricant and Their Purpose in the Cold Rolling of Steel

Lubricant Component	Purpose
Ester	Acts as a base lubricant and as a solvent carrier for other components; a weak boundary lubricant; forms the largest proportion of the lubricant formulation, thus major contributor to the bulk film and is important in EHD lubrication
Mineral oil	Acts as a base lubricant and as a solvent carrier for other components; a very weak boundary lubricant; may form a large proportion of the formulation, thus can be a major contributor to the bulk film and is important in EHD lubrication; reduces saponification value of the lubricant, which reduces its boundary lubrication properties and can be useful to reduce over lubrication that could lead to a slippage condition
Fatty acids	Boundary lubrication
Antioxidant	Protects lubricant from oxidation and polymerization
Emulsifier	Reduces the interfacial surface tension between the lubricant and water and allows the two phases to mix in mill solution tanks
Phosphorus-containing additives	Form strong boundary shear films and gives the lubricant antiwear properties
Sulphur-containing additives	Extreme pressure additive; forms strong shear films under severe conditions; useful in preventing welding and inhibiting frictional transfer of metal

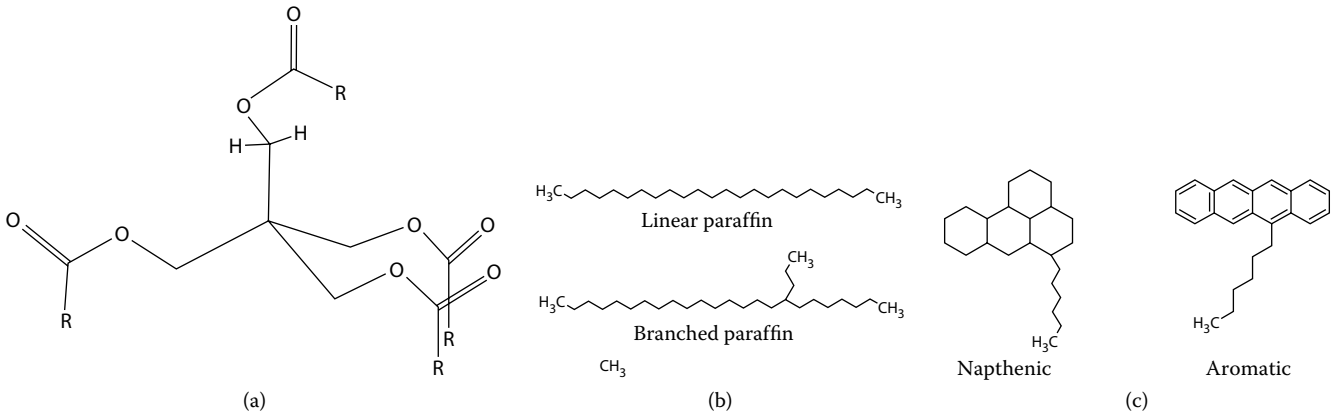


FIGURE 17.4 Examples of base oils used in cold-rolling lubricants: (a) pentaerythritol ester, where R is an alkyl chain, typically C8–C18; (b) paraffinic mineral oil; (c) napthenic/aromatic mineral oil. (From Burton, I., *Proceedings of Iron and Steel Conference*, 2007, 2: 307–319. With permission.)

geometry in the laboratory. A pilot plant laboratory mill could be utilized for this purpose; however, this is expensive and time-consuming. Consequently, it was decided to utilize a tribological instrument that has a nonconformal contact geometry, similar to that of the rolling process, in which a ball on disc geometry mimics roll on strip; this is shown in Figure 17.5a. In this configuration, the film formed is not a true tribofilm due to the presence of the glass disc (Olver and Spikes 1998). Thus friction-generated tribochemical films can be negated, and pure EHD film forming properties of the rolling lubricant can be obtained. The instrument determines the film thickness h by interferometry (Figure 17.5b) from low speed (boundary condition) to high speed (EHD condition). Most of the white light incident upon the disk is reflected by the chromium layer, while some of the light passes through the glass disk and silica spacer layer and through the oil film. This light is then reflected back from the steel ball. Depending if the two electromagnetic waves are in phase or out of phase, this procures wavelengths of light that either constructively or destructively interfere. Using a spectrometer and optical imaging devices, the thickness of the lubricant film can be obtained.

Hamrock and Dowson (1977) have determined film thickness h experimentally in the form of Equation 17.4. Here a, b, and c are constants and most authors assign values of 0.60–0.74 for a, 0.5–0.6 for b, and approximately −0.1 for c. k is dependent upon the overall geometry of the two surfaces involved in the tribological contact (Olver and Spikes 1998).

$$\frac{h}{R'} = k\left[\frac{U\eta_o}{E'R'}\right]^a (\alpha E')^b \left[\frac{W}{E'R'^2}\right]^c \tag{17.4}$$

where

R' = reduced radius of the interacting solids
E' = reduced Young's modulus
U = mean speed of the two surfaces, $(U_1 + U_2)/2$
α = pressure–viscosity coefficient
η_o = dynamic viscosity
W = applied load

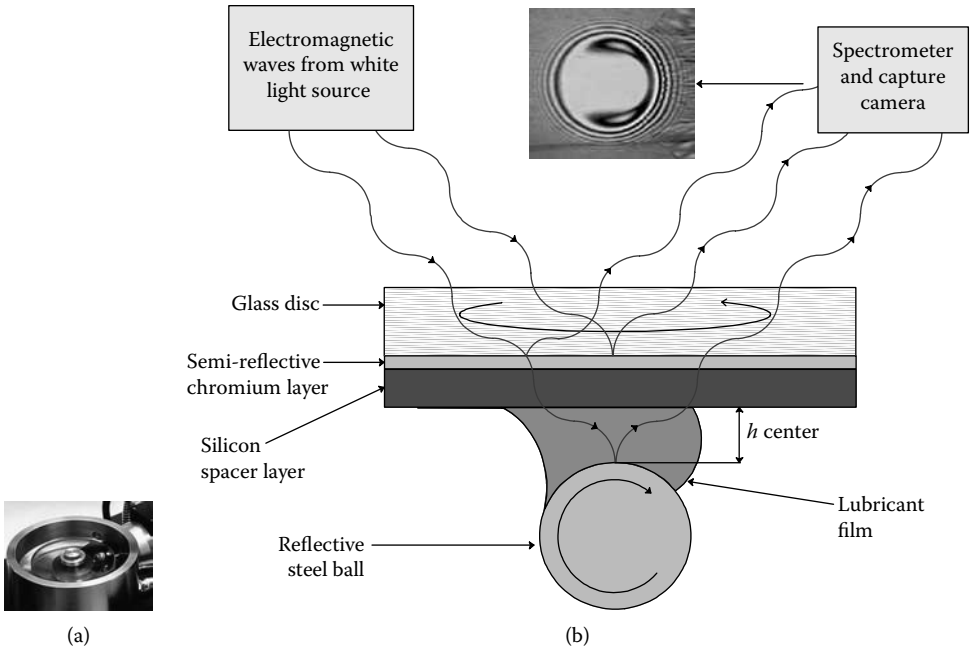


FIGURE 17.5 Elastohydrodynamic interferometry: (a) test apparatus with ball on disk geometry; (b) schematic representation of the elastohydrodynamic interferometric technique and the determination of h versus speed. (From Burton, I., *Proceedings of Iron and Steel Conference*, 2007, 2: 307–319. With permission.)

TABLE 17.2
Fully Formulated Cold-Rolling Lubricants Evaluated in This Study

Cold-Rolling Lubricant	Material Description	Sulfur Additive	Phosphorus Additive	Bulk Film
1	Fully formulated rolling oil	Yes	No	Linear polyol synthetic ester, low mol wt
L1 Ester	100% linear polyol ester	No	No	Linear polyol synthetic ester, low mol wt
2	Fully formulated rolling oil	Yes	No	Branched chain polyol synthetic ester, high mol wt
L2 Ester	100% branched polyol ester	No	No	Branched chain polyol synthetic ester, high mol wt
3	Fully formulated rolling oil	Yes	Yes	Linear polyol natural ester, medium mol wt
4	Fully formulated rolling oil	Yes	Yes	Linear polyol natural ester, medium mol wt

17.2.4 Determination of Film Thickness *h* of Fully Formulated Cold-Rolling Lubricants

In this new study, four fully formulated rolling lubricants were investigated. They are shown in Table 17.2. The ester components, present in lubricants 1–4, accounted for more than 80% of their composition by weight. For comparative purposes, the pure esters, $L1^{est}$ and $L2^{est}$ utilized in lubricants 1 and 2, respectively, were also evaluated. All test lubricants 1–4 contained a sulfur additive of the same molecular structure. Lubricants 3 and 4 also contained a phosphorus additive, but its molecular structure was different in each lubricant.

Film thickness h for lubricants 1–4 and the two pure esters $L1^{est}$ and $L2^{est}$ was determined by EHD interferometry, as described in Section 17.4.1. Measurements were carried out in a pure rolling contact, to minimize shear, at 50°C, 100°C, and 150°C, 0.54 GPa Hertz contact pressure, and at a mean rolling speed from 0.01 to 4.25 ms^{-1}. Results of this analysis are tabulated in Table 17.3 and shown graphically in Figure 17.6. Log h (film thickness) is plotted against log U (mean rolling speed) for each lubricant. The values presented are true film thicknesses, calculated using the measured refractive index for the lubricant concerned, at the relevant test temperature. It must be noted that the plots are logarithmic, which tends to make the results appear more similar in the thick film region than they actually are.

Lubricant 1 (Figure 17.6a) exhibits an almost linear dependence of log h versus log U at all three test temperatures, as predicted from Equation 17.4. At low speeds (0.01 ms^{-1}) film thicknesses h are generally low and in the range of 3.32–0.68 nm, while at high speeds (4.25 ms^{-1}) h is in the range of 210.34–39.07 nm. The variation in h reported at the same speed arises from a reduction in lubricant viscosity, as temperature increases, resulting in thinner films.

TABLE 17.3
Lubricant Film Thickness for Lubricants 1–4 and Esters L1^{est} and L2^{est}, under Various Speed and Temperature Conditions

Test Conditions	Lubricant Film Thickness *h* (nm)					
	Lubricant 1	Ester L1^{est}	Lubricant 2	Ester L2^{est}	Lubricant 3	Lubricant 4
0.01 ms^{-1}, 5 0°C	3.32	3.08	19.58	21.06	10.27	10.08
0.01 ms^{-1}, 100°C	1.33	1.12	6.49	6.84	7.00 first run 12.58 second run	3.78
0.01 ms^{-1}, 150°C	0.68	0.52	4.39	5.47	17.31	22.9 Acceleration 10.84 Deceleration
4.25 ms^{-1}, 50°C	210.34	194.76	659.21	745.79	408.84	374.58
4.25 ms^{-1}, 100°C	72.4	60.84	241.76	265.35	158.34	140.69
4.25 ms^{-1}, 150°C	39.07	36.02	111.97	125.71	97.87	93.7

Clearly, at low speeds, the motion of the tribological surfaces is slow, resulting in insufficient lubricant entrainment into the convergence and tribocontact zones, thus resulting in a thin film that relies on boundary lubrication. Conversely, at high speeds, an excess of lubricant is supplied to the tribological interface resulting in thicker films that provide EHD lubrication. It appears that the influence of other additives in lubricant 1 have actually produced a slight increase in film thickness at all temperatures and speeds compared to the pure ester, L1^{est}, with the largest deviation (15.58 nm) recorded at the lowest temperature and highest speed (50°C, 4.25 ms^{-1}). Generally, however, film thickness measurements for the fully formulated rolling lubricant were similar to the base ester, L1^{est} (Figure 17.6b), from which it was produced. This is not surprising as L1^{est} represented more than 80% of the final formulation. The data do, however, support the hypothesis that the efficacy of EHD lubrication is characteristic of the bulk film, and this is predominantly a function of the major component in the lubricant, rather than individual polar molecules.

Lubricant 2 (Figure 17.6c) also exhibits normal, linear EHD behavior at all test temperatures. As expected, thicker films were seen at lower temperatures. Film thickness values *h* were generally found to be much larger, particularly at higher mean rolling speeds, than those observed for lubricants 1, 3, and 4. At 50°C at 4.25 ms^{-1}, the film thickness *h* is 659.21 nm, conversely for lubricant 1, under the same conditions, a film thickness of 210.34 nm was recorded. Such differences are attributable to variations in the molecular structure of the base esters, within the rolling lubricants and how the corresponding bulk film will respond under load (Piezoviscous Effect) in the tribological contact, and this is discussed further in Section 17.2.7. Lubricant 2 also inherits characteristics of its parent ester L2^{est} (Figure 17.6d). Unlike lubricant 1, the film thickness for lubricant 2 had been reduced slightly by the additional additives present. This modification to film thicknesses in the case of lubricants 1 and 2 is clearly a function of the additive and its concentration and as this increases, it starts to represent more of the bulk film, and it is that dilution influence that is observed. It is proposed that a concentration gradient versus *h* can be imagined for the base ester in the lubricant formulation: as it is reduced, in a stepwise manner, the bulk EHD film exhibits characteristics of the components that replaced it.

Lubricant 3 exhibits linear film thickness versus speed behavior at 50°C, but at 100°C and 150°C nonlinear behavior, not predicted by Equation 17.4, was observed (Figure 17.6e). At medium to low speeds (0.4–0.01 ms^{-1}), a thicker film than expected was formed. A more detailed analysis shown in Figure 17.6f reveals two log *h* versus log *U* plots at 100°C. The lower series is the first run where speed is increased incrementally from 0.01 to 4.25 ms^{-1}. Close observation of this plot with that of the 50°C plot in Figure 17.6e actually reveals an almost parallel line, indicating almost normal EHD behavior. From 0.01 to 0.02 ms^{-1}, however, some nonlinear behavior is still evident (h = 7 nm at 0.01 ms^{-1}, 100°C). The second plot (higher series) was conducted immediately after the first run, and again, speed was increased incrementally from 0.01 to 4.25 ms^{-1}. The nonlinear behavior was, however, more pronounced in this second run with a greater increase in film thickness (12.58 nm at 0.01 ms^{-1}). At 150°C the deviation from EHD theory (Equation 17.4) was quite severe (h = 17.31 nm at 0.01 ms^{-1}) and prevalent up to speeds of 0.8–1 ms^{-1}.

Lubricant 4 (Figure 17.6g) exhibited predicted EHD behavior at 50°C and 100°C, but at 150°C, nonlinear behavior, which was more severe than found with lubricant 3, was evident. To simplify the graphs, a plot of log *h* versus log *U* for lubricant 4 at 150°C is shown in Figure 17.6h. The first plot was obtained through incremental acceleration to 4.25 ms^{-1}, whereas the second plot was recorded during deceleration from 4.25 to 0 ms^{-1}. During acceleration, the film is already thick (22.9 nm) at a very slow speed of 0.01 ms^{-1}, indicating facile formation of a boundary film at 150°C. This nonlinearity continues up to 1 ms^{-1}, after which normal EHD behavior is seen. During deceleration, the log *h* film thickness becomes

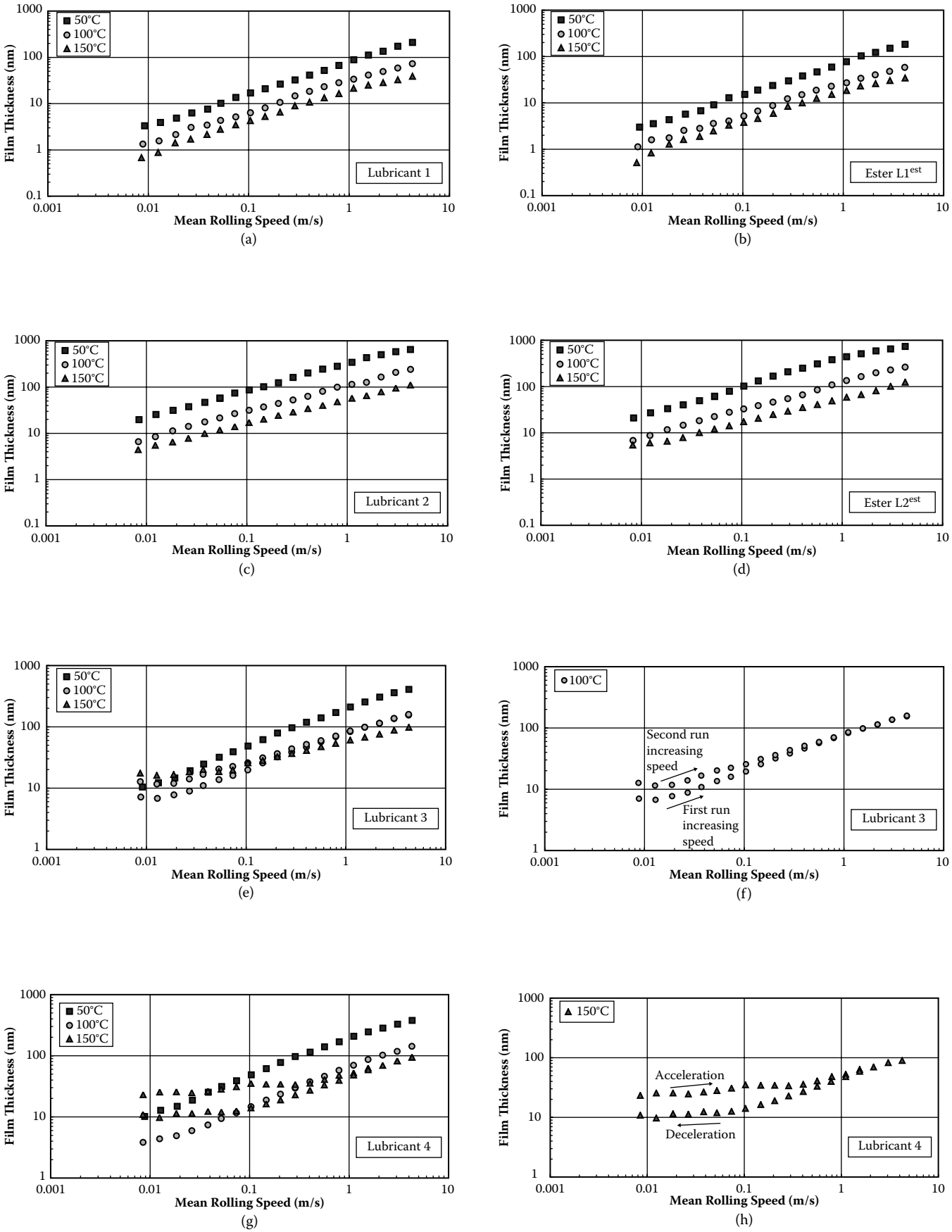


FIGURE 17.6 (a)–(h). Log h (film thickness) versus log U (mean speed) determined by elastohydrodynamic interferometry for lubricants 1–4 and esters $L1^{est}$ and $L2^{est}$.

more linear down to speeds of 0.1 ms^{-1} with a final film thickness of 10.84 nm at 0.01 ms^{-1} compared to 22.9 nm at 0.01 ms^{-1} during acceleration. This decrease in film thickness indicates a shearing of the boundary film. It is possible that the film had grown too large with time at the elevated temperatures encountered and sheared in the contact zone, when the EHD film had started to deteriorate at slower speeds, during deceleration. Below 0.1 ms^{-1} the nonlinear behavior continued to be prevalent, during deceleration, indicating the presence of a thinner boundary film. This type of data can be exploited in formulation design, applicable to Continuous Pickle–Continuous Mills (CPCM) process lines; (see Section 17.2.8).

17.2.5 Nonlinear Film Growth

The nonlinear film growth observed in lubricants 3 and 4 appeared to be independent of speed, but temperature and kinetically (time) dependent, indicative of a chemically reacted film that was facile in its formation, as friction at the glass–steel interface was minimal, with the absence of sliding motion. The nonlinear film was probably forming on the surface of the steel ball in the test apparatus. It is unlikely that the chemical film was attributable to the sulfur additive, as it was present in all the test lubricants 1–4, but lubricants 1 and 2 did not exhibit any nonlinear behavior. In addition, at these temperatures (100°C–150°C) and lack of severe friction, the activation energy (ΔE_{act}) for sulfur reactions with the steel surface would be prohibitive. Cold-rolling lubricants 3 and 4, unlike 1 and 2 did, however, contain phosphorus-based antiwear additives (Table 17.2). Lubricant 3 utilizes phosphorus chemistry known to have a low activation energy (ΔE_{act}) for chemisorption to take place, whereas the phosphorus additive in Lubricant 4 requires a higher activation energy for boundary film formation. This correlates well with the observed nonlinear film formation as a function of temperature and time. It is proposed that the nonlinear film is attributable to the formation of a polyphosphate boundary layer.

A possible reaction mechanism for phosphate film growth on a steel surface is shown in Figure 17.7. FeO or FeOH on the surface of the steel attacks the electrophilic phosphorus centre in a nucleophilic associative addition reaction. The author believes that this forms a sp^3d^1 trigonal bipyramidal species. Collapse of this structure, via a dissociative mechanism, leads to the chemisorbed product. When steric hindrance is low, which is the case with small R groups that occupy minimal geometric and rotational space, the major rate-determining step is collapse of the trigonal bypyramidal intermediate with expulsion of R_1—O-. Factors that affect the stability of this anionic species will determine the final rate of reaction. If the R groups are large, however, the active phosphorus center is too sterically hindered for nucleophilic attack and the rate-determining step will be the formation of the sp^3d^1 species. It is envisioned that this step would be highly reversible, if it took place at all.

Najman et al. (2002) proposed an alternative reaction mechanism in which FeO or FeOH undergoes a simple acid–base reaction with oxyphosphorus compounds (Figure 17.8). The author believes, however, this would not explain the reaction of trialkylphosphates with the surface, where no acidic groups are present within the molecule. It is likely that this mechanism would, however, prevail over the associative/dissociative mechanism described earlier (Figure 17.7), if acidic moieties are present in the additive molecule. This is attributable to the higher ΔE_{act} required for the associative/dissociative mechanism and is a function of steric hindrance in the intermediate and transition states. Such phenomena are absent in the acid/base mechanism.

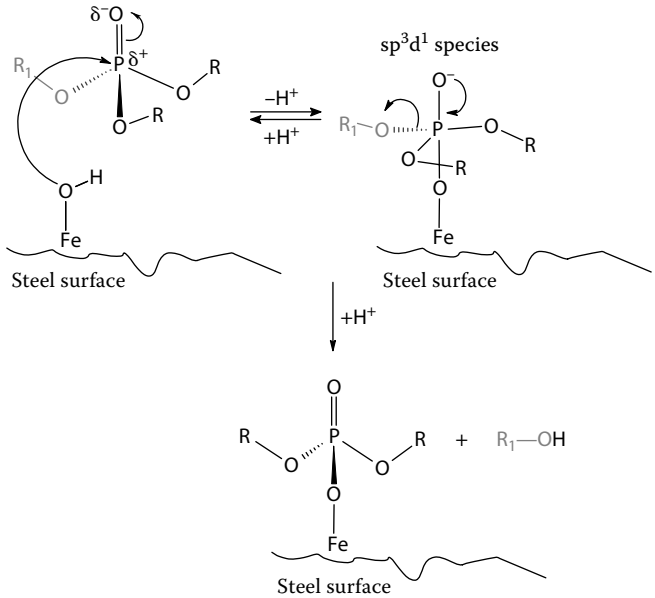


FIGURE 17.7 Suggested nucleophilic association/dissociation mechanism for the reaction of tetrahedral phosphate molecules on the surface of steel.

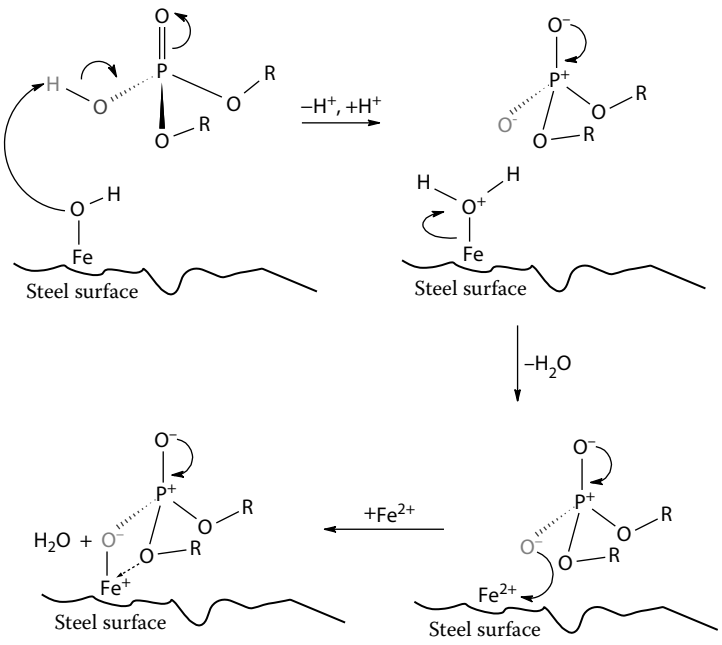


FIGURE 17.8 Acid–base mechanism for the reaction of phosphorus compounds on a steel surface.

Wang and Wood (2007) have shown that iron phosphide formation in the tribochemical film is not normally observed, with iron phosphates being the dominant species. Gao et al. (2005) have suggested phosphide formation is dependant on the absence or presence of a surface iron oxide. In its absence, phosphide formation may be possible. Minfray et al. (2008) in similar work with iron oxides also observed only phosphate formation. An alternative postulate for the lack of iron phosphide formation is that it may be attributable to the high susceptibility of phosphorus to oxidation.

17.2.6 Modeling the Boundary and Elastohydrodynamic Films

The nonlinear behavior of lubricants 3 and 4 made it difficult to analyze the film thickness attributable only to the EHD component h_{EHD} because of the presence of a boundary film, which was far more severe than expected in these examples. Normally, the calculation of EHD film thickness h_{EHD} at any mean speed U can be achieved with a simplified form of Equation 17.4, shown below as Equation 17.5. This assumes that the pressure–viscosity coefficient and viscosity are maintained constant, enabling k_1 and a to be constants. Because log h and log U are known, k_1 and a can be calculated.

$$h_{EHD} = k_1(U)^a \tag{17.5}$$

The measured film thickness h_{meas}, obtained from EHD interferometry (Figure 17.6e—h), is made up of the bulk film h_{EHD} and the boundary film h_b, consequently Equation 17.5 has to be modified thus to give Equation 17.6:

$$h_{meas} = k_1(U)^a + h_b \tag{17.6}$$

To obtain only film thickness attributable to the bulk film h_{EHD}, Equation 17.6 becomes Equation 17.7:

$$h_{EHD} = (h_{meas} - h_b) = k_1(U)^a \tag{17.7}$$

To resolve this problem, a number of data manipulations had to be undertaken. First, the thickness of the boundary film had to be estimated. This was achieved by extrapolating a line down toward the x-axis from the data points to the right of the data convergence in Figure 17.6f—h. At the point that $U = 0.01$ ms^{-1} intersected the extrapolation line, equated to a theoretical EHD film thickness on the log h axis. Subtracting the measured film thickness from the extrapolated film thickness then gave an estimation of the film thickness attributable to the boundary component h_b. Data points of $(h_{meas} - h_b)$ then gave the effective h_{EHD}. A plot of log h_{EHD} versus mean speed log U was constructed and then treated to linear regression and fitted to Equation (17.7). For regression purposes, the nonlinear component of the data points to the left of the data convergence in Figure 17.6f and h were ignored. Only data points on the linear part of the graph at higher speeds and thicker films were used to perform the analysis, and this was to minimize the error that may occur from the semiquantitative estimation of the boundary film h_b. Results of this analysis are shown in Table 17.4 along with constants k_1, a, and estimated h_b values.

A plot of log h versus log U, after linear regression and the resulting fitted equations, is shown for lubricant 4 during acceleration (Figure 17.9a) and deceleration (Figure 17.9b) at 150°C. The fitted equations and knowledge of boundary film thickness can predict total film thickness or film thickness attributable to EHD alone. On observing Figure 17.6h the measured film thickness h_{meas} at 0.01 ms^{-1} was recorded as

TABLE 17.4
Fitted Equations for EHD Film Thickness at 50°C, 100°C, and 150°C

Cold-Rolling Lubricant	50°C	100°C	150°C
3 EHD Fitted Line (nm)	$h_{EHD} = 191.49U^{0.578}$	$h_{EHD} = 63.599U^{0.6265}$	$h_{EHD} = 41.214U^{0.5057}$
3 Boundary Film h_b (nm)	0	10	15.31
4 EHD Fitted Line (nm)	$h_{EHD} = 185.33U^{0.5248}$	$h_{EHD} = 61.133U^{0.6089}$	$h_{EHD} = 21.804U^{0.8989}$ (Acceleration) $h_{EHD} = 35.069U^{0.635}$ (Deceleration)
4 Boundary Film h_b (nm)	0	1.4	21.5 (Acceleration) 9.4 (Deceleration)

[a] *Note:* U is in ms^{-1}.

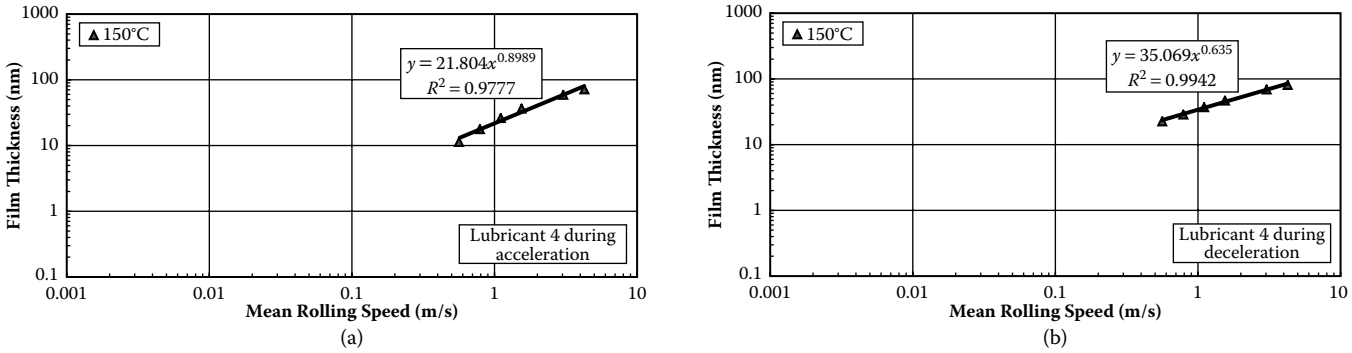


FIGURE 17.9 Effective elastohydrodynamic film thicknesses log h_{EHD} versus log U mean speed for lubricant 4 at 150°C, after removal of boundary component film thickness h_b and linear regression of resulting data points according to Equation 17.7: (a) lubricant 4 during acceleration; (b) lubricant 4 during deceleration.

22.9 nm during acceleration. Comparing this with the fitted equation (Lubricant 4, 150°C, acceleration) from Table 17.4, the film thickness due to the EHD component h_{EHD} was calculated to be 0.35 nm, a true boundary condition as expected at these slow speeds and high temperatures. At 4.25 ms^{-1} a measured film thickness of 93.7 nm was observed. Using the same fitted equation, an EHD film thickness h_{EHD} of 80.06 nm was calculated. Adding the boundary film of 21.5 nm gives a predicted total film thickness of 101.56 nm versus 93.7 nm as measured. This model works reasonably well for predicting film thicknesses at various entrainment speeds, even in the presence of nonlinear behavior.

17.2.7 Pressure–Viscosity Coefficients α

From film thickness measurements, it is evident that speed is a major component of the EHD mechanism. It acts as a vehicle to carry a continuous supply of lubricant into the tribocontact zone, and this occurs through motion of the surfaces. In the contact, load is applied through roll force to the lubricant, and its bulk modulus (K) is modified as a function of molecular structure, of the major constituent in the bulk film, with pressure. It is envisaged that under standard pressure conditions (1.01325×10^{-4} GPa) linear alkyl chains of the polyol ester, present in lubricant 1, will occupy a high molecular volume due to entropic effects (Figure 17.10a and c). Under high pressure (0.5–2 GPa), however, as found in the EHD environment, the linear alkyl chains will compress significantly to a minimum volume and exhibit a low bulk modulus (K) (Bekefi and Barett 1987). Conversely, ester molecules that contain branched alkyl chains, as present in lubricant 2 (Figure 17.10b and d), start to compress under high pressure but large intramolecular, nuclear, and electron repulsions are felt that provide an elastic resistance to the compression (1/K), thus preventing total collapse of the molecular volume.

The viscosity of the branched chain esters will be much higher due to pressure-induced reduction in density and intramolecular/intermolecular entanglement. This increase in viscosity with pressure known as the Piezoviscous Effect will carry the load better than the linear chain molecules and leads to a significant reduction in the coefficient of friction as h increases.

Pressure–viscosity coefficients α describe how the bulk film will respond under load in the tribological contact and this is summarized in the Barus (1893) Equation 17.8.

$$\eta = \eta_o e^{\alpha p} \tag{17.8}$$

Burton (2007) reported that temperature acts antagonistically, with pressure, upon viscosity and modified Equation 17.8 to give a temperature viscosity coefficient β term in Equation

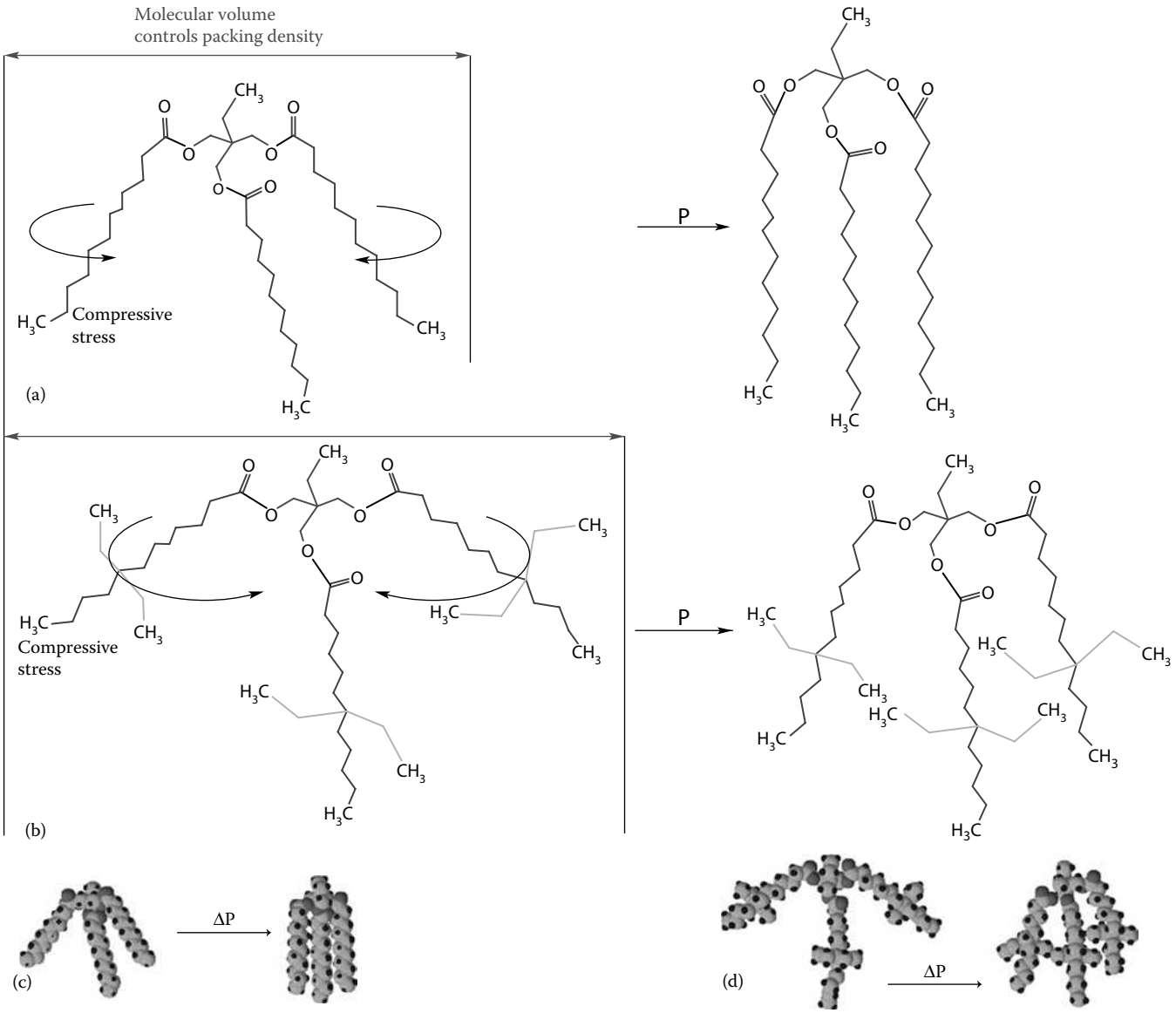


FIGURE 17.10 Effect of compressive forces on alkyl chains: (a) linear chains, (b) branched chain, (c) linear chains spacefill representation, and (d) branched chains spacefill representation. (From Burton, I., *Proceedings of Iron and Steel Conference*, 2007, 2: 307–319. With permission.)

17.9 that is also absent from the isothermal Wilson–Walowit Model (Equation 17.1).

$$\eta = \eta_o e^{\alpha p} e^{-\beta(T - T_o)} \tag{17.9}$$

where

η = actual viscosity in the material pair interface
β = temperature viscosity coefficient
η_o = viscosity at 1.01325×10^{-4} GPa
T = actual temperature in the material pair interface
α = pressure–viscosity coefficient
T_o = temperature at which η_o is measured
p = pressure at interface

Calculations of the pressure–viscosity coefficient α and temperature viscosity coefficient β have been made for lubricants 1–4 and esters $L1^{est}$ and $L2^{est}$, and they are tabulated in Table 17.5.

α was determined by EHD interferometry, indirectly, through back calculation of a modified power form of Equation 17.4. This protocol has been shown to produce results that are 10% lower than actual values, due to shear thinning. β was calculated by viscometry as detailed in the experimental protocol 4.3. Calculations of the pressure–viscosity coefficient α revealed values that ranged from 2.7 GPa^{-1} at 150°C to 18.9 GPa^{-1} at 50°C. As expected, α values decreased as temperature increased. Lubricant 2, which contained branched molecules, understandably gave the highest α values, while lubricant 1, which contained low-molecular-weight, linear molecules, gave the lowest α values and this correlated well with film thickness measurements (Figure 17.6a–h). Not surprisingly, lubricants 1 and

TABLE 17.5
Dynamic Viscosity, Pressure–Viscosity Coefficients α and Temperature Viscosity Coefficients β for Lubricants 1–4 and Esters L1^{est} and L2^{est} at 50°C, 100°C, and 150°C

Lubricant Sample	Dynamic Viscosity at 50°C (mPa s)	Dynamic Viscosity at 100°C (mPa s)	Dynamic Viscosity at 150°C (mPa s)	Pressure–Viscosity Coefficient (α) at 50°C (GPa^{-1})	Pressure–Viscosity Coefficient (α) at 100°C (GPa^{-1})	Pressure–Viscosity Coefficient (α) at 150°C (GPa^{-1})	Temperature Viscosity Coefficient (β) at 100°C	Theoretical Viscosity η at 100°C, Hertz Contact Pressure 0.54 GPa Equation 17.9 (mPa s)	Viscosity Ratio η100°C/η50°C
1	11.251	3.792	2.695	8.9	5.1	2.8	0.021751	59.555	5.293
L1^{est}	10.873	3.5172	2.4859	8.8	5.0	2.7	0.022572	52.34	4.81
2	94.901	16.758	10.127	18.6	16	6.6	0.034679	94739.305	998.296
L2^{est}	96.501	17.152	10.393	18.9	16.3	6.8	0.034548	114022.86	1181.57
3	32.9	9.501	5.324	17.1	11.1	10.1	0.024842	3809.955	115.804
4	34.03	9.581	5.321	17.3	10.2	6.2	0.025349	2363.249	69.446

2 gave α values similar to their respective esters L1^{est} and L2^{est}. Lubricants 3 and 4 exhibited comparable α values that were intermediary of lubricants 1 and 2. This was expected as the bulk esters used in lubricants 3 and 4, while of the linear polyol type (unbranched), were of a higher molecular weight than those found in lubricant 1, resulting in increased entropic motion and entanglement. One anomaly was that lubricant 3 exhibited the highest α value at 150°C. This might be attributable to microelastohydrodynamic lubrication reported by Kaneta and Nishikawa (1999). Theoretical calculations of η have been made at 100°C under a Hertz contact pressure of 0.54 GPa and assumed shear thinning was absent in the contact. If a sliding component is present in the contact, as is the case in cold rolling, the effective viscosity will be less than that predicted from Equation 17.9 (Olver and Spikes 1998; Bair et al. 2005).

The data do, however, indicate the huge viscosity increases that can take place in a nonconformal rolling geometry, under load. Lubricant 2 exhibits an increase in viscosity at 100°C, a ΔT of +50°C, that is still nearly 1000 times that of the original value measured at 1.01325×10^{-4} GPa, 50°C. This correlates well with film thickness measurements in which lubricant 2 (Figure 17.6c) produced the largest h values of all lubricants tested (659 nm), and its pure parent ester L2^{est} produced h values of 746 nm. If the β temperature coefficient was ignored from Equation 17.9, then the theoretical viscosity would have been 536506.65 mPa s for lubricant 2, which represents a 5653 times increase of the original value. Lubricant 2, with its high α value, will form a very rigid hydrodynamic film and it is this feature of the EHD mechanism that is responsible for the elastic deformation (flattening) of work rolls. Although speed is a primary feature of EHD lubrication, it is pressure applied to the lubricant that completes the EHD mechanism.

17.2.8 Mill Validation Testing

In order to test the validity of the work, a mill trial was conducted with lubricant 4, which was chosen because its nonlinear film behavior coupled with reasonable EHD film-forming properties might be conducive to CPCM designs, where there are constant cycles of acceleration/deceleration to allow shearing and welding of the strip. It is at these junctures in the rolling process where roll forces and friction can be high. A comparison was made to a control lubricant known to have poor EHD properties. Trials were held on a continuous pickle–continuous cold-rolling five-stand tandem mill, using coils of the same metallurgy and dimensions. Stand five specific roll force versus speed as taken from the mill computer are shown for the control after 10 coils (Figure 17.11a) and lubricant 4 after 1 coil (Figure 17.11b) and after 10 coils (Figure 17.11c).

In the boundary lubrication region, between 0 and 300 m min^{-1}, the specific roll force is high for the control at 17.97 MN m^{-1}. Comparing this with lubricant 4 after one coil and after 10 coils rolling, there is a progressive reduction in roll force of up to 2.5 MN m^{-1} and 3.69 MN m^{-1}, respectively. The stepwise reduction in roll force is probably attributable to two factors. First, there is a progressive growth of the polyphosphate film on the roll surface, which is absent in the control. At the same time, it is likely that the work rolls are wearing to their equilibrium roughness, thus reducing point contacts. The corollary of this is that h_{EHD} is also dependent on surface roughness and is preferable when lambda values of 1–2.5 are achieved (Burton 2007).

As the mill starts to accelerate further, EHD lubrication starts to dominate, and there is a significant decrease in specific roll force for lubricant 4, to 12 MN m^{-1} at 350 m min^{-1} (Figure 17.11c) compared with 14 MN m^{-1} for the

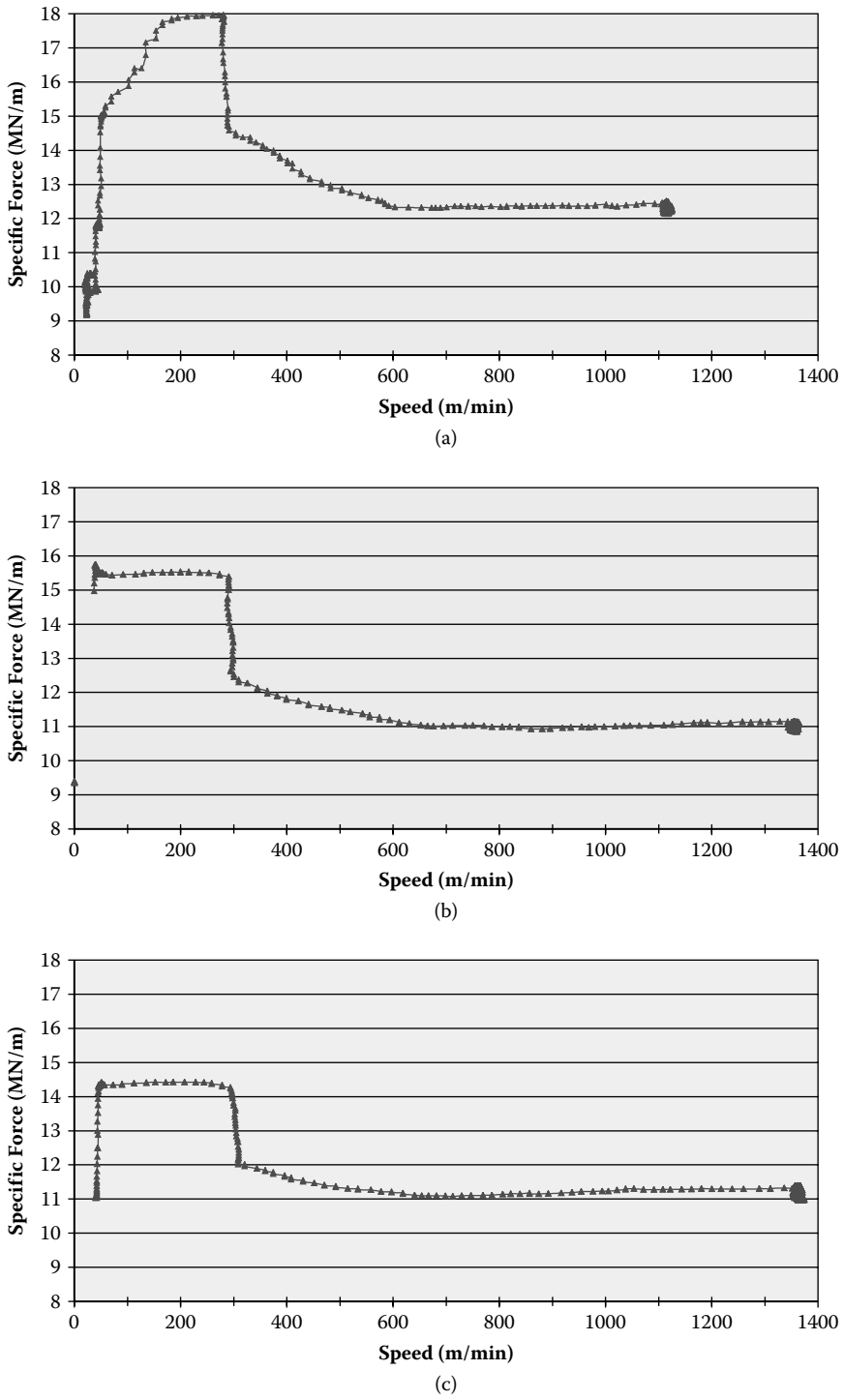


FIGURE 17.11 Stand 5-specific roll forces versus speed: (a) control lubricant after 10 coils; (b) lubricant 4 after one coil; (c) lubricant 4 after 10 coils.

control (Figure 17.11a). At 600 m min^{-1}, lubricant 4 exhibited a further drop in roll force to 11 MN m^{-1}, which allowed maximum speed (1400 m min^{-1}) to be obtained. For the control, however, the EHD mode of operation was not significant until a speed of 600 m min^{-1} was achieved and only a reduction in specific roll force to 12.3 MN m^{-1} was achieved, limiting final speed to 1130 m min^{-1} due to vibration. The reduction in roll force, at high speed, is attributable to the EHD effect, which flattens the work rolls and distributes the normal load over a larger Hertz contact area. Mill data gave good correlation with EHD interferometry, which is a useful technique for predicting boundary and EHD lubrication.

17.3 CONCLUSION

Film thickness h measurements were determined on four fully formulated lubricants and two pure esters, designed for the cold rolling of steel on multi-stand tandem mills, by EHD interferometry at 50°C, 100°C, and 150°C, 0.54 GPa Hertz contact pressure, and at a mean rolling speed U from 0.01 to 4.25 ms^{-1}. Film thickness h was found to increase with speed and pressure but decrease with temperature. Lubricants 1 and 2 and their respective base esters $L1^{est}$ and $L2^{est}$ exhibited an almost linear dependence of a log h versus log U at all three test temperatures, as predicted from Equation 17.4. At low speeds (0.01 ms^{-1}), h values of 0.52 to 21 nm were observed, typical of boundary lubrication, whereas at high speeds (4.25 ms^{-1}), h was in the range of 36–746 nm, typical of EHD lubrication. h decreased by over 547 nm at constant speed and pressure, for lubricant 2, with a ΔT of 100°C and is attributable to a reduction in viscosity in the contact zone. Lubricants 1 and 2 inherited characteristics of their respective base esters $L1^{est}$ and $L2^{est}$ but the additional additives in the fully formulated lubricants had diluted the bulk film and variations in h were observed. Lubricants 3 and 4 both exhibited quite severe nonlinear behavior with lubricant 4 producing film thicknesses of up to 23 nm at 150°C, between 0.01 and 1 ms^{-1}. This was not predicted by EHD theory and was attributable to the formation of a polyphosphate film. Modeling of the nonlinear behavior enabled the film thickness attributable to EHD and the phosphate film to be separated. Using fitted models gave results that correlated well with measured values and would facilitate calculation of film thicknesses at any entrainment speed and in the presence of nonlinear behavior.

The large variation in h between lubricants 1–4, recorded at the same speed and temperature, were attributable to variations in the molecular structure of the bulk film forming components and how they behaved under pressure (Piezoviscous Effect) in the tribological contact. Calculations of the pressure–viscosity coefficient α revealed values that ranged from 2.7 GPa^{-1} at 150°C to 18.9 GPa^{-1} at 50°C. Lubricant 2, which contained a more branched ester, $L2^{est}$, gave a higher α value, whereas lubricant 1 which contained the linear polyol ester, $L1^{est}$, gave a lower α value and this correlated well with film thickness measurements. Lubricants 3 and 4 also contained linear polyol esters but exhibited α values that were intermediary of lubricants 1 and 2, and this was attributable to the higher relative molecular mass of the esters employed. It was found that under a Hertzian contact pressure of 0.54 GPa, lubricant 2 increased its theoretical viscosity nearly 1000 times compared to its viscosity at 1.01325×10^{-4} GPa. The viscosity would have increased 5653 times if β (Equation 17.9) had been ignored. Although speed acts as a carrier of lubricant into the tribocontact, it is the large increases in viscosity with pressure that will facilitate the formation of a very rigid hydrodynamic film, producing a concomitant EHD flattening of the work rolls.

Mill trials were conducted comparing a control lubricant with lubricant 4. Its nonlinear behavior coupled with its good EHD forming properties was exploited to cover the lubrication spectrum. Reductions in specific roll force of up to 3.69 MN m^{-1} were observed in the boundary lubrication mode compared to the control lubricant. In the EHD region, a reduction in specific roll force of 1.3 MN m^{-1} was recorded with an increase in speed of 300 m min^{-1} over that of the control. A good correlation of film thickness measurements h by EHD interferometry and mill performance was obtained.

17.4 EXPERIMENTAL PROTOCOL

17.4.1 Determination of Film Thickness h by Elastohydrodynamic Interferometry

Measurements were made between a 19.0-mm diameter, AISI 52100, steel ball in nominally pure rolling contact with the flat surface of a glass disc. The disc surface was coated with a 20 nm thick chromium layer, covered by a 500 nm thick silica layer. The Young's moduli of the two surfaces were 210 and 75 GPa for steel and glass, respectively. The load applied was 20 N, corresponding to a maximum Hertz contact pressure of 0.54 GPa. The test rig is shown in Figure 17.5a and b.

The test rig was cleaned thoroughly with Analar toluene and isopropanol. Lubricant was then added to the test rig to cover the steel ball. After setting the temperature of the test rig to 50°C, a period of 45 min was allowed for the lubricant temperature to fully stabilize. The contact was then loaded and the EHD apparatus ran at 0.3 ms^{-1} for 5 min. Finally, the speed was adjusted to 0.01 ms^{-1} and measurements at that speed and a series of speeds up to 4.25 ms^{-1} were made over a total time of about 5 min. This whole procedure, including the 45-min stabilization time, was then repeated at 100°C and 150°C. Temperature was controlled to ±1.0°C.

17.4.2 Determination of the Pressure–Viscosity Coefficient α

Pressure–viscosity coefficients were determined by EHD interferometry, indirectly, through back calculation of a modified power form of Equation 17.4. It has been shown that this protocol has produced results that are 10% lower than actual values, due to shear thinning.

17.4.3 Determination of the Temperature–Viscosity Coefficient β

The dynamic viscosity and density were measured at 50°C and 100°C using an Auto Paar Stabinger SWM 3000 viscometer. Values at 150°C were calculated via kinematic viscosity values using ASTM D341 and assuming linear variation of density with temperature. Temperature–viscosity coefficients β were determined at two temperatures, in the region of interest utilizing Equation 17.10.

$$\ln\left[\frac{\eta_o}{\eta}\right] = -\beta(T_o - T) \tag{17.10}$$

where

η_o = viscosity at 1.01325×10^{-4} GPa
β = temperature viscosity coefficient
η = actual viscosity in the material pair interface
T_o = temperature at which η_o is measured
T = actual temperature in the material pair interface

ACKNOWLEDGMENTS

I would like to thank D. A. Stuart Company and others who have contributed to this work. I would also like to thank Melinda Burton.

REFERENCES

Bair, S., Vergne, P., and Querry, M. (2005) A unified shear-thinning treatment of both film thickness and traction in EHD. *Tribology Letters* 18: 145–152.

Barus, C. (1893) Isothermals, isopiestics and isometrics relative to viscosity. *American Journal of Science* 45: 87–96.

Bekefi, G., and Barett, A. H. (1987) *Electromagnetic Vibrations, Waves and Radiation*. Cambridge, MA: MIT Press, pp. 11.

Bowden, F. P., and Tabor, D. (1950) *The Friction and Lubrication of Solids*. London: Oxford University Press.

Burton, I. (2007) Elastohydrodynamic lubrication in rolling geometries. In *Proceedings of Iron and Steel Conference*, Vol. 2, AIST, Warrendale, PA, pp. 307–319.

Gao, F., Kotvis, P. V., Stacchiola, D., and Tysoe, W. T. (2005) Reaction of tributyl phosphate with oxidized iron: Surface chemistry and tribological significance. *Tribology Letters* 18: 377–384.

Hamrock, B. J., and Dowson, D. (1977) Isothermal elastohydrodynamic lubrication of point contacts: Part III—Fully flooded results. *Transactions ASME Journal of Lubrication Technology* 99: 264–276.

Hertz, H. (1882) Uber die beruhrung feter elastischer korper. *Journal für die Reine und Angewandte Mathematik* 92: 156–171.

Kaneta, M., and Nishikawa, H. (1999) Experimental study on microelastohydrodynamic lubrication. *Proceedings of the Insti-tution of Mechanical Engineers* 213 Part J: 371–380.

Minfray, C., LeMogne, T., Martin, J. M., Onodera, T., Nara, S., Takahashi, S., Tsuboi, H., Koyama, M., Endou, A., Takaba, H., Kubo, M., Del Carpio, C. A., and Miyamoto, A. (2008) Experimental and molecular dynamics simulations of tribochemical reactions with ZDDP: Zinc phosphate-iron oxide reaction. *Tribology Transactions* 51: 589–601.

Najman, M. N., Kasrai, M., Bancroft, G. M., and Miller, A. (2002) Study of the chemistry of films generated from phosphate ester additives on 52100 steel using x-ray absorption spectroscopy. *Tribology Letters* 13: 209–218.

Nakayama, K., and Fujimoto, T. (2004) The energy of electrons emitted from wearing solid surfaces. *Tribology Letters* 17: 75–81.

Olver, A. V., and Spikes, H. A. (1998) Prediction of traction in elastohydrodynamic lubrication. *Proceedings of the Institution of Mechanical Engineers* 212: 321–332.

Spikes, H. A. (1989) Additive-additive and additive-surface interactions in lubrication. *Lubrication Science* 2: 3–23.

Sutcliffe, M. P. F., and Johnson, K. L. (1990) Lubrication in cold strip rolling in the 'mixed' regime. *Proceedings of the Institution of Mechanical Engineers* C204: 249–261.

Timoshenko, S., and Goodier, J. N. (1951) *Theory of Elasticity*. New York: McGraw Hill, pp. 137.

Wang, L., and Wood, R. J. K. (2007) The influence of contact conditions on surface reaction layers formed between steel surfaces lubricated by an aviation oil. *Tribology International* 40: 1655–1666.

Wilson, W. R. D., and Walowit, J. A. (1971) An isothermal hydrodynamic lubrication theory for strip rolling with front and back tension. *1971 Tribology Convention*, London, U.K. pp. 164–172.

Yuen, W. Y. D., Popelianski, Y., and Prouten, M. (1996) Variations of friction in the roll bite and their effects on cold strip rolling. *Iron Steelmaker* 23: 33–39.

Section III

Measurement, Automation, and Process Control

18 Multivariable Hot Strip Mill Control

Gerald Hearns, T. Bilkhu, and Peter Reeve

CONTENTS

18.1 Introduction 209
18.2 System Modeling 210
18.3 Conventional Gauge and Mass Flow Control 213
18.4 Multivariable Controller Design 213
18.4.1 State Feedback 213
18.4.2 State Estimation 214
18.4.3 Performance Optimization 215
18.5 Mill Trials 215
18.6 Conclusions 217
References 218

18.1 INTRODUCTION

Hot strip mills are processes with very high throughput of product. They are highly developed, capital intensive, and competitive businesses where control systems are essential to maintain product quality and production efficiency. Even small improvements in the accuracy of the product and mill availability yield significant savings for the steel producer. This chapter describes the development of a multivariable controller to control the gauge and mass flow for one stand and interstand in a tandem hot strip mill. A feature of the design is that no new or additional equipment to that installed for the conventional control system is required for the multivariable design.

Gauge control is essential to product quality, while regulating mass flow is important for stable operation of the complete mill. Gauge and mass flow are tightly coupled. The control design, which uses state feedback and estimation, is described along with the issues necessary for a practical implementation. Inherent in the multivariable design is the explicit ability to trade off gauge and mass flow performance against each other.

This chapter focuses on an important aspect of the dynamic control of the finishing mill: the stand's speed and gap controls. These controls ensure that the product reaches its required dimensions at the mill exit and that the strip is rolled in a stable manner. It is achieved by controlling each stand and interstand unit as a subsystem. The stand exit gauges are controlled to a reference calculated by the mill setup. The mass flow out of the upstream and into the downstream stands is controlled to avoid any mass flow mismatch and disturbance to the interstand strip tension. Figure 18.1 shows schematically two stands in the finishing mill and the interstand gap. To avoid a buildup or reduction in the length of strip between the stands, the speed of the upstream stand is modulated to maintain the looper at a reference angle. The looper is a metal arm with a roller on the end that is held in contact with the strip by applying a torque to the looper arm pivot. The looper arm movement provides a degree of variation in strip storage length between the two stands, giving the system some leeway to respond to disturbances. The arm angle also provides a measurement of the length of strip between the two stands (the loop length) that is used to control the upstream stand speed. The looper pivot torque is also modulated according to the measured looper angle to keep the strip tension at its setup reference. The stand gap is modulated to keep the exit gauge at its setup reference. Note, however, that the system is highly interactive or coupled, in other words, changing the gap affects gauge, and thereby, mass flow/strip tension/looper angle. That is, the system is multi-input/multi-output with a strong cross coupling.

Since the early 1980s, there has been a substantial international research effort devoted to developing multivariable controllers for the hot strip mill looper/strip tension system. The use of multivariable controllers is particularly appropriate for the coupled two input (looper torque, stand speed), two output (looper angle, strip tension) system. The control techniques proposed have included: decouplers (Kotera and Watanabe 1981), multivariable proportional integral derivative (PID) control (Duysters et al. 1994), linear quadratic (Seki et al. 1991), H-infinity (Imanari et al. 1997), quantitative feedback theory (Hearns and Grimble 2000a), and advanced nonlinear control (Hesketh et al. 1998). Most work (both simulation and physical trials) has concentrated on controlling

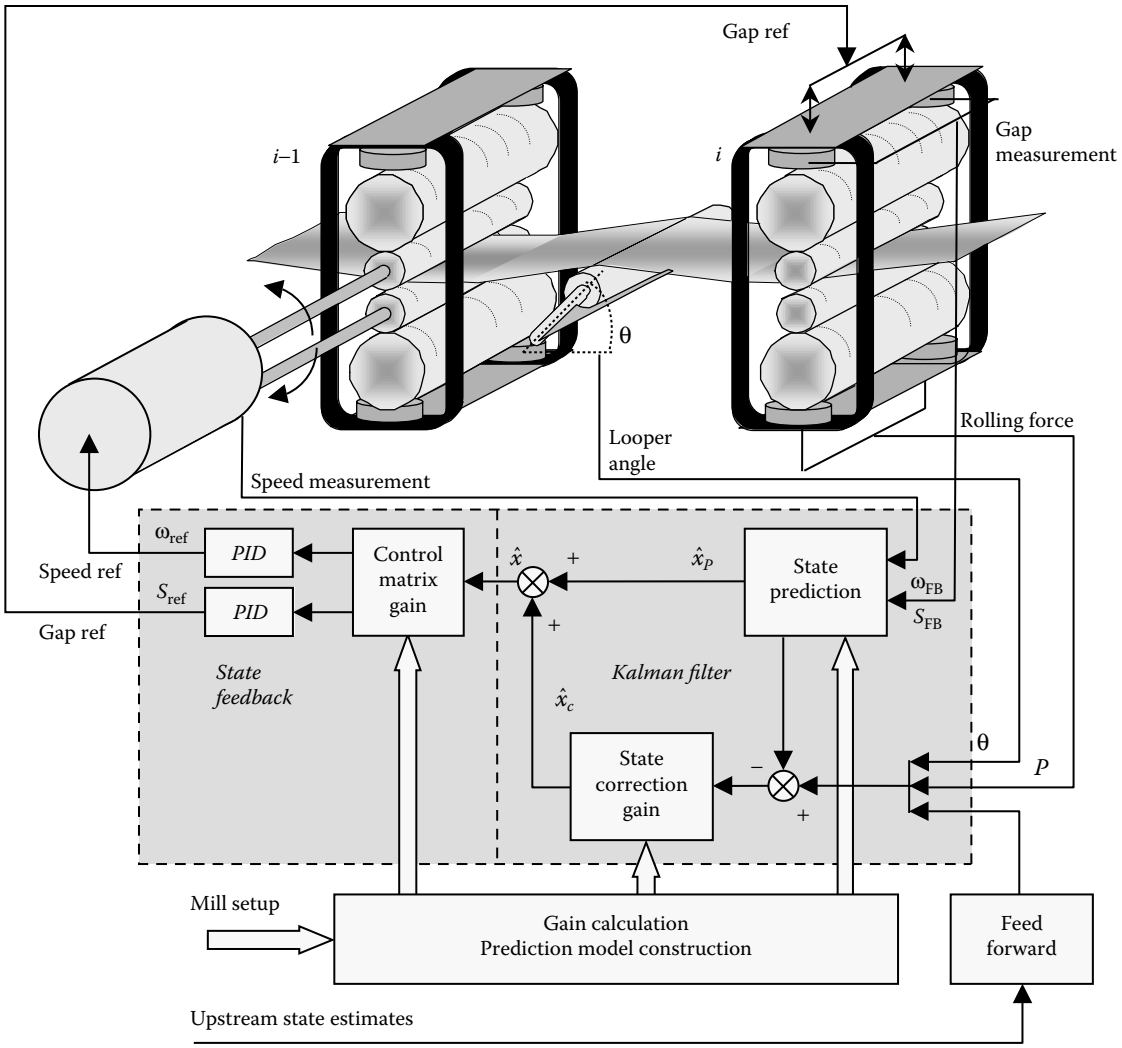


FIGURE 18.1 Multivariable control of gauge and looper angle.

the looper angle and strip tension using a direct measurement of tension. Less common has been the development of controllers that include the interactions to the strip gauge (Miura et al. 1993; Hearns and Grimble 2000b). Systems using a direct measurement of strip tension require special instruments. On most hot strip mills, the instruments are not available and would need to be specially installed. Conventional strip tension control is by high bandwidth looper, drive motor torque control. The torque reference is calculated as a nonlinear function of the looper angle, because it varies. With good loop length control, conventional looper control produces good performance. Further, the cross couplings from tension to rolling force/exit gauge are small compared to the large gauge to loop length coupling.

The aim of the controllers developed here is to control the strip exit gauge and mass flow (loop length, looper angle), while assuming that the strip tension is already well regulated. The design will only use the conventional hot strip mill equipment. This will particularly help in the retrofitting of the design to existing mills. Designing gauge and mass flow control loops in a multivariable structure directly addresses the limiting factor on speed of gauge response, which is mass flow regulation. Figure 18.1 shows the basic control structure where looper angle (θ) and rolling force (P) are used to control the upstream speed reference (ω_{ref}) and downstream gap reference (S_{ref}).

18.2 SYSTEM MODELING

The stand process models required for the control system design are the rolling force and the mill stretch models. Rolling force (P) is a nonlinear function of entry gauge (H), exit gauge (h), and the strip hardness (k):

$$P = F_P(H,h,k) \tag{18.1}$$

Strip exit gauge depends on the roll gap (S) controlled by the hydraulic capsule and the mill stretch, which is a function of the rolling force:

$$h = S + F_S(P) \tag{18.2}$$

To calculate the exit gauge, these simultaneous nonlinear equations must be solved. Both the roll force and mill stretch are smooth functions, but are significantly nonlinear across the product range, both in terms of the arguments and of other factors not shown in Equations 18.1 and 18.2. However, as a coil is rolled through the mill deviations from linearity about the setup values are small. This property is exploited in the control design.

Through the stand, the mass flow must balance, hence if the strip width remains constant,

$$VH = vh \tag{18.3}$$

where V is the strip entry speed and v the exit strip speed. The exit speed depends on forward slip (f), roll radius (R), and roll speed (ω):

$$v = (1+f)R\omega \tag{18.4}$$

The rate of change of strip length ($\dot{L}_s$) in the interstand is equal to the difference of the strip speed leaving the upstream stand (v_{i-1}) and entering the downstream stand (V_i):

$$\dot{L}_s = v_{i-1} - V_i \tag{18.5}$$

The strip tension (σ) is the strain multiplied by Young's modulus (E)

$$\sigma = E\left(\frac{L_\theta - L_s}{L_s}\right) \tag{18.6}$$

where the strain depends on the difference between the geometric length (L_θ) and the material length (L_s). L_θ is a nonlinear function of the looper angle and the mill geometry. For hot steel, Young's modulus $E \approx 1 \times 10^{11}$ N m^{-2} and nominal tension is 1 MN m^{-2} < σ < 20 MN m^{-2}. Therefore,

$$L_s = \frac{E}{\sigma + E} L_\theta \tag{18.7}$$

and, even for large changes in tension, $L_s \approx 0.999 L_\theta$. The geometric loop length, which is a function of looper angle, is extremely close to the physical loop length (L_s), which depends on the amount of strip leaving one stand and entering the next.

The control design method uses linear models. These are derived from the nonlinear process models, Equations 18.1 through 18.5, by linearizing them about the coil setup values, $\overline{H}$, $\overline{h}$, and $\overline{\omega}$. Figure 18.2 shows a linear dynamic model of the stand and upstream looper/strip. The top part of the model represents the dynamics of the looper arm with inertia J_L, nonlinear torque T applied to the looper, which is a function of looper angle and strip tension.

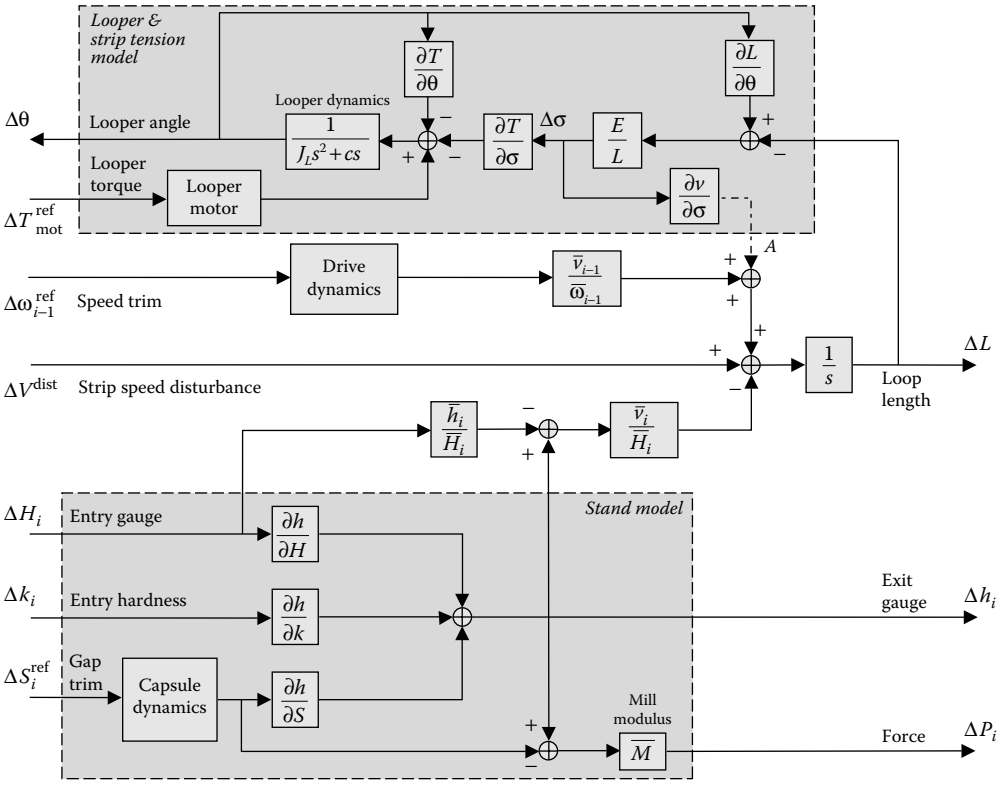


FIGURE 18.2 Full dynamic model of looper and stand.

It is common to use the measured looper angle to calculate a reference looper motor torque that will regulate the strip tension despite looper angle variations. The strip tension will change the exit slip of the upstream stand, which changes the exit velocity and loop length. While this interaction is important in helping to stabilize the strip tension, it is less important for control of loop length. Therefore, the loop can be broken at point *A* and the diagram simplified, as shown in Figure 18.3 for the control of gauge and loop length with the assumption that the strip tension is already being controlled and is a weak interaction to gauge and loop length.

The two control inputs are the upstream speed trim $\Delta\omega_{i-1}^{\text{ref}}$ and the downstream gap trim ΔS_i^{ref}. The two main measurements are downstream stand force ΔP_i and interstand strip loop length ΔL. The latter measurement is calculated from the looper angle using the looper/stand geometry. Three disturbances to the system are considered. Two are strip disturbances, the stand entry gauge ΔH_i and hardness Δk_i. The third is a speed disturbance ΔV^{dist} to the mass flow balance between the upstream and downstream stands. This is to represent mass flow disturbances caused by roll diameter changes, slip changes, modeling errors, etc. In general, the disturbances comprise two components: a known component, such as gauge and hardness errors fed-forward from the upstream stand, and an unknown or random component. Note that strip disturbances or gap changes made for control purposes directly affect the stand exit gauge and force of the downstream stand. Because of mass flow conservation across the stand (see Equation 18.3) the strip entry speed changes, which in turn disturbs the loop length. That is, there is strong cross coupling between the downstream exit gauge and loop length, meaning the stand/interstand is a tightly coupled dynamic multivariable system.

The upstream drive model is second order with speed PI control (K_{P}, K_{I}), inertia (J), and motor constant (K_{m}), while the capsule is modeled with a first order lag. The generalized design system is

$$\begin{aligned} \dot{x} &= Ax + B_1\varsigma + B_2u, \\ z &= C_1x + D_{11}\varsigma + D_{12}u, \\ y &= C_2x + D_{21}\varsigma + D_{22}u \end{aligned} \tag{18.8}$$

with actuator input (u), disturbances (ς), regulated variables (z), and observations (y):

$$x = [\Delta I_\omega, \Delta\omega_{i-1}, \Delta S_i, \Delta L]^{\text{T}},\ y = [\Delta L, \Delta P_i]^{\text{T}},\ z = [\Delta L, \Delta h_i]^{\text{T}},$$
$$u = [\Delta\omega_{i-1}^{\text{ref}}, \Delta S_i^{\text{r}}]^{\text{T}},\ \varsigma = [\Delta H_i, \Delta k_i, \Delta V^{\text{dist}}]^{\text{T}}$$

ΔI_ω is the drive motor current and all variables are deviations from setup values. The state space matrices are

$$A = \begin{bmatrix} 0 & -1 & 0 & 0 \\ \dfrac{K_{\text{m}}K_{\text{I}}}{J} & \dfrac{-K_{\text{m}}K_{\text{P}}}{J} & 0 & 0 \\ 0 & 0 & -\dfrac{1}{\tau_{\text{C}}} & 0 \\ 0 & \dfrac{\bar{v}_{i-1}}{\bar{\omega}_{i-1}} & -\dfrac{\bar{v}_i}{\bar{H}_i}\dfrac{\partial h}{\partial S} & 0 \end{bmatrix} \tag{18.9}$$

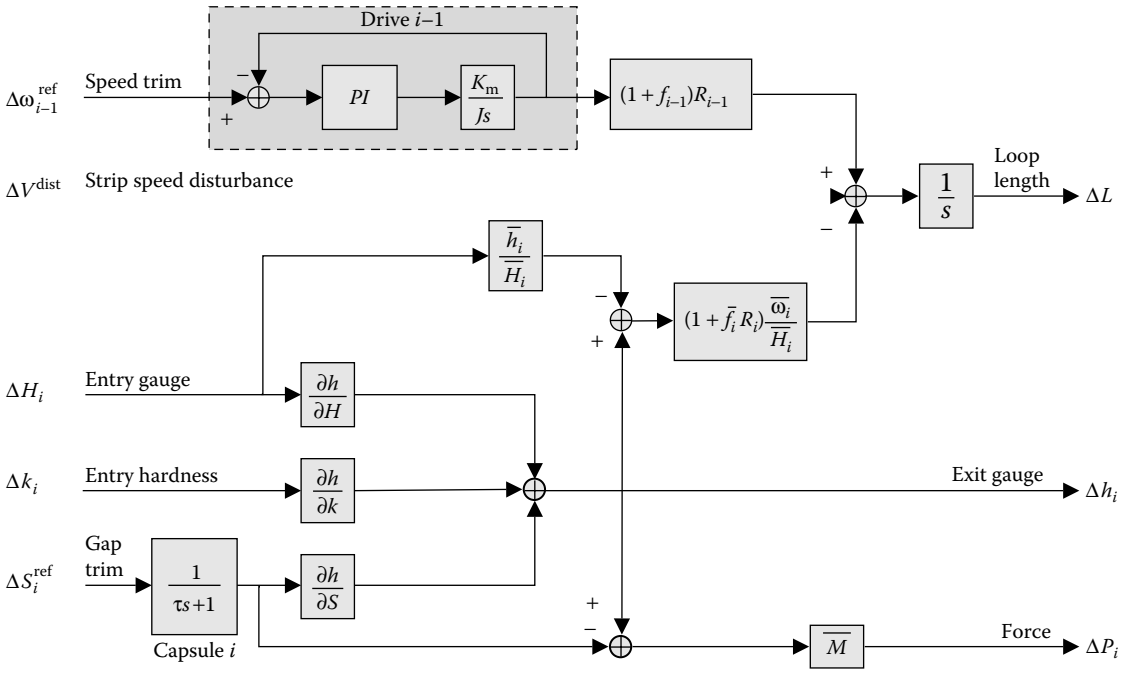


FIGURE 18.3 Linear design model.

$$B_1 = \begin{bmatrix} 0 & 0 & 0 \\ 0 & 0 & 0 \\ 0 & 0 & 0 \\ \frac{\bar{v}_i}{\bar{H}_i}\left(\frac{\bar{h}_i}{\bar{H}_i} - \frac{\partial h}{\partial H}\right) & -\frac{\bar{v}_i}{\bar{H}_i}\frac{\partial h}{\partial k} & 1 \end{bmatrix}, \quad B_2 = \begin{bmatrix} 1 & 0 \\ \frac{K_m K_P}{J} & 0 \\ 0 & \frac{1}{\tau_C} \\ 0 & 0 \end{bmatrix} \tag{18.10}$$

$$C_1 = \begin{bmatrix} 0 & 0 & 0 & 1 \\ 0 & 0 & \frac{\partial h}{\partial S} & 0 \end{bmatrix}, \quad C_2 = \begin{bmatrix} 0 & 0 & 0 & 1 \\ 0 & 0 & M\left(\frac{\partial h}{\partial S} - 1\right) & 0 \end{bmatrix} \tag{18.11}$$

$$D_{11} = \begin{bmatrix} 0 & 0 & 0 \\ \frac{\partial h}{\partial H} & \frac{\partial h}{\partial k} & 0 \end{bmatrix}, \quad D_{12} = \begin{bmatrix} 0 & 0 \\ 0 & 0 \end{bmatrix} \tag{18.12}$$

$$D_{21} = \begin{bmatrix} 0 & 0 & 0 \\ M\frac{\partial h}{\partial H} & M\frac{\partial h}{\partial k} & 0 \end{bmatrix}, \quad D_{22} = \begin{bmatrix} 0 & 0 \\ 0 & 0 \end{bmatrix} \tag{18.13}$$

18.3 CONVENTIONAL GAUGE AND MASS FLOW CONTROL

The looper angle is usually controlled by converting the angle to a loop length error, which is then input to a PID controller to provide a speed trim reference to the upstream stand. Any change in the downstream stand speed is compensated by feeding forward the speed change to the upstream stand in the proportion of the setup speeds. Mass flow compensation adjusts the speed of each stand to accommodate for changes in entry and exit gauge to prevent any loops forming or strip breakage. It can be shown that

$$\frac{\Delta V_{i-1}}{V_{i-1}} = \frac{\Delta h_i}{h_i} - \frac{\Delta H_i}{H_i} \tag{18.14}$$

The dominant change to Δh_i will be due to the gap change ΔS_i; therefore, the speed trim to the upstream stand will be

$$\Delta\omega_{i-1}^{r} = \frac{\partial h_i}{\partial S_i}\frac{\Delta S_i^{r}}{\bar{h}_i}\bar{\omega}_{i-1} \tag{18.15}$$

where $\bar{h}$ and $\bar{\omega}$ are setup gauge and speed, respectively.

The primary purpose of automatic gauge control (AGC) is to compensate for the mill stretch by using the measured force and mill modulus (gradient of mill stretch function) to decrease the gap:

$$\Delta S^{r} = -\frac{P}{\bar{M}} \tag{18.16}$$

The actual gauge control is more sophisticated, allowing it to cope with errors in the mill modulus ($\bar{M}$), filter out disturbances it cannot control such as backup roll eccentricity, and react to gauge reference changes.

18.4 MULTIVARIABLE CONTROLLER DESIGN

It is important to note that every strip the mill rolls may have different dimensions and different metallurgical properties. Also, the mill stretch changes with time and is measured periodically. Because of the large variations in the product that are possible, it is necessary to calculate the model sensitivities from the full nonlinear model as each strip is presented to the mill. The strip-specific model is then used to calculate the controller gains. The calculations must be quick, robust, and automatic. The multivariable control design method chosen is linear quadratic state feedback with the states estimated by a Kalman filter (LQG control). The process model based design is valuable because the physical meaning of the states is preserved, and the estimated states, which include disturbances, may be used by other control systems in the mill, for trouble shooting and for general plant monitoring.

18.4.1 State Feedback

To provide design flexibility, the actuator references are divided into three parallel channels: one is a direct path, one is augmented with an integrator, and one is augmented with a filtered differentiator $\{A_D, B_D, C_D, D_D\}$. Note the integral path ensures the controller has integral action. Each of the three channels has its own control weight, thus in effect the multivariable controller can be tuned with the same intuition that a PID controller provides. Modeling the disturbances as random walks adds the states ς^I. The full design model is

$$\frac{d}{dt}\begin{bmatrix} x \\ \varsigma^I \\ u^I \\ u_D \end{bmatrix} = \begin{bmatrix} A & B_1 & B_2 & B_2 C_D \\ 0 & 0 & 0 & 0 \\ 0 & 0 & 0 & 0 \\ 0 & 0 & 0 & A_D \end{bmatrix}\begin{bmatrix} x \\ \varsigma^I \\ u^I \\ u_D \end{bmatrix} + \begin{bmatrix} 0 \\ I \\ 0 \\ 0 \end{bmatrix}\varsigma$$

$$+ \begin{bmatrix} B_2 & 0 & B_2 D_D \\ 0 & 0 & 0 \\ 0 & I & 0 \\ 0 & 0 & B_D \end{bmatrix}\begin{bmatrix} u_r^P \\ u_r^I \\ u_r^D \end{bmatrix}$$

$$\begin{bmatrix} z \\ y \end{bmatrix} = \begin{bmatrix} C_1 & D_{11} & D_{12} & D_{12}C_D \\ C_2 & D_{21} & D_{22} & D_{22}C_D \end{bmatrix} \begin{bmatrix} x \\ \varsigma^I \\ u^I \\ u_D \end{bmatrix} + \begin{bmatrix} 0 \end{bmatrix} \varsigma + \begin{bmatrix} D_{12} & 0 & D_{12}D_D \\ D_{22} & 0 & D_{22}D_D \end{bmatrix} \begin{bmatrix} u_r^P \\ u_r^I \\ u_r^D \end{bmatrix} \tag{18.17}$$

To calculate the state-feedback matrix gain, the continuous system ($D_{12} = D_{22} = 0$) from the control inputs is converted to a discrete system:

$$\begin{aligned} x_{k+1} &= \hat{A}x_k + \hat{B}_2 u_k, \\ z_k &= \hat{C}_1 x_k \end{aligned} \tag{18.18}$$

The linear quadratic cost function to optimize is

$$J = \sum_{k=1}^{\infty} z_k^T Q_C z_k + u_k^T R_C u_k \tag{18.19}$$

where

$$z_k = [L - L_{ref} \quad \Delta h - \Delta h_{ref}]^T$$

and $$u_k = \left[\begin{bmatrix} \omega_P \\ S_P \end{bmatrix}^T \quad \begin{bmatrix} \omega_I \\ S_I \end{bmatrix}^T \quad \begin{bmatrix} \omega_D \\ S_D \end{bmatrix}^T \right]^T$$

L_{ref} is the geometric loop length at the reference looper angle. The state feedback matrix gain can be found by solving the difference Ricatti equation sequentially (Astrom and Wittenmark 1997)

$$S_n = A^T S_{n-1} A - A^T S_{n-1} B[B^T S_{n-1} B + R_C]^{-1} B^T S_{n-1} A + C^T Q_C C \tag{18.20}$$

$$K_n = [R_C + B^T S_{n-1} B]^{-1} B^T S_{n-1} A \tag{18.21}$$

until it is believed a steady-state solution is reached. Q_C and R_C are, respectively, the output and control weightings. The controller output is $u_k = -Kx_k$.

18.4.2 State Estimation

The system structure is such that with the two measurements of force and loop length the observer can only resolve two of the disturbances. As careful study of the linear design model (Figure 18.3) shows, appropriate combinations of V^{dist} and H_i or V^{dist} and k_i will give the same force and loop length responses. The two disturbances chosen are hardness and velocity. In the Kalman filter, these disturbances are modeled as random walks. The entry gauge disturbance estimate can be obtained by feeding forward the exit gauge estimate from the upstream stand, which is calculated using the mill stretch model. The main measurements driving the filter are the change in rolling force from setup force, the change in loop length, which is generated, from the looper angle error. In the practical design use is also made of the measured roll rotational speed ($\Delta\omega_{i-1}^{meas}$) and the relative gap position (ΔS_i^{meas}). It is convenient to split the required state estimation into three Kalman filters for the physical process, drive motor, and capsule. The process Kalman filter estimates the hardness disturbance, speed disturbance (or unmeasured speed error), and the change in loop length. The measurements driving the filter are change in rolling force from setup force and the change in loop length, which is generated from the looper angle error. Since it is assumed that the strip tension is already regulated then there should be little difference between the physical loop length (from the strip entry and exit speeds) and the geometric length from the looper angle. For the process Kalman filter, the design model is

$$\frac{d}{dt}\begin{bmatrix} \Delta k \\ \Delta V \\ \Delta L \end{bmatrix} = \begin{bmatrix} 0 & 0 & 0 \\ 0 & 0 & 0 \\ -\frac{\partial V}{\partial k} & 1 & 0 \end{bmatrix} \begin{bmatrix} \Delta k \\ \Delta V \\ \Delta L \end{bmatrix} + \begin{bmatrix} 0 & 0 \\ 0 & 0 \\ \frac{\partial v}{\partial \omega} & -\frac{\partial V}{\partial S} \end{bmatrix} \begin{bmatrix} \Delta\omega_{i-1}^{filt} \\ \Delta S_i^{filt} \end{bmatrix} + \begin{bmatrix} 1 & 0 \\ 0 & 1 \\ 0 & 0 \end{bmatrix} \begin{bmatrix} k_\xi \\ V_\xi \end{bmatrix} \tag{18.22}$$

$$\begin{bmatrix} \Delta L \\ \Delta P \end{bmatrix} = \begin{bmatrix} 0 & 0 & 1 \\ \frac{\partial P}{\partial k} & 0 & 0 \end{bmatrix} \begin{bmatrix} \Delta k \\ \Delta V \\ \Delta L \end{bmatrix} + \begin{bmatrix} 0 & 0 \\ 0 & \frac{\partial P}{\partial S} \end{bmatrix} \begin{bmatrix} \Delta\omega_{i-1}^{filt} \\ \Delta S_i^{filt} \end{bmatrix} + \begin{bmatrix} 0 & 0 \\ 0 & 0 \end{bmatrix} \begin{bmatrix} k_\xi \\ V_\xi \end{bmatrix} \tag{18.23}$$

The continuous model should be converted to a discrete time system

$$\begin{aligned} x_{k+1} &= Ax_k + Bu_k + Ew_k, \\ y_k &= Cx_k + Du_k + v_k \end{aligned} \tag{18.24}$$

where w_k is a zero mean random process disturbance with covariance matrix Q_f and v_k is a zero mean random measurement noise with covariance matrix R_f. The Kalman filter (one step ahead predictor) system is

$$\hat{x}_{k+1} = A\hat{x}_k + Bu_k + N(y_k - C\hat{x}_k - Du_k) \tag{18.25}$$

and the Kalman gain N is

$$N = APC^T[CPC^T + R_f]^{-1} \tag{18.26}$$

where P is the solution of the algebraic Riccati equation

$$P = APA^T - APC^T[CPC^T + R_f]^{-1} CPA^T + EQ_f E^T \tag{18.27}$$

18.4.3 Performance Optimization

A significant advantage of the multivariable control design compared to conventional control is that by manipulating the output weightings the engineer is able to trade off mass flow control against gauge control. It is possible to speed up the mass flow control response by relaxing the weight on stand exit gauge and using the high bandwidth, stand gap control to maintain interstand loop length. Figure 18.4 compares the frequency responses of the conventional controllers (dashed) and the multivariable controller with varying weights. For both, the AGC (force to gap) has a fairly similar response and the multivariable loop length to speed has the characteristic of a PID controller. When the weightings are changed to improve the mass flow control (increase loop length weight, decrease gauge weight), the gain from loop length to gap increases. It is possible in the limit to control the looper angle using only the downstream gap trim. Such a control strategy may be valuable if there is a predictable material phase change occurring in the mill, in which case the weights can be changed to ensure that the mill remains stable at the expense of exit gauge control from the downstream stand.

An important feature of the controller is the recalculation of the optimum control gains on a coil-by-coil basis, that is, the controller is schedule dependent. To maintain a consistent performance across the schedule it is necessary to adjust the design weightings according to the primary data. Rules have been devised so that the dynamic response (controller bandwidth, etc.) is independent of the primary coil parameters. In addition, the design weights can be set to produce a different performance characteristic for individual products should they require it.

18.5 MILL TRIALS

The multivariable controller was implemented between stands 4 and 5 on a seven-stand hot strip mill. Figures 18.5 and 18.6 show the main controller variables for a representative coil under multivariable control. The looper angle for a consecutive coil with conventional control is also plotted. The controller is responding to the normal product disturbances. The figures show the large initial transient response on the strip nose as the mill threads and, in-coil, the response to disturbances primarily caused by temperature variations along the coil. It can be seen that with multivariable control the angle reaches its reference more quickly and has less variation during the body. As expected, the gauge error is within target performance limits, the noise being due to roll eccentricity. The strip hardness and velocity error estimates (Figure 18.6) both have upward trends due to strip cooling and mill speed acceleration. Once the looper has made contact with the strip, the controller moves in the correct direction of slowing down the upstream speed and increasing the downstream gap, thus bringing the looper angle back to the reference. There is less overshoot at the head of the strip and tighter control in the body of the strip.

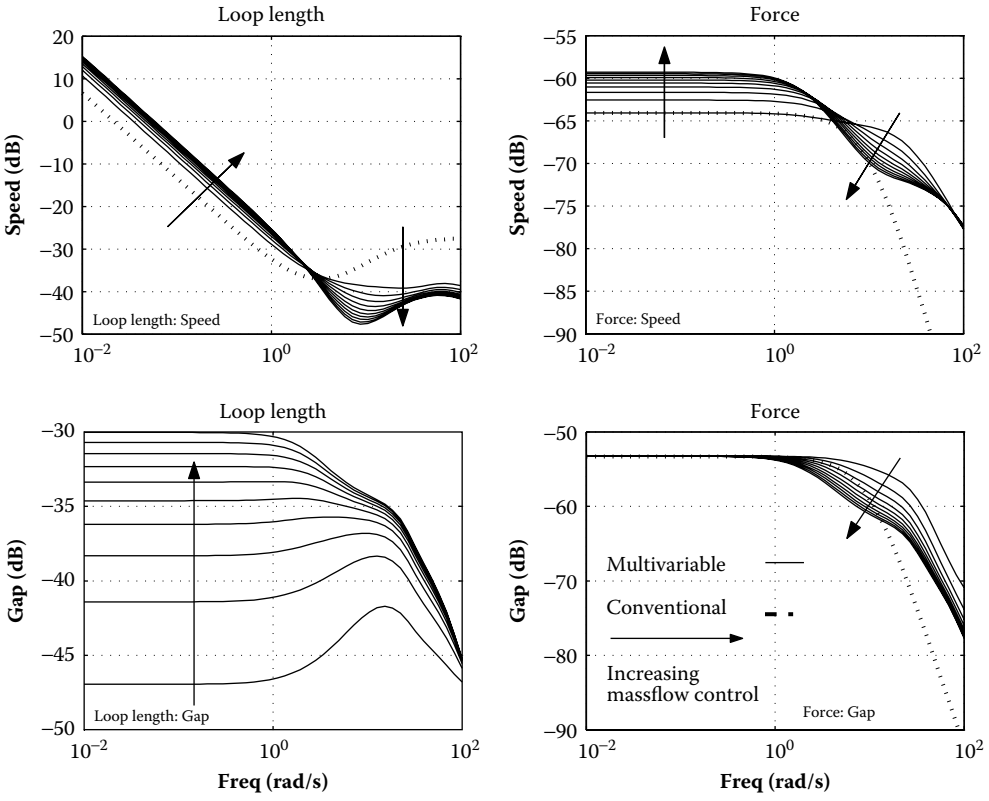


FIGURE 18.4 Controller magnitude with varying weights for increased mass flow control.

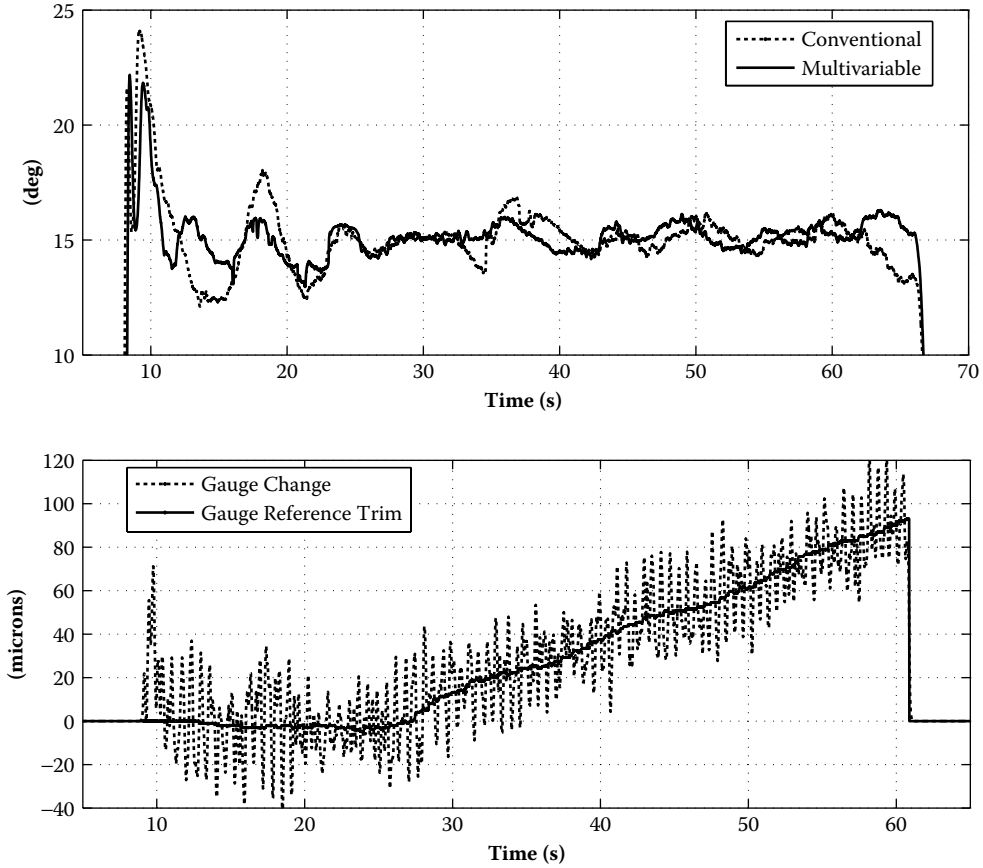


FIGURE 18.5 Multivariable/conventional looper angle, multivariable control gauge change, and gauge reference.

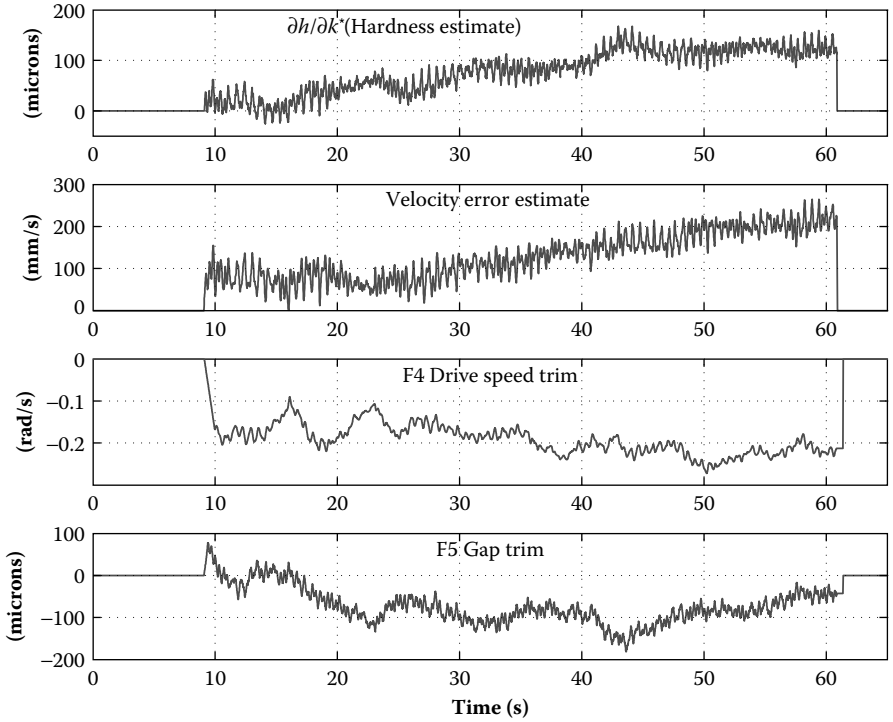


FIGURE 18.6 Multivariable disturbance estimates and control outputs.

It is difficult to improve on the unconstrained performance of a conventional gauge meter controller using a multivariable controller. However, in practice the operation of the gauge meter controller is often constrained because of the interaction between gauge and loop length, by the need to maintain good loop length control for mill stability and product quality reasons. One of the advantages of the multivariable control approach is that it directly addresses the gauge/loop length interaction.

A statistical analysis of the multivariable controller performance compared to the conventional controllers is carried out using approximately 250 coils and plotted in Figure 18.7. The main criterion of control performance is the looper angle. The tension performance can be assessed using an estimated strip tension derived from the measured looper angle and looper motor current. With multivariable control, the head end angle overshoot and area (degrees × seconds) is significantly less. The time for the looper angle to go from its maximum to reference is significantly less with multivariable control, 2.3 s as opposed to a mean of 3.8 s with conventional control. It is during the large initial looper angle transient at the head end of the strip that mill stability is critical. The faster the angle is brought to its reference the better. The spread of the overall maximum tension during the strip body is less with multivariable control although the mean maximum is more. Note also that the numbers of outliers in the multivariable case are less than with the conventional control.

The control improvements with multivariable control appear small. However, as was pointed out in the introduction, for such high throughput and highly developed processes as a hot strip mill small performance improvements yield significant cost benefits. The reduction in the number of outliers is particularly significant. The outlier coils are the ones more likely to result in catastrophic loss of control of the process, a mill "cobble." Any mill cobble results in loss of the coil, mill downtime, and can possibly cause damage that must be repaired before production can continue. A loss of throughput results.

18.6 CONCLUSIONS

It is believed that this is the first application of a multivariable controller for gauge and mass flow that has been tested on a hot strip mill. The innovative structure of the multivariable cost function to give a PID characteristic ensures engineers trained in classical control can readily apply the new techniques with minimal knowledge of advanced methods. The improved looper angle control provides more stable conditions for the control of strip tension.

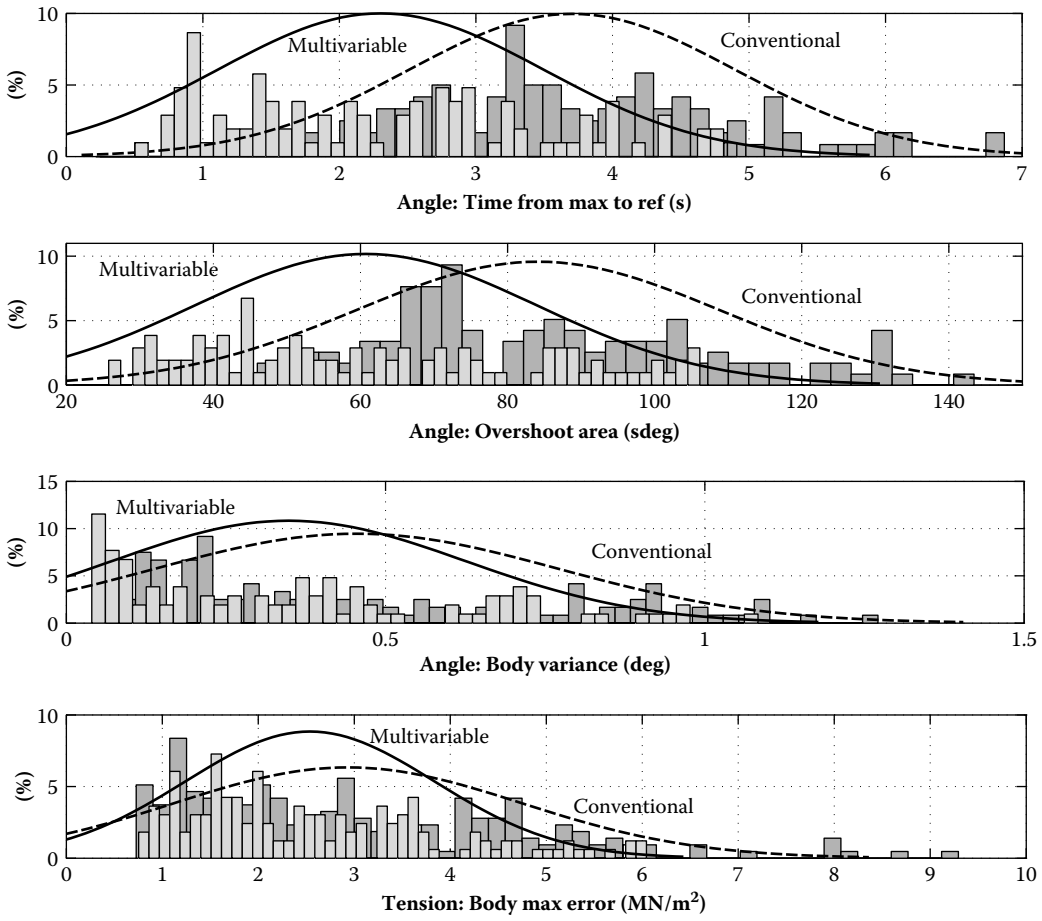


FIGURE 18.7 Statistical performance analysis.

Analysis of the multivariable controller performance compared to the existing loop height PID, AGC and mass flow compensation shows that most improvements have been made at the coil head end. Looper angle overshoot and undershoot is less, and the time to reach the reference angle is less with the multivariable controller. There is a smaller improvement in the body of the coil with a smaller angle variance and a smaller maximum error. As expected, the gauge performance for the multivariable and existing AGC was similar although one objective of the multivariable controller was to be able to use more aggressive gauge control without compromising the mass flow stability. Though the performance improvement appears small, in the very high throughput hot mill process, these small improvements can yield significant cost benefits. It was seen in the frequency analysis of the controller and the mill trials that there is a trade-off between improving the mass flow control and the bandwidth of gauge control. It is possible to go to the extreme where the looper angle is only controlled using the capsule. A practical application of this would be to weight the controller only for mass flow control if there is a known event, such as a material phase change, which may affect the mill stability. The trade-off between mass flow and gauge control may be different for each stand/looper in the mill.

An important feature of the design is that only conventional hot strip mill instruments and actuators are required. Also, the existing models are used to calculate the sensitivities for the design model and controller gain calculations are relatively simple. The multivariable controller is therefore very practical and suited to retrofitting to existing mills.

REFERENCES

Astrom, K. J. and Wittenmark, B. 1997. *Computer Controlled Systems.* Upper Saddle River, NJ: Prentice Hall International.

Duysters, S., Govers, J. A. J., and van der Weiden, A. J. J. 1994. Process interactions in a hot strip mill: Possibilities for multivariable control? *3rd IEEE Conference on Control Applications*, pp. 1545–1550, Glasgow, U.K.

Hearns, G. and Grimble, M. J. 2000a. Inferential control for rolling mills. *IEE Proceedings—Control Theory and Applications* 147(6): 673–679.

Hearns, G. and Grimble, M. J. 2000b. Robust multivariable control for hot strip mills. *ISIJ International* 40(10): 995–1002.

Hesketh, T., Jiang, Y. A., Clements, D. J., Butler, D. H., and van der Laan, R. 1998. Controller design for hot strip finishing mills. *IEEE Transactions on Control Systems Technology* 6(2): 208–219.

Imanari, H., Morimatsu, Y., Sekiguchi, K., Ezure, H., Matuoka, R., Tokuda, A., and Otobe, H. 1997. Looper H-infinity control for hot-strip mills. *IEEE Transactions on Industry Applications* 33(3): 2133–2139.

Kotera, Y. and Watanabe, F. 1981. Multivariable control of hot strip mill looper. *8th IFAC World Congress*, Vol. 18, pp. 1–6, Kyoto, Japan.

Miura, H., Nakagawa, S., Fukushima, S., and Armasaki, J. 1993. Gauge and tension control system for hot strip finishing mill. *19th IEEE Industrial Electronics, Control and Instrumentation Conference*, Vol. 1, pp. 463–468, Maui, Hawaii.

Seki, Y., Sekiguchi, K., Anbe, Y., Fukushima, K., Tsuji, Y., and Ueno, S. 1991. Optimal multivariable looper control for hot strip finishing mill. *IEEE Transactions on Industry Applications* 27(1): 124–130.

19 Finishing Mill Predictive Temperature Control

Gerald Hearns, Chris Fryer, and Peter Reeve

CONTENTS

19.1 Introduction 219
19.2 Setup Calculations 219
19.3 Dynamic Control 220
19.4 Finishing Mill Interactions 220
19.5 Finishing Mill Predictive Temperature Control 221
19.5.1 Finishing Mill Temperature Modeling 222
19.5.2 Temperature State Estimation 223
19.5.3 The Control Algorithm 224
19.5.4 Application of the Control Algorithm 225
19.5.5 Velocity Feedforward from the Setup 227
19.6 Temperature Control Results 227
References 228

19.1 INTRODUCTION

The key dimensional and mechanical properties of flat-rolled products are developed during rolling in the finishing train of the hot strip mill (HSM). The finishing mill (FM) is required to produce material within ever more restrictive thickness, temperature, flatness, width, and surface-finish tolerances. Operations have to take place within the context of scheduling, pacing, and motion control systems that ensure maximal productivity and efficiency.

The FM consists of a sequence of multivariable processes. Segments of material are transported through the process sequence at velocities that vary through the coil. The control task includes not just the problem of coping with velocity-dependent transport lags for each segment, but also dealing with the fact that the segment is transformed with time and by the thermomechanical operations carried out upon it. The relationships between variables are highly nonlinear.

Although the final quality parameters are usually measured online with instruments of reasonable accuracy and response, these instruments are expensive and cost considerations, as well as practical difficulties, limit the instrumentation available for intermediate measurement. Hence, there is an emphasis in an HSM control on predictive modeling and feedforward control. Lack of instrumentation in the harsh environment makes model-based control a necessity. Predictive control has been applied in many areas of HSMs: reheating furnaces (van Ditzhuijzen et al. 2002), width control (Umeda et al. 1995), and looper control (Choi et al. 2004).

This chapter addresses the problems associated with the control of temperature at the exit of the FM of an HSM. The mill setup calculations and use of intermediate variables for dynamic control are reviewed. The basic FM interactions are described, along with a more detailed description of the FM temperature modeling. The model-based predicted controller (MBPC) for temperature, along with the required state estimator are developed. Finally, some results from the application of this controller on a seven-stand mill are presented.

19.2 SETUP CALCULATIONS

We distinguish between head-end control and in-piece control noting the emerging need for a hybrid dealing with continuous rolling. For the head-end setup, a group of predictive process models is used to generate optimized set points for threading each part of the line. At any point, a best estimate of piece state is used as the starting point for the calculation of downstream references. State update involves the following:

- Direct measurement
- Directly modeled responses to plant controls or events
- Inference using measurements of intermediate parameters

Note that a key element of the last technique is the identification of downstream process model parameters, as well

as piece parameters. It is important to make as much use as possible of the limited instrumentation because material behavior in one stand/pass is often closely correlated with its downstream behavior. For this reason, it is customary to merge most state updates into a common identifier; see, for example MacAlister (1989), which includes a description of an extended Kalman filter being applied to a roughing train, and Randall (1996), which deals with a finishing train. Superimposed on the in-piece identifier is the update of models through piece-to-piece learning.

19.3 DYNAMIC CONTROL

For in-piece dynamic control, the principles are similar to those for head ends, but two additional factors apply, as follows:

- Information from preceding segments of material can be used to improve control of later segments.
- Actuation is subject to dynamic nonlinearities—most notably rate limits.

The basic building blocks are feedback control loops acting to control not only the final targets, but also a number of intermediate variables distributed along the plant. The controllers have to rely heavily on modeling—sometimes, as in the case of direct feedback, by using the latest adapted models to supply the expected sensitivity of control variable to actuator movement; sometimes, in the case of intermediate variables, to supply a pseudo-measurement based on models using auxiliary measurements.

Figure 19.1 shows a generalized arrangement with an intermediate variable (Control variable n) and a final variable (Control variable $n + 1$). Added to the basic feedback loops are the following:

- Feedforward based on information from the intermediate control loop. Because of the transport delays, this requires accurate delay lines. The data fed forward usually comprises a state estimate but may also include direct actuator trims. The output trims to the plant are selected from suitable points in the delay line to anticipate the expected actuator delays.
- Feedback based on final measurements (and often state estimates) acting on intermediate variable control. The feedback may be in the form of a reference trim or an adjustment to the models used by the intermediate variable controller.

Such an approach has been used for many years in the control of FM exit gauge (see, for example, Hicks 1990) and run-out temperatures (see, for example, Lawrence 1996).

19.4 FINISHING MILL INTERACTIONS

Modeling of the complex operations in the FM is an important element in designing an effective feedforward/feedback dynamic controller. Figure 19.2 shows the interactions of key variables for one stand and interstand gap at constant line speed. Measurements are usually limited to screw/hydraulic position, roll force, bending cylinder pressures, motor torque, motor speed, tension (via looper), and speed mismatch (via looper).

Physical models can be fitted to data collected over many pieces and can be refined to achieve a good thread at the required tolerances. In addition, some of the secondary effects required to enable high tolerances from head to tail can be derived from within coil data. Because of the time-varying nature of the process, these calculations need continual updating—hence, the use of online identification techniques.

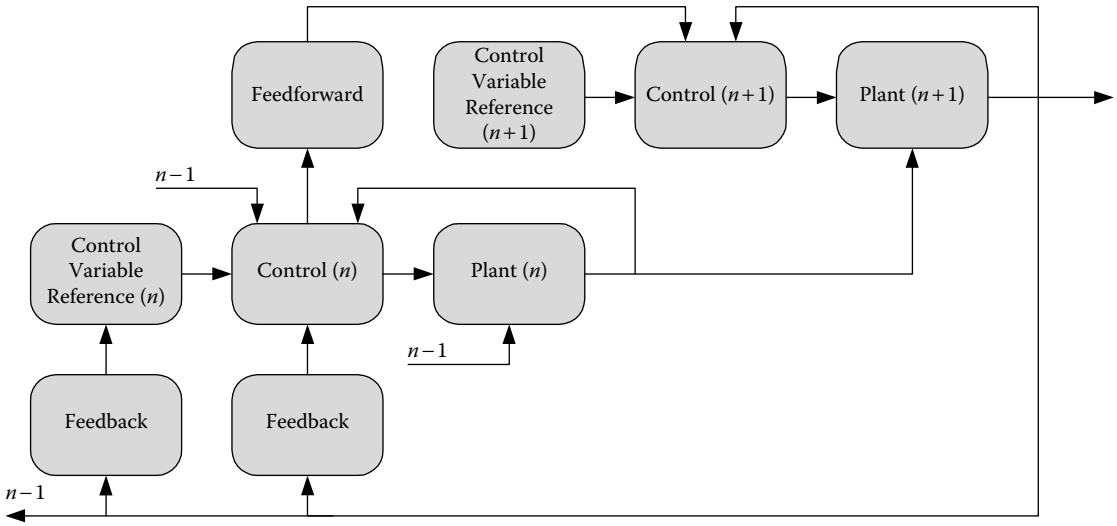


FIGURE 19.1 Control using intermediate variables.

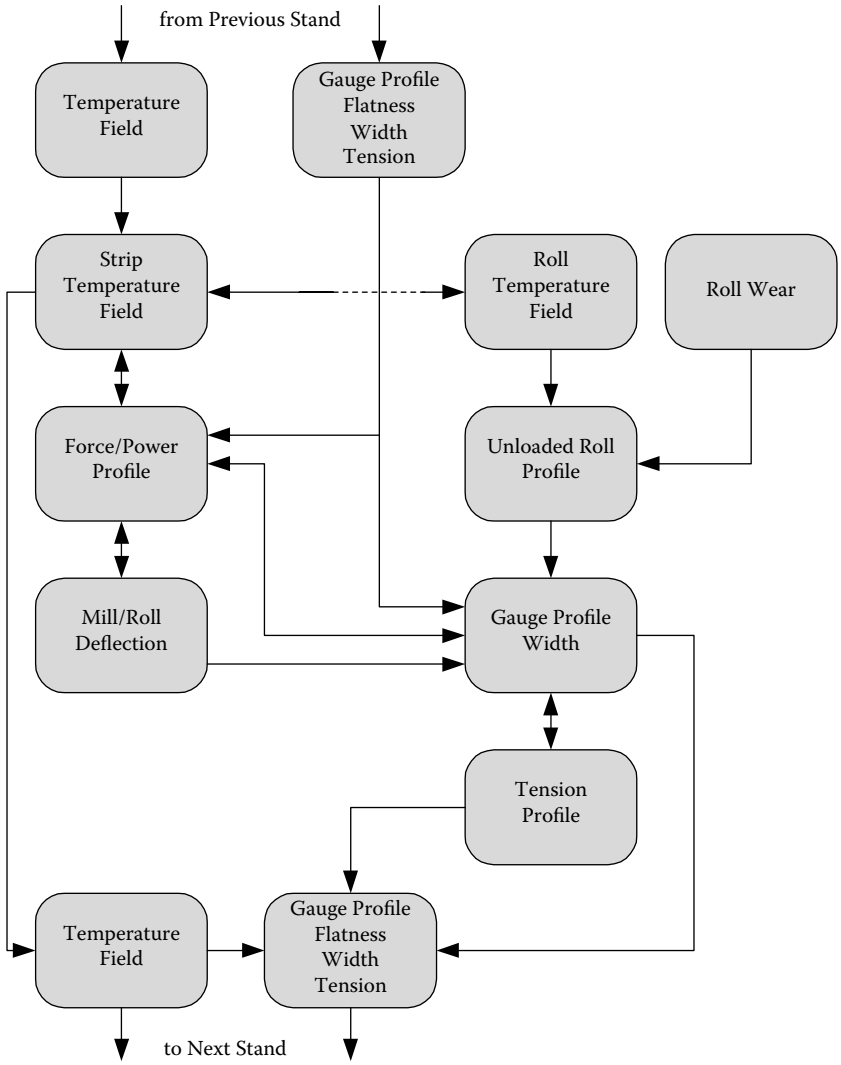


FIGURE 19.2 Finishing mill interactions for one stand/interstand.

The prime cause of in-piece variations in finishing temperature is entry temperature. Disturbances arise from furnace irregularities (notably skid chills and hot ends), head-to-tail trends (run-down due to the tail spending longer than the nose on the delay tables; run-up due to reversal in the coil box), speed variations through descaler sprays, and other end effects (especially severe where there is a coil box). Temperature is a key model in hot rolling because it is always changing and it affects all mill physical processes. The temperature model across the FM is physically based, taking into account internal diffusion, radiation, convection, conduction to rolls, conduction to water, scale formation, crystalline state, and deformation energy.

19.5 FINISHING MILL PREDICTIVE TEMPERATURE CONTROL

Consider a seven-stand finishing train fitted with cooling sprays between the early stands. Temperature can be controlled using the mill speed and sprays. The prime control parameter is the mill exit temperature, which is an important input to the run-out table spray control and determines the phase and grain structure of the coiled strip.

The temperature between the stands is also important, particularly upstream where hot strip surface can result in excessive scale formation. Steep temperature gradients along the strip length should be avoided, as the resulting hardness change may prove problematic for gauge control. Finally, there are obvious throughput advantages to running the mill at the highest possible speed. Fortunately, these control requirements are complementary. Accelerating the mill for throughput requires the spray flows to increase if the finishing temperature is to be held constant. Increasing the spray flow between the early stands chills the strip surface and suppresses scale formation.

The time taken for the strip to travel from the first interstand spray to the mill exit pyrometer can be as long as 30 s, depending on the product being rolled. Intermediate measurements of strip temperature are often not available due to the difficulty of maintaining a clear line of sight in the presence

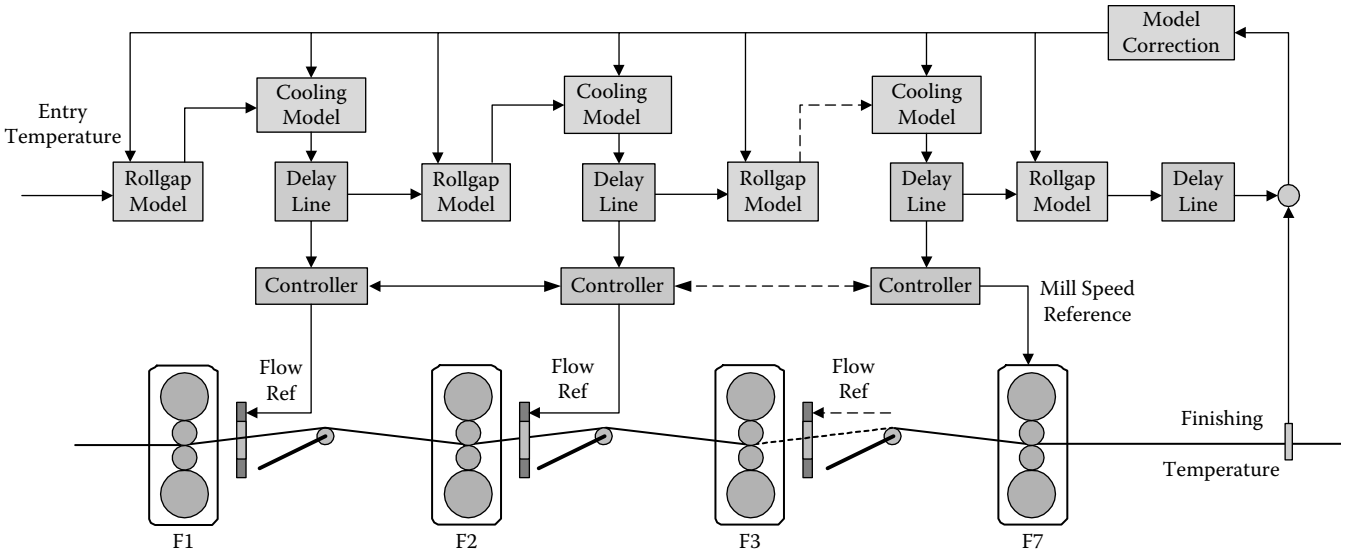


FIGURE 19.3 Model-based predictive control structure.

of water and steam. Coping with transport delays is therefore an important part of the control function. This is done by modeling the evolution of strip temperature through the mill, so that estimated temperatures are available at each actuator. The models are dynamically calibrated using the mill exit pyrometer and intermediate pyrometers, if available.

The controller, having information about strip temperature all the way through the finishing train, optimizes the use of the available actuators to achieve the multivariable control objectives within the operating constraints of the mill. The overall model-based predictive control structure is shown in Figure 19.3.

19.5.1 Finishing Mill Temperature Modeling

Heat is lost to the environment from the strip surface due to:

$$\text{Radiation} \quad q = \lambda \cdot \sigma \cdot (T_{SS}^4 - T_\infty^4) \tag{19.1}$$

$$\text{Convection with the air} \quad q = h_c \cdot (T_{SS} - T_\infty) \tag{19.2}$$

$$\text{Conduction to the water sprays} \quad q = h_{wt} \cdot (T_{SS} - T_{wt}) \tag{19.3}$$

$$\text{Conduction to the work rolls} \quad q = h_r \cdot (T_{SS} - T_r) \tag{19.4}$$

where

q is the rate of heat loss (W/m^2)
λ is the strip surface emissivity
σ is the Stefan–Boltzmann constant
h_c, h_{wt}, and h_r are the heat-transfer coefficients between the strip and the air, sprays, and work rolls, respectively (W/m^{2}K)
T_∞, T_{SS}, T_{wt}, and T_r are the ambient, strip surface, water, and work roll temperatures, respectively (K)

The strip is heated by the energy of deformation in the roll bite. Heat flows throughout the strip due to conduction. For the thin, wide strip in the FM, conduction in the length and width directions can be neglected, and so a one-dimensional implementation of Fourier's equation through the strip thickness is adequate:

$$k \cdot \frac{\partial^2 T}{\partial x^2} = c \cdot \rho \cdot \frac{\partial T}{\partial t} \tag{19.5}$$

where

k is the strip thermal conductivity (W/mK)
ρ is the strip density (kg/m^3)
c is the strip specific heat capacity (J/kgK)
x is the distance through the strip thickness
t is time

The strip is divided into slices through its thickness, and a finite-difference method is used to solve the simultaneous equations. Typical results are shown in Figure 19.4.

As the strip travels through the descale sprays before the first finishing stand, the top and bottom surfaces are chilled rapidly. Heat then flows back from the strip center, and the surface temperatures recover. When the strip enters the first stand, the top and bottom surfaces are chilled by contact with the work rolls. The core temperature increases because of the deformation energy. Again, heat diffuses back from the center. In this example, the interstand sprays affecting the top and bottom surfaces are not the same distance from the upstream stand, hence the different cooling pattern top and bottom. This process of cooling and recovery continues through all seven stands to the exit of the mill. Temperature evolution is very nonlinear. The effects of mill speed and spray flows, in particular, are highly interactive.

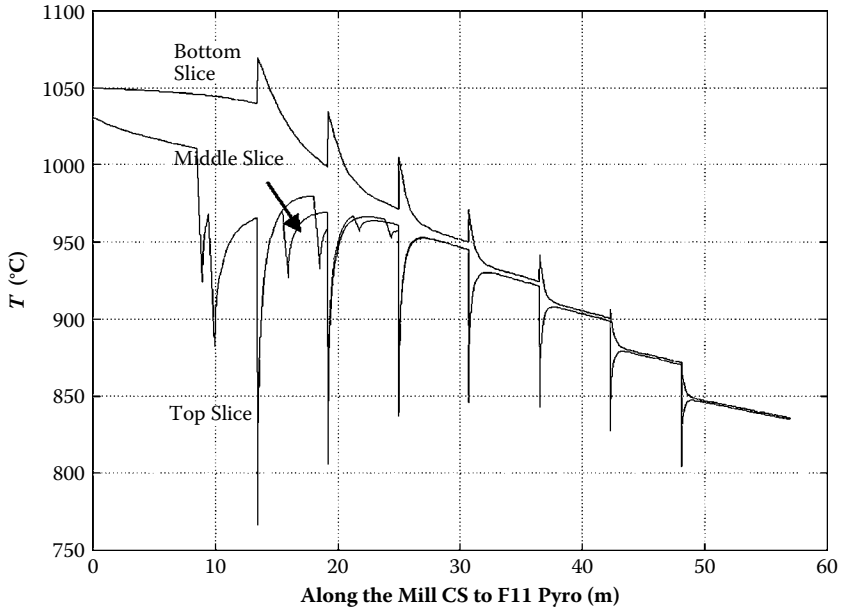


FIGURE 19.4 Evolution of strip temperature slices along the mill.

19.5.2 Temperature State Estimation

Most mills have a pyrometer located at the crop shear, before the descale sprays, but often, its measurements are of poor quality because of steam and scale. In the absence of good measurements, the temperature of the strip entering the FM can be estimated from the variation in yield stress obtained from the first stand force and gap. The slice temperature models are then used to evolve the temperature through the mill using measured plant speeds, powers, forces, gaps, and spray flow rates. A table of temperatures at many points along the mill length is maintained in this way.

The coordinates (see Figure 19.5) at which temperatures are predicted are chosen based on the following criteria:

- There are points immediately before and immediately after each stand.
- There are points at each spray.
- There are points at each pyrometer.
- The grid of coordinates is sufficiently dense for the required control bandwidth.

The models are continuously calibrated by comparing the estimates at each available pyrometer with the pyrometer measurements as the strip is rolled. Model correction is performed with a high gain at the start of each coil to quickly remove any steady-state model error, then more slowly in the body to reduce susceptibility to measurement noise.

The model used in the predictive controller comprises two important components: the strip temperature evolution model and the transport delay model. The strip temperature evolution models are those used in the FM setup calculation:

$$T(i+1) = F[T(i), \phi(i), v(i), \text{Pwr}(i), \text{Troll}(i), \text{Twater}(i)] \qquad (19.6)$$

where

$T(i)$ is the strip temperature at stand i
$\phi(i)$ is the spray flow at spray i
$v(i)$ is the speed profile the strip element experiences moving from stand i to stand $i + 1$
Pwr(i) is the deformation power on stand i
Troll(i) is the roll temperature on stand i
Twater(i) is the cooling water temperature

For setup there is no need to model the transport delays explicitly. However, for dynamic control sufficiently accurate

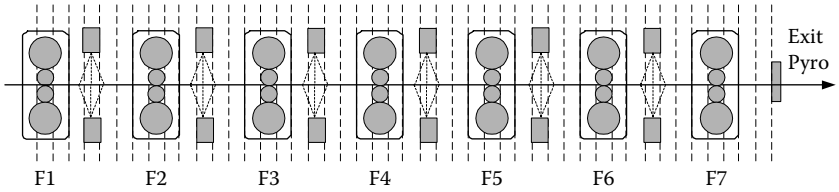


FIGURE 19.5 Estimator coordinate system.

modeling of the material transport through the process is essential. There are two methods of doing this: one using a coordinate system attached to the material and moving through the process with it, and one using a fixed coordinate system through which the material moves. In this application of MBPC, both are used. The estimator uses the fixed and the controller uses the moving coordinate system.

The MBPC system operates at regular time intervals through the rolling of a coil and has two components:

- The in-coil temperature estimator—using the latest measurements from the mill, the temperature model, and tracking the strip through the FM.
- An in-coil model-based predictive control calculation to compute individual adjustments to the mill speed and interstand spray flows from the calibrated estimates of temperature at each stand.

19.5.3 The Control Algorithm

On each timed entry of the MBPC, the control actions to be applied to the mill in the next time interval are calculated from the latest estimates of the strip temperature.

To reduce the complication in the control calculations, only a subset of the temperature estimates, those at the exit of each stand (the control station), is used to drive the controller. Given predictions of the mill speed profile and stand and spray actuator settings, the future evolution of the temperature through the mill of each element of strip at the control stations can be predicted. (In the controller, the coordinate system is attached to the strip and moving through the mill with it.) The control problem is to calculate the future spray flow setting and the mill speed in order to satisfy the control requirements of good exit temperature, secondary scale suppression, and throughput.

Using the model Equation 19.6, a set of equations relating the spray flows and mill speed to the predicted temperatures downstream of the stand exit estimates can be set up. For any control station j, the future evolution of the temperature of the strip element through the mill is

$$\underline{T}(j) = F[\hat{T}(j), \underline{\Phi}(j), \underline{Vp}(j), \underline{\mathrm{Pwr}}(j), \underline{\mathrm{Troll}}(j), \underline{\mathrm{Twater}}(j)] \quad (19.7)$$

where

$\underline{T}$ is the vector of downstream temperatures $[T(k|j); k = j + 1,...n]$ predicted from the current estimate $T(j)$

$\underline{\Phi}$ is the vector of spray flows $[\Phi(k|j); k = j, j + 1,...n]$ that the element of strip at control station j will experience as it passes under spray k

$\underline{Vp}(j)$ is the mill speed profile $[Vp(k); k = j, j + 1,...n - 1]$, where $Vp(k)$ is the mill speed that applies when element $k + 1$ has passed the exit pyrometer, that is, left the system, until the element of strip at control station k leaves the system

The temperatures to be controlled are the entry temperatures to each downstream stand, $T(j + 1|j)$, $T(j + 2|j)$, etc. and at the mill exit, $T(n|j)$. The start temperature for these predictions is $T(j)$ stand j exit estimate.

In principle, the equations for all control stations can be used to recognize one optimization problem that can be solved using a suitable method to find the optimal controls. The resulting calculations can become very burdensome, particularly as spray flow and mill speed limits become active.

Using the structure of the FM, a much simpler, though suboptimal, solution is possible. The controller works backward from the mill exit. It calculates a mill speed trim and a change in the flow of the last set of sprays so that the section of strip about to pass under the last set of sprays (control station $n - 1$) achieves the control objectives. Next, the section of strip about to pass under the penultimate set of sprays (control station $n - 2$) is evolved through the models using the control trims just found, and further trims to speed and sprays calculated. This process is repeated up to the first control station.

$$\Delta\underline{T}(j) = \underline{T}(j) - \underline{Tp}(j) = \frac{\partial \underline{Tp}(j)}{\partial Vp(j)}\Delta Vp(j) + \sum_{k=j}^{n-1} \frac{\partial \underline{Tp}(j)}{\partial \phi(j)}\Delta\phi(k|j) \quad (19.8)$$

At each stage, knowledge that no deviations to speed or sprays upstream of the current control station can affect the strip at that station is used to simplify the model.

When the algorithm reaches control station j, the "optimum" spray flows $\Phi^*(k|j+1)$ and speeds $Vp^*(k)$, $k = j + 1,...n$ for the downstream control stations have been calculated. Using these, together with the current setting of spray flow $\Phi_{\mathrm{mill}}(j)$ and setting the value of $Vp(j) = Vp(j + 1)$, equations (see Equation 19.7) are used to calculate *a priori* prediction of all the downstream temperatures $Tp(j)$ and their sensitivities to the spray flows $\Phi(k|j)$ and speed $Vp(j)$. From these sensitivities, a linear model can be constructed for use by the controller, which has the following cost function:

$$\begin{aligned} J(j) = {} & [\Delta\underline{T}\mathrm{aim}(j) - \Delta\underline{T}(j))' \cdot Q_1 \cdot (\Delta\underline{T}\mathrm{aim}(j) \\ & - \Delta\underline{T}(j)) + 2 \cdot R_{1'} \cdot \Delta\underline{T}(j) + (\Delta\underline{\Phi}\mathrm{aim}(j) \\ & - \Delta\underline{\Phi}(j))' \cdot Q_2 \cdot (\Delta\underline{\Phi}\mathrm{aim}(j) - \Delta\underline{\Phi}(j)] \\ & + 2 \cdot R_{2'} \cdot \Delta\underline{\Phi}(j) + q_3 \cdot (\Delta Vp_{\mathrm{aim}}(j) \\ & - \Delta Vp(j))^2 + 2 \cdot r_3 \cdot \Delta Vp(j) \end{aligned} \quad (19.9)$$

subject to the equality constraint representing the linear temperature model:

$$\Delta\underline{T}(j) = K_1 \cdot \Delta\underline{\Phi}(j) + K_2 \cdot \Delta V(j) \quad (19.10)$$

which has the structure,

$$\begin{bmatrix} \Delta T(1) \\ \Delta T(2) \\ \vdots \\ \\ \\ \Delta T(6) \\ \Delta T(7) \end{bmatrix} = \begin{bmatrix} \frac{\partial T(1)}{\partial \phi(1)} & 0 & 0 & \cdots & 0 \\ \frac{\partial T(2)}{\partial \phi(1)} & \frac{\partial T(2)}{\partial \phi(2)} & 0 & & 0 \\ & \vdots & & & \vdots \\ \frac{\partial T(6)}{\partial \phi(1)} & & & & \frac{\partial T(6)}{\partial \phi(6)} \\ \frac{\partial T(7)}{\partial \phi(1)} & \frac{\partial T(7)}{\partial \phi(2)} & & \cdots & \frac{\partial T(7)}{\partial \phi(6)} \end{bmatrix} \times \begin{bmatrix} \Delta\phi(1) \\ \Delta\phi(2) \\ \vdots \\ \\ \\ \Delta\phi(6) \end{bmatrix} + \begin{bmatrix} \frac{\partial T(1)}{\partial V} \\ \frac{\partial T(2)}{\partial V} \\ \vdots \\ \\ \frac{\partial T(7)}{\partial V} \end{bmatrix} \cdot \Delta V \tag{19.11}$$

The aims of the control are to minimize deviations of the control temperatures from their setup values and to reduce scale risk by keeping the interstand temperatures low while increasing line speed (throughput). This should be achieved without excessive control actuator changes. These aims can be achieved by finding the spray flows and mill speed that minimizes the cost function.

Q_1, Q_2, and q_3 weight the deviation from target in a least-squares sense; R_1, R_2, and r_3 weight positive deviations. K_1 and K_2 represent the sensitivities of the control temperatures to changes in flow and speed. K_1 and K_2 are equivalent to $\partial Tp/\partial\Phi$ and $\partial Tp/\partial V$.

Normally, it is important that the temperature of the strip exiting from the mill be kept close to the aim value. Intermediate temperatures can be allowed more variability. This freedom can be exploited by setting the costs R_1 and R_2 to force down the intermediate temperatures early in the mill so reducing scale formation while still achieving good mill exit temperature control. Further, the linear cost on speed, r_3, can be used to increase line speed. The process dynamics are favorable to achieving this aim. As mill speed increases, the temperature drop across the mill reduces, and so to maintain the desired mill exit temperature, the interstand spray flows must increase. More spray flow depresses the strip surface temperature so suppressing surface oxide scale formation.

Minimizing the cost function, assuming no actuator or process limits are active, yields a linear controller,

$$\begin{aligned} \Delta\underline{\Phi}^*(j) = G_1 \cdot \Delta\underline{\Phi\text{aim}}(j) + G_2 \cdot \Delta\underline{T\text{aim}}(j) \\ + G_3 \cdot \Delta V^*(j) + G_4 \end{aligned} \tag{19.12}$$

and

$$\begin{aligned} \Delta Vp^*(j) = G_5 \cdot \Delta Vp_{\text{aim}}(j) + G_6 \cdot \Delta\underline{T\text{aim}}(j) \\ + G_7 \cdot \Delta\underline{\Phi\text{aim}(j)} + G_8 \end{aligned} \tag{19.13}$$

In practical application, the controller will encounter absolute and rate limits to the spray flows and mill speed from time to time. These limits can be handled directly using quadratic programming in place of linear/quadratic optimization. Also, the iterative structure used to calculate the controls lends itself to simpler heuristic methods of dealing with limits.

When the iteration through the control stations is complete, the spray and speed setting for the next time interval are

$$\begin{aligned} \phi_{\text{mill}}(j) &= \phi^*(j \mid j) \\ V_{\text{mill}} &= Vp^*(n-1) \end{aligned} \tag{19.14}$$

19.5.4 Application of the Control Algorithm

Referring to Figure 19.6, consider first the final interstand spray at sample time i. We know the estimated temperature

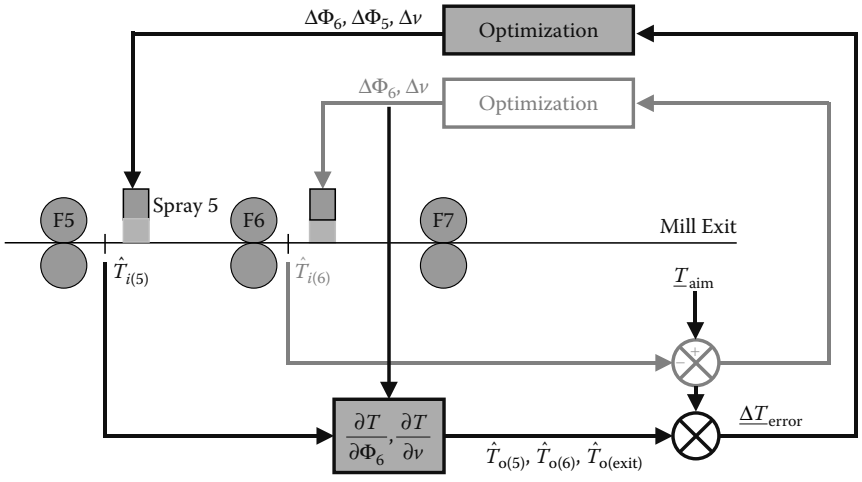


FIGURE 19.6 Control algorithm for stands 5 and 6.

of the element of strip just before the final spray 6 (the control point) $T_{i(6)}$. The control calculation computes the change in spray flow and strip speed required to achieve the optimal tradeoff between aim and measured exit temperature, maximizing throughput (speed) for the element of strip at the control point.

The key steps are

1. Predict the FM exit temperature for the strip at the control point using the strip temperature evolution models with the current values of mill speed and spray 6 flow as inputs.
2. Calculate the sensitivities of the exit temperature to changes in spray flow and mill speed.
3. Using the error between the aim temperature and the predicted exit temperature together with the sensitivities, calculate the spray and speed changes that minimize the trade-off cost function between temperature error, flow change, and speed change.
4. The resulting values of spray 6 flow and mill speed are output to the mill as the new set points for the next sample period.

We now move up the mill and consider the penultimate interstand spray 5 at sample time *i*. Again, we know the estimated temperature of the element of strip just before spray 5. The control calculation now computes the changes in sprays flow 5 and 6 and the part of the strip speed profile in the future that is free to change (i.e., after the strip at the control point before spray 6 has passed the exit pyro). Again, the key steps are

1. Predict the FM exit temperature for the strip at the control point using the current value of the spray 5 flow and the future mill speed profile predicted so far (for this spray, the current mill speed plus the speed change calculated for element of strip before spray 6) and the expected spray 6 flow (for this spray, the current flow for spray 6 plus the change calculated for the element of strip before spray 6) as inputs.
2. Calculate the sensitivities of the exit temperature to changes in spray flows and mill speed.
3. Using the error between the aim temperature and the predicted exit temperature together with the sensitivities, calculate optimum speed change and

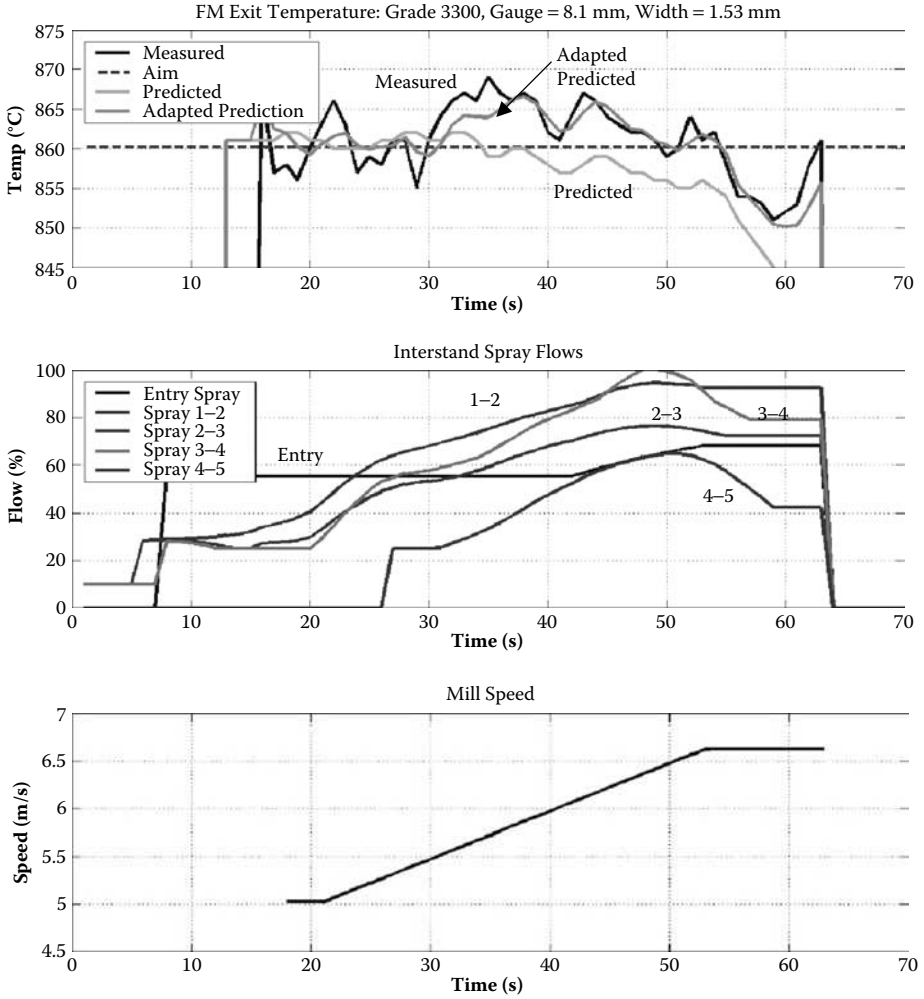


FIGURE 19.7 Finishing mill exit temperature, interstand spray flows, mill speed for 8.1-mm gauge.

spray flows. The resulting values of spray 5 flow are output to the mill as the new set point for the next sample period. The new values of spray 6 flow and the change in mill speed profile are not output to the mill. However, they are included in the predictions for the next upstream spray 4. We are building future speed and spray profile, in other words, a profile of anticipated speed changes to be used in the upstream predictions.

19.5.5 Velocity Feedforward from the Setup

For each coil, the thread mill speed and head-end spray flows are calculated to achieve finishing temperature. An acceleration profile is also calculated that will maintain temperature through to tail out. This acceleration profile is used to introduce a further feedforward element to the controller via the $\Delta\Phi_{aim}$ and Δv_{aim} terms of the cost function. This makes the control less reactive, and results in much smoother and predictable acceleration rates, which is beneficial to run-out table spray control.

19.6 TEMPERATURE CONTROL RESULTS

The results shown in Figure 19.7 are from a seven-stand coil-box mill with interstand sprays after stands 1 through 4, and before stand 1. Mill speed has increased throughout the bar, even though thermal run down for a coil box mill is not as pronounced. It can be seen that as the mill speed increases, the interstand spray flows have to increase to maintain aim temperature. All the control objectives are met: temperature is held within 10°C of reference from nose to tail, the mill accelerates smoothly for throughput, and the spray flows increase for scale suppression. The predictive nature of the controller can be seen toward the tail, where the spray flows begin to decrease before the exit pyrometer measures cold strip. Figure 19.8 shows results from the same mill for a coil with exit gauge of 2.11 mm. The sprays have a minimum flow

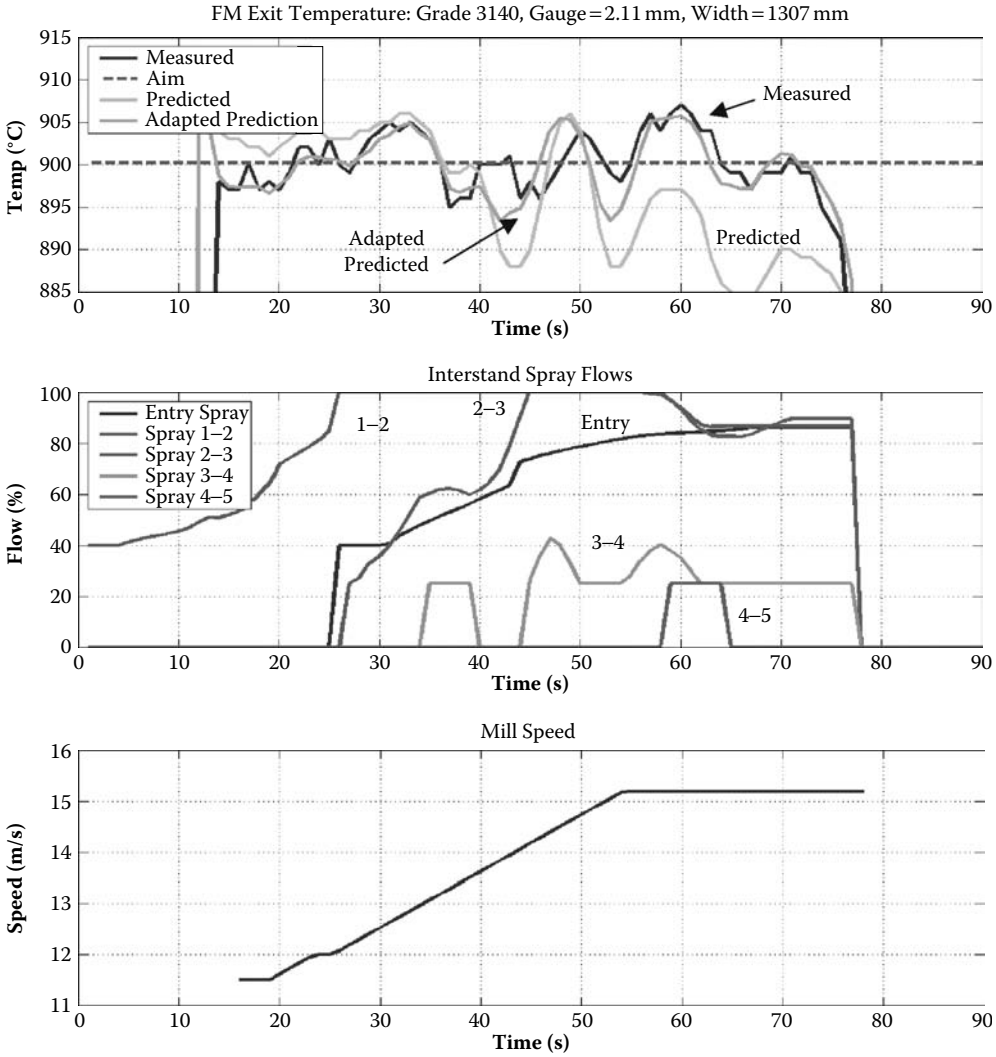


FIGURE 19.8 Finishing mill exit temperature, interstand spray flows, mill speed for 2.11-mm gauge.

achieved through a control constraint. The flows are reduced toward the end of the bar before the temperature is seen to go below aim at the mill exit.

REFERENCES

Choi, I. S., Rossiter, J. A., and Fleming, P. J. 2004. An application of the model based predictive control in a hot rolling mill. *IFAC Symposium on Automation in Mining, Mineral and Metal Processing*, September 8–10, Nancy, France.

Hicks, C. J. 1990. Aspect of gauge control for hot and cold mills. *Institute of Metals 5th International Conference*, London, U.K.

Lawrence, W. J. 1996. Online modelling and control of strip cooling. *Ironmaking and Steelmaking*, 23(1): 74–78.

MacAlister, A. F. 1989. Modelling and adaptive techniques for rolling mill automation. *Iron and Steel Engineer*, 12(12).

Randall, A. 1996. Disturbance attenuation in a hot strip rolling mill via feedforward adaptive control. *13th IFAC World Congress*, June 30–July 5, San Francisco, CA.

Umeda, H., Kikuchi, T., Yokota, S., Kanou, H., Takekoshi, A., and Motoyashiki, Y. 1995. Application of predictive control theory in hot strip mill. In *Proceedings of the 1995 IEEE International Conference on Industrial Electronics*, *Control, and Instrumentation*, pp. 786–791, Orlando, FL.

van Ditzhuijzen, G., Staalman, D., and Koorn, A. 2002. Identification and model predictive control of a slab reheating furnace. In *Proceedings of the 2002 International Conference on Control Applications*, Vol. 1, pp. 361–366, Glasgow, U.K.

20 Digital Visual Inspection of Coils

Mohammad B. Assar, Larry Romanauski, Matt Kremer, Margaret Krolikowski, Joe Franklin, Mike L. Elliott, and Randy A. Stankie

CONTENTS

20.1 Introduction 229
20.2 Objectives 230
20.3 Technical Description 230
20.4 Solution 231
20.5 Applications and Results 233
20.5.1 Temper Mill System 233
20.5.2 Pickle Line System 234
20.5.3 Weld-Tracking Analysis and Verification 236
20.5.4 Tandem Mill System 236
20.6 Conclusions 238
References 238

20.1 INTRODUCTION

Evaluation of quality problems within mills has always been a difficult undertaking. Quality engineers rely heavily on inspectors to locate defects and report them accurately. When defects are reported, the product is often diverted to reinspect/rewind lines where quality personnel verify the defects and make disposition on the coil. The process of rewinding and checking is time-consuming, causing delays and adding significant costs. Quality problems that are reported back by customers are even more difficult and often impossible to research and resolve.

Similarly, troubleshooting mill equipment problems can also be extremely difficult (Edwards and Boulton 2001). Engineers frequently spend large amounts of time trying to find out what actually caused a mill wreck or an equipment failure. Since engineers are not watching each operating unit 24 hours a day, they rely on various tools to help troubleshoot problems. These tools include operator descriptions of what has occurred, strip chart recorders, high-speed memory review data, alarm logs, and computer-generated reports.

Video has also become an important tool used to help troubleshoot both strip quality and mill equipment problems. Originally, cameras were installed on mills and video recorded using VCRs. The stored video provided engineers with a method to see what the strip quality actually looked like or to see what really happened on the mill. The problem with the VCR/tape method was that it did not provide the speed or flexibility that was required to quickly resolve mill production and quality problems. Searching a VHS tape, fast forwarding/rewinding, or trying to find the desired coil was extremely difficult and time-consuming. Many times, the VCR clock had wandered, and attempting to synchronize VCR time with the coil-produced time was challenging or impossible. Since the data were stored on tapes, only one person could perform analysis at a time and a dedicated television and VCR were required for the review. A number of inconvenient maintenance issues also arose with tape storage. The life of VCRs and VHS tapes was limited, especially in a mill environment. VCR heads got dirty, and deteriorated VHS tapes resulted in extremely poor image quality. Management of the tapes (changing, labeling, storing) was a nightmare, often requiring entire rooms to archive the video for long periods of time. Missing tapes, nonloaded VCRs, and powered-off VCRs were just a few more of the problems that existed.

The issues associated with the VCR/tape systems frequently caused them to be more of a problem than a solution. There was nothing more frustrating than spending hours searching through a tape for a specific defect within a coil, only to find that the image quality was too poor to make the images useable.

The shortcomings of VCR/tape systems mentioned above inspired the in-house development of the state-of-the-art video capture system (VCS) using existing cameras and adding some new ones. This was a contribution by Benchmark Automation, which built the system, and the quality department's engineers, who came up with the needs that the system must address. The system will be explained in detail in the next section.

The newer alternative for surface inspection, automated surface inspection systems, only recently came to market. These systems digitally map the surface of the coil, and by

TABLE 20.1
Comparison of Different Techniques with VCS

System Features	VCS	Automated Surface Inspection Systems	VHS Tape
Average cost	$25,000	$400,000	$50,000
Average time to retrieve data	30 s	30 s	10 min
Data storage type	Digital	Digital	Tape
Portability	Yes	No	Yes
Selectable retrievable coil image	Yes	Yes	No
Retrievable individual defect image	No	Yes	No
Automated defect detection	No	Yes	No
Defect classification	No	Yes	No
Image quality	Good	Good	Fair/poor
Use for process monitoring	Yes	No	No
Use for troubleshooting	Yes	No	No

Source: M. B. Assar, C. D. Romanauski, M. Kremer, et al. 2007. *Iron & Steel Technology*, January 2007, pp. 74–84. With permission.

using image processing schemes, identify surface defects. Although these systems are strong tools for defect classification, they need higher capital, training, and can only be used for surface quality, and not process monitoring and maintenance. The following table compares the current available techniques with VCS.

20.2 OBJECTIVES

The objective of the project was to upgrade the existing analog VCR/tape video system to a digital video storage system that would provide the unique functionality required in a finishing mill. Two key goals had to be met. One was to ensure that image quality would be excellent and consistent, without degradation. The other was to find the exact location of a defect or questioned area in a coil within seconds, not hours.

In addition to the two key goals, the following features were desired in a new system:

- Flexibility to retrieve images by entering coil number or timeframe
- Allow for images to be stored based on either time, strip footage, or mill event
- Provide variable storage rate capabilities for different cameras
- Provide extended storage of critical images for several years
- Provide open interface to mill computers/programable logic controllers (PLCs) to incorporate critical mill data into the images
- Allow remote access from any office computer
- Allow simultaneous and multiple user access
- Require little or no maintenance
- Scalable for future camera requirements
- Interface with existing wiring and cameras
- Support high-resolution, network-based digital cameras for future installations

20.3 TECHNICAL DESCRIPTION

The video capture system (VCS) is a network video recording system. The VCS takes the existing analog camera video signals and converts the images to motion JPEG files via D/A converters. Images from internet protocol (IP)/digital cameras are captured directly in motion JPEG format. These image files are transferred to the VCS, which then stores them for as long as needed. Since the VCS is network based, any computer that has a standard web browser or the VCS client software is capable of connecting to the VCS and displaying both live and archived images. Another key factor is the open interface of VCS, which allows production computers (Level 1 or Level 2) to control the VCS via data, which includes key information such as heat, bar, slab, and coil numbers, as well as relative process data including footage, width, thickness, speed, temperature and any other critical data, as production occurs. All of this information is linked with an image and stored for easy retrieval. Figure 20.1 shows the network architecture of the VCS system.

There are a number of other features the VCS can provide:

- Create multimedia reports that visually explain what happened
- Include process images in email, reports, and studies
- Use images or movies for operational and safety training
- Use remote pan-tilt-zoom control from any Internet-enabled computer to position cameras
- Create a time-lapse video of any archived images (JPEG or MPEG)
- Provide unlimited user access to troubleshoot various problems at the same time

The flexibility of choosing the right camera for the job is also critical. The VCS is designed to easily integrate with many

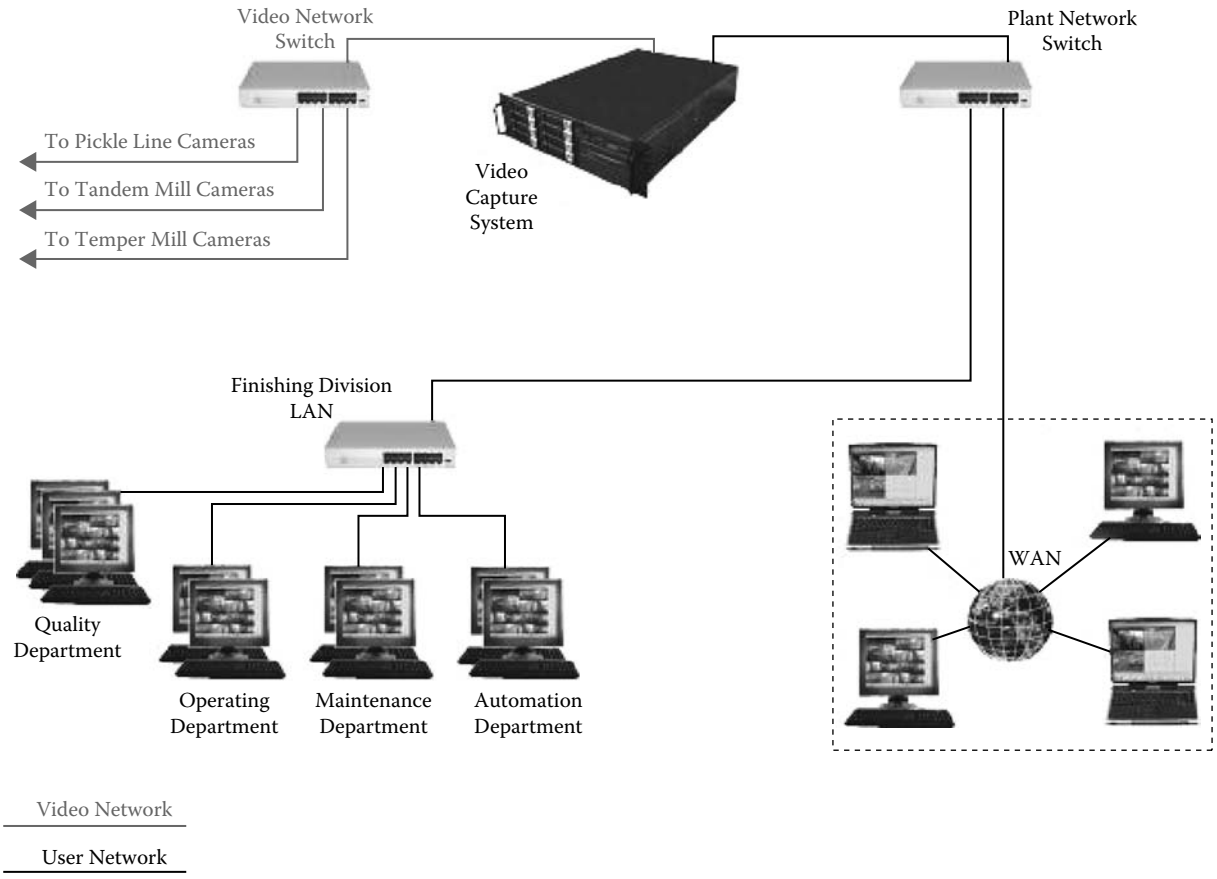


FIGURE 20.1 Network architecture of the video capture system. (From M. B. Assar, C. D. Romanauski, M. Kremer, et al. 2007. *Iron & Steel Technology*, January 2007, pp. 74–84. With permission.)

different camera manufacturers. It also allows for multiple types of cameras, so that analog, IP digital, wireless, high-resolution, and pan-tilt-zoom cameras are all integrated into one system. The VCS client software shields the users from differences between the camera types.

The VCS is based on the concept of total images per second (ips). For example, one can choose to utilize 400 ips in different ways. There can be 100 cameras recording 4 ips, or 400 cameras at 1 ips, or in any other combination. Images from critical cameras can be stored for longer periods of time and at a higher frame rate than images from less critical cameras. For example, images from a camera pointed at the exit of a mill are saved for months for quality reasons. Cameras pointed between stands could be saved for 5 or 7 days, enough to troubleshoot cobble or off-level mills. This concept also allows for only one system being needed compared to multiple 16-port DVR solutions when 17 or more cameras are installed.

Three VCS rack mount servers are available: an 8-, 16-, and 24-disk drive system. Each VCS is customized for each application. It is based on a number of parameters: total number of cameras, ips capture rate, storage length, percent recording activity, and future expansion plans. A VCS requiring 12-disk drives will have four spare slots in the 16-disk system, and 12 spare slots in the 24-disk system for future cameras or the decision to increase storage times.

In addition to the applications mentioned in this chapter, Benchmark Automation has also developed additional applications to meet the changing requirements of the mill environment. The installations include most areas of steelmaking, from primary operations to hot and cold rolling. The applications include production monitoring, slab surface, cobble, off-level mill analysis, emissions monitoring, safety compliance, and security surveillance.

20.4 SOLUTION

All of the VCR/tape systems in the finishing mill were replaced with the state-of-the-art video capture system (VCS). The VCS system is capable of footage-based recording, with easy video retrieval by coil number or timeframe, and has the ability to overlay critical mill data on the images in real time. Other DVRs (that were actually designed for security surveillance application) offered none of these critical features.

The VCS interfaced easily with the existing analog cameras. This meant no additional wiring had to be installed. The system converts the analog camera signals to digital image files, processes the image files, and archives the required images to a hard disk array. The VCS provides two separate networks: one used exclusively for video camera interfaces and the second to interface to the plant network. This

architecture insures that 24 × 7 video traffic does not interfere with the plant network. Management screens provide an easy mechanism to set the different recording rates and archive durations for each camera.

Seventeen cameras are currently tied into the VCS system. Two of these cameras are located on the 84-in. Pickle Line. One Pickle Line camera views the top of the strip, while the other views the bottom of the strip. Images are captured from these cameras every 2 feet of strip during processing. The Pickle Line coil images are archived for a period of 4 months. Eleven cameras on the 84-in. Tandem Mill were attached to the VCS system. The 11 Tandem Mill cameras are set up to view various areas of the mill and are used for troubleshooting mill equipment and production problems. Two recently installed cameras automatically take snapshots of both the operator and drive sidewalls of all produced coils to evaluate coil winding. These cameras are high-resolution, capturing information at 1 ips and retaining the images for a period of 10 days. Four cameras are located on the 84-in. Temper Mill. One camera views the top of the strip as it enters the mill, while the other views the exit end of the mill. The third camera on the Temper Mill monitors the coil sidewall on the entry uncoiler and is used to assist in troubleshooting loose winding, entry damage, and friction dig problems. The fourth Temper Mill camera monitors the delivery conveyor of the mill. The VCS captures images from the Temper Mill cameras after every 5 ft of processed strip. These cameras have also been set up to capture an image every 2 s when the mill is not running to help troubleshoot equipment problems. The Temper Mill camera images are archived for a period of 3 months. Table 20.2 describes the camera locations, type of camera, and the image capture rate.

The VCS provides many of the tools that are critical for mill troubleshooting. Personnel in any department can access the VCS simultaneously, viewing live or archived images from any cameras at any time. Images are setup to be stored in a manner that best suits the needs of the mill. There is no longer the need to search for the video associated with a particular coil. Personnel simply enter a coil number and view the video, just as one would retrieve a production or quality report. The VCS displays all required information, such as coil ID numbers, line speeds, thicknesses, widths, grade, temperature, and mill forces stamped on the images, allowing mill personnel to view critical data along with the video. This feature is critical to troubleshooting mill problems and wrecks. Quality personnel are frequently able to make coil dispositions directly from the video review, reducing reprocessing and improving on-time delivery.

TABLE 20.2
Camera Setup and Specifications

Production Unit	Location	Camera Type	Image Capture Rate
84-in. Pickle Line	Top of strip	Analog	Every 2 ft
84-in. Pickle Line	Bottom of strip	Analog	Every 2 ft
84-in. Tandem Cold Mill	Entry conveyor	Analog	High resolution @ 1 ips
84-in. Tandem Cold Mill	Uncoiler	Analog	High resolution @ 1 ips
84-in. Tandem Cold Mill	Entry holding shelves	Analog	High resolution @ 1 ips
84-in. Tandem Cold Mill	Right side guide (Std 1)	Analog	High resolution @ 1 ips
84-in. Tandem Cold Mill	Left side guide (Std 1)	Analog	High resolution @ 1 ips
84-in. Tandem Cold Mill	Entry stand 1 roll bite	Analog	High resolution @ 1 ips
84-in. Tandem Cold Mill	Tension reel	Analog	High resolution @ 1 ips
84-in. Tandem Cold Mill	Mill overview	Analog	High resolution @ 1 ips
84-in. Tandem Cold Mill	ADS conveyor	Digital/network	High resolution @ 1 ips
84-in. Tandem Cold Mill	Exit conveyor–oper. side	Digital 1.3 Mpixel	Five high-resolution snapshots of each produced coil
84-in. Tandem Cold Mill	Exit conveyor-drive side	Digital 1.3 Mpixel	Five high-resolution snapshots of each produced coil
84-in. Temper Mill	Mill entry	Analog	Every 5 ft when running and every 2 s when not running
84-in. Temper Mill	Mill exit	Analog	Every 5 ft when running and every 2 s when not running
84-in. Temper Mill	Uncoiler	Digital/network	High resolution @ 15 ips
84-in. Temper Mill	Delivery conveyor	Analog	High resolution @ 1 ips
Slitter Line – future	Strip surface	Digital high res	High resolution camera for strip inspection

Source: M. B. Assar, C. D. Romanauski, M. Kremer, et al. 2007. *Iron & Steel Technology*, January 2007, pp. 74–84. With permission.

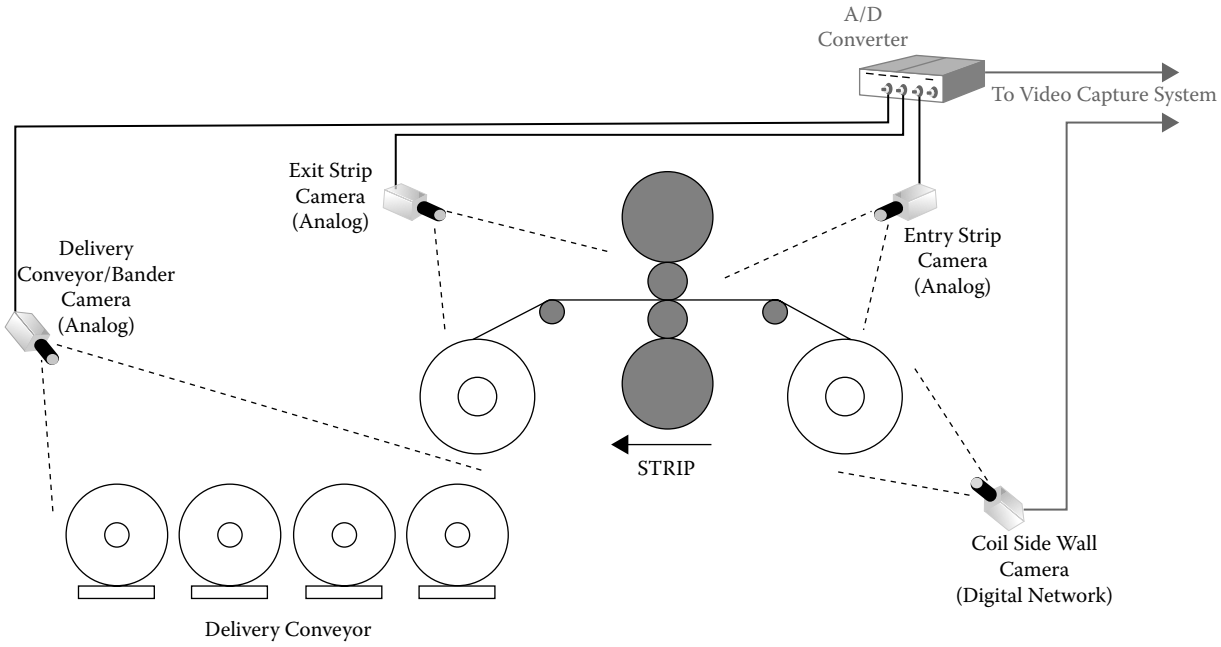


FIGURE 20.2 Location of cameras at 84-in. Temper Mill and the related network architecture. (From M. B. Assar, C. D. Romanauski, M. Kremer, et al. 2007. *Iron & Steel Technology*, January 2007, pp. 74–84. With permission.)

20.5 APPLICATIONS AND RESULTS

20.5.1 Temper Mill System

Four cameras are currently located on the 84-in. Temper Mill. One camera views the top of the strip as it enters the mill, while the second camera views the exit end of the mill. Images from each camera are captured every 5 ft of strip. A third camera views the operator sidewall of coils on the uncoiler. This camera records with the frequency of 5 ips and is used to troubleshoot sidewall shifting problems and incoming coil damage problems. The fourth Temper Mill camera monitors the delivery conveyor. This camera records on motion and is used to track safety procedures around the coil bander and to assist with investigation of mixed coil problems. Figure 20.2 shows a schematic of the location of camera installation at 84-in. Temper Mill, along with the related network architecture.

The VCS system provides an additional set of eyes that monitor Temper Mill operations and strip quality 24 hours a day. Quality personnel now have the ability to go back and view any 5-ft section of strip rolled during the previous three months. Coil data are retrieved either by produced coil ID or by selected timeframe. The top of each image is imprinted with the incoming and exit coil numbers, footage, line speed, and X-ray gauge readout to aid the troubleshooting process.

Figure 20.3 shows what anyone with network access can see during coil production. Quality engineers frequently review these images to make coil dispositions and investigate customer claims.

The ability to make coil dispositions based on review of the images has greatly reduced reprocessing rates on the mill. The video is used to verify reported defects, pinpoint their location, check for additional similar defects, make coil dispositions, and schedule reprocessing. The system has also been extremely effective in investigating/confirming conditions reported by the customer, such as pre-Temper Mill stain, shape problems, and scratches. Customers who make a claim expect an action plan that prevents the problem from occurring again in the future. By reviewing images from the processing of the coil, the source of the problem can frequently be identified and resolved. In the past, there was no reliable method to visually investigate customer claims. Resolving coil-tracking issues has been perhaps the greatest advantage. Going back and reviewing images alongside production records have resolved many misidentified coil issues. Most of the tracking issues are operator/computer input errors or exit end tag errors.



FIGURE 20.3 Online/offline production images include parameters like coil number, gauge, speed, footage, etc., making the disposition of the coil much quicker. (From M. B. Assar, C. D. Romanauski, M. Kremer, et al. 2007. *Iron & Steel Technology*, January 2007, pp. 74–84. With permission.)

In summary, the VCS system has helped in the following areas:

- Acts as a second set of eyes
- Review customer claims
- Troubleshooting mill problems (i.e., mill wrecks, friction scratches, soft incoming coils)
- Product tracking (i.e., coil number verification)
- Live production review from the comfort of the office desk
- Review images for verification at quality meetings
- Unit productivity

The cameras pick up most conditions that would be visible to the naked eye, but unlike the naked eye, cameras have pause and rewind buttons. The cameras have also detected many operating issues that caused quality problems, which include the following:

- Friction digs that were the result of improper arbor insertion
- Edge breaks damage that was not repaired prior to temper rolling
- Torn edges and stickers from poor incoming winding
- Mill wrecks resulting from people not reacting correctly to incoming conditions
- Oiler not in position for product (dry up/oiled down)
- Exit saddle left in the up position (responsible for many wrecks)
- Exit table failed to lower (resulting in mill wrecks)
- Creases on the exit reel due to bad start (see Figure 20.4)
- Belt wrapper problems (broken or binding belt)

The live view allows quality personnel to keep track of the status of the mill at any given time with the push of a button.

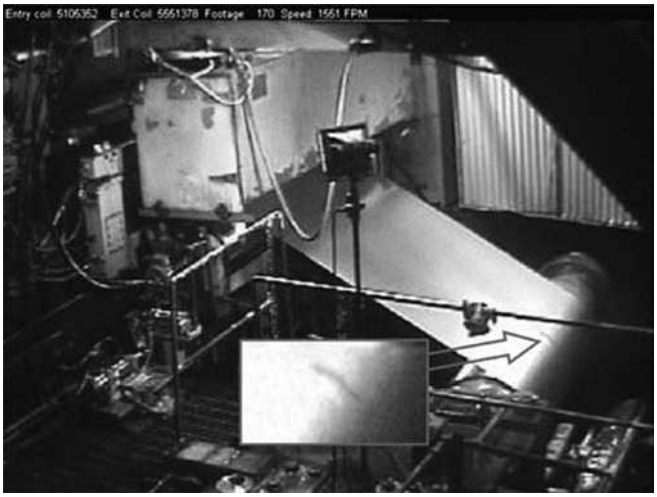


FIGURE 20.4 Mill backed up after belt wrapper came in causing crease that carried through entire coil. (From M. B. Assar, C. D. Romanauski, M. Kremer, et al. 2007. *Iron & Steel Technology*, January 2007, pp. 74–84. With permission.)

Quality personnel no longer have to rely on operators to notify them when they are needed to observe trial coils. Delay times, operating practices, and roll changes can also be reviewed.

The following two figures exemplify a Temper Mill wreck caused by poor incoming winding. Figure 20.5 shows the coil being loaded with a damaged sidewall. Figure 20.6 shows the mill wreck with the coil running at high speed instead of being processed at a lower speed. The coil would have been acceptable if processed at a lower speed.

Figure 20.6 shows a crease that carried through the entire coil. Review of the video images showed that shortly after the coil entered the belt wrapper, the mill was reversed. This caused the defect to occur throughout the coil.

20.5.2 Pickle Line System

Figure 20.7 shows a schematic of the location of cameras installed at the 84-in. Pickle Line and the related network

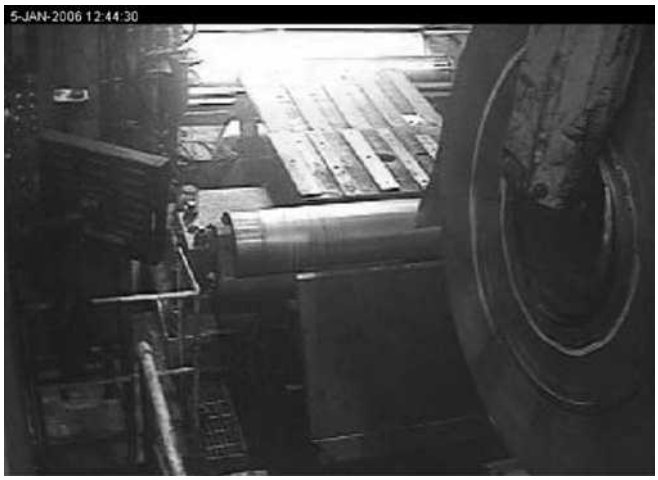


FIGURE 20.5 Coil is chalk-marked with winding problem as it is loaded. (From M. B. Assar, C. D. Romanauski, M. Kremer, et al. 2007. *Iron & Steel Technology*, January 2007, pp. 74–84. With permission.)



FIGURE 20.6 Coil breaks entering the mill. (From M. B. Assar, C. D. Romanauski, M. Kremer, et al. 2007. *Iron & Steel Technology*, January 2007, pp. 74–84. With permission.)

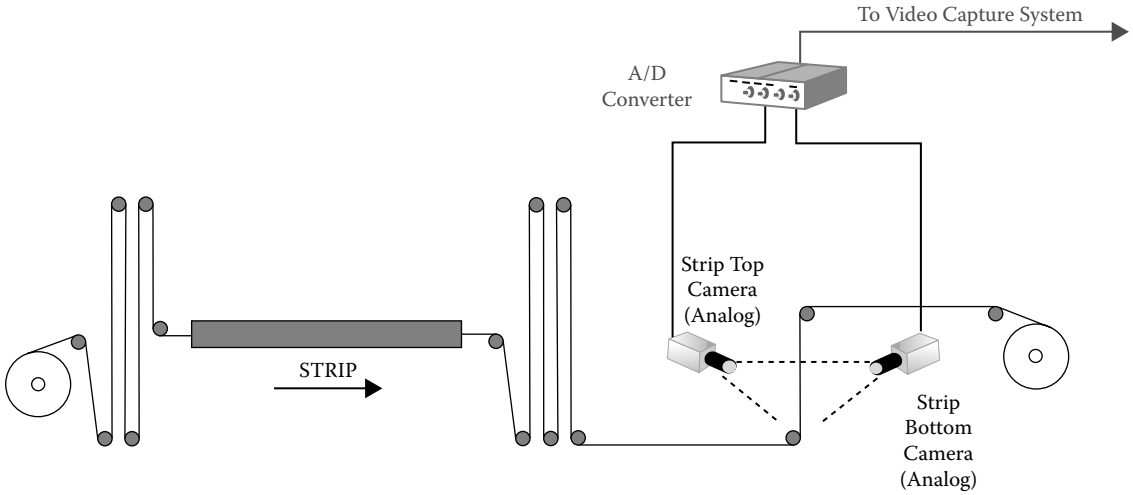


FIGURE 20.7 Location of cameras at 84-in. Pickle Line. (From M. B. Assar, C. D. Romanauski, M. Kremer, et al. 2007. *Iron & Steel Technology*, January 2007, pp. 74–84. With permission.)

FINISHING UNIT QUALITY EXCEPTION REPORT

Unit: 84" Pickle live **Date:** 1-11-06 **Turn:** 7.3 **Inspector:** A

Charge coil	Produced coil	Size	Customer	Part	Weight	Comment	Final dispo
382750	5085636	0.128×71.43		Drums	64,730	L–Bolt Tem Btm CTR At 200' Area	

FIGURE 20.8 Inspector reports indicating possibility of a defect on one coil. (From M. B. Assar, C. D. Romanauski, M. Kremer, et al. 2007. *Iron & Steel Technology*, January 2007, pp. 74–84. With permission.)

architecture. As this figure shows, both the top and bottom surface of coils are being monitored and recorded post acid tanks. The images are stored along with the incoming and outgoing coil numbers, as well as the footage and speed.

The VCS system for the pickle line is used in the following ways:

- Inspection aid (second set of eyes)
- Production tracking
- Live review
- Review and print images for quality evaluation
- Weld-tracking analysis and verification

Utilizing the inspectors' comments and the video images, personnel have the ability to identify and disposition a class of defects that would be detrimental to future units or customers. Disposition may include coil rejection. Another possible disposition is to process the coil with a feedforward note to alert future units about the defective areas for potential removal in either small coils or blank forms. Other software programs also have been developed that simplify the identification of defective locations by calculating their positions after the coils have been cold reduced, including edge and footage locations.

As with the Temper Mill system, benefits are received through production tracking and live review. In most cases,



FIGURE 20.9 The image of the suspected coil was reviewed and the exact location of the defect was found. (From M. B. Assar, C. D. Romanauski, M. Kremer, et al. 2007. *Iron & Steel Technology*, January 2007, pp. 74–84. With permission.)

the printed image of a defect satisfies the visual need for confirmation. Figure 20.8 shows the inspector report in comparison to the actual video image.

After reviewing the inspector's comments, the video image confirms the severity of the defect, but shows that the defect actually occurred at 98 ft (see Figure 20.9).

CURRENT LOCATION OF PICKLER DEFECT

LOCATION OF DEFECT AT PICKLER

EAST/WEST (E/W)	W
TOP/BOTTOM (T/B)	B
FEET FROM WELD	2050
TANDEM MILL COIL NUMBER	5197453
TANDEM MILL ENTRY GAUGE	0.1105
TANDEM MILL EXIT GAUGE	0.0298
TANDEM MILL COIL LENGTH	9399
CALC PKL COIL LENGTH	2535

CURRENT DEFECT LOCATION

FEET FROM CURRENT OD	**1516**
CURRENT TOP/BOTTOM	**B**
LAST UNIT EAST/WEST	**E**
CURRENT LEFT/RIGHT	**L**

	Y/N	Entry Reel Orient-ation	Delivery Reel Orient-ation
PKL	Y	O	O
TCM	Y	O	O
SLTA1			
SLTA2			
SLTA3			
TMP1	Y	O	O
TMP1		O	O
SLTB1		O	O
SLTB2			
SLTB3			
TMP2		O	O
TMP2		O	O
SLTC1			
SLTC2			
SLTC3			

Notes:
1. Does not acount for coils run on Slitter after Pickler, before Tandem Mill
2. Assumes 3% scrap loss from Temper Mill entry pup and that this is Pickler tail
3. Assumes no scrap loss at Tandem Mill or Temper Mill prep shear

FIGURE 20.10 Pickle Line defect spreadsheet. (From M. B. Assar, C. D. Romanauski, M. Kremer, et al. 2007. *Iron & Steel Technology*, January 2007, pp. 74–84. With permission.)

Knowing the position of the defect in the pickled coil, the future units operator can maximize production by running at a higher speed until the defect arrives, then slows down to look for the defect. A simple Excel program was developed to calculate the defect location. Figure 20.10 shows a sample spreadsheet. This program calculates the defect position, as it would appear post-temper pass. It enables the reinspection unit to go directly to the noted footage running at a normal speed of 800–900 feet per minute (fpm), eliminating the need to run the entire coil at re-inspect speed, which is 315–350 fpm.

Figure 20.10 shows a typical Excel spreadsheet used to predict the location of defects at different locations, knowing the position of defects in the pickled coil. The yellow shaded fields are filled in and the software does the rest. The slitter operator would know to slow down at 1516 from the outer and the defect would be on the bottom east or left edge of the strip.

20.5.3 Weld-Tracking Analysis and Verification

Figure 20.11 is an example of a pickle-weld and punched hole that is detected at the Tandem Mill to identify the correct point to split coils. Occasionally, the weld was not detected and was processed through the Tandem Mill, resulting in roll mark and premature roll change.

After installation of VCS, engineering personnel analyzed the video images containing the affected strip footage and saw that an occasional weld did not have a punched hole. Maintenance personnel corrected the problem at the punch and verified the reliability at the weld-tracking at the Tandem Mill. This investigation resulted in savings by reducing the number of roll changes at the Tandem Mill and eliminated reprocessing costs. See Figure 20.11.

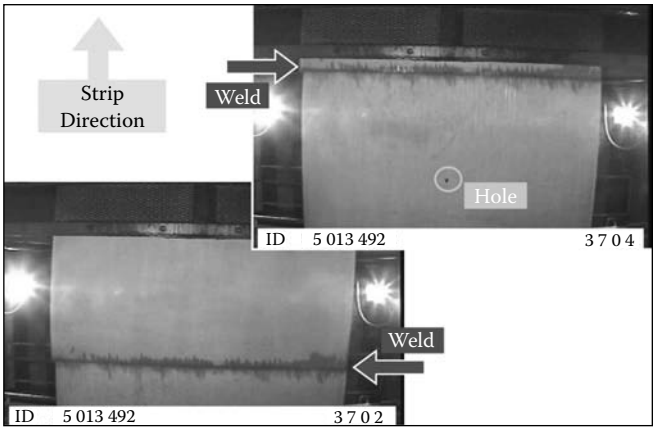


FIGURE 20.11 Pickle weld with hole used for tracking. (From M. B. Assar, C. D. Romanauski, M. Kremer, et al. 2007. *Iron & Steel Technology*, January 2007, pp. 74–84. With permission.)

20.5.4 Tandem Mill System

Figure 20.12 shows a schematic of the location of camera installation at 84-inch Tandem Mill along with the related network. There are 11 cameras installed at the Tandem Mill. The system is being used for monitoring the mill operation and performing wreck analysis.

Numerous problems have been resolved using the VCS system. Two such problems are described in the following.

A coil falling into the pit raised safety concerns regarding the proper functionality of the equipment. The coil was being

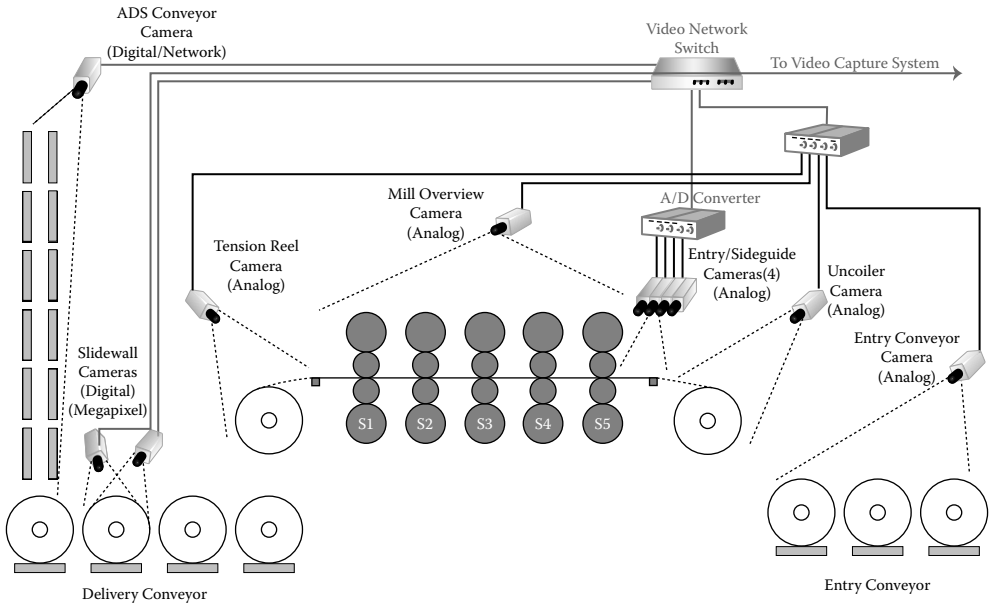


FIGURE 20.12 Location of cameras at 84-in. Tandem Mill and the related network architecture. (From M. B. Assar, C. D. Romanauski, M. Kremer, et al. 2007. *Iron & Steel Technology*, January 2007, pp. 74–84. With permission.)



FIGURE 20.13 During removal of the coil, a buckle formed between saddle and coil. (From M.B. Assar, C. D. Romanauski, M. Kremer, et al. 2007. *Iron & Steel Technology*, January 2007, pp. 74–84. With permission.)

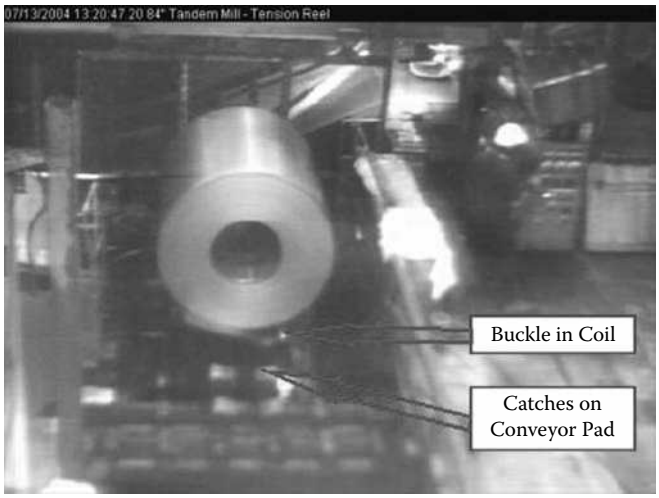


FIGURE 20.14 Buckle about to hit the conveyor pad. (From M. B. Assar, C. D. Romanauski, M. Kremer, et al. 2007. *Iron & Steel Technology*, January 2007, pp. 74–84. With permission.)

moved from the tension reel to the exit conveyor. No one saw what happened, so the cause was not known. Figure 20.13 shows the removal of this coil from the tension reel after the mandrel collapsed. A buckle can be seen on the outer lap of this coil.

Figure 20.14 has the pictures of the troubled coil being transferred to the exit conveyer. The pictures show the buckle will not clear the conveyor pad.

Figure 20.15 shows the transfer car moving the coil toward the exit conveyor. The conveyor pad stops the coil. As the transfer car moves, the coil starts to slide off the transfer car and fall into the pit.

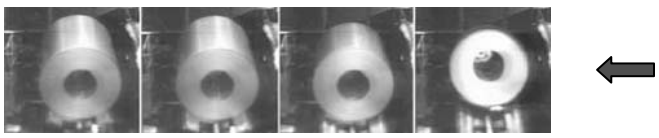


FIGURE 20.15 The coil sliding off the transfer car and falling into the pit. (From M. B. Assar, C. D. Romanauski, M. Kremer, et al. 2007. *Iron & Steel Technology*, January 2007, pp. 74–84. With permission.)

The images above show that the equipment was operating properly, saving investigation time of a nonexistent mechanical, electrical, or safety problem.

Another example involved unexplainable stand #1 wrecks that were occurring two to three times per month. Review of the VCS video after one such wreck showed that during mill delays, the uncoiler would slowly rotate forward, loosening the laps and causing the coils to telescope due to loose tension. See Figures 20.16 and 20.17.

When the mill would restart, the arbor-centering system was unable to compensate for the severe telescope resulting in the strip going over the side guides and causing a wreck. Maintenance personnel reviewed the video and traced the cause to out-of-adjustment brakes on the uncoiler motors. The brakes were repaired and the stand #1 mill wrecks were virtually eliminated.

Evaluation of winding is a recent application of VCS. There are two cameras, at the drive and operator sides of coil, at the exit conveyer. Cameras look at both sides of the coil wall. These cameras show whether the sidewall is straight or if there is any telescoping in the inner or outer diameter of coil. Telescoping is a major source for coil handling damage, which results in significant yield loss (Edwards and Boulton 2001). These cameras help monitor the winding condition of each individual coil, and thereby help take the mystery out of coil winding by monitoring it and finding a correlation between winding condition and process variables. Figure 20.18 shows an example of these cameras.

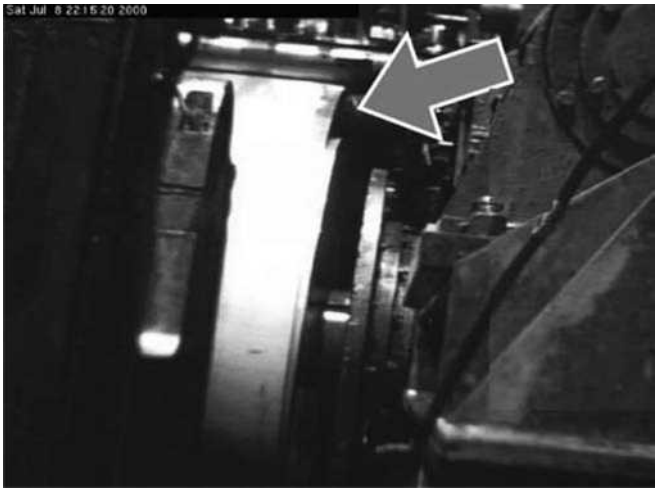


FIGURE 20.16 Incoming coil is wound tight without telescoping. (From M. B. Assar, C. D. Romanauski, M. Kremer, et al. 2007. *Iron & Steel Technology*, January 2007, pp. 74–84. With permission.)

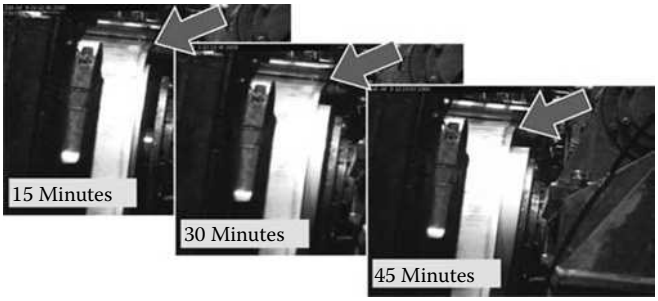


FIGURE 20.17 Uncoiler drifts forward causing coil to loosen and telescope. (From M. B. Assar, C. D. Romanauski, M. Kremer, et al. 2007. *Iron & Steel Technology*, January 2007, pp. 74–84. With permission.)



FIGURE 20.18 Coil winding is a major source of yield loss being monitored by vcs for every coil.

20.6 CONCLUSIONS

The VCS was installed at the Finishing Division—Mittal Steel USA-Cleveland in 2001. The system is being used successfully for wreck analysis, troubleshooting, coil quality evaluation, claim review, and production tracking. Significant savings have resulted since video investigation was implemented. The number of reprocess coils as well as the number of mill wrecks has been greatly decreased. Improvements in the following areas have also been attained:

- Increased productivity
- Improved yield
- Reduced maintenance costs
- More efficient in troubleshooting techniques
- Reduced downtime

REFERENCES

M. B. Assar, C. D. Romanauski, M. Kremer, et al. Digital visual inspection of coils. *Iron & Steel Technology*, January 2007, pp. 74–84.

W. J. Edwards, G. Boulton. *The Mystery of Coil Winding*, Pittsburgh, PA: AISE, 2001.

R. Gonzalez, R. Wood. *Digital Image Processing,* 2nd edition, Upper Saddle River, NJ: Prentice Hall, 2001.

A. Kamrani, W. Rong, R. Gonzalez. A generic algorithm methodology for data mining and intelligent knowledge acquisition. *Computer and Industrial Engineering*, 40: 361–377.

T. MacDougall, E. Dillon. Implementation of surface inspection technology on noisy surfaces. *Iron & Steel Technology*, August 2008, pp. 98–105.

21 Yield Improvement through Better Crop Optimization

Robert L. Ricciatti

CONTENTS

21.1 Introduction 239
21.2 Crop Optimization 239
21.2.1 Imaging 241
21.2.2 Cut Line Determination 241
21.2.3 Tracking 241
21.2.4 Shear Control 242
21.2.5 How Far to Go? 242
21.3 Laser Velocimeters 242
21.4 Summary 243
References 243

21.1 INTRODUCTION

There are still some parts of the world today in which the domestic market for steel is so large that every steel (or aluminum) mill can sell every last ton of metal rolled without regard to its quality.

However, in most highly developed steel-producing countries, competition between mills is so great that the failure to improve yield and quality continuously can mean not only reduced business but also even eventual bankruptcy.

For steel mills, there is an almost endless list of projects that could improve both quality and yield, but most are so expensive that they are simply unaffordable to mills short of working capital. But there is one affordable improvement that has come to the forefront because of its remarkable return on investment when applied correctly: crop optimization.

21.2 CROP OPTIMIZATION

Crop optimization is the process by which the head and tail ends of the transfer bar produced by a hot strip mill (HSM) roughing stand are trimmed by a special cropping machine (shear) before entering the HSM finishing stands. If not cropped, the head and tail ends would be elongated during rolling, requiring expensive trimming downstream, or worse—they could catch between runout table rolls to cause a cobble that stops production altogether.

Most existing mills have had some kind of cropping system in use for decades, even if it comprises only a video camera and a button that allows an operator to judge where best to cut a slowed down or stopped transfer bar manually. New HSM are supplied with an automatic cropping system of some kind to crop transfer bars on the fly. Some are very simple, cropping only a fixed length from the ends of the transfer bar, but others are much more complicated, recording and then analyzing the shape of head and tail ends, and then attempting to control the shear to crop in the ideal places (Figure 21.1).

George Kelk Corporation (KELK) is an engineering company located in Toronto, Canada, but well known all over the world for the superiority of its rolling mill sensors. Beginning with its roll force load cells—immune to errors from uneven loading and so strong that they are guaranteed against any kind of failure for 5 years—KELK has developed a wide range of mill-worthy sensor products that have the reputation of always being technically the very best available.

KELK started to make components for crop optimization systems in the mid-1980s, but it was not until 1993 that it introduced a revolutionary new shear control system that raised cropping accuracy to an entirely new level. The better the cropping accuracy, the higher the increase in yield, with the bonus of less trimming required downstream.

For ease of analysis, crop optimization can be divided into four distinct processes:

1. Imaging of head and tail ends
2. Determination of optimum virtual cut lines
3. Tracking of virtual cut lines to the shear
4. Control of shear blades to hit the cut lines

Each of these processes contributes individual errors to overall cropping performance. By developing and using components with the least possible errors, the accuracy of

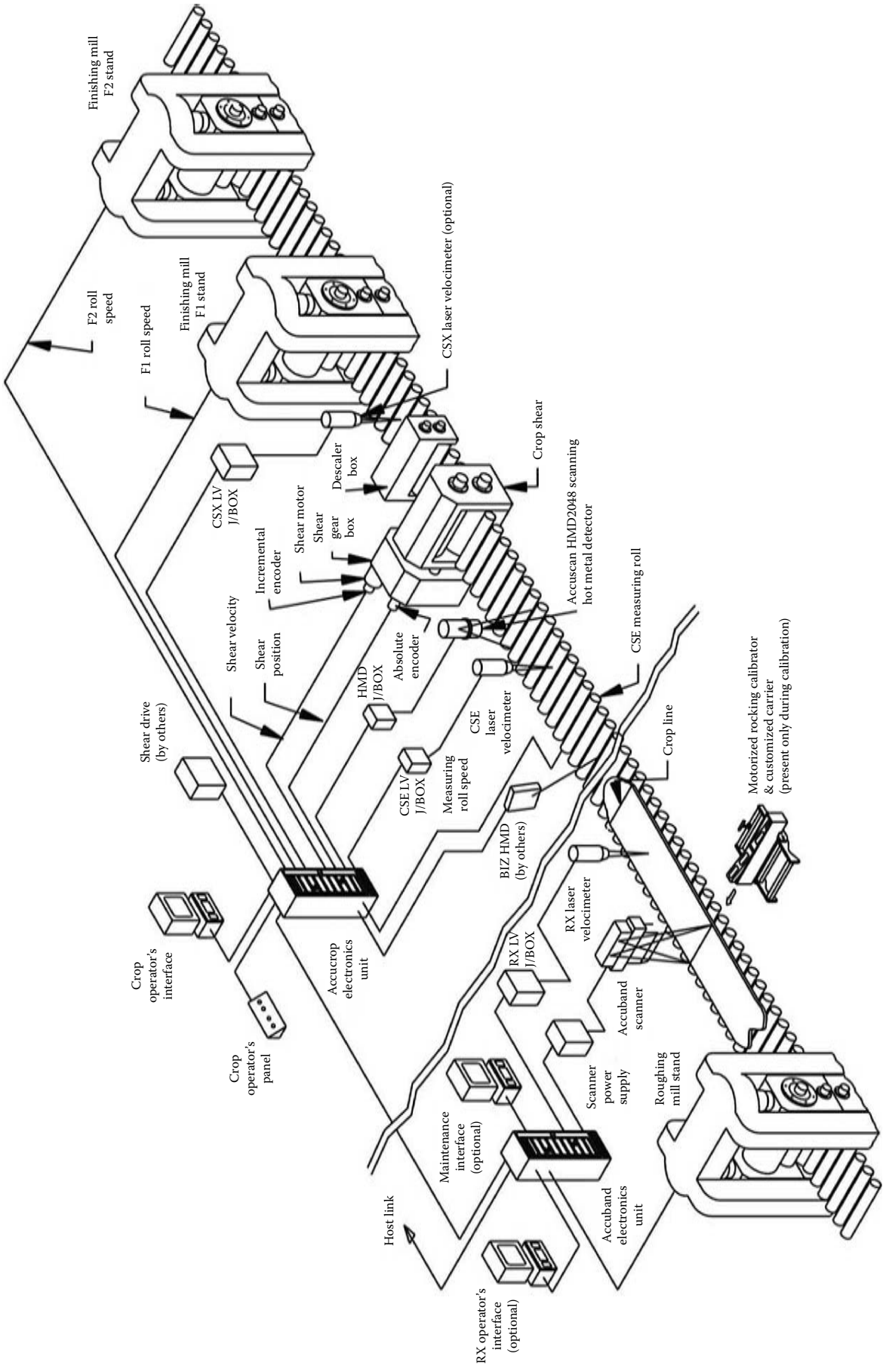


FIGURE 21.1 A modern crop optimization system.

each individual process can be maximized, and therefore, so can total overall accuracy. This is the philosophy behind the KELK system.

21.2.1 Imaging

There are several ways to generate an image or picture of the head and tail ends of a transfer bar. The simplest way is to use what's called a monoscopic area array video camera to take snapshots of the transfer bar ends. While very economical, area array cameras cannot photograph the bar if there is any steam in the field of view, so it is left to the end user to remove the steam typical of crop shear environments with heavy fans, an almost impossible task. Since the bar ends are usually curled above the rolling table as they pass under the camera, their size will be distorted when viewed by a monoscopic camera, appearing shorter and wider than they really are.

A linescan camera has a field of view much more easily cleared of steam and is low cost but is also monoscopic and must be used together with an accurate speed measuring device in order to construct head and tail images.

Stereoscopic width gauges solve the problem of distorted images, but cannot normally "see" through steam. But KELK has one that can measure well in spite of the presence of considerable amounts of steam—the Accuband Strip Width Gage (Figure 21.2). Since the Accuband is also the most accurate width gauge in the world, it is easy to understand why head and tail images captured with an Accuband will contribute less error to the overall imaging process.



FIGURE 21.2 The KELK Accuband Strip Width Gage.

21.2.2 Cut Line Determination

Once accurate head and tail images are obtained, they must be analyzed to determine the best place to cut. This is more difficult than it would seem because it is not optimal to cut straight across the head end of a transfer bar. If cropped that way, ears are developed during finishing rolling that can interfere with coiling. Instead, shoulders of precise dimension must be left on the head end.

Most crop optimization systems are designed to leave such shoulders but are programmed for only one specific shape of head end. If an unexpected shape is observed, such systems may be unable to assign a cut line or may cause the transfer bar to be cut in the wrong place. In actuality, several different shapes can occur, and each requires a different cut line location (Figure 21.3). One of the most important features of the KELK system is that it analyzes the head (and tail) end shapes to determine the proper rules to apply before location of the virtual cut lines.

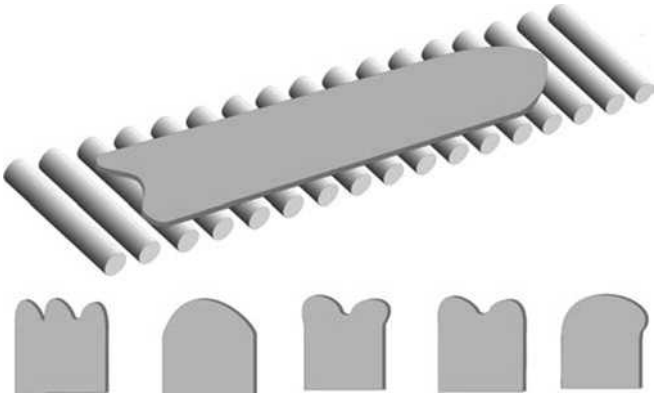


FIGURE 21.3 Transfer bar head/tail shapes.

21.2.3 Tracking

Once the optimum cut line locations have been determined, they must be referenced to an identifiable part of the transfer bar and then tracked all the way into the shear.

Tacho generators attached to rolling table rolls or contact wheels lowered onto the bar are two inexpensive ways of tracking the bar continuously, but they are not often used anymore because of significant errors from slippage between bar and rolls.

A linescan video camera mounted in the direction of bar travel is a better choice but subject to be blinded by steam. Moreover, these cameras cannot tolerate more than one transfer bar in the field of view at the same time, so there must be a deliberate spacing left between successive transfer bars, which slows down the entire hot rolling process.

The best choice for continuous, noncontact bar tracking is a laser velocimeter. Once exceedingly expensive, these devices are now quite affordable and offer superb accuracy, even if the transfer bar accelerates, decelerates, or stutters from contact with side guides. KELK uses the best one, the Accuspeed Laser Velocimeter (Figure 21.4), which is from 2 to 100 times more accurate than other known products (depending on bar speed) and can be mounted at a much greater distance from the hot transfer bar, out of harm's way from cobbles.



Model ASD3500A Model ASD2100B

FIGURE 21.4 The KELK Accuspeed Laser Velocimeter.

If it is not possible to track the transfer bar continuously into the shear—for example, when the HSM uses a coil box between roughing stand and shear—the location of the foremost end of the transfer bar must be reacquired as it nears the shear. Many crop systems use hot metal detectors for this purpose, usually mounted under the center line of the rolling table. The assumption is that the transfer bar will travel down the center of the table, but if it moves sideways, a different part of the head end will be detected than was expected, sometimes introducing a very large error.

Rather than using the center of the head end as a reference, the KELK system uses the extreme tip and then reacquires its location with an Accuscan hot metal detector looking across the direction of bar travel. The Accuscan has a much tighter triggering field than any competing sensor and so eliminates a major source of error from the overall system performance.

21.2.4 Shear Control

For decades, similar methods of shear control were used by various suppliers of crop control systems. In essence, the initiation of the shearing cycle was made without considering several very important factors, such as the change of the bar speed, acceleration of the bar, and backlash in the crop shear gears. The resulting best reported accuracy with which the shear blades could be made to hit the bar was in the range of ±10–15 mm.

In 1993, KELK changed everything with the introduction of its Accucrop Shear Control, a clever adaptation of military smart bomb technology. A smart bomb is not fired from a warplane ahead of, for example, a moving tank, in the hope that the tank will not change speed or direction before being hit. Instead, the tank is tracked by a laser designator, and the smart bomb continuously changes its point of aim as it accelerates, guided by the laser, so that it hits the tank with extreme accuracy.

In the KELK Accucrop system, the Accuspeed Laser Velocimeter is used as the laser designator, and the shear blades are accelerated slowly from standstill to a calculated optimum impact speed, guided by continuous input from the Accuspeed. With updates every 4 ms, the shear blades are accelerated continuously without any backlash and hit the intended cut lines within 1 mm, and within 1% of the intended optimum impact speed every time.

Some mills have been told that they must install a new, powerful shear motor before they can consider upgrading their crop optimization, but this is only a requirement of non-KELK systems. The Accucrop shear control never requires maximum acceleration of the shear blades, so even old, weak shear motors can be used. Also, because the blades are made to impact the transfer bar without excessive speed, blade wear is always less, and the intervals between blade change-outs greatly extended.

21.2.5 How Far to Go?

If each component of a crop optimization system is examined separately, it will not be difficult to effect positive improvements in one part or another, and any number of sensor suppliers stand ready to help. KELK, for example, can supply just imaging components or imaging plus tracking, with the end user or mill builder left with the responsibility to control the shear. But for maximum improvement, all components should be optimized [1].

By replacing even a modern crop optimization system with a complete KELK system, substantial savings will accrue. Application specialists study the site conditions and logistics at each HSM, determine which components to use and where to locate them, and then calculate the expected improvement in accuracy over any existing system. KELK is prepared to guarantee this improvement in writing.

Knowing the amount of otherwise wasted steel they are guaranteed to save, mills can then calculate the amount of money they will save per year, and use that figure to justify investment in a new system and to propose meaningful site tests to prove the mill is truly realizing the savings promised [2].

Just how much can be saved? A conservative minimum is 4000 tons of steel per year for mills already using a modern, European crop optimization system, while the record so far is held by a Russian steel mill that had been cropping manually. Their savings? An astonishing 30,000 tons of steel per year, with a payback period of only 18 days!

Moreover, the life of shear blades is always extended by the implementation of a KELK system, and for many mills, this represents a substantial saving in downtime otherwise required for blade replacement.

21.3 LASER VELOCIMETERS

The ability to measure both speed and length in rolling mills, through the use of laser-based sensors, has improved so much in recent years that it deserves special mention.

Traditionally, speed and length have been measured by counting the rotations of a wheel in contact with, for example, a steel strip or a toothed gear wheel attached to the axle of a roll over which the strip is made to pass. Neither of these methods is particularly expensive, but both exhibit fairly large errors—typically 3% or more—because of slippage

between strip and wheel or roll. This level of measurement error was considered acceptable until the mid-1990s, when mill-quality laser velocimeters first became available.

The idea that a laser beam aimed at a strip can tell its speed may sound strange to many people, but the science involved is relatively simple. A laser beam is light of a constant wavelength, and therefore, frequency. When bounced off a moving strip, that frequency will be changed by the motion of the strip (the Doppler principle). If the new frequency can be measured, the change in frequency can be plugged into a simple formula (the Doppler formula) to calculate strip speed. Velocimeters that work in this way are commonly called laser Doppler velocimeters or LDVs.

There are other ways to derive speed using lasers, but so far, only LDVs have proven practical for use in steel mills.

The secret to good laser speed measurement is in the way in which the frequency of the reflected laser light is determined. Too small to be observed directly, the change in frequency must be estimated by means of frequency analysis. Several methods of frequency analysis are used by different sensor manufacturers (correlation techniques, fast Fourier transforms (FFTs), etc.), but the results are surprisingly similar—accuracy approaching 0.05% under good measuring conditions.

An accuracy of 0.05% will certainly be an improvement in any mill automation system in which 3% accuracy is the norm, but it must be noted that LDVs are variable accuracy devices—accuracy decreases with strip speed. For crop optimization applications, with transfer bar speeds of only 3–4 m/s, LDV accuracy is reduced to 2%–6%, which is certainly not an improvement over measuring wheels or tacho generators.

In 1995, KELK introduced a new velocimeter—the Accuspeed—which was promoted as "not an LDV." This was because it incorporated an optical system different from that of LDVs, as well as an entirely new and unique method of frequency determination. The result was a device with a constant speed measuring accuracy of 0.025%—twice as good as LDVs in cold mills but more than 100 times better at transfer bar speeds [3].

Offered today in a variety of mill-worthy models with standoff distances of up to 3.5 m (ideal for crop optimization applications), the Accuspeed has become a requirement whenever the highest speed measuring accuracy is required for process improvement.

Laser velocimeters measure length as well as speed, but are not usually considered to replace other less expensive methods of length measurement because LDVs have a fixed-length measurement accuracy in the range of 2.0%–0.05%. For long strips, this is not precise enough to represent an improvement. But here, too, the KELK Accuspeed is different: it exhibits variable accuracy which actually improves with the length of the measured strip.

For example, for strips of 2000 m long, the KELK Accuspeed has a length measuring accuracy of ±0.0014% (±28.0 mm). This means that laser velocimeters can now be used to effect improvements in flaw detection monitoring, weld tracking, and a myriad of similar applications throughout the strip rolling and finishing processes—but only if the KELK product is specified!

21.4 SUMMARY

The development and improvement of many different kinds of process control sensors and systems has resulted in new possibilities for yield improvement. In particular, modern crop optimization systems can almost always deliver significant savings for a relatively modest investment. But not all sensors and systems are equal in performance. It is well worthwhile to search out and specify the very best.

REFERENCES

1. T. Dozier. Crop optimization—beyond the obvious, *Iron and Steel Technology*, August 2006, 81–84.
2. Newsletter of Dunaferr Steelworks, Hungary. Sheet bar cropped accuracy. November 2002, 7.
3. A. Gluzmann and R. Ricciatti. State of the art laser velocimetry. Paper presented at the *Institute of Metals U.K. Conference*, April 27–28, 1999.

22 State-of-the-Art, Noncontact Infrared, Laser, and Microwave Intelligent Sensors and Systems for Steel Mills

François Reizine, Bingji Li, and John Nauman

CONTENTS

22.1 Current Sensor Technologies 245
22.2 Principles of Selected Applications 246
22.2.1 Continuous Caster Optimization of Cut 246
22.2.2 Width Measurement of Slab 248
22.2.2.1 Strip Centering/Camber and Width Measurement 248
22.3 Sensor Systems 248
22.3.1 Systems Developments 248
22.3.2 Systems Techniques 251
22.3.3 System Examples in Slab Casting 252
22.3.4 System Examples in Hot Rolling 253
22.3.5 System Examples in Finishing 254

22.1 CURRENT SENSOR TECHNOLOGIES

Accuracy and reliability are very important in the harsh steel mill environment, filled with steam, water, dust, scale, and heat. This leads to very high requirements for the sensors and systems used in detection, position of edges of steel products on the move, and measurement of temperatures, levels, dimensions, and so on. Therefore, in hot metal detectors and infrared scanners, automatic gain control, adjustable threshold, continuous monitoring of infrared energy, and Bluetooth wireless communication have been developed for ease of use, increased reliability, accuracy, safety and reduced waste, and maintenance. As a leader of sensors and systems providers in the world, ASC (American Sensors Corp.) has applied those advanced technologies to its infrared, laser, microwave, sensor, and systems technologies.

Infrared sensors include static and scanning detectors, edges positioning sensors, and temperature emissivity measurement sensors. The scanning and positioning sensors (ASC IS-3000) are noncontact sensors for loop control and width and speed measurement of any hot and cold products. They provide analog and digital and serial Ethernet or Bluetooth wireless outputs. Another positioning detector is the static hot metal detector (ASC HMD-3000) with automatic gain control that allows the sensors to choose the best gain setting so that the energy of the signal is always between 3000 and 8000 mV. In other words, the sensors are never saturated (over 9969 mV) and never less than three times the threshold. The temperature measurement sensors are the pyrometers, (ASC PM-3000) which use one-, two-, and multiple-color (wavelength) pyrometry systems that allow the accurate measurement of emissivity and, consequently, of the true temperature even in the presence of scale, slag, and fumes. They are accurate even if the temperatures to be measured are as low as 200°C (390°F) and even with targets that have low emissivity and variable roughness and surface conditions. Such sensors are being used in blast furnaces, basic oxygen furnaces/converters, continuous casters, hot rolling mills flat and long products, and galvanizing and galvanneal lines.

Laser-based sensors use different principles of physics, mainly time-of-flight, pulsed infrared lasermeters for level measurement and dimensional length measurements; triangulation lasermeters for width and thickness measurements; and laser Doppler velocimeters for velocity and length measurements, including mass flow, elongation, tension control, and cut-to-length applications. All of these measurements are noncontact (without slippage that causes inaccurate and non-repeatable measurements that reduce quality and causes more waste and accidents).

Microwave sensors are designed to measure the level, volume, and refection of liquids, pastes, slurries, and solids, through particulate materials. They can be operated in storage and process ladles and tanks, as well as in wells. The measuring systems consist of the electronic units with wave guides and cone-shaped antennas, all made of stainless steel.

TABLE 22.1
Applications of Sensor Technology in the Flat Processing of the Steel Industry

Continuous Caster	Continuous caster optimization of cut	LM-3000 Infrared time-of-flight
	Laser	Auto-focus laser Doppler
	Width measurement of slab	LM-3000 Triangulation lasermeter
	Snapshot or length measurement	HMD-3000-D Infrared sensor + LM-3000-F laser sensor
	Temperature control fiber	PM-500 two- or PM-3000 multiwave Infrared pyrometers, with or without optic cables and reimaging lens
	Positioning of the loop	MWS-3000 Microwave sensor or IS-3000-LS infrared sensor
	Temperature profile along the width	PM-3000 multiwave length scanning pyrometer
Reheat Furnace	Width, taper measurement of slab at entry	LM-3000/LM-500-LR7 Triangulation lasermeter
	Snapshot and positioning length measurement at entry	OB-3000-F Infrared sensor + LM-3000-F laser distance sensor
	Automatic positioning at exit	LM-3000-F Laser distance sensors
	Product detection at exit of reheat furnace	OB-3000-F Retro reflective single sensor
	Automatic positioning at entry	LM-3000-F Laser distance meters
Hot Rolling Mills	Coil diameter	LM-3000/LM-500-LR7 Triangulation lasermeter
	Strip centering/camber and width measurement	IS-3000-HW Infrared sensor
	Crop shear optimization	Dual IS-3000-HW Scanners
	Snapshot or length measurement	IS-3000 Infrared sensor + OB-3000 optical barrier
Cold-Rolling Mills	Mass flow	LM-3000-F Laser sensor
	Cut to length at shear	LM-3000-F Laser sensor + OB-3000-F retro reflective single sensor
	Coil diameter	LM-3000/LM-500-LR7 Triangulation lasermeter
	Strip centering/camber and width measurement	IS-3000 Infrared sensor + radiant bar
	Pin hole detection	PHD-3000 Infrared sensor + radiant bar
Processing Lines	Mass flow	LM-3000-F Lasermeter
	Loop control	LM-3000-F Lasermeter
	Coil diameter	LM-3000/LM-500-LR7 Triangulation lasermeter
	Pin hole detection	IS-3000 Infrared sensor + radiant bar
	New control of ladle preheater	IS-3000 Infrared sensor
	Level of metal in pot	LM-3000/LM-500-LR7 Triangulation lasermeter

In the FMCW (frequency modulated continuous wave) (ASC MWS-3000) the frequency difference is transformed via a Fourier transformation into a frequency spectrum, and then the distance is calculated from the spectrum. Since measuring frequency is easier than measuring time, the measurement is more precise. Pulse radar sensors are also available (ASC PR-3000), and in both cases, the measurement is unaffected by environmental conditions such as dust, heat, vapor, or light.

These sensors and systems are based on state-of-the-art technical development to improve productivity and quality and to reduce maintenance and downtime. Table 22.1 shows the major applications of the sensor technologies in the production process of steel, including blast furnaces, mines, lime and pelletizing coke plants, melt shops, continuous casters, reheat furnaces, hot- and cold-rolling mills and processing lines.

22.2 PRINCIPLES OF SELECTED APPLICATIONS

22.2.1 Continuous Caster Optimization of Cut

This application uses either two lasermeters (ASC LM-3000-F), or one lasermeter and one auto-focus laser Doppler velocimeter (ASC LM-3000-LSV). The lasermeter has visible laser alignment capability in a mill-duty, water-cooled, positive-pressure, air-purged housing. The LM-3000-F is used to position the torch cut machine and the second lasermeter, down the caster line (or the laser Doppler velocimeter, after the straightener segment and before the home-position of the torch cut machine) positions the head of the uncut slab. The top view of the application at the 3D overall caster is shown in Figure 22.1.

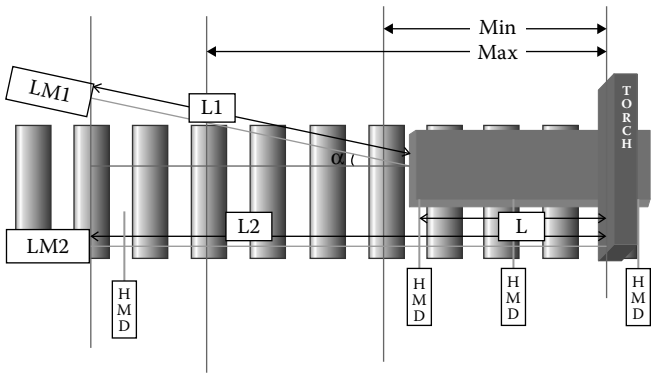


FIGURE 22.1 Top view of the continuous caster optimization of cut application.

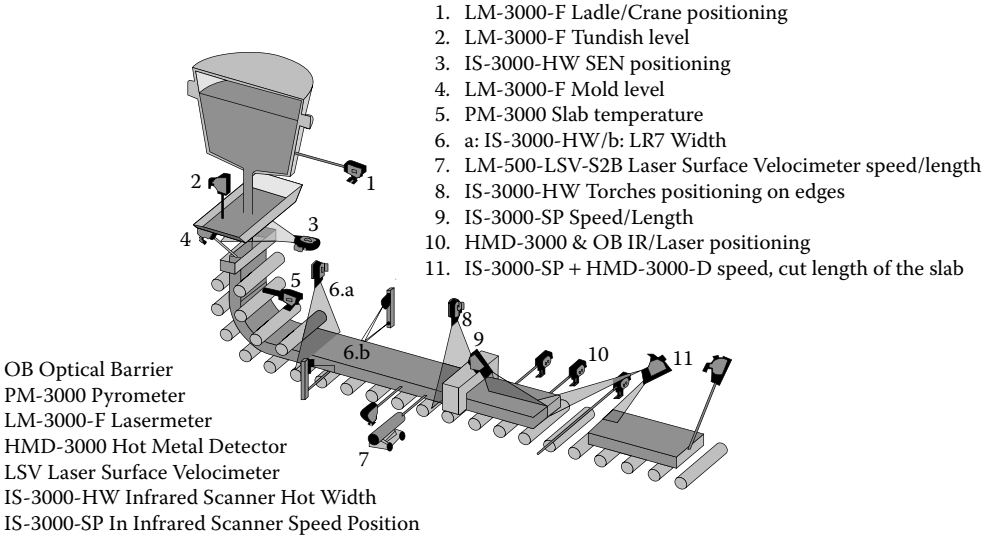


FIGURE 22.2 Applications for sensors in a continuous caster.

The principle of the application is that the first lasermeter positions the front of the torch machine, and the second lasermeter or laser Doppler positions the head of the slab. From the first laser (LM1), we get the distance L1. Since it is mounted in an angle α, the product of L1 and the cosine of this angle will give the perpendicular distance. The distance between the front edge of the slab and the torch machine L can be calculated as:

$$L = L2 - L1\cos\alpha$$

There are four hot metal detectors (HMD) mounted in different locations for self-calibration, first cut, and alarm if the cut slab is not moved away. The first HMD is mounted just before the torch-cut machine, and it is used for the first cut. The second and third HMD are mounted between the torch-cutting machine and the minimum length. This is used for self-calibration of the system and for the generation of an alarm if systems fail. The fourth HMD is used to generate the alarm if the cut slab is not removed from the roller table.

All these sensors are controlled by a dedicated processor with integral display unit, called the MAB-3000, through which we give the precut and cut commands to the torch-cutting machine. The program in the MAB-3000 records all the data for analysis and also displays a user-friendly screen to view the online data, such as length from torch, velocity of slab, position of torch, speed of torch, precut command, and cut command. Figure 22.2 shows applications for sensors in a continuous caster. Figures 22.3 through 22.7 show applications using lasermeters and laser Doppler velocimeters in casters.

Continuous caster optimization of cut is currently in use at U.S. Steel, ArcelorMittal, and VM Star.

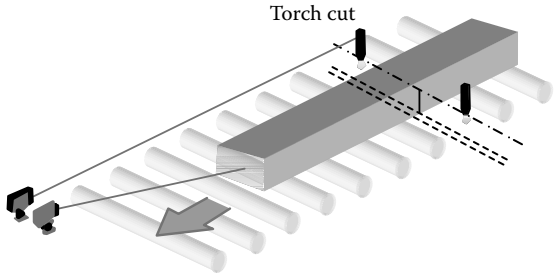


FIGURE 22.3 Billet, bloom, and slab cut to length.

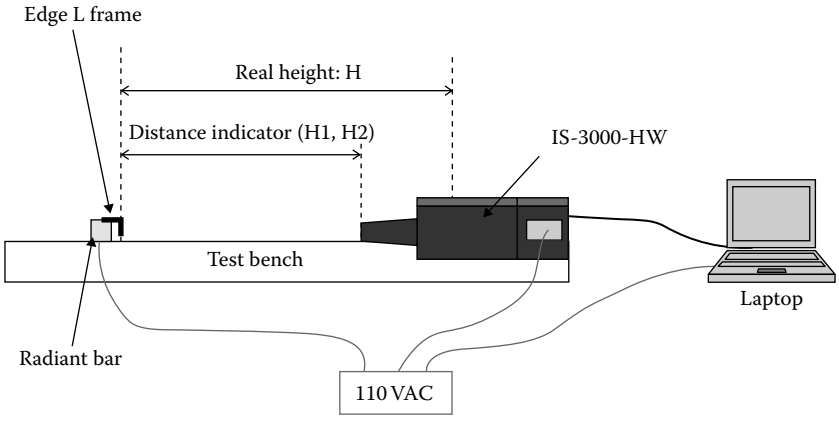


FIGURE 22.4 Slab positioning and length.

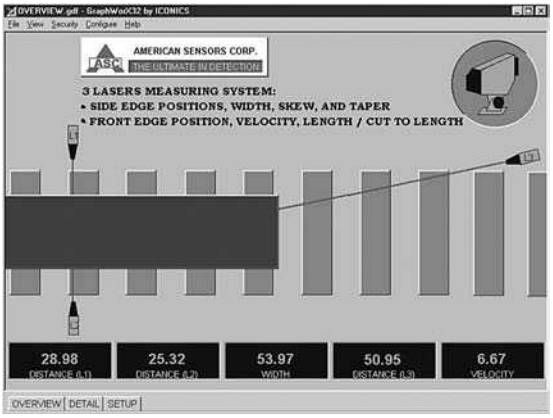


FIGURE 22.5 Overview display of measurement recordings.

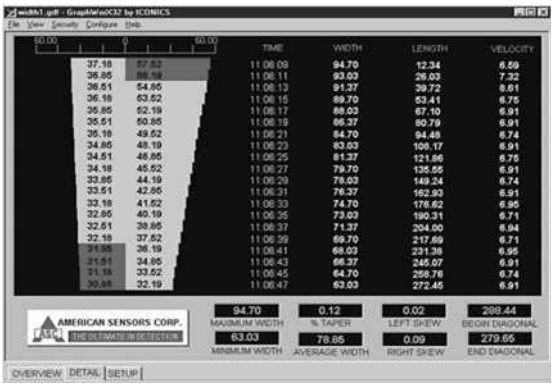


FIGURE 22.6 Detail display of measurement recordings.

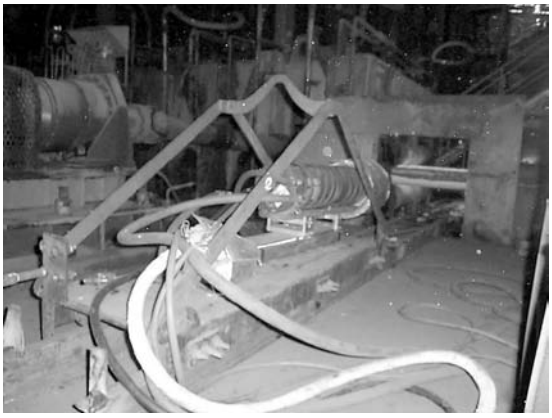


FIGURE 22.7 Auto-focus laser Doppler velocimeter in a slab caster measuring speed and length.

22.2.2 Width Measurement of Slab

This application uses two triangulation lasermeters (LM-3000-LR7D) to measure the width of the slab at slab caster or roller tables at entry of reheat furnaces. The system continuously measures and graphically displays the slab edge distance from the center line of the machine and the overall width (profiling option available also). The system can interface with level 1 and 2 systems to position torches for cutting and control automatic width adjustments. The measurement principle used by the sensor is optical triangulation. The sensor emits a laser beam. The diode array R observes through focalization optics L the image of the impact A of the beam onto the surface to be measured. The distance OA is related in a one-to-one way to the address N of the enlightened control diode (Figure 22.8).

Figure 22.9 shows how the sensors are mounted. The minimum and maximum measuring distance and measurement range are described in Table 22.2.

Figures 22.10 and 22.11 show applications using the ASC LM-3000-LR7D for width and thickness measurement.

Table 22.3 describes the major application requirements, such as sample rate, background light elimination, sensitivity, and strongest and weakest signal for this application. Table 22.4 describes the specifications and accuracy of the triangulation lasermeter in this application.

Width measurement of slab is currently in use at ArcelorMittal, AK Steel (Armco), and U.S. Steel.

22.2.2.1 Strip Centering/Camber and Width Measurement

This application uses infrared sensor (ASC IS-3000-HW) to detect strip centering/camber and width measurement. The sensor is placed vertically or at an angle so that the scanner is perpendicular to the axis of the roller table. The sensor detects infrared radiation emitted by the work piece, and provides an analog output and serial outputs proportional to the angular position of hot products within its field of view.

Communication via HyperTerminal is used to send/receive data with the sensor. The sensor is linked to a laptop via RS232 or RS485 duplex. The sensor software setup is shown in Table 22.5.

Figure 22.12 shows the IS-3000-HW installed at ATI. Figure 22.13 is a typical application for the IS-3000-HW.

Strip centering/camber and width measurement is currently being used at Alcoa, Alcan and ATI.

22.3 SENSOR SYSTEMS

22.3.1 Systems Developments

Complementing the improvements in the accuracy and reliability of noncontact sensors, the supporting electronic systems have expanded the use of the sensors. Advances in the resolution and speed of graphics have allowed sensor outputs to be more clearly and dynamically displayed in pulpits and to be coupled with other measurements and information. Databases have been implemented in level 1.5 and level 2 systems, so noncontact measurements are stored and searched rapid diagnosis of process failures and quality defects.

The most dramatic developments supporting noncontact sensors have been the use of analysis software to estimate conditions that cannot be measured for the data and the use of learning software for optimum productivity and quality. Some of these developments are discussed only briefly. They

TABLE 22.2
Minimum and Maximum Measuring Distances and Measurement Ranges

Minimum measuring distance (Dmin)	The distance from the front face of the sensor at which measurement can start
Maximum measuring distance (Dmax)	The distance from the front face at which measurement ends
Full scale span or working measurement range	Dmax-Dmin, the distance range over which the sensor will measure displacement

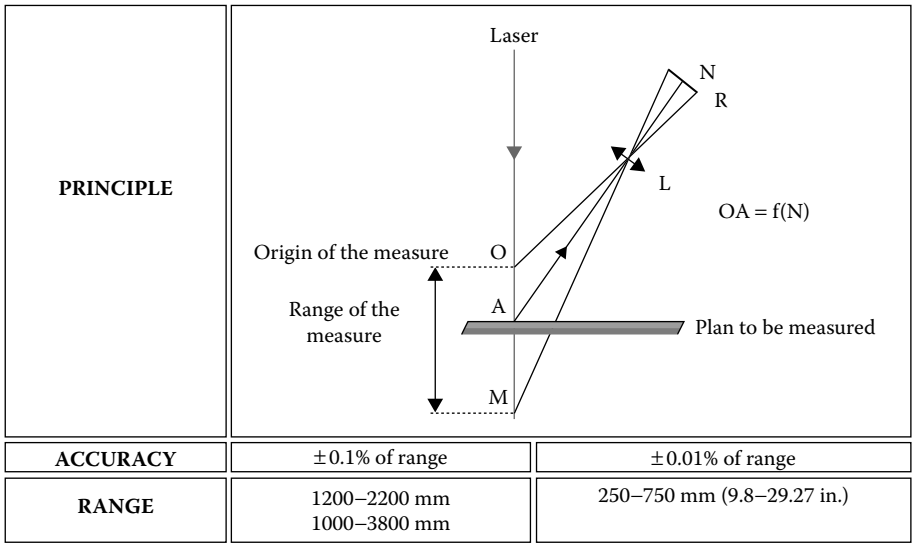


FIGURE 22.8 Principle of triangulation lasermeter (ASC LM-500-LR7D).

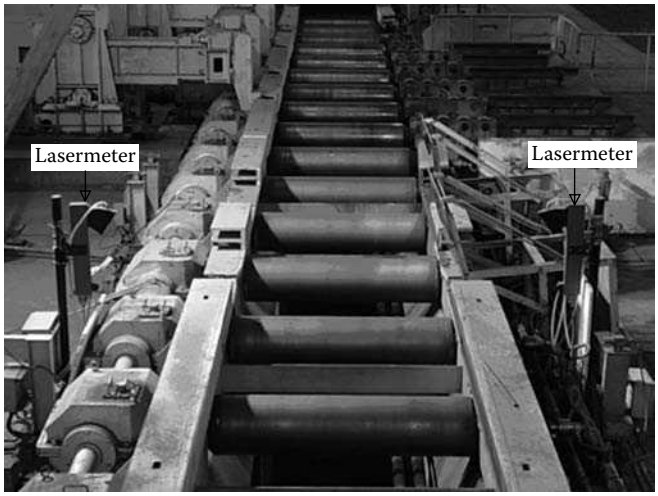


FIGURE 22.9 How the sensors are mounted in the width measurement of slab application.

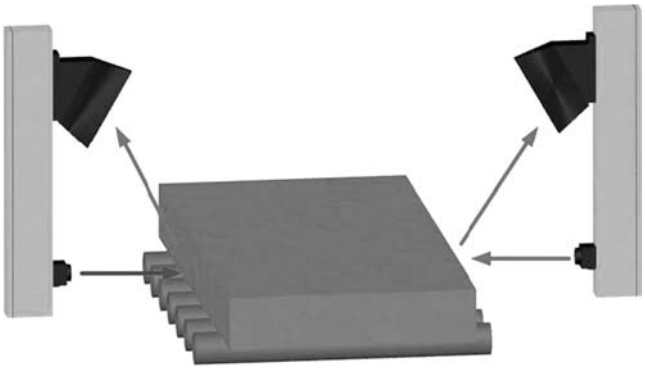


FIGURE 22.10 Width measurement.

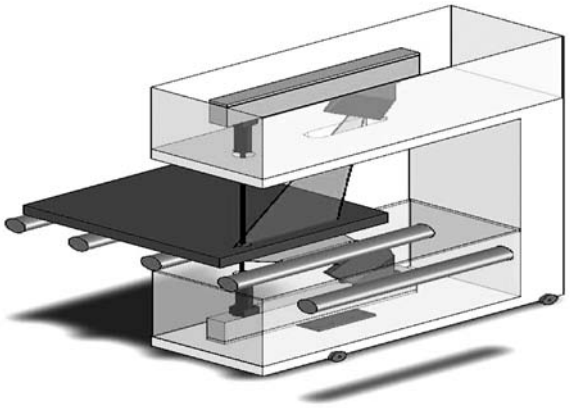


FIGURE 22.11 Thickness measurement.

are in various stages of use, including some that are routinely used and others that have only been tested in production.

To simplify the integration of the sensors discussed in this article, into a customer's existing control system, ASC provides an interface unit called the MAB-3000. This unit receives all sensor inputs associated with the application and provides a local visual display to allow for easy set up and troubleshooting. The MAB-3000 provides local display of the application results and provides data storage of the various inputs and calculations. The MAB-3000 also provides

TABLE 22.3
Application Requirement

Sample rate	The rate at which data samples are obtained from the sensor. The maximum attainable sample rate is determined by the operating mode chosen and the reflectance of the target.
Background light elimination	A user-selected operating mode in which the sensor captures an image with the laser off and subtracts it from the subsequent image taken with the laser on. The maximum sample rates are lower, but performance in brightly lit areas is improved.
Sensitivity	A measure of the relative ability to detect small amount of reflected light. Since different models use different laser power levels and have differing distances to the target surface, sensitivity varies with the model. The better the sensitivity, the higher the attainable sample rate on surfaces, such as clear glass, gloss black paint, or shiny plastic.
Strongest signal	The triangulation lasermeter cannot be overloaded and measures accurately even when a mirror reflects the entire beam back into the detector.
Weakest signals	On surfaces of polished glass or water, almost the entire beam passes through or is reflected away. The LR7 can operate on the small remaining amount of scattered light.

TABLE 22.4
Optics and Accuracy Specification

Specification	LM-500-LR7						
	LR7-F	LR7-G	LR7-H	LR7-I	LR7-J	LR7-K	LR7-L
Dmin	7 in. 178 mm	3.5 in. 89 mm	2.25 in. 57.2 mm	2.5 in. 63.5 mm	0.9 in. 22.9 mm	0.6 in. 15.2 mm	0.5 in. 12.7 mm
Full scale span	6 in. 152 mm	4 in. 102 mm	2 in. 50.8 mm	1 in. 25.4 mm	0.5 in. 12.75 mm	0.25 in. 6.35 mm	0.125 in. 3.175 mm
Dmax	13 in. 325 mm	7.5 in. 190 mm	4.25 in. 108 mm	3.5 in. 89.9 mm	1.4 in. 35.6 mm	0.85 in. 21.6 mm	0.625 in. 15.87 mm
Laser class	II	II	II	II	II	II	II
Accuracy	±0.006 in. 0.15 mm	±0.004 in. 0.10 mm	±0.002 in. 0.05 mm	±0.001 in. 0.025 mm	±0.0005 in. 0.012 mm	±0.0003 in. 0.007 mm	±0.00015 in. 0.0038 mm
Target standoff	10 in. 254 mm	5.5 in. 139.7 mm	3.25 in. 82.55 mm	3.0 in. 76.2 mm	1.15 in. 29.21 mm	0.725 in. 18.415 mm	0.5625 in. 14.288 mm
Laser spot size (microns)							
@Span center	95	70	65	60	40	35	30
@Span endpoints	350	300	220	200	130	100	500

TABLE 22.5
Infrared Sensor Software Setup

Gain	Threshold	Delta H1	Delta H2	Output Rate	Window	Average	Units	Max Angle
2	50 mV	0	0	Low	Off	Normal	mm	4010



FIGURE 22.12 Camber measurement application installed at ATI.

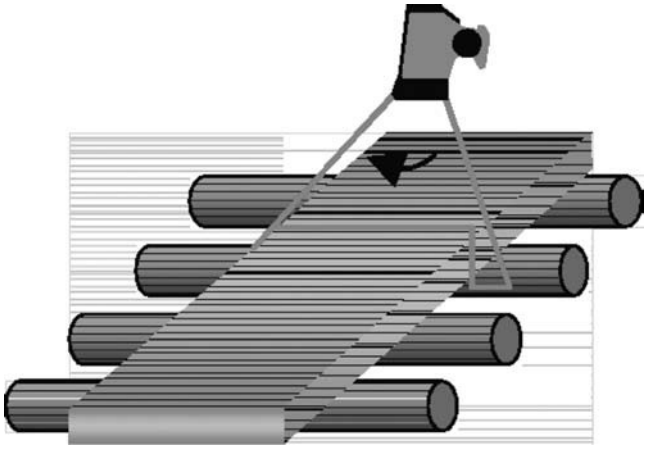


FIGURE 22.13 Typical application for the IS-3000-HW.

output communication bus capability, in a number of standard formats, such as Ethernet, Profibus and Serial Link, as well as hard-wired analog and digital outputs, to feed the sensor data and application results to the customer control system.

22.3.2 Systems Techniques

In many installations, noncontact sensors are being protected from the environment of casters, rolling mills, and hot processing with wireless transmitters and receivers. This has involved the use of various types of technology to move data from the sensors to the analysis and display processors, including simple wireless connections (like Bluetooth) that are used to access the sensors and sensor database for diagnostics. The advantage of a wireless connection is its ability to avoid damage to the connecting wires from water, heat, scale, and collision with metal products in the process environment.

Data from sensors are now routinely stored in structured files that comply with standard programming tools for searching, sorting, and displaying. Such databases were developed for business data, but have become robust and generally available where hard drives are installed. The standard software tools with these systems allow more complex and complete displays of the data at minimal cost.

Graphic trending has become standardized in the form of real-time spreadsheets or similar tools. These graphics tools provide two- and three-dimensional displays of the output from the sensors. There are more colors, patterns, and methods of mixing the trend of variable with diagrams of the equipment, so the meaning of the displays is more evident.

The use of multivariable analysis is being applied to sensor systems so that conditions like crack potential or cleanliness ratings can be detected and conveyed to the operators during the processing. These conditions are derived from historical and theoretical relationships between a desirable attribute and a measurable parameter. There are a number of statistical and theoretical methods used to develop these relationships. They can be mathematically simple, like polynomials, or complex like simultaneous nonlinear differential equations.

Quality models or quality engines are being developed in software to predict key quality properties from the sensors. The predicted properties then are used in real time to recommend manual or automatic adjustments to process speed, guidance, temperature, and other parameters. These models are largely theoretical and involve element mathematics to estimate stress, grain size, porosity, and phase structure of the metal. These models seek to control cracking, inclusions, pores, chemical segregation, and dimensional deviations in the processing of flat-rolling products.

In some systems, statistical models of parameters are derived from least square error analysis of the sensor data to set up target conditions to minimize quality problems and to operate at the highest possible speeds. Programming methods are automatically applied in systems to support quality objectives.

Expert systems or neural-network models are used to establish limits and optimum settings of process parameters. Expert systems use a set of rules that are automatically

adjusted from the measurements, even if the measurements are taken long after the parameters have been applied. For example, noncontact temperatures are measured along the surface of a cast slab and then related to spray water settings in the secondary spray area on future casts. The rules that evolve from these measurements can be used to change or limit the operation of the water sprays. Neural networks operate in a similar fashion, but instead of mathematical rules, neural networks use equations that simulate the operation of biological neurons that are automatically adjusting to the feedback from the sensors.

22.3.3 System Examples in Slab Casting

The slab caster has many examples of systems with noncontact sensors in hot-rolled product. The level of liquid in the mold involves several sensors and complex systems analysis. The objective of most of these complex systems is to control the cracking and uniformity of the four surfaces of the slab in the mold. Multivariable analysis has been applied to the laser scanning of the exposed surface in the mold and has been tied to the speed, the submerged nozzle condition, and observations of the surface by experienced inspectors. This analysis was used in real time to set casting speed and the rates of lubrication on the surface in the mold.

There are several complex systems involved in the use of noncontact level measurements, like the radioactive isotope and eddy current sensors that track the movement of the liquid in the mold. Expert systems and simulation models are used to predict the level from the weight of the tundish, the weight of the ladle, the conditions of the submerged nozzle, and the casting speed. The noncontact sensors are then used to calibrate those models, so the level can be controlled to follow a series of ramping and holding steps, which improve the quality and reliability of the startup, the changes in the width, or the changes in the tundish. These models are quite complex and involve level 1 and level 2 systems.

Another control system with noncontact sensors involves the measurement of width and thickness to optimize the shape of the slab. Because the slab thickness is dynamically changing with hydraulic cylinders in the segments, the slab thickness needs to be measured and modeled for thermal shrinkage, cooling and compression with the hydraulic cylinders, speed, and water cooling. The measurement of the thicknesses and the width are supplemented by models predicting the bulging and guttering of the surfaces, which are displayed to alert the operators and to feed back to the cooling system. Multivariable analysis and finite element models are used to tie these variables together to establish a basis to minimize changes in slab shape.

The estimation of the weight from the length and width of the cut slabs has evolved in sensor systems. The weight of the slab is critical to the yield of flat-rolled products, and noncontact velocity measurements are beginning to be preferred over contact sensors as a reliable means of gauging the length of the slab sensors. The noncontact velocity measurements involve tracking surface features that require special algorithms and learning systems. Once the velocity is determined from the data, the weight of the slab is estimated from the width and thickness measurements. These measurements are adjusted for the expected shape of the cross section, which is never perfectly rectangular, and learning systems are used to estimate the cross section from the noncontact measurements, history of the type of slab, and the prior measurements of weight.

In other systems, there is a control of internal quality with the use of the noncontact measurement of speed and dimension. The slab caster uses a soft reduction in thickness of 5% to 10% just before the last liquid solidifies at the center, and the location of this reduction is determined with an estimation of the liquid present throughout the caster, which involves finite element models and feedback from the speed and dimensions. Expert-system rules are often involved in the final setting of the strategy for control, once a history of the center porosity and chemical segregation have been determined.

Another critical internal quality issue is cracks. Similar to the soft reduction control, cracks are estimated from the measured speed and dimensions, using multivariate analysis and models with finite element simulations that calculate the strain on the solidifying surfaces inside the slab as they are bent and supported through the machine. The casting speed and the distribution of water in the various zones are adjusted with those of the models, and in some installations, an optimum speed and a water flow are recommended based on these models to minimize the potential for internal cracking. This recommendation is used dynamically as the noncontact sensors for velocity and thickness update the models.

Systems are being tested that use noncontact optical devices to improve the surface quality of the slab. Pattern recognition software is being applied to the data from lasers or cameras directed at the surface of the slab. The severity of the oscillation marks is estimated, and the oscillation pattern is being modified in real time. With the use of hydraulic oscillators, it is possible to change the frequency, the positive amplitude, and the negative amplitude of the oscillation, which have different effects on different steel grades. The adaptive software, like expert systems and neural networks, has been applied to this problem, and different noncontact sensors have been evaluated, including eddy current and infrared sensors.

Another problem that is being tackled by advances in systems with noncontact sensors is the slip of the dive rolls. In the past, the driven rolls controlling the speed of the slab have been allowed to slip or they fail to drive the slab at all. The noncontact sensors tracking the velocity of the rough surface can now be used in combination with the infrared temperatures and the position of the tundish nozzle to determine the severity of the slip. As needed, the hydraulic pressure on the drive rolls is increased to reduce the slip or the operator is alerted to take other action. Early action can mitigate the sticking of the slab in the caster.

Comparison between the target velocity and the noncontact velocity can be used to alert the operator to the blockage of the submerged nozzle in the tundish or the slide gate on the

ladle. Action can be taken to increase argon shrouding or to change the nozzles before the cast must be aborted. The criteria for these control actions have been developed from the historical data of the noncontact sensors for particular grades and sizes. Various methods of analysis of the data have been used to determine and adapt the criteria.

Many applications for the slab caster have been proposed to utilize surface inspection devices that are also noncontact. In general, the pilot studies with digital cameras and associated software have not provided confident identification of defects, such as cracks, excessive mold powder, or pinholes. The state of the pattern recognition software is considered one of the weaknesses of these devices, and as better software is developed, it is believed the digital cameras will be used to help control the surface quality.

Current systems to protect the machine from breakout of the liquid metal in the mold are becoming more complex and effective. These systems rely primarily on contact thermocouples in the mold, but they are being improved by adding the signals from noncontact infrared pyrometers in the secondary spray system. The systems now include models to estimate the shell thickness. The expected temperature in the spray area is compared to the signal from the pyrometer to determine automatically if the caster needs to be slowed down to avoid a thin-shell breakout.

22.3.4 System Examples in Hot Rolling

In the next processing step for flat-rolled products, the slab moves into the reheat furnace to be prepared for hot rolling. The systems that control the firing of these furnaces now utilize noncontact measuring devices for width, thickness, and length to position the slabs and select zone temperatures. These systems utilize thermal models of the heat flow in the slabs to estimate the temperatures along the length and width. The models are particularly critical when slabs with different thicknesses are charged into the furnace together. The feedback from the infrared pyrometers at the exit of the furnace is used to adapt the models for each type of steel and its associated surface conditions.

At the hot mill, a number of systems are being used to improve the use of noncontact sensors. Analysis of laser velocity and position sensors has provided width measurement at the mill and estimations of camber and surface flatness. Even the amplitude of the waves on the edge or the center of the rolled product are determined and fed back to the operator for adjusting the roll bending or roll gap. The analysis for these applications involves Fourier transforms and digital filters in the systems.

There are also pattern and shape analysis systems for the head end of the products as it emerges from the rolling mill. The objective of these systems is to determine the severity of turn up or turn down on the head end. Severe changes in shape of the head can lead to damage to the equipment or cobbling of the product in the mill. Laser and noncontact devices are used to measure the position of the head, and pattern software is used to classify the shape for the system. The shape of the head is also used in systems that control the threading of coiling furnaces and the automated cropping of the ends. These systems often include adaptive functions for the tuning and input from the operator manual offset.

Noncontact lasers and other devices are used to measure the eccentricity and vibration around the rolling mill. These are coupled to analysis systems that determine eccentricity of the rolls, or problems with the mechanical system, such as chatter or slip. The eccentricity analysis is used in real time to regular the gap between the rolls for control of the product thickness. Vibrational analysis systems are used to alert maintenance personnel to the need to perform further work on the mill.

There have been limited trials on using noncontact measuring devices to automatically steer the flat products through the mill. Differential forces using contact measuring across the width of the rolls has been used with some success, but now the additions of the laser measurements of edge position, velocity, and thickness across the width may allow these systems to provide automatic steering and decrease camber and hook. It also appears that these systems may be improved by adaptive software to deal with the changing friction and temperature in the mills. Historical data and different models may need to be utilized before automatic steering becomes a reality.

Infrared temperature sensors continue to be used in more and more sophisticated control systems at the hot rolling mill. The feedback from the sensor is used in systems to predict forces in the mill. The relationship between the hardness of the metal and the temperature is modeled in the controls for setting the gap between the rolls, and the measured temperature is used with the models of heat transfer to estimate the temperature inside the steel. Various methods are used by different systems to adapt and learn the temperatures and hardness under different conditions and products.

The infrared sensors are critical for the systems that regulate the quenching of the product after rolling. Heat transfer models are combined with the sensors to estimate temperature inside the product and to estimate the effectiveness of the quench headers on the top and bottom. Some effort is being made to use this feedback to estimate the size of the grains in the metal and the metallurgical phases that are present. The sensors are being expanded to scan the entire width, and this data is stored in databases to be used for the quenching and for control of thickness. Metallurgical models are proposed for these systems as the data and the devices become more reliable.

Noncontact sensors are routinely used to determine the true velocity and shape of the products coming through the hot mill. These devices can be used to estimate the mass flow by the control systems with the proper models and adjustments. Mass flow control is critical to the control of tensions and thickness in a tandem mill with multiple stands. Width control is also dependent on the complex analysis of the width sensors combined with the models for the roll gap and the edge rolling. A number of elastic and plastic effects for different alloys are considered in these systems before the sensor measurements can be used to tune the width control.

The signals from the noncontact measurements of velocity can be used to determine the slip of the product in the mill. This is critical for accurate control of the thickness, width, and flatness from the level 1 and level 2 systems. The signals are also used in the diagnoses of chatter and lubrication with the appropriate models in the systems.

Systems are being evaluated to use noncontact eddy current, laser, and ultrasonic sensors to estimate the quality of the product coming out the mill. With effective software, these systems appear to indicate the porosity, grain size, and phases present in the steel. These systems are in the early stages of evaluation in rolling mills.

Noncontact optical systems are also being used in the rolling mills to inspect the surface for cracks, porosity, roll marks, and scale. As the software and the adaptive approaches in these systems improve, the effectives of the inspection will improve.

22.3.5 System Examples in Finishing

Cold mills have complementary systems that use the noncontact sensors for velocity and dimensional control. The use of noncontact devices in systems for controlling the flatness and the roll gap are the most mature. There are also optical inspection systems used in these mills. Between and after rolling, many steel products are annealed and cleaned, where noncontact infrared and optical inspection devices are used. There are systems that estimate the temperature, where it cannot be accurately measured, with existing infrared devices and heat transfer models.

There are loop controllers and steering systems in the annealing and cleaning operations that use position, hole-detection, or infrared sensors. Most of these systems employ dynamic models of mass flow, and compensate for thermal expansion and alloy properties to accurately control the movement of the flat-rolled product. Where automated welding is required to complete the processing, the sensors are provided with heat transfer models to complete the control and tuning of the welding operation.

Finally, there are systems that use noncontact devices in the tracking of flat rolled products, such as coils, stacked plate, and sheet. These tracking systems use mapping and dynamic simulation software to estimate where each piece is located and are coupled to the noncontact sensors that confirm the positions. Bar codes and other identifying tags are used, when possible, but otherwise, complex software is coupled to position sensors to improve the reliability of the tracking with pattern recognitions and learning.

23 Cold-Rolling Mill Vibration and Its Impact on Productivity and Product Quality

Tom Farley

CONTENTS

23.1 Introduction 255
23.2 Background Vibration Theory 255
23.3 Modeling Natural Resonant Vibrations of a Rolling Mill Stand 256
23.4 Low-Frequency Forced Vibrations 256
23.5 Torsional Chatter Vibration 256
23.6 Third Octave Gauge Chatter Vibration 257
23.7 Fifth Octave Chatter (Roll and Strip Chatter Marks) 259
23.8 Summary 262
References 263

23.1 INTRODUCTION

This chapter describes the common types of mill vibration that can be experienced during the cold rolling of steel and aluminum. Two main problems are highlighted in more detail, namely third octave gauge chatter and fifth octave chatter. Third octave gauge chatter still poses a difficult problem for the metal rolling industry, in some instances causing significant financial loss due to a reduction in cold-rolling speeds. Fifth octave chatter is more common in mills and can cause significant surface quality issues.

23.2 BACKGROUND VIBRATION THEORY

All machines vibrate during operation, and most of these vibrations do not cause any problems. Typically, the most damaging vibrations involve a natural resonance of the machine, which significantly increases the displacement of critical components. It is important to understand the difference between forced and resonant vibrations. Looking at a simple mass on a spring, as shown in Figure 23.1a, can help with this. For simplicity, we can assume that the mass on the spring has a single natural resonance where the mass moves up and down, compressing and stretching the spring. The mode shape associated with the resonance is defined as the motion of the mass, and the natural frequency of vibration, ω_n, is proportional to the square root of the spring stiffness, k, divided by the mass, m. Any damping within this system can be denoted by the fraction of critical damping, ζ, equal to the ratio of the damping constant, c, to the critical damping of the system. Damping will reduce the resonant frequency slightly and will cause an exponential decrease in the amplitude of the mass if it is disturbed from its resting position.

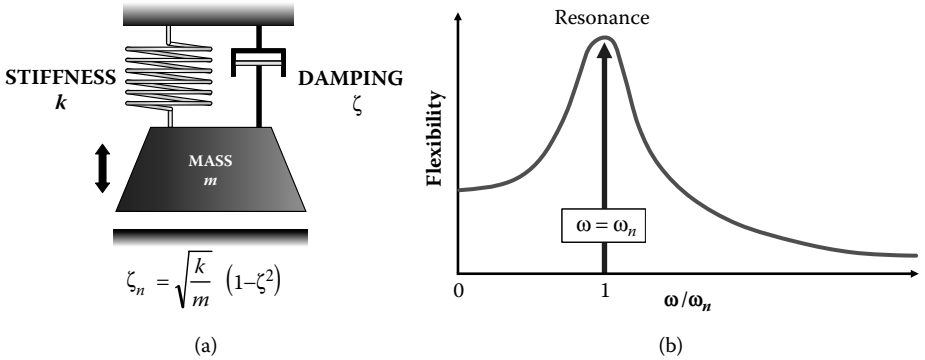


FIGURE 23.1 (a) Simple mass and spring system with (b) the forced response (or flexibility) of this system when subjected to a cyclic force over a range of frequencies.

Figure 23.1b shows the forced vibration response for a simple mass on a spring, where flexibility is defined as the displacement of the mass per unit of exciting force. If a periodic disturbance or exciting force is applied to the mass at a frequency equal to the natural resonant frequency, then the mass will move through a very large displacement (limited by any damping associated with the resonance). It is clear that the system is very flexible when excited at or near its resonance. If the periodic exciting force is applied at a frequency below or above the resonant frequency, then the flexibility is less and relates to the stiffness or mass of the system, respectively. In the limiting case, at zero frequency, the flexibility of the system will be given by Hooke's law.

There is a special class of vibration called *self-excited vibration*. Self-excited systems begin to vibrate of their own accord spontaneously, the amplitude increasing until some nonlinear effect limits any further increase. The alternating force that sustains the motion is created by the motion itself and stops when the motion stops. A natural resonance is often involved in the self-exciting behavior, providing the structural flexibility. Common examples include machine tool chatter, the sounds from some musical instruments, aeroplane wing tip flutter, chimney sway, and bridge vibration. A famous example of self-excited bridge vibration is the Tacoma Narrows Bridge in 1940. Here, aerodynamic instability at high wind velocities produced extreme amplitudes of structural vibration ending in the destruction of the bridge. It is important to note that there was no independent external cyclic force exciting this structure. The force that sustained the vibratory motion came from the motion of the bridge itself, requiring only a small initial disturbance to get it started.

Third octave gauge chatter, one common type of mill vibration, falls into this self-exciting category. The physical mechanism that produces the sustaining alternating force relates to the continuity of mass flow through the rolling mill bite. Like the bridge, the mill will vibrate without an independent external cyclic force to excite it.

It should be noted that the terms third and fifth octave relate to the definition of musical frequency ranges and were used historically to distinguish these two problems.

23.3 MODELING NATURAL RESONANT VIBRATIONS OF A ROLLING MILL STAND

To provide a better understanding of this phenomenon, a *finite-element* computer model was developed to predict the natural modes of vibration of any mill stand (Farley et al. 2002, 2006). The model required input of physical dimensions and elastic properties of the materials making up the mill stand frame, rolls, bearings, and hydraulic actuators. To capture effects of roll and frame bending, the mill stand frame and rolls were modeled as multiple beam elements, each with two or three degrees of freedom. Hertzian contact was assumed between the work and backup rolls. The stiffness of the aluminum strip was calculated automatically using a roll gap model, based on the mill geometry, the material being rolled and the rolling schedule. The model also included one-dimensional springs to account for hydraulic connections and discrete masses to account for interconnecting drive shafts and chocks. The model could be asymmetric (top vs. bottom and operator vs. drive side). The model automatically assembles large mass and stiffness matrices, with up to 250 degrees of freedom (depending on the mill), before calculating the eigenvalues or natural vibration frequencies of the structure. The model was used to understand the key mill stand resonant vibration modes responsible for third and fifth octave problems, as described in Sections 23.6 and 23.7.

23.4 LOW-FREQUENCY FORCED VIBRATIONS

The simplest type of mill vibration is found in all mills and is a forced vibration such as that due to roll eccentricity. These frequencies are usually lower than any of the resonant frequencies of the mill stand, and so gauge variation is a result of the stiffness of the mill and material being rolled. This type of gauge variation from roll eccentricity can represent a significant proportion of the total gauge variation of the product delivered to the customer. In some cases, it is possible for this vibration to be worsened by excitation of torsional resonances of the main, unwind, and rewind drives of the mill.

Typically, the resonant vibration modes of a rolling mill involving translational motion of the rolls have frequencies greater than 50 Hz. If excited, most of these modes will not be detrimental to rolling, but some specific modes can be very damaging to mill productivity and/or product quality. These modes are responsible for the main types of what is termed *mill vibration* and are described in this chapter.

23.5 TORSIONAL CHATTER VIBRATION

Torsional chatter vibration involves cyclic angular speed variation of components in the rolling mill drive system, often amplified by excitation of natural resonances of the drive. Such motion can produce variations in surface finish on the strip being rolled and/or gauge variation. Typical frequencies of torsional chatter occur between 5 and 25 Hz.

Torsional chatter usually occurs as a result of malfunctioning or instability of the motor control system, an instability of the lubrication in the roll bite, or a forced vibration within the drive. Moller and Hoggart (1967) showed that unstable torsional chatter could be considered to be self-exciting when the coefficient of friction decreases with increasing speed, as found in the mixed hydrodynamic-boundary lubrication regime.

Solutions to torsional chatter problems involve the stabilization of mill drive controllers, minimization of roll eccentricities, and other forced vibrations that could excite torsional resonances, as well as the avoidance of certain roll speeds and excessive rolling reductions that cause lubricant breakdown and instability.

23.6 THIRD OCTAVE GAUGE CHATTER VIBRATION

A third octave gauge chatter problem can produce significant gauge variation from a few percentages of nominal gauge up to higher percentages, and can even cause strip breaks. This is due to excitation of one of the natural resonances of the mill stand. Commonly, these natural resonances have frequencies between 90 and 150 Hz, but sometimes are as high as 300 Hz. These frequencies are much higher than the bandwidth of many gauge control systems, so the gauge variation is averaged over several vibration cycles and not seen by the system. The onset of gauge chatter vibration occurs at high rolling speed and usually can only be stopped by reducing the speed. It is rarely possible to stop the vibration by increasing speed if the mill is truly unstable. Typically, the amplitude of vibration will rise very rapidly (in less than a second) and the vibration will become audible at the vibration frequency. Without vibration monitoring equipment, this audible noise is often the only indication to the mill operator that the mill is vibrating. Some lower frequency modes will also be felt in the ground supporting the mill housing.

In tandem steel and aluminum cold-rolling mills, the vibration typically originates in one of the final high-speed stands. However, as observed in single-stand cold rolling of aluminum, the problem can be just as severe and therefore is not a consequence of tandem rolling itself. It is inherent in every individual rolling stand for reasons described below.

During gauge chatter, the gauge variation will be fairly uniform and in-phase across the strip width. It is often only detected by careful off-line thickness measurements of the final product. Figure 23.2 shows a simulated gauge variation produced by vibration with several vibration cycles per meter length of strip.

Figure 23.3 shows the typical rolling mill resonances that can become excited to produce gauge chatter (Farley et al. 2002). The most common mode for a four-high mill is shown in Figure 23.3a and involves the top two rolls moving vertically in antiphase against the bottom two rolls. The mill stand housing is also involved in the vibration mode. There is very little deflection of the work roll barrels, which helps us understand why the gauge variation is similar at all positions across the strip width. Figure 23.3b shows a less common gauge chatter vibration mode involving significant bending of the roll barrels.

As stated earlier, this type of vibration is self-exciting. There is a feedback mechanism that provides a sustaining force to increase the mill vibration amplitude, which is a consequence of the vibration motion itself. This mechanism has its origins in the roll bite and is a consequence of the continuity of mass flow through the stand.

$$H_i V_i = H_o V_o \tag{23.1}$$

where H_i and H_o are the entry and exit gauges and V_i and V_o are the entry and exit strip speeds. Figure 23.4 illustrates the mechanical feedback loop that exists in every mill stand (Evans et al. 1996).

On the basis of continuity of mass flow through the mill stand during rolling, it can be shown that a change of exit

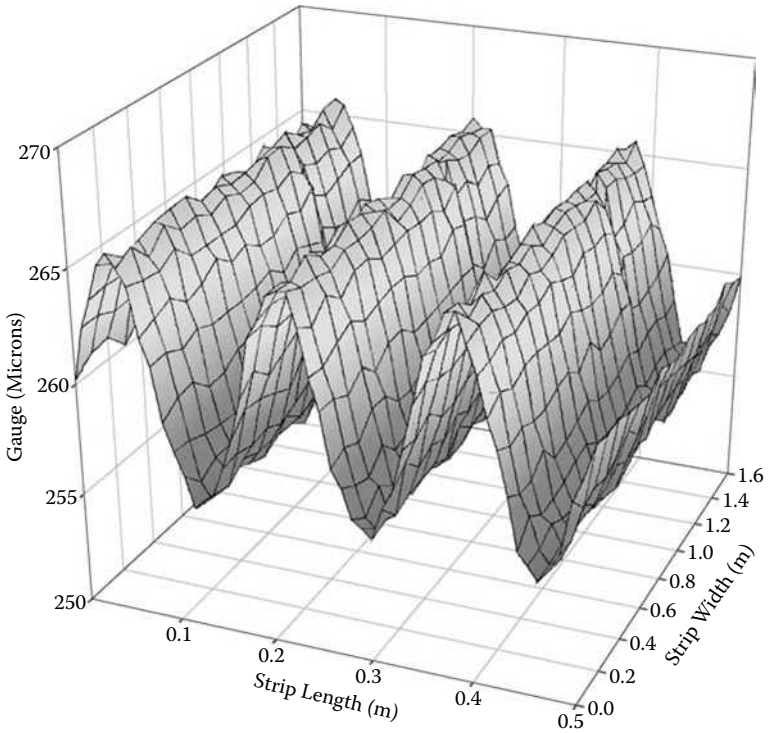


FIGURE 23.2 Simulated three-dimensional gauge trace for a 0.5-m section of sheet product showing ±2% gauge variation due to third octave gauge chatter.

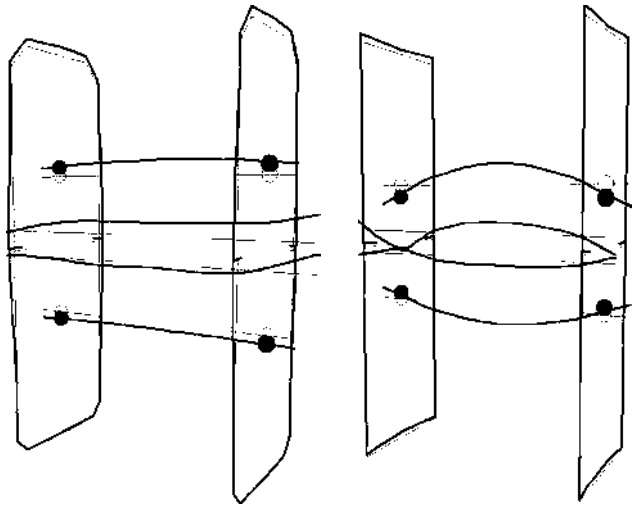


FIGURE 23.3 Typical mode shapes of rolling mill resonances that become excited during third octave gauge chatter, as predicted by the mill stand vibration model described above: (a) most common mode with a frequency between 100 and 150 Hz; (b) less common higher frequency mode. The lines represent the central axes of the rolls and housing frames in a four-high mill. (After Farley, T. W. D., Rogers, S., Nardini, N. 2006. *Proceedings of the IOM3 Conference: Vibration in Rolling Mills*, London, U.K.)

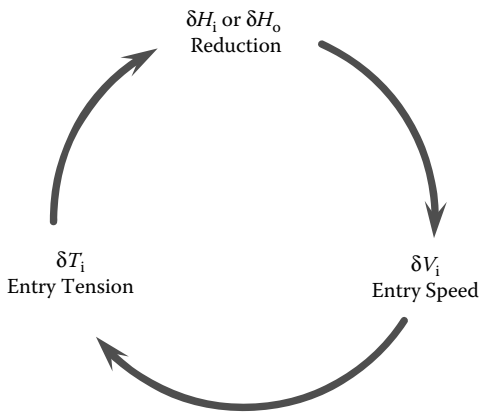


FIGURE 23.4 Mechanical feedback loop that exists in every mill stand with the potential to cause self-excited third octave gauge chatter.

gauge will produce a change in entry strip speed, assuming that the entry gauge and exit speed remain constant.

$$\delta V_i = \frac{V_o}{H_i}\delta H_o \tag{23.2}$$

The change in strip speed at one end of the entry strip compared to the other, V_c, will produce a change in entry strip tension, T_i, as follows:

$$\delta T_i = K_s \int (\delta V_i - \delta V_c)dt \tag{23.3}$$

where K_s is the stiffness of the entry strip given by the following equation:

$$K_s = E\frac{WH_i}{L} \tag{23.4}$$

where E is the elastic modulus of the material being rolled, W is the strip width, and L is the length of the entry strip over which the speed difference was applied.

A change in entry tension will produce a change in exit gauge, thus completing the loop as follows:

$$\delta H_o = \left(\frac{\partial H_o}{\partial F}\right)\left(\frac{\partial F}{\partial T_i}\right)\delta T_i \tag{23.5}$$

where F is the rolling load for the pass. The ratios in Equation 23.5 are roll gap sensitivities that will depend on rolling variables, such as the roll gap friction.

There is a 180-degree phase change around the mechanical feedback loop in Figure 23.4, 90 degrees coming from the mill vibration mode and 90 degrees from the integration required to convert strip velocity to tension in Equation 23.3.

Analogous to electrical control system instabilities, if there is a 180-degree phase change around the loop, then the loop will go unstable as the gain is increased above a certain threshold value. From the above equations coupling each term in the loop, it can be seen that gain is proportional to the exit speed of the strip (Equation 23.2). This explains why rolling mills prone to gauge chatter vibration exhibit the problem suddenly as the speed is increased above a threshold value. Normally, this threshold speed cannot be exceeded, and to do so would cause strip break and/or damage to the mill.

It can be shown that relaxing the assumption of constant exit speed in the above formulation and allowing a variation in forward slip has a small stabilizing influence on the chatter vibration due to a slight reduction in the gain of the feedback loop.

It is possible to formulate the above feedback equations in the Laplace domain and to then apply a standard condition

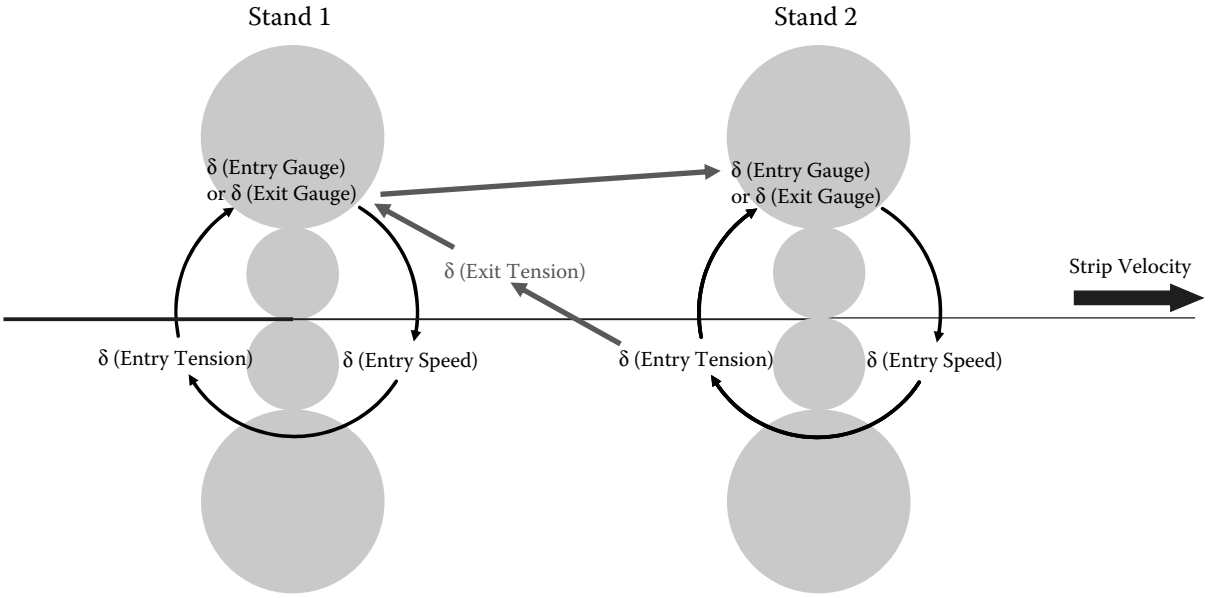


FIGURE 23.5 Interactions between two neighboring stands in a tandem cold mill during mill vibration showing feedback of strip tension variation and feedforward of strip gauge variation.

for the threshold of self-excitation. This results in the following equation for the critical rolling speed, V_{critical}, at which the mill would start to vibrate (Farley et al. 2006).

$$V_{\text{critical}} = \frac{-2LM_{\text{eq}}\zeta\omega_n^3}{\frac{dF}{dT_{\text{i}}}EW} = \frac{-2L\zeta\omega_n^{3/2}}{\frac{dF}{dT_{\text{i}}}EWM_{\text{eq}}^{1/2}} \tag{23.6}$$

where M_{eq} is the equivalent mass of the rolling mill that is vibrating during resonance. From Equation 23.6 it can be seen that factors such as the material being rolled, the rolling conditions, and the natural damping of the mill stand resonance will all affect the threshold rolling speed for vibration. However, these are difficult to change, and none varies as significantly as the speed during a particular rolling pass.

The problem is more complex in cold tandem mills as each mill stand will exhibit the mechanical gauge chatter feedback loop, and these loops will interact as shown in Figure 23.5. If a downstream mill stand starts to exhibit gauge chatter, then the change in entry tension will be felt by the previous mill stand as a change in exit tension. This change in exit tension can excite the upstream mill stand to vibrate. If the upstream stand vibrates, it will produce an exit gauge variation that will travel with the strip and excite vibration of the downstream stand.

The rolling speeds on cold mills suffering from this type of gauge chatter vibration are often constrained for certain products. For these products, the rolling speeds are kept below the threshold speed at which mill vibration occurs, sometimes with the use of online vibration monitoring equipment. This can represent a significant loss of productivity if the mill is a bottleneck machine.

From Equation 23.6, it can be seen that the critical speed of a rolling mill limited by third octave vibration can be increased by:

- Increasing the length of the entry strip
- Increasing the damping associated with the chatter mode
- Increasing the frequency of the chatter mode
- Decreasing the mass of the chatter mode
- Decreasing the sensitivity of rolling load to entry tension

In the case of the entry strip length, in principle, this is correct. However, the situation is more complex due to the presence of other mechanical equipment, such as entry rolls, that can interact with the main feedback loop in a positive or negative way. Increasing the damping is a textbook approach to this type of problem and can be achieved in passive and active ways (Benhafsi and Durrant 2006). Researchers have experimented with tuned mass dampers and hydraulically inflatable mill liners (Critchley and Paton 1987; Musto and Viens 1998). The latter may also stabilize the mill through a stiffening of the resonant mode. The sensitivity of rolling load to entry tension can be affected by rolling variables such as friction and roll roughness.

23.7 FIFTH OCTAVE CHATTER (ROLL AND STRIP CHATTER MARKS)

Fifth octave chatter marks usually develop on the backup roll barrel and print onto the strip surface with a spacing between 10 and 40 mm. Figure 23.6 shows an example of severe chatter marks around the barrel of a backup roll before grinding (Farley et al. 2002). The markings are parallel to the roll axis

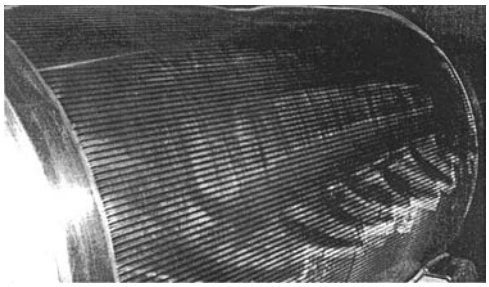


FIGURE 23.6 Example of severe fifth octave chatter marks on the barrel of a backup roll that would produce similar surface markings on the strip. (After Benhafsi, Y., Farley, T. W. D., Wright, D. S. 1999. *Proceedings of the 1999 IOM Conference*, London, U.K.)

and often have uniform intensity across the backup roll barrel. With very sensitive surface proximity measurements, it is possible to measure surface features on the roll with an amplitude of a few microns that relate to the marking spacing.

When mills suffer from this type of chatter mark problem, the backup rolls have to be changed frequently, ideally before the onset of marking. A high frequency of backup roll changes results in reduced mill productivity, shortened overall lifetime of the backup rolls, and potential strip marking, as well as customer rejection of product if the problem goes undetected.

The chatter mark problem requires a source of forced vibration within the mill, and the vibration frequency associated with fifth octave chatter is usually within the range of 600–1200 Hz. Typical sources on the mill may result from forced vibrations from defective gear teeth, roll bearings, and drive couplings. If the forced vibration excites a fifth octave resonance of the mill stand, then the vibration amplitude will be increased by the flexibility of the mill resonance and the marking problem will be more severe. Once the markings have begun to form on a roll, the marks themselves can excite the vibration mode at certain roll speeds and the formation of marks becomes self-exciting. This causes the intensity of the markings to build up in an exponential manner, such that a product quality issue can build up within several coils, after many days or weeks of problem-free service. Nevertheless, the timescale for the roll marks to become self-exciting is much longer than for the third octave chatter described above. Another source of forced vibration in the mill is due to periodic submicron features on the roll surface produced during roll grinding. These are created by forced vibrations within the roll grinder that usually also excite a natural resonance of the grinding machine.

Very careful vibration measurements are required to identify the source of the marking before this problem can be solved.

It can be helpful to understand the fifth octave resonant frequencies of the mill stand. This can be approached through experimental modal analysis and/or computer simulation. If the grinder is involved in the problem, then a full modal analysis of the grinder is also useful.

Several authors have debated the shape of the mill stand vibration mode excited during fifth octave chatter. One previous experimental modal study (Moore and Peters 1990) showed this mode to be in good agreement with simple theories that the mode essentially involves the work rolls moving together as a pair, bouncing between the backup rolls that remain relatively stationary. However, at these higher frequencies, all the rolls are bending, which complicates the motion (Nessler and Cory 1989, 1993; Nieb and Nicolas 1991). The chocks may also be moving through much larger amplitudes, causing bending of the roll necks.

Experimental modal testing of a mill stand has been undertaken by AMTRI (Benhafsi et al. 1999) using an instrumented hammer and accelerometers to accurately identify the shape of a fifth octave mill resonance and also to verify predictions from computer simulation.

As an example, Figure 23.7 shows the baseline inertance transfer function (acceleration/force) of the mill for various mill loads at a constant +35% bending force. The fifth octave resonant mode at around 800 Hz is the most prominent of all of the resonant peaks. Its frequency can be seen to increase

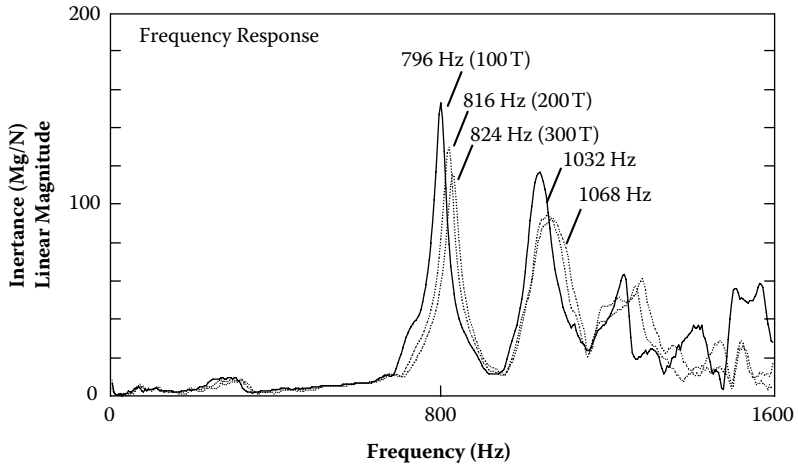


FIGURE 23.7 Frequency response of mill at various mill loads, measured on the bottom work roll. (After Benhafsi, Y., Farley, T. W. D., Wright, D. S. 1999. *Proceedings of the 1999 IOM Conference*, London, U.K.)

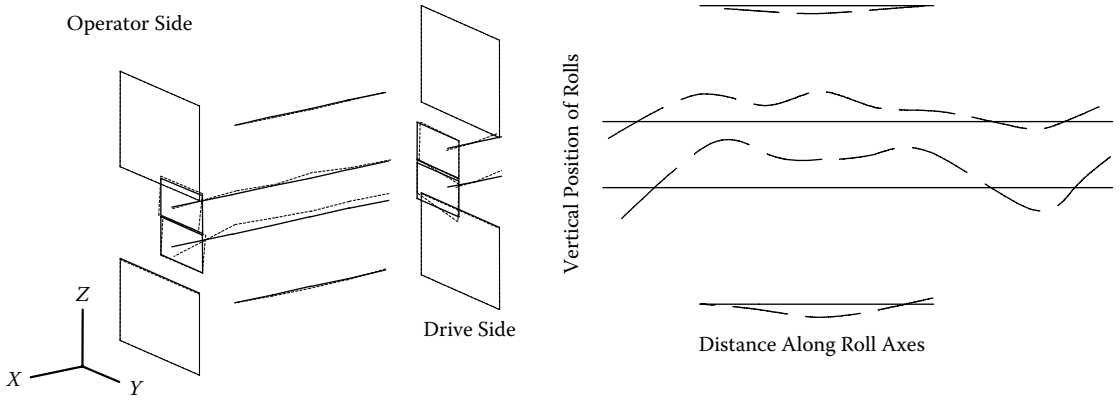


FIGURE 23.8 Measured fifth octave mode shape at ~822 Hz shown in 3-D (left) and also parallel to the strip direction (right). (After Benhafsi, Y., Farley, T. W. D., Wright, D. S. 1999. *Proceedings of the 1999 IOM Conference*, London, U.K.)

as the mill load is increased, indicating a stiffening characteristic. Varying the bending force at constant mill load was also observed to change the fifth octave peak frequencies.

Having identified the baseline mill resonances, a complete modal analysis of the mill stand was performed at a mill load of 200 tons and at a +35% bending force. The impact response was measured using an accelerometer mounted in three orthogonal directions at 62 accessible points around the mill structure, encompassing all the rolls, chocks, and couplings. The fifth octave resonance, occurring at around 822 Hz, is shown in Figure 23.8. The modal shape shows the two work rolls moving in phase, mostly rigidly, between the two backup rolls, in a largely vertical plane. It is this particular motion, when excited, which results in the marking of the backup rolls. The operator-side roll necks are bending significantly, largely within the clearance in the chocks. The lower coupling and drive-side work roll chock are also in motion.

The mill vibration model described above was used to predict the mode shape for the same mill; the results are shown in Figure 23.9. There is close agreement in frequency and shape with the fifth octave resonant vibration mode identified from the model and the one measured on the mill. This work was the first clear evidence that fifth octave chatter marks are caused by excitation of this type of mill resonance (Benhafsi et al. 1999).

It should be noted that this type of mode belongs to a family of fifth octave modes, all capable of damaging the backup roll through relative motion between the work roll and backup roll.

If the effect of roll bending is ignored, then the fifth octave mode can be simplified to a single work roll mass oscillating on a spring represented by the Hertzian stiffness between the work roll and the relatively stationary backup roll. Such a model was put forward by Roberts (1978) and resulted in a simple formula for calculating an approximate fifth octave frequency for a mill stand as follows:

$$\text{Fifth Octave Frequency (Hz)} = \frac{1.21\times10^{6}}{D_{\mathrm{W}}\sqrt{\log_{\mathrm{e}}\left[\dfrac{1.80\times10^{5}(D_{\mathrm{B}}+D_{\mathrm{W}})}{F_{\mathrm{S}}}\right]-0.333}} \tag{23.7}$$

where F_S is the specific rolling load (N/mm^{-1}), and D_W and D_B are the work and backup roll diameters (mm), respectively (Roberts 1978).

There is discussion in the early literature relating to the effect of roll diameters. The main roll diameter effect worthy of mention here is due to the difference in backup roll diameters and critical rolling speeds, V_n (m/min), and was first calculated by Nessler and Cory (1989), as follows:

$$V_n = \frac{0.06\pi\,(D_{\mathrm{B}}^{\mathrm{T}} - D_{\mathrm{B}}^{\mathrm{B}})f_{\mathrm{C}}}{n} \qquad n = 1, 2, 3, \ldots \tag{23.8}$$

where D_B^T and D_B^B are the top and bottom backup roll diameters (mm), respectively, and f_C is the fifth octave resonant frequency (Hz) of the mill responsible for the chatter marks.

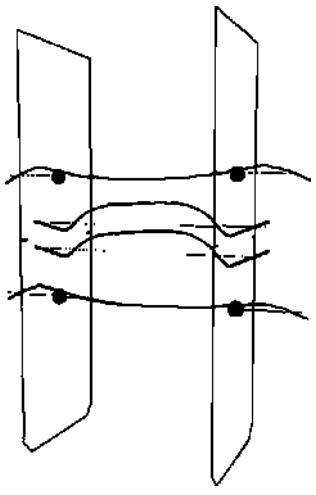


FIGURE 23.9 Typical mode shape of a rolling mill resonance that can become excited during fifth octave chatter, as predicted by the Alcan mill stand vibration model described above. The lines represent the central axes of the rolls and housing frames in a four-high mill. (After Benhafsi, Y., Farley, T. W. D., Wright, D. S. 1999. *Proceedings of the 1999 IOM Conference*, London, U.K.)

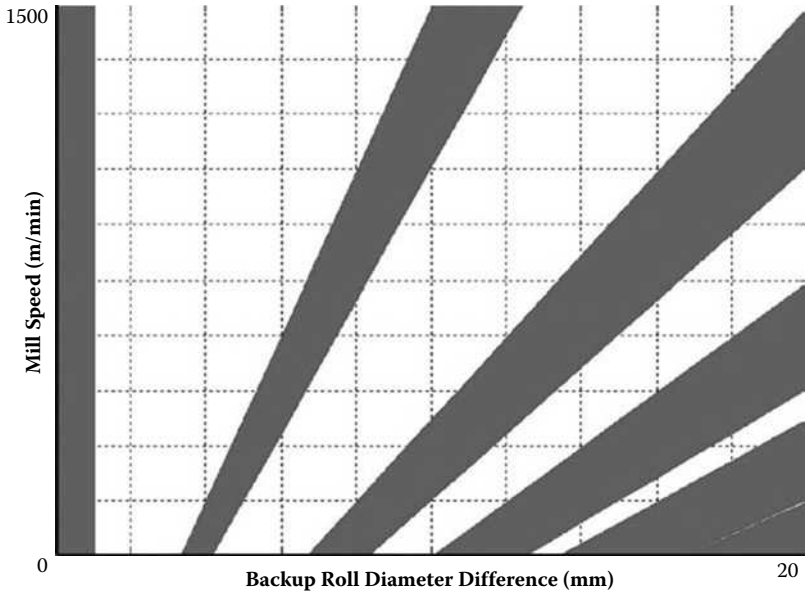


FIGURE 23.10 Example of a stability chart for a single-stand cold mill with a fifth octave mode resonant frequency range of 640–790 Hz. (After Hardwick, B., Tordi, A., Farley, T. W. D. 2006. *Proceedings of the IOM3 Conference: Vibration in Rolling Mills*, London, U.K.)

The critical rolling speeds should be avoided because they correspond to speeds when an integer number of chatter marks would form around both backup rolls at the same time, a situation considered more likely to lead to a buildup of chatter marks. These critical rolling speeds can be calculated using Equation 23.8 and represented on a stability chart, as shown in Figure 23.10. The shaded regions represent speeds and diameter differences of lowest stability. If the mill is run for prolonged periods at speeds lying in the shaded areas, then the process of wearing chatter marks into the backup rolls as a result of the presence of exciters is likely to be promoted, or accelerated. By contrast, mill speeds that fall in the white regions of the chart will result in suppression of the marking process (Hardwick et al. 2006).

Some solutions to this problem may require an online monitoring strategy on the grinder and/or the mill to identify the source and then minimize its impact. This is an effective operational strategy to maximize productivity while maintaining high quality of the strip surface.

The AMTRI Vibration Analysis System, now marketed by UNIVIB Ltd in the UK, has been developed with the above considerations in mind. It is a mill-wide, integrated monitoring and analysis system for application to single and multistand mills and roll grinding machines. Data-acquisition systems measure and analyze vibration occurring when grinding and rolling, and store roll and coil vibration histories to a central database. As well as providing immediate early warning to operators, warnings are also issued to operators of downstream processes when rolls or coils have suffered high levels of vibration during processing. Furthermore, the system is designed to provide an indication of possible marking of the strip in the form of a coil quality index. Similarly, a roll quality index has also been developed. The database can be queried to help trace the sources of strip marking. In a further development, bearing and gear vibration will be tracked and trended on a coil-by-coil basis so that developing faults can be identified. This integrated approach to vibration monitoring in rolling mills has recently proved to be successful in helping identify incidences of abnormal vibration, allowing appropriate remedial action to be taken to eliminate the sources of these vibrations (Benhafsi et al. 1999; Hardwick et al. 2006).

23.8 SUMMARY

The two common forms of mill vibration that are most difficult to solve are third octave gauge chatter and fifth octave chatter. Both can cause significant strip quality issues if they occur on a mill. There is always a source of vibration responsible for fifth octave chatter, so a solution can usually be found to this type of problem.

Third octave gauge chatter vibration, however, is particularly difficult to solve because it is self-exciting and so can occur with no source of forced vibration. The problem usually represents a speed limit on cold mills and can cause significant loss of productivity. For this reason, gauge chatter is still the subject of significant ongoing research and development. In principle, there should be a threshold rolling speed on all cold mills where gauge chatter vibration will become self-exciting. For most mills, this threshold speed is greater than the current maximum rolling speed, so vibration is not experienced. However, as cold mill speeds increase, this problem is likely to become more of an issue unless a good solution can be found.

REFERENCES

Benhafsi, Y., Farley, T. W. D., and Wright, D. S. 1999. An approach to on-line monitoring of fifth octave mode mill chatter to prolong back-up roll life. *Proceedings of the 1999 IOM Conference*, London, U.K.

Benhafsi, Y. and Durrant, J. 2006. Some practical means to attenuate 3rd octave chatter. *Proceedings of the IOM3 Conference: Vibration in Rolling Mills*, London, U.K.

Critchley, S. and Paton, D. 1987. Tandem mill vibration. *Proceedings of the 4th International Steel Rolling Conference*, Deauville, France.

Evans, P. R., Hill, D. E., and Vaughan, N. D. 1996. Dynamic characteristics of a rolling mill. *Proceedings of the Institution of Mechanical Engineers* 210: 259–271.

Farley, T. W. D., Nardini, D., Rogers, S., and Wright, D. S. 2002. An approach to understanding mill vibration. *Proceedings of TMS 2002: 131st Annual International Meeting*, Seattle, WA.

Farley, T. W. D., Rogers, S., and Nardini, D. 2006. Understanding mill vibration phenomena. *Proceedings of the IOM3 Conference: Vibration in Rolling Mills*, London, U.K.

Hardwick, B., Tordi, A., and Farley, T. W. D. 2006. Identification and solution of fifth octave mode mill chatter problems. *Proceedings of the IOM3 Conference: Vibration in Rolling Mills*, London, U.K.

Moller, R. H. and Hoggart, J. S. 1967. Periodic surface finish and torque effects during cold strip rolling. *Journal of the Australian Institute of Metals* 12(2): 155–165.

Moore, J. M. and Peters, J. 1990. Rolling mill vibration measurement by modal analysis. *Proceedings of 1990 Conference on Dimensional Control in Rolling Mills*, London, U.K.

Musto, F. and Viens, D. L. 1998. Reduction of rolling mill vibration through the use of expandable housing liners. *Proceedings of 40th Mechanical Working and Processing Conference*, Pittsburgh, PA: pp. 469–476.

Nessler, G. L. and Cory, Jr., J. F. 1989. Cause and solution of fifth octave back-up roll chatter on 4-high cold mills and temper mills. *Iron and Steel Engineer* 66(12): 33–37.

Nessler, G. L. and Cory, Jr., J. F. 1993. Identification of chatter sources in cold rolling mills. *Iron and Steel Engineer*, January 1993, pp. 40–45.

Nieb, J. R. and Nicolas, V. T. 1991. Automated monitoring and control of vibration and chatter in rolling processes. *Iron and Steel Engineer* 68(7): 33–42.

Roberts, W. L. 1978. Four-high mill stand chatter of the fifth octave mode. *Iron and Steel Engineer*, 55: 41–47.

24 IMPOC©: An Online Material Properties Measurement System

Klaus Herrmann and Matthias Irle

CONTENTS

24.1 Introduction 265
24.2 Principle of Operation 265
24.3 System Components and System Operation 265
24.3.1 IMPOC Sensor 266
24.3.2 IMPOC Data Processing Unit 266
24.4 Data Modeling and System Performance 266
24.5 Technical and Economic Benefits 268
24.5.1 Process Optimization 268
24.5.2 Reduction of Coil Logistics Expenses 268
24.5.3 Reduction of Destructive Testing Costs 268
24.5.4 Skin Pass Mill Control 269
24.6 Summary 269
References 269

24.1 INTRODUCTION

Online material properties measurement has itself been established as an important tool for optimizing the product quality of rolled flat steel products. Increasing demand from the automotive industry for more reliable product quality has led to a search for measuring instruments that overcome the drawbacks of standard mechanical properties testing methods. In order to optimize the product quality and to achieve narrow production tolerances, a continuous monitoring of the mechanical properties during production is mandatory. Only online measurements of these properties provide fast and immediate feedback and enable the producer to react during the processing of the steel. This chapter describes the industrial operation and economic benefits of an Impulse Magnetic Process Online Controller (IMPOC©). This online material properties measurement system allows automatic nondestructive testing of ferromagnetic steel strips. The system periodically magnetizes the steel strip and measures the residual magnetic field. Based on mathematical models, the mechanical properties' tensile strength and yield strength are calculated online along the length of the coil. The system was developed by the Institute of Applied Physics, Minsk [1–3], has been further optimized for industrial applications in close cooperation with ThyssenKrupp Steel [4], and is now in use at several steel-producing plants worldwide.

24.2 PRINCIPLE OF OPERATION

The basic underlying physical operating principle is magnetic induction. Based on the fact that there are well-known physical relations between the mechanical properties and the magnetic properties of ferromagnetic strip steel [5,6], the IMPOC system periodically magnetizes the strip and subsequently measures the residual magnetic field strength of the material. In order to operate at the high speed of typical steel production lines, such as hot-dip galvanizing lines or continuous annealing lines, a pulsed magnetic field is used.

The amplitude of the magnetic field pulse is fixed and is chosen to magnetically saturate the strip steel material locally. After the external magnetic field pulse has decayed, only the remanent magnetic induction (remanence) of the magnetized strip is left. This remanence is measured by a high-sensitivity fluxgate magnetic field sensor.

24.3 SYSTEM COMPONENTS AND SYSTEM OPERATION

The IMPOC measuring system is designed for automatic, nondestructive, online testing of ferromagnetic steel strips with thicknesses from 0.15 to 3 mm. It operates at line speeds of up to 900 m/min. Larger strip thicknesses up to 12 mm can be measured up to line speeds of 300 m/min.

The main system components are the IMPOC sensor and the IMPOC Data Processing Unit (DPU).

24.3.1 IMPOC Sensor

The IMPOC sensor consists of one magnetizing coil and one magnetic field sensor mounted 300 mm apart on a nonmagnetic fixture. This compact design facilitates easy and quick integration into existing production lines. (See Figure 24.1.)

Rigid spacers provide a minimum required distance of 500 mm of this assembly to other steel parts in the line. The distance of the IMPOC sensor to the passline is typically 25 mm.

The residual magnetic field of the magnetized strip is measured by a highly sensitive magnetic field sensor. This magnetic field sensor is the well-known second harmonic fluxgate sensor [7].

This sensor consists of a ferromagnetic core with primary excitation windings and a secondary pickup coil. The ferromagnetic core is periodically driven into saturation by a drive current through the excitation coil. An external magnetic field is then superimposed on this alternating field. The nonlinear ferromagnetic hysteresis of the core material leads to an alternating voltage at the pickup coil containing second and even higher harmonics of the drive signal frequency. A suitable electronic readout scheme then detects the second harmonic, which is proportional to the magnitude of the external field. To provide a linear magnetic-field-to-voltage transfer characteristic and to achieve a stable operating point near zero, a feedback loop is used. This feedback loop consists of a compensation coil, which generates a magnetic field that is directed opposite to the external magnetic field and thereby effectively nulls the total magnetic field.

To further suppress any disturbing ambient magnetic fields, the fluxgate sensor is operated as a gradiometer with two pickup coils wound in the opposite direction canceling out uniform external magnetic fields and measuring only the gradient of the residual magnetic field. The measuring error of the gradient of the residual magnetic field amounts to a maximum 5%.

Typical installations have one IMPOC sensor on either side of the strip in order to compensate for any strip oscillations by averaging the measurements from each sensor.

Therefore, an additional error caused by strip oscillations is less than 2% for residual magnetic field for a maximum horizontal passline variation of ± 5 mm.

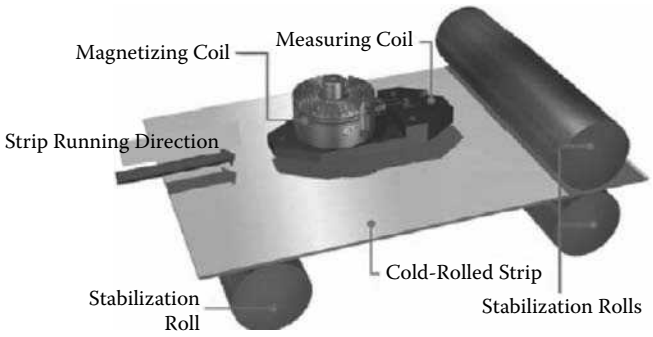


FIGURE 24.1 IMPOC.

24.3.2 IMPOC Data Processing Unit

The IMPOC DPU contains the main electronics for the magnetizing coils, and also the main data acquisition and processing unit. It consists of the generator, the data acquisition unit, the calibrator and the IMPOC PC.

The generator supplies the current for the magnetizing coils. It generates a pulsed magnetic field with a frequency of 0.05–7 Hz. This corresponds to line speeds of 6–900 m/min. The generator is synchronized with the speed of the production line.

The data acquisition unit synchronizes the measurement of the gradient of the magnetic field with the magnetization of the strip. The measured magnetic field signals are transferred to the IMPOC PC for the calculation and display of the mechanical properties.

The calibrator is used for the calibration of the magnetic field sensors and the data acquisition unit. An additional calibrator head is mounted between the upper and lower IMPOC sensor, and a controllable pulse simulates the magnetic field of the strip.

24.4 DATA MODELING AND SYSTEM PERFORMANCE

Data modeling is essential for deriving the mechanical properties from the magnetic field measurements. At present, there are phenomenological models for calculating the mechanical properties' tensile strength and yield strength from the IMPOC measurements.

These linear models take five variables into account: the results of the destructive testing, the measured IMPOC value, the sheet thickness, degree of skin-pass rolling, and yield degree either in combination or separately. All variables are measured online, and the calculation is performed during the strip production.

The steel grades are classified into different material classes and then analyzed using multiple-linear regression. Linear functions of the following type are calculated:

$$F(x_1, x_2, x_3, x_4) = k_1 + k_2 \cdot H_I + k_3 \cdot d + k_4 \cdot \mathrm{SKD_s} + k_5 \cdot \mathrm{YD} + k_6 \cdot R_x$$

where

R_x = Results of destructive test
which can be: $R_{p0,2}$ (yield strength)
R_{eL} (lower yield point)
R_{eH} (upper yield point)
R_m (tensile strength)

k_i = Regression coefficients

H_I = Measured IMPOC value

d = Sheet thickness

$\mathrm{SKD_s}$ = Skin pass degree (ratio of changes in strip length before and after skin pass mill, similar to skin pass elongation)

YD = Yield degree (ratio of changes in strip length before and after tension leveller)

The different material classes were grouped together based on similar chemical composition and similar processing conditions. Several groups, such as low carbon steels, IF steels, high-strength–low alloy steels, and bake-hardening steels, are formed. Typical standard deviations of tensile strength and yield strength for these models are approximately 6–10 MPa. Provide Table 24.1 an overview of the results of regression calculation for the tensile strength (R_m) and yield strength ($R_{p0,2}$). (See also Figures 24.2 and 24.3.)

TABLE 24.1
Standard Deviation in MPa

	Standard Deviation (MPa)	
	R_m	$R_{p0,2}$
Low Carbon Steel	6	8
IF Steel	6	8
Bake-Hardening Steel	6	10

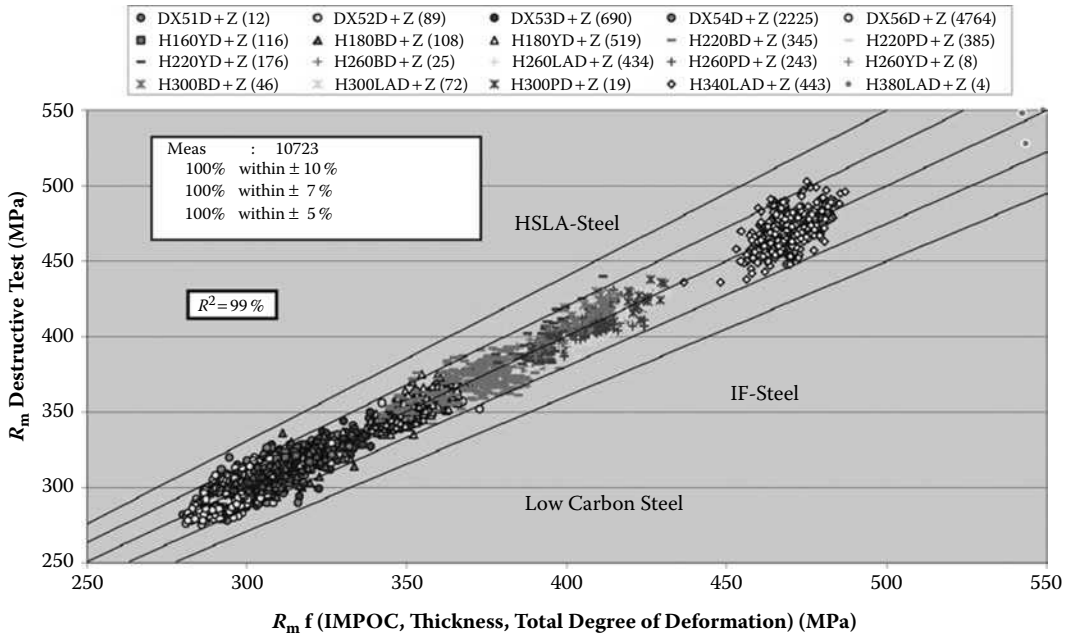


FIGURE 24.2 Regression analysis, tensile strength.

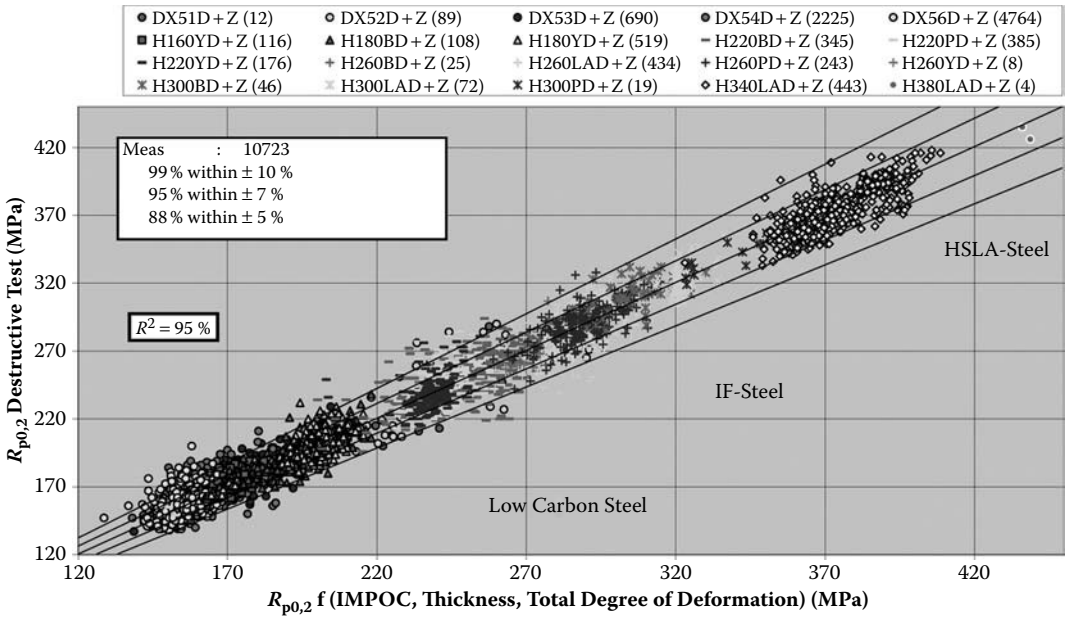


FIGURE 24.3 Regression analysis, yield strength.

24.5 TECHNICAL AND ECONOMIC BENEFITS

The industrial operation of these systems has several benefits for the customer. Some of the benefits can be easily quantified in technical and economic terms; some benefits are easier to justify on a technical basis.

24.5.1 Process Optimization

One clear and immediate benefit is certainly the advantage of monitoring the steel quality online during production. The traditional way of destructive testing does not allow recognizing changes in the material properties on time, and the operator cannot directly interact with the process, for example, react on faulty annealing processes. (See Figure 24.4.)

With IMPOC, the operator can block faulty coils or a whole production sequence before they are processed further in the plant or sent to the customer. This in-time reaction possibility certainly has important benefits, not only in technical terms, but also because it enables the producers to optimize their coil management logistics.

24.5.2 Reduction of Coil Logistics Expenses

Without an online measurement system, a typical scenario for the coil quality management in a hot dip galvanizing line is as follows.

The results of the destructive testing are typically available 8–24 h after production. A reasonable assumption for the amount of blocked coils in a hot dip galvanized line due to strong deviations of the mechanical properties is 3%–6%. Normally, these coils are brought to an inspection line or, in some cases (e.g., if the yield point is too low), to a skin pass mill for a second skin pass path. Again, typically, 5% of the material will be cut off and a new sample for material testing will be taken. After 8–24 h, the coil is either finally released, brought again to the inspection line, or finally downgraded. With the availability of online IMPOC results, the situation changes substantially.

Coils that show severe deviations from the target values visualized by the IMPOC system can be immediately identified for further inspection or rework measures. These coils will not be packaged, and waste of packaging material is avoided. This packaging loss can be up to $150,000/year. Further, by comparison of the IMPOC values and the results of potentially additional destructive testing, the finishing department can easily decide where to cut the material or whether the coil needs to be downgraded to 2A qualities. The resulting cost reduction comprises the following main elements:

- Reduced packaging costs
- Reduced inspection line utilization costs
- Reduced yield loss
- Reduced storage costs
- Reduced delivery time

An estimate for the total cost for inspection line utilization and yield loss can go up from $195,000 to $650,000/year.

These costs can be substantially reduced with an IMPOC system with immediate online information. A typical target for an IMPOC application is 30%–40% cost reduction for coil logistics expenses.

24.5.3 Reduction of Destructive Testing Costs

The reduction of the destructive testing can also be described in economic terms. Typical destructive testing procedures for automotive qualities require sample taking at the beginning and at the end of each coil. By implementing an IMPOC system, the steel producer can save at least one destructive testing per coil. This can also amount to $40,000 to $65,000/year.

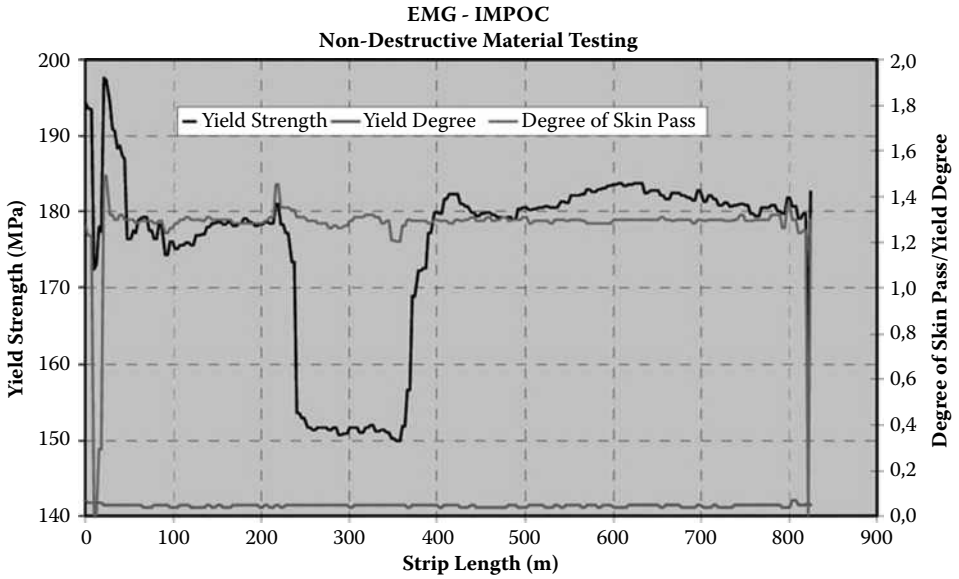


FIGURE 24.4 Influence of faulty annealing process on IMPOC yield strength measurement.

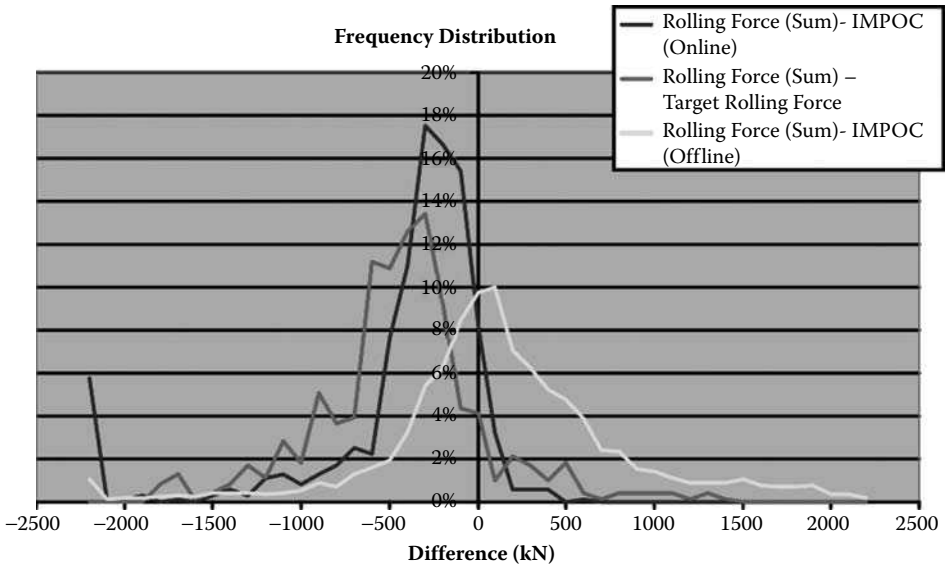


FIGURE 24.5 Change of rolling forces of skin pass mill based on IMPOC measurement.

Destructive testing cannot be completely replaced by online testing methods, but they complement each other giving reliable results along the strip length together with one reference value per coil by a destructive sample test.

24.5.4 Skin Pass Mill Control

A prototype application where two IMPOC systems are incorporated into a closed loop, skin pass mill control is done in cooperation with ArcelorMittal Eisenhuettenstadt GmbH. In this project, one IMPOC system is installed before the skin pass mill and one after. Besides the target values for the tensile strength and yield strength, the roughness is the main optimization criterion. For measuring that, an online roughness measurement system EMG SORM 3plus is used after the skin-pass mill in the same process.

The first IMPOC before the skin pass mill gives the necessary preset values for the rolling force. After that preset correction and based on the allowed rolling force range, the elongation is changed in the allowable ranges to see the effects in the resulting roughness measured with SORM 3plus.

The Figure 24.5 graph shows how the real rolling force at the start of the coil is changed (gray line, increased in average) by taking the IMPOC presets of the incoming coil (white line) and additional customer presets into account. Without that correction the rolling force at the beginning of the coil would have always been too low (black line). The resulting material properties are measured after the skin pass mill by the second IMPOC.

24.6 SUMMARY

IMPOC has been in continuous operation for several years in various industrial applications, such as in pickling lines and hot-dip galvanizing lines. Based on the online availability of the values for tensile strength and yield strength, it has proven the advantage of online material properties measurement and has demonstrated its benefits both technically and economically.

REFERENCES

1. Matyuk V.F., Delendikh M.N., Osipov A.A., Pinchukov D.A., Hartmann H., Reichelt H., and Schmidt R. 2006. The plant for pulse magnetic on-line testing of mechanical properties of rolled products. *Paper presented at the 2006 European Conference on Non-Destructive Testing*, September 25–29, Berlin, Germany.
2. Matyuk V.F. 1998. Pulsed magnetic testing of strengthening characteristics of ferromagnetic articles. *Ser. Fiz.-Tekhn. Navuk* (4):114–118.
3. Matyuk V.F. and Osipov A.A. 1995. Pulsed magnetic testing of separately moving sheets in the production line. *Defektoskopiya* (6):56–62.
4. Dürr W. and Irle M. 2003. Magnetic inductive online measurement system for mechanical properties within a hot-dip galvanizing line. *Stahl & Eisen* 123(10):73–77.
5. Kneller E. 1962. *Ferromagnetismus*. New York: Springer Verlag.
6. Seeger A. 1965/1956. *Moderne Probleme der Metallphysik. Band I und II*. Berlin: Springer Verlag.
7. Blumenhauer H. 1994. *Werkstoffprüfung*. Stuttgart: Deutscher Verlag für Grundstoffindustrie.

25 Technologies for the Prediction and Control of Microstructural Changes and Mechanical Properties

Kazuhiro Ohara

CONTENTS

25.1 The Need for Prediction and Control of Microstructural Changes and Mechanical Properties 271
25.2 Overall Structure of the Calculation for Microstructural Changes and Mechanical Properties 271
25.3 Details of the Models for Predicting Microstructural Changes and Mechanical Properties 272
25.3.1 Grain Growth during Slab Reheating 272
25.3.2 Hot Deformation Model 272
25.3.2.1 Recovery 273
25.3.2.2 Recrystallization 273
25.3.2.3 Grain Growth after Deformation 273
25.3.3 Transformation Model 273
25.4 Mechanical Properties Prediction Model (Structure–Mechanical Properties Relationship) 274
25.5 Trends in the Development of Material Properties Models 274
25.5.1 Material Properties Model for Ultra-Low-Carbon Steel 275
25.5.2 Material Properties Model for Ultra-Fine-Grain Microstructure Steel 275
25.5.3 Mesoscopic Model 275
References 275

25.1 THE NEED FOR PREDICTION AND CONTROL OF MICROSTRUCTURAL CHANGES AND MECHANICAL PROPERTIES

Characteristics such as the strength and ductility of iron and steel are referred to as mechanical properties. These properties are determined by microstructural characteristics, such as grain size and the volume fraction of each phase, and material properties prediction models can be used to predict microstructural changes and the resulting mechanical properties under various rolling and process conditions. The strength of iron and steel increases with finer grain size, and each phase has a different hardness. Accordingly, the mechanical properties are determined by the grain size and the volume fraction of each phase.

A system for predicting microstructural changes and the resulting mechanical properties uses a model to predict microstructural changes based on the rolling conditions, such as the processing and cooling conditions, and then uses a materials prediction model to determine how to produce a coil or a plate with the desired mechanical properties. Control of microstructure and mechanical properties is achieved by predicting the microstructure after rolling, and then using these results as input to the control of the actual rolling line so that the rolling conditions can be modified to obtain the desired result. This section outlines the model used to predict the changes in microstructure during rolling and the changes in metallurgical structure during cooling at transformation, and also describes the model used to predict the mechanical properties using this metallurgical information.

25.2 OVERALL STRUCTURE OF THE CALCULATION FOR MICROSTRUCTURAL CHANGES AND MECHANICAL PROPERTIES

Figure 25.1 shows a block diagram of the system for predicting microstructural changes and mechanical properties in a hot strip mill. Grain growth occurs in the slab-reheating furnace when the slab is reheated. A reheating furnace model simulates this grain growth to estimate the grain size to use as an input to the hot deformation model, which simulates the structure transitions during hot rolling. The result of this hot deformation model gives the final austenite grain diameters at the exit of the finishing mill. Next, the transformation model

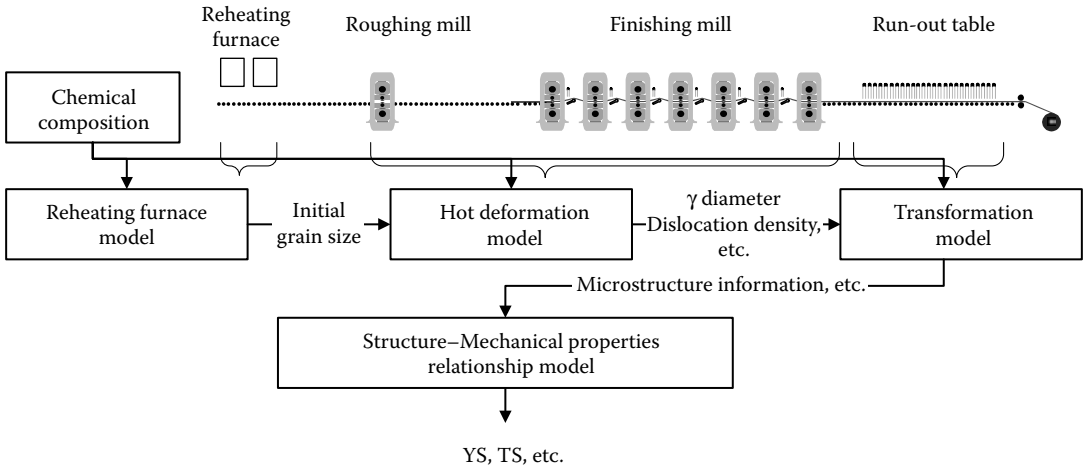


FIGURE 25.1 An example of a microstructure and material properties prediction system.

simulates transformation during cooling on the run-out table and calculates the transformed structure. The mechanical properties are then calculated from this transformed structure using a model of the relationship between microstructure and mechanical properties.

25.3 DETAILS OF THE MODELS FOR PREDICTING MICROSTRUCTURAL CHANGES AND MECHANICAL PROPERTIES

To simulate microstructural changes during rolling, it is necessary to establish models for metallurgical phenomena over the entire rolling process.

1. Initial structure model (grain growth during slab reheating)
2. Hot deformation model
   a. Recovery
   b. Recrystallization
   c. Grain growth after deformation
3. Transformation model
4. Mechanical properties prediction model (structure–mechanical properties relationship)

Each of these models is summarized below.

25.3.1 Grain Growth during Slab Reheating

The initial grain size at extraction is determined by grain growth during slab reheating and is predicted using the initial austenite–grain size prediction model. In hot-tandem rolling, the initial grain size generally has little influence on the final austenite grain size because of the large cumulative strain during rolling. However, there are cases such as plate rolling, when the initial austenite grain size does affect the calculation results and cannot be neglected. The grain growth model uses different formulations for the cases when carbides of Nb or Ti, etc., do and do not precipitate. For the case of no precipitation (normal carbon steel), the grain size is expressed as follows [1]:

$$(\bar{D})^n - (\bar{D}_0)^n = k_1 \cdot t \tag{25.1}$$

where
$\bar{D}$ = average austenite grain diameter
$\bar{D}_0$ = initial grain diameter
k_1 = coefficient
t = time of grain growth
$n = 2$ for single structure steel
$n = 3$ for dispersion structure steel

The case when precipitation does occur requires calculation of dissolution and Ostwald ripening, and the third power law is employed for particles as follows [2]:

$$(\bar{d})^3 - (\bar{d}_0)^3 = k_2 \cdot t \tag{25.2}$$

where
$\bar{d}$ = average particle diameter
$\bar{d}_0$ = initial diameter for $\bar{d}$
k_2 = coefficient
t = time of particle growth

In addition to the above, formulas are also used to consider the solute drag effect due to solute elements and the pinning effect due to dispersion particles.

25.3.2 Hot Deformation Model

In some cases during tandem rolling, the subsequent pass occurs before recovery and recrystallization have fully released the strain resulting from the previous pass. In this case, it is necessary to consider the effect of accumulated

strain on recovery and recrystallization. These effects should be considerable in cases when the interstand time is short or the material contains chemical components that delay recovery and recrystallization. The hot-deformation model calculates the austenite grain size, dislocation density, and other parameters based on the dynamic phenomena in the roll bite and the static phenomena interstand or between passes. These can be broadly divided into the following three phenomena.

25.3.2.1 Recovery

Before recrystallization, elimination of point defects and diffusion-assisted reorganization of dislocations occurs and subgrains are formed.

25.3.2.2 Recrystallization

Dynamic recrystallization occurs during deformation if the strain exceeds the critical strain value. Static recrystallization, in contrast, occurs after recovery during the interpass interval. For example, Senuma [3] expressed the volume fraction of dynamic recrystallization X_{dyn} using the Avrami equation [4–6] as follows:

$$X_{dyn} = 1 - \exp\left(-0.693\left(\frac{\varepsilon - \varepsilon_c}{\varepsilon_{0.5}}\right)^2\right) \tag{25.3}$$

where

X_{dyn} = volume fraction of dynamic recrystallization
ε = strain
$\varepsilon_{0.5}$ = strain at 50% dynamic recrystallization
ε_c = critical strain for dynamic recrystallization

For static recrystallization also, Senuma [3] expressed the volume fraction of static recrystallization based on the Avrami equation.

$$X_{st} = 1 - \exp\left(-0.693\left(\frac{t - t_s}{t_{X_{st}=0.5}}\right)^2\right) \tag{25.4}$$

where

X_{st} = fraction of static recrystallization
t = time
t_s = static recrystallization starting time
$t_{X_{st}=0.5}$ = 50% static recrystallization time

25.3.2.3 Grain Growth after Deformation

Compared to normal grain growth during slab reheating, grain growth after recrystallization occurs very quickly. Rapid grain growth also occurs briefly due to dynamic recrystallization after deformation at constant temperature. The driving force for grain growth is the difference in dislocation density between grains, and this is accentuated in dynamic recrystallization. In contrast, grain growth after static recrystallization is driven by the grain boundary energy when recrystallization completes. For example, the time and temperature dependence of grain growth can be modeled using the following formula by Sellars [7]:

$$d^n = d_{rex}^n + A_5 t \exp\left(-\frac{Q_{gg}}{\mathrm{R}T}\right) \tag{25.5}$$

where

d = grain diameter after grain growth
d_{rex} = recrystallized grain diameter
T = temperature
A_5 = constant
t = time
Q_{gg} = activation energy
R = gas constant
n = 10 for C-Mn steel

25.3.3 Transformation Model

During cooling after hot deformation, transformation occurs from deformed austenite to ferrite, pearlite, bainite, martensite, and so on. The transformation model calculates the metallurgical parameters during transformation to predict the resulting metallurgical microstructure. Three main methods of calculation are known:

1. Parameters k and n in the Avrami equation [4–6] are calibrated experimentally:

$$X = 1 - \exp(-kt^n) \tag{25.6}$$

   where

   X = volume fraction of transformed
   k = coefficient dependent on chemical composition and temperature
   n = coefficient
2. Functional formulation based on measured values
3. Modeling based on theoretical considerations such as nucleation and growth

When using the Avrami equation, the effects of chemical composition and austenite grain size must be taken into consideration when determining parameters k and n. To allow the equation to be applied more broadly, the effect of chemical composition on nucleation and growth should also be considered using the Johnson-Mehl [8] equation or Cahn equation [9].

The following formulation for transformation describes the use of a model from Suehiro [10], which is used to make the system applicable to hot-strip rolling. Two different transformation rates are applicable when a nucleation site for transformation occurs on a grain surface and the nucleation rate and growth rate are constant with respect to time. One is the case when nucleation and growth proceed at the same time.

The other is when the nucleation sites become saturated and only growth occurs. The Cahn equations [9] for the transformation rate with respect to time for each case are as follows.

Nucleation and growth:

$$\frac{dX}{dt} = 4\left(\frac{\pi}{3}\right)^{1/4} (IS)^{1/4}\, G^{3/4}\left(\ln\left(\frac{1}{1-X}\right)\right)^{3/4}(1-X) \quad (25.7)$$

Nucleation saturated (growth only):

$$\frac{dX}{dt} = 2SG(1-X) \quad (25.8)$$

where

X = transformed fraction
I = nucleation rate per unit volume
S = grain boundary area of nucleation site
G = growth rate

Because the formula for the progress of transformation is expressed as a time differential, the transformation rate can be obtained from the Continuous-Cooling-Transformation diagram. This procedure is useful because accurate measurement of the Time-Temperature-Transformation diagram is difficult for the low-carbon steels commonly used in strip rolling.

The above equations are used to calculate the ferrite, pearlite, and bainite transformations. The progress of transformation during cooling is calculated based on the following assumptions: the ferrite transformation starts when the temperature reaches A_{e3}, the pearlite transformation starts when the quantity of carbon (which becomes concentrated in nontransformed austenite) reaches A_{cm}, and the transformation of nontransformed austenite into bainite starts when further cooling brings the temperature down to B_S (the bainite transformation start temperature). The A_{e3} and A_{cm} points are calculated from thermodynamics. An experimental equation is used for B_S.

In this way, the ferrite grain diameter and the volume fraction of each phase after transformation can be calculated based on the chemical composition, austenite grain diameter, cooling rate, and other factors.

25.4 MECHANICAL PROPERTIES PREDICTION MODEL (STRUCTURE–MECHANICAL PROPERTIES RELATIONSHIP)

The model for predicting the relationship between structure and properties is formulated from structural considerations. The mechanical properties to be predicted include tensile strength (TS), yield stress (YS), total elongation (T-El), uniform elongation (U-El), and toughness. It is well known that TS is dependent on the transformation temperature because the dislocation density at transformation is closely related to the transformation temperature. Suehiro et al. calculated the hardness of each phase as a function of the average transformation temperature and then determined TS by multiplying by the volume fraction of each phase. The theoretical bases of the other mechanical properties are not well established and therefore they are estimated using empirical equations. Examples are described below.

The Irvine and Pickering formula for ferrite–pearlite steels [11,12] are:

$$\mathrm{TS[MPa]} = 15.4\{19.1 + 1.8(\mathrm{Mn\,\%}) + 5.4(\mathrm{Si\%}) + 0.25 f_p + 0.5 d_f^{-0.5}\} \quad (25.9)$$

where

d_f = ferrite diameter (mm)
f_p = volume fraction of pearlite (%)

The Yada et al. formula for ferrite-pearlite-bainite steels [10] are:

$$\mathrm{TS[MPa]} = a\{f_f(H_f + b\sqrt{d_\alpha}) + H_p f_p + H_b f_b\}, \quad (25.10)$$

$$H_f = 361 - 0.357T_f + 50[\%\mathrm{Si}],\ H_p = 175,\ H_b = 508 - 0.588T_b + 50[\%\mathrm{Si}]$$

where

H_f, H_p, and H_b = microhardness of each phase subscripts f, p and b denote ferrite, pearlite, and bainite
d_α = ferrite grain size (mm)
a and b = constants, T_f, T_p
and T_b = average transformation temperature of each phase

The average transformation temperature is obtained from the study by Suehiro et al. [10]:

$$T_M = \frac{\int T dX}{\int dX} \quad (25.11)$$

where

T = transformation temperature
dX = transformed portion

However, these equations are intended for use with materials that do not contain elements that cause precipitation hardening. Therefore, to extend the scope of the model, the precipitation hardening mechanism must also be considered. In addition, neural network techniques are used to improve the prediction accuracy of the model.

25.5 TRENDS IN THE DEVELOPMENT OF MATERIAL PROPERTIES MODELS

This section considers the current situation for material properties models.

25.5.1 Material Properties Model for Ultra-Low-Carbon Steel

Ultra-low-carbon steel and interstitial free steel contain very little carbon. This gives them high ductility and allows their use in the fabrication of complex geometries involving severe sheet-forming processes. Although the rate of phase transformation is often controlled by diffusion processes, for ultra-low-carbon steel, it is controlled by movement across the phase interface between ferrite and its adjacent austenite. Consequently, transformation models based on diffusion processes are not suitable for analyzing this mechanism. Empirical models have been produced, and work has been undertaken on the development of theoretical equations.

25.5.2 Material Properties Model for Ultra-Fine-Grain Microstructure Steel

Many researchers have recently undertaken studies of the ultra-fine-grain microstructure (around 1 micron) of hot rolled steel without the addition of special alloys. There are several ways of achieving this objective. One is high-reduction deformation of the steel in the two-phase state (austenite–ferrite region) or supercooled austenite region. Another is to accumulate strain by having a short interpass interval while in the austenite region close to A_{r3} in order to reduce the rolling force. To simulate ferrite transformation under severe deformation, methods for considering nucleation and growth from dislocation lines inside the austenite grain have also been proposed.

25.5.3 Mesoscopic Model

In recent times, the Monte–Carlo method [13] and phase-field method [14] have been used to simulate microstructure evolution including grain growth, recrystallization, and phase transformations, and work in this field is continuing. The advantage of these methods is that they can predict the grain size distribution or morphology, not just the average values at each pass. These methods are expected to offer further improvements in the accuracy of material properties models.

REFERENCES

1. J.E. Burke. 1949. Grain control in industrial metallurgy. *ASM* 1:1.
2. T. Nishizawa. 1984. Grain growth in single- and dual-phase steels. *Tetsu-to-Hagane* 70:1984–1992.
3. T. Senuma, H. Yada, Y. Matsumura, T. Futamura. 1984. Structure of austenite of carbon steels in high speed hot working process. *Tetsu-to-Hagane* 70:2112–2119.
4. M. Avrami. 1939. Kinetics of phase change I. *Journal of Chemical Physics* 7:1103–1112.
5. M. Avrami. 1940. Kinetics of phase change II: Transformation–time relations for random distribution of nuclei. *Journal of Chemical Physics* 8:212–224.
6. M. Avrami. 1941. Granulation, phase change, and microstructure: Kinetics of phase change III. *Journal of Chemical Physics* 9:177–184.
7. C.M. Sellars, J.A. Whiteman. 1979. Recrystallization and grain growth in hot rolling. *Metal Science* 14:187–194.
8. W.A. Johnson, R.F. Mehl. 1939. Reaction kinetics in process of nucleation and growth. *Transactions of the AIME* 135:416–458.
9. J.W. Cahn. 1956. The kinetics of grain boundary nucleated reactions. *Acta Materialia* 4:449–459.
10. M. Suehiro, K. Sato, Y. Tsukano, H. Yada, T. Senuma, Y. Matsumura. 1992. Computer modeling of microstructural change and strength of low carbon steel in hot strip rolling. *Transactions ISIJ* 32:439–445.
11. K.J. Irvine, F.B. Pickering. 1957. Low-carbon bainitic steels. *JISI* 187:292–309.
12. F.B. Pickering. 1978. *Physical Metallurgy and the Design of Steels.* London: Applied Science Publishers.
13. Y. Saito, M. Enomoto. 1992. Monte Carlo simulation of grain growth. *ISIJ International*, 32:267–274.
14. I. Steinbach, F. Pezzolla, B. Nestler, M. Seeselberg, R. Prieler, G.J. Schmitz, J.L.L. Rezende. 1996. A phase field concept for multiphase systems. *Physica D* 94:135–147.

26 Metallurgical, Modeling, and Software Engineering Issues in the Further Development of the Steel Mill Level 2 Models

Bingji Li and John Nauman

CONTENTS

26.1 Level 2 Model 277
26.1.1 Force and Flow Stress 277
26.1.2 Force Learning 278
26.2 Metallurgical Issues in Level 2 278
26.2.1 Retained Strain 278
26.2.2 Rolling in the Two-Phase Region 279
26.2.3 Metallurgical Aspect of the Flow Stress 279
26.2.4 Others 279
26.3 Modeling Issues in Level 2 279
26.3.1 Limitation of the Adaptive Learning 279
26.3.2 The Guided Two-Parameter Learning (FIT2G) 280
26.3.3 Flow Stress Valid Range 281
26.3.4 Temperature-Dependent Properties 281
26.3.5 Intelligent Learning 281
26.4 Software Engineering Issues in Level 2 281
26.4.1 System Architecture Based on the Interactive Relationship of Mill Process Models 281
26.4.2 Web-Based Level 2 Systems 282
26.4.3 Others 282
26.5 Next-Generation Level 2 Systems 283
References 283

26.1 LEVEL 2 MODEL

The rolling mill Level 2 model is a substantial portion of the rolling mill Level 2 system. The Level 2 model is, in traditional sense, an expanded roll-pass design program, which creates pass schedule (draft distribution and stage plan) based on a long list of influence parameters. One of the primary parameters the Level 2 model takes into account in creating draft schedule is the roll-separating force. For a given mill, the roll separating force is the one to determine whether the limits (force and torque, etc.) of the mill are reached. On the one hand, a higher draft is preferred to reduce number of passes and to achieve better mechanical properties (in view of controlled rolling); on the other hand, a lower draft is helpful for better shape, especially in the finish passes. The draft schedule should compromise those two conflicting factors. Further factors that have to be considered for the good flatness of the rolled steel include roll crown (thermal, mechanical, and wearing), roll deflection, roll flattening, roll bending, and stand deformation, and so on. In particular, any variation in temperature, composition, entry slab size, and so on, should be compensated. The high complexity of the problem is far beyond the reach of human experience; a computer system (Level 2 model) has to be used.

One of the most critical areas for the Level 2 model is the Level 2 force prediction. Therefore, in the following sections, particular attention is paid to the force model.

26.1.1 Force and Flow Stress

The roll separating force is the multiplication of the mean flow stress, the projective contact area, and the shape factor

(Q-factor) [1]. Steel rolling in a pass starts at strain 0 (at the entrance) and ends at the maximum strain (pass strain, at the exit), so the mean flow stress rather than the instant flow stress should be used. The projective contact area increases with roll flattening. The shape factor (Q-factor) accounts for both deformation-zone geometry and friction.

Among the factors affecting the roll separating force, the flow stress is the one that bears the effect of material, strain, strain rate, and temperature. The strain is usually used as pass strain in the hot rolling, but it should be accumulated strain in the cold rolling. Many rolling passes in the hot mills could be considered as cold-rolling passes as long as the recrystallization cannot be completed (and so, the strain from previous passes cannot be fully removed). Some people term it warm rolling to avoid confusion. Understandably, the flow stress formula derived for the above rolling conditions is not applicable for the cases when phase transformation occurs during rolling.

Depending on the rolling practice, various formulas for flow stress prediction should be used. In many Level 2 systems, the following formula is used:

$$\sigma = C_1 e^{C_2/T} \cdot \varepsilon^{C_3} \cdot u^{C_4} \tag{26.1}$$

The four parameters C_1, C_2, C_3, and C_4 represent the coefficients of material, temperature (T in K), strain (ε), and strain rate (u), respectively. A good feature for this simple formula is that the flow stress and the mean flow stress enjoy the same form and share the same value of C_3. The potential problem is a very narrow valid range for the strain: the wider the strain range, the poorer the result. In particular, it is not valid for the strain below 0.1 (draft below 10%). In view of the strain rate, this formula applies to most flat rolling practices but is not valid for the high-speed rolling with strain rate over 100 (e.g., finish passes of wire-rod rolling).

26.1.2 Force Learning

To increase accuracy of the rolling force prediction, the flow stress model maintains separate sets of flow stress coefficients for each model grade. A model grade is created based on the steel grade (chemical composition), the product (type and dimension), and the production practice (e.g., with or without hold). For each model grade, three sets of coefficients are automatically adjusted by the long-term learning function to cover the three ranges (either thickness or temperature) expected during rolling. A Level 2 model should pursue not only high accuracy, but also good robustness (accuracy over a wide range of operating conditions).

Many Level 2 models use adaptive learning. The learning includes the short-term learning to shift the values upward or downward based on the error in the previous pass, and the long-term learning to recalculate and adjust all parameter coefficients (such as flow-stress coefficients and heat-transfer coefficients) after a qualified piece is rolled. The long-term learning of the Level 2 may use four fitting mechanisms (FIT), as shown in Table 26.1. If a coefficient is not used for learning (e.g., C_4 in FIT3A), it should be set to a medium value rather than zero.

TABLE 26.1
Four Fitting Mechanisms for Flow Stress Learning

FIT	Learning Coefficient	Fixed Coefficient
FIT2	C_1, C_2	C_3, C_4
FIT3A	C_1, C_2, C_3	C_4
FIT3B	C_1, C_2, C_4	C_3
FIT4	C_1, C_2, C_3, C_4	

26.2 METALLURGICAL ISSUES IN LEVEL 2

26.2.1 Retained Strain

In a project to improve the Level 2 model force accuracy, flow stress coefficient C_3, as indicated in the Equation 26.1, was studied. The C_3 for FIT4 (Table 26.2) indicated a medium value of about 0.22. The experimentally verified medium value for the hot forming is about 0.18 [2] from German colleagues, or 0.21 suggested for hot rolling Level 2 by Japanese researchers [3].

The question now is how to explain the difference between the values, and which is the right value.

In fact, both the German and Japanese colleagues are right, and their data are consistent. If the value from the Japanese colleagues is used, the pass strain should be used; while if the German colleagues' data are accepted, the true strain (the pass strain plus the retained strain) should be used.

Modern rolling practice has significantly reduced the rolling temperature to achieve better mechanical properties (tensile strength, yield strength, etc.). The rolling practice with high draft plus low temperature is the basis for the modern controlled rolling. Due to the low rolling temperature, the recrystallization often cannot be completed, and some strain from the previous pass would be retained. Table 26.3 shows the retained strain published by I. Tamura, et al. [4] with Nb steel at an inter-pass time of 20 s, and the value of the

TABLE 26.2
C_3 Values for the FIT4

Avg. C_3	Count	Weight%
≤0.12	492	12
0.14	308	8
0.16	164	4
0.18	334	8
0.20	514	13
0.22	382	10
0.24	295	7
0.26	563	14
0.28	244	6
≥0.3	674	17

TABLE 26.3
Retained Strain

T (°C)	1000	900	850	800	750
T (°F)	1830	1650	1560	1470	1380
IT (%)	2	25	35	55	70
BL (%)	0	15	21	33	42

Note: Nb steel, with inter-pass time: I. Tamura (IT) 20 s; B. Li (BL) 30–40 s.

retained strain estimated by the author (BL) for a plate mill assuming an inter-pass time of 30–40 s. At an inter-pass time of of 1 s and rolling temperature of 750°C (1380°F), almost the entire pass strain was retained [4].

26.2.2 Rolling in the Two-Phase Region

When rolling some thin gauges, large errors occur in predicting the roll separating force in the last two passes. It seems that the distribution of measured flow stress is off the trend: the measured value in the last pass is a bit too low. In Figure 26.1, the measured flow stress is calculated into a reference condition with strain 0.3 and strain rate 10 1/s; the only effect left is the temperature for the given grade. From the second to last pass to the last pass, the flow stress reduces with the decreasing temperature.

It is very likely that there was an α–γ phase transformation in the last pass, so much softer ferrite was generated.

Research report from Suzuki et al. [5] shows that for low- and medium-carbon steel, there can be phase transformation in the temperature 800°C–1000°C (1470°F–1830°F), sometimes in the range of 900°C–1000°C (1650°F–1830°F). Frequently, some low-carbon steels and some high strength low alloy (HSLA) grades conduct phase transformation in the temperature range of 850°C–900°C (1560°F–1650°F). This is the temperature range for the second last passes or the last pass of quite a number of grades rolled in many mills. The phase transformation temperatures for the newer grades rolled in recent years are much more difficult to determine, especially for those with addition of micro-alloys.

In general, one set of flow-stress coefficients only applies to one material in a given temperature region, but the phase transformation here actually involves two materials: the austenite (γ-phase) and the ferrite (α-phase). If we have to model this process, two different sets of coefficients have to be known: one for austenite and the other for ferrite. The difficulty is that the integrated coefficients also depend on the percentages of the two phases.

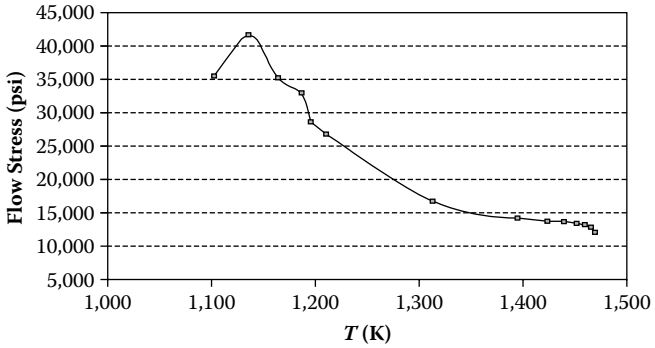


FIGURE 26.1 Flow stress at strain 0.3 and strain rate 10 1/s.

26.2.3 Metallurgical Aspect of the Flow Stress

In view of modern rolling technology, the flow stress has more metallurgical than mechanical sense, though most Level 2 models only treat it as a mechanical property. Metallurgically, the hot deformation of the metal is a very dynamic process: the grain size and grain shape are under constant change; some strains can be quickly removed (by recrystallization, etc.), while others from the past deformation (the retained strain) may need to be added to the current deformation stage.

As showed in Table 26.4, the material in the flow stress section (left) is associated with both the phase and the grain size (right), and the strain is affected by the retained strain. In high-speed rolling, the portion of the strain rate contribution to the flow stress is affected by the temperature due to the significant heat generation. In addition, the phase transformation involves heat release or heat absorption, as well as the change of the material, and thus, has a great impact on the flow stress. The metallurgical process would get much more complicated when the precipitation, etc., exists during processes such as hold.

TABLE 26.4
Flow Stress and Metallurgical Parameters

Flow Stress	Metallurgical Parameter
Material	Phase
Strain	Grain size
Strain rate	Retained strain
Temperature	Temperature

26.2.4 Others

For some X-grade and HSLA grades, the steel is held in the air for a certain length of time after a certain number of passes of rolling, and before it is rolled in the next pass, the so-called resume pass. In the hold period, there is precipitation and microstructure evolution. As a result, the flow stress changes. Many Level 2 models have no reflection on this change in the flow-stress model.

26.3 MODELING ISSUES IN LEVEL 2

26.3.1 Limitation of the Adaptive Learning

A project was completed to examine a mill Level 2 model because of the large force prediction errors, with the fitting mechanism FITs showed in the Table 26.1. It was detected

that there was a fluctuation of the flow-stress coefficients (C_3 and C_4) in a large range. This fluctuation of the flow-stress coefficients was identified to be due to a design logic problem of the model. For example, if the coefficient C_3 was not used for learning, the existing system set the C_3 to zero. This means that the contribution of the strain to the force was pushed to the strain rate factor C_4 (and other parameters). This caused the C_4 to fluctuate and thus hurt the long-term learning. The proposes solution was to replace the zero with an average value (C_{3m} or C_{4m}), if a coefficient was not used for learning.

Studies also indicated that C_3 and C_4 from FIT3A and FIT3B, respectively, were much larger than those from four-parameter learning. Continued studies also showed that either a low C_3 plus a high C_4, or a high C_3 plus a low C_4, would work well, in addition to a medium C_3 plus a medium C_4. In further studies, it was found that C_3 and C_4 from learning had great dependence on each other and roughly followed the relationship:

$$C_3 = -1.3203C_4 + 0.3677 \tag{26.2}$$

Equation 26.2 satisfies values from Hensel and Spittel [2] for traditional hot rolling: $C_3 = 0.174$, $C_4 = 0.139$ (roughly, $C_3 = 0.18$, $C_4 = 0.14$). Following this equation, if $C_4 = 0$ (as the case of FIT3A), then $C_3 = 0.3677$ would be twice as high as its theoretical value (0.18); or if $C_3 = 0$, then $C_4 = 0.278$ is also twice as high as its usual value (0.14) for hot rolling. Level 2 log data did confirm the higher values of C_3 and C_4 received from FIT3A and FIT3B, respectively, than the other fits.

Even with a four-parameter learning, the (C_3, C_4) value pair received from a qualified piece still can be at any point in the line described by the Equation 26.2, and so, both C_3 and C_4 can be in a wide range, from negative value, zero to a value twice as high as the best value. Therefore, there is a limitation for the blind learning, simply because C_3 and C_4 depend on each other. It is very hard to achieve the best value by combining those widely scattered numbers. This means that the learning itself can only reach a certain level of accuracy, but no further improvement. Human intervention or other improved logic is needed to achieve high-quality learning.

26.3.2 The Guided Two-Parameter Learning (FIT2G)

From the above discussion, if we slide the value pair C_3, C_4 to the middle point on the line described by Equation 26.2, by referencing the theoretical values of C_3 and C_4 published earlier, the preferred C_3, C_4 value pair can be determined. This preferred C_3, C_4 pair would fit both the theoretical values and the Level 2 real operation data.

Of course, in designing a new Level 2 system, the preferred value pair mentioned above could be used to improve the long-term learning. However, for an existing Level 2, in order not to make too many changes to the logics, use of carefully designed stable values for C_3 and C_4 is preferred, and it is sufficiently accurate, say, with an error below 5% as indicated in the results of a past mill project (Table 26.5). At least, it is much better than the blind learning (including the four-parameter learning). Further learning will be conducted only through C_1 (material coefficient) and C_2 (temperature coefficient), the two primary components of the flow stress. This learning procedure can be called the Guided Two-parameter Learning (FIT2G).

TABLE 26.5
Force Error and Quality Level Based on FIT2G

Before Improvement	After 1st Improvement
57% passes: <5%	Over 80% passes: <5%
87% passes: <10%	Over 90% passes: <10%
94% passes: <15%	Over 99% passes: <15%
Model failed for some grades (40% force error, bad shape)	No occurrence of quality problem found yet since use of new model

Note: The data here were based on the troubled grades. Regular grades may have still better results.

The result showed in Table 26.5 was actually after the first of the two improvements for an existing Level 2 model for a Steckel mill to roll steel plates. The first improvement was primarily to solve the learning logical problems, including the following:

- System learning: applied the guided two-parameter learning
- Metallurgical interaction: considered effects of retained strain, etc.

The second improvement, which was on the formula valid range and for the resume pass after hold, further improved the model quality.

Besides accuracy, the great benefit for FIT2G solution exists in the high-speed calculation because it only needs to recalculate two parameters C_1 and C_2 instead of four (C_1 to C_4). The fast calculation also provides a perfect opportunity for the web-based Level 2 system that Metal Pass is developing. In addition, FIT2G makes it possible to minimize the number of passes in the third temperature region, increase force prediction accuracy, and finish product geometry.

To perform the FIT2G learning, a great number of the carefully designed flow-stress coefficients (C_1, C_2, C_3, and C_4) are needed. For the mill with the results shown in Table 26.5, over 2000 model grades are rolled. For each model grade, there are three sets of the coefficients designed for the three temperature regions. Coefficients C_1 and C_2 were supplied in addition to C_3 and C_4; this was to satisfy the rolling for the first piece right after the new coefficients are loaded into the Level 2 system.

The design of the C_3 and C_4 values for each model grade in each temperature region can be based on the following three principles:

1. The initial values of the coefficients C_3 and C_4 in typical hot rolling

2. The pattern of the initial values (C_3 and C_4) in different temperature regions; in higher temperature there often are higher values of C_3 and C_4
3. The retained strains in different temperature regions; a lower temperature region has higher retained strains

26.3.3 Flow Stress Valid Range

Equation 26.1 is one of the oldest flow-stress formulas and has very limited coverage of nature of the flow stress. Modern forming process has called for comprehensive formulas for flow stress. A summary of the current flow-stress formulas is available online [6]. Based on requirements, four possible ways for expanding Equation 26.1 are described below.

1. Creating equivalent strain. Scale up the strain for the range (0, 0.15), and scale down the strain in the strain range over 0.35. This is a rough and easy solution. For existing Level 2 model, it only needs to change several lines of the source code, in the strain definition [7].
2. Adding a multiplication factor $\exp(C_5/\varphi)$ to Equation 26.1, to expand its valid range for strain from (0.1, 0.5) to (0.05, 1.5) [6], in which φ is strain and C_5 is the coefficient.
3. Adding a multiplication factor u^{C_6*T} to Equation 26.1, to expand its valid range for strain rate from (0.1, 100) to (0.1, 500) [6], in which u is strain rate and C_6 is the coefficient.
4. Adding a multiplication factor $d^{-0.5}$ to Equation 26.1, to expand its valid range from single grain size to variable grain size [6], in which d is the grain diameter.

To be noted is that the modification (2) leads to a change of the mean-flow stress formula. Please refer to [6] for the right formula of the mean-flow stress. The valid ranges mentioned above are for most steels, but with exceptions, especially for some alloys, alloy steels, and some nonferrous metals [8].

Flow-stress modeling for the rolling in the two-phase region is still a difficult problem. Because different materials are involved, theoretically the entire set of the coefficients, C_1, C_2, C_3, C_4, and so on, should be different.

One problem that remains unsolved in the metal forming community is modeling the flow stress for high-speed deformation with a strain rate over 500/s. It is difficult to model flow stress as such a high strain rate because the strain rate becomes unstable. Strain rate can easily reach 8000/s when hammering a sample, but because there is no way to maintain a constant strain rate, the results of such models are questionable.

26.3.4 Temperature-Dependent Properties

Temperature-related parameters are among the most critical factors in the steel hot mill Level 2 model. Almost all the mechanical or physical properties used in the Level 2 models are strongly temperature dependent. Examples of the properties are specific heat, thermal expansion coefficient (or density), E-modulus, Poisson ratio, etc. Using fixed values in the model calculation introduces prediction error. An example for the collection of the temperature-dependent properties for various steel grades is shown in [9].

26.3.5 Intelligent Learning

The limitation for the adaptive learning discussed above opens the door for the intelligent learning techniques, such as neural network, though for the existing Level 2 system, the guided two-parameter learning is much easier to implement.

Here is an example to apply an intelligent learning. Many Level 2 systems use a reference table to predict steel width change. With a varied environment, the table content and table length may need to be changed through learning, but many systems have difficulty achieving it. In this aspect, a neural network can be designed like a table-like system to update the table content and table length dynamically, based on a long list of factors such as production condition, fuzzy logic rules, and contents in the expert system. The learning system can be designed to be so flexible that a simple change in the database of the expert system can modify the entire learning logics and learning behavior.

Intelligent learning techniques can greatly improve the accuracy of some models with high complexity, such as the microstructure model, the microstructure-integrated flow stress model, and the model of rolled steel properties. The learning should be based on the rolling process models, in which the neural network provides the correcting factors for the model coefficients. Fuzzy logic rules and an expert system can provide guidelines (upper and lower boundaries) for the learning. A hybrid intelligent learning system can be designed with a combination of mathematical models and an intelligent learning system.

26.4 SOFTWARE ENGINEERING ISSUES IN LEVEL 2

26.4.1 System Architecture Based on the Interactive Relationship of Mill Process Models

Highly efficient rolling mill Level 2 model systems can be designed based on the object-oriented principle together with the interactive relationship of the mill process models. For example, in the structure design, the relationship between microstructure and flow stress could be reflected, and similarly, draft, flow stress, and roll force. The aim is that at least 80% of the classes should be consistent with the corresponding data structures. The design of the Database Management System (DBMS) should also follow the structure design.

In the design, one single set of the parent classes should be created based on general features of the mill. The classes for roughing mill, intermediate mill, and finishing mill, etc. should be derived from the parent classes during which time the special features for each mill stages can be added.

Consistently, a single set of general structures can be designed for the general mill, and the composite structures designated for roughing mill, intermediate mill, and finishing mill, etc. should use the general structures as data types. Every class, parent or derived, should take the corresponding structure (general or composite) as its data type to define its properties. In this way, every variable (e.g., the property) in the class may represent dozens or even hundreds of mill parameters. Any data type (either structure or composite structure) can be used in various mill stages (roughing, intermediate, and finishing, etc.) and in various scopes (local, module, and global). One example to apply the object-oriented principle is a program suite to calculate roll force for nine pass-sequences [10]. Almost all the calculations were done in a single class, the parent class. The eight derived classes (for those other than the general pass) only made minimal modifications to the parent class, primarily in the calculation for cross-section and contact areas.

Currently, some poorly designed Level 2 systems are with, for example, over 400 letter-size pages for parameter definition. This makes it tremendously difficult for newly hired engineers to modify or support such systems. It is believed that a well-designed Level 2 may only need one tenth of those parameters (about 40 pages).

26.4.2 Web-Based Level 2 Systems

Some of our clients still run the steel rolling facilities without Level 2, while some other clients, especially those in Asia, bought the Level 2 systems but had to retire them due to the lack of skills to support them (OpenVMS-based) [13]. It seems that a web-based Level 2 system can help those mills without Level 2 or with Level 2 of limited functionality. We tested the capacity of the web for engineering applications by running a computing-intensive program. This programs is a finite-differential program to calculate the temperature distribution over the cross-section of the rolled steel, say, in every 0.05 s along the 28 passes of the rolling and controlled cooling in water-boxes [11]. The result is satisfactory. The data transfer for Level 2 should be sufficiently fast. The numbers and text files really don't take very long to transfer, and the model calculation should have lower computing intensity as the finite differential method (FDM) program.

Level 2 developers know that a great portion of the Level 2 programming is usually spent in the data communication and memory management. However, in a web-based Level 2, those functions have been included in the web servers! While financial institutions use the web to run much more mission-critical applications than the steel mill Level 2, there should not be any concern about data security or availability. If the user prefers, the web server can be put inside the mill, the same as the Windows-based Level 2. New technologies such as Microsoft.Net enable the developers to write a web-based application in exactly the same way as the Windows-based one. Web servers are usually free of charge and are available for most versions of Windows (e.g., Windows 2000 Professional) and for other operating systems. Technologies are mature in this area. The cost of development and thus purchase of such a web-based Level 2 system should be much lower than a traditional one. In addition, it is very easy to use, support, and upgrade.

26.4.3 Others

In the software engineering aspect, the steel industry is usually 10 to dozens of years behind the IT industry. Software systems have evolved from client-server architecture to three-tier (client, server, and database) and multiple tier architecture, and to the distributed architecture and further to today's service-oriented architecture (SOA). Technologies, such as SOA and component object model plus (COM+), make it possible to develop powerful software systems with little effort. SOA allows various sub-systems and applications from various platforms to be easily integrated [12]. Applications

TABLE 26.6
Mechanical Factors of Roll Gap

Parameters	Issues	Modeling Note
Roll diameter	Ratio of the work and backup diameters, forward slip	
Draft	Draft in the last two passes: not too big (for shape), but not too small either (for mechanical property)	
Roll flattening	Increases contact area; needed for hot flat rolling model; critical for cold rolling	Formulas initially for cold rolling need to be fully expanded to fit hot rolling
Roll crown	Mechanical crown, thermal crown, roll wear, roll bending, etc.; may cause difference in draft between center and side	Empirical + FEM
Roll deflection	May cause difference in draft between center and side	Elastic FEM model preferred
Stand deflection	May cause variation in roll gap	Empirical + FEM
Friction	Critical for cold rolling and high-speed rolling	Depends on lubricant, temperature, roll gap, speed, contact material pair, etc.
Heat transfer	Steel/Roll, roll cooling, roll lubrication, etc.	Coefficient depends on scale formation, pressure, cooling and lubrication, etc.

based on the old platform cannot take advantage of the new information technologies. Currently, it is still quite popular in the steel industry to use the DOS-like OpenVMS to run the Level 2 application. Most OpenVMS-based Level 2 systems are still in the client-server architecture, with data stored in only short term.

26.5 NEXT-GENERATION LEVEL 2 SYSTEMS

The new-generation Level 2 system should have the following features:

1. *Full metallurgical principles integrated.* For example, a rolling mill Level 2 system may be integrated with over 100 rolling process models, an expert system, and advanced intelligent learning. Microstructure simulation is performed pass by pass to determine parameters such as retained strain, flow stress, grain size, grain shape, phase proportion, etc. The modeling, such as microstructure simulation, is integrated with the artificial intelligence (AI) learning techniques and with an expert system and is continuously learned through history data. Finite element method will be used to determine, e.g., roll deflection and local draft over width [14]. Hybrid systems will be established by combining the AI learning techniques with the empirical models so that the models are not black boxes (as many neural networks are) and will be continuously improved with the history data.
2. *Uninterrupted upgrade.* The Level 2 system can be upgraded frequently using vendor-supplied or user-developed components, without system shutdown. It will be fully modularized and fully object oriented. The system facilitates uninterrupted upgrade at three levels: service, component and dynamically linked library (DLL). A service usually consists of multiple components (including software applications) and is developed following certain IT standards (e.g., SOA, COM+). A component may be created from multiple class DLLs. A DLL is created from a single class, which may call other classes following object-oriented methodology. An upgrade in the DLL level may be done, for example, by simply replacing an old DLL with the new one, or by adding new DLLs to the existing Level 2 system. Therefore, with the changing industry practice, the Level 2 vendor (or the third party) can supply new DLLs, components, or services to the user. There is, therefore, no need to retire an old system and buy a new one every 10 years. The upgrade cost in this way can be minimal.
3. *State-of-the-art software engineering technologies.* Fully object-oriented programming technique will be combined with the interactive relationship of the mill process models. SOA will be used to integrate various applications and components, which may be initially designed for various platforms. The source code is expected to be concise, easy to understand, and easy to maintain. As to the architecture, it may be a four-tier system, consisting of operator interface (HMI, tier 1), Level 2 management system (tier 2), Level 2 model system (tier 3), and DBMS (tier 4). The tier 2 and tier 3 can either reside in a single server or be separated in two or more servers. Due to the large number of model calculations (microstructure, FEM, Neural Network, etc.), separate servers for the tier 3 is preferred.

The next-generation Level 2 model may include following components:

- Rolling process models—The models calculate several parameters, including roll force, temperature, roll flattening, roll deflection, thermal crown, roll wear, and steel deformation. It calls the metallurgical modules to determine microstructure, retained strain, and flow stress, etc.
- Metallurgical models—The models determine retained strain, grain size, rolled steel properties, etc., by combining with intelligent learning such as neural network, fuzzy logic, and expert system.
- Expert systems—The systems include logics, data, and influence factors on the mechanical, thermal, and metallurgical parameters, depending on rolling and thermal processes. Past mill experiences should be programmed as a portion of the expert system.
- Learning programs—The programs be based on rolling process models, in which the neural network provides the correcting factors for the model coefficients, and fuzzy logic rules and expert system provide guidelines (upper and lower boundaries, etc.) for the learning.
- Draft scheduling—The scheduling be based on various requirements (shape, properties, etc.) and various algorithms, with special attention paid to nonlinear algorithms. Microstructure and finish properties will be predicted for every newly generated pass schedule.

REFERENCES

1. B. Li. *Compared Experimental and Theoretical Investigations of Forming Technical Parameters in Shape Rolling with Example of the Hot Rolling of Angle Steels*. Freiberg, Germany: TU Bergakademie Freiberg, 1996.
2. A. Hensel and T. Spittel. *Kraft- und Arbeitsbedarf-bildsamer Formgebungsverfahren*. Leipzig, Germany: VEB Deutscher Verlag für Grundstoffindustrie, 1977.
3. Y. Saito, et al. The mathematical model of hot deformation resisitance with reference to microstructural changes during rolling in plate mill. *Transactions of the Iron and Steel Institute of Japan*, 1985, 25(11): 1146–1155.
4. I. Tamura, et al. *Thermomechanical Processing of High-Strength Low-Alloy Steels*. London: Butterworth & Co, 1988.

5. H. Suzuki, et al. *Studies on the Flow Stress of Metal and Alloys*. Tokyo: University of Tokyo, 1968.
6. B. Li. *Flow Stress*. http://www.metalpass.com/flowstress. Accessed February 2008.
7. B. Li, D. Cyr, and P. Bothma. *Level 2 Model Improvements at Evraz Oregon Steel Mills*. To be published in *AISTech*, May 4–7, 2009.
8. B. Li. *Steel Mill Process Modeling and Computer Application*. To be published in 2009.
9. B. Li. *High Temperature Properties*. http://www.metalpass.com/hit. Accessed February 2008.
10. B. Li. *Mill Load*. http://www.metalpass.com/millload. Accessed February 2008.
11. B. Li. *Rod temperature*. http://www.metalpass.com/cool. Accessed February 2008.
12. T. Erl. *Service-Oriented Architecture – Concept, Technology, and Design*. New York: Prentice Hall, 2005.
13. B. Li and J. Nauman. *Metal Pass 108 Mill-Related Projects*. http://www.metalpass.com/consulting. Accessed February 2008.
14. B. Li. Compared numerical and experimental studies of angle steel production process. *39th MWSP Conference Proceedings*, Vol. 35, pp. 705–719, 1998.

Section IV

Strip Profile and Flatness Control

27 Methods of Describing, Assessing, and Influencing Shape Deviations in Strips

Gert Mücke, Paul Dieter Pütz, and Frank Gorgels

CONTENTS

27.1 Shape Deviations in Strips 287
27.1.1 Flatness Deviations 288
27.1.2 Straightness Deviations 290
27.2 Measurement of Strip Flatness under Strip Tension 290
27.2.1 Methods for Measuring Strip Shape: Strip Flatness 291
27.2.1.1 Radial Force Measuring Systems 291
27.2.1.2 Strip Displacement Measuring Systems 291
27.2.1.3 Strip Waviness Measuring Systems 292
27.2.1.4 Strip Permeability Measurement 293
27.2.2 Requirements on Flatness-Measuring Systems 293
27.2.2.1 Measuring Accuracy 293
27.2.2.2 Influence of Measuring Zone Width 293
27.2.2.3 Influence of Temperature Deviations across the Strip Width 293
27.3 Quantitative Evaluation of Flatness Deviations, with Specific Regard to Waviness 294
27.4 Strip Flatness Control Methods 297
27.4.1 Strip Flatness Control Inside the Rolling Mill 297
27.4.2 Strip Flatness Control Outside the Rolling Stand 297
27.4.2.1 Conventional Strip Leveling Methods 297
27.4.2.2 New Strip Leveling Process 298
References 298

27.1 SHAPE DEVIATIONS IN STRIPS

Strip shape deviations may result in significant process disruptions and can give rise to defects and quality nonconformances up to the point where the product has to be rejected. Achieving an optimized strip geometry is, therefore, a priority goal both in producing strip via hot- and cold-rolling lines and in downstream processing and finishing operations.

The causes of strip shape deviations may be manyfold. Deformation may occur at the following times:

- In the roll gap during rolling
- In strip deflection, coiling, or uncoiling operations
- During heating or cooling, particularly of coiled product

Shape deviations are the result of plastic deformation varying locally across the strip width and/or strip thickness, which in turn produces inherent stress variations within the strip. A deviation from the ideal flat strip condition will occur, for instance, when the inherent stresses in the material exceed a critical level referred to as the critical buckling stress. The full extent of the shape deviation will not become visible until the process-induced strip tension is removed, in other words, the strip is no longer under load.

There exist numerous different types of strip shape deviations, which can be classified, for instance, as illustrated in the overview in Figure 27.1. Thus, one basic distinction is made between strip flatness and straightness deviations [1]. Flatness deviations are, in turn, divided into three major defect patterns: waviness, bow-shaped faults, and a nonplane-parallel strip thickness profile. Straightness deviations are commonly described as strip camber. Waviness is further subdivided into developable types (bounded by straight lines) and nondevelopable types (bounded by curved lines). Bow-shaped faults are further classified into length bow, cross bow, and twist, as illustrated in Figure 27.1.

A more comprehensive description of the shape deviations encountered will be presented in the following text. This description will be followed by a look at their causes and the associated measuring techniques and remedies, including methods for a quantitative evaluation of shape deviations, with specific regard to waviness.

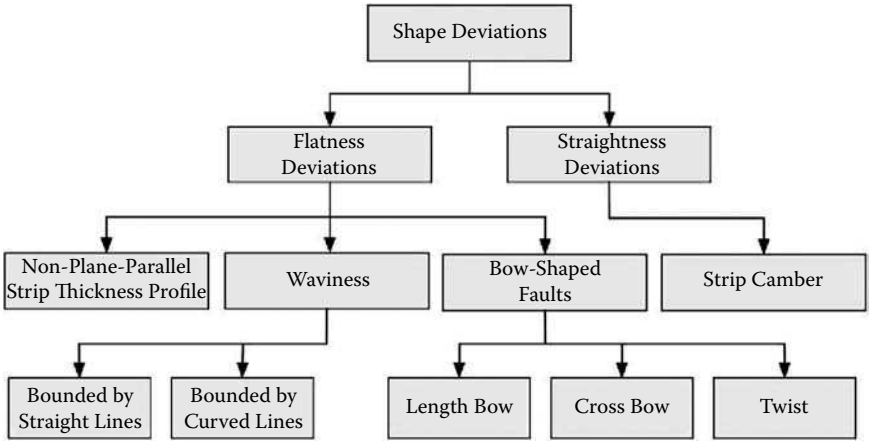


FIGURE 27.1 Classification of shape deviations.

27.1.1 Flatness Deviations

Strip waviness, the most frequently encountered shape deviation in cold rolling, can be described via the two measurable parameters, wave height and wavelength, as illustrated schematically in Figure 27.2. The wave height is the maximum distance of the bottom strip edge from a flat support surface. The wavelength refers to the length of strip buckling away from the support.

Waviness may occur in several forms. In some instances, it is bounded by straight lines (Figure 27.3). This is the result of tensile and compressive strains alternating across the strip thickness in the direction of rolling, resulting in opposed longitudinal inherent stresses at the top and bottom side of the strip. In the cross-strip direction, the magnitude of such stresses is virtually constant.

When a strip exhibiting such flatness defects is longitudinally slit, the slit sections will be found to be of equal length. Since this shape deviation can be removed by a simple bending process, without increasing the strip tension, the flatness of the strip surface can be restored. This phenomenon is generally described as developable waviness.

Another type of waviness (Figure 27.4) is characterized in that it is circumscribed by curved lines. This shape deviation cannot be eliminated by simple bending; it is due to plastic stretching of the longitudinal strip fibers that varies in intensity in the cross-strip direction. The amount of plastic elongation of the longitudinal fibers remains constant over the strip thickness. An uneven distribution of inherent stresses in the longitudinal and transverse direction is present in the material. The resulting length differences are balanced by residual stress, up to a level determined by the material's buckling strength. If this buckling strength is reduced by decreasing the elastic stability of the strip, for example, through further roll down, local buckling of the strip will occur. The magnitude of the critical buckling stress σ_k (refer to the formula in Figure 27.4.) depends on the modulus of elasticity E, the Poisson ratio v, the width b, and thickness h of the strip, and the strip length-to-width ratio α.

Waviness defects bounded by curved lines are referred to as nondevelopable waviness. This type of flatness defect is not amenable to elimination via a simple bending process. To remove such shape deviations, the strip must be subjected to locally adapted plastic stretching across the strip width so

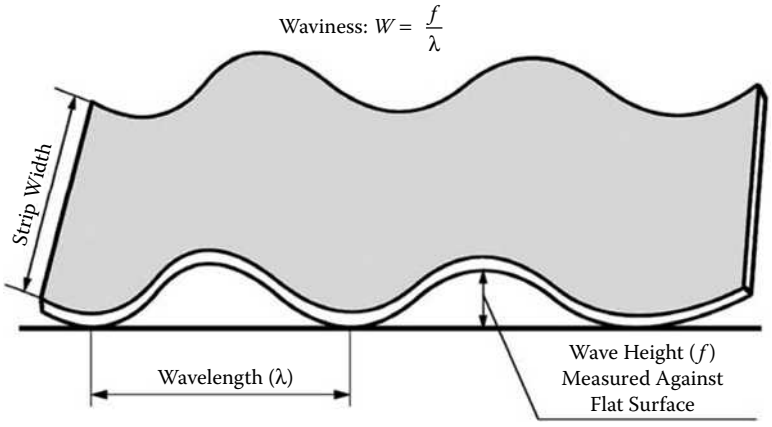


FIGURE 27.2 Waviness.

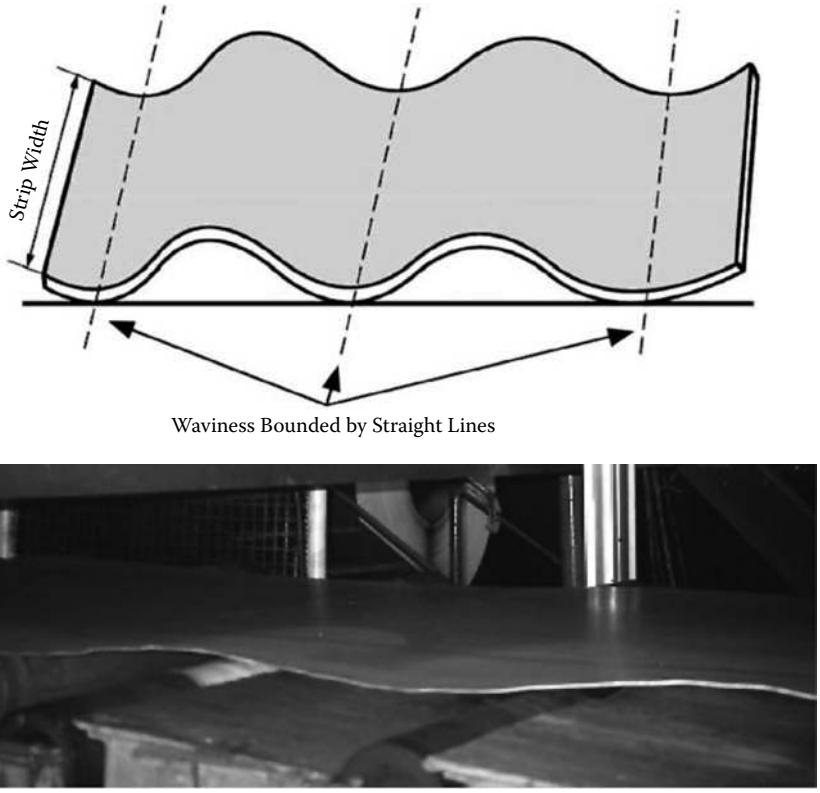


FIGURE 27.3 Waviness bounded by straight lines.

$$\sigma_k = k \times \sigma_e \text{ (Critical Buckling Stress)}$$

$$\sigma_e = \underbrace{\frac{E \times h^3}{12 \times (1 - \nu^2)}}_{\text{Bending Strength } N} \times \frac{\pi^2}{b^2 \times h} = N \times \frac{\pi^2}{b^2 \times h} \text{ (Euler's Stress)}$$

$$k = \left(1 - \frac{\nu^2 \times \alpha}{1 + \alpha}\right) \frac{1}{\alpha^2} \text{ (Buckling Value)}$$

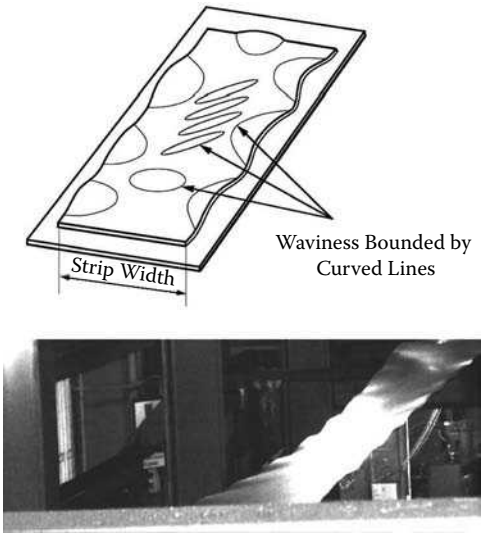


FIGURE 27.4 Waviness bounded by curved lines.

that the shortest strip fiber will be plastically elongated to at least the length of the originally longest fiber.

Bow-shaped faults constitute a class of shape deviations that, like waviness, may take various forms, such as:

- Strip curvature across the strip length (so-called "length bow" or "coil set")
- Strip curvature across the strip width (so-called "cross bow")
- Torsion about the longitudinal strip axis (so-called "twist")

Bow defects arise when the strip undergoes varying degrees of plastic stretching across the strip thickness in longitudinal strip direction. Under applied strip tension, nonuniform residual stresses endure in the lengthwise direction at the top and bottom sides of the strip. These stresses are constant across the entire strip width. When the applied longitudinal tension is removed, the residual stresses will give rise to strip curvature in the lengthwise strip direction, and the phenomenon known as *coil set* will be observed.

As the longitudinally curved strip is laid out in a flat plane, its outside (which has undergone more plastic stretching) undergoes elastic upsetting. Cross-strip compression stresses will form on this strip side. On the shorter inside surface, reverse conditions apply. The resulting inhomogeneous distribution of inherent stresses produces a bending moment,

which the material seeks to overcome by elastic deformation, for example, by buckling in the cross-strip direction. The strip is said to exhibit *cross bow.*

Coil set and cross bow (Figure 27.5) both constitute symmetrical buckling phenomena. Asymmetrical buckling in the form of twist (Figure 27.5) reflects lengthwise torsion of the strip.

Coil set, cross bow, and twist can each be eliminated by plastic bending without superimposing tension. Thus, they belong to the class of defects referred to as developable faults.

Another type of flatness deviation to be included here, along with waviness and bow-shaped faults, is non-plane-parallelism of the strip thickness profile (Figure 27.6). In producing hot strip for a downstream cold-rolling process, it is usually desirable to create a thickness profile that departs from the plane-parallel ideal. The aim is to achieve the cigar-shaped section illustrated in Figure 27.6 so as to adapt the strip thickness profile to the convex roll gap that is caused by mill spring at the cold-rolling stage.

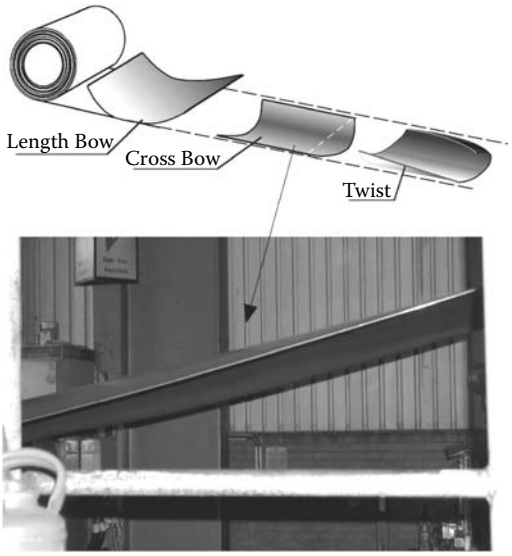


FIGURE 27.5 Types of bow-shaped fault.

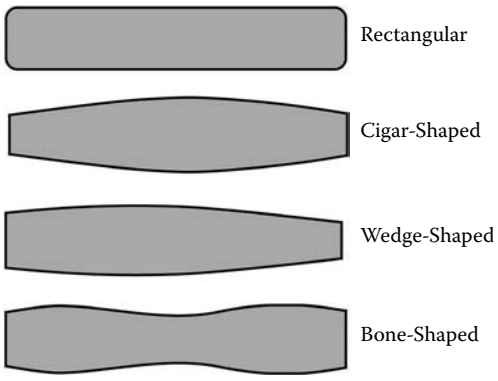


FIGURE 27.6 Various thickness profiles.

An unfavorable strip thickness profile may cause flatness deviations to occur in the roll gap if the latter cannot be adapted to the thickness profile of the incoming strip via appropriate mechanical or thermal control mechanisms.

Even minuscule variations in the thickness profile of the incoming strip may result in pronounced strip waviness or strip camber. Thus, a 1-μm variation in the thickness profile of a 1-mm-gauge strip will cause the strip to lengthen by about 1000 μm/m in the longitudinal direction.

It may be mentioned in this context that a pronounced risk of camber formation exists specifically in rolling of slit strip, given the asymmetrical nature of the strip thickness profile in the cross-strip direction.

27.1.2 Straightness Deviations

Strip straightness is measured by the amount of curvilinear deviation of the strip edges from an ideal straight line in the direction of rolling (Figure 27.7). This defect type is usually referred to as lateral strip camber. Strip camber occurs if, during rolling, the thickness of the strip increases or decreases at a uniform rate across its width. This shape defect constitutes a nondevelopable fault. Nonuniform stretching of the strip fibers in the cross-strip direction is required to remove it.

Basically, it can be said that developable shape defects can be removed by a mere plastic bending operation resulting in a uniform plastic elongation of the strip fibers in the cross-strip direction. The elimination of nondevelopable shape faults, however, requires a nonuniform plastic elongation across the strip width.

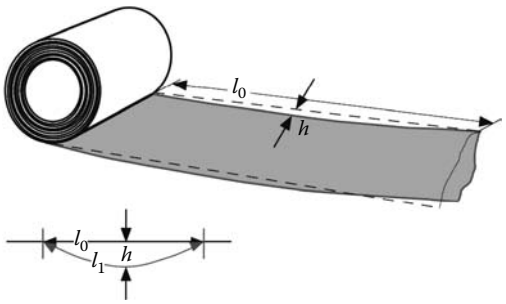


FIGURE 27.7 Strip camber.

27.2 MEASUREMENT OF STRIP FLATNESS UNDER STRIP TENSION

In hot- and cold-rolling mills, as well as in downstream treatment lines, the strip is processed under tension. Length deviations of different strip fibers across the strip width that are present in the material are stretched out by the applied tension in such a way that the strip appears to be flat during processing. However, latent flatness deviations are present in the strip and will later become apparent during uncoiling.

In order to be able to influence flatness deviations during the rolling process itself, using the adjustment systems of rolling stands, flatness-measuring systems are required. These measuring systems have to be capable of being used in diverse types of rolling mills and strip treatment lines and must deliver precise results, irrespective of the steel grade and its dimensions. Since the strip is subjected to longitudinal tension in most strip treatment lines, the tensile stress distribution, which itself is dependent on the length distribution according to Hook's law, is used for the determination of deviations in strip flatness.

27.2.1 Methods for Measuring Strip Shape: Strip Flatness

For the determination of the local strip length distribution over the strip width, measuring methods are applied; these methods can be classified in four groups [2], as shown in Figure 27.8:

- Radial force measuring systems
- Strip displacement measuring systems
- Strip waviness measuring systems
- Strip permeability measuring system

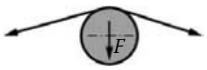
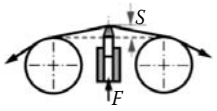
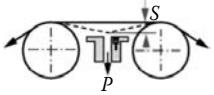
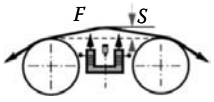
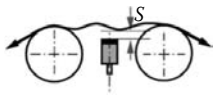
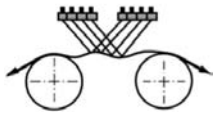
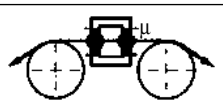
Measuring Method	Schematic Measuring Principle	Remark
1. Measuring of local bending forces in the strip		The measuring roll has to be driven in some systems and specific applications.
2. Measuring of displacement of the strip Deflection produced by a) contact method (mechanically)		Strip deflection depends on strip thickness and tension gradients over strip width.
b) contactless method (negative pressure)		Strip deflection depends on strip thickness and tension gradients over strip width.
c) contactless method (magnetic)		Strip deflection depends on strip thickness and tension gradients over strip width. Suitable for ferromagnetic material only.
3. Measuring of waviness in the strip a) inductive		Suitable for ferromagnetic material only.
b) optical		Suitable for low strip tension only. This method does not detect length differences that have been compensated by elastic elongation.
4. Measuring of permeability in the strip		Suitable for ferro magnetic material only. Magnetic anisotropy over the strip width should be considered.

FIGURE 27.8 Flatness measuring methods.

27.2.1.1 Radial Force Measuring Systems

The methods most commonly used to measure strip flatness deviations detect the radial force exerted by the longitudinally tensioned strip as it is deflected around the deflector roll. This radial force varies locally as a function of differences in tensile strength distribution across the strip width. By using suitable measuring rolls with measuring zones distributed across the width of the roll cylinder, it is possible to determine the local radial force and to calculate the tensile stress and hence the length distribution across the strip width (Figure 27.9a).

The well-known flatness-measuring rolls of the BFI and ABB types, of which more than about 1000 each are now in operation around the world in a wide variety of cold-rolling mills and strip treatment facilities, also operate on this deflection-roll principle. The strategy is to replace the deflector rolls—which are, in any case, required in front of the coiler—with measuring rolls designed to operate as deflector rolls at the same time. This avoids the installation of separate measuring systems occupying additional space (Figure 27.9b).

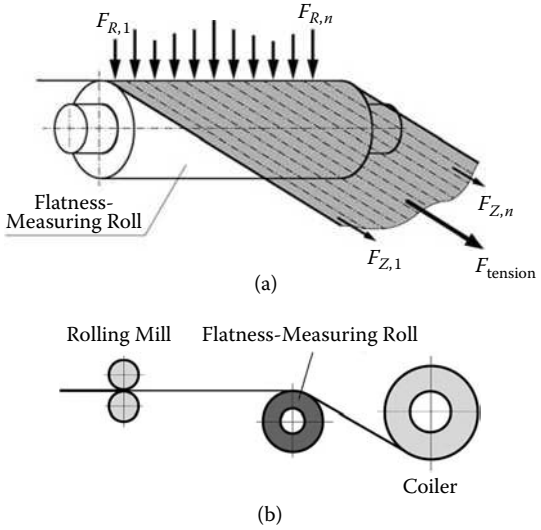


FIGURE 27.9 Measurement of local radial forces by deflection rolls. (a) Flatness measuring roll; (b) Separate measuring systems.

27.2.1.2 Strip Displacement Measuring Systems

This group of measuring systems uses the varying deflection of the strip over the strip width perpendicular to the direction of rolling under the influence of an external force. When forces are applied to the strip in the cross-strip direction, the individual fibers of the rolled material will deflect according to the tension acting on them. This deflection can be produced by contact, such as by a specially designed diamond head, with no surface damage resulting. Strip deflection can, however, also be achieved by contactless devices using oscillating negative-gauge pressure (vacuum principle) or by magnetic fields. In the first case, inductive position transducers

are used to measure the distance covered by the strip at the deflection point. In the second case, this is done using eddy current measuring sensors. In the third case, contactless inductive sensors are applied.

The measurement of local strip displacement serves to determine an equivalent distribution of longitudinal strip tension across the strip width. When using this method, it must be remembered that the deflection of the strip depends on the strip thickness and on the gradient of tension in the cross-strip direction.

Displacement measuring systems are normally installed between the roll gap of the rolling mill and the deflector roll before the coiler (Figure 27.10a). In thin strips, the longitudinal tensile stress acting on the material may therefore result in elastic necking and folding (Figure 27.10b). Such folds generate a bending resistance similar to that of corrugated plate/sheet, which will restrict the extent of strip displacement under the applied displacement forces and will cause errors in flatness measurement.

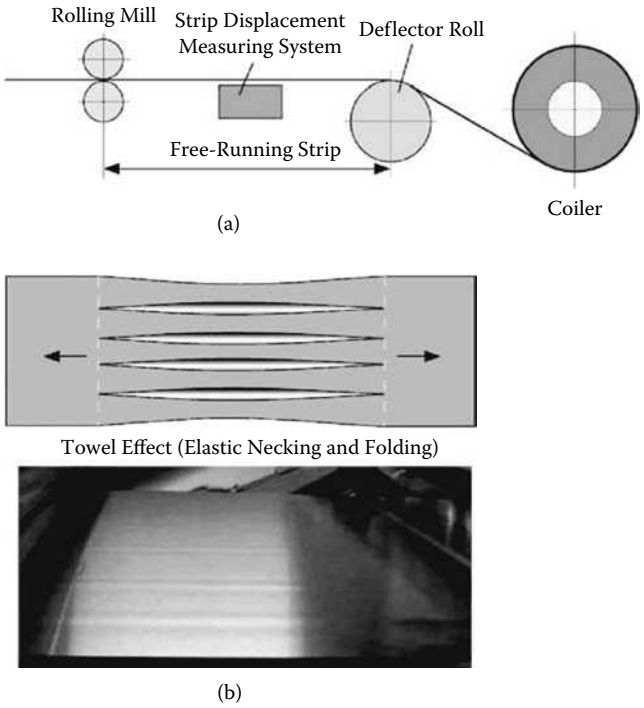


FIGURE 27.10 Measuring error due to formation of folds. Normally installed systems (a) can result in elastic necking and folding (b) in thin strips.

In thick strips, bending of the strip around the deflector roll will generate a length bow, which in turn results in a cross bow due to cross contractions (Figure 27.11a). If this cross bow has superimposed flatness deviations, such as long strip edges, the direction of the cross bow will change from upward to downward in an uncontrolled manner during displacement of the strip. The flatness-measuring system then wrongly registers this change of direction as a flatness deviation.

There is another bow-induced factor influencing the result of flatness measurements obtained with displacement measuring systems. If the length bow becomes more pronounced, the distance between the strip surface and measuring unit will increase as well, which may result in values that are outside the range of the measuring system (Figure 27.11b).

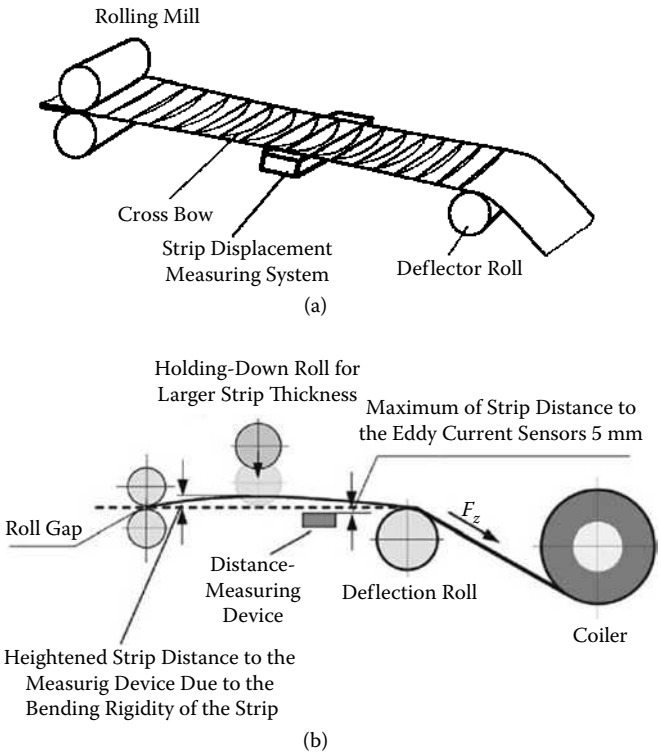


FIGURE 27.11 Measuring errors caused by strip length bow and cross bow (a), which, if pronounced, will result in increased distance from strip surface to measuring unit (b).

Displacement methods using the vacuum principle have an additional drawback. The positive atmospheric pressure prevailing at the strip edges results in an undefined pressure condition in this zone, which will affect the precision of the measurements. Knowledge of the state of flatness especially at the strip edges is, however, essential for flatness control.

27.2.1.3 Strip Waviness Measuring Systems

Here the measuring principle is based on detection of the strip distance to a reference position, for instance, by using inductive or optical sensors, without effecting a targeted strip displacement by supporting forces as in Section 27.2.1.2. Consequently, this measuring principle is suitable only for lines operating at low-strip tension, which do not even out length differences of strip fibers. The amplitudes of the local strip waves are measured in the cross-strip direction and converted into local-strip length deviations.

However, since the strip is unsupported and moves freely through this space, strip displacements may occur that are not attributable to longitudinal length deviations of strip fibers and will therefore cause spurious measurements [3].

27.2.1.4 Strip Permeability Measurement

Another method of determining strip flatness relies on the fact that ferromagnetic material will change its magnetic permeability under mechanical stress. This method is therefore limited to ferromagnetic strip products. Moreover, the correlation between permeability and tension in the cross-strip and longitudinal directions must be known for each material. This technique has therefore seldom been used in recent years.

27.2.2 Requirements on Flatness-Measuring Systems

27.2.2.1 Measuring Accuracy

Given the widely differing conditions under which flatness-measuring equipment is used today, for instance, in cold tandem mills or different types of reversing stands, the requirements regarding measuring accuracy vary widely as well.

In general, a minimum resolution of 10 µm/m in the measured values for strip length differences is considered necessary. This corresponds to a longitudinal stress difference of approximately 2 N/mm^2 on steel strip and of approximately 0.7 N/mm^2 in the case of aluminum. The demands on measuring accuracy are highest if very low differences in measured values are to be determined at a high stress level. Figure 27.12 shows the relationship between the required measuring accuracy and the level of tensile stress for different areas of use. Because of its low modulus of elasticity, the requirements for aluminum strip are substantially higher than those for steel [4]. Additionally, the figure clearly shows the difference between the accuracies required for measurements on tandem mills and on reversing stands, in which rolling generally takes place at considerably higher longitudinal stresses. Still higher measuring accuracies are needed if the same plant rolls strip of widely differing thickness at varying angles of wrap around the measuring roll. Frequently, it is necessary to detect deflection forces varying by a factor of up to 100 with the same relative accuracy in the same plant.

27.2.2.2 Influence of Measuring Zone Width

This width has a major impact on the accurate determination of the tensile stress or length distribution over the strip width. The measuring zone width is particularly important in strip edge areas and where large gradients of length deviations are present in the cross-strip direction [4]. For example, if there are large tensile stress gradients in the edge zone of thin strip, sufficiently accurate measurements can only be delivered by the outermost loaded measuring element and provided that the strip edge position is known (Figure 27.13). If the edge position is not known, which is often the case, then—for the example shown—a zone width of 50 mm would result in the flatness control adjusting mechanism being set in the wrong direction. Without the additional cost of strip edge detection, this error can only be avoided through narrower measuring zones.

27.2.2.3 Influence of Temperature Deviations across the Strip Width

For accurate flatness measurement, the cross-strip differences in strip temperature should also be taken into account since temperature gradients may result in nonuniform strip expansion. In material rolled on reversing stands, for instance, such cross-strip temperature variations may amount to as much as 5°C–8°C, which in the case of low-alloyed steels corresponds to length differences of between 60 and 100 µm/m.

These temperature-related length differences will be reflected in the online flatness readings, although they will disappear once the strip temperature has equalized. When using flatness-measuring systems, it is therefore recommended to

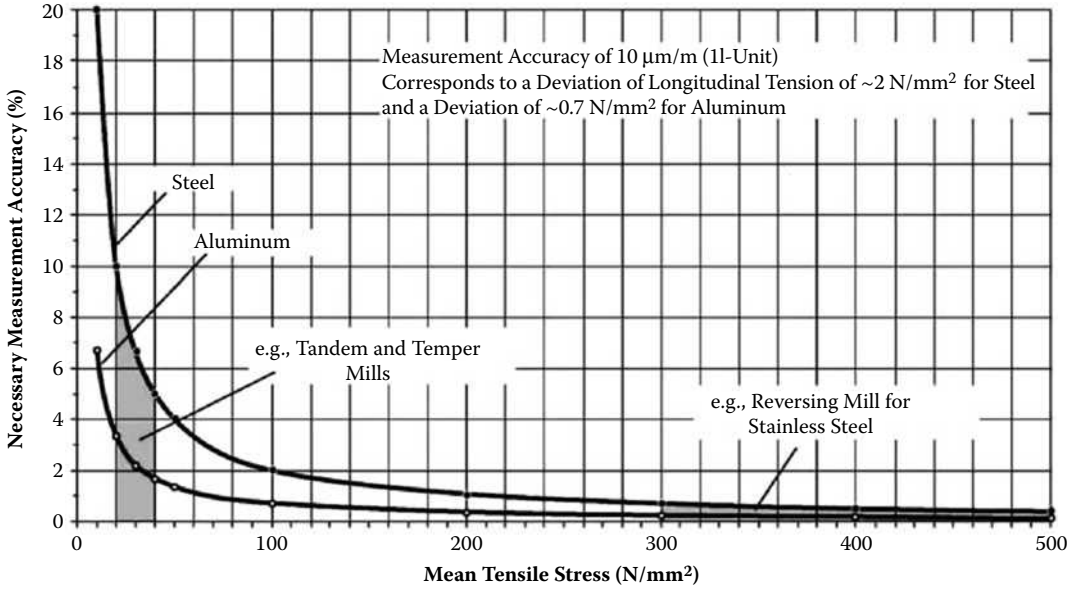


FIGURE 27.12 Required measuring accuracy with various strip tensions.

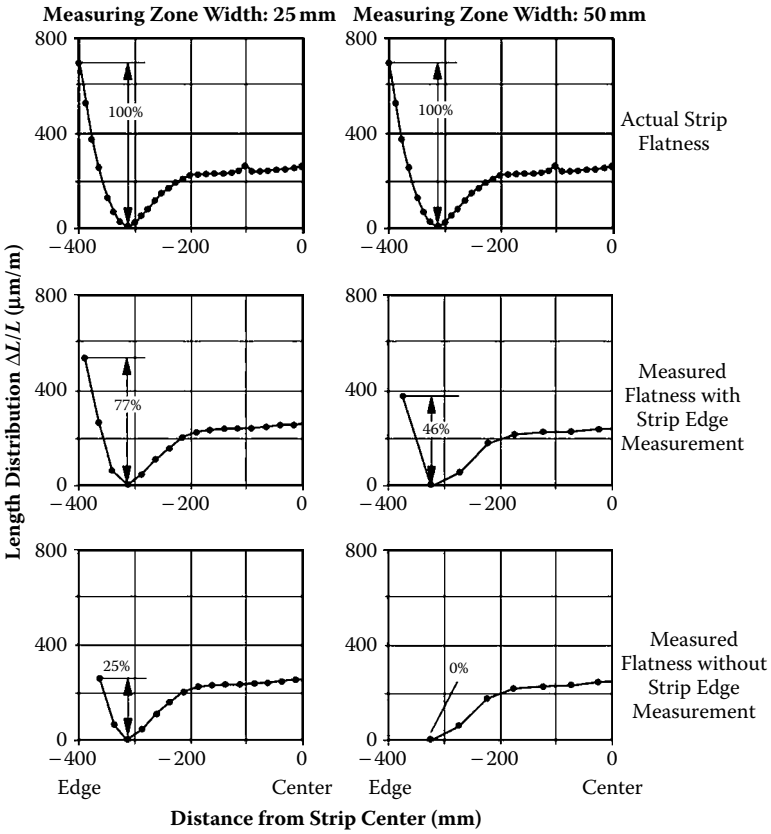


FIGURE 27.13 Effect of measuring zone width on flatness readings.

measure the strip temperature at the point where the readings are taken so that the measurement can be temperature-adjusted if major temperature differences are noted. This is particularly advisable where cooling conditions differ over the strip width.

27.3 QUANTITATIVE EVALUATION OF FLATNESS DEVIATIONS, WITH SPECIFIC REGARD TO WAVINESS

The qualitative and quantitative assessment of shape deviations is of great significance in industrial practice for:

- Manufacturers of rolling mill and strip finishing equipment in defining their warranties
- Measuring instrument manufacturers in demonstrating instrument capability
- Rolling mill and finishing line operators for process analysis and improvement
- Processors of semifinished products in drawing up specifications

Strip flatness requirements may be variously specified, depending on the downstream processing purpose. For deep-drawing processes, for instance, it may suffice to stipulate the maximum acceptable strip lift-off from a flat support surface. Where strip is intended for printing in multiple operations, on the other hand, the wave frequency may likewise be of interest.

The intention is always to describe the characteristics of a shape distribution in the longitudinal and cross-strip directions in an unambiguous quantitative manner using a minimum of parameters. Strip flatness is usually determined on strip sections having a reference length L which are cut, for instance, out of a rolled coil as required. These strip sections are then slit across their width into several strips whose length L_i is measured. The flatness index I_E used to describe the strip flatness is then obtained from the length difference ΔL_i of a local longitudinal strip fiber to the reference length L, related to the reference length of the strip section examined:

$$I_E = \frac{\Delta L_i}{L}$$

The flatness index is thus a dimensionless variable, although it is usually expressed in μm/m or I-units, with one I-unit being equal to 10 μm/m.

If the measurement is performed on a flat table assuming sine-shaped wave forms, the index can be calculated from the wavelength λ_i and the amplitude f_i as follows:

$$I_E = \left(\frac{\pi f_i}{2\lambda_i}\right)^2$$

As an alternative to this description method, one often finds the waviness W calculated in terms of the steepness ratio, which can also be converted directly into the flatness index.

$$W = \frac{f_i}{\lambda_i} = \frac{2}{\pi} \cdot \sqrt{I_E}$$

In assessing flatness deviations in a continuous manufacturing process in which the product is under tension, the shape deviation is normally determined continuously across the width and length of the strip using tension-measuring rolls. Here the shape deviation can be expressed via the shape deviation index I_P as follows:

$$I_P = \frac{\sigma_i - \sigma_m}{E}$$

In this equation σ_i is the longitudinal tensile stress of a strip fiber i, determined from the radial force measurement, while σ_m denotes the mean longitudinal stress across the strip width according to the strip tension applied. E is the modulus of elasticity of the specific strip.

According to Hooke's law, the tensile stress difference is directly proportional to the difference in elongation of individual strip fibers. Under the influence of external longitudinal tension, the originally shortest strip fibers undergo the greatest stress increase. Thus, the shape deviation index I_P corresponds to the negative value of the flatness index I_E.

In practice, the online measurements recorded under tension cannot always be correlated with the values measured offline with the aid of instruments. This is because strip flatness will be further influenced by the coiling processes, temperature changes, and strip deflection operations taking place downstream of the rolling mill. It should also be noted that flatness deviation measurements performed under tension can only identify nondevelopable faults, that is, those defects that are not attributable to inherent stress effects across the strip thickness.

An objective assessment of shape deviations can only be accomplished with the aid of suitable parameters. The available options are described below, using a deliberately exaggerated example. Figure 27.14 shows a measured flatness deviation from a defined target graph in the form of a cross-strip distribution. The material considered is industrial aluminum, rolled with a pass reduction of 0.7–0.3 mm. In the present case, the rolling mill was started without preheating following a work roll and backup roll change. The lack of thermal roll camber resulted in pronounced initial flatness deviations in the form of edge waviness and an elongated strip center, which could only be evened out as rolling progressed.

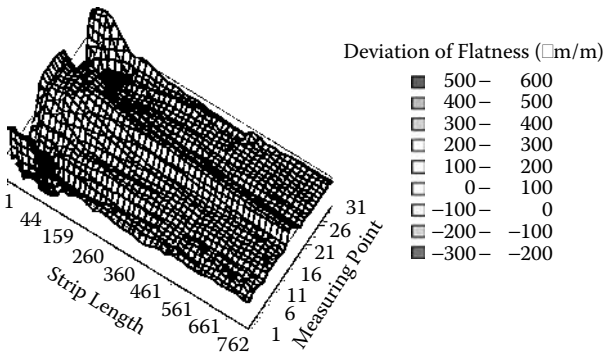


FIGURE 27.14 Measured flatness deviation.

In the most straightforward case, a description of the flatness situation can be given in the form of a limit value, for example, the statement that all shape deviations within 200 m of rolled strip lie within 150 µm/m. In addition, the measured values can be described statistically, which will usually yield a frequency distribution with defect probability statements. In the present case, the entire strip exhibited a standard deviation of σ = 54 µm/m and an average absolute defect of F_m = 31 µm/m. To describe the nonstationary area separately, one would obtain σ = 104 µm/m and F_m = 206 µm/m for the first 200 m of strip and σ = 28 µm/m and F_m = 22 µm/m for the remaining strip. For a direct comparison of the various scenarios, the shape deviation can be visualized, for example, in the form of a cumulative frequency function, as illustrated separately for the two strip areas in Figure 27.15. However, all information on the shape of the deviations and on their longitudinal and cross-strip distribution will be lost in this case.

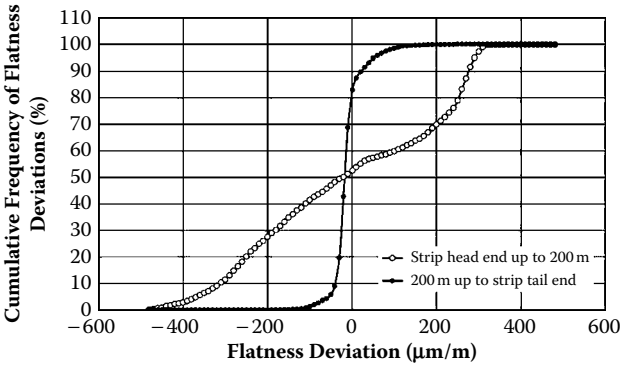


FIGURE 27.15 Cumulative frequency of flatness deviations.

A much used and more detailed shape description that is capable of describing cross-strip defect shapes for a given strip length position is achieved via a polynomial regression using the following equation:

$$\frac{\Delta L}{L} = a_0 + a_1 \cdot \left(\frac{b}{2} - x\right) + a_2 \cdot \left(\frac{b}{2} - x\right)^2 + a_3 \cdot \left(\frac{b}{2} - x\right)^3$$

$$+ a_4 \left(\frac{b}{2} - x\right)^4 \quad (0 \le x \le b)$$

where x is the variable coordinate across the strip width b and $a_0 - a_4$ are the regression coefficients. These coefficients

can each be assigned a geometrical meaning so that they will describe the following:

a_0: a constant portion
a_1: a linear wedge shape
a_2: parabolic defect portions
a_3: third order asymmetrical defects
a_4: symmetrical defects in strip edge areas

With the aid of these five coefficients, a large number of standard flatness deviations can be mapped and described with fairly high precision. It should be mentioned here that other functional relationships, such as cosine terms, are also frequently used in a regression analysis of the above type in order to achieve a still more detailed description of certain defect types. The above coefficient has gained particular importance in a strip-shape control context since it allows the various mill stand actuators to be separately controlled. Since the usual control functions such as crown, roll bending, and roll shifting act on the symmetrical portions, the control map of a rolling stand can be rendered in a single diagram for various rolling scenarios by plotting a_4 over a_2.

If the above polynomial description is applied to measured flatness deviation distributions, one basic problem will be encountered. In a shape-deviation measurement using segmented measuring rolls with a width of sensor elements of, say, 52 mm, a 1700-mm-wide strip will yield 32 measuring signals per cycle with which the cross-strip distribution of flatness deviations can be described. With extremely pronounced shape deviations, as depicted in Figure 27.14, a polynomial of the fourth order may not provide sufficient accuracy. To improve the description, one may increase the order of the polynomial, but then the values of all coefficients will change as well. Moreover, polynomials of an arbitrarily high order cannot be numerically computed with adequate stability. An additional drawback of the polynomial description is that even minor changes in the flatness profile will result in major changes in coefficient magnitude.

A useful tool in this context is the Chebyshev analysis [5]. The Chebyshev polynomial of the order n is described by:

$$T_n(x) = \cos(n \cdot \arccos x)$$

and provides the following explicit expressions by trigonometric transformation:

$T_0(x) = 1$ constant shifting

$T_1(x) = x$ wedge portion

$T_2(x) = 2 \cdot x^2 - 1$ parabolic portion

$T_3(x) = 4 \cdot x^3 - 3 \cdot x$ asymmetrical portion with one inflection point

$T_4(x) = 8 \cdot x^4 - 8 \cdot x^2 + 1$ symmetrical portion with two inflection points ("W")

The individual Chebyshev coefficients remain constant for a given shape profile, regardless of the order of the polynomial used. Their magnitude directly reflects the amount of the respective shape deviation, and polynomials of any degree can be computed in a stable manner.

Here, too, the term T_4 can be plotted over the quadratic term T_2. It should be noted that with Chebyshev coefficients, the control window generated is defined differently than with the $a_2 - a_4$ polynomial regression diagram. High values of T_4 indicate too short fibers in the quarter positions of strip having long strip centers and edges, while high T_2 values point to a parabolic defect with long fibers in the strip edge areas. On the other hand, a_2 coefficients indicate the same defect type, but high values of a_4 testify to long fibers along the strip edges. Since the plot can be drawn over the strip length at any time of the in-process measurement, a longitudinal path will be generated in the respective diagram. If the analysis is performed, not for the absolute strip shape but for the shape deviation from the target value, a zero level must be reached if the strip is perfectly flat.

Figure 27.16 plots the polynomial coefficients for the above example. The correct form of the defect is evident in the form of a trend represented by the superimposition of high a_4 values (long strip edges) and negative a_2 values (long strip center) at the start of the strip. In the course of deviation control, the coefficients approach the zero point. The order of magnitude of the coefficients is arbitrary, however, resulting from the sum of the superimpositions with other terms not shown here.

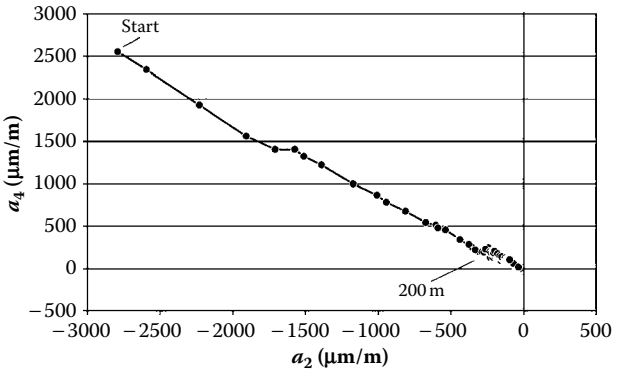


FIGURE 27.16 Flatness deviation diagrams, $a_2 - a_4$ from polynomial.

The Chebyshev plot in Figure 27.17, on the other hand, shows plausible values for the above example. The fact that all deviations fall within a tolerance window of 200 µm/m after a strip length of 200 m can be directly read off the diagram. The high values of T_4 indicate a strong W-phenomenon in excess of 300 µm/m, while the negative T_2 values point to a further elevation of the strip centre fibers.

By plotting the T_2 and T_4 coefficients from a Chebyshev analysis, it thus becomes possible to visualize the symmetrical flatness deviations in the cross-strip and longitudinal direction in an easily comprehensible form and to quantify the magnitude of each deviation at the same time.

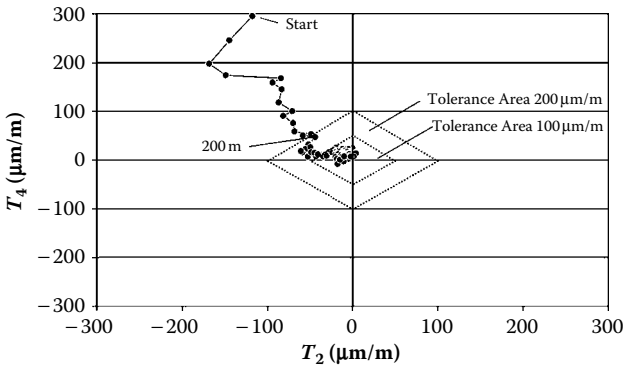


FIGURE 27.17 Flatness deviation diagrams, $T_2 - T_4$ from Chebyshev.

27.4 STRIP FLATNESS CONTROL METHODS

Strip flatness defects can be influenced during the rolling process by using effective mill actuators, as well as outside the rolling mill by subjecting the strip to various leveling operations.

27.4.1 Strip Flatness Control Inside the Rolling Mill

Figure 27.18 shows the most common and most frequently described methods used to control the length distribution over the strip width [2]. Alongside a schematic of the respective adjusting method, the basic effect of the adjustment on strip-length distribution is shown. By tilting the rolls, the strip sides can be elongated to differing degrees depending on the direction of tilting, as the length distribution drawings show. Bending the roll necks in the one or other direction achieves elongations either of the strip sides or center. More differentiated length distribution can be achieved by bending the rolls and applying different forces to the roll barrel. This method is, for example, used in multiroll rolling mills. Another effective method is axial shifting of the rolls. Conically ground intermediate rolls can be used to specifically influence the strip edge. The strip edges can be elongated by shifting the cone toward the outside or, conversely, they can be shortened. Axial shifting of work rolls with a particular ground barrel contour basically has the same effect as changing the crowning of the rolls. Continuous adjustment of roll crowning, with a corresponding effect on the strip-length distribution, can also be achieved by selective heating or cooling of the rolls or by changing the internal hydraulic pressure of a purpose-designed roll.

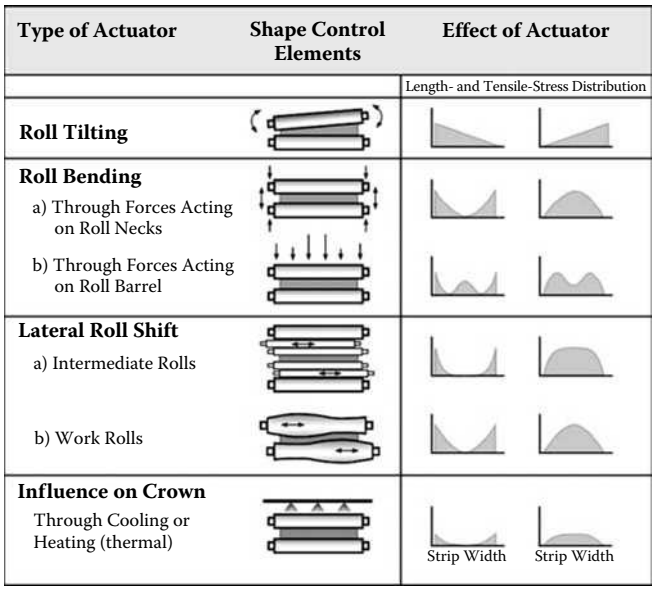


FIGURE 27.18 Means of controlling strip shape.

27.4.2 Strip Flatness Control Outside the Rolling Stand

In practice, the flatness of hot- or cold-rolled strip is improved through leveling methods designed to stretch the strip fibers plastically to a uniform length over the strip width so as to eliminate center or edge waves, for example, by equalizing strip length differences. Leveling equipment may be either of the stand-alone type or integrated into process lines, such as annealing or pickling lines, but may also operate continuously downstream of a temper rolling stand.

27.4.2.1 Conventional Strip Leveling Methods

In terms of equipment operating principle, a distinction can be made between stretch leveling and tension leveling. Tension leveling is by far the more important of these two. A feature common to both processes is that the required strip tension is raised above the line strip tension via entry and exit-side bridle rolls (Figure 27.19), [6]. In pure stretch-leveling the strip is plastically stretched by applying a tension load only. In tension leveling, plastic deformation of the strip is achieved by superimposing longitudinal tension and bending loads. It follows that the amount of stress bias required to achieve identical amounts of stretching is significantly lower in tension leveling. At the same time, the risk of strip cracking or fracture is reduced. On the other hand, a more inhomogeneous distribution of inherent strip stresses is to be expected from tension leveling as compared to stretch-leveling because of the nonuniform stress distribution across the strip thickness that results from bending.

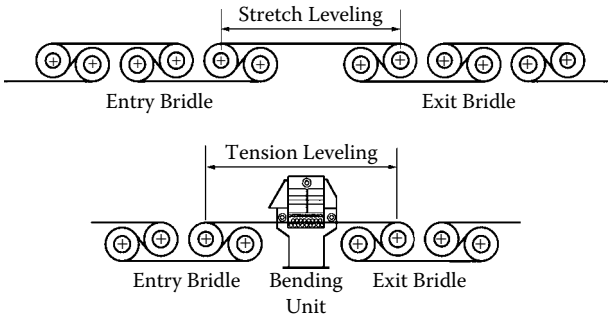


FIGURE 27.19 Methods of leveling strip.

27.4.2.2 New Strip Leveling Process

Conventional tension leveling requires high strip tension not only to support the plastic elongation achieved by bending but also for controlling the effective wrap angle around the bending roll. In addition to the bending roll radius and the amount of vertical screw down of the upper bending cartridge, the longitudinal strip tension is of great importance for adjusting the effective bending contour of the strip so as to achieve the targeted leveling result (Figure 27.20a).

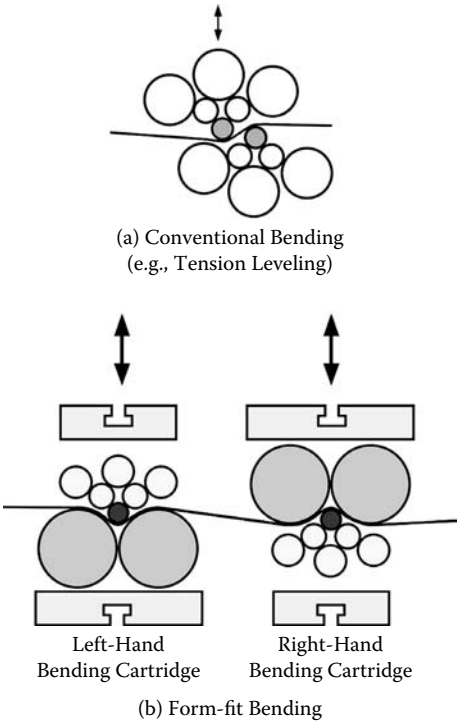


FIGURE 27.20 Tension leveling (a) compared with form-fit-bending (b).

The form-fit bending machine takes a different approach [7]. Its action principle is shown schematically in Figure 27.20b. Due to the design and arrangement of the form-fit-bending rolls and the bending roll force applied, the strip will assume a bending contour quite independently of the prevailing longitudinal strip tension rates. Vertical adjustment of the bending roll thus allows targeted control of the effective bending geometry irrespective of the tension. This operating principle makes it possible to run the bending process with reduced tension rates, down to the level commonly used for strip transport in processing lines.

REFERENCES

1. Mücke, G., Karhausen, K.F., Pütz, P.D. 2002. Methods of describing and assessing shape deviations in strips. *MPT International* 3: 58–65.
2. Neuschütz, E. Planheitsmessung und regelung beim warm- und kaltwalzen von bändern. *Walzen von Flachprodukten Symposium* 1987, pp. 7–26.
3. Mücke, G., Gorgels, F. 2007. Flatness measurement for high quality cold strip production. *MPT International* 1: 70–75.
4. Neuschütz, E., Mücke, G., Thies, H. 1994. New generation BFI flatness measuring system. *MPT International* 1: 86–88.
5. Bronstein, I.N., Semendjajew, K.A. 1996. *Taschenbuch der Mathematik [Mathematics Pocketbook]*. Stuttgart, Germany: Teubner Stuttgart.
6. Wieser, V. 1997. Simulation des Zugreckens von dünnen, breiten Bändern. Dissertation Montanuniversität Leoben.
7. Gorgels, F., Heßler, A., Mücke, G., Polzer, J., Pütz, P.D., Wolff, A., Boguslawsky, K. New method for the optimization of the strip geometry in strip processing lines. Paper presented at the *9th International and 4th European Steel Rolling Conferences*, Paris, France, 2006.

28 Local Shape Defects in Cold Rolling: Simulation, Causes Identification, and Reduction

Yuli Liu, Jian Fan, and Mike Levick

CONTENTS

28.1 Introduction 299
28.2 Strain Rate–Based Strip 3D Deformation Model 300
28.2.1 Analysis Model of Deformation Zone 300
28.2.2 Strip Thickness Distribution in the Roll Bite 300
28.2.3 Strain Rate and Velocity Field Model 300
28.2.4 Yield Criterion and Plastic Flow Equation 301
28.2.5 Surface Friction Model 301
28.2.6 Longitudinal Equilibrium Equation 301
28.2.7 Entry and Exit Tension Stress Model 302
28.2.8 Transverse Equilibrium Equation 302
28.2.9 Numerical Scheme 302
28.3 Work-Roll Thermal Crown Model 303
28.4 Roll Stack Deformation Model 303
28.4.1 Roll Separating Forces 303
28.4.2 Roll Equilibrium Equations 303
28.4.3 Roll Deflection Equations 303
28.4.4 Roll Deformation Compatibility Equation 304
28.4.5 Roll Gap Profile 304
28.4.6 Calculation Procedure 304
28.5 Stresses Unloading Model 305
28.6 Flowchart of the Main Program 305
28.7 Model Tuning and Verification 305
28.8 User Interface 306
28.9 Base Case for Local Shape Defects Simulation 306
28.10 Effects of Entry Strip Profile Ridge 308
28.11 Effect of Local Yield Stress Drop 311
28.12 Roll-Cooling Nozzle Clog or Work-Roll Crown Ridge Effect 314
28.13 Identification of Causes and Reduction of Local Shape Defects 316
Acknowledgments 316
References 316

28.1 INTRODUCTION

With the development of new shape control technologies, the shape quality of cold-rolled strip has improved significantly in recent years. Since simple shape defects, such as edge waves and center waves, are not difficult to control by advanced control actuators and close-loop shape control technologies, local shape defects become more outstanding. In some cases, they become the number one reason for customer rejection of cold-rolled strip.

Local strip shape defects are shape defects resulting from the local increase in the strip elongation along a line at any position across the strip width. Unlike simple waves, local shape defect is usually related to abnormal rolling conditions, such as feed stock ridges, yield stress local drop, roll cooling nozzle clogging, etc., and therefore, difficult to control. Quad Engineering Inc. carried out a research project to develop a three-dimensional shape simulation model for cold-rolling process [1,2], in which local shape defects can be simulated.

This chapter summarizes the results of the research project. In addition, by analyzing the simulation results, methods to identify the causes of the local shape defects and methods to reduce the occurrence of the local shape defects are proposed.

28.2 STRAIN RATE–BASED STRIP 3D DEFORMATION MODEL

28.2.1 Analysis Model of Deformation Zone

Figure 28.1 shows the strip-deformation zone and the stresses acting on an element in the roll bite. The nomenclatures of geometrical dimensions and stresses are also shown in this figure.

28.2.2 Strip-Thickness Distribution in the Roll Bite

The strip-thickness profile in the roll bite along rolling direction is assumed to be parabolic,

$$h(x,y) = h_2(y) + (h_1(y) - h_2(y))\left(\frac{x}{l_d}\right)^2 \tag{28.1}$$

where

l_d = Contact length between roll and strip
$h_1(y)$ = Strip entry–thickness profile in width direction
$h_2(y)$ = Strip exit–thickness profile in width direction

The entry thickness profile of the first stand is equal to the hot rolled–band profile $h_0(y)$. Under normal rolling conditions, the hot-band profile is fitted with following function:

$$h_0(y) = a_0 + a_2\left(\frac{y}{b/2}\right)^2 + a_4\left(\frac{y}{b/2}\right)^4 \tag{28.2}$$

where a_0, a_2, a_4 are fitting coefficients and b is the width of the strip.

If the hot band has a ridge, another parabolic term is added to the above function within the ridge width to form the ridged profile,

$$h_{0r}(y) = \begin{cases} h_0(y) + \Delta h_r\left(1 - \left(\dfrac{y - y_r}{w_r}\right)^2\right) & y_r - w_r \le y \le y_r + w_r \\ h_0(y) & y < y_r - w_r \quad \text{or} \quad y > y_r + w_r \end{cases} \tag{28.3}$$

where

$h_{0r}(y)$ = Hot-band profile with a ridge
Δh_r = Maximum height of the ridge
y_r = y coordinate of the ridge center
w_r = Half width of the ridge

28.2.3 Strain Rate and Velocity Field Model

It is assumed that the ratio of transverse strain rate to longitudinal strain rate β is constant along the rolling direction:

$$\beta(y) = \frac{\xi_y}{\xi_x} \tag{28.4}$$

With this assumption and by applying the constant volume principle, the strain rate field (ξ_x, ξ_y, ξ_z, η_{xy}) and velocity field (v_x, v_y) in the roll bite can be derived:

$$\xi_z \approx \frac{1}{h}\frac{\partial h}{\partial x} v_x \tag{28.5}$$

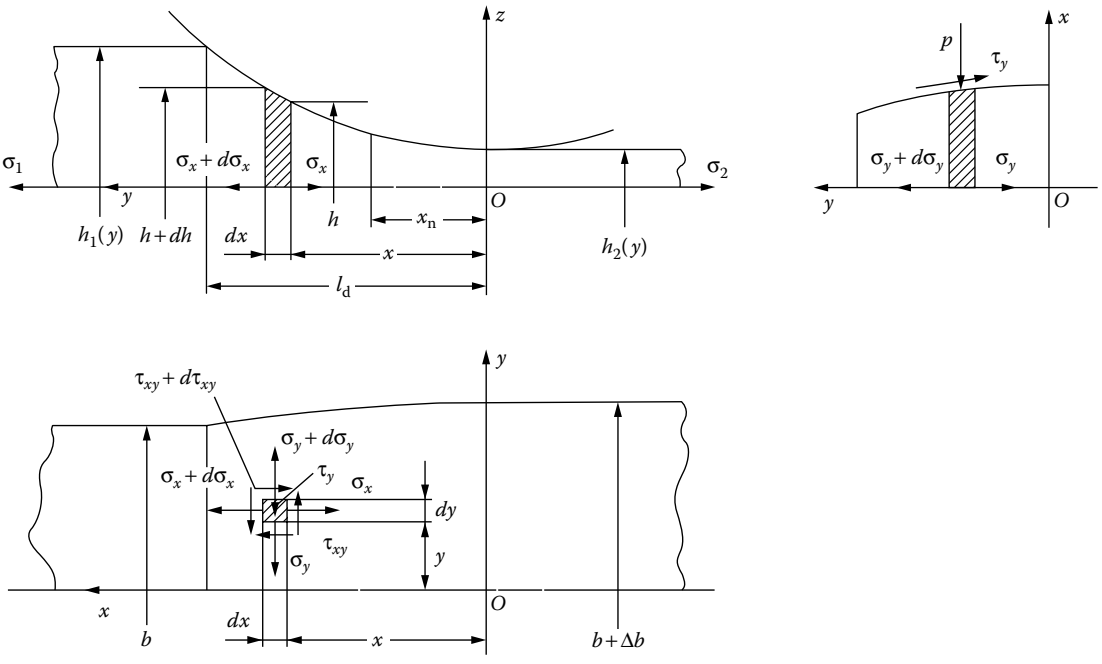


FIGURE 28.1 Sketch of strip 3D deformation model. (From Y. Liu et al. 2007. *Iron and Steel Technology* 4(8): 70–80. With permission.)

$$\xi_y = -\frac{\beta}{1+\beta}\xi_z \tag{28.6}$$

$$\xi_x = -\frac{1}{1+\beta}\xi_z \tag{28.7}$$

$$\eta_{xy} = \frac{\partial v_x}{\partial y} - \frac{\partial v_y}{\partial x} \tag{28.8}$$

$$v_x = v_n (h_n/h)^{\frac{1}{1+\beta}} \tag{28.9}$$

$$v_y = \int_0^y \frac{\beta}{1+\beta}\frac{1}{h}\frac{\partial h}{\partial x} v_x dy \tag{28.10}$$

where h_n, v_n are the thickness and longitudinal velocity distribution at the neutral plane, respectively.

28.2.4 Yield Criterion and Plastic Flow Equation

Considering the yield stress variation along width direction, the von Mises yield criteria and Levy–Mises plastic flow equation can be expressed by the stress field (σ_x, σ_y, σ_z, τ_{xy}) as follows:

$$(\sigma_x - \sigma_y)^2 + (\sigma_y - \sigma_z)^2 + (\sigma_z - \sigma_x)^2 + 6\tau_{xy} = 6(k(y))^2 \tag{28.11}$$

$$\frac{\xi_x}{\sigma_x - \sigma_m} = \frac{\xi_y}{\sigma_y - \sigma_m} = \frac{\xi_z}{\sigma_y - \sigma_m} = \frac{\eta_{xy}}{\tau_{xy}} = \frac{H}{k(y)} \tag{28.12}$$

where

$\sigma_m = \frac{1}{3}(\sigma_x + \sigma_y + \sigma_z)$

H = Effective shear strain rate

$k(y)$ = Yield stress in shear, which is considered to be a function in width direction in the case of local yield stress variation

$$k(y) = \begin{cases} k_0 + \Delta k\left(1 - \left(\dfrac{y - y_r}{w_r}\right)^2\right) & y_r - w_r \le y \le y_r + w_r \\ k_0 & y < y_r - w_r \quad \text{or} \quad y > y_r + w_r \end{cases} \tag{28.13}$$

where k_0 is the average yield stress in shear in the roll bite, considered to be a constant value and Δk is the maximum value of local yield stress increase (positive) or drop (negative).

Combining the yield condition, the plastic flow equation and the strain rate equations, the following stress–strain rate relationships can be obtained:

$$\begin{cases} \sigma_y = \sigma_x + \dfrac{2k(y)}{H}(2\xi_y + \xi_z) \\ \sigma_z = \sigma_x + \dfrac{2k(y)}{H}(\xi_y + 2\xi_z) \\ \tau_{xy} = \dfrac{k(y)}{H}\eta_{xy} \end{cases} \tag{28.14}$$

28.2.5 Surface Friction Model

The surface friction τ_f is divided into components in longitudinal and transverse direction τ_x, τ_y:

$$\tau_x = \tau_f \cdot \frac{v_x - v_n}{\sqrt{(v_x - v_n)^2 + v_y{}^2}} = \tau_f \cdot \frac{v_{sx}}{v_s} \tag{28.15}$$

$$\tau_y = \tau_f \cdot \frac{v_y}{\sqrt{(v_x - v_n)^2 + v_y{}^2}} = \tau_f \cdot \frac{v_y}{v_s} \tag{28.16}$$

$$\tau_f = \begin{cases} \mu p & \mu p \le k(y) \\ k(y) & \mu p > k(y) \end{cases} \tag{28.17}$$

where

p = Specific roll force

μ = Friction coefficient

v_s = Relative speed of roll and strip surfaces

v_{sx} = Longitudinal component of relative speed of roll and strip surfaces

28.2.6 Longitudinal Equilibrium Equation

Using slab analysis, the longitudinal equilibrium equation can be obtained [3]:

$$\frac{\partial(\sigma_x h)}{\partial x} + \frac{\partial h}{\partial x} p - 2\tau_x = 0 \tag{28.18}$$

Introducing stress–strain rate relationships and surface friction equations into the longitudinal equilibrium equation and making further simplifications, the following equations can be derived:

$$\frac{\partial \sigma_x}{\partial x} + \frac{2\mu v_{sx}}{h v_s}\sigma_x - \frac{k(y)}{hH}\left(\frac{2\mu v_{sx}}{v_s} - \frac{\partial h}{\partial x}\right)\sqrt{\frac{H^2 - \eta_{xy}^2}{1+\beta+\beta^2}}\left(2+\beta\right) = 0 \qquad \mu p \le k(y) \tag{28.19}$$

$$\frac{\partial \sigma_x}{\partial x} - 2k\frac{v_{sx}}{h v_s} + \frac{\partial h}{\partial x}\frac{k(y)}{Hh}\sqrt{\frac{H^2 - \eta_{xy}^2}{1+\beta+\beta^2}}\left(2+\beta\right) = 0 \qquad \mu p > k(y) \tag{28.20}$$

Equations 28.19 and 28.20 can be solved numerically.

28.2.7 Entry and Exit Tension Stress Model

The entry and exit tension stress models developed in Reference 1 are assumed to be still valid under hot-band ridge or yield-stress ridge conditions. For entry tension stress, it is

$$\sigma_1 = \bar{\sigma}_1 + \frac{E_s}{1-\upsilon_s^2}\left(\frac{v_{x1}}{\bar{v}_{x1}} - 1\right) + \sigma_0$$

$$= \bar{\sigma}_1 + \frac{E_s}{1-\upsilon_s^2}\left(\frac{v_n (h_n/h_1)^{\frac{1}{1+\beta}}}{\bar{v}_{x1}} - 1\right) + \sigma_0 \qquad (28.21)$$

where

$\bar{\sigma}_1$ = Average entry tension stress
v_{x1} = Entry velocity distribution induced by the plastic deformation in the roll bite
$\bar{v}_{x1}$ = Average entry velocity
σ_0 = Residual stress of the incoming strip (from previous stand or hot band, feed stock local residual stress included)
E_s = Elastic modulus of the strip
υ_s = Poisson's ratio of the strip

For exit tension stress, it is

$$\sigma_2 = \bar{\sigma}_2 + \frac{E_s}{1-\upsilon_s^2}\left[1 - \frac{v_{x2}}{\bar{v}_{x2}}\right]$$

$$= \bar{\sigma}_2 + \frac{E_s}{1-\upsilon_s^2}\left[1 - \frac{v_n (h_n/h_2)^{\frac{1}{1+\beta}}}{\bar{v}_{x2}}\right] \qquad (28.22)$$

where

$\bar{\sigma}_2$ = Average exit tension stress
v_{x2} = Exit velocity distribution induced by the plastic deformation in the roll bite
$\bar{v}_{x2}$ = Average exit velocity

28.2.8 Transverse Equilibrium Equation

The finite difference format of the transverse equilibrium equation is used to avoid the discontinuity of the partial derivatives to the y coordinate:

$$h\frac{\Delta\sigma_y}{\Delta y} - h\frac{\Delta\tau_{xy}}{\Delta x} - 2\tau_y = 0 \qquad (28.23)$$

To get a better converge, a simplified format of the transverse equilibrium equation is adopted here based on the method of weighted residuals to get an approximate solution [4]:

$$\int_0^{l_d}\left(h\frac{\Delta\sigma_y}{\Delta y} - h\frac{\Delta\tau_{xy}}{\Delta x} - 2\tau_y\right)dx = 0 \qquad (28.24)$$

with the boundary condition at the strip edge $y = b/2$

$$\int_0^{l_d} h\sigma_y dx = 0 \qquad (28.25)$$

28.2.9 Numerical Scheme

The above equations are solved using finite difference methods. The flowchart of the calculation procedure is shown in Figure 28.2. The stress fields are calculated from entry to exit by solving the longitudinal equilibrium (Equations 28.19 and 28.20) with the initial values determined by Equation 28.21. There are two main iterative loops in the calculation procedure. The inner loop calculates the lateral spread ratio by satisfying the transverse equilibrium Equation 28.24 and the strip edge boundary condition Equation 28.25. The outer loop determines the neutral plane profile by matching the exit tension stress calculated by the longitudinal equilibrium equation with the tension stress determined by the exit tension model Equation 28.22.

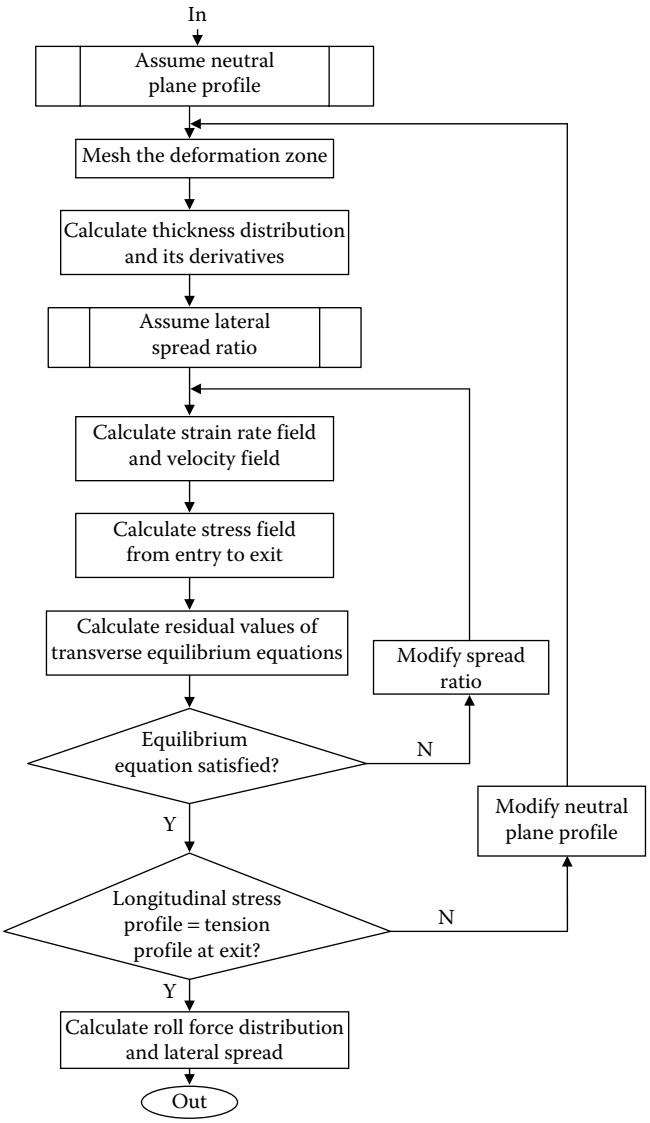


FIGURE 28.2 Flowchart of strip 3D deformation model.

28.3 WORK-ROLL THERMAL CROWN MODEL

An axisymmetric two-dimensional finite difference model is developed to calculate the work-roll temperature field and thermal crown. Since there are several different heat-transfer zones along circumferential direction, the weighted average of heat fluxes during one revolution is used in the calculation. The heat-transfer coefficient formulations used in References 5–8 are adopted to calculate the heat fluxes in different zones. The status of roll-cooling nozzles can be controlled independently; therefore, roll-thermal crown ridge effect can also be simulated by turn-off one or two nozzles. The governing equation and solving procedure used in Reference 5 are closely followed. The details of the formulation are neglected here. Extensive measurements of work-roll temperature field and work-roll thermal crown were carried out at a Coupled Pickle-Line and Cold Mill (CPCM). The work-roll thermal crown model was tuned and verified using the data collected during the measurements.

28.4 ROLL STACK DEFORMATION MODEL

The roll stack deformation calculation model for a four-high mill considering possible work-roll crown ridge and kiss rolling condition is shown in Figure 28.3.

28.4.1 Roll Separating Forces

The roll separating forces at the drive side and operator side can be different. They can be obtained by balancing the force and moment of the roll system as follows:

$$P_L = P_1 + P_k + F_L + F_R - P_R \tag{28.26}$$

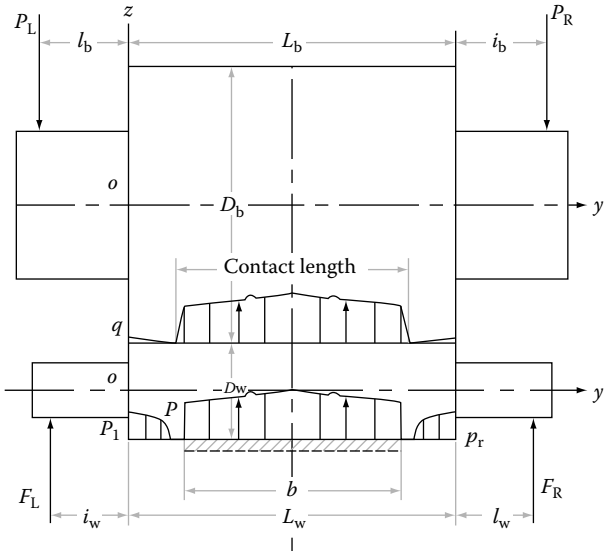


FIGURE 28.3 Roll stack deformation calculation model. (From Y. Liu et al. 2007. *Iron and Steel Technology* 4(8): 70–80. With permission.)

$$P_R = \frac{1}{(L_b + 2l_b)}\left[l_b(P_1 + P_k + F_R + F_L) + \sum_{j=1}^{m} p_{cj}\Delta y_j y_j \right.$$
$$\left. - F_L\left(l_w + \frac{L_w - L_b}{2}\right) + F_R\left(l_w + \frac{L_b - L_w}{2}\right)\right] \tag{28.27}$$

where

P_L = Roll separating force at the left side (drive side)
P_1 = Total rolling force
F_L = Work-roll bending force on the left side (drive side)
F_R = Work-roll bending force on the right side (operating side)
P_R = Roll separating force on the right side (operating side)
P_k = Total contact force between top and bottom work rolls
L_b = Backup roll barrel length
L_w = Work-roll barrel length
l_b = Backup roll neck length
l_w = Work-roll neck length
p_c = Combined work-roll contact pressure and rolling pressure

$$p_c = \begin{cases} P & \textit{rolling zone} \\ p_k & \textit{work roll to work roll contact zone} \\ 0 & \textit{noncontact zone} \end{cases}$$

P = Rolling pressure per unit width
p_k = Work-roll contact pressure per unit width
y_j = Coordinate of the jth element in the y direction (roll-axial direction)
Δy_j = The length of the jth element
m = Number of elements

28.4.2 Roll Equilibrium Equations

Two independent roll equilibrium equations are used to determine the inter-roll pressure distribution:

$$\sum_{j=1}^{m} q_j \Delta y_j - P_L - P_R = 0 \tag{28.28}$$

$$\sum_{j=1}^{m} q_j \Delta y_j y_j - l_b(P_R - P_L) - P_R L_b = 0 \tag{28.29}$$

where q is the contact pressure between backup roll and work-roll.

28.4.3 Roll Deflection Equations

With the formulation of influence functions, the backup roll deflection Z_b can be expressed as:

$$Z_{bi} = \sum_{j=1}^{m} \alpha_{bij} q_j \Delta y_j + \alpha_{bL} P_L + \alpha_{bR} P_R + \frac{y_i}{L_b}\sum_{j=1}^{m} \alpha_{\Delta bj} q_j \Delta y_j$$
$$+ \sum_{j=1}^{m} \alpha_{obj} q_j \Delta y_j \quad i = 1, 2 \ldots m \tag{28.30}$$

the work-roll deflection Z_w can be expressed as:

$$Z_{wi} = \sum_{j=1}^{m} \alpha_{wij} p_{cj} \Delta y_j - \sum_{j=1}^{m} \alpha_{wij} q_j \Delta y_j - \alpha_{FL} F_L - \alpha_{FR} F_R + \Delta_{wz} \frac{y_i}{L_c} + K_{wz} \quad i = 1, 2 \ldots m \tag{28.31}$$

where

L_c = Contact length between rolls
Δ_{wz} = Work-roll rigid skewing parameter
K_{wz} = Work-roll rigid movement
α = Influence functions respective to different cases
i = Suffix counter denotes the position of an element in axial direction

28.4.4 Roll Deformation Compatibility Equation

The deformation compatibility between the backup roll and the work-roll can be expressed as follows:

$$Z_{bi} + \delta_{bwi} = Z_{wi} + C_{Rbi} + C_{Rwi} \quad i = 1, 2 \ldots m \tag{28.32}$$

where

C_{Rb}, C_{Rw} = Backup roll and work-roll crown (radius) relative to the middle of roll barrel
δ_{bw} = Contact deformation between work-roll and backup roll, calculated using the formula derived in Reference 9

The roll crown profile consists of roll initial crown and roll thermal crown. If there is no crown ridge, the roll initial crown profile is assumed to be parabolic. Another parabolic term will be added to the roll initial crown profile if roll crown ridge exists.

$$C_{Rw}(y) = \begin{cases} C_w(y) + \Delta C_{wr} \left(1 - \left(\dfrac{y - y_r}{w_r} \right)^2 \right) & y_r - w_r \le y \le y_r + w_r \\ C_w(y) & y < y_r - w_r \quad \text{or} \quad y > y_r + w_r \end{cases} \tag{28.33}$$

where

$C_{Rw}(y)$ = Work-roll initial crown including a ridge
$C_w(y)$ = Parabolic work-roll initial crown
ΔC_{wr} = Maximum height of the work-roll crown ridge

28.4.5 Roll Gap Profile

The roll gap profile can be expressed as:

$$h_i = h_z + (Z_{wi}^u - Z_{wz}^u) + (Z_{wi}^d - Z_{wz}^d) + 2(\delta_{wwi} - \delta_{wwz}) - 2(C_{Rwi} - C_{Rwz}) \quad i = 1, 2 \ldots m \tag{28.34}$$

where

h_z = Exit thickness at center
u = Superfix denotes top work-roll
d = Superfix denotes bottom work-roll
z = Suffix denotes the center of the strip
δ_{ww} = Work-roll flattening, using the 3D work-roll flattening model in Reference 4

28.4.6 Calculation Procedure

The kernel part of the roll deformation calculation is to solve the equation system consisting of roll deformation compatibility and roll equilibrium equations. The flowchart of the calculation procedure is shown in Figure 28.4. Considering the inter-roll pressure peaks due to work-roll crown ridge, the iteration to determine the inter-roll pressure distribution

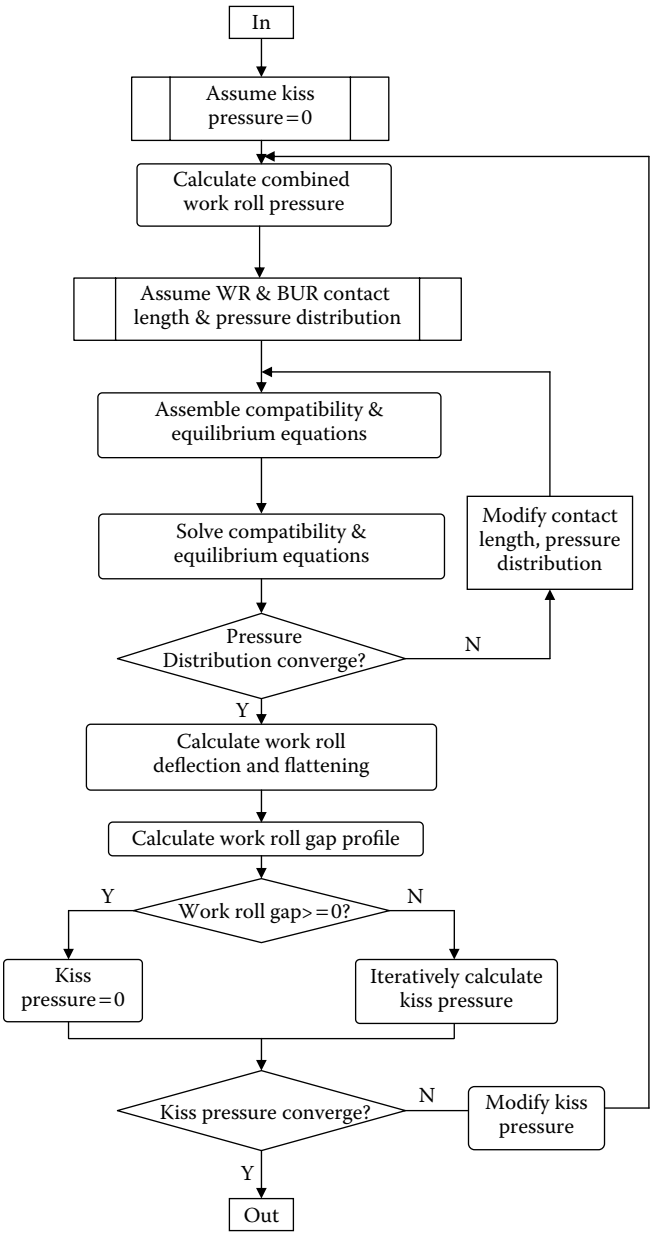


FIGURE 28.4 Flowchart of roll stack deformation calculation model. WR = work roll, BUR = backup roll.

is used in the program. This iteration can also determine the inter-roll contact length at the same time. Another iteration loop calculates the kiss pressure if kiss rolling occurs.

28.5 STRESSES UNLOADING MODEL

The analytical stresses unloading model derived in Reference 10 is adopted in this program to calculate the residual stress. Using the coordinate system from Figure 28.5, the residual stress σ_{xr} can be expressed as follows:

$$\sigma_{xr} = \sigma_{x2} - \upsilon_s(\sigma_{y2} + \sigma_{z2}) - \frac{\int_0^{b_2/2} \{\sigma_{x2} - \upsilon_s(\sigma_{y2} + \sigma_{z2})\} h_2 dy}{\int_0^{b_2/2} h_2 dy} \tag{28.35}$$

where h_2 is the strip thickness at exit of roll bite and b_2 strip width at exit of roll bite, and suffix 2 denotes the exit of roll bite.

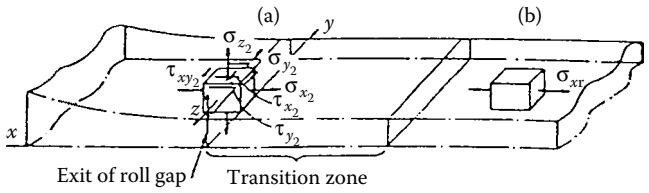


FIGURE 28.5 Stresses at the exit of roll gap and residual stress.

28.6 FLOW CHART OF THE MAIN PROGRAM

Combining the strip 3D deformation model, roll thermal crown model, roll stack deformation model and stresses unloading model results in a program capable of simulating the local shape phenomena in a tandem cold mill. The program is designed in a way that a multi-coil lineup can be simulated in one run. The main flowchart of the shape simulation program is shown in Figure 28.6.

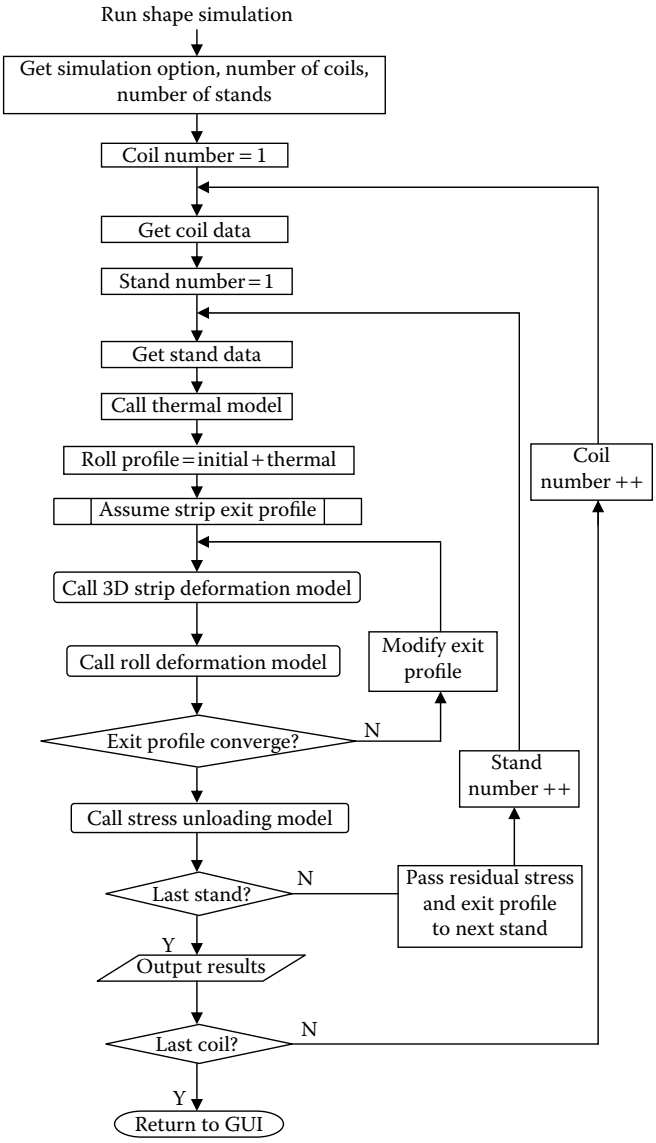


FIGURE 28.6 Main flowchart of the shape simulation program. (From Y. Liu et al. 2007. *Iron and Steel Technology* 4(8): 70–80. With permission.)

28.7 MODEL TUNING AND VERIFICATION

The model was tuned and verified under no-ridge conditions using the data collected from a CPCM to establish the base cases for the simulation. The shape meter readings of 20 coils in two lineups were used for the model tuning and verification. The shape readings in I-units were translated into residual stress distributions and tension stress distributions acting on the shapemeter. For each coil, the average value of 200 readings in a stable rolling period was used as the shape reading of the coil. The corresponding process parameters for each coil were then extracted from the database of the mill. A tuning factor was added to modify the work-roll crown to compensate for some effects that are not considered in the model such as roll horizontal deflection, effects of roll wear and errors in roll grinding, etc. This tuning factor was determined by fitting the shape readings of one coil for each lineup. With the fixed tuning factor, the shape readings of other coils in the lineup were used to verify the model. The model provided a consistent shape prediction for all the coils in each lineup. The shapes of sample coils of the lineups are shown in Figures 28.7 and 28.8.

Although there are still discrepancies, the consistency of the overall match of the measured and predicted shape proves the validity of the model.

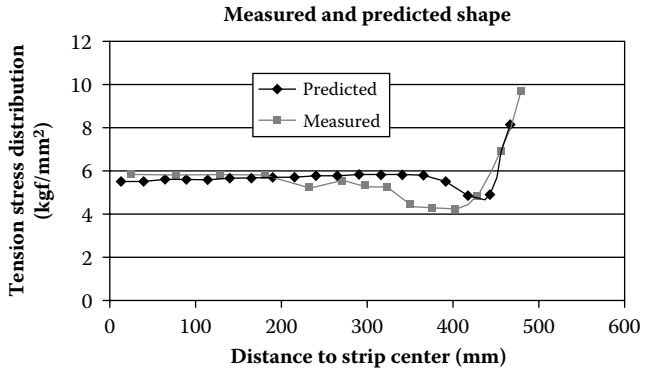


FIGURE 28.7 Sample comparison of 1st lineup. (From Y. Liu et al. 2007. *Iron and Steel Technology* 4(8): 70–80. With permission.)

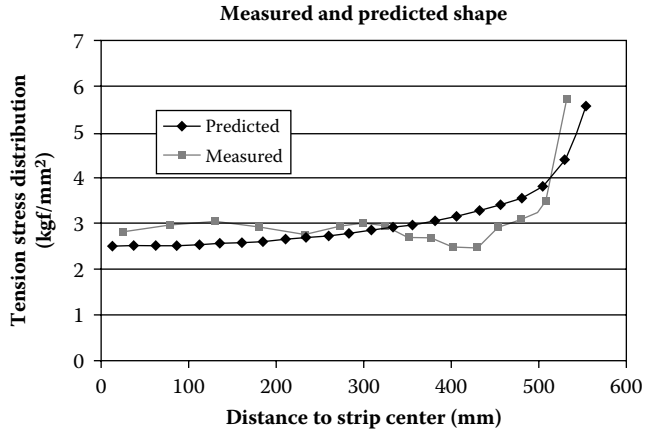


FIGURE 28.8 Sample comparison of 2nd lineup. (From Y. Liu et al. 2007. *Iron and Steel Technology* 4(8): 70–80. With permission.)

28.8 USER INTERFACE

A graphic user interface has also been developed to integrate the sub-models and manage the simulation options, the input and output data, and then graphically display the simulation results. The main screen of the user interface and the simulation options are shown in Figure 28.9. The simulation results are output to data files, which can be further processed by the user. They can also be graphically displayed in the user interface, as shown in Figure 28.10. The major results currently selected for graphical display in the user interface include 3D longitudinal stress, 3D transverse stress, 3D vertical stress, 3D shear stress, lateral spread ratio, neutral plane profile, exit velocity profile, entry tension stress profile, exit tension stress profile, residual stress distribution, inter-roll contact pressure distribution, exit thickness profile, roll thermal profile, and roll force distribution.

Since the local shape defects are the main focus of this simulation program, three abnormal rolling conditions are listed as the main simulation options. These abnormal rolling conditions are simulated and discussed in subsequent sections.

28.9 BASE CASE FOR LOCAL SHAPE DEFECTS SIMULATION

To simulate the local shape defects from various sources, a real rolling case is selected as the base case in which no local shape defect was produced. The various causes of local shape defects are then added to the base case by assumptions to see their effects. The rolling mill and process data of the base case are shown in Figures 28.11 and 28.12, respectively.



FIGURE 28.9 User interface and simulation options.

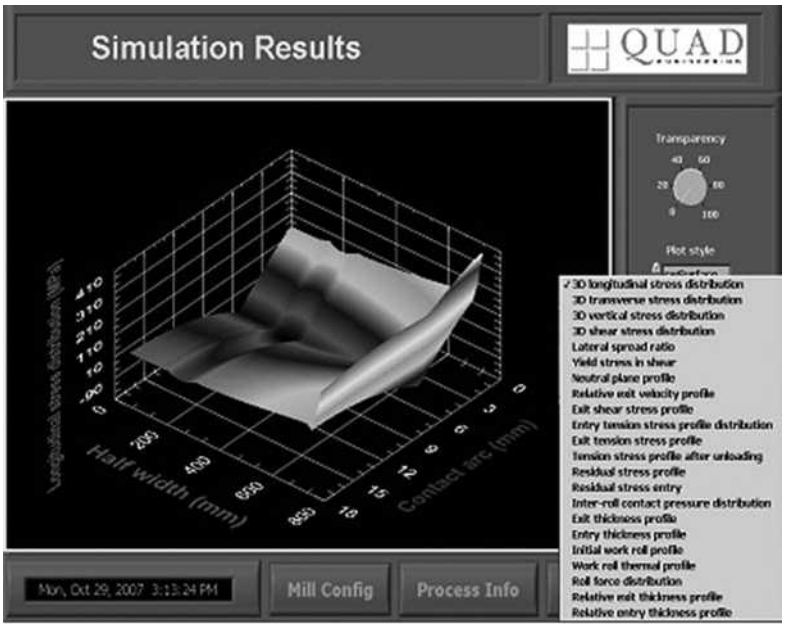


FIGURE 28.10 Display screen and results for display.

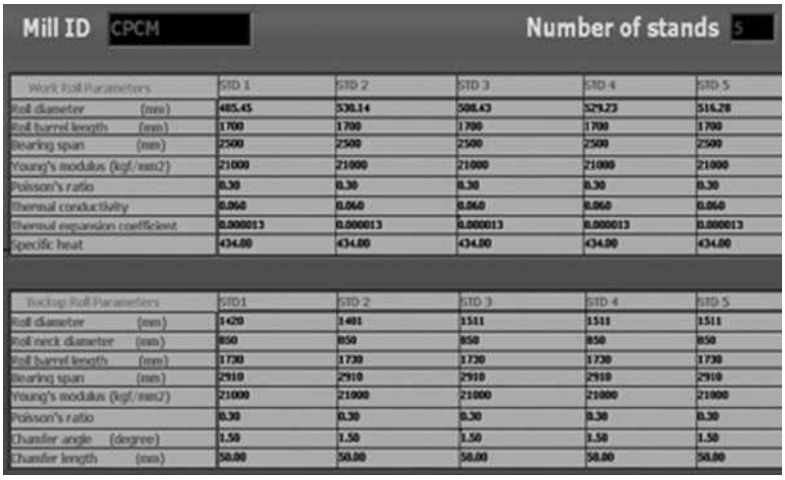


FIGURE 28.11 Mill data of the base case.

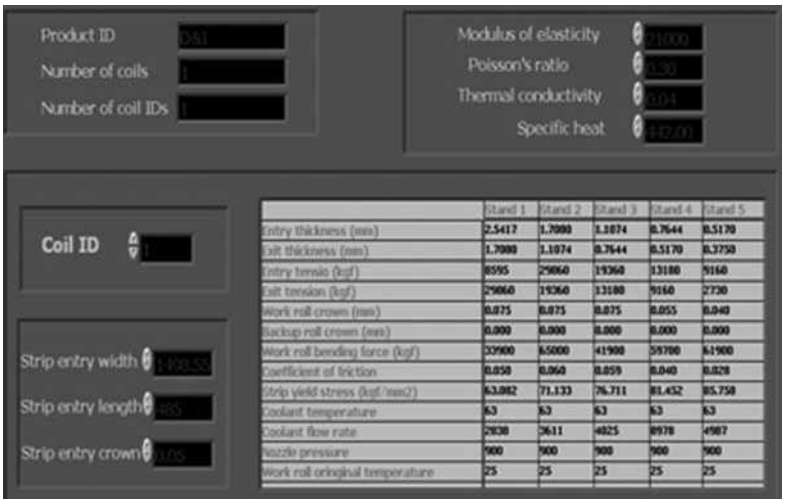


FIGURE 28.12 Process data of the base case.

28.10 EFFECTS OF ENTRY STRIP PROFILE RIDGE

One major reason for local strip buckles is to cold roll a strip with thickness profile ridges. The feed stock of cold-strip mills is normally coils rolled by hot-strip mills. If abnormal conditions, such as excessive roll wear, occur in the hot-strip mill, thickness profile ridges may be produced on the hot-rolled strip. When the hot-rolled strip with ridges is subsequently fed into a cold mill, local buckles may be produced in the cold-rolled strip. The extra material forming the thickness ridge will be divided into three portions in subsequent cold rolling. A portion of the material will remain in the form of a thickness ridge in cold-rolled strip due to a local roll flattening increase, which is caused by the higher local roll force when rolling the thickness ridge. The second portion of the material will produce a local elongation increase, which will cause a local strip compression increase that may induce local buckles. The third portion of the material will spread laterally, which actually has the effect of attenuating the local buckles and the thickness ridges of the cold-rolled strip. The percentage of each portion depends on the parameters of the rolls, products, and rolling process and may vary over a wide range. This shape simulation program is capable of quantitatively determining what happens when rolling a thickness profile ridge.

Figures 28.13 through 28.21 show the major simulation results when cold rolling a coil with two thickness ridges in a five-stand fully continuous tandem mill. The height of the thickness ridges is assumed to be 2% of the entry strip thickness, about 0.051 mm. The thickness ridges are assumed to be parabolically distributed in 100-mm width and symmetric to the center line of the strip.

The strip thickness profiles after each stand are shown in Figure 28.13. Even though the height of the ridges is continuously reduced from stand to stand, the ridges could not be totally eliminated. There are still thickness ridges, about 0.004 mm in height, left in the final product. The additional reductions to the thickness ridges will cause peaks in the roll force distribution, as shown in Figure 28.14.

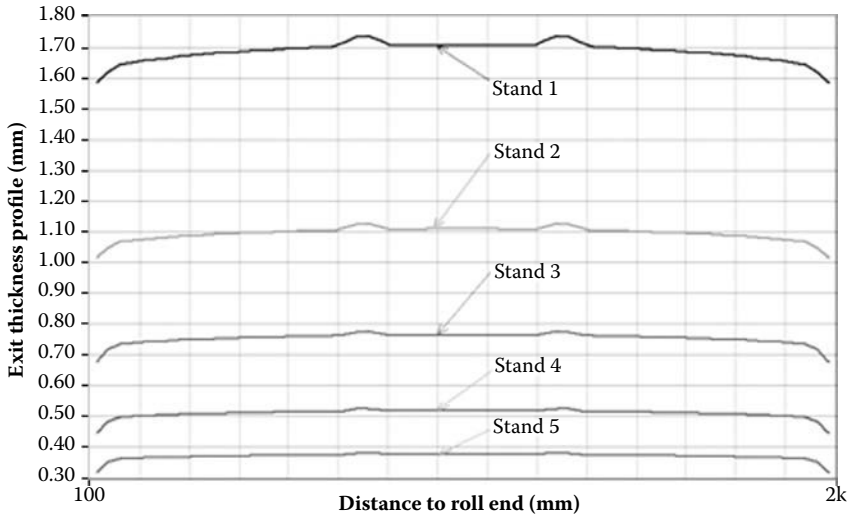


FIGURE 28.13 Exit thickness profile.

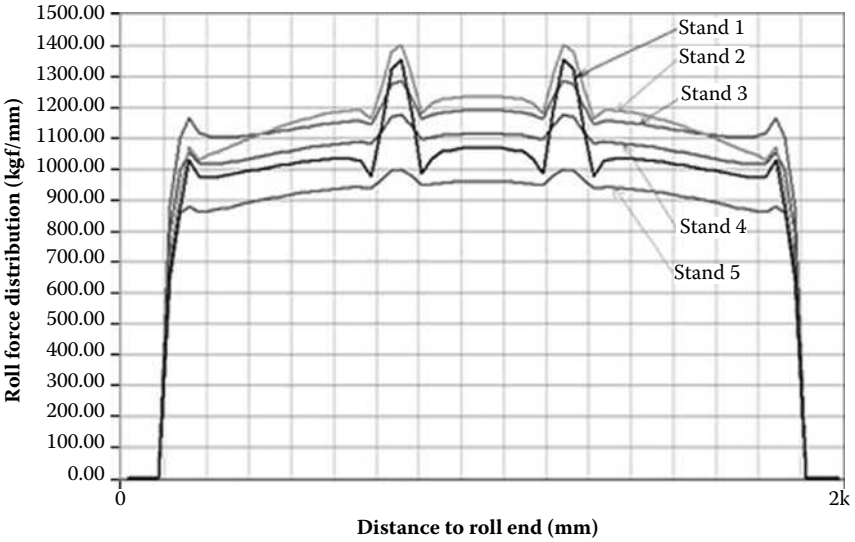


FIGURE 28.14 Roll force transverse distribution. (From Y. Liu et al. 2007. *Iron and Steel Technology* 4(8): 70–80. With permission.)

Figure 28.15 shows the three-dimensional stress distributions in the roll bite when rolling a thickness ridge. It is clear that the thickness ridges cause normal stress drops locally in all three directions. The ridges also induce local shear stress variation due to lateral spread and speed variation.

The thickness ridge will also induce lateral spread around it. However, the altitude of the lateral spread ratio, which is defined as the ratio between lateral strain rate and longitudinal strain rate, is much smaller in the region of thickness ridge than that in the strip edge. The lateral spread ratio in the region of thickness ridge also decreases from first stand to last stand, as shown in Figure 28.16. The lateral spread ratio at the strip edge, however, may not always decrease from first stand to last stand.

Because of the thickness ridge and lateral spread at the edge, the neutral planes are not "planes" anymore. They are curved by the material flow variation and lateral spread, as shown in Figure 28.17. The curved portions are mainly at the region of the ridge and the strip edge.

The relative exit speed profile, which is defined as the ratio of strip longitudinal speed at the roll bite exit to roll linear speed, are also curved around the ridge and the strip edge, as shown in Figure 28.18. The entry tension stress profile, which mainly depends on the residual stress formed in the previous

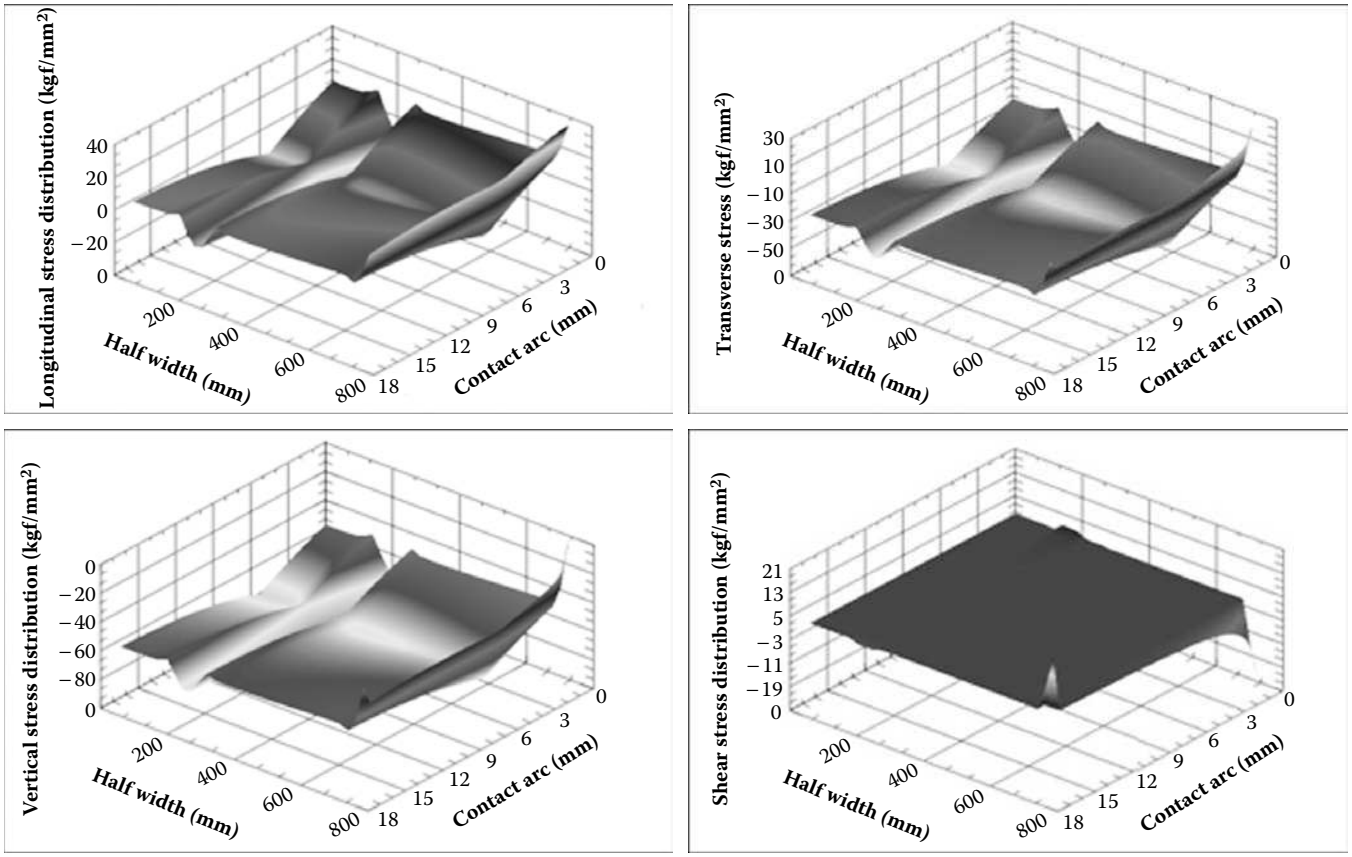


FIGURE 28.15 Three-dimensional stress distributions in roll bite. (From Y. Liu et al. 2007. *Iron and Steel Technology* 4(8): 70–80. With permission.)

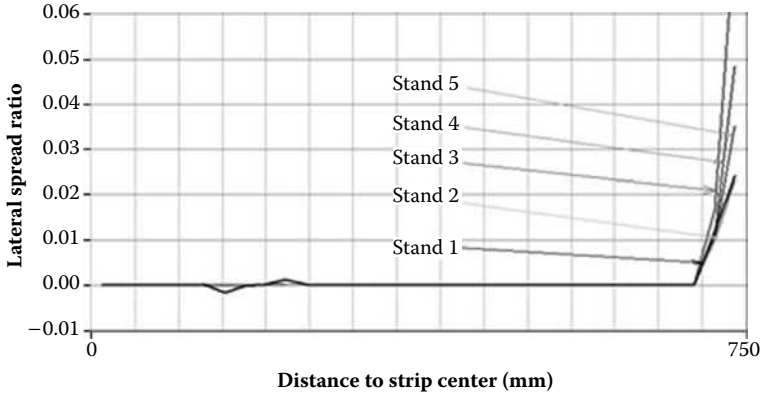


FIGURE 28.16 Lateral spread ratio distribution. (From Y. Liu et al. 2007. *Iron and Steel Technology* 4(8): 70–80. With permission.)

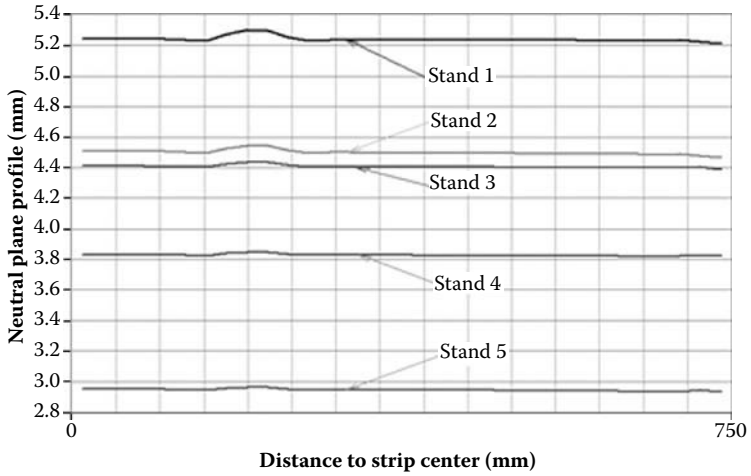


FIGURE 28.17 Neutral plane profile. (From Y. Liu et al. 2007. *Iron and Steel Technology* 4(8): 70–80. With permission.)

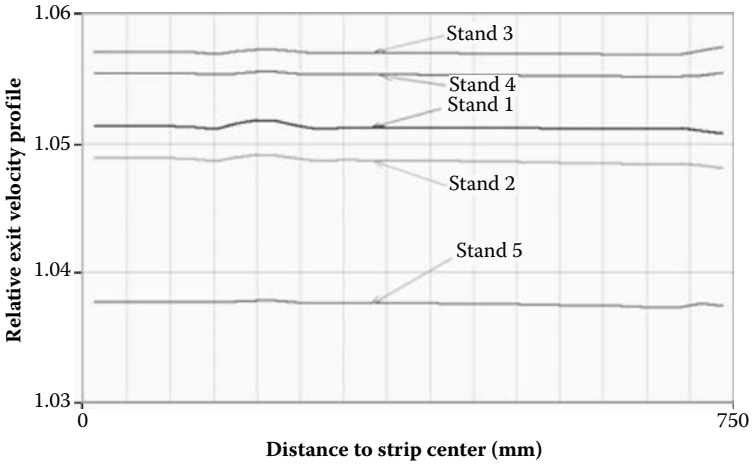


FIGURE 28.18 Relative exit speed profile. (From Y. Liu et al. 2007. *Iron and Steel Technology* 4(8): 70–80. With permission.)

stand and the entry speed profile of current stand, are also influenced by the thickness ridge, as shown in Figure 28.19.

The exit tension stress drops around the ridge area are obvious, as shown in Figure 28.20. However, the amount of tension stress drop decreases substantially from the first stand to the last stand. The exit tension stress drop in stand 5 is only about a quarter of that in stand 1. A similar phenomenon also occurs in the residual stress profile, as shown in Figure 28.21. The interaction among reduction, lateral spread, tension, residual stress, roll bending, and flattening of all stands determines the final residual stress due to thickness ridge rolling, which will dictate the local shape of the product.

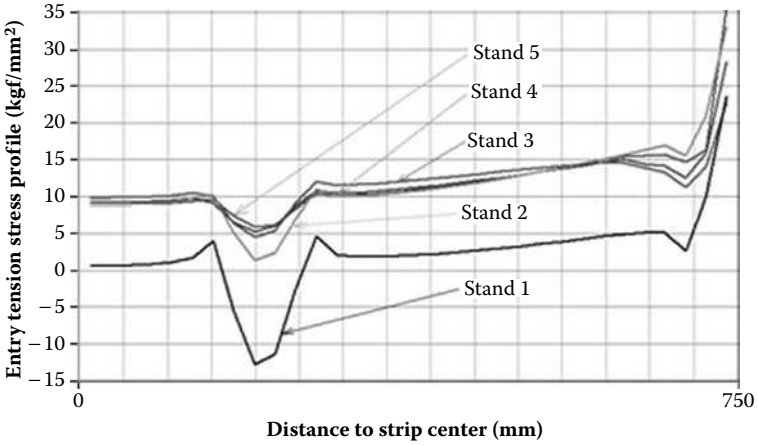


FIGURE 28.19 Entry tension stress profile. (From Y. Liu et al. 2007. *Iron and Steel Technology* 4(8): 70–80. With permission.)

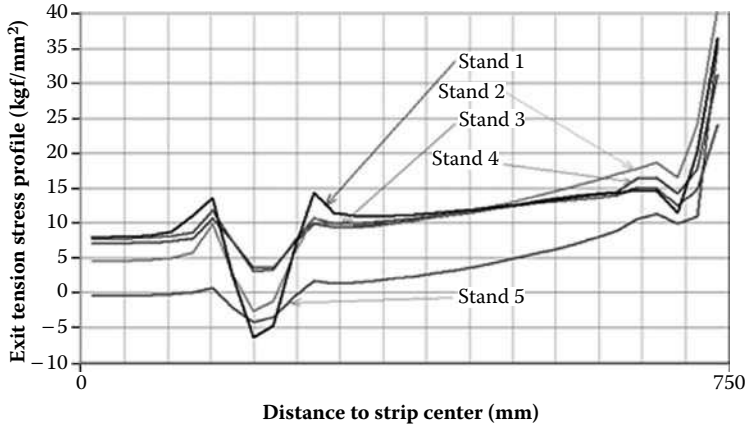


FIGURE 28.20 Exit tension stress profile. (From Y. Liu et al. 2007. *Iron and Steel Technology* 4(8): 70–80. With permission.)

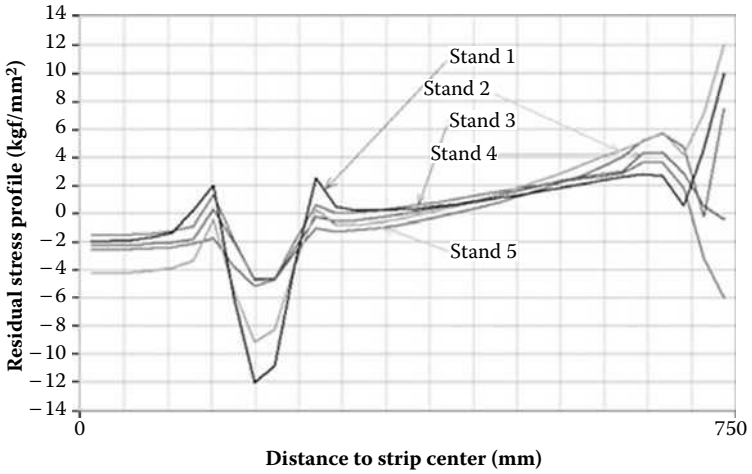


FIGURE 28.21 Residual stress profile. (From Y. Liu et al. 2007. *Iron and Steel Technology* 4(8): 70–80. With permission.)

One feature that distinguishes local hot band–ridge defects from other causes, such as yield stress drop or roll crown ridge, is that both local thickening and local buckles exist at the same position in the cold-rolled strip, as shown in Figures 28.13 and 28.21.

28.11 EFFECT OF LOCAL YIELD STRESS DROP

There are abnormal metallurgical or physical conditions that may cause nonuniform yield stress across the strip width. For example, microstructure changes occurring in the finishing mill as a result of temperature variation in zones of the strip may result in yield stress variations in the hot band. If a narrow slice of the hot-rolled strip is softer than the rest, local buckles may be induced as a result of cold rolling. To see the effects of local yield stress drop, a parabolic yield stress valley with 15% yield stress drop in a 100-mm-wide slice is assumed. Yield stress distributions for each stand are shown in Figure 28.22.

The local yield stress drops will induce a roll force drop at corresponding positions, as shown in Figure 28.23. However, the percentage of roll force drop is only about 2%–3%, which is much smaller than the 15% yield stress drop. The reason is that the local roll force drops reduce the local roll flattening, which reduces the local roll gaps and increases the local reductions slightly, which in turn offsets part of the roll force drops.

The slightly increased local reductions cause strip exit speeds to locally increase as shown in Figure 28.24, which in turn changes the neutral plane profiles, as shown in Figure 28.25.

The slightly increased local reductions also cause compression at the entry and exit of the roll bites, producing local tension stress drops at the entry and exit side, as shown in Figures 28.26 and 28.27.

Because of the local exit tension stress drops, there are local compressions in the residual stress profile after unloading, as shown in Figure 28.28. The local compressions in the residual stress profile would produce local buckles if they exceed certain limits. Contrary to the local shape defects produced by hot band ridges, in which strip local thickening occurs at the location of the local buckles, local strip thinning would occur at the position of the local buckles if the local buckles were caused by local yield stress drops, as shown in Figure 28.29.

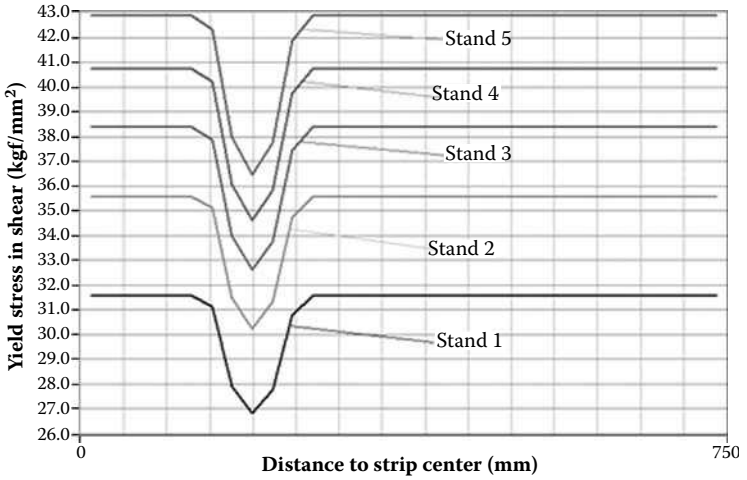


FIGURE 28.22 Assumed yield stress profile. (From Y. Liu et al. 2007. *Iron and Steel Technology* 4(8): 70–80. With permission.)

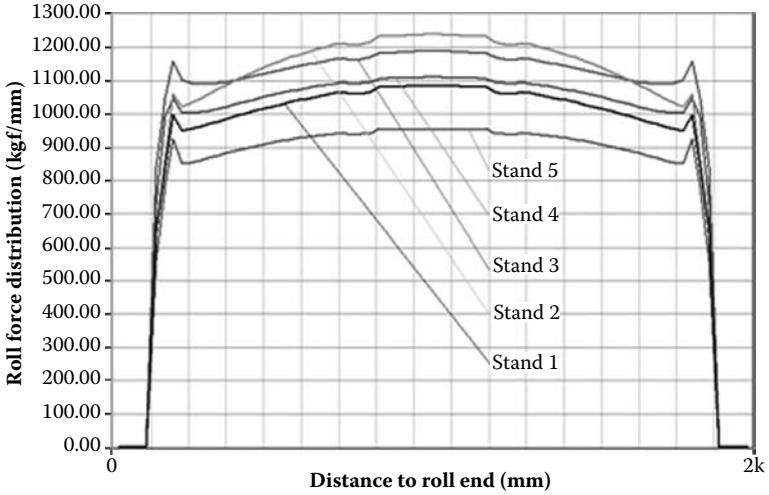


FIGURE 28.23 Roll force profile. (From Y. Liu et al. 2007. *Iron and Steel Technology* 4(8): 70–80. With permission.)

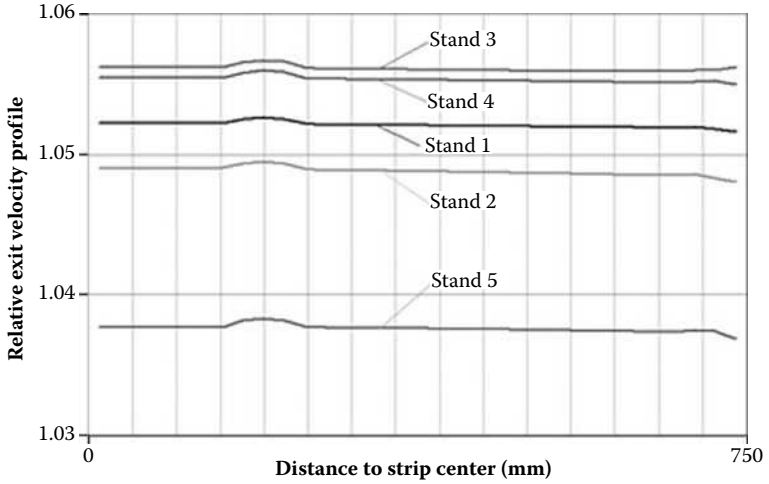


FIGURE 28.24 Relative exit velocity profile. (From Y. Liu et al. 2007. *Iron and Steel Technology* 4(8): 70–80. With permission.)

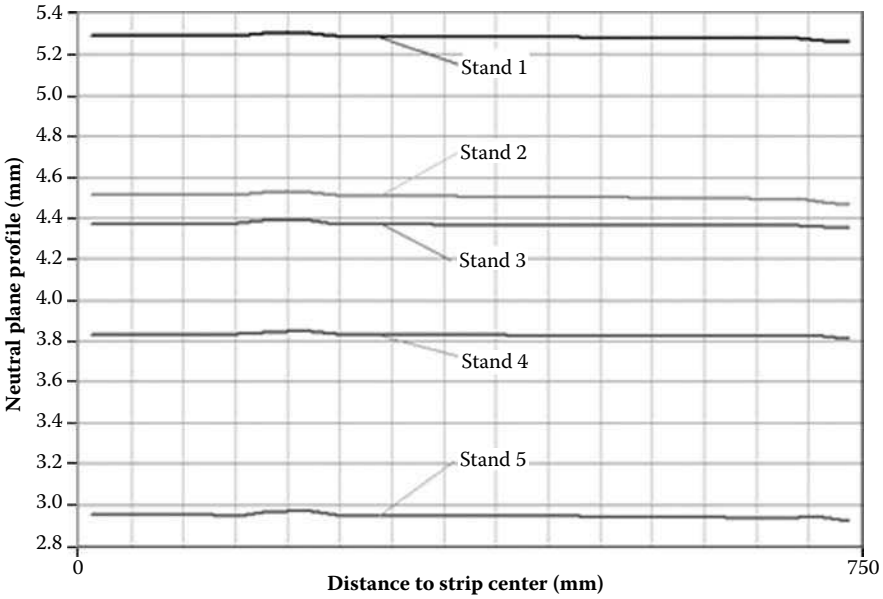


FIGURE 28.25 Neutral plane profile. (From Y. Liu et al. 2007. *Iron and Steel Technology* 4(8): 70–80. With permission.)

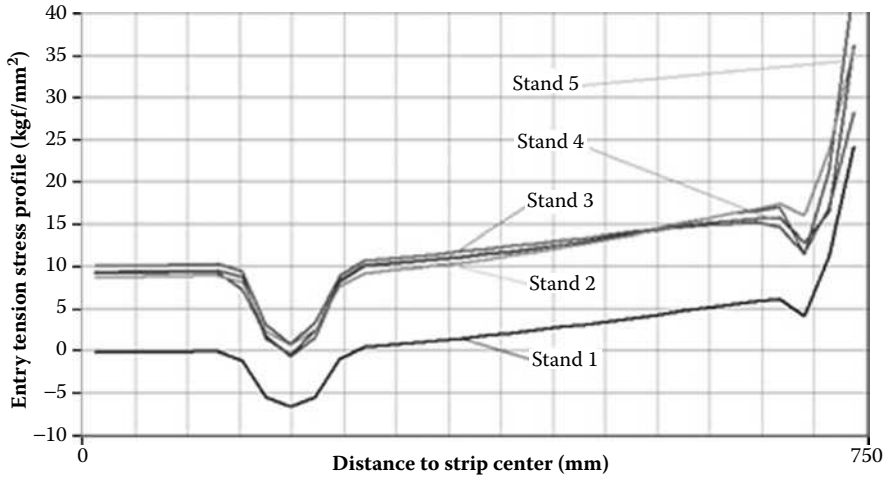


FIGURE 28.26 Entry tension stress profile. (From Y. Liu et al. 2007. *Iron and Steel Technology* 4(8): 70–80. With permission.)

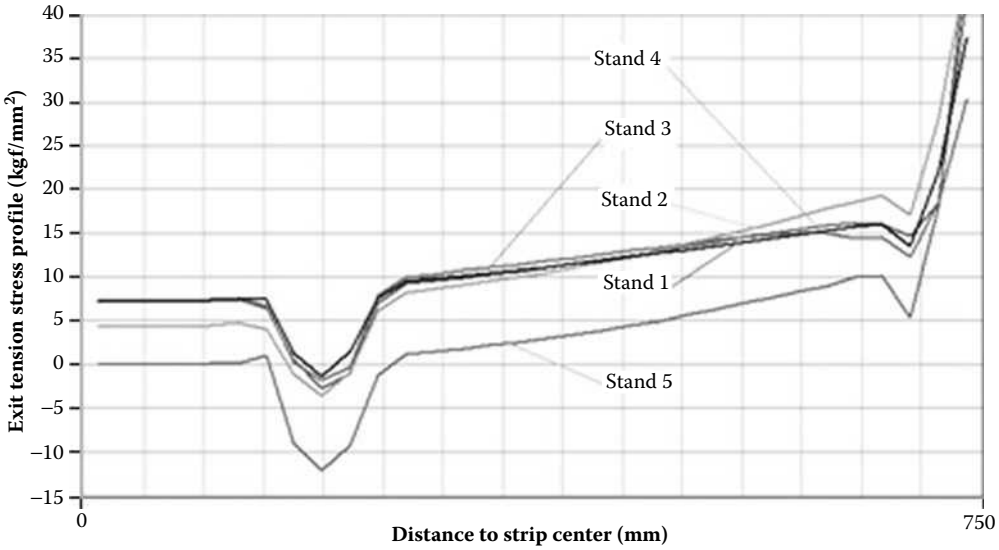


FIGURE 28.27 Exit tension stress profile. (From Y. Liu et al. 2007. *Iron and Steel Technology* 4(8): 70–80. With permission.)

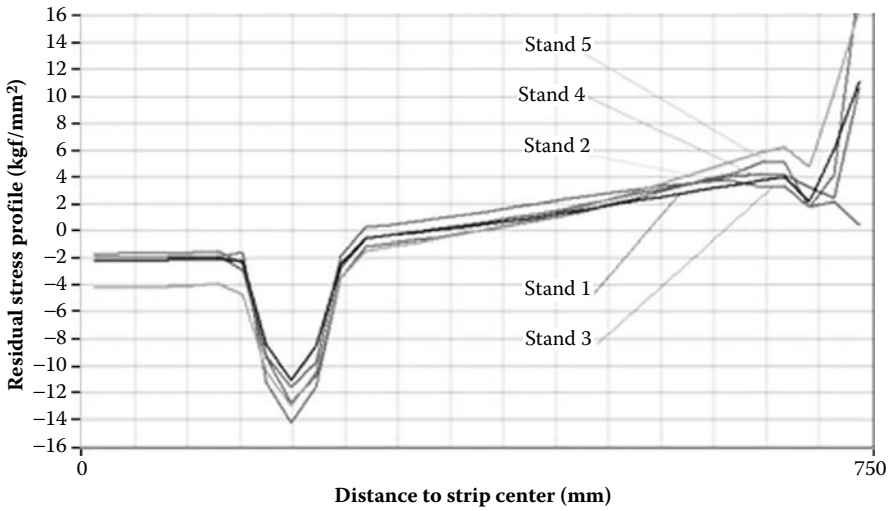


FIGURE 28.28 Residual stress profile. (From Y. Liu et al. 2007. *Iron and Steel Technology* 4(8): 70–80. With permission.)



FIGURE 28.29 Thickness profile after stand 5. (From Y. Liu et al. 2007. *Iron and Steel Technology* 4(8): 70–80. With permission.)

28.12 ROLL-COOLING NOZZLE CLOG OR WORK-ROLL CROWN RIDGE EFFECT

Local shape defects due to hot-band profile ridges and local yield stress drop are caused by the abnormal conditions in upstream processes such as the hot mill. The abnormal conditions in the cold mill itself may also cause local shape defects. For example, if some roll cooling nozzles are clogged, the corresponding position may form a roll thermal ridge, which may cause local strip buckles.

As an example, assuming two adjacent work-roll cooling nozzles are clogged, a 0.007-mm work-roll thermal crown ridge will be produced at thermal steady-state conditions for the base case simulated. If the roll ridge occurs in the early stands, the potential local shape defects produced by the ridge could be ironed flat by subsequent stands before buckles occur. However, if the work-roll thermal ridge is in the last stand, local buckles may be produced in the final product.

Figure 28.30 shows the roll force distributions assuming that four roll-cooling nozzles are clogged at stand 5, two in each half of strip width and symmetric to the strip center line. Max 0.007-mm roll thermal crown ridges are built up at thermal steady-state conditions of stand 5, which will produce the roll force peaks in stand 5, as shown in Figure 28.30. Local reduction increases induced by the roll force peaks will cause local drop of the entry tension stress profile, as shown in Figure 28.31, and a local drop in the exit tension stress profile, as shown in Figure 28.32.

The local drop in exit tension stress profile will cause a local compression in the residual stress profile after unloading, as shown in Figure 28.33. Local buckles may occur if the local compression exceeds certain limits.

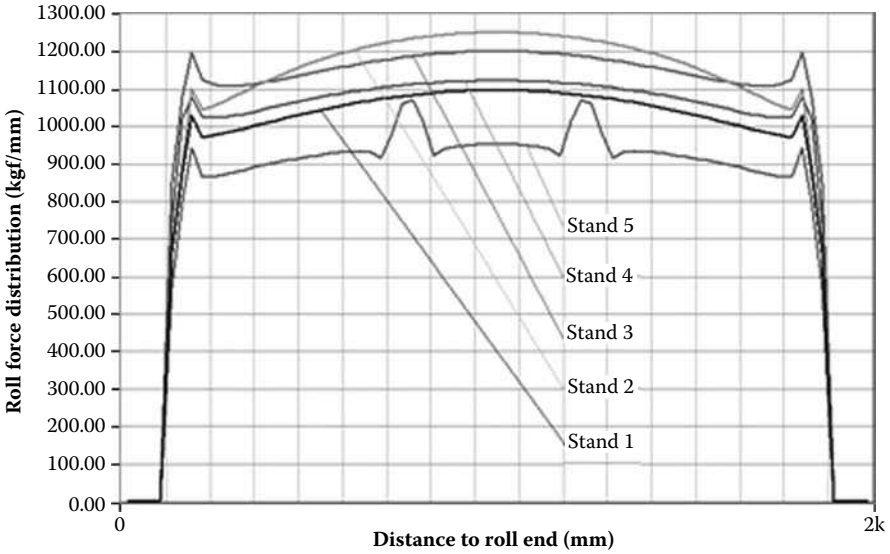


FIGURE 28.30 Roll force profile. (From Y. Liu et al. 2007. *Iron and Steel Technology* 4(8): 70–80. With permission.)

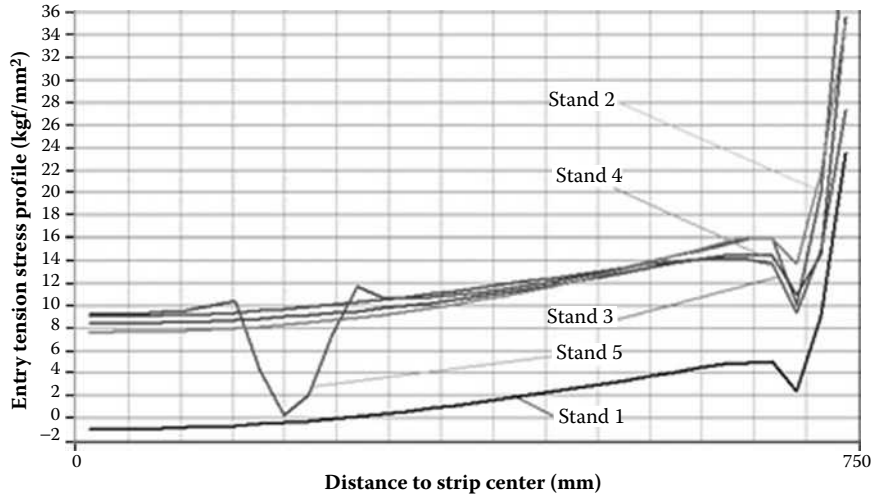


FIGURE 28.31 Entry tension stress profile. (From Y. Liu et al. 2007. *Iron and Steel Technology* 4(8): 70–80. With permission.)

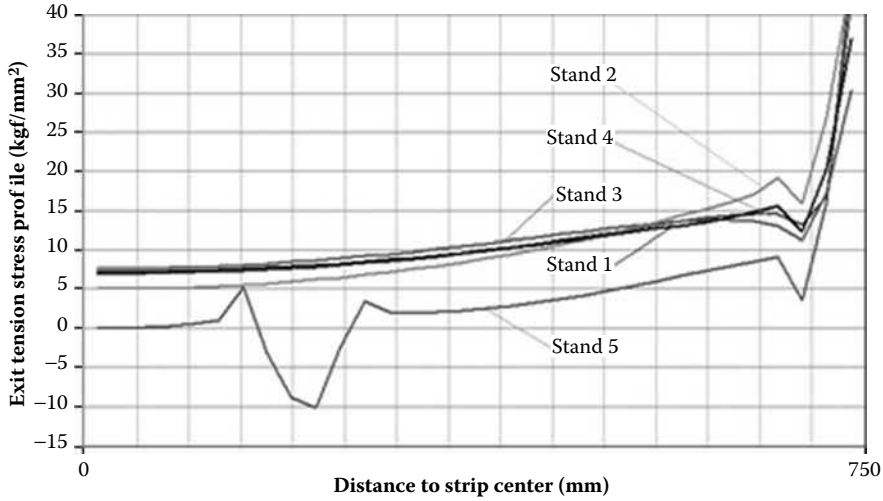


FIGURE 28.32 Exit tension stress profile. (From Y. Liu et al. 2007. *Iron and Steel Technology* 4(8): 70–80. With permission.)

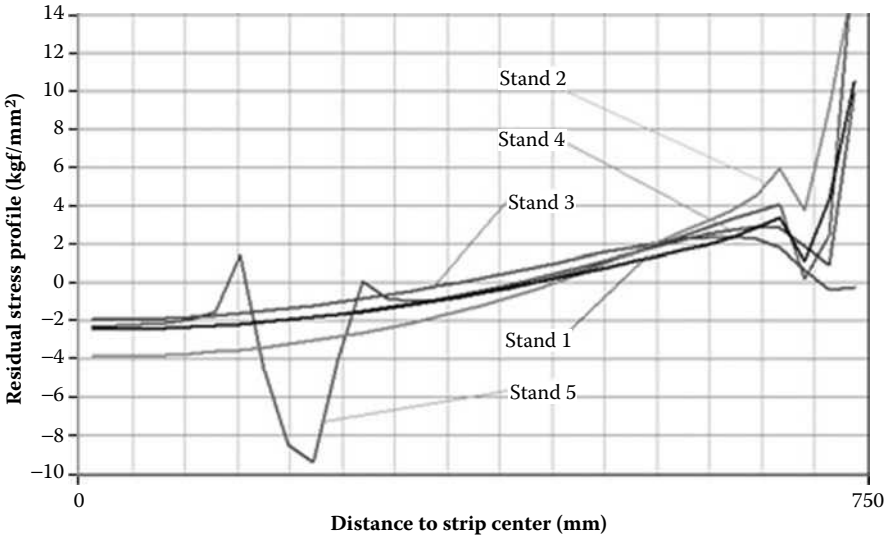


FIGURE 28.33 Residual stress profile. (From Y. Liu et al. 2007. *Iron and Steel Technology* 4(8): 70–80. With permission.)

28.13 IDENTIFICATION OF CAUSES AND REDUCTION OF LOCAL SHAPE DEFECTS

The effects of friction coefficient variations in width direction and feed stock local residual stress are also simulated. In the practical variation range, they are unlikely to cause local shape buckles. Therefore, they are excluded from the possible causes of the local shape defects. Since the local residual stress induced by upstream stands can be ironed out, if they are not manifest, the working conditions of upstream stands are excluded from the causes of the local buckles. The remaining possible causes of local shape defects are the above three factors, hot band ridge, yield stress local drop, and abnormal rolls or operating conditions in the last stand. With above simulation results, the causes of local shape defects can be identified as follows. The thickness profile should be measured first with more attention paid to the buckled regions. If local buckles are caused by local decrease of the strip yield strength or abnormal operation conditions of the last stand, local thinning and local buckles should be observed at the same position. Therefore, if both local thickening and local buckles are observed at the same position, hot band ridge should be the cause of the local shape defect. If both local thinning and local buckles are observed at the same position, the work-rolls and its cooling system as well as the operating conditions of the last stand should be checked to see if there is anything abnormal in the last stand. If the working conditions of the last stand are perfect, the local shape defect should be caused by yield stress local drop.

Even though any of the above three factors can cause local buckles, the majority of them are caused by hot-band ridges [11]. Therefore, properly monitoring the hot band profile and producing ridge-free hot band will be the first choice for reducing local buckles. Since hot-band ridges are most likely related to uneven roll wear, the measures to uniform the roll wear, such as on-line roll grinding and work-roll axial shifting, are suggested for reducing local buckles. If all measures in hot-strip mills fail, ridges are produced on the hot band. Flattening the ridges before cold rolling or using the localized shape control actuators, such as segmented roll cooling and rolls with multiple pressure zones [12], are helpful in reducing local buckles. The uniformity of the metallurgical related factors in the hot-strip mills and casters should be properly maintained to avoid yield stress local drop and reduce local buckles. Finally, rolls, roll-cooling system, and other operation conditions of the last stand of the cold mill need to be carefully maintained to avoid the local shape defects produced solely by the cold mill.

ACKNOWLEDGMENTS

We wish to thank Quad Engineering Inc. for permission to publish the material contained in this chapter. We also want to thank Mr. J.J. Fitzpatrick and Mr. B.D. Nelson of Dofasco Inc. for their cooperation in this project. Yuli Liu wishes to thank Professor T. Ishikawa of Nagoya University, Japan for his kind help regarding the application of stress unloading model.

REFERENCES

1. Y. Liu, J. Biglou, J.J. Fitzpatrick, J. Fan, B. Nelson. 2005. Strip shape simulation software for continuous cold rolling process. *Iron and Steel Technology* 2(4): 180–190.
2. Y. Liu, J.J. Fitzpatrick, J. Fan, B.D. Nelson, M. Levick. 2007. Three-dimensional simulation of local shape defects in continuous cold rolling. *Iron and Steel Technology* 4(8): 70–80.
3. Y. Tozawa. 1984. Analysis for three-dimensional deformation in strip rolling, taking deformation of rolls into consideration. *1st International Conference on Technology of Plasticity*, Tokyo, Japan, pp. 1151–1160.
4. T. Ishikawa, et al. 1987. Analytical approach to occurrence and suppression of flatness defect in strip rolling. *4th International Steel Rolling Conference*, Deauville, France, E7.1–E7.10.
5. V.B. Ginzburg. 1997. Application of coolflex model for analysis of work roll thermal conditions in hot strip mills. *Iron and Steel Engineer* 74(11): 38–45.

6. A.A. Tseng, S.R. Wang. 1996. Effects of interface resistance on heat transfer in steel cold rolling. *Steel Research* 67(2): 44–51.
7. G.V. Steden, J.G.M. Tellman. 1987. A new method of designing a work roll cooling system for improved productivity and strip quality. *4th International Steel Rolling Conference*, Deauville, France, A.29.1–A29.12.
8. C. Devadas, I.V. Samarasekera. 1986. Heat transfer during hot rolling of steel strip. *Iron and Steelmaking* 13(6): 311–321.
9. J.C. Lian, et al. 1995. *Shape and Gauge Control*. Beijing: Military Industry Press.
10. N. Yukawa, T. Ishikawa, Y. Tozawa. 1987. Calculation of residual stress in cold rolled strip. *Journal of the JSTP* 28(312): 28–33.
11. W. Melfo, R. Dippenaar, C. Carter. 2006. Ridge-buckle defect in thin-rolled steel strip. *Iron and Steel Technology* 3(8): 54–61.
12. V.B. Ginzburg. 1993. *High-Quality Steel Rolling Theory and Practice.* New York: Marcel Dekker.

29 Fundamentals of Online Flatness Measuring Devices

Fabio Miani and Paolo Patrizi

CONTENTS

29.1 Introduction 319
29.2 Causes of Flatness Deviation 320
29.3 Contact Flatness Measuring Devices 320
29.3.1 Contact Shapemeter for Cold Strip Mills 320
29.3.1.1 Strengths 321
29.3.1.2 Weaknesses 321
29.3.2 Contact Shapemeter for Hot Strip Mills 321
29.3.2.1 Strengths 321
29.3.2.2 Weaknesses 321
29.3.3 Shapemeter–Looper 322
29.3.3.1 Strengths 322
29.3.3.2 Weaknesses 322
29.3.4 Contactless Flatness Measuring Devices 322
29.3.5 Linear Laser Method 323
29.3.5.1 Strengths 324
29.3.5.2 Weaknesses 324
29.3.6 Laser Points Method 324
29.3.6.1 Strengths 325
29.3.6.2 Weaknesses 325
29.3.7 Fringe Method 325
29.3.7.1 Strengths 326
29.3.7.2 Weaknesses 326
29.3.8 Moirè's Topography Method 326
29.3.8.1 Strengths 327
29.3.8.2 Weaknesses 327
29.3.9 Contactless Nonoptical Shapemeter 327
29.3.9.1 Strengths 327
29.3.9.2 Weaknesses 327
29.4 Conclusions 327
References 328

29.1 INTRODUCTION

The big issue in strip and plate production—both by cold and hot flat rolling processes—is to obtain the desired profile of the finished product without exceeding the required flatness value, normally fixed by specific needs. The profile and flatness are also directly linked to the quality of the finished product itself. The flatness of a strip or a plate is not only one of the primary parameters that decides its price, but when waviness appears on a strip in production it can easily amplify its features if not properly controlled, and result in a partial or total break or jamming of the metal strip in the machine, making it necessary to stop the production process. This results in increased costs for the producer.

In the last 20 years many different technologies and mathematical models have been proposed to solve this problem. While automatic strip width and gauge controls have attained great accuracy and guarantee this aspect of strip quality, the automatic control of flatness still lacks precision, especially for the hot rolling process. For closed loop automatic flatness control systems good analysis software has been developed, leaving the measuring devices as the weak link.

In this chapter, we review the most common devices for flatness measurement, to give the reader a complete overview of the present situation and to improve understanding of the strengths and weaknesses of each.

The existing devices for flatness measurement can be divided into two different groups. Contact devices are directly in contact with the strip and they are typically placed inside specific kinds of rolls. Contactless devices are generally based on optical measurement systems. We will show that the appropriate technology should be chosen based on consideration of its intrinsic technological limits and the specific production situation.

We wish to stress that it is of primary importance to select the correct flatness measurement device because the wrong choice can lead to a worthless increase in maintenance and production costs, with a direct effect on the processing operation and the quality of the strip itself; minimum material waste, stable strip production, high superficial finishing and low processing costs are not secondary objectives in strip production.

29.2 CAUSES OF FLATNESS DEVIATION

To understand the reasons for the difficulties in performing a good measurement of the flatness it is vital to describe the three basic causes of strip flatness deviation, as represented in Figure 29.1.

A common cause of flatness deviation is the nonuniform elongation of the strip fibers along the strip length because of uneven stresses acting across the strip width. When the corresponding internal stresses across the strip width are not uniform and the strip internal latent forces are not strong enough to withstand the internal stresses, then the quality of the strip deteriorates. In this case, we speak of *strip manifest shape*, which can appear in different forms: strip camber, center waves, edge waves, quarter buckles, edge buckles, center buckles, and so on [1,2].

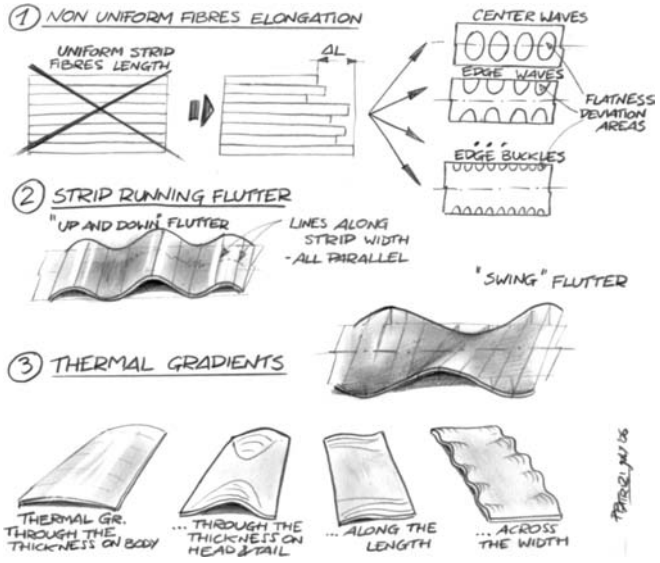


FIGURE 29.1 Causes of flatness deviation.

Another reason for strip waviness is linked to high rolling speeds, which can sometimes cause the strip to flutter. This anomalous movement of the strip—which is frequently observed on the hot strip mill runout table—can become visible as a uniform wave along the whole strip (up and down flutter) or a waviness of the two sides of the strip which does not affect the strip center (swing flutter).

Furthermore, the deviation of strip flatness is not mechanical in nature, but it is linked to uneven thermal gradients across the strip. This defect occurs when there is inhomogeneous heating or cooling of the strip and the appearance of internal stresses that can locally overcome the yield stress of the material. At this point, plastic deformation of the strip takes place. Even though thermal gradient problems can normally be easily identified because of their peculiar characteristics, when they occur across the width of the strip, they can sometimes be confused with edge waves or edge buckles, leading to difficulties in controlling them [3].

From the nature of the strip waviness, it can be understood that these defects are difficult to control, especially when we have to deal with very thin strips, where a difference in fiber elongation greater than 0.01% can be enough for superficial defects to appear; for a 1-mm-thickness strip we must be able to spot a variation of 10 μm in the fiber length.

29.3 CONTACT FLATNESS MEASURING DEVICES

Contact flatness measuring devices are commonly known as *contact shapemeters*. This kind of device is the oldest and most frequently used, so we can find many different models designed by many different companies. This type of tool is commonly placed between the last rolling stand and the coiler, where the strip is experiencing the tension necessary for rapid and correct coil wrapping (the final rolling process on the strip). Normally, this is the best position because there is room to position the apparatus and the device remains accessible. The tension that the strip is standing in this position can hide the waviness on the strip surface, increasing the precision necessary to measure the flatness. In this situation, contactless measuring devices can barely detect strip surface deformations and only contact shapemeters are helpful, but in a hot rolling process, contactless sensors are preferred because of the high temperatures involved. In other words, for cold strip production contact measurement devices are the best choice, while for plate flatness measurement contactless systems should be chosen.

To clarify the different kinds of contact shapemeters available on the market, we subdivide them into three different groups, based on their common characteristics.

29.3.1 Contact Shapemeter for Cold Strip Mills

Contact shapemeters, which include the Stressometer and the Betriebsforschungsinstitut (BFI) flatness roll technologies,

have been in use for more than 40 years, and they are known as the world standard in strip flatness measurement [4–6]. This kind of technology is used in over 1500 installations worldwide. It is manufactured by many different companies, but always built to the same basic design. This flatness measurement device consists of a deflection roll, which is a segmented roll having different sets of sensors across its width (Figure 29.2). The Stressometer is based on pressductor measuring transducers and the BFI flatness roll is based on piezoelectric force sensors. These sensors can measure the pressure distribution along the roll length, and from these values, the variation of tensile stress across the strip width is calculated. From the tensile stress, it is possible to calculate the waviness of the strip using the mathematical relationship:

$$\frac{\Delta L}{L} = \frac{\Delta \sigma_x}{E_s} \tag{29.1}$$

where ΔL is the difference between the shorter and the longer fiber across the width of the strip, L is the length of the wave, $\Delta\sigma_x$ is the variation of tensile stress across the strip, and E_s is the modulus of elasticity for the material.

To more clearly evaluate this measuring device, we identified the following strengths and weaknesses.

29.3.1.1 Strengths

This device gives accurate measurements that are not affected by fluctuations in the strip tension, long-term accuracy and stability if used in cold-rolling processes, a wide range of sensitivity in force measurement (from approximately 120,000 N to less than 1 N), wide distribution with consequent competitive prices, a long history in the market, and actual mean time between failure graphs available to establish device life and maintenance features.

29.3.1.2 Weaknesses

This is intrusive flatness measurement technology; using deflection rolls in direct contact with the metal strip risks scratching and stretching its surface, vibrations, humidity, and continuous variation of maximum to minimum load differences—at tension and compression—can result in a reduction of reliability and stability of the sensors. In addition, this technology cannot be applied to hot rolling mills, mainly because the high temperatures involved cause rapid wearing of the roll and a reduction in the sensors' life.

29.3.2 Contact Shapemeter for Hot Strip Mills

To partially overcome the deflection roll problems on hot rolling mills, a special technology was studied, the shapemeter. This technology is based on the same working principle as the deflection roll, but the sensors are attached in an external position to place them away from the rolled strip (Figure 29.3). The shapemeter designed by Hoesch Stahl AG, Germany [7], is an example of this kind of device, and it is used in hot strip mills. In this shapemeter, some sensors are attached externally to the arms holding the shapemeter roll that is segmented across its width, measuring the force applied to it while in contact with the hot strip.

An innovative evolution of this system allows adjustment of individual segments and direct control of each (Shape Actimer [8]—United Engineering and International Rolling Mill Consultants). This detail is particularly useful when we have to measure both the hidden and visible components of the strip shape.

In comparison with the deflection roll, we can identify the following strengths and weaknesses [9].

29.3.2.1 Strengths

The sensors are much more protected from temperature effects and more easily cooled. Even with the hot strip temperature between 800°C and 1200°C, they can be applied to hot rolling. The sensors' special position reduces the peak loads they normally experience because the tensile load applied to the roll is not directly transmitted to them, resulting in fewer breaks and greater stability.

29.3.2.2 Weaknesses

The nonuniform wear of the roll reduces the accuracy of the load measurement. Consequently, the accuracy of the waviness measurement is reduced and maintenance costs

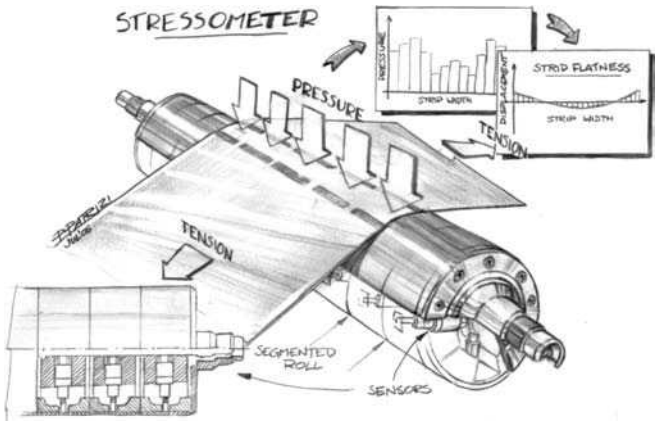


FIGURE 29.2 Stressometer.

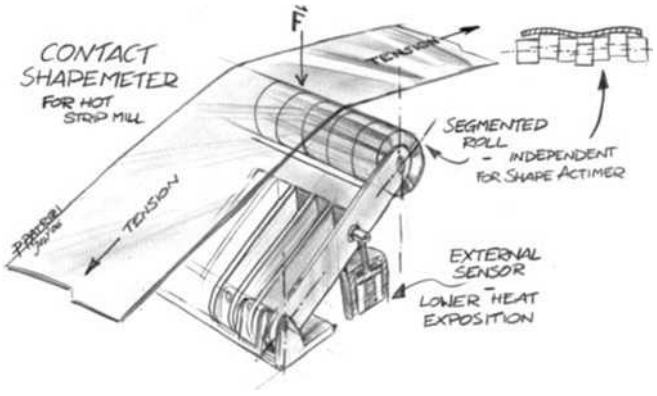


FIGURE 29.3 Contact shapemeter.

eventually increase. Rolls in contact with a hot strip must be changed frequently, slowing down the rolling process. This type of device is usually free to move around the looper shaft, exposing the sensors to excessively strong impacts (because the looper works like a dumper), thus reducing the sensors' life.

29.3.3 Shapemeter–Looper

Shapemeter–loopers are an evolution of the flat measuring devices described above [10]. This technology is designed using the basic concept of the contact shapemeter for hot rolling, but can measure the strip tension as well. At the same time it works like a traditional strip looper. It maintains a constant strip tension between two rolling stands (Figure 29.4). In recent years, shapemeter–looper devices have experienced rapid evolution thanks to the interest of many groups of developers.

29.3.3.1 Strengths

The shapemeter–looper can be used to measure both strip tension and shape. It can substitute for common loopers and the most recently designed models can provide the sensors better protection from high temperature and impact, thus extending the sensors' life. One particular kind of shapemeter–looper [11] is subdivided into many split rolls whose movement in the tangent and normal directions can be controlled to compensate for the wear of each split roll. With this method, it is possible to balance the lack of measurement precision due to wearing of the rolls.

29.3.3.2 Weaknesses

Those weaknesses identified for the previous contact systems, linked to the wearing of the roll in contact with the strip, also apply, even if they are not as pronounces. The inertia of the mass-spring system, typical of the looper, must be chosen within certain limits and controlled during the normal process downtime. The system design is more complex because it must take into account the specific characteristics of the looper in the particular mill configuration, which affects the device costs.

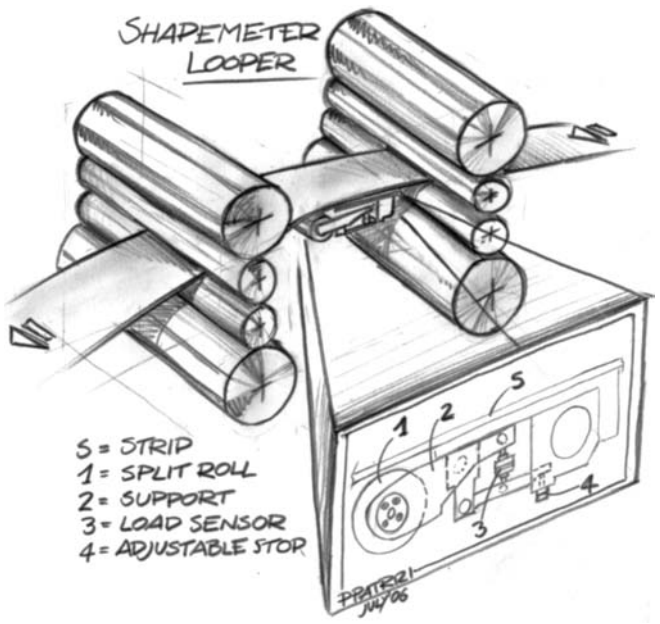


FIGURE 29.4 Shapemeter–looper.

29.3.4 Contactless Flatness Measuring Devices

Contactless measurement systems are less intrusive and much more flexible compared with the contact devices, but they are clearly less precise. For this reason, cold-rolling mills should normally use contact shapemeters. Even in this case, this choice is sometimes not the right one, because the contact with the roll can affect the strip surface itself so that it becomes incompatible with the stringent demands on the strip surface; for instance, in bright-annealed, stainless steel production, we must avoid the appearance of superficial scratches. In this case, special roll coatings must normally be used, with consequent increasing of initial roll costs and additional maintenance costs; the roll coatings are normally changed every 3 to 6 months when working with cold strips. Another frequent problem with contact devices is linked to hot rolling, where we have to cope with the high temperature of the strip, easily rising above 900°C and affecting the wear of the roll coating and, as a result, the strip surface. Furthermore, contact shapemeters cannot be used to measure the flatness of plates, because the plate surface is not in tension, and so measurements cannot be performed. Given these technological limits to contact shapemeters, in recent years contactless flatness measurement systems have been developed.

Nowadays, there are many different kinds of contactless shapemeters, and most of them are based on optical methods. These optical devices commonly work by projecting, with a laser or a special light source, a particular pattern onto the strip surface. This pattern is read by a charge coupled device (CCD) camera and processed by a computer, calculating the deviation from the same pattern when projected onto a completely flat surface. From this difference, we can compute the divergence of the measured strip from flatness and build a 2D (and sometimes 3D) representation of the strip surface.

In the following, we list and explain the most common techniques, on which almost all commercial contactless devices are based. By not considering any single measurement device, we keep our discussion more generic and, at the same time, we try to give to the reader the basics, to allow analysis using other contactless shapemeters on the market.

The different measurement processes are reviewed following a logical order that proceeds from what we consider the simplest device to the most complex.

Before examining the details of specific systems, it is useful to clarify the concept that is the basis of any optical measurement system, the optical triangulation method [12].

Optical triangulation can be realized in many different ways, but fundamentally we need a light source (a normal

light projector or laser projector) and a receiver (commonly a CCD camera). Usually there are two setups for the relative positions of source and receiver (Figure 29.5): either the source or receiver is fixed, normal to the projection plane, or both source and receiver fixed obliquely to the projection plane.

The measurement system is very simple and rapid, which is one reason for its widespread and popular use. A point (or a line, as we can see later) is projected onto the surface, called "S," by a source, called "L," and its position is captured by a receiver, called "R." When the projection plane moves up, or down, by a distance y, the displacement is sensed by R as a movement Y. The relationship between y and Y can be mathematically expressed as:

$$y = \frac{aY\cos\theta_1}{b\sin(\theta_1+\theta_2) - Y\cos(\theta_1+\theta_2)} \tag{29.2}$$

where a is the distance between the projected point and the lens of the receiver, b is the focal length of the camera (the distance between the lens of the camera and the light sensor), θ_1 is the angle between the laser beam axis and a normal line to the projection plane, and θ_2 is the angle between the segment a and the normal line to the projection plane.

To understand the difference between these two setups, we have to consider that a polarized light beam is reflected by an ideal smooth surface (that behaves like a mirror) at an angle equal to the incidence angle, as stated by the second law of reflection. From this observation, we can understand that if the receiver is positioned on the ideal trajectory of the reflected light beam it will receive the maximum possible quantity of light, resulting in a better signal sensed by the camera.

Thus, for setup 1 we would expect a weaker signal perceived by the camera in comparison with setup 2. When we have to deal with highly scattering surfaces, this consideration can be significant, because the quality of the image "seen" by the receiver is directly proportional to the measurement precision.

On the other hand, when the projector is perpendicular to the reference surface, the position of the projected point is not affected by the strip movement, a problem that appears in the alternative setup.

29.3.5 Linear Laser Method

This technique, used for example by Shapeline and Inline Measurement Systems contactless shapemeters [13], is a basic application of the optical triangle method. By projecting a laser line or a sequence of points, with a defined angle from the vertical position, onto a body, we can measure the height of the body by processing the images captured by a camera placed perpendicular to the reference plane. The idea of the process is sketched in Figure 29.6, in which a generic body is considered first (to better understand the logic principle) and then an example of a distorted strip is shown.

Proceeding with a continuous measurement of the different height of points across the width of the strip, we can

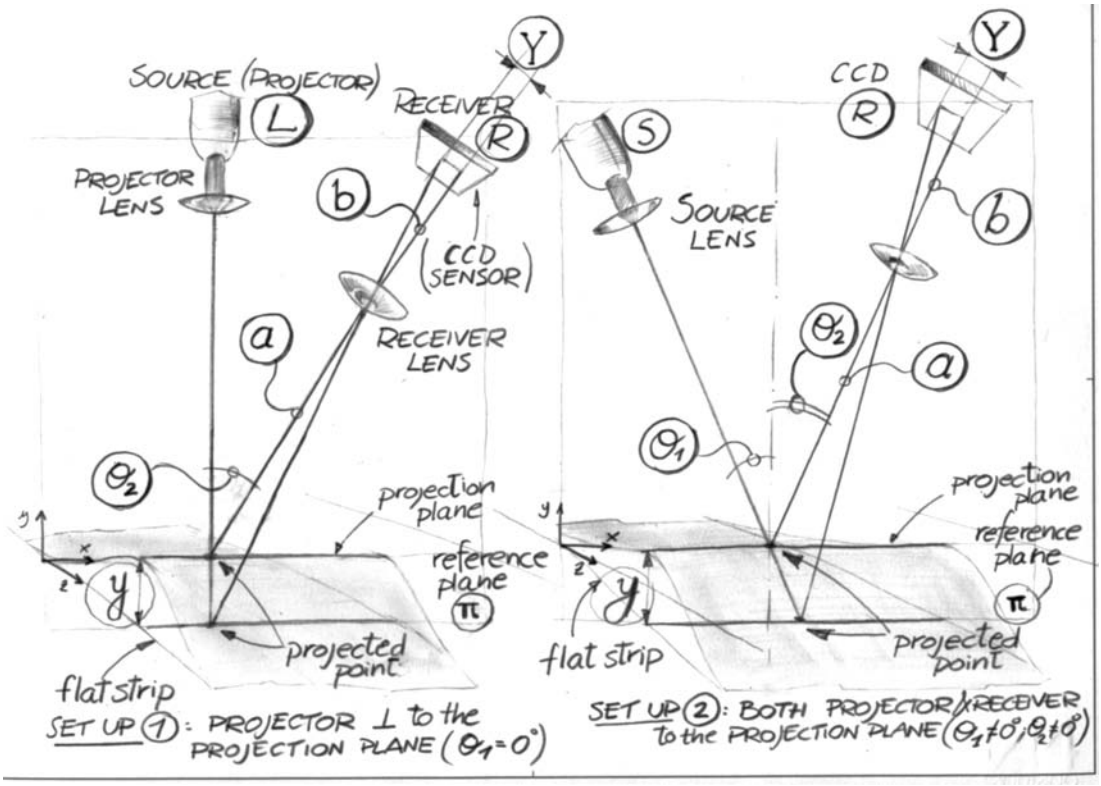


FIGURE 29.5 Contactless flatness measuring devices—optical triangulation.

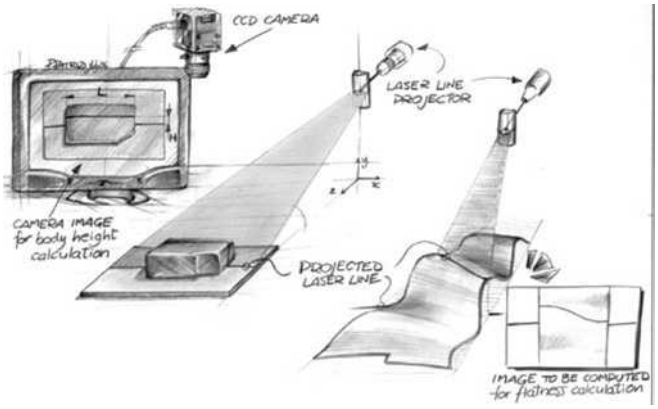


FIGURE 29.6 Linear laser method.

compute a 2D model of the strip surface. To comprehend how this happens, we have to consider a single fiber along the strip length (Figure 29.7).

After we have measured the height of different points along the fiber, we can calculate a linear approximation to the actual fiber length, expressed by the equation

$$L_j = \sum_{i=0}^{n} \sqrt{(y_i - y_{i-1})^2 + V_i^2 (t_i - t_{i-1})^2}$$
$$(i = 0,1,2,\ldots,n;\ j = 1,2,\ldots,m) \qquad (29.3)$$

where L_j is the actual length of each fiber, from 1 to m, corresponding to the m-points across the width of the strip measured simultaneously by the system; y_i and v_i are, respectively, the height and the speed of the i-th point at time t_i.

Similarly, we can calculate the ideal fiber length L for a completely flat strip:

$$L = \sum_{i=1}^{n} v_i (t_i - t_{i-1}) (i = 0,1,2,\ldots,n) \qquad (29.4)$$

From L_j and L we can calculate the elongation ε of the fibers, and therefore the flatness I expressed in I-units ($I = \varepsilon \times 10^5$):

$$\varepsilon = \frac{L_j - L}{L} \qquad (29.5)$$

29.3.5.1 Strengths

The linear laser method allows fast calibration of the system and easy flatness calculation, so we do not need extremely powerful computers to perform the calculations and we can increase the number m of points measured at the same time, giving proportional improvement of the precision of the device; the system consists of few parts, reducing the possibilities for failure and lowering maintenance costs.

29.3.5.2 Weaknesses

With this system only a finite number m of fibers can be considered in the flatness measurement, which contributes to a lack of precision. Using a single camera means we have fewer calculations todo, but only a 2D model of the strip can be built, limiting the final flatness accuracy to a value of around 5 μm. Also, the strip movement influences the measurements, thus limiting the maximum speed of the strip.

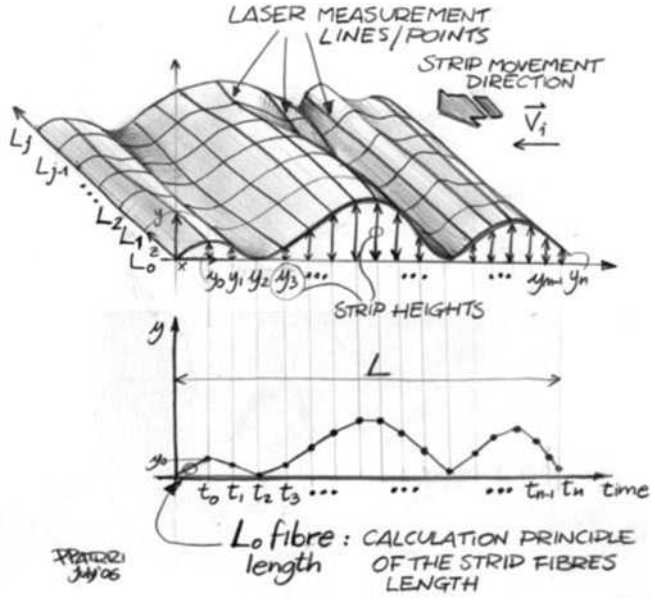


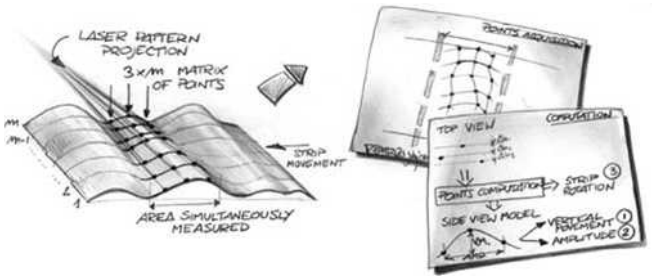
FIGURE 29.7 Linear laser method—measurement.

29.3.6 Laser Points Method

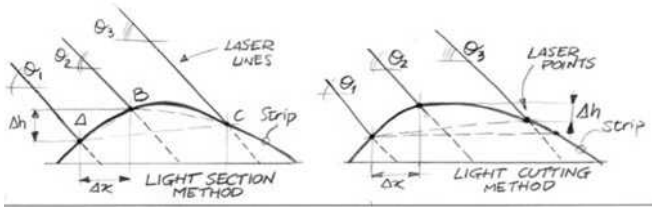
This technique provides the basis of the most commonly used contactless shapemeter, the ROMETER by IRM, Belgium [14]. The system consists of projecting a complete pattern of points onto the strip surface and using an array of cameras to convert the spatial location of these points to a measure of strip flatness. Normally, the light pattern, simultaneously projected and computed, is composed of a finite number of points m across the width of the strip (depending on the desired accuracy, strip speed, and computing power) and three points, for each of the m fibers considered, along its length.

Using this pattern, rather than a single line of points or a single line, permits the evaluation of a supplementary spatial coordinate, with the possibility of building a 3D model of the strip. This result is achieved using geometrical relationships based on the triangulation procedure. The three points, measured simultaneously for each fiber, feed a system of three equations with three variables: the vertical strip movement, strip rotation, and flatness amplitude (Figure 29.8a). From the values of these variables, a complete 3D description of the strip surface is obtained. In a subsequent step, the data for the amplitude variations for each fiber are integrated to compute the fiber lengths and flatness values.

There have been several different mathematical methods proposed to calculate the three variables for each fiber. Once



(a)



(b)

FIGURE 29.8 (a) Laser points method; (b) Light section method and light cutting method.

again, the most common method is the optical triangulation technique, because it is extremely easy and it results in rapid data processing. In 1997, Xilin et al. [15] proposed the idea of the light cutting method, as an evolution from the light section method and first studied by the Japanese company Sumitomo Metal Industries [16]. In the Figure 29.8 it is possible to understand the ideas behind these two methods.

Referring to the Figure 29.8b sketch, the elongation of each fiber can be measured as follows, for the light section method and the light cutting method.

$$\varepsilon = \frac{\overline{AB} + \overline{BC} - \overline{AC}}{\overline{AC}} \tag{29.6a}$$

$$\varepsilon_N = \frac{\overline{AB} + \overline{BC} - \overline{AD}}{\overline{AC}} \tag{29.6b}$$

29.3.6.1 Strengths

A 3D model of the strip can be computed, offering a detailed representation of the strip surface. The technique uses innovative technology with respect to projection of a single line of points.

29.3.6.2 Weaknesses

3D system needs are more complex and must be calibrated with respect to the 2D systems. Even if various geometrical methods were proposed to measure the strip fiber details (the optical triangulation, light section, and light cutting methods), the accuracy of the data collected is still not optimal, resulting in an imprecise flatness calculation. The amount of data to be concurrently processed is relevant, needing faster mathematical algorithms or using faster computers. Single points are more difficult for the CCD camera to locate than lines when disturbing elements are present, for instance strip vibrations, smoke, or hot strip fluorescence. For the ROMETER the external disturbing factors are attenuated using a multi-stereoscopic correction.

29.3.7 Fringe Method

The fringe method is a further improvement in the development of contact-free shapemeters with an example being the TopPlan system, an invention of BFI, Thyssen Krupp Stahl, and Gesellschaft für optische Meßtechnik [17]. A pattern of parallel lines (fringe pattern) is projected onto the hot strip using a specific light or laser projector. As with other optical devices it is of primary importance that the light pattern projected onto the strip stands out from the background, so it can be precisely recognized by the CCD camera and subsequently computer processed.

This method is based on the idea of the stereoscopic view that forms the basis of the human visual system. A stereoscopic view is obtained by observing the same object from two different points of view and using the slight differences between the two images to obtain 3D data. This view can be simulated using two cameras observing the same object from different positions. With a stereo system, we can obtain 3D volumetric imaging and thus a full reconstruction of the objects. This result is something completely different from the 3D depth imaging acquired with the previous laser points method, where only the depth and not the volume of the surface can be defined [18]. To understand the concept of volumetric imaging, we can think of 3D stereoscopic images as used in 3D cinema, books, and images; the left and right components of the stereo image can be represented in a single image, if one is shown in red and the other in green and the viewer uses glasses with a red lens for one eye and a green lens for the other. In this situation, we not only have the illusion of the object's depth, but we can also see all its volume; this is, therefore, a 3D volumetric image.

The stereoscopic view can be re-created even replacing one camera by a light source, but it is necessary to identify from which direction the illumination is coming. This requirement is to compensate for the missing information of image disparity (the apparent difference in position of an object when it is viewed from slightly different angles). From this reasoning is born the idea of a fringe pattern, a continuous sequence of dark and bright strips (we normally use black and white CCD cameras to view the image) projected over the object of interest, giving volumetric information on each point of the projection area.

For the specific case of strip flatness measurement, the fringe pattern will appear distorted if the surface is not flat, and from the mutual deformation of the projected lines, it is possible to compute a 3D volumetric model of the strip surface (Figure 29.9).

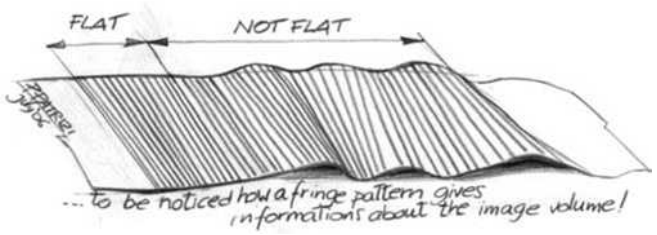


FIGURE 29.9 Fringe method.

With the fringe method, the calculation of the flatness is not as simple as with the other processes, but greater accuracy can be achieved. Without getting into too much detail, we can say that the first step in analyzing the image is a digital filtering, to remove the effect of external disturbances and to reduce the fringes to a unique, one pixel width line. Subsequently the lines are computed and compared with the ideal pattern that should appear for a completely flat strip. From the comparison, the deviation of the actual fringe pattern is calculated. In the next step the deviation is displayed on the z axis, to obtain a complex 3D volumetric model, from which all flatness data can be retrieved.

The most recently proposed variations of the fringe method are based on projecting a grid pattern consisting of parallel vertical and horizontal lines. The image data processing is slightly different from method to method, but the basic idea is always the same.

29.3.7.1 Strengths

This is an innovative contactless measuring method with fast calibration of the system. It creates a complete 3D volumetric image of the strip surface with superior accuracy in flatness definition. This method can use both a laser and white visible light projector. The flatness information is gained from one frame of image without the problem of time integral; therefore, it can completely overcome the flatness measurement error results from strip vibration and swing on the roll table. As a consequence, the whole strip is uniformly checked, with good precision at the critical edge areas, and there is the possibility of detecting local defects that are not repeated.

29.3.7.2 Weaknesses

A large amount of data has to be processed at the same time, slowing down the flatness measurement. The actual software for the digital image processing still needs to be studied and improved. More expensive technology is involved, increasing the cost of the device.

29.3.8 Moirè's Topography Method

The Moirè's topography method can be considered to be the most precise technique for cold strip and plate flatness measurements despite the complexity of its setup. The Moirè-based method has the advantage of covering, without exception, the entire area of interest, providing measurements for all points of the strip surface and using, at the same time, a fast data acquisition method. Another extremely positive characteristic of this method is that it overcomes all the problems that normally confuse all the other contactless shapemeters measurements. These include an extreme strip surface reflective index (a mirror surface or scattering surface) and the many tedious external disturbing factors such as vibrations, smoke, dust, water, oil, and so on [19].

The Moirè method (Figure 29.10a) is based on an interference phenomenon generated by the superposition of two identical gratings G_1 and G_2 with a grid constant l [20]. When they are exactly parallel, with α (the angle between the grating axes) equal to zero, we observe only a completely dark or white image. If we move the gratings with respect to each other so that α is different from zero a peculiar interference figure appears, with a width T proportional to the angle α and the grating pattern module length l. Mathematically,

$$T = \frac{l}{2 \sin \frac{\alpha}{2}}$$

which for small α can be written as

$$T = \frac{1}{\alpha}$$

The typical setup for a flatness measurement is shown in Figure 29.10b, where a grating is placed in the projector and another one in the image acquisition camera. The system must be as symmetrical as possible; both projector and camera must use the same optical system, they have to be placed at the same height above the strip, and both gratings must be securely fixed in a specific position with respect to the lens focusing points.

To understand what happens when the strip flatness has to be measured, we must consider Figure 29.10b.

In this image a strip deviation from the flat situation (plane P) is represented by the plane M. The projection of the grating G_1 appears curved when it is viewed through the grating G_2 because the projected pattern is distorted by the plane M, which is not flat. The deviation C of the Moirè $l' = \beta \cdot l$ pattern from the one that we should have for a flat surface can be calculated as a function of the grid constant (where β is the magnification of the projection system), the incidence angle θ_1, the viewing angle θ_2, the inclination surface angle ω, and the angle φ between the normal to the NO plane and the AOB plane [18]:

$$C = \beta \cdot l \cdot \frac{1 + \tan\omega \tan\theta_2 \cos\varphi}{\tan\theta_1 + \tan\theta_2} \tag{29.7}$$

If C is known, the deflection of two Moirè fringes gives information about the local vertical $N_3 - N_4$ deviation Δz

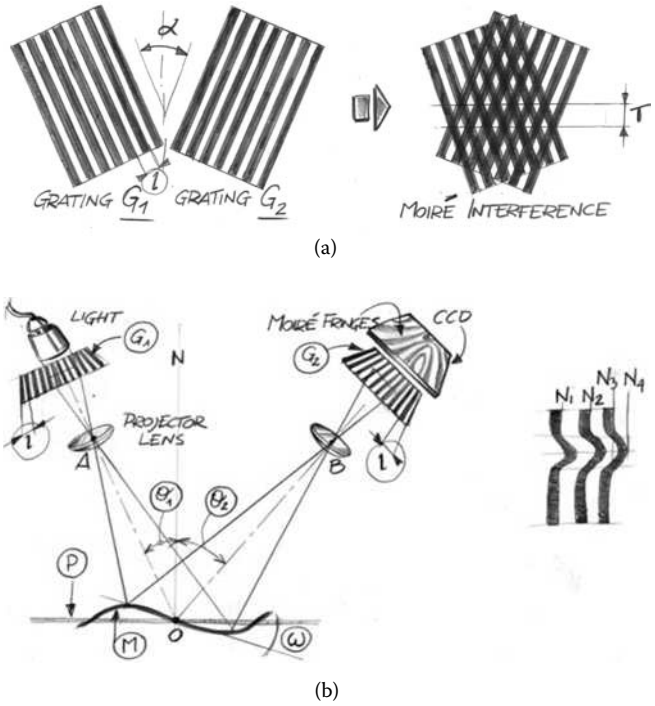


FIGURE 29.10 (a) Moirè method—superposition of two identical gratings; (b) Moirè method—typical setup.

$$\Delta z = C \cdot \frac{N_3 - N_4}{N_1 - N_2} \tag{29.8}$$

where $N_1 - N_2$ is the distance between two neighboring fringes (Figure 29.10b).

In the past, many methods for automatic analysis of Moirè image contours have been developed for different kinds of applications. For strip flatness measurement, real-time operation and reliability are the key objectives, within a defined range of precision. These needs are normally satisfied by using a intensity-based cumulative phase calculation algorithm that locally deduces the fringe contours by the changes of light intensity in the Moirè pattern. Advanced digital processing of the captured images is then used for noise filtering and correction of the signal profile and intensity. The images obtained are then compared with a preprocessing calibration pattern and differences in phase information are converted into strip flatness information.

29.3.8.1 Strengths

This technique produces very accurate results in real time. The whole strip is examined. Vibrations, high surface reflection and refraction indexes, oil, water, and dirt do not generally influence the measurement precision.

29.3.8.2 Weaknesses

Best results are obtained with surface temperatures at a maximum of 100°C, so this measurement system cannot be used in hot rolling mills. The initial setup is difficult, due to the precision required for the projector–camera system symmetry. Manufacturing costs are high and a high degree of maintenance is required.

29.3.9 Contactless Nonoptical Shapemeter

Not many kinds of contactless nonoptic shapemeter have been proposed, and at present, only one is actually used. This system is called SI-Flat and is produced by Siemens [21,22]. The principle of this device is to induce a precise vibration in the strip, and by computing the consequent excitation along the strip width, it can calculate the tension distribution in this same direction. Because this system is unique, schemes and detailed information can be easily retrieved.

29.3.9.1 Strengths

Vibrations of the strip and dirt on the surface do not influence the measurement precision. It can easily be applied to strips with different thicknesses. It reduces the problems of surface damage. There is no wear experience by the measuring device and so costs are correspondingly low. The measurement is independent of the strip speed. Calibration of the system is easy and rapid using a flat calibration sample.

29.3.9.2 Weaknesses

This measuring system cannot be used in hot rolling mills, so it can only be considered as a substitute for the commonly used contact shapemeters.

29.4 CONCLUSIONS

Nowadays automatic flatness control is a common requirement for all cold and hot flat-rolled strip or plate production. Many studies have been carried out in this field showing that flatness measurement devices are the weak link of close loop control systems. The reason for the slow development of contact and contactless shapemeters is the complexity behind the problem of flat strip deformation and the design requirements. These devices must guarantee constant accuracy even when working in completely hostile environments. For cold-rolling mills, contact devices are preferred and the available technologies can provide optimum measurement results. Many similar solutions are proposed to cover different needs of production and costs. For hot rolling mills and for special cold-rolling processes, contactless devices are appropriate. Unfortunately, the available systems still lack precision and much study is still required.

Contactless shapemeters are essentially an answer to the problem of exposure of the measurement devices to high temperatures (900°C–1200°C) in hot rolling mills. The temperature causes the contact devices to rapidly wear and drastically limit the sensors' lifetime. The flatness measurement by optical devices uses the optical triangulation method, in which the displacement of projected points or lines from a reference position allows the device to calculate the waviness of the strip surface. These optical methods can output 2D and

3D representations of the strip surface that can be used to change the rolling parameters and thus control the flatness.

Among the optical measurement systems, particular attention must be given to the Moirè topography method that is based on evaluating interference figures that are generated with a particular system setup. This device is actually the one that gives the best results in terms of accuracy and precision, but it can be used only for cold-rolling mills and it is difficult to set up and maintain.

Finally, representing contactless nonoptical devices and only for cold-rolling mills, we considered the SI-Flat system manufactured by Siemens, which is based on inducing a certain vibration in the strip. The flatness can be determined from the corresponding strip excitation.

Even if techniques of measuring strip flatness are further improved, it remains essential to match the right measuring device to the specific production situation to obtain the maximum accuracy and precision. In this way, good strip quality can be assured and the rate of production can be maximized. To choose the right shape measuring device we have to consider not only the specific limits of each device but also all its characteristics and how they might be influenced by disturbances such as temperature, humidity, smoke, water, and oil. All factors must be considered to obtain the best solution.

REFERENCES

1. MacDonald, D.J. 1980. *Shape Defects in Tinplates—Mechanical Working and Steel Processing XVIII*. Warrendale, PA: AIME Iron and Steel Society.
2. Ginzburg, V.B. 1993. *High-Quality Steel Rolling: Theory and Practice.* New York: Marcel Dekker.
3. Ginzburg, V.B., Ballas, R. 2000. *Flat Rolling Fundamentals*. New York: Marcel Dekker.
4. ABB product information. 1997. Flatness measurement Stressometer system. http://www.abb.com.
5. Keck, R., Neuschütz, E. 1980. German system brings accuracy to flatness measurement. *Iron and Steel International* 53: 215–220.
6. Vollmer America. 2009. Shapemeter Roll—System for Tension Levelers. http://vollmeramerica.com/vollmer_usa/brochures.
7. Fabian, W., et al. 1985. On-line flatness measurement and control of hot wide strip. *Metallurgical Plant and Technology* 8(4): 68–75.
8. Ginzburg, V.B. 1987. June 23rd. U.S. Patent No. 4,674,310.
9. Wortberg, H.J. 1976. Operative experiences with the Stressometer installed in cold mills at Alunorf GmbH, Federal Republic of Germany. *Shape Control*. London: Metal Society, 71–75.
10. Kelk, G.F., Hellis, R.H., Ginzburg, W.B. 1986. New developments improve hot strip shape: Shapemeter-looper and shape-actimeters. *Iron and Steel Engineer*, August 1986, pp. 48–56.
11. International Patent Classification: B21B 38/02, January 25th 2001. Patent Title: Apparatus for measuring the strip flatness.
12. Pirlet, R., Mulder, J., Adriaensen, D., Boelens, J. 1983. A noncontact system for measuring hot strip flatness. *AISE Year Book*, pp. 284–289.
13. Shapeline product information. Shapeline Strip System 500 Series. http://www.shapeline.com/products/shapeline_500_en_low.pdf.
14. I.R.M. Publication P107 E-001, 1984. *ROMETER Hot Strip Flatness Gage*. Belgium: Industry Research and Metallurgy.
15. Xilin, Y., Hui, M., Zhongyi, Q., Guofan, J. 1997. Image processing system in shape meter for hot strip mill. *Intelligent Processing Systems* 2: 1027–1030.
16. Matsui, K. 1989. Shape meter for hot strip mill. *Sumitomo Search* 38: 105–114.
17. Degner, M., Müller, U., Thiemann, G., Winter, D. 1998. Topometric on-line flatness measuring system for improved flatness control of hot strip. *Proceedings of the 1998 International Conference on Steel Rolling*, Chiba, Japan.
18. Jahne, B. 2002. *Digital Image Processing—5th revisited and Extended Edition*, Heidelberg: Springer-Verlag.
19. Paakkari, J. VTT Electronics: On-line flatness measurement of large steel plates using Moirè topography, Ph.D. Dissertation, University of Oulu.
20. Bartl, J., Fíra, R., Hain, M. 2001. Inspection of surface by the Moirè method. *Measurement Science Review* 1 (1).
21. Spreitzhofer, G., Dümmler, A. 2002. SI-FLAT improves measurement of strip flatness in cold rolling mills. *Metals and Mining International News* 4: 1–2.

30 Recent Developments in Strip-Profile Calculation

Arif S. Malik and Ramana V. Grandhi

CONTENTS

30.1 Introduction 329
30.2 Strip Profile and Crown 329
30.3 Strip Flatness or Shape 330
30.4 Strip-Profile Prediction and Control Models 330
30.4.1 Tasks Requiring Accurate and Rapid Strip-Profile Calculation 331
30.4.1.1 A New Simplified Mixed Finite Element Method for Strip-Profile Calculation 331
30.4.2 Strip-Profile Model Development 332
30.4.2.1 Modeling Strip-Profile Control Devices 334
30.4.2.2 Strip-Profile Calculation 334
30.5 Strip-Profile Model Applications 335
30.5.1 Four-High Cold Plate Mill 335
30.5.1.1 Comparison with Large-Scale Finite Element Analysis 336
30.5.2 20-High Sendzimir Mill 337
30.6 Summary 339
Acknowledgments 339
References 339

30.1 INTRODUCTION

Two critical aspects in attaining high-quality rolled metal strip are the cross-sectional strip thickness profile and its related flatness (or shape). While these geometric attributes of the strip have been extensively studied (Ginzburg 1989; Roberts, 1978), the requirements for higher quality and increasingly thinner strip compel the development of more rapid and accurate mathematical models for predicting and controlling strip profile and flatness. Following a brief review of existing approaches, we introduce a new mathematical method to calculate the strip profile and related flatness.* Comparison of the calculated deflections with those predicted by large-scale finite element analysis (FEA) is also shown. The new method employs a *simplified mixed finite element* approach, and it applies to both hot mills and cold mills—including complex cluster-type cold-rolling configurations. The new method accommodates the typical profile and flatness control mechanisms such as roll crowning, roll bending, roll shifting, and roll crossing, in addition to thermal and wear effects. Straightforward application of the model to dynamic analysis is also possible, including determination of natural frequencies and mode shapes of vibration for rolling mills.

* U.S. Patent pending, US/686,381, Malik and Grandhi, 2007.

30.2 STRIP PROFILE AND CROWN

The strip thickness profile refers to the variation in thickness (or gauge) of the strip in the lateral direction, transverse to the direction of rolling. In other words, it is the thickness variation across the width of the strip. Although the strip profile can assume any form, depending on mill parameters and the action of profile control mechanisms, in practice, it tends to assume a convex parabolic form, as shown in Figure 30.1a, because of the natural mill deflection characteristics. The strip profile may become concave due to mechanical roll crown and thermal roll expansion. A parameter commonly associated with the strip profile is the strip *crown*, which is a measure of the increase in thickness at the center of the strip width relative to other lateral locations. As defined in Equation 30.1 and shown in Figure 30.1b, the strip crown, denoted here as $C(x)$, is the difference between the center thickness, $H(0)$, and the thickness $H(x)$ at an arbitrary location x along the strip width.

$$C(x) = H(0) - H(x) \tag{30.1}$$

It is customary to record the average strip crown relative to a small distance from either edge of the strip. When this reference distance, indicated as "a" in Figure 30.1b, is 25 mm, the

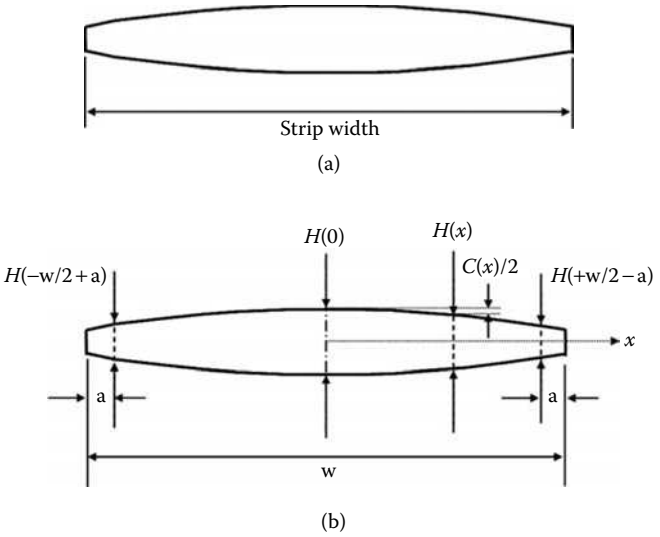


FIGURE 30.1 (a) Parabolic form of naturally occurring strip thickness profile. (b) Thickness parameters used to determine strip crown.

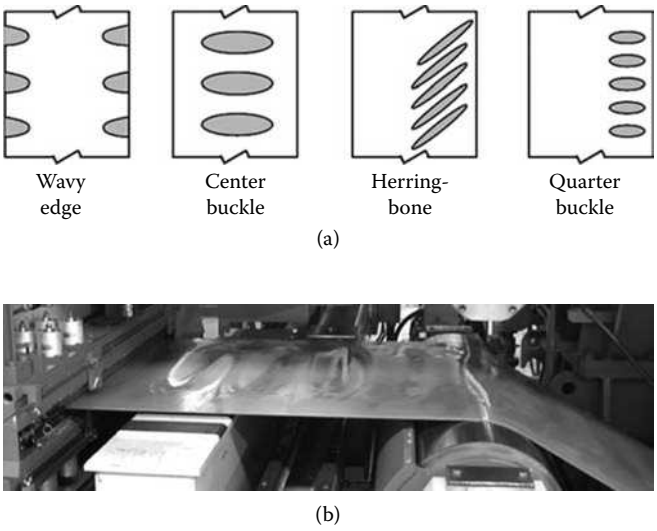


FIGURE 30.2 (a) Common strip flatness defect classifications. (Adapted from Malik, A. and Grandhi, R. 2008. *Journal of Materials Processing Technology* 206: 263–274.) (b) Example of center-buckle flatness defect in stainless cold rolling.

crown is referred to as *C*25 strip crown. If the strip profile is equally convex, as shown earlier in Figure 30.1a, then the crown $C(x)$ will be positive at all points x away from the center. Negative crown values indicate concavity in the thickness profile. Magnitudes of crown should not be so great as to violate standard thickness tolerances, nor should they cause problems during subsequent processing operations or in end-use applications.

30.3 STRIP FLATNESS OR SHAPE

Strip flatness (or shape) is related to the strip profile, and it is equally important to the dimensional quality parameter describing the geometry of flat-rolled metals. Whereas crown is the variation in thickness across the strip width, flatness is the variation in length or longitudinal strain across the strip width. Crown and flatness are strongly related since plastic deformation of the strip is incompressible and expansion of the strip width is comparatively small, especially in cold rolling. Common types of flatness defects are illustrated in Figure 30.2a. Flatness defects may be large enough to appear as buckles or waves, even when the strip is under tension during rolling. An example of this type of visible or *manifest* flatness defect is shown in Figure 30.2b. In contrast, *latent* flatness defects can only be detected by flatness meters that indirectly measure the lateral variation in the longitudinal stresses. Besides the adverse aesthetic impact on customer applications, strip having poor flatness can render mill operations and downstream processing difficult or impossible.

Strip flatness changes during rolling occur primarily as a result of *relative* changes in the strip thickness profile—because of the principle of mass conservation. This means that flatness control is most often performed indirectly via strip profile control. Accordingly, pass schedule set-up models are frequently designed to maintain a constant pass-to-pass strip crown ratio, in which the ratio of crown to center thickness, $C(x)/H(0)$, is often used. For a given pass, a change in the manifest strip flatness will only occur when relative changes to the strip profile exceed a certain range known as a flatness *deadband*. Several investigators, including Shohet and Townsend, Somers, Guo and Schunk, Ishikawa, and Takashima, previously identified empirical relationships for the flatness deadband (Ginzburg and Ballas 2000). As is clear to rolling mill operators, these empirical relationships generally indicate that the flatness deadband decreases exponentially as the ratio of strip width to thickness increases. In addition, the sensitivity of flatness to changes in the strip profile becomes more pronounced for relatively thinner and wider strip. For this reason, strip profile control is more important in the final stands of hot strip mills and is more difficult when cold rolling thin gauge products.

30.4 STRIP-PROFILE PREDICTION AND CONTROL MODELS

As mill operations become more productive, with pass schedules pushing the rolling envelope, the use of sophisticated strip-profile calculation models for both prediction and control becomes even more important. Practical techniques applied to control strip profile and related flatness are numerous, but they principally involve distributing the rolling force across the width of the strip in such a manner that the localized thickness reductions yield a desirable strip thickness profile. The most rudimentary means to control strip profile on even the most basic rolling mills include roll crowning together with the assignment of an appropriate reduction schedule. Other profile and flatness control mechanisms that can be adjusted during the rolling of a strip include roll bending, roll shifting, roll crossing, and roll cooling. Successful

TABLE 30.1
Strip–Profile Calculation Methods

Method	Year	Investigator	Advantages	Disadvantages
Single Beam on Elastic Foundation Method	1965	Stone and Gray	Simplicity	Neglects shear deformation; limited to two-high and four-high mills; no dynamic analysis
Influence Coefficient Method	1968	Shohet and Townsend	No linear assumption; applicable to two-high, four-high, and six-high mills; widely adapted method	Iterative solution; difficult to apply to cluster mills; no dynamic analysis
Transport Matrix Method	1980, 1990, 2005	Poplawski et al., Guo, Guo and Malik	Noniterative rapid solution; very compact spring-beam-gap system; applicable to two-high, four-high, six-high, and cluster mills	Discrete nodal springs; linearized at mill operating point; piecewise linear displacement field; no dynamic analysis
Large-Scale Commercial Finite Element Method	1984, 1987	Eibe, Chen and Zhou	No linear assumption; ability to model complex geometries; stress fields readily available; can couple with strip deformation; dynamic analysis possible	Extensive computation time; large RAM; large number of elements; convergence difficulties due to contact; memory requirements limit number of rolls
Fuzzy / Neural Network Methods	1992	Hattori et al.	Ability to model complex rolling phenomena; can couple with strip deformation; readily applicable to cluster mills	Nonphysics-based model; requires significant "training" with mill data
Simplified Mixed Finite Element Method (presented method)	2007	Malik and Grandhi	Noniterative rapid solution; continuous elastic foundations; third-order displacement field; compact global system; applicable to two-high, four-high, six-high, and cluster mills; straightforward dynamic analysis	Linearized at mill operating point

implementation of these profile control techniques requires either extensive trial-and-error or the preferred use of an effective strip-profile calculation model. Table 30.1 summarizes the major developments (over four decades) in strip-profile calculation methods, including the new simplified mixed finite element method presented in this chapter.

30.4.1 Tasks Requiring Accurate and Rapid Strip-Profile Calculation

The demands for increased quality and productivity, and the challenges of rolling ultra-thin gauge products, require that accurate strip-profile and flatness calculations be incorporated into the following rolling mill–related tasks:

1. Mill design
2. Profile/flatness control mechanism design
3. Roll crown determination
4. Pass schedule set-up calculation
5. Online strip-profile/flatness control (via bending, shifting, crossing, or cooling of rolls)

For application to pass schedule set-up and online profile (crown) and flatness control, the strip-profile calculation must be rapid. Historically, with the exception of Fuzzy/Neural Network techniques, the methods in Table 30.1 were not fast enough to directly perform pass schedule set-up or online profile and flatness control. They were therefore used in conjunction with surrogate modeling techniques such as polynomial curve-fitting and/or look-up table approximation. Today, however, depending on the specific implementation, computing speeds may allow other models (such as those derived from the Transport Matrix Method) to be deployed directly for pass schedule calculation or profile and flatness control.

30.4.1.1 A New Simplified Mixed Finite Element Method for Strip-Profile Calculation

Presented next is a new simplified mixed finite element method for predicting and controlling the strip-profile and its related flatness. The model is based on a global stiffness-based linear system that is coded in the same manner as the conventional finite element method (FEM), from which it draws many benefits. Unlike conventional FEM, however, the new simplified mixed finite element method does not require a large number of elements to accurately represent the rolling mill deflection behavior. As described in Table 30.1, the method provides a rapid, noniterative solution, making it ideal for applications such as pass schedule set-up and online flatness control. Theoretical accuracy is improved over the traditional spring-beam-gap systems because the method uses continuous (rather than discrete) elastic foundations to represent the strip-work roll interaction, and the contact interactions between adjacent rolls. Inherent third-order (cubic) displacement fields provide a high-fidelity solution with very few elements. Application to cluster mills such as

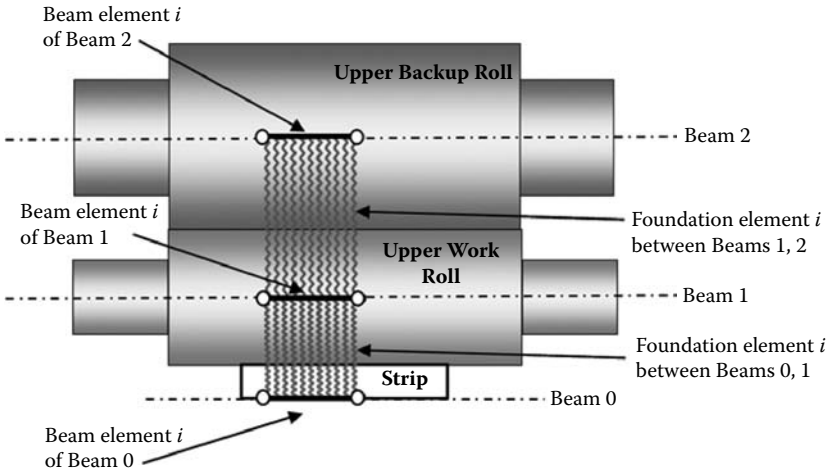


FIGURE 30.3 Simplified mixed finite element model of four-high mill upper section. (Adapted from Malik, A. and Grandhi, R. 2008. *Journal of Materials Processing Technology* 206: 263–274.)

the 20-high Sendzimir cold mill is straightforward and easier to program than conventional models. Further, because the method employs a global stiffness-based linear system, dynamic analysis can be performed using natural frequencies and mode shapes of vibration computed by solving the standard eigenvalue problem.

30.4.2 Strip-Profile Model Development

As illustrated in Figure 30.3, construction of a strip-profile model using the simplified mixed finite element method is accomplished by coupling Timoshenko (shear deformable) beam elements with continuous elastic Winkler foundation elements. The beam elements represent bending and shear deflection rigidities, while the continuous foundation elements characterize the flattening contact resistance between adjacent rolls, and between the work rolls and the strip. The total number of elements used is arbitrary, but very few node points (element ends) are required compared to conventional methods because the vertical displacements are modeled using cubic polynomials that are inherent to the displacement solution. In addition, symmetry in the roll stack and loading can be exploited to create very compact models. The minimum number of elements required is determined by assigning nodes at the ends of each roll, at the edges of the strip, and wherever the roll diameters change. Figure 30.4 shows the minimum number of nodes and their corresponding locations for a one-quarter symmetric model of a four-high mill. Additional nodes and accompanying elements can be used to increase accuracy.

The simplified mixed finite element method produces a global stiffness-based linear system, [K] **u** = **f**, where [K] is the global stiffness matrix, **u** is the vector of nodal displacements, and **f** is the vector of applied nodal loads and/or nodal reactions. The global matrix system is created by combining the individual Timoshenko beam elements and elastic foundation elements in the same manner as the conventional finite element method. This makes the strip-profile model simpler to program than conventional models. Referring to Figure 30.5, a simplified mixed finite element stiffness matrix, $[K_T^{1,2,i}]$, is created to characterize the bending, shear, and flattening deflections for an element i of two adjacent beams, denoted as Beam 1 and Beam 2, respectively. In the case of a simple four-high mill, Beam 1 may represent the work roll (WR) and Beam 2 the backup roll (BUR). Alternatively, if the element of Figure 30.5 is used to represent the interactive deflection between the strip and upper work roll, then Beam 1 (representing the strip) will carry zero bending and shear deflection terms. In addition, the continuous linear elastic foundation terms in $[K_T^{1,2,i}]$ will account for a series-combination of the work roll flattening stiffness and a strip *modulus*. The strip modulus characterizes the rolling force per unit strip width, per unit thickness reduction at a given mill operating point. A similar approach that represented the strip as discrete linear springs was taken by Guo (1986). When examining rolling data for 1880-mm-wide mild steel at up to 80% thickness reduction, Guo found the use of a linear strip modulus to be satisfactory. The new method employs the same concept of a linear strip modulus, but uses a more accurate continuous elastic foundation rather than several discrete nodal springs. The disadvantage of the strip modulus concept is that a given modulus is valid only in the vicinity of a specific mill operating condition according to the nature of the actual load-reduction curve.

The matrices $[K^{1,i}]$ and $[K^{2,i}]$ in Figure 30.5 govern the bending and shear deflections for Beams 1 and 2, respectively, and are merely conventional four-by-four Timoshenko beam element stiffness matrices for the vertical displacement. In the case of cluster-type rolling mills where the adjacent rolls may not be aligned in a vertical stack, the Timoshenko beam element matrices include both horizontal and vertical displacement terms, and are eight-by-eight in size.

The global stiffness matrix [K] in the system [K] **u** = **f** is computed by summing the contributions of all individual

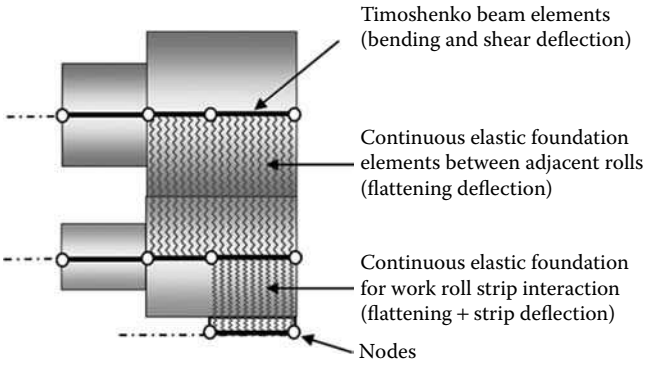


FIGURE 30.4 Quarter symmetric model of four-high mill indicating minimum number of nodes and corresponding locations.

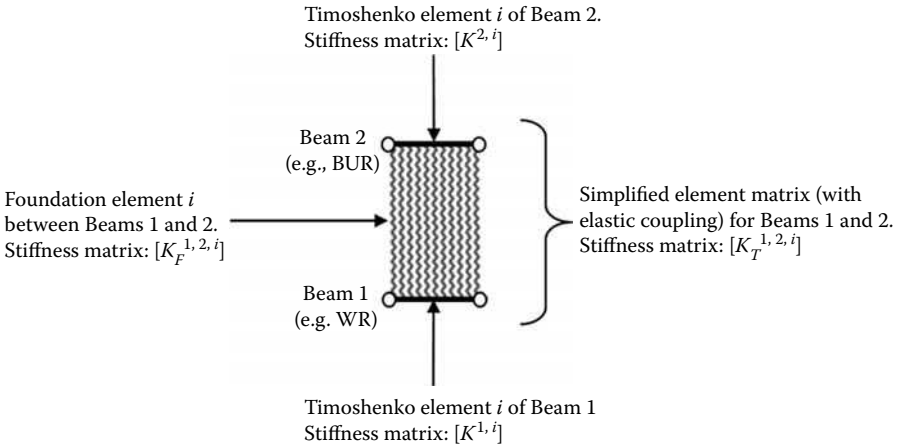


FIGURE 30.5 A simplified mixed finite element to model shear, bending, and flattening deflection for two rolls.

beam element and foundation element matrices, as shown in Equation 30.2, where N is the total number of simplified mixed finite elements.

$$[\mathrm{K}] = \sum_{i=1}^{N} [K_T^{1,2,i}] = \sum_{i=1}^{N} ([K^{1,2,i}] + [K_F^{1,2,i}]) \tag{30.2}$$

The term $[K^{1,2,i}]$ in Equation 30.2 is simply the matrix combination of $[K^{1,i}]$ and $[K^{2,i}]$, as shown in Equation 30.3.

$$[K^{1,2,i}] = \begin{bmatrix} [K^{1,i}] & [0] \\ [0] & [K^{2,i}] \end{bmatrix} \tag{30.3}$$

The term $[K_F^{1,2,i}]$ in Equation 30.2 represents the elastic coupling, or roll flattening stiffness contribution, and is calculated as follows:

$$[K_F^{1,2,i}] = \begin{bmatrix} \left[\int_0^L k(x)F_{11}(x)dx\right] & -\left[\int_0^L k(x)F_{12}(x)dx\right] \\ -\left[\int_0^L k(x)F_{21}(x)dx\right] & \left[\int_0^L k(x)F_{22}(x)dx\right] \end{bmatrix} \tag{30.4}$$

where $k(x)$ is the elastic foundation modulus, L is the element length, and terms F_{11}, F_{12}, F_{21}, and F_{22} are defined by Equation 30.5, for $p = 1, 2$ and $q = 1, 2$.

$$F_{pq} = N_{vp}^T N_{vq} \sin^2\theta + N_{wp}^T N_{wq} \cos^2\theta + N_{vp}^T N_{wq} \sin\theta\cos\theta + N_{wp}^T N_{vq} \sin\theta\cos\theta. \tag{30.5}$$

The angle θ in Equation 30.5 accounts for cluster-type roll stack configurations, as shown in Figure 30.6 for the 20-high Sendzimir mill. Terms N_{vn} and N_{wn} (for $n = 1, 2$) are the vertical and horizontal shape function submatrices of the

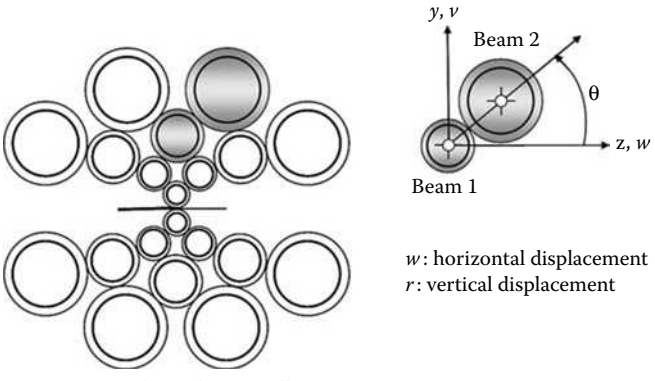


FIGURE 30.6 Definition of angle θ for modeling cluster-type mills.

full third-order Timoshenko beam element shape function matrix (Bazoune and Khulief 2003).

A flowchart of the procedure for assembling and solving the global system of equations to compute the deflection behavior for a given rolling mill is depicted in Figure 30.7. There is no difference between the procedure shown and that of the conventional finite element method, except for the use of the simplified mixed finite element stiffness matrices, $[K_T^{1,2,i}]$. Tasks identified with an asterisk (*) are only performed if dynamic analysis is required, using conventional techniques, such as those outlined by Cook et al. (2004).

30.4.2.1 Modeling Strip-Profile Control Devices

In addition to pass schedule adjustment, common techniques to control strip profile and flatness in rolling mills include roll crowning, roll bending, roll shifting, roll crossing, and roll cooling, among others (Figure 30.8). The effects of these upon the strip thickness profile can be predicted with the use of the simplified mixed finite element method by assigning corresponding nodal loads in the case of roll bending or by assigning the appropriate element geometry and elastic foundation terms in the case of other profile control devices. Since the foundation modulus terms, $k(x)$ in Equation 30.4, are functions of the axial position along their corresponding rolls, they can readily account for arbitrary roll crowns, incoming strip crowns, and roll cooling patterns.

30.4.2.2 Strip-Profile Calculation

To calculate the strip crown using Equation 30.1, the vertical position, $y(x)$, of the common generator surface between the strip and the work roll at the desired axial location x must first be computed. The common generator vertical position, $y(x)$, between any two arbitrary beams (1 and 2) can be obtained using Equation 30.6. The two beams in Equation 30.6 represent either two adjacent rolls, or the strip and an adjacent work roll.

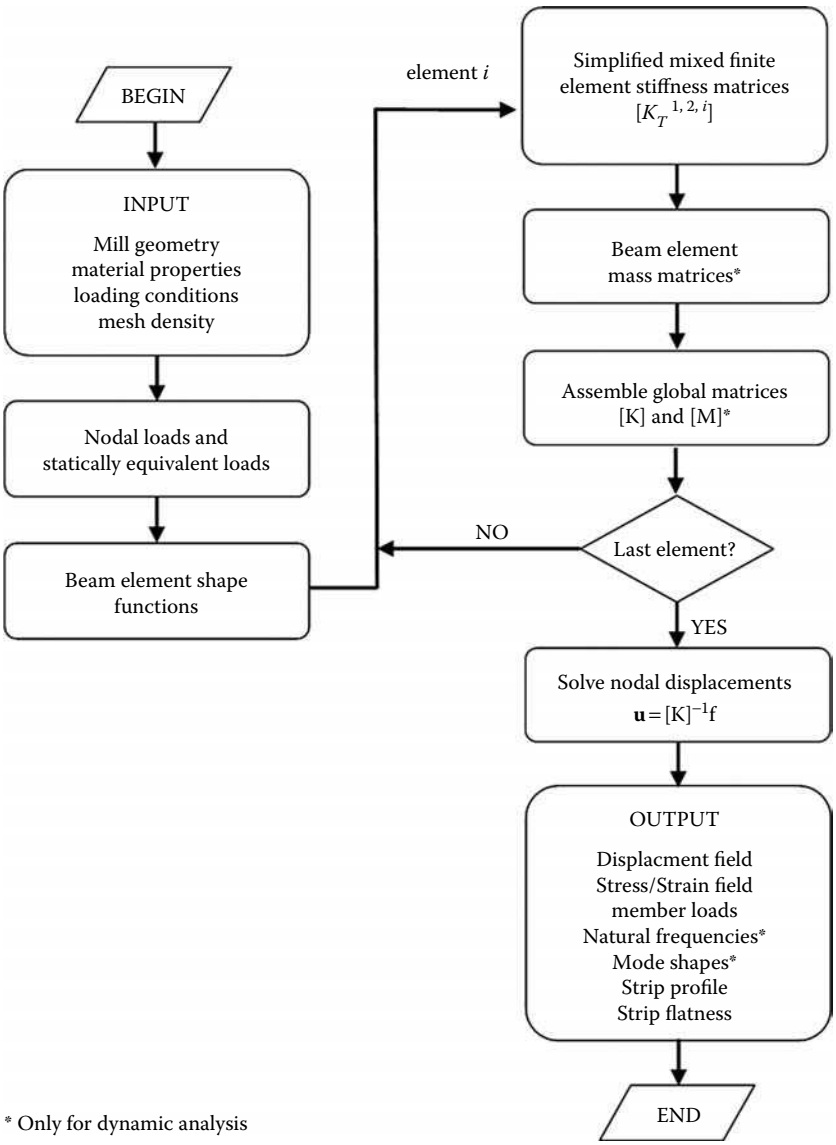


FIGURE 30.7 Procedure for computing mill deflection using simplified mixed finite element method.

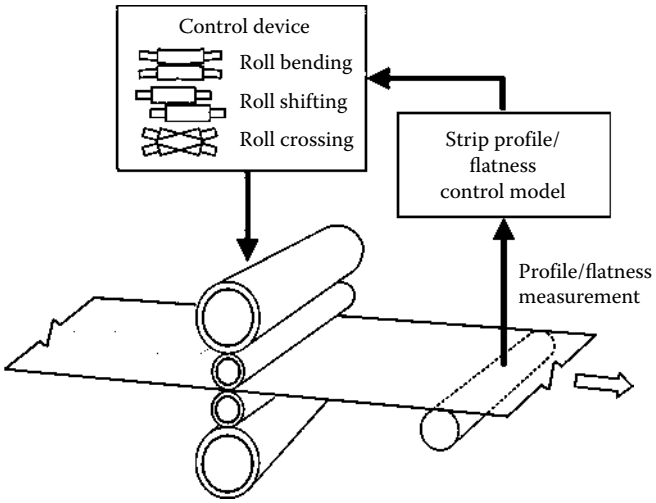


FIGURE 30.8 Strip profile and flatness control.

$$y(x) = y_{1j}(x) + \left(\frac{D_1(x)}{2} - \frac{k(x)}{k_1(x)} I(x) \right) \sin\theta \qquad (30.6)$$

The term $y_{1j}(x)$ in Equation 30.6 is the vertical position for node j at the axial coordinate x of Beam 1 (where Beam 1 is the strip when determining thickness profile). $D_1(x)$ is the original diameter of Beam 1, which is the initial strip thickness if $y(x)$ corresponds to the strip/work roll common generator. The term $k(x)$ is the equivalent series-combined foundation modulus for the strip and the adjacent work roll, and $k_1(x)$ is the foundation stiffness contribution of only Beam 1, which corresponds to the strip modulus. Roll angle θ is as defined previously in Figure 30.6. The term $I(x)$ in Equation 30.6 represents the total interference between the adjacent beams, as determined from the original nodal coordinates, roll diameter profile(s), initial strip crown, and the nodal displacements.

30.5 STRIP-PROFILE MODEL APPLICATIONS*

30.5.1 Four-High Cold Plate Mill

In this section, the simplified mixed finite element method is applied to calculate the strip profile for a 1270-mm-wide, four-high mild steel cold plate mill. A comparison of the displacement results with those predicted using large-scale commercial FEA is also provided. In the next section, a complex 20-high Sendzimir cold-rolling mill is modeled. Basic geometric parameters for the four-high mill example are shown in Table 30.2, with corresponding model parameters indicated in Table 30.3. Using partial symmetry, a total of 48 Timoshenko beam elements and associated coupling foundations are used to model the upper half of the roll stack (use of full symmetry would lead to a one-quarter model with 24 elements). The strip foundation modulus, $k(x)$, is assigned a constant value of 13,790 N/mm^2, except for a modification to decrease this value by a factor of two at the strip edges, starting at a distance of 25 mm from either strip edge.

Based on the input data in Tables 30.2 and 30.3, Figure 30.9a illustrates the resulting contact force distribution at the interface between the strip and the upper work roll, and between the upper work roll and the upper backup roll. Figure 30.9b shows the thickness profile of the upper half of the strip relative to the strip edge. By Equation 30.1, the strip crown $C(x)$ corresponding to $C25$ locations ($x = \pm 229$ mm) is 1.118 mm, since the semithickness is 0.559 mm greater at the strip center than at the $C25$ edge locations. Table 30.4 summarizes the results for the four-high plate mill simulation. The model predicts that for a 17.02% reduction in thickness at the strip center, the thickness at a distance of 25 mm from either edge of the strip is 1.118 mm less than the center thickness (19.959 mm vs. 21.077 mm). Hence, the $C25$ strip crown is 1.118 mm, or 5.304% of the center thickness. Since this simulation includes no crown control devices, Figure 30.9a and b illustrate the typical deflection and load characteristics that occur in a four-high rolling mill. It can

TABLE 30.2
Geometry Parameters for Four-High Plate Mill Example

Four-High Mill Geometry Parameter	Value
Strip entry thickness, H (mm)	25.400
Strip center exit thickness, h (mm)	21.077
Strip width, w (mm)	508.00
Work roll diameter, D_w (mm)	254.00
Work roll length, L_w (mm)	1270.0
Backup roll diameter, D_b (mm)	508.00
Backup roll length, L_b (mm)	1270.0

Source: Adapted from Malik, A. and Grandhi, R. 2008. *Journal of Materials Processing Technology* 206: 263–274.

TABLE 30.3
Model Parameters for Four-High Plate Mill Example

Four-High Mill Model Parameter	Value
Strip foundation modulus, $k(x)$ (N/mm^2)	13,790
Back-up roll boundary condition type on end nodes	Pinned
Work roll boundary condition type on end nodes	Free
Strip lower edge vertical displacement boundary condition (mm)	6.35
Backup roll elastic modulus, E_b (GPa)	206.84
Backup roll Poisson ratio, v_b	0.30
Work roll elastic modulus, E_w (GPa)	206.84
Work roll Poisson ratio, v_w	0.30
Number of Timoshenko beam elements	48

Source: Adapted from Malik, A. and Grandhi, R. 2008. *Journal of Materials Processing Technology* 206: 263–274.

* Adapted from Malik, A. and Grandhi, R. 2008. *Journal of Materials Processing Technology* 206: 263–274.

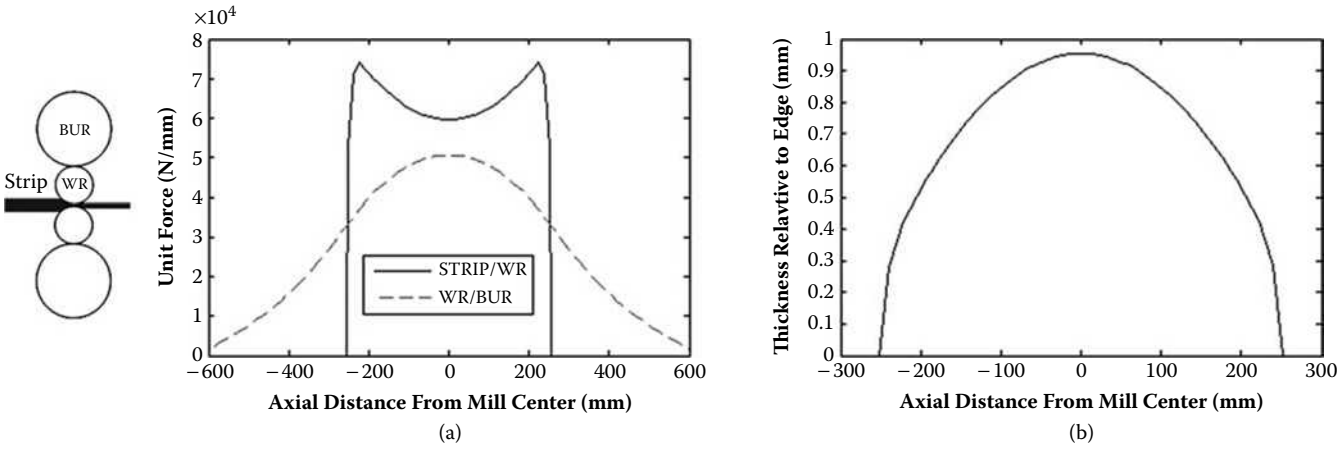


FIGURE 30.9 Contact force distribution (a), and strip crown for strip upper half (b). (Adapted from Malik, A. and Grandhi, R. 2008. *Journal of Materials Processing Technology* 206: 263–274.)

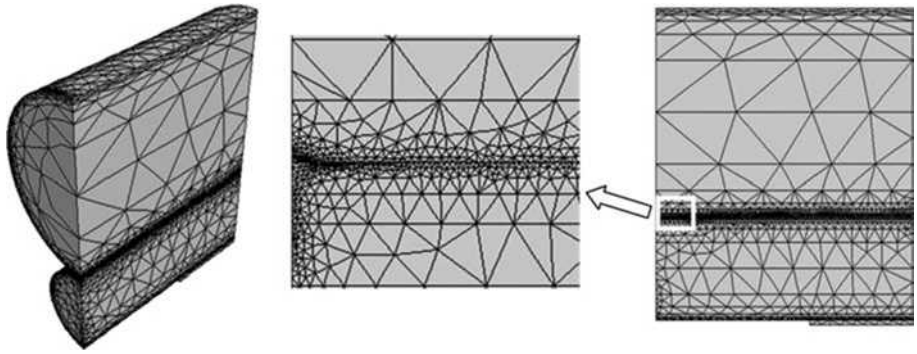


FIGURE 30.10 FEA model of upper section of four-high mill (64,054 3D tetrahedral elements).

TABLE 30.4
Results for Application of Simplified Mixed Finite Element Method to Four-High Plate Mill

Four-High New Model Result	Value
Strip center thickness, h_0 (mm)	21.077
Strip *C*25 thickness, h_{c25} (mm)	19.959
Strip crown, *C*25 (mm)	1.118
Strip crown, *C*25 (%)	5.304
Total force, *F* (MN)	33.949

Source: Adapted from Malik, A. and Grandhi, R. 2008. *Journal of Materials Processing Technology* 206: 263–274.

be seen that the increase in the contact force distribution in the vicinity of the strip edges leads to greater corresponding thickness reduction in those areas.

30.5.1.1 Comparison with Large-Scale Finite Element Analysis

A comparison of the displacement results obtained using the simplified mixed finite element method with those predicted using a commercial FEA package (ABAQUS® version 6.6-1) is now given. Figure 30.10 illustrates the one-eighth symmetric FEA model, in which, like the new model, the strip is represented by an equivalent elastic foundation (Malik and Grandhi 2008). While this simplification does not accommodate the strip's plastic behavior, it provides a direct comparison for which to evaluate the new method with similar assumptions. Table 30.5 provides a comparison of selected displacements (at the strip center location, *C*25 position, and strip edge location) obtained using both commercial FEA and the new mixed finite element model. The commercial FEA simulation undergoes three iterations to achieve satisfactory convergence, and terminates with 64,054 elements. Each of the iterations requires several hours computing time, prohibiting use in online control applications. In contrast, the simplified mixed finite element model achieves similar displacement results obtained in less than one second (on the same computer) with only 48 Timoshenko beam elements. Table 30.6 lists the "error" of the new method relative to the large-scale commercial FEA simulations. Interestingly, as the number of elements is increased in the large-scale FEA, the displacement results move closer to those predicted by the new simplified mixed finite element method.

TABLE 30.5
Vertical Displacement Comparison Between Large-Scale FEA and New Model

Four-High Model Type	Number Elements	Strip Center Displacement (mm)	Strip C25 Displacement (mm)	Strip Edge Displacement (mm)
FEA iteration 1	44,716	4.3896	3.7315	3.3650
FEA iteration 2	42,672	4.2718	3.6640	3.3147
FEA iteration 3	64,054	4.2459	3.5884	3.2408
New model	48	4.1891	3.6316	3.1521

Source: Adapted from Malik, A. and Grandhi, R. 2008. *Journal of Materials Processing Technology* 206: 263–274.

TABLE 30.6
Vertical Displacement Error of New Model Relative to Large-Scale FEA

Four-High Model Type	Number Elements	Center Displacement Error (%)	C25 Displacement Error (%)	Edge Displacement Error (%)
FEA iteration 1	44,716	–4.59	–2.68	–6.33
FEA iteration 2	42,672	–1.95	–0.88	–4.90
FEA iteration 3	64,054	–1.35	1.20	–2.73

Source: Adapted from Malik, A. and Grandhi, R. 2008. *Journal of Materials Processing Technology* 206: 263–274.

TABLE 30.7
Geometry Parameters for 20-High Cluster Mill Example

20-High Geometry Parameter	Value
Strip entry thickness, H (mm)	0.9779
Strip exit thickness, h (mm)	0.9063
Strip width, w (mm)	508.00
Work roll diameter, D_w (mm)	50.80
Work roll length, L_w (mm)	1270.0
First intermediate roll diameter, D_f (mm)	101.60
First intermediate roll length, L_f (mm)	1270.0
Second intermediate roll diameter, D_s (mm)	172.72
Second intermediate roll length, L_s (mm)	1270.0
Backing bearing outer diameter, D_{bb} (mm)	292.10
Backing bearing shaft length, L_{bb} (mm)	1270.0
Backing shaft outer diameter, D_{bs} (mm)	127.00
Number of backing bearings per shaft, N_{bb}	6

Source: Adapted from Malik, A. and Grandhi, R. 2008. *Journal of Materials Processing Technology* 206: 263–274.

TABLE 30.8
Model Parameters for 20-High Sendzimir Cluster Mill

20-High Model Parameter	Value
Strip foundation modulus, $k(x)$ (N/mm^2)	52,472
Backing bearing boundary condition type on all nodes	Pinned
Other roll boundary condition type on end nodes	Free
Strip lower edge vertical displacement boundary condition (mm)	0.5588
Elastic modulus of all rolls, E_r (GPa)	206.84
Poisson ratio of all rolls, v_r	0.30
Number of Timoshenko beam elements	252

Source: Adapted from Malik, A. and Grandhi, R. 2008. *Journal of Materials Processing Technology* 206: 263–274.

30.5.2 20-High Sendzimir Mill

Flexibility of the simplified mixed finite element method is now demonstrated by simulating the deflection behavior for a complex 20-high Sendzimir cluster mill (shown earlier in Figure 30.6). Traditionally, this type of mill has been very difficult to model using the conventional strip-profile calculation methods discussed earlier in Table 30.1.

Dimensions of the strip and rolls for the 20-high mill example are shown in Table 30.7. The entry and exit thickness at the center of the strip are 0.9779 mm and 0.9063 mm, respectively, giving a 7.32% reduction. The strip width is 508 mm and the length of all rolls is 1270 mm. The roll diameters increase progressively from the work roll to the backing bearing rolls. Each backing bearing roll has six equally spaced bearings of 292.10-mm diameter, mounted on common solid shafts of 127.0-mm diameter. Parameters assigned to the 20-high mill model are shown in Table 30.8. The upper half of the 20-high mill is modeled using 252 Timoshenko beam elements and associated coupling foundations. A constant strip foundation modulus, $k(x) = 52{,}472$ N/mm^2, is assigned over the strip width, w, except that the same "strip edge"

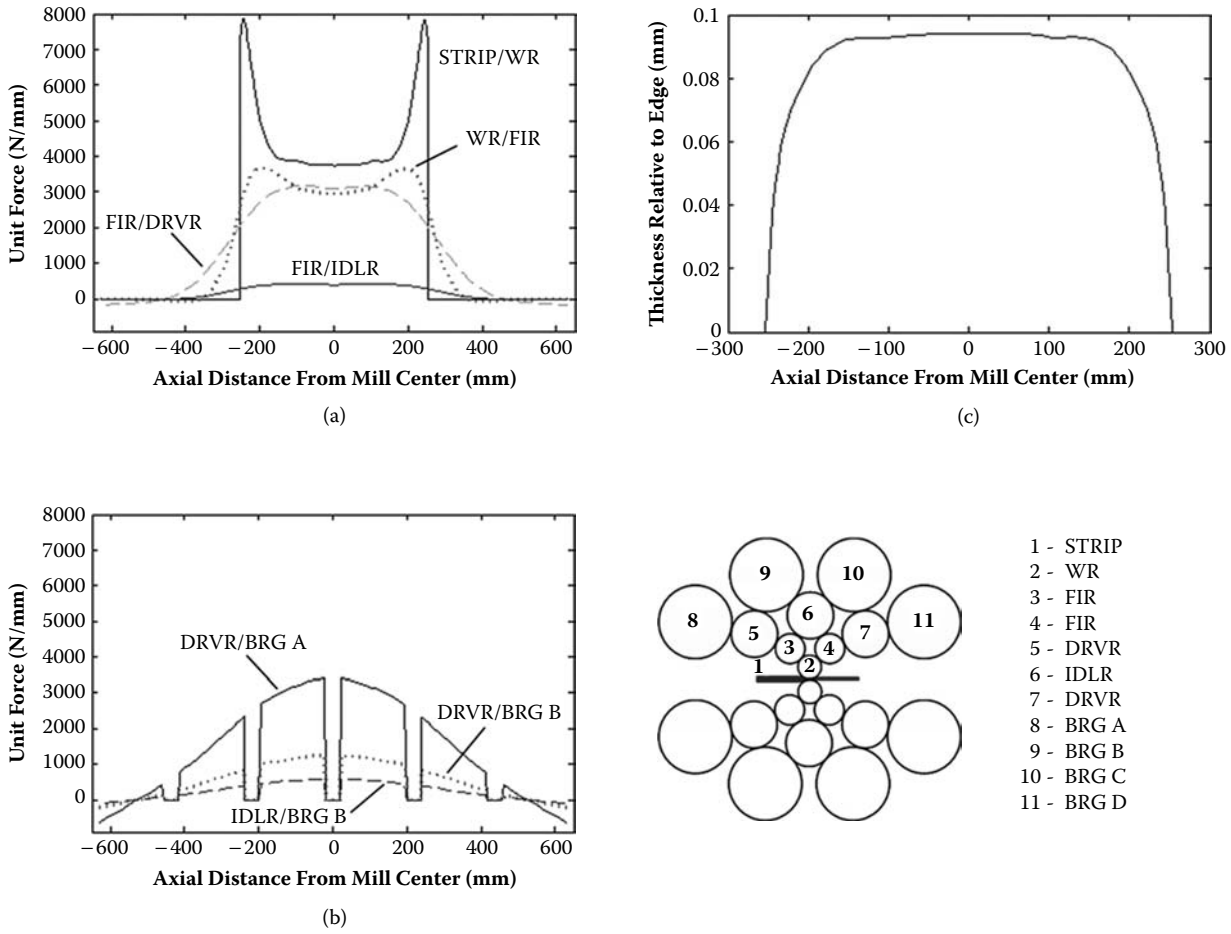


FIGURE 30.11 Twenty-high contact force distribution (a, b), and upper strip semithickness relative to edge (c). (Adapted from Malik, A. and Grandhi, R. 2008. *Journal of Materials Processing Technology* 206: 263–274.)

modification applied in the four-high example is also used here. To simulate the thickness reduction, a uniform vertical displacement boundary condition of 0.5588 mm is subjected to the lower nodes of the strip upper half section.

Figure 30.11a and b illustrate the results following simulation. Shown is the contact force distribution at the interface between the strip and the work roll, and between the other various rolls. As was observed for the four-high mill, in the absence of any strip-profile control devices, the contact force between the strip and the work roll increases in the vicinity of the strip edges, leading to a large "natural" strip crown. An interesting and useful characteristic of the 20-high mill is its ability to horizontally transfer much of the vertical roll-bite load. This is evidenced when comparing the general magnitude contact force between the second intermediate driver roll (DRVR) and backing bearings A and B, respectively (BRG A, BRG B).

Table 30.9 summarizes the results for the 20-high mill simulation. The *C*25 strip crown is 0.0605 mm, since the upper half thickness is 0.0302 mm greater at the strip center than at the *C*25 edge locations. This crown corresponds to 6.675% of the exit thickness at the strip center. Such a large strip crown is normally unacceptable, and must be reduced through the use of roll crowns (or tapers) and other profile control devices. Figure 30.11c illustrates the cross-sectional thickness of the upper half of the strip relative to that of the strip edge. The increased rigidity of the 20-high mill, in comparison to the four-high mill, causes it to "flatten" the natural strip-profile over a majority of the strip width, but significant edge-drop is present. The tendency to create such a large edge-drop leads most users of 20-high mills to

TABLE 30.9
Results for Application of Simplified Mixed Finite Element Method to 20-High Cluster Mill

20-High New Model Result	Value
Strip center thickness, h (mm)	0.9063
Strip $C25$ thickness, h_{c25} (mm)	0.8458
Strip crown, $C25$ (mm)	0.0605
Strip crown, $C25$ (%)	6.675
Total force, F (MN)	2.292

Source: Adapted from Malik, A. and Grandhi, R. 2008. *Journal of Materials Processing Technology* 206: 263–274.

decrease the diameters of the first intermediate rolls near their ends. Shifting of these tapered first intermediate rolls provides control of the force distribution near the strip edges, and hence increases control over the magnitude of edge-drop. Although not included in this example, the simplified mixed finite element method is capable of including the effects of shifting tapered rolls, in addition to the effects of roll bending mechanisms on 20-high mills.

30.6 SUMMARY

In this chapter, a brief review of conventional models for predicting and controlling strip profile and related flatness in hot and cold-rolling mills was provided. Introduced subsequently was a new simplified mixed finite element method, which has several advantages over traditional methods, including rapid calculation time, enhanced theoretical accuracy, and straightforward application to complex cluster-type rolling mills. While this new method still does not couple the elastic mill stand deflections with the plastic deformation of the strip, it provides an enhancement to the existing practical models designed to meet the requirements for online control applications.

ACKNOWLEDGMENTS

The National Science Foundation is acknowledged for supporting this work (Award No. 0758539).

REFERENCES

Bazoune, A. and Khulief, Y. A. 2003. Shape functions of three-dimensional Timoshenko beam element. *Journal of Sound and Vibration* 259: 473–480.

Chen, X. and Zhou, J. 1987. A specificalized finite element model for investigating controlling factors affecting behavior of rolls and strip flatness. *4th International Steel Rolling Conference*, E4.1–E4.7. Deauville, France.

Cook, R. D., et al. 2004. Finite elements in structural dynamics and vibrations. In *Concepts and Applications of Finite Element Analysis, 4th ed*, 373–451. New York: Wiley.

Eibe, W. W. 1984. Inflatable crown rolls—Characteristics, design and applications. *Iron and Steel Engineer* 61: 426–432.

Ginzburg, V. B. 1993. *High-Quality Steel-Rolling: Theory and Practice*. New York: Marcel Dekker.

Ginzburg, V. B. and Ballas, R. 2000. Strip profile and flatness analysis. In *Flat Rolling Fundamentals*, 685–701. New York: Marcel Dekker.

Guo, R. M. 1986. Computer model simulation of strip crown and shape control. *Iron and Steel Engineer* 63: 523–530.

Guo, R. M. 1990. Development of a mathematical model for strip thickness profile. *Iron and Steel Engineer* 67(9): 32–39.

Guo, R. M. and Malik, A. S. 2005. Development of a new crown/shape model for cluster mills. *Iron and Steel Technology* 2: 31–40.

Hattori, S., et al. 1992. Fuzzy control algorithm and neural networks for flatness control of a cold rolling process. *Hitachi Review* 41: 31–38.

Malik, A. and Grandhi, R. 2008. A computational method to predict strip profile in rolling mills. *Journal of Materials Processing Technology* 206: 263–274.

Malik, A. S. and Grandhi, R. V. 2007. Analytical method for use in optimizing dimensional quality in hot and cold rolling mills. U.S. Patent and Trademark Office, Application no. 11/686,381.

Poplawski, J. V., et al. 1980. Bethlehem's contribution to the mathematical modeling of cold rolling in tandem mills. *AISE Yearbook* 391–402.

Robert, W. L. 1978. Strip shape: Its measurement and control. In *Cold Rolling of Steel*, ed. G. Boothroyd and G. E. Dieter, 655–716. New York: Marcel Dekker.

Shohet, K. N. and Townsend, N. A. 1968. Roll bending methods of crown control in four-high plate mills. *Journal of the Iron and Steel Institute* November 1968, 1088–1098.

Stone, M. D. and Gray, R. 1965. Theory and practice aspects in crown control. *Iron and Steel Engineer* 42: 657–667.

31 Hot Band Profile Irregularities Related to Thermal Contour of Work Rolls*

Eugene Nikitenko

CONTENTS

31.1 Introduction 341
31.2 Roll Cooling Pattern 341
31.3 Improving Flatness and Crown Performance 342
31.4 Impact of Rolling Strip with Offset from Mill Centerline 344
31.5 Conclusions 346
References 347

31.1 INTRODUCTION

It is well known that the relative profile of the hot-rolled strip does not noticeably change after the cold reduction in a tandem mill. Moreover, as the strip gets thinner in the subsequent cold-rolling passes, any irregularities of the strip profile, such as buildup on both edges of the strip or a one-side edge buildup accompanied by a wedge condition, can cause local shape deterioration. Through simulations of the thermal conditions of the work rolls in the finishing stands of the hot strip mill, it has been established that the particular pattern of the roll cooling and the strip deviation from the mill centerline are among the root causes of the above-mentioned hot band profile irregularities. Experimental data have proved the findings.

31.2 ROLL COOLING PATTERN

Although specifics of the design of the work roll cooling headers in the finishing stands may vary from one hot-strip mill to another, there is a common feature among almost all mills. Specifically, the pattern of the cooling water flow applied to a work roll has a maximum in the middle section of the roll and tapers down toward the edges, as shown in Figure 31.1. In some cases, due to a particular mill condition, an opposite pattern is used with lower water flow in the middle than at the edges.

Even when the actual cooling pattern is nonuniform, the majority of the work roll thermal expansion models that are used for finishing mill setup assume that the heat transfer coefficient in cooling is constant along the roll length. At the same time, from comparing computer simulations of the conditions of uniform and nonuniform cooling during rolling the wide products, it becomes obvious that the work roll temperatures resulting from these two cases are noticeably different, as shown in Figure 31.2.

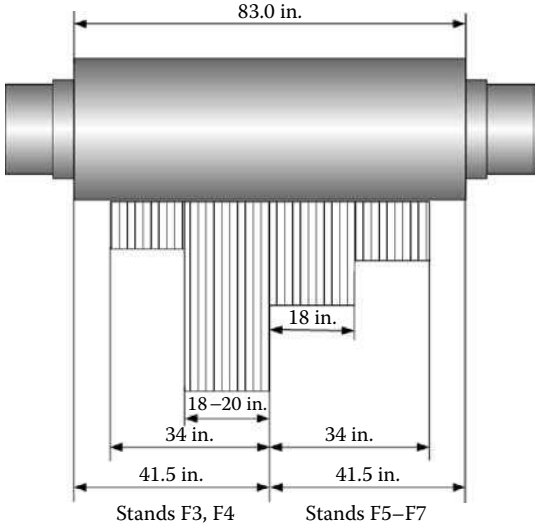


FIGURE 31.1 Cooling water flow pattern.

A characteristic feature of the roll temperature distribution along the roll length in the case of nonuniform cooling (see Figure 31.2), is the presence of two maxima located symmetrically between the centerline and edges. Such an appearance differs from what is usually measured at the end of the roll campaign after rolling narrow products, when a familiar bell-shape temperature pattern is detected.

* The material in this chapter is intended for general information only. Any use of this material in relation to any specific application should be based on independent examination and verification of its unrestricted availability for such use, and a determination of suitability for the application by professionally qualified personnel. No license under any United States Steel Corporation patents or other proprietary interest is implied by the publication of this chapter. Those making use of or relying upon the material assume all risks and liability arising from such use or reliance.

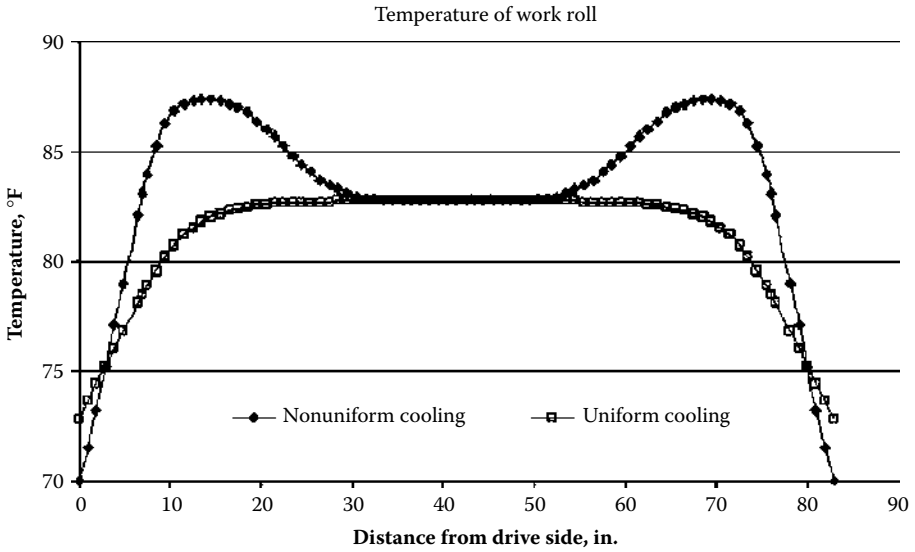


FIGURE 31.2 Comparison of roll temperature with uniform and nonuniform cooling.

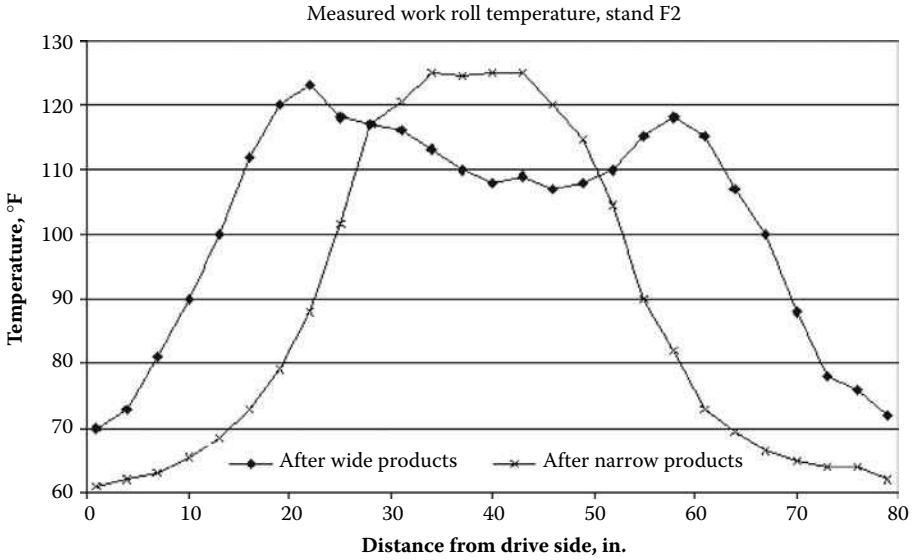


FIGURE 31.3 Work roll temperature after rolling wide and narrow products.

Nevertheless, measurements of the roll temperature taken after rolling wide products show the temperature distribution similar to the predicted, as presented in Figure 31.3.

The assumption of a constant heat-transfer coefficient in cooling, when the actual cooling water flow is applied nonuniformly, will have an adverse effect on accuracy of prediction of strip profile of wide products and will lead to producing wrong references for roll bending and shifting actuators. Figure 31.4 presents strip profiles computed for the conditions of uniform and nonuniform cooling of the work roll of the last finishing stand.

To verify the significance of cooling pattern influence on the strip profile and to validate the accuracy of the computations, a comparison was done of the predicted and measured strip profiles. In general, good agreement is observed, as shown in Figure 31.5. Higher variation of the measured thickness in the edge areas, within 4 in. from each side, is believed to be due to a greater local roll wear.

Now, when the degree of the impact of nonuniform cooling is evaluated and validated, the effect of roll cooling pattern can be taken into account to produce hot bands with minimal flatness imperfections and consistent crown.

31.3 IMPROVING FLATNESS AND CROWN PERFORMANCE

With the aid of a Shape and Crown Simulator [1–3], an analysis has been performed of one of the actual schedules of wide products rolled on an 80-in. hot-strip mill for the purpose of comparing the shape and the crown of the coils produced with uniform (simulated) and nonuniform (actual) roll cooling. The target crown of all coils was set at 0.002 in. in both

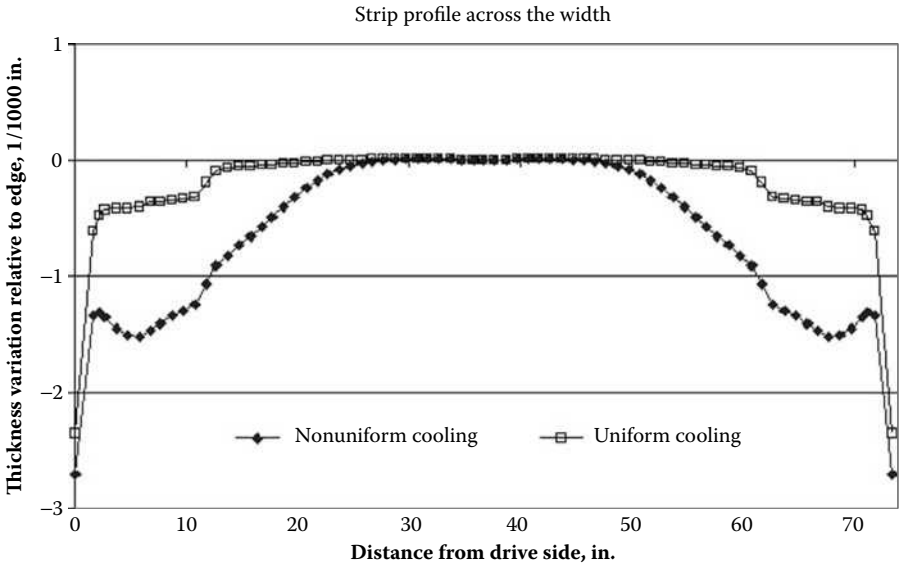


FIGURE 31.4 Strip profile with uniform and nonuniform roll cooling.

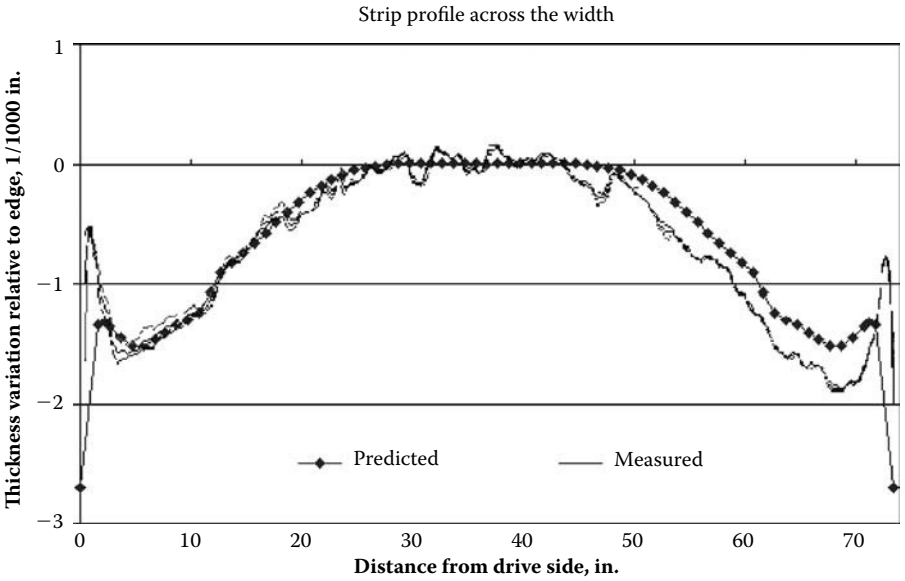


FIGURE 31.5 Comparison of computed and measured strip profiles.

cases. Coil number 1, 20, 80, and 100 were selected and compared. Because uniform cooling results in lower strip crown, as shown in Figure 31.2, the ground crowns of the work rolls in the case of uniform cooling were modified to meet the target. Optimized work roll bending was used in both cases.

The calculated transverse thickness profile of the selected coils is shown in Figure 31.6a and b. The benefit of using the uniform cooling pattern is obvious. Uniform cooling produces a desired profile of the hot bands without edge buildups. A comparison of the calculated strip crowns for all coils rolled in the schedule is shown in Figure 31.7. While the average crown increases from 1.87 thousands of an inch or mils (nonuniform) to 2.07 mils (uniform), the standard deviation of strip crown decreases from 0.727 mils (nonuniform) to 0.056 mils (uniform).

There is also the benefit of minimizing flatness imperfections. Figure 31.8 presents the strip flatness for all coils. Average flatness can be reduced from 69.2 to 11.0 I-units, while the standard deviation decreases from 31.2 to 12.9 I-units, by using uniform cooling in place of nonuniform cooling.

Another benefit of uniform cooling during rolling wide products is illustrated by Figure 31.9, which provides comparison of roll bending references in case of nonuniform (initial bending) and uniform (optimized bending) cooling. Though bending was optimized in both cases, lower bending

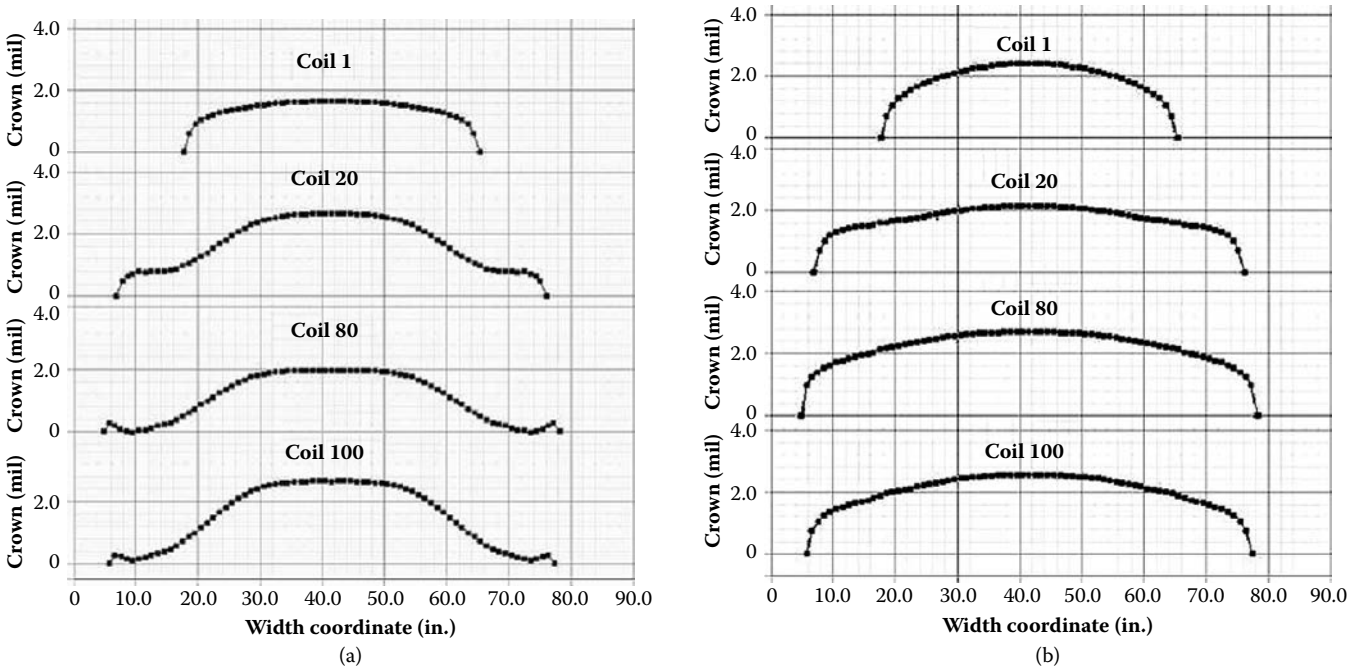


FIGURE 31.6 Transverse profile of coils rolled with nonuniform (a) and uniform (b) cooling.

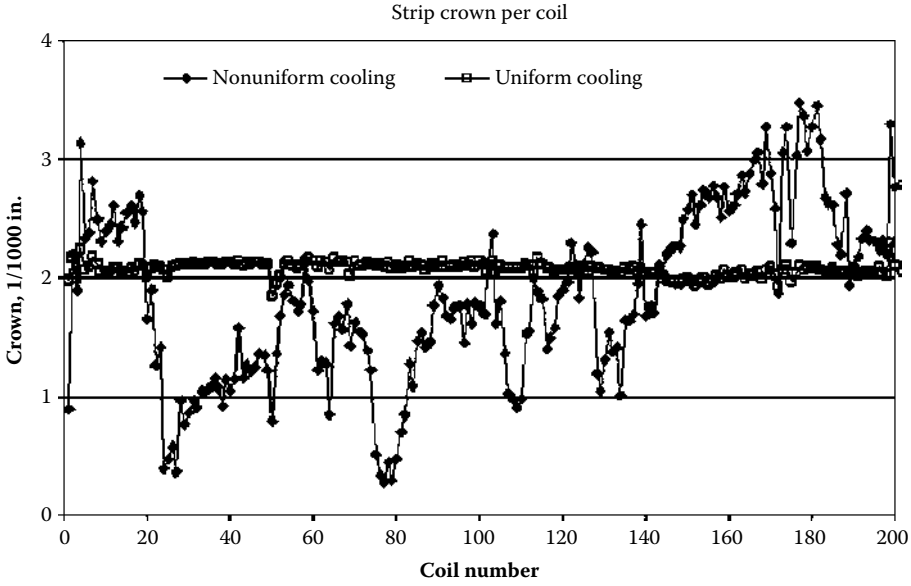


FIGURE 31.7 Strip crown for each coil rolled in the analyzed schedule.

is required with uniform cooling to produce the target crown while maintaining good shape.

31.4 IMPACT OF ROLLING STRIP WITH OFFSET FROM MILL CENTERLINE

One-side buildup with a wedge condition, as shown in Figure 31.10, is another irregularity of the hot band transverse profile, although it is not related to a cooling pattern but is still associated with the roll thermal profile.

Deviation of a bar being rolled in the finishing stands from the mill centerline is common for any hot strip mill, especially when rolling head and tail ends of the bar, where an offset in a range of 1–3 in. can be observed. To evaluate the effect that such a deviation could have on the strip profile, computer simulations were performed of rolling strip in the finishing stands with various offsets from the mill centerline.

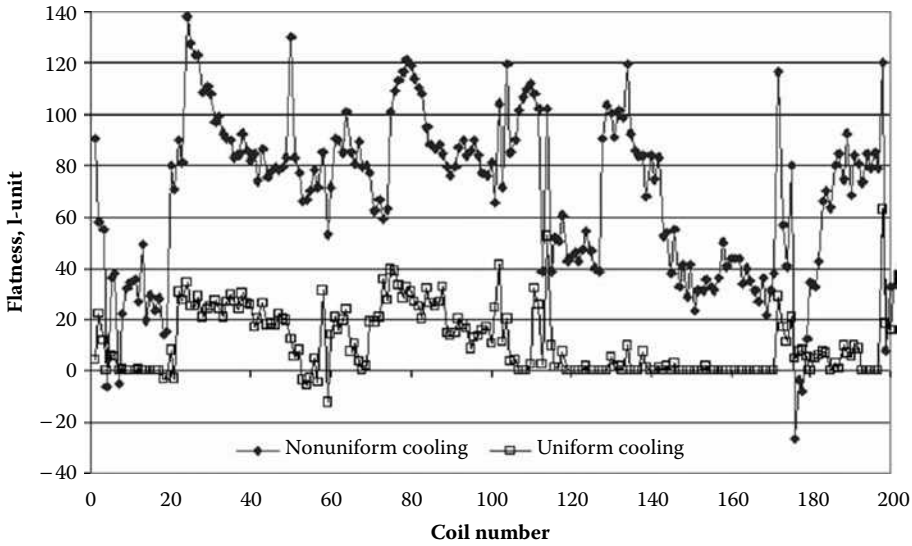


FIGURE 31.8 Strip flatness for each coil rolled in the analyzed schedule.

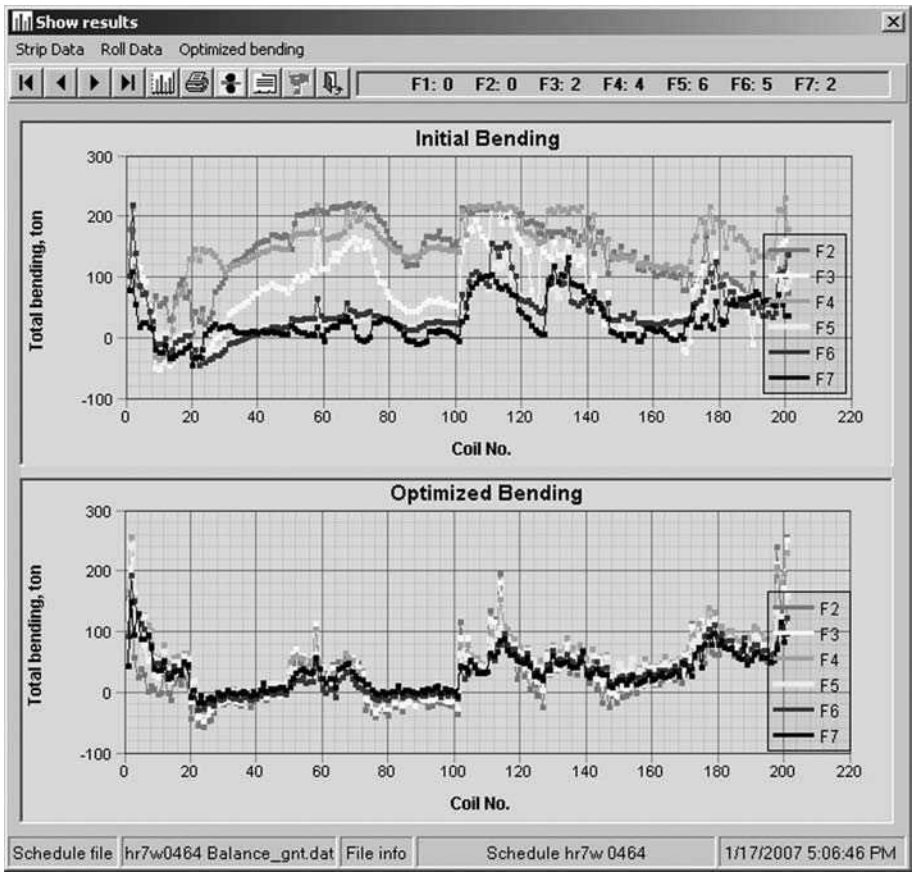


FIGURE 31.9 Optimized bending references for nonuniform (initial bending) and uniform (optimized bending) cooling.

Offsets varied from 0 to 5 in. toward the operator side (right). The results are shown in Figure 31.11. For comparison, all profiles were positioned on the graph symmetrically with respect to the strip centerline.

Simulations were conducted for the conditions when the work rolls had zero thermal crown as well as when a thermal crown was developed after rolling 20 bars. A simulation with cold rolls failed to produce a profile similar to that shown in

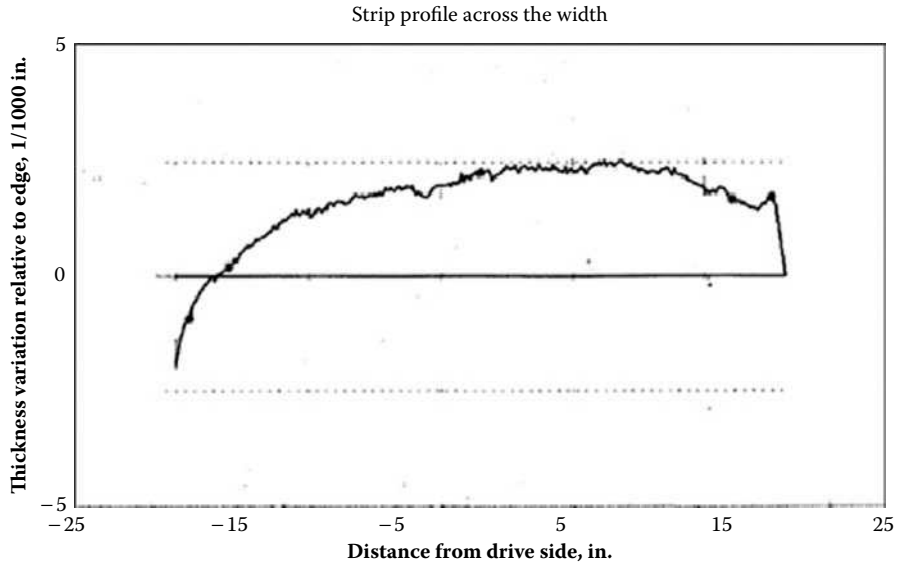


FIGURE 31.10 One-side buildup with wedge condition.

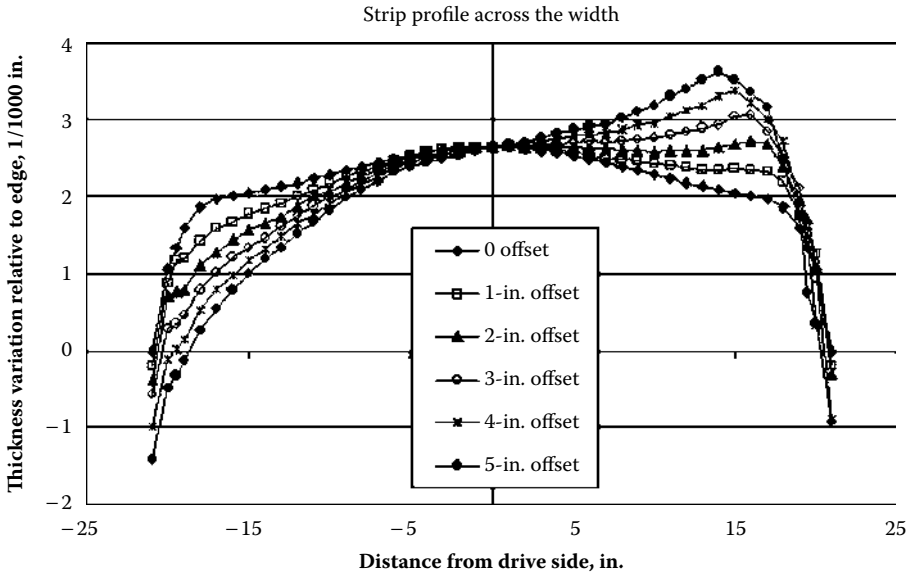


FIGURE 31.11 Change in strip profile when rolled with various offsets from mill centerline.

Figure 31.10. Conversely, a simulation with the rolls possessing a certain thermal crown showed that a deviation from the mill centerline in excess of 2 in. could result in an asymmetrical profile, similar to the actual strip profile pictured in Figure 31.10.

31.5 CONCLUSIONS

Uniform cooling of the work rolls in the finishing stands during rolling wide strip can significantly stabilize strip profile and improve flatness. While making the target crown, standard deviation of the strip crown from the target can be reduced more than 10 times. Average flatness can be reduced more than five times.

The analysis presented here should not lead the reader to the conclusion that uniform roll cooling is a universal solution for shape and crown improvement of all products of a hot strip mill. As a matter of fact, nonuniform cooling is required for rolling narrow products, especially while rolling with a very short time between bars in the finishing stands. The purpose of this chapter is to highlight the benefits of uniform cooling for rolling wide hot bands of the highest compliance of flatness and crown to the specifications of the customers. Ideally, the best configuration of the cooling header should

allow for selection between uniform and nonuniform cooling pattern depending on the products being rolled.

To minimize the occurrence of one-side buildup accompanied by a wedge condition, deviation of strip from the mill centerline should be kept within ±1 in.

REFERENCES

R. Somers, et al. Verification and applications of a model for predicting hot strip profile, crown and flatness. *Iron and Steel Engineer*, 1984, (9): 35–44.

E. Nikitenko. Changes made to date to RollSim, interface, thermal, and structural modules. U.S. Steel Internal Research Memorandum, July 2005.

E. Nikitenko. Updates to the WinRollSim interface, thermal, and structural modules. U.S. Steel Internal Research Memorandum, November 2007.

32 Analysis of the Transverse Temperature Distribution in the Hot Strip Mill of a Compact Strip Production Plant

Jie Zhang, Lili Tian, Paolo Patrizi, and Fabio Miani

CONTENTS

32.1 Hot-Rolled Strip Transverse Temperature Distribution: State of the Art 349
32.2 Experimental Setup 350
32.2.1 Experimental Devices 350
32.2.2 Measured Data 350
32.3 Experimental Results 351
32.3.1 Temperature Distribution in the Strip Central Area 352
32.3.2 Temperature Distribution in the Strip Edge Regions 352
32.3.3 The Relationship Between Transverse Temperature Distribution and Strip Width 352
32.3.4 The Relationship Between Transverse Temperature Distribution and Strip Temperature 353
32.4 Conclusion 353
References 353

32.1 HOT-ROLLED STRIP TRANSVERSE TEMPERATURE DISTRIBUTION: STATE OF THE ART

The current experimental research on the hot-rolled strip transverse temperature distribution is following two main paths: the numerical simulation of the problem and the measured data analysis.

Numerical simulation is mainly used to calculate the strip thermal field with the finite-element method (FEM) or the finite differences method (FDM), to predict how it affects the strip flatness, and thus the final strip quality [1–5]. By means of FEM, Sun et al. [5] got the strip temperature evolution at the surface and core, for a common hot-rolling process. Biggs [6] created a two-dimensional elastic finite element model to predict the different shapes of possible temperature distributions (parabolic, hyperbolic or curved and irregular) in relation with the strip camber. Zhou and Shen [7] built a 3D thermal-mechanical strip temperature distribution simulation model by using FDM, to describe simply how the rolling speed affects the strip edge temperature gradient.

Along with numerical simulations, the other way to investigate the problem is to use some experimental data, acquired with an infrared thermal vision system (or pyrometer), to get the strip surface transverse temperature distribution. The results obtained are subsequently used to set the temperature compensation needed to control the strip final quality [4]. This is what Biggs [6] and Sun [3] did in their work, where they use the temperature data measured at the inlet of the first stand of a finishing rolling mill as initial strip temperatures for their models.

Both the simulated and measured results are subsequently used for two main fields of research. The first is to understand the transverse temperature distribution characteristics and their evolution during the rolling process, usually by using numerical simulation methods: strip temperature changing from the reheat furnace to the roughing mill, from the last roughing stand to the first finishing stand, during the finishing process and from the last finishing stand to the coiler. The second group of investigations is based on the measured data to find out the reasons behind a specific temperature distribution.

The major findings of these studies can be summarized as follows:

1. During the whole rolling process, from the furnace to the coiler, the transverse temperature distribution is uniform in 4/5th of the strip width, while for the remaining strip surface we have a temperature variation around 100°C [5].
2. Before the first stand of the finishing mill, the strip superficial temperature peaks are approximately

positioned 100 mm from the edges, with the highest temperature negative gradient at the edges [2–5].
3. Out of the last finishing stand, the temperature distribution over the strip width is quite marked, with a difference from the center to the edge of approximately 70°C, and minimum at the edges [7, 8].
4. From the last finishing stand to the coiler, the maximum temperature difference over the strip width can be between 60°C and 80°C, generally with the center temperature higher than the edges [4].

Most of these results are obtained from numerical simulations and they are not verified by using production data because of the difficulties linked to transverse temperature measurement and the lack of effective measurement equipments mounted on the production facilities. Even when it is possible to have some measured data, they can differ quite a bit one from another, and this is still a big problem in the research and investigation of strip transverse temperature distribution.

As we said above, measured results of strip transverse temperature profiles are obtained mainly from infrared pyrometer [9] and infrared line-scanning systems mounted at the entry and exit of the finishing mill. Even if the measurement systems are not good enough to accomplish an online temperature control, the results can be used to verify the simulation results and subsequently to control the transverse temperature distribution.

32.2 EXPERIMENTAL SETUP

32.2.1 Experimental Devices

All the transverse strip temperature data were collected from a compact strip production (CSP) 1800-mm hot-strip rolling line by using a Radiometrie RM 312–Instantaneous Multi-Function Gauge measuring system. The measuring device was mounted at the finishing mill exit, in the position showed in Figure 32.1.

The measuring device is able to determinate, instantaneously and continuously, the strip transverse profile, thickness and temperature. By using noncontact line scanning pyrometers the radiometer can give the thermal profile for the whole strip width, as shown in Figure 32.2. The measuring system temperature working range is from 600°C to 1200°C, with an accuracy of ±5°C and a resolution of 0.5°C.

32.2.2 Measured Data

In the following, we will consider the data collected from the infrared line-scanning system installed at the finishing mill exit.

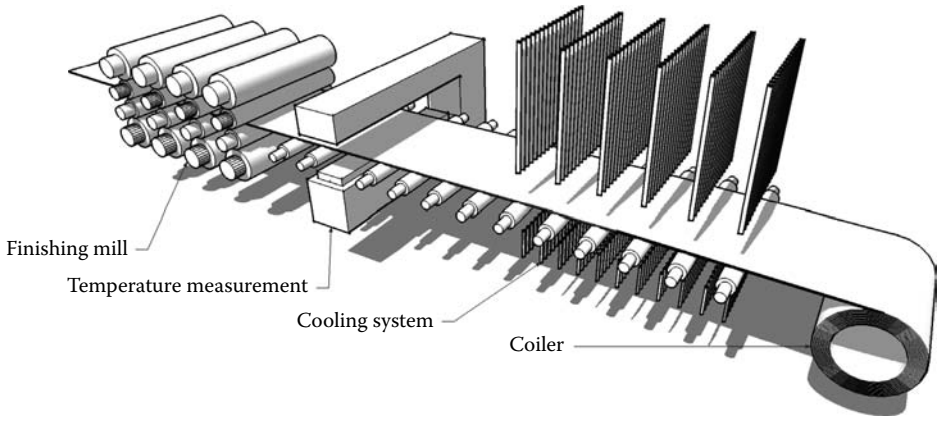


FIGURE 32.1 Location of temperature measurement.

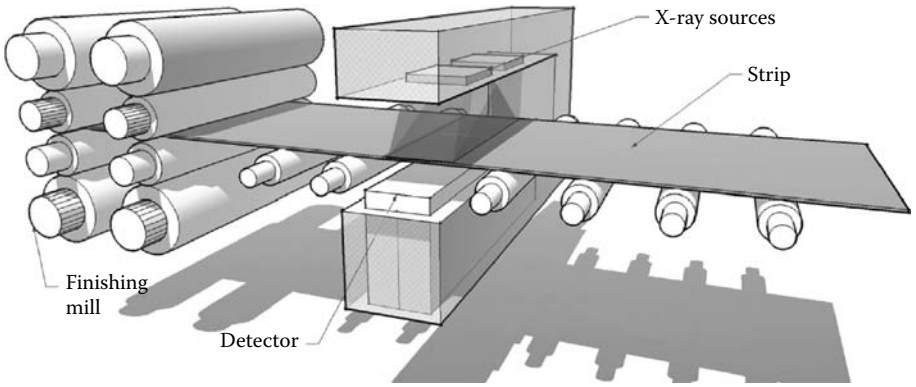


FIGURE 32.2 Scheme of line scanning system.

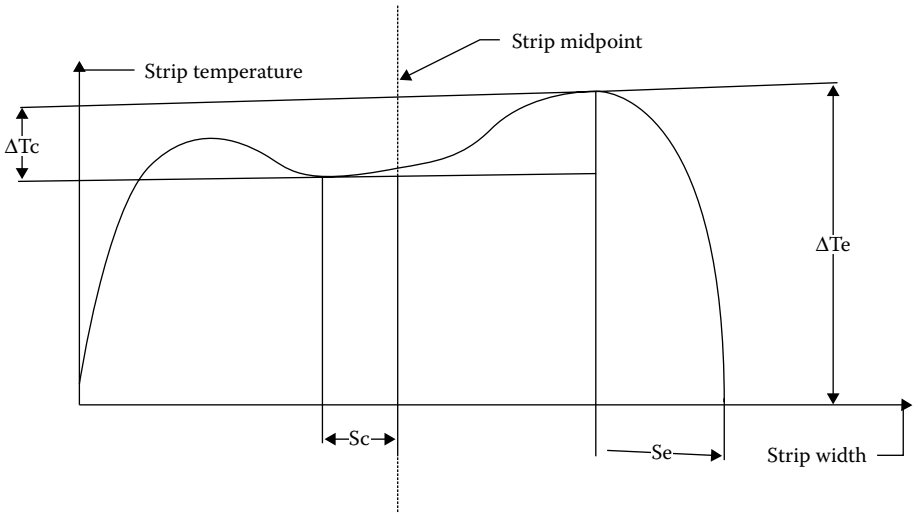


FIGURE 32.3 Strip transverse temperature distribution: main parameters.

To define the main features of the transverse temperature distribution, 228 pieces of strip were measured. Table 32.1 summarizes the characteristics of the measured strip.

TABLE 32. 1
Measured Strip Characteristics

Strip grade (GB standard)	SPHC-1, SS400-3
Strip thickness (mm)	From 1.5 to 7
Strip width (mm)	From 1023 to 1542
Strip temperature at finishing mill exit (°C)	From 846 to 923

Figure 32.3 shows the most typical temperature distribution over the strip surface, resulting from our experiments. It can be described as follows: an average temperature in the middle of the strip that reaches a maximum going from the center to the edge direction, and then there is a drop in temperature from this point to the corresponding edge.

In consideration of the measured data, our target is to identify the main factors influencing the strip temperature profile, to more clearly describe the strip thermal contour, and to deeper investigate the reason of uneven transverse temperature distributions.

After a thorough evaluation, we defined four new parameters that we used to classify each temperature measurement. These parameters are two temperature differences between two particular points on the strip surface, and two correspondent geometrical values to identify the position of these points on the strip. The group of parameters we propose here are

Se: distance from the maximum temperature point to the edge
ΔTe: difference between the maximum temperature and edge temperature
Sc: distance between the central minimum temperature point and the strip midpoint
ΔTc: difference between the maximum temperature and strip center lowest temperature

32.3 EXPERIMENTAL RESULTS

From an overall point of view the first differentiation of our experimental results can be made in consideration of the temperature distribution over the strip width. Three main temperature distributions had been defined:

1. Numerous peak points unevenly distributed over the strip width, as shown in Figure 32.4b
2. Two peak points close to the edges region, with a rough distribution of temperatures in the middle region, as shown in Figure 32.4c
3. Relative minimum of temperature in the middle, with a smooth temperature increase going in the edge direction up to the peak points, as shown in Figure 32.4d and e

To conclude this general evaluation of the experimental data obtained, we made some basic physical considerations. Every 1°C of temperature difference between two points of the strip, in transverse direction, leads to a difference in extension of 1.05×10^5 mm, which in flatness is equal to 1.05 IU. In terms of forces, we can accordingly say that the difference in internal stresses between the same two points on the strip surface is of 2.205 N/mm^2. When the stresses overcome a specific value, obviously defined for each type of steel grade, they result in waviness of the strip, and thus strip profile defects [10]. To overcome the occurrence of strip superficial defects, we must compensate them in consideration of the allowed flatness value.

On the basis of the new four parameters we defined above we finally classified more specifically the experimental data

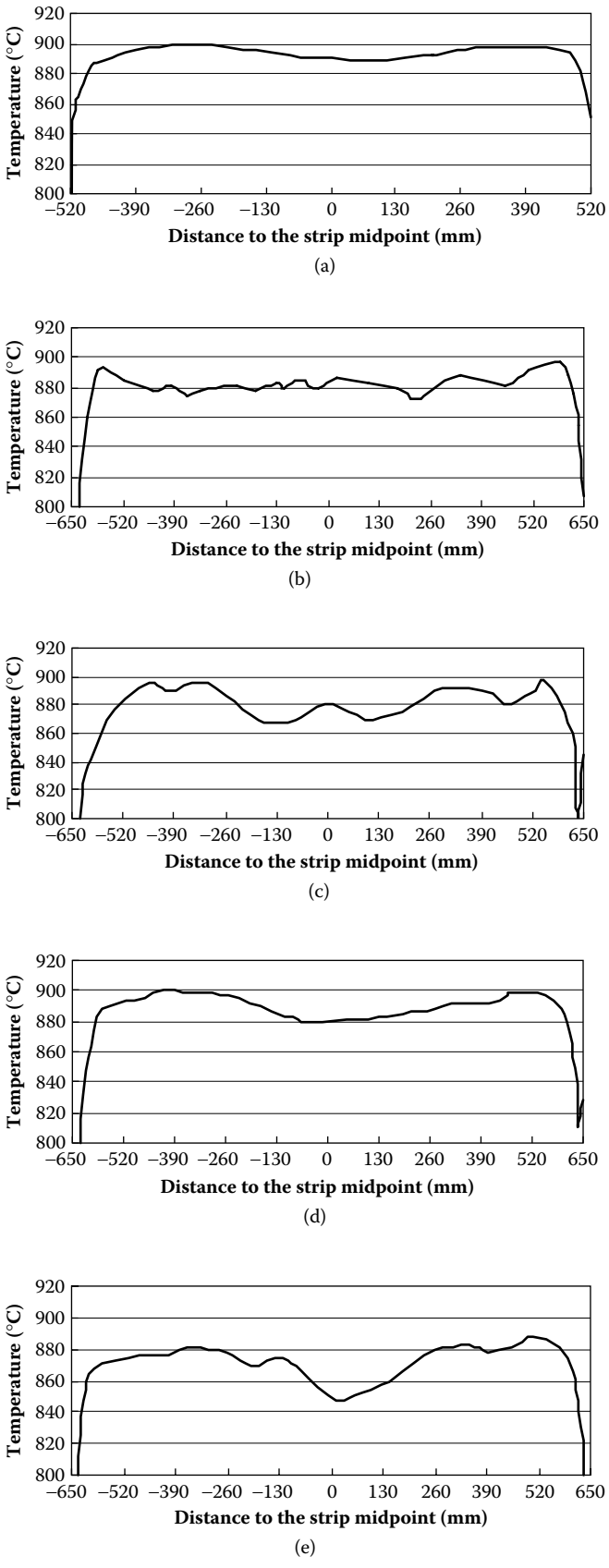


FIGURE 32.4 Curves of transverse temperature distribution.

measured on the 228 strip pieces. The results are described in Sections 32.3.1 through 32.3.3.

32.3.1 Temperature Distribution in the Strip Central Area

Considering the new parameters that we defined above, we first focus on the temperature distribution in the strip central area, which is linked to the values of ΔTc and Sc:

- ΔTc has a value between 5.2°C and 46.5°C.
- Sc has a value between 0 and 588.8 mm.
- Almost 58% of ΔTc values are around 20°C, as shown in Figure 32.4a.
- Nearly 42% of ΔTc values are above 20°C.

33.3.2 Temperature Distribution in the Strip Edge Regions

In the strip edge regions, it is possible to spot the highest drop in temperature, going from the peak points to the edge. In accordance with the parameters defined in this chapter, thus ΔTe and Se, we can summarize our data with the following observations:

- ΔTe has a value between 53°C and 130°C.
- Se has a value between 40 and 405.6 mm.
- For almost 79% of the measured strips, Se < 200 mm; thus most of the temperature drop occurs in the range of 200 mm from the strip edges.

More generally, we can state that only when the strip has a thickness between 2.5 and 3.5 mm, and a width between 1275 and 1525 mm, we can easily spot a peak point in the edge area (shown in Figure 32.4c), while the other temperature distributions can randomly appear for any other geometry among the ones considered in our experiment. After further analysis, there is no evident relationship between the Se and Sc and the strip geometrical details.

32.3.3 The Relationship Between Transverse Temperature Distribution and Strip Width

Starting from the data collected in our experimentation, we build a statistical analysis of the transverse strip average temperature variation appearing on a strip surface, expressed in Centigrade for the strips having the same thickness but different widths. The widths considered are 1035, 1285, and 1540 mm, and the results are shown in Figure 32.5. In the graph, it is easy to define the general trend of the data: the transverse temperature difference grows almost linearly with the increase in the strip width. In addition, it is possible to confirm that an increase of 200 mm in strip width leads to a temperature difference of roughly 7°C.

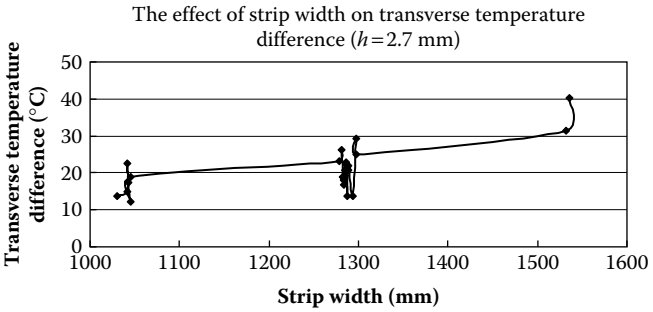


FIGURE 32.5 Strip transverse temperature differences for different strip widths (for a strip thickness of 2.7 mm).

32.3.4 The Relationship Between Transverse Temperature Distribution and Strip Temperature

Another interesting topic in our data analysis is to spot the transverse temperature average variation related to the average strip temperature, by considering a constant strip thickness. The results can be seen in Figure 32.6. From this graph, it is easy to understand that for higher strip temperatures the transverse average temperature variation gets smaller, as we should have expected.

As a further consideration, we want to point out how the cooling conditions have a considerably effect on the temperature distribution over the strip width. Since the strip surface temperature is almost uniform in the first rolling stands, the transverse temperature difference is linked to some subsequent steps of the process: the higher longitudinal cooling efficiency, the quantity of cooling water used the water flux relative speed, and the nozzle position. Consequently, the key point in controlling the strip transverse temperature distribution is to control the cooling efficiency over the strip width, thus controlling the cooling efficiency in the inter-stand cooling system.

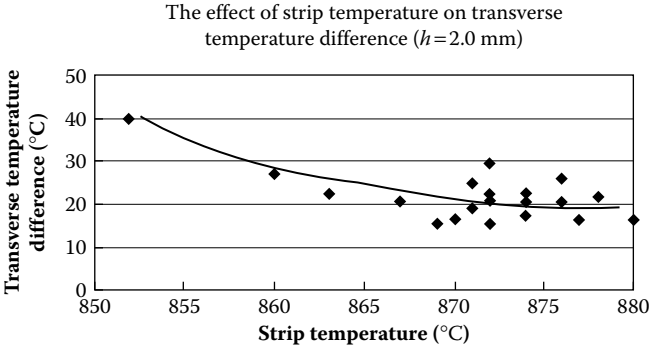


FIGURE 32.6 Strip average transverse temperature variations for different strip average temperatures.

32.4 CONCLUSION

In considering all the simulation methods and results presented in the literature about the issue of strip transverse temperature distribution, we found a large amount of different data. This uneven amount of results clearly shows the need to fit the simulation models with some real measurements, which unfortunately are still difficult to obtain because of measuring hardware limitations and measuring difficulties.

In this chapter, we present the transverse temperature distribution data collected for 238 pieces of strip, with different geometrical characteristics. To give an order to our data, we isolated four main parameters—that we first introduce here—by which it is possible to describe the different transverse temperature distributions. By the combination of these parameters and by using statistical analysis methods, we found some relationship among transverse temperature distribution, strip width, and strip average temperature.

Despite the results presented, we acknowledge that much experimental work must still be undertaken. By defining these new parameters to describe the problem of strip transverse temperature distribution, we hope to suggest a logical and ordinate approach to the problem, to find a quick and efficient solution to understand and connect the large amounts of data.

REFERENCES

1. Japanese Association of Iron and Steel. 1990. *Theory and Practice of Strip Rolling.* Beijing: Railway Press of China.
2. Chen, S. and Y. Zhang. 2000. Influence of the edge heating on the flatness of hot rolled strip. *Shanghai Metals* 22: 28–31.
3. Sun, C.G. 2002. Prediction of three dimensional strip temperatures through the entire finishing mill in hot strip rolling by finite element method. *ISIJ International* 42: 629–635.
4. Sun, K., et al. 2004. Compensating tactics of flatness control for hot strip mills. *Journal of University of Science and Technology Beijing* 26: 545–547, 559.
5. Sun, W., G. Wang, and G. Wu. 1994. Analysis of temperature field on transverse section of piece in the process of rolling hot strip. *Shandong Yejin* 16: 30–35.
6. Biggs, D.L. 1998. Finite element modeling of camber development during hot rolling of strip steel. *Ironmaking & Steelmaking* 25: 81–89.
7. Zhou, J. and B. Shen. 2003. Numerical simulation on temperature field of hot strip in finish rolling process. *Journal of Iron and Steel Research* 15: 14–18.
8. Shen, B., J. Zhou, and Z. Han. 2003. Progress in numerical simulation on temperature field of hot rolling strip. *Research on Iron and Steel* 31: 48–51.
9. Devadas, C. 1986. Heat transfer during hot rolling of steel strip. *Ironmaking & Steelmaking* 13: 311–321.
10. Qi, X., J. Li, and J. Lian. 2005. Influence of hot strip local hardness on cold strip shape. *Iron & Steel* 40: 40–43.

33 Innovations in Shape Measurement and Control for Cold-Rolled Flat Strip Products

Mark E. Zipf

CONTENTS

33.1 Introduction 355
33.2 Innovations in Shape Measurement Technologies 358
33.2.1 Noncontact Shape Measurement 358
33.2.2 Seamless Roll Technologies 359
33.3 New Methods in Mill Modeling and Simulation 360
33.4 Advancements in Shape Control Technologies 362
33.4.1 Singular Value Decomposition Method 363
33.4.2 Model Predictive Control Methods 364
33.5 Conclusion 364
References 365

33.1 INTRODUCTION

The fundamental objective of online shape measurement and closed-loop control is to provide a rolled product whose resulting flatness adheres to the specified geometric tolerances when relaxed (off-line, nontensioned, and at ambient temperature).* Flatness is a descriptive indication characterizing the nature and extent of the strip's manifest geometric departure from a reference plane. These manifest departures are the direct result of the relaxed strip finding an equilibrium condition of its rolled-in, internal stress patterns, by deflecting out of plane, in localized regions whose transverse differential strain-induced compressive stresses exceed the material's buckling threshold. Latent (hidden) stresses may be present in relaxed, "still water flat" strip, but their couplings to adjacent components of the parent strip constrain, distribute, and diffuse these stress patterns to amplitudes that do not induce visually apparent buckles or other geometric/flatness distortions. However, these stored latent stress patterns may become exposed and form manifest distortions if the parent strip is later slit, punched, sheared, cut, etc., allowing a decoupling of the internal stress patterns from their former diffusing, adjacent constraints.

The key to achieving flatness in cold-rolled strip products is the correction, control and progression of the strip's internal stress patterns during tensioned, multipass rolling activities.

The control and achievement of strip flatness is a multifaceted problem, involving complex machine setup, measurement and control, along with the inclusion of a certain element of human experience and intuition. The underlying physics, technologies and operational practices associated with online, active measurement and multivariable closed-loop control of strip shape are well understood and are now a common fixture in the industry. Figure 33.1 provides a block diagram illustration of this process.

The required resulting flatness is dependent on the planned application of the rolled material [1,2]. For certain products (e.g., ultralight gauge and foil class high-strength materials) it may be desirable to induce narrow, manifest over-rolled edges (i.e., pie crust edge waves) to avoid edge crack–induced strip breaks while rolling. Other products may require subtly over-rolled centers with tight edges, to assist strip tracking in downstream processes. Some applications may require the slit segments of the resulting strip be as flat as possible.

* The terms "shape" and "flatness" are often used in an arbitrary or interchangeable manner, and there are no universally accepted definitions. For the purposes of this discussion, the following terms will adhere:
Shape—The transverse distribution of differential strain/elongation induced stress within the material with respect to the material's average/nominal applied stress. This terminology implies a tensioned condition and is inherently bipolar, accounting for regions looser/longer and tighter/shorter than the nominal strip condition.
Flatness—The geometric departure of the strip from a reference plane. These distortions are associated with internal differential strain/elongation-based stress patterns that exceed the material's buckling threshold, and obtain a lower potential stress equilibrium by manifesting out of the reference plane.

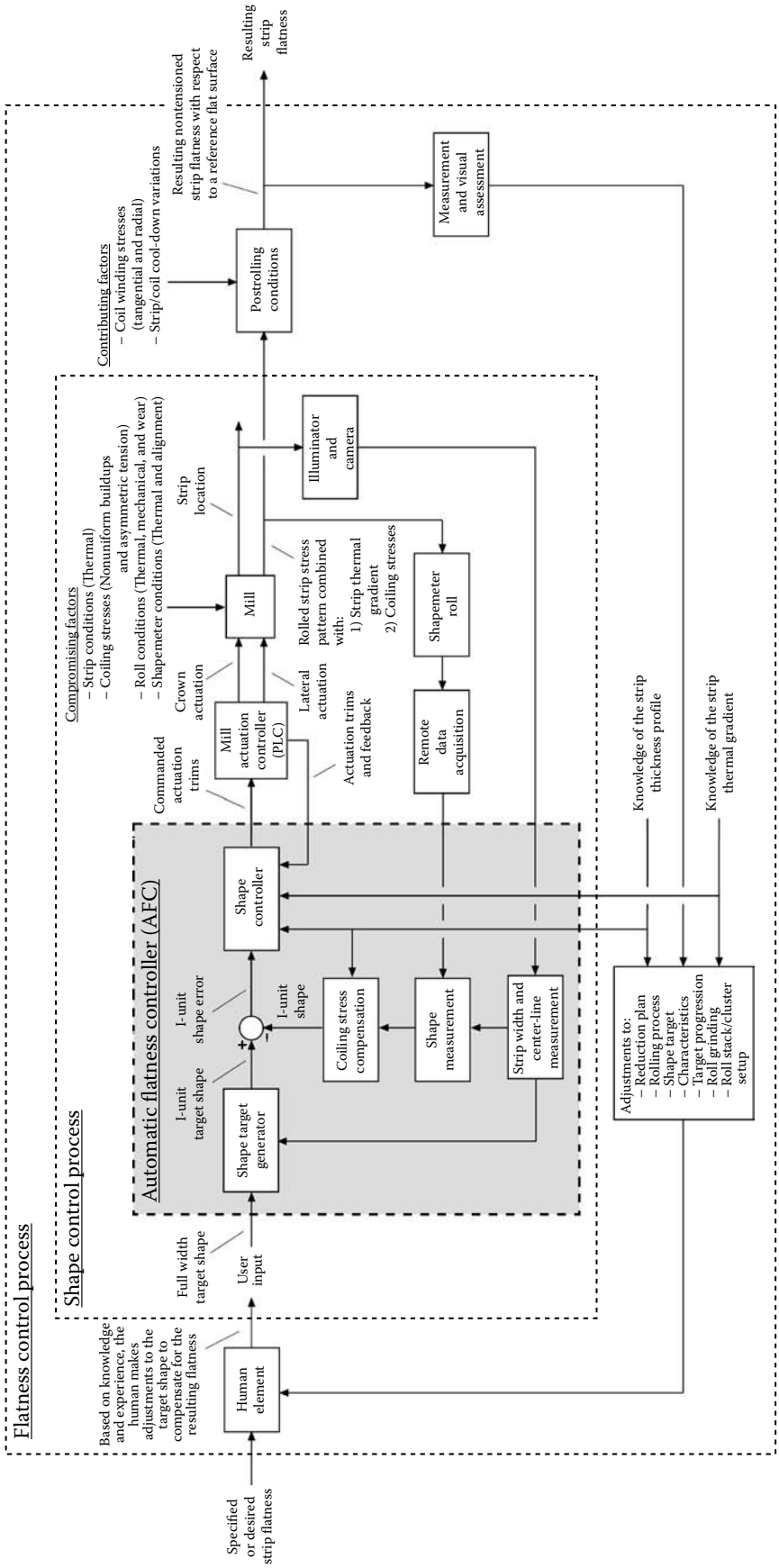


FIGURE 33.1 Block diagram illustration of the overall strip shape/flatness control problem.

The online shape control problem becomes one of consciously rolling-in specific transverse stress patterns whose presence will induce the necessary equilibrium conditions in the cooled, relaxed end product. The desired, rolled-in transverse stress pattern is often described by a target function. The shape control system coordinates and adjusts the available mill actuators to induce a transverse pressure distribution within the roll bite that causes the online, measured stress pattern in the existing strip to approach that of the target function.

Online shape measurement resolves the transverse differential strain and/or stress distribution(s) within the rolled/exiting strip. It involves directly measuring the rolled strip's transverse tension distribution with a shapemetering device. Depending on the precision of the mill and process requirements, it may be necessary to also measure the strip's instantaneous width and center-line to have an understanding of the strip's physical relation to the shapemeter sensing array and the mill's mechanical geometry. Compensations are then applied for strip thickness and thermal profiles, applied tension distribution, coiling behavior, strip width and transport center-line, shapemeter thermal influences, mechanical misalignments, adjacent roll crowns and deflections, oil film buildups, etc.

The selection of the target function and its pass-to-pass progression is a complex black art that must be coordinated and compromised with a number of competing concerns, including the ground roll profiles and wear behavior, vertical stack/cluster setup, pass schedule, material characteristics and thickness profile, desired rolling conditions, thermal characteristics of the mill and strip, nature of the coiling and applied transverse tension distribution, desired flatness, the envelope of the mill's shape adjustment actuation capabilities, and many, many more.

In reversing mill applications, during early, heavy gauge passes, it may be desirable to adjust the target to provide short/tight edges to promote good tracking and coil buildup. During intermediate passes, it may be desirable to progress the target function to provide a more uniform/flat stress distribution. While during later, light gauge passes it may be desirable to have the target provide a slightly full center (for downstream process strip-tracking assistance), with narrow long/loose edges to avoid applying strip tension to potentially edge cracked regions. The exact, pass-by-pass shape and progression of the target function is dependent on the mill, the material, the nature and extent of the reduction plan, and the needs of the rolling operations, and downstream processes.

Although a mature subject matter, the methods and equipment involved in shape/flatness measurement and control are not without a need for refinement and improvement. Modern shape/flatness tolerances and material surface quality requirements (e.g., bright-annealed stainless steel) have reached unprecedented levels of tightness. Many of the existing and contemporary systems are no longer able to reliably obtain the necessary performance and quality levels.

Recent innovations and developments have overcome the fundamental difficulties inherent to past states of the art. These can be consolidated into the following three categories of interest:

1. Shape Measurement
   - Noncontact Techniques—A novel method for measuring the strip's tension distribution using a cyclic, noncontacting, deflecting force (induced by a modulating vacuum) and eddy current–based strip deflection measurement transducers [3] now offers complete freedom from surface quality concerns associated with sensors directly in contact with the moving strip.
   - Seamless Contact Rolls—Long-established methods of roll contact sensing, involving zonal rings and/or transducers embedded in the roll surfaces, have a history of imparting characteristic surface defects (scratches, indentations and markings), leading to aesthetic quality issues. New incarnations of these approaches [4,5] employ hardened, seamless sleeve and coating technologies to eliminate surface defect concerns.

2. Mill Modeling and Simulation
   - Advanced Mill Modeling Techniques—New methods of roll stack/cluster and shape control actuation modeling [6–8] provide improved prediction capabilities over wider ranges of mill configurations, setups, and operating conditions. Certain techniques [7,8] offer full three-dimensional analytic descriptions of the roll stack/cluster interactions and deflections (especially in multiroll cluster configurations), offering new insight into the mill's envelope of shape actuation capabilities, the impact of ground roll profiles, reductions plans, etc., while also offering improved internal models for multivariable control systems.
   - Fully Coupled Pass Scheduling and Shape Targeting—Traditionally, the practices of pass scheduling and shape targeting have taken separate and often competing paths, when in fact, they are inherently coupled and interdependent. The above-mentioned, three-dimensional analytic models offer the ability to optimize pass scheduled reduction plans and separating force/tension calculations with an understanding of the expected mill setups and transverse deformations. In addition, desired shape targeting progressions and nominal conditions on shape actuators can be directly involved in the constraining of the scheduled passes and resulting mill deformation conditions.

3. Shape Control
   - Advanced Multivariable Control Techniques—Multivariable control methods [9–18] are uniquely suited for accommodating the nonlinear, highly

coupled interactions between the shape actuators, mill components, and strip behavior. These techniques offer improved closed-loop shape control performance, enhanced stability, and actuator coordination by employing internal models of the mill/material interactions and associated mill deformations (i.e., spatial sensitivity influence functions) to determine the appropriate (often optimal) actuation adjustments.

This chapter is divided into four sections. Section 33.2 discusses the advances in shape measurement techniques. Section 33.3 addresses new applications of multivariable shape control methods. Section 33.4 considers advances in analytical modeling of the mill, material, and roll stack/cluster interactions and deformations. Section 33.5 concludes with some insights into current aspects of research and development in these fields.

33.2 INNOVATIONS IN SHAPE MEASUREMENT TECHNOLOGIES

Accurate online shape measurement is a critical component of the overall shape/flatness control problem. Through the years, a great many methods and technologies have been considered and implemented [19–22].

Most methods measure the strip's shape through a direct measure of the transverse tension and related (strip profile dependent) stress distribution, then determine the transverse strain distribution and associated shape. Localized/zonal strip tension measurements are taken by individual sensing elements (typically 25–125 mm in width) arranged in transverse arrays. A large number of sensing technologies have been applied [19–21] and until recently, all involved a means of direct contact with the strip, employing elements ranging from independent zonal rings to sensors embedded in the roll surfaces to linear displacement transducers, employing sensing technologies extending from pneumatic pressure differentials to embedded strain gauges/load cells to piezoelectric methods. Depending on its sophistication, the shape measurement system may take into account and compensate for a number of compromising issues: strip profile asymmetries, coil geometry (crowned, coned, etc.), strip offset from the mill center-line, roll/strip temperature gradients, nonuniform tension application, diagonal stresses, roll misalignment, etc.

Other methods directly measure the strip's flatness from direct observation of manifesting/buckling departures from the plane of an ideal flat strip [23–26]. These later (flatness related) methods measure only those shape defects whose localized stress amplitudes are great enough to manifest in the presence of an applied tension. Although new and innovative, we will not consider these direct flatness measurement methods since they do not provide important insight into the strip's internal stress patterns.

33.2.1 Noncontact Shape Measurement

The most interesting and innovative advancement has come in the area of noncontact shape measurement with the introduction of the Siemens SI-Flat system [3]. Figure 33.2 provides a diagram illustrating the basic sensing system components and organization.

The shape measurement component of the system is relatively compact and consists of a horizontal plate (170 mm wide) mounted beneath the strip (~1–6 mm below pass-line), typically local to a deflector (billy) roll. The horizontal plate contains an array of uniformly distributed vacuum apertures through which the suction force is applied to the strip and an array of eddy current induction distance measuring sensors (typically spaced 30–60 mm on center). The sensors generate

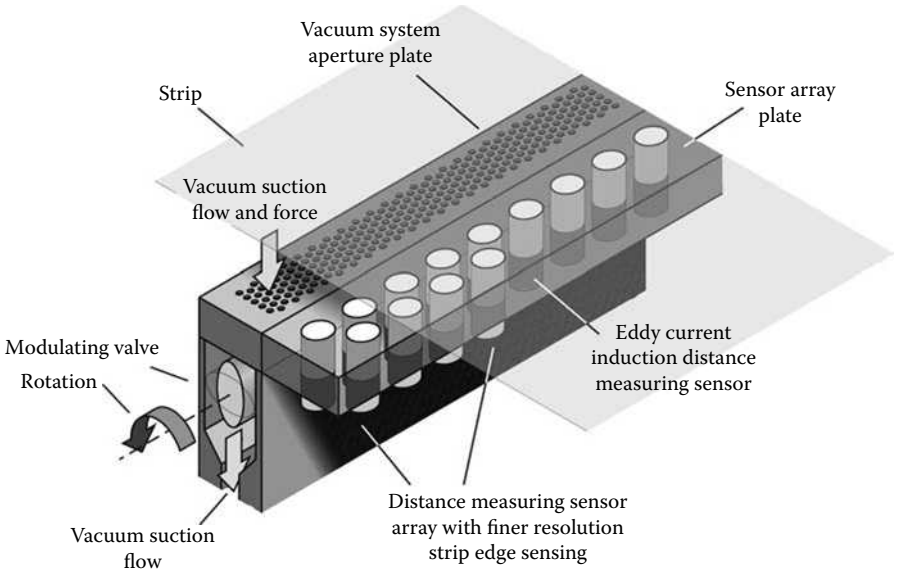


FIGURE 33.2 Illustration of the shape measurement components involved in the Siemens SI-Flat noncontact strip-shape measurement system.

an electromagnetic field, which interacts with the conductive strip-inducing eddy currents and forms a circuit whose impedance changes in proportion to the separation between the sensor and strip. The controlled nominal suction force is provided by an external vacuum and pressure regulating system. A rotating modulating valve resides beneath the vacuum aperture plate, providing a known, cyclic suction force (~2.5–7.5 Hz) uniformly across the strip width.

The strip's transverse tension distribution is measured by observing the amplitude of zonal strip displacement (typically, 100–200 μm) induced by the known, calibrated, modulating suction force applied across the strip. As shown in Figure 33.3, the suction force causes the strip to deflect downward from the pass line.

A transverse array of distance measuring sensors provide zonal measurements of the amplitude of the deflections across the strip width. Signal conditioning, signal processing, and fast Fourier transform techniques [27] are applied to extract the underlying deflection displacements from the modulating vacuum excitation, in a manner similar to lock-in amplification [28,29]. The relative degree of measured zonal deflection, as a function of the calibrated suction force, is an indication of localized tension deviations about the nominal strip tension. Collectively, these zonal indications form the transverse tension distribution. From a knowledge of the strip alloy, gauge, and profile, the stress distribution is formed and subsequently the measured strip shape.

The eddy current sensors also offer the ability to judge the location of the strip edges, providing the ability to accommodate partially covered edge zones and strip tracking off centerline. Finer shape measurements local to the strip edges are provided by a smaller, secondary arrays of offset sensors, as shown in Figure 33.2, or by more tightly spacing the sensors.

The innovative, noncontact Siemens SI-Flat shape measurement system is truly a creative departure from the well-established, traditional methods involving direct contact with the strip. By its very nature, there is no means of imparting strip surface damage, a long-endured problem associated with contact rolls employing zonal ring or surface-embedded sensors, in surface critical products (i.e., bright annealed stainless steels, etc.). Further, there is no need for an inertial helper motor and drive. The SI-Flat is inherently suited for light gauge products (<1 mm). The strength of the vacuum suction force ultimately limits the thickness of strip that can be measured (typically, no more than 4 mm).

33.2.2 Seamless Roll Technologies

Traditional methods of shape measurement have involved rolls in contact with the strip. Typically, these shapemeter rolls employed either sensors contained within ringed zonal segments or sensors embedded directly in the roll surface [19–21]. Both techniques provide direct, sound measure of the strip's tension distribution; unfortunately, minor imperfections in the zonal ring edge boundaries or in the sensor-cap-to-roll-surface interface often create patterned marks and abrasions of the strip surface. Surface marking in critical surface quality products cannot be tolerated.

Until recently, only the Siemens/Voest-Alpine/Clecim Planicim Roll [20,30] provided a truly seamless (nonmarking) contact roll surface with its displacement sensor mounted beneath a solid shell. Shape measurement industry vanguards, ABB and Andritz-Sunwig/BFI have now addressed concerns about the marking characteristics of their long-embraced product lines by developing seamless contract roll surface technologies of their own [4,5]. Figure 33.4 illustrates both of these new shapemeter arrangements.

As shown in Figure 33.4a, Andritz-Sundwig/BFI [5] has chosen to radically depart from its former sensor array distribution. Six transverse arrays of sandwiched piezoelectric sensors are embedded within full-width axial bores of the solid roll body, arranged at 60-degree intervals. The roll surface is then covered with a tungsten carbide coating. This arrangement provides six measurements per roll rotation, a notable improvement over the previously provided one measurement per rotation.

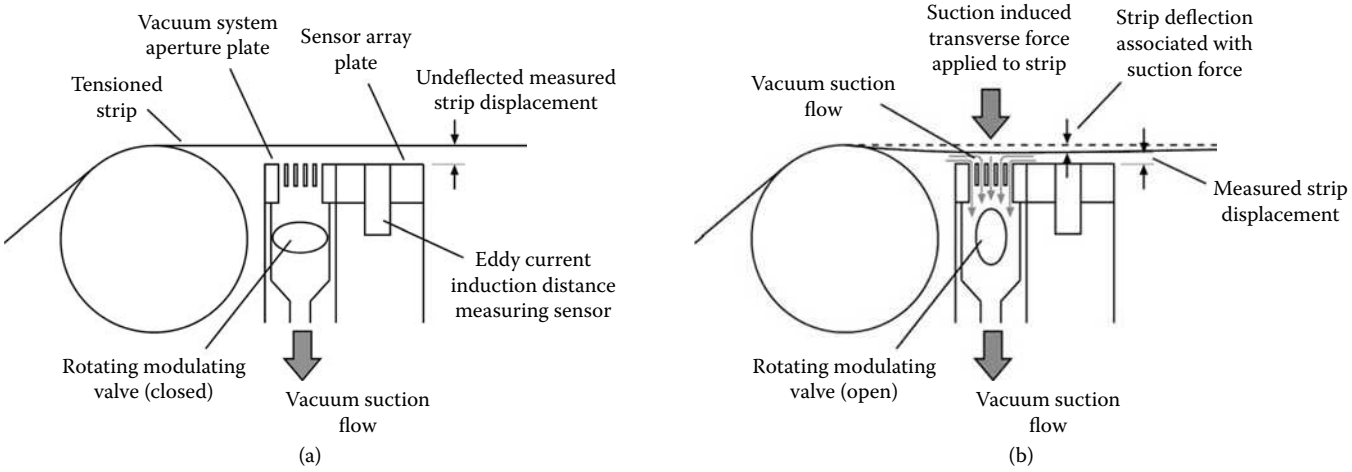


FIGURE 33.3 Cross-sectional illustration of the vacuum suction force inducement of strip deflections: (a) modulating valve rotated to a closed orientation suppressing the suction force; (b) modulating valve rotated to the full open orientation inducing maximum suction force and a measurable strip deflection.

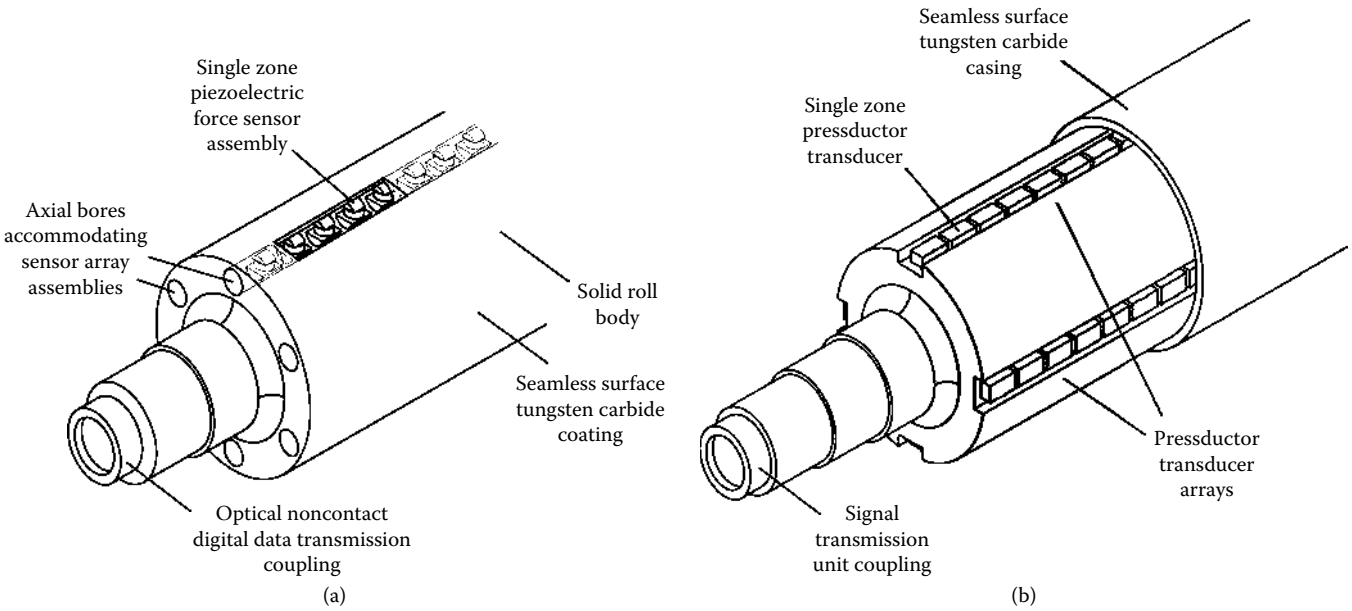


FIGURE 33.4 Illustrations of the physical arrangements of the new seamless roll technologies: (a) Andritz-Sundwig/BFI Shapemeter system; (b) ABB Stressometer system.

As shown in Figure 33.4b, ABB Automation has approached this issue by creating a completely new Stressometer roll architecture [4]. Four transverse arrays of Pressductor sensors are embedded within grooved recesses in the solid roll body, arranged at 90 degree intervals. The assembly is then sleeved with a thin, seamless tungsten carbide casing. This arrangement follows the historic four measurements per roll rotation, employed in the former ringed zonal segment Stressometer roll configuration [20].

Both of these new seamless contact roll technologies provide the needed smooth surface required in surface critical products (i.e., bright annealed stainless steels, etc.), while also providing a convenient means of upgrade for those possessing existing shape measurement equipment of the respective manufacturers.

33.3 NEW METHODS IN MILL MODELING AND SIMULATION

Cold-rolling mills adjust the strip's shape by coordinating their shape control actuators to provide changes in the transverse pressure distribution (across the roll gap) that modify the localized strip reductions/elongations, thereby altering the stress/strain patterns (and resulting shape/flatness) of the rolled strip. In changing the transverse pressure distribution, the roll stack/cluster physically reacts and deforms, influencing other regions of the roll-bite.

Each actuator induces a unique stress adjustment pattern on the strip's transverse stress distribution that can be characterized as a continuous spatial sensitivity influence function. From the ensuing equilibrium-finding roll stack/cluster reactive deformations, the geometry of the pattern is not localized to the vicinity of the actuator, but spans the strip width. This creates a highly coupled and potentially compromising interaction with the activities of the other actuators. The extent of the spatial frequencies of the influence functions are limited by the mechanical interactions within the roll stack/cluster (e.g., roll bending, flattening, multiple contact points, housing, etc.). To further complicate matters, these patterns change with strip width, yield stress, tension, incoming thickness, etc.

Multivariable control techniques [9–18] accommodate this form of nonlinear, highly coupled actuation behavior by employing analytical models of the mill actuators' responses in the determination of their control reactions. The models provide a description of the mill shape actuators' spatial sensitivity influence functions (in a transverse sense) evaluated at the point of shape measurement. Essentially, this is a multivariable mapping (possibly nonlinear and typically nonsquare) from the transverse actuator space to the transverse measurable shape space. Figure 33.5 illustrates the modeling of a Sendzimir mill (20-high cluster arrangement) employing As-U-Roll (AUR) top-crown eccentrics (B&C) and the tapered lateral first intermediate rolls. These same mathematical models offer predictive capabilities for applications to mill setup, roll grinding profile selection, evaluation of the mill's shape actuation capabilities envelope, shape target selection, pass scheduling, and diagnostic assistance in resolving complex shape control troubleshooting.

The key issues in model development and application are the classical compromises between model accuracy, complexity/sophistication, computational overhead requirements, and the range of model applicability/robustness. As model range and accuracy improve, model complexity and computational requirements increase, limiting the applicability to online shape control and rapid assessments of mill setups, schedules, roll grinding profiles, and achievable shape targets.

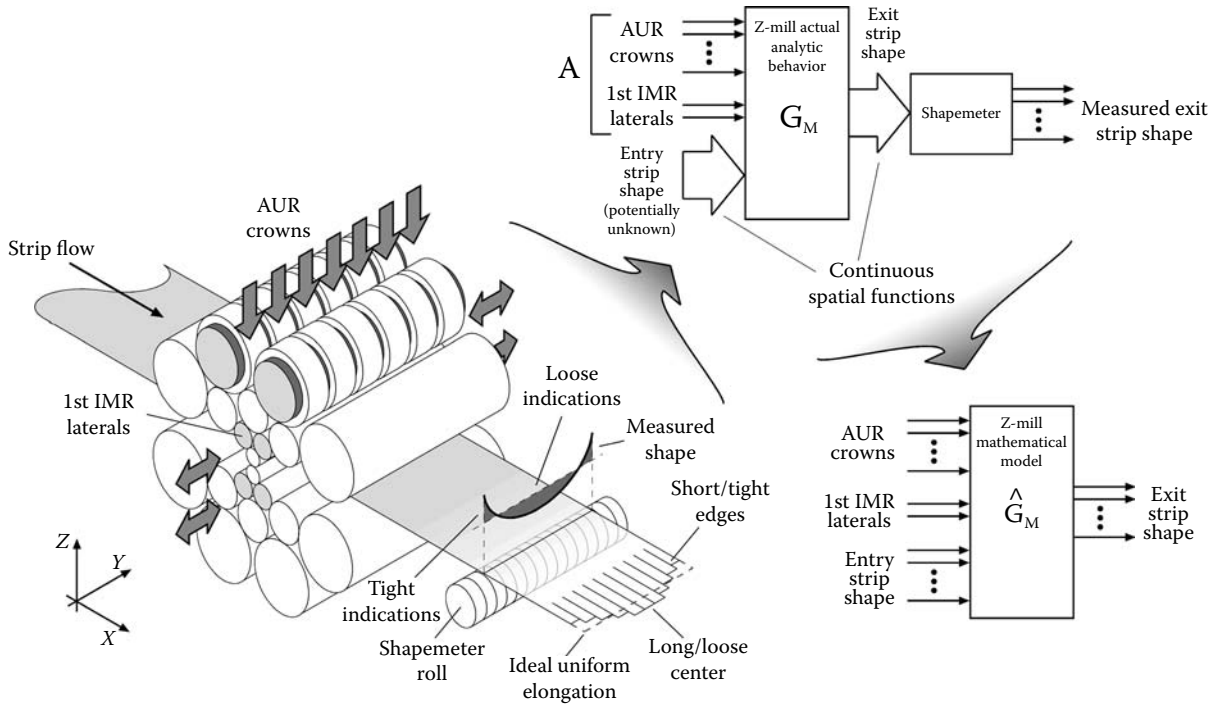


FIGURE 33.5 Illustration of the Sendzimir mill and its shape control actuators, along with the general form and structure of its characterization and modeling.

A wide variety of analytic and empirical/heuristic modeling methods has been developed and can be categorized as follows:

- Single-beam on elastic foundation method [31]
- Influence coefficient/point-match method [32,33]
- Transport matrix method [34,35]
- Empirical/pattern recognition/heuristics method [36,37]
- Large-scale finite element method [38,39]
- Combinational methods [7,8,40]

In many respects, the results of the analytic model developments are preferable (over the empirical/heuristic) since they inherently offer the ability to provide extrapolating predictions of mill/material performance and response characteristics when considering new/different product mixes, mill setups, schedules, and operating practices. The empirical/heuristic techniques are very quick and useful in direct, well-defined applications, but can/will provide suspect results when asked to predict outside their range of experience. The finite element methods are undoubtedly the most flexible and potentially accurate techniques, but they fundamentally suffer from extreme computational overhead and are not applicable to online/real-time shape control or mill setup and scheduling predictions/evaluations.

The analytic models typically originate from first principle physics and mechanics in combination with certain complexity reducing assumptions. Traditionally, these models are formulated along the transverse vertical plane (*YZ* plane of Figure 33.5) and employ simplifying assumptions and transformations to consolidate the contributions of the longitudinal components and influences (*X*-axis related) to resultants operating only in the *YZ* plane. In vertical stack configurations, these modeling techniques have shown satisfactory prediction properties. However, in clustered roll arrangements, these practices do not properly accommodate the true three-dimensional nature of the roll interactions and cluster deformations and their effects on the roll bite dynamics.

Further, the fundamental nature of the individual modeling principles and methodologies induce characteristic limitations and inaccuracies in the results. Models using single beam on elastic foundation methods employ a range of simplifying assumptions and therefore can only yield approximate results. Accuracy in influence coefficient/point-match and transport matrix methods is associated with sufficient continuity in their piecewise linear displacement fields requiring potentially large numbers of closely spaced nodes. The transport matrix approach also has problems representing the contact regions of the roll-on-roll and roll-on-strip interfaces, due to its use of discrete nodal springs as opposed to continuous elastic foundations. The discrete spring arrangement experiences certain problems in accommodating the discontinuities local to the component ends/edges [41].

The two-dimensional methods [42] have been shown to have adequate prediction properties in cluster mill models, about narrowly defined operating conditions and roll cluster setups, and are commonly used to obtain reduced order actuator influence/spatial sensitivity function descriptions suitable for the internal models of closed-loop shape/flatness controls of sufficient robustness. Unfortunately, these models do not

possess the necessary prediction capabilities to confidently assist in the determination of roll cluster setups during commissioning activities, the introduction of new product mixes, or the evaluation of difficult shape distortions.

Recently, new three-dimensional techniques have been introduced that offer enhanced accuracy and prediction capabilities from their considerations of the full three-dimensional contributions of the cluster's multiroll interactions.

Guo and Malik [6] extended off-line transport matrix descriptions of four-high mill setups to cluster mill configurations. The method considered the full three-dimensional characteristics of the mill's shape actuators and multiroll arrangement. The resulting model was complex, having a large number of rolls and contact regions. The convergence stability and computational overhead were prohibitive for consideration in online control application.

Malik [7] has developed a novel method of three-dimensional modeling that has direct applicability to multiroll cluster mill arrangements and complex roll geometries. The semianalytic technique couples the finite-element method (FEM) with classical solid mechanics to render a compact model, suitable for online consideration.

Mill component deflections are obtained through the formation of a linearized global stiffness system that is valid in the vicinity of the expected nominal loading conditions. This approach does not require knowledge of the force distribution at the work roll/strip interface in advance of the solution (similar to transport matrix techniques) and can accommodate any combination of distributed or concentrated loads, coincident nodal locations, and so on. Third-order displacement fields and the associated roll gap geometry result from the solution of the nodal displacements. Full, three-dimensional, high-resolution, finite-element analysis (FEA) was used to validate modeling results and assist in model refinement, through the evaluation of foundation moduli between rolls based on diameters, length, contact force, friction, and position along the roll.

This method offers the advantages of the continuity of elastic foundations, noniterative solution when using predetermined foundation moduli, continuous third-order displacement fields, simple stress-field determination, and a reasonable computational overhead. It is highly applicable to the determination of rolled strip thickness profiles (and associated strip shape/flatness), shape control internal models, shape target validation, roll profile selection and optimization, and pass schedule optimization.

A recent extension of this approach considers pass schedule/reduction planning optimization in cluster mill configurations [8]. This work focused on achieving a uniform, transverse reduction/elongation profile (i.e., no rolling imparted changes to strip shape/flatness) by maintaining a constant crown ratio between the entry and exit strips. Optimization of an existing pass schedule was based on the iterative adjustment of the pass-by-pass exit gauges to induce loaded roll cluster deformations (within the constraints of the available shape actuation capabilities) that achieve the desired strip crown ratio as a function of the complete three-dimensional roll cluster influences and restrictions (i.e., roll profiles, shape actuator conditions, etc.).

This is the first step toward the development of methods that simultaneously solve the coupled problems of pass scheduling, roll profiles, and cluster setup, and achievable shape target selection, as a single combined action in a full three-dimensional setting. This class of future model will provide unprecedented insight into the cluster's internal behavior and interaction. It will also provide an indication of the mill's shape control capabilities envelope, describing the transverse extent of the mill actuation–induced changes/adjustment in the exit strip shape, for a given situation, having direct application to specifying the achievable range of shape targets available for pass-by-pass shape target progressions.

33.4 ADVANCEMENTS IN SHAPE CONTROL TECHNOLOGIES

As shown in Figures 33.1 and 33.6, the objective of shape control is to achieve a rolled, exit strip transverse stress pattern/distribution that approaches a reference target shape by coordinating the activities of the available, mill configuration dependent shape control actuators.

This is a highly coupled, potentially nonsquare, multivariable control problem that has been approached in a variety of ways [9–22]. A number of popular methods involve internal model principles coupled with transformations to square, lower-dimensional curvatures spaces [9,10,43]. The typically nonsquare internal model transforms (maps) shape actuator inputs (in actuator space) to predicted perturbations in the transverse measured shape (in shape space—typically of higher dimension). It consists of a collection of the individual shape actuators' spatial sensitivity influence functions having potentially high-order spatial frequency content.

Essentially, the problem becomes one of obtaining a pseudo-inverse of the nonsquare internal model that will map shape errors to corrective trims to be applied through the shape actuation. Unfortunately, the model's rank deficient, nonsquare architecture precludes inversion, and direct applications of Moore–Penrose techniques offer no means of imposing controls design priorities.

Alternatively, it is possible to represent the mill/actuator model and transverse differential error between target and measured shape as spectral content in a lower-dimensional curvature space [9,11]. The transformation to curvature space typically involves projections via orthogonal polynomials, Fourier or eigenstructure methods, that result in a square, invertible pseudo-model. The lower-dimensional, finite order of the curvature space limits the extent of spatial frequency content that can be represented or considered. All loop-closing control determination actions are carried out within the curvature space (via a chosen loop closing methodology), resulting in the spectral content of the actuator trims required to correct the measured shape (i.e., zero the spectral content of the shape error). Therefore, the number of control loop closures equals the dimensional order of the

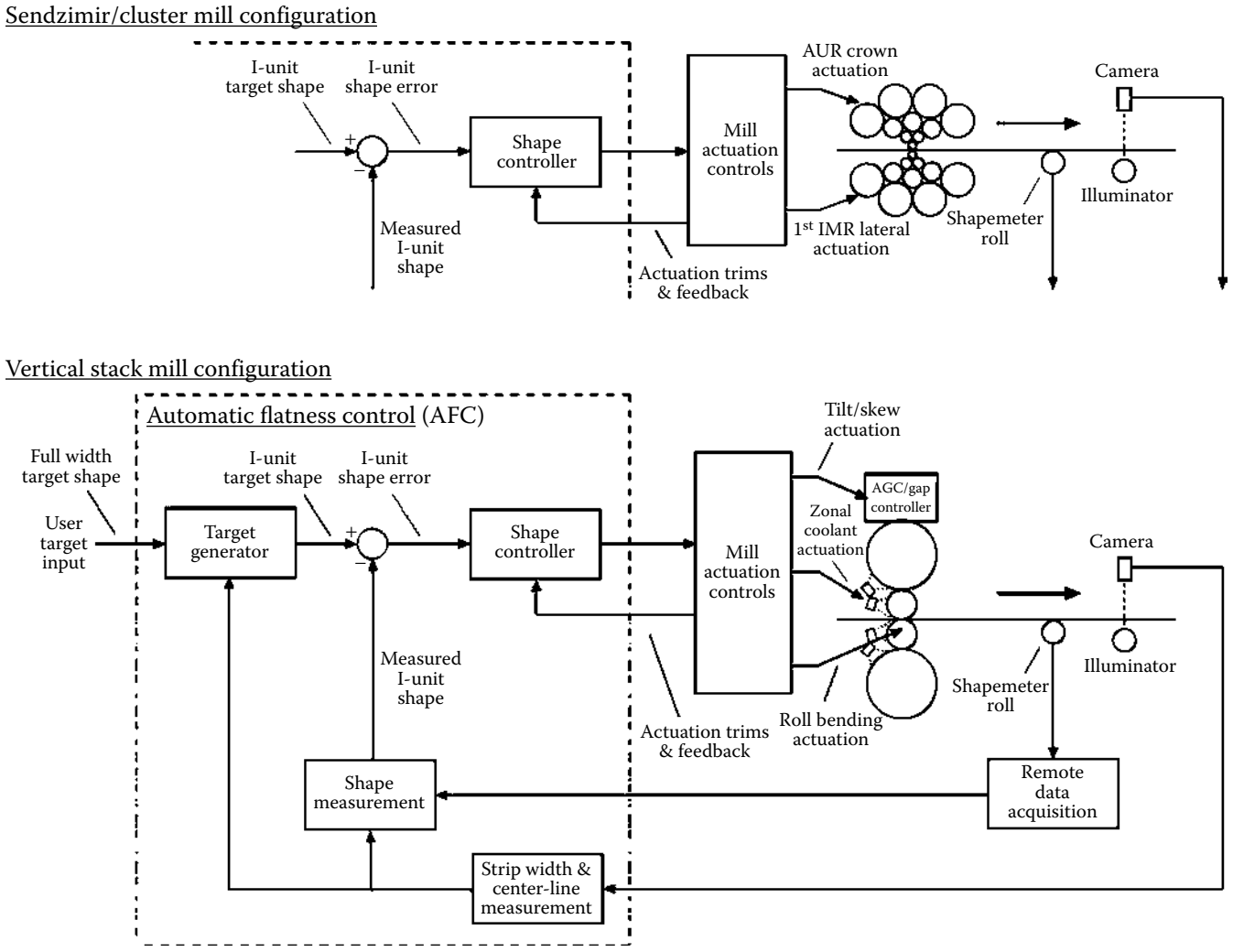


FIGURE 33.6 Block diagram illustration of the primary components involved in closed-loop shape control for both vertical stack and cluster configurations.

curvature space. Corrective actuator trims are determined through an inverse transformation of this spectral content to actuator space, and applied to the mill. The transformation to/from the lower-dimensional curvature space results in a suboptimal control and a reduction in robustness due to truncation of higher-order spatial frequency content considered in the controls decisions. This is, of course, dependent on the chosen spectral extent (dimensional order) and basis functions defining the curvature space, and the manner in which control decisions utilize the constrained information. Ringwood [10] provides an interesting comparison of multivariable methods.

Recently, new methods of advanced multivariable control strategies have been employed, offering improved control optimization and robustness.

33.4.1 Singular Value Decomposition Method

Singular value decomposition (SVD) is a method of matrix factorization that can be used to decompose nonsquare internal models into canonical, reduced order, diagonalized forms [10,12]. This diagonalized form is a representation of the internal model within a unique, natural space spanned by the model's own right and left singular vectors and corresponding singular values. Essentially, this is a decoupling transformation to a space whose basis system is unique to (and aligned with) the natural degrees of freedom of the model (mill) itself. This diagonalized representation offers a straightforward means of nonsquare model inversion.

Ringwood [12] introduced this approach by considering that the resulting SVD-based pseudo-inverse is the unique solution to the least squares minimization of the two-norm. Further, while operating in the diagonalized form, it was shown to be possible to partition the singular value spectrum, and focus attention and control decisions away from the dimensions of the internal model's natural basis that correspond to relatively small singular values requiring considerably larger control efforts and actuator dynamic range. This partitioning reduces the likelihood that the resulting closed-loop controller will make exaggerated (possibly

saturating) actuation adjustments in a vain attempt to correct minor shape error components that are not well aligned with the capabilities of the mill. It was shown [12] that this trait improves robustness and reduces overall coordinated actuation effort, with a lower computational overhead.

ABB Automation [44] has recently incorporated SVD as a parameterizing transformation and a means of reducing the number of control loops requiring closure. This "Fine SVD Control" technique resides among a pool of selectable control strategies, and is typically invoked during the final series of passes, when the material is thin, work-hardened and sensitivities of the actuators' spatial influence functions have substantially increased.

33.4.2 Model Predictive Control Methods

Andritz-Sundwig [5] has recently incorporated Model Predictive Control (MPC) techniques as part of a commercially available shape control system. MPC refers to a class of recursive, discrete time, sampled data algorithms that employ explicit internal models to predict the future response of the plant under control (a mill, in this case) to determine coordinated actuation inputs as part of an online, real-time optimization problem, in the presence of constraints (primarily on the inputs) and cost function performance weighting factors [14–17]. During each computational interval, the MPC algorithm attempts to optimize future plant response characteristics by computing an optimal sequence of future plant input adjustments. The algorithm applies the first element of the calculated optimal input sequence (as the actuation input), discarding rest. This process is cyclically repeated in subsequent computation intervals.

MPC is formulated as a state space representation [14,15] with the optimization actions focusing on the minimization of a quadratic cost function, often involving the weighted differences between the desired and instantaneous system states and inputs, along with the rate of change of the applied actuation inputs. It is often necessary to incorporate Luenberger or Kalman Filter state estimation techniques [45–50] to reconstruct (in real-time) nonmeasurable state vector elements from the available plant input and output vectors. The state estimator also employs an explicit internal model of the plant (mill), further reinforcing the need for accurate modeling practices.

MPC implementations are quite complex. Care must be taken in the formulation of the internal model and nature of the optimization process. The internal model employed is used to generate future-looking predictions and also in the reconstruction of the system state vector, making these techniques susceptible to modeling uncertainties, the presence of unmodeled nonlinearities, and estimator/controller interactions [18]. Further, the constrained optimization problem must be specifically formulated to ensure that a unique, optimal solution is feasible. Nikolaou [16] provides a detailed discussion on the critical issues that influence the resulting controller's stability, robustness, and fragility.

33.5 CONCLUSION

The prediction, measurement, and closed-loop control of cold-rolled strip shape/flatness are mature subjects, but still active areas of interest and developmental work.

- New techniques in shape measurement provide equipment suitable for use in surface critical applications. An innovative, noncontact system has been developed and successfully deployed, while established strip contact roll technologies are now supplied with seamless surfaces.
- Improvements in the accuracy and applicability of mill modeling techniques offer new three-dimensional insight into the complex internal behavior of the mill's roll stack/cluster, shape actuators, and material interaction.
- Advanced multivariable control techniques have been successfully applied to commercially available online/real-time shape/flatness control systems. These approaches offer new potentials in optimized shape control and stable actuator coordination.

The primary focuses of ongoing developmental work are in coupled fields of three-dimensional mill modeling and multivariable shape control techniques.

- Initial work has been undertaken in the development of methods that simultaneously solve the coupled problems of pass schedule optimization, roll profiles and cluster setup, and achievable shape target selection in a full three-dimensional setting. This iterative approach employs an existing pass schedule (generated by classical methods [51–53]) whose exit gauge constraints are adjusted from the results of transverse crown ratio prediction and analysis. Current work involves the development of a unified, three-dimensional model that directly incorporates the simultaneous determination of optimized pass scheduling and achievable shape target progressions, as a single noniterative result. Initial findings indicate the existence of a successive series of pass-by-pass boundary conditions that define and constrain the families of surfaces describing regions of achievable solutions. The presence of these surfaces suggests the existence of multiple solution pathways (as experienced in operational practices) that may provide a means of supporting constrained optimization methods.
- Certain interests are focused on the incorporation of improved nonlinear techniques applicable to the shape control problem. The ongoing work is twofold. One focus is on using nonlinear methods to expand the closed-loop robustness about the given operating point, while the other is directed at applying nonlinear controls to better accommodate the more accurate nonlinear models. Still other work focuses

on the use of adaptive techniques, primarily the use of online parameter identification coupled with self-tuning regulation, as a means to accommodate ever-present modeling uncertainties, the presence of unmodeled nonlinearities, or the unusual behavior of asymmetric strip profiles and their associated coiling/tracking behaviors.

- The exceptional processor speeds available in contemporary computer systems now allow the consideration of far more complex and computationally rigorous control and modeling techniques in online, real-time applications. Strategies once condemned to the domain of off-line processing, are now being experimentally employed and evaluated in the support of online systems. Issues of performance definable model convergence and computational stability are a main focus in determining the ultimate applicability.

The recent innovations and advancements in shape measurement and control technologies have been well received and are currently exceeding customer expectation and industry specifications. Time will surely reveal the staying power of the technological high watermark set by the contemporary methods or if these innovations and advancements will be eclipsed by some newly developed equipment, strategies, and/or technologies. It will certainly be interesting.

REFERENCES

1. Duprez, J.L. and Turley, J.W. *The Sendzimir Manual*, Waterbury, CT: T. Sendzimir, Inc./Jean-Louis Duprez Publications, 2000.
2. Duprez, J.L. and Duprez, A. *Cold Rolling Practice for Flat Products*, Bavans, France: SARL Duprez, 2005.
3. Siemens VAI Metals Technologies GmbH & Co. *SI-FLAT: Contactless Flatness Measurement System for Cold Rolling Mills*, Equipment manual, 2007.
4. ABB Automation GmbH. *Measure^{IT} Stressometer Systems*, Equipment manual, 2006.
5. Andritz-Sundwig GmbH. *Shape Control Systems*, Equipment manual, 2003.
6. Guo, R.M. and Malik, A. Development of new crown/shape control model for cluster mills. *Iron and Steel Technology*, 2005, 2(8): 31–40.
7. Malik, A.S. Rolling Mill Optimization Using an Accurate and Rapid New Model for Mill Deflection and Strip Thickness Profile. Dayton: Wright State University, Ph.D. Dissertation, 2007.
8. Malik, A.S., Grandhi, R.V., and Zipf, M.E. Optimal cluster mill pass scheduling with an accurate and rapid new strip crown model. *Proceedings of the 9th International Conference on Materials Processing and Design: Modeling, Simulation and Applications*. Proto, Portugal: American Institute of Physics, June 17–21, 2007: 1041–1046.
9. Grimble, M.J. and Fotakis, J. The design of strip shape control systems for Sendzimir mills. *IEEE Transactions on Automatic Control*, 1982, AC-27(3): 656–666.
10. Ringwood, J.V. Shape control systems for Sendzimir steel mills. *IEEE Transactions on Control System Technology*, 2000, 8(1): 70–86.
11. Ringwood, J.V. and Grimble, M.J. Shape control in Sendzimir mills using both crown and intermediate roll actuators. *IEEE Transactions on Automatic Control*, 1990, 35(4): 453–459.
12. Ringwood, J. Multivariable control using the singular value decomposition in steel rolling with quantitative robustness assessment. *Control Engineering Practice*, 1995, 3(4): 495–503.
13. Bates, D.G., Ringwood, J.V., and Holohan, A.M. Robust shape control in a Sendzimir cold-rolling steel mill. *Control Engineering Practice*, 1997, 5(12): 1647–1652.
14. Rawlings, J.B. Tutorial overview of model predictive control. *IEEE Control Systems Magazine*, 2000, 20(3): 38–52.
15. Qin, S.J. and Badgwell, T.A. A survey of industrial model predictive control technology. *Control Engineering Practice*, 2003, 11: 733–764.
16. Nikolaou, M. *Model Predictive Controllers: A Critical Synthesis of Theory and Industrial Needs*, Advances in Chemical Engineering Series, New York: Academic Press, 1998.
17. Findeisen, R. and Allgower, F. *An Introduction to Nonlinear Model Predictive Control*, Stuttgart, Germany: Institute for Systems Theory in Engineering, University of Stuttgart, 2003.
18. Hovd, M. and Bitmead, R.R. Interaction between control and state estimation in nonlinear MPC. *Modeling, Identification and Control*, 2005, 26(3): 165–174.
19. Roberts, W.L. *Cold Rolling of Steel*, New York: Marcel Dekker, 1978.
20. Roberts, W.L. *Flat Processing of Steel*, New York: Marcel Dekker, 1988.
21. Ginzburg, V.B. *High-Quality Steel Rolling: Theory and Practice*, New York: Marcel Dekker, 1993.
22. Spooner, P.D. and Bryant, G.F. Analysis of shape and discussion of problems of scheduling set-up and shape control. *Proceedings of the Shape Control. Conference of the Metals Society*, Chester, 1976, pp. 19–29.
23. Friedrich Vollmer GmbH. *Shape Control Systems*, Equipment manual, 1992.
24. Lap GmbH, *Lap Laser: Non-Contact Flatness Measuring Systems*, Equipment manual, 2006.
25. Shapeline AB, *Shapeline 500*, Equipment manual, 2006.
26. Paakkari, J. On-Line Flatness Measurement of Large Steel Plates Using Moire Topography, Oulu: University of Oulu, Ph.D. Dissertation, 1998.
27. Bose, N.K. *Digital Filters: Theory and Applications*, New York: North-Holland, 1985.
28. Cooper, W.D. *Electronic Instrumentation and Measurement Techniques, 2nd edition*, Englewood Cliffs, NJ: Prentice-Hall, 1978.
29. Motochenbacher, C.D. and Fitchen, F.C. *Low-Noise Electronic Design*, New York: John Wiley & Sons, 1973.
30. Siemens VAI Metals Technologies GmbH & Co. *SIROLL$_{CIS}$ ALU—Solutions for Aluminium Rolling Mills*, Technical brochure, 2006.
31. Stone, M.D. Theory and practical aspects in crown control. *Iron and Steel Engineer*, 1965, 8: 73–90.
32. Shohet, K.N. and Townsend, N.A. Roll bending methods of crown control in four-high plate mills. *Journal of the Iron and Steel Institute*, November 1968, 1088–1098.
33. Shohet, K.N. and Townsend, N.A. Flatness control in plate rolling. *Journal of the Iron and Steel Institute*, October 1971, 769–775.
34. Poplawski, J.V. Bethlehem's contribution to the mathematical modeling of cold rolling in tandem mills. *AISE Yearbook*, 1980, 391–402.

35. Guo, R.M. Development of a single-stage transport matrix method using the beam on elastic foundation theory. *19th Southeastern Conference on Theoretical and Applied Mechanics*, Ft. Lauderdale, FL, 1998.
36. Hattori, S., Nakajima, M., and Morooka, Y. Applications of pattern recognition and control techniques to shape control of rolling mills. *Hitachi Review,* 1993, 42: 165–170.
37. Zhu, H.T., Jiang, Z.Y., and Tieu, A.K. A fuzzy algorithm for flatness control in a hot strip mill. *Journal of Materials Processing Technology*, 1993, 140: 123–128.
38. Eibe, W. Inflatable crown rolls—Characteristics, design and applications. *Iron and Steel Engineer*, 1984, 61: 426–432.
39. Chen, X. and Zhou, J. A specificalized finite element model for investigating controlling factors affecting behavior of rolls and strip flatness. *4th International Steel Rolling Conference*, Deauville, France, 1987: E4.1–E4.7.
40. Zipf, M.E., Godwin, C.K., and Wisti, D.R. Modeling and simulation of Sendzimir mill shape control actuation sensitivities and capabilities envelope with applications to multivariable shape control. *Proceedings of the Associação Brasileira de Metalurgia e Materiais, 43rd Rolling Seminar—Processes, Rolled and Coated Products*, Curitiba, Brazil: ABM Brasil, October 17–20, 2006: 856–866.
41. Cook, R.D., Malkus, D.S., Plesha, M.E., and Witt, R.J. *Concepts and Applications of Finite Element Analysis*, New York: John Wiley & Sons, 2002.
42. Gunawardene, G.W.D.M. Static Model Development for the Sendzimir Cold Rolling Mill, Sheffield: Sheffield City Polytechnic, Ph.D. Dissertation, 1982.
43. Smith, P. *Flatness Control in Cold Rolling*, Pittsburgh, PA: International Rolling Mill Academy, 2005.
44. ABB Automation GmbH. *Automatic Flatness Control System: Commissioning of Flatness Control in Cluster Mills*, Technical brochure, 2007.
45. Luenberger, D.G. An introduction to observers. *IEEE Transactions on Automatic Control*, 1971, AC-16(6): 596–602.
46. Luenberger, D.G. Observer for multivariable systems. *IEEE Transactions on Automatic Control*, 1966, AC-11(2): 190–197.
47. Middletown, R.H. and Goodwin, G.C. *Digital Control and Estimation—A Unified Approach*, Englewood Cliffs, NJ: Prentice-Hall, 1990.
48. Saberi, A., Chen, B.M. and Sunnati, P. *Loop Transfer Recovery: Analysis and Design*. London: Springer-Verlag, 1993.
49. Friedland, B. *Control System Design: An Introduction to State Space Methods*, New York: McGraw-Hill, 1986.
50. Brown, R.G. *Introduction to Random Signal Analysis and Kalman Filtering*, New York: John Wiley & Sons, 1983.
51. Bland, D.R. and Ford, H. The calculation of roll force and torque in cold strip rolling with tensions. *Proceedings of the Institute of Mechanical Engineering*, 1948, 159: 144–153.
52. Stone, M.D. Rolling of thin strip: Part I. *Iron and Steel Engineering*, 1953, 2: 61–74.
53. Stone, M.D. Rolling of thin strip: Part II. *Iron and Steel Engineering*, 1956, 12: 55–76.

Index

3D deformation model, 300–302, 305
3D volumetric image, 325–326
20-High Sendzimir mill, 332–333, 335
  characteristics of, 338
  geometry parameters for, 337
  model parameters for, 337
  simplified mixed finite element method for, 337–339

A

Abor-centering system, 238
Acceleration profile, 227
Accuband Strip Width Gage, 241
Accucrop shear control, 242
Accuscan hot metal detector, 242
Accuspeed Laser Velocimeter, 241–242
Acid-base mechanism, 198–199
Adamite rolls, 63
Adaptive learning, limitation of, 279–280
AGC, *See* Automatic gauge control
AIU, *See* Alternative iron units
Alloys
  creep-strength, 83, 85, 89
  heat-resisting, 87
Alternative iron units (AIU), 7, 10, 11
American Petroleum Institute (API), 169
American Society for Testing Materials (ASTM), 166
AMTRI Vibration Analysis System, 260, 262
Andritz-Sunwig/BFI shapemeter, 359–360
Artificial intelligence (AI) learning techniques, 283
ASC (American Sensors Corp.), 245–246
As-U-Roll (AUR) top-crown, 360
Austenite grain coarsening, avoidance of, 104
Austenite grain size, 272–274
Automated surface inspection systems, 229–230
Automatic flatness control, 319, 327
Automatic gauge control (AGC), 19, 213
Automatic width control, 19
Automation system upgrades, 36–43
Automotive industry, 171, 265
Avrami equation, 273

B

Backup roll bending (BUB), 147
Backup roll (BUR), 65, 69, 122–124, 332
Bainitic products, material properties for, 51
Basic oxygen process (BOP), 4
Benchmark automation, 229, 231
Bending moment, 128–130
Bending stresses, 84–85, 88, 129–130, 136
Bernoulli equation, 92
Betriebsforschungsinstitut (BFI) flatness roll, 320–321
BHP Steel, *See* BlueScope North Star Steel
Big steel, oil crisis in, 4–6
Biot indexes, 166
BlueScope North Star (BHP) Steel, 6, 9
  design parameters of CR line at, 23–24
BOP, *See* Basic oxygen process
Bottom headers
  cooling efficiency, 163
  modification of, 163
Boundary film
  modeling, 199
  shearing of, 198
BUB, *See* Backup roll bending
Buckling phenomenon, 156–157
BUR, *See* Backup roll

C

Carbide-enhanced chrome steel, 65
Carbides, 71–72
Carbide volume percentage (CVP), 75
Casters
  design parameters of, 21, 27
  optimization, 246–248
Casting and rolling (CR) lines, 15–32
  coilers of, 19
  components of, 17–20
  descalers of, 18
  design features of, 20
  design parameters of, 22–23
  finishing mills of, 18
  groups of, 19–30
  heat conservation devices of, 17–18
  layout of, 20
  reheat furnaces of, 17
  roughing mills of, 18
  shears of, 17
  slab casters of, 17
  supercompact, 30–31
    for endless hot rolling, 31
    for hot rolling of discrete coils, 31
  vertical edgers, 18
  water cooling systems of, 18
Cast slab width range, 50
Cauchy–Schwartz conditions, 173
Charge coupled device (CCD) camera, 322, 325
Chebyshev coefficients, 296
Chemisorbed films, 191
China Steel Corporation (CSC), 43
  China Steel HSM #1, 43–50
Chrome steel rolls, 64–65
Classical cooling control, 172, 175–176
Cluster mill
  20-high Sendzimir, 337
  models, 361, 363
CO_2 emissions, 12
Coiler controllers, regulating functions in, 45
Coilers area, 48–49
Coilers of CR lines, 19
Coiling pyrometer, 175
Coiling temperature control (CTC) model, 45–46
  performance of, 51
Coil parameters, 51
Coil quality, 45, 268
Coil set, 289–290
Coil shape defects, 52
Coil surface defects, 52
Coil telescopicity, 44, 51
Coil width performance, 50
Coil winding, evaluation of, 232, 238
Cold-rolled sheets, ultra-thin, 179
Cold-rolled strip, 299, 308, 355
Cold rolling
  elastohydrodynamic lubrication of, 191–205
  lubricant, 193
    determination of film thickness of, 195–198
  process modeling, 179
    analysis, 183–184
    theory basics, 180–188
  tribocontact geometries of, 192–193
Cold-rolling mills, 179, 183–184, 290
  energy–force calculations of, 188
  technology improvement, 188–189
Cold strip mills, contact shapemeters for, 320–321
Compact Steel Plant (CSP), 6, 12, 15–16
  Hylsa, 6, 20, 22
  Nucor Steel, 15, 20–21
  optimum slab thickness of, 16–17
  SeverCorr, 20, 22
Compact strip production (CSP), 350
  process, 83
  tunnel furnaces, 84, 88
Compressive force, 156, 201
Computational fluid dynamics (CFD) software, 100
Connectivity solutions, identification of, 41–42
Contact flatness measuring devices, *See* Contact shapemeters
Contact shapemeters
  for cold strip mills, 320–321
  for hot strip mills, 321–322
  shapemeter–loopers, 322
  strengths and weaknesses, 321–322
  technological limits of, 322
Contact stresses, 115, 180–181, 184
  calculation procedure, 118–121
  for elastic regions and plastic region, 118–121
  formulas for, 121–122
  of thin wide strips, 118, 121
  in working stands of wide-strip mills, 121–122
Contactless flatness measuring devices, *See* Contactless shapemeters
Contactless shapemeters
  nonoptical devices, 327
  optical devices, 322–327
  for plate flatness measurement, 320, 326
  strengths and weaknesses, 324–327
Continuous casting (CC), 3, 5, 10
Control algorithm, application of, 224–227
Controlled heating, 100
Controllers, 38–39, 41
  multivariable, 209–210, 215, 217
Controlling strip shape, 297
Control outputs, 216
Control shadowing, 41–42
  level 1 control, 41–42
  level 2 control, 42

Control systems
downcoilers, 45
features of, 36
slab sizing press installation, 47
Convection heat flux, 106
Conventional gauge control, 213
Conventional looper angle, 216
Cooling systems
accelerated, 56–57
water, 18–19
Cooling temperature control, 172
Cost function, 142–143, 148
Coupled Pickle-Line and Cold Mill (CPCM), 303
Crawfordsville plant, 6
Creep-strength alloys, 83, 85, 89
CR lines, *See* Casting and rolling lines
Crop optimization system, 239–242
cut line determination, 241
imaging, 241
shear control, 242
tracking, 241–242
Cropping system, 239
Crossbow, 161, 166, 290
at cut-to-length line, 167
elimination, 167
vs. strip dimension, 168
Cross-strip temperature variations, 293
CSC, *See* China Steel Corporation
CSP, *See* Compact Steel Plant; Compact strip production
CTC model, *See* Coiling temperature control model
Cumulative distribution function, 151
Cumulative frequency, 295
Curved skid riders
and boundary conditions, 107
impact on skid marks, 108
temperature comparison between straight and, 108
CVP, *See* Carbide volume percentage

D

Data-acquisition systems, 262
Database management system (DBMS), 281
Data modeling, 266
Datapaq's Furnace Tracker®, 112
Data processing unit (DPU), 266
Deflection roll, 321
Deformation model
3D, 300–302, 305
roll stack, 303
calculation procedure, 304
Deformation zone, 180, 300
analysis model of, 300
calculation formulas for rolling values, 123
elastic-plastic model of, 181, 187
elastic region of, basic expressions for, 118
plastic region of, basic expressions for, 119
stick zone in, 115–116
tangential stresses in, 116–117
versions of structural schemes for, 187–188
working stands, structural parameters of, 122
Descalers of CR lines, 18
Descale systems, 91–95
design, 95
header stations, 95
impingement pressure, 92–94
spray nozzle interference, 94–95
Digital front ends (DFEs), *See* Firing circuits replacement
Direct current (DC) drives, 37
Direct strip production complex (DSPC), 23
Doppler principle, 243
Double-stand Steckel mill, 29
Downcoilers, 17–18, 44–45
Dry rolls, 84
conversion, 88
heat losses for, 87–88
DSPC, *See* Direct strip production complex
Dual-phase steel, 171
Dynamically linked library (DLL), 283
Dynamic control, 220

E

EAF, *See* Electric arc furnace
Eccentric bottom tapholes (EBTs), 5
Eccentricity analysis, 253
Eddy current sensors, 359
EHD interferometry, *See* Elastohydrodynamic interferometry
EHD lubrication, *See* Elastohydrodynamic lubrication
Elastic deformation of work rolls, 193
Elastic foundation elements, 332
Elastic instability phenomenon, 156
Elastic-plastic model, 187
Elastohydrodynamic (EHD) interferometry, 193–195
Elastohydrodynamic (EHD) lubrication, 191–205
Elastoplastic deformation zone, contact stresses in, 181
Electrical drives upgrade solutions, 36–38
Electrical equipment, 45–48
Electrical motors, 37
Electrical systems upgrades, 36–43
Electric arc furnace (EAF), 5
flat-rolled minimills, cumulative production of, 7
reduction in chemical and electrical energy in, 13
Energy balance formulation, 163
Entry tension stress model, 302, 310, 313
Equipment control upgrade solutions, 38–39
Exit tension stress model, 302, 311, 313
Expert systems, 251–252, 283

F

Fabrication technology, developments in, 56
Factor-of-safety design, 144
Factory system test, 41
FDM, *See* Finite differences method
FEM, *See* Finite element method
Ferrite-pearlite-bainite steels, 274
Ferrite–pearlite steels, 274
Ferritic rolling, 26
Ferromagnetic core, 266
Ferrous martensitic matrix, 71
Fifth octave chatter, 259–262
Finishing mills
of CR lines, 18
design parameters of, 21–22, 28
exit temperature of, 226
interactions in, 220–221
predictive temperature control in, 221–227
temperature modeling for, 222–223
velocity feedforward in, 227
Finishing rolling temperature, 104–105
Finite differences method (FDM), 282, 349
Finite-element computer model, 256
Finite element method (FEM), 349, 361–362
for computing mill deflection, 334
for 20-High Sendzimir mill, 337–339
for strip profile calculation, 331–332
width necking simulation using, 136–137
Firecracks, 75, 78
Firing circuits replacement, 37
FIT2G, *See* Guided two-parameter learning
Flatness, 355
control, 19
measuring devices, 319–328
of rolled steel, 277
Flatness deviations, 287–290
bowshaped faults, 287, 289
causes of, 320
cumulative frequency, 295
defect patterns, 287
strip waviness, 287–288
Flatness index, 295
Flatness reliability, 151–152
Flat-rolled steel minimills, 3–13
Flat-rolled products, 253
Flow stress, 277
learning, fitting mechanisms for, 278
metallurgical aspect of, 279
valid range, 281
FLUENT®, 100
Four-high cold plate mill
FEA model of, 336
geometry parameters for, 335
model parameters for, 335
simplified mixed FEM of, 332, 335–337
Four-high mill
force and moment calculation scheme for, 123
quarter symmetric model of, 333
Four-high temper mill, 147–150
Fourier indexes, 166
Frequency modulated continuous wave (FMCW), 246
Friction law, 115–116
Friction stress model, 117
Fringe method
stereoscopic view, 325
strengths and weaknesses, 326
Furnace design models, 100
Furnace dynamic control models, 100–101
Furnace heating practice models, 100–113
case application of, 110–112
implementation results, 112–113

G

Gauge control, 209
Ghost bar rolling, 42–43
Gibbs' free enthalpy, 173–174
Global stiffness matrix, 332
Grain coarsening temperature, 104
Grain growth, 104
after deformation, 273
during slab reheating, 272
Grain refinement mechanisms, 56
Guided two-parameter learning (FIT2G), 280

H

Hall–Petch equation, 174
Hasofer–Lind method, 152
Heat checks, 75
Heat conductivity, 165

Heat conservation devices of CR lines, 17–19
Heat diffusion, 163
Heating curves
  fast and slow, 108–110, 112
  of slab, 108–110, 112
Heat loss
  by convection, 165
  by radiation, 164
Heat removal, 169–170
Heat-resisting alloys, 87
Heat transfer, 106, 161, 165, 253
Hertz–Belyaev formula, 123, 185
Hertz formula, 182
High carbon steel grades, 173
High chromium irons, 71, 78
High chromium steel, 71, 76–78
High-speed steel (HSS) rolls, 64–65, 71–72
  applications of, 76–78
  behavior in lab test, 73–76
  considerations of, 78
  results of
    in continuous roughing stands, 76–77
    in early finishing stands, 78–79
    in reversing roughing stands, 78–79
  safe and cost-efficient use of, 68–69
  wear and damaging of, 78
High strength low alloy (HSLA) steel, 100, 104, 161, 169, 279
High-strength plate, aspects of marketplace for, 55–56
HIsmelt direct iron process, 11
HMD, *See* Hot metal detector
HMI systems, *See* Human-machine interface systems
Hooke's law, 130
Hot band profile irregularities, 341–347
Hot band ridges, 316
Hot deformation model, 272–273
Hot metal detector (HMD), 245, 247
Hot rolling, 253–254
  mode of St1PS strip, 124–125
  plastic deformation in, 130
  of thin wide strips, 115–125
  width variation behavior during, 127–139
Hot rolling mills, 24
  arrangements of, 29
Hot strip mill (HSM), 16, 239, 242
  basic mill data, 44
  modernization projects, 43–52
  configuration, 43
  contact shapemeters for, 321–322
  CSC HSM 1, configuration, 44
  roughing stands in continuous, 76–77
  transverse temperature distribution of, 349–353
  upgrades of, 43
Hot Strip Mill Model (HSMM), 102
Hot-tandem rolling, 272
HSLA, *See* High strength low alloy
HSM, *See* Hot strip mill
HSS rolls, *See* High-speed steel rolls
Human–machine interface (HMI) systems, 39, 42
Hydraulic oscillators, 252
Hysteresis, nonlinear ferromagnetic, 266

I

Impingement pressure, 92–94
IMPOC© (Impulse Magnetic Process Online Controller), 265–269
  data modeling and system performance, 266–267
  data processing unit, 266
  operating principles, 265
  sensor, 266
  system components and system operation, 265–266
  technical and economic benefits, 268–269
Impulse Magnetic Process Online Controller, *See* IMPOC©
Induction welding, 31
Infrared sensors, 245, 248, 253
  software setup for, 251
Inline Strip Production (ISP) plant, 27
Integrated system, 42
Intelligent learning, 281
Intermediate variables, 220
Internal energy, 164
International Association of Steckel Mill Operators (IASMO), 128
Iron, strength of, 271
Iron-base castings, solidification of, 67
Iron oxide (scale) layer, 91–92
Iron unit supply, 9–11
Irvine and Pickering formula, 274
Irvine's equations, 103
Iverson, Ken, 4

J

JFE Steel Corporation, 159
Johnson–Mehl–Avrami approach, 173

K

Kalman filter, 214
Kelk Corporation (KELK), 239, 241–243

L

Laminar cooling systems, 45–46
Laminar flow
  bottom flow to top flow ratio, 168
  distribution, 167–169
  heat removal by, 169–170
  yield strength, 169
Laminar flow-cooling system, 161
  composed of, 162
  hardware modification, 163
  layout of, 162
Laser-based sensors, 245
Laser Doppler velocimeters (LVDs), 243, 245–248
Lasermeters, 246–247; *See also* Triangulation lasermeters
Laser points method, 324–325
Laser velocimeters, 241–242
Laser velocity, analysis of, 253
Ledeburitic steel, 71
Level 2 model, 277–283
  AI learning techniques, 283
  force and flow stress, 277–278
  force learning, 278
  issues in
    metallurgical, 278–279
    modeling, 279–281
    software engineering, 281
  next-generation, 283
  rolling in two-phase region, 279
  temperature-dependent properties, 281
  web-based, 282
Light cutting method, 325
Light section method, 325
Limit state functions, 152
Linear design model, 212
Linear dynamic model of looper and stand, 211
Linear laser method, 323–324
Linear temperature model, 224
Linepipe, 55–56
Local shape defects, 299, 314
  identification of causes, 316
  reduction of, 316
  simulation, 306
Longitudinal equilibrium equation, 301
Looper angle, 212, 215
  control of, 213
  multivariable, 216
Low-frequency forced vibrations, 256
Lubricants
  dynamic viscosity, 202
  film, 195–198
Lubrication mode, 192
LVDs, *See* Laser Doppler velocimeters

M

MAB-3000, 249
Mandrel power, 44
Martensitic products, 51
Mass flow control, 213, 215
Material properties models
  trends in development of, 274–275
  for ultrafine-grain microstructure steel, 275
  for ultra-low-carbon steel, 275
Mathematical optimization, 142
  cost function, 142–143
  design variables, 142–143
MBPC, *See* Model-based predicted controller
Mechanical equipment, 44–45, 47
Mechanical properties prediction model, 274
Medium-slab casters, 15–32
Melt shop, design parameters of, 21
Mesoscopic model, 275
Microalloying, 56, 172
Microalloy precipitates, dissolution of, 103–104, 107
Microporosities, 67
Microstructure modeling, 172–174
  and cooling section control, 171–172
  evolution, 172
Microstructure Monitor system, 176
Microstructure simulation, 283
Microwave sensors, 245
Mill modeling and simulation, 357
  analytic models, 361
  empirical/heuristic models, 361
  methods in, 360–362
  pass scheduling, 362
  process models, interactive relationship of, 281
  setup calculations, 219–220
  shape control actuators, 360–361
  shape target selection, 362
Mill stands, 16–17
Mill wrecks, 229, 234, 236
Minimills, history of, 3–13
Minimill sector, restructuring of, 12
Model-based predicted controller (MBPC), 219, 224
Model predictive control (MPC), 172, 175–176
  structure of, 177
  techniques, 364

Modern rolling practice, 278
Moirè's topography method, 326–327
Mono-cast rolls, 63–64
Monte–Carlo method, 275
Monte–Carlo simulations, 145–146, 275
MO-RE®-2150, 85, 88
MPC, *See* Model predictive control
MULPIC (Multi-purpose interrupted cooling) system, 56–58
Multibody dynamics simulation, 158
Multivariable control gauge change, 216
Multivariable controller design, 213–217
  advantage of, 215, 217
  application of, 209
  of gauge and looper angle, 210
  performance optimization, 215
  state estimation and feedback, 214
  statistical performance analysis of, 217
Multivariable disturbance estimates, 216
Multivariable hot strip mill control, 209–218
Multivariable looper angle, 216
Multivariable shape control techniques, 360, 362

N

Neural-network models, 251
Nitrogen oxide (NO_x) emission, 100
No-crystallization temperature, 104–105
Nonconformal rolling contacts, elastohydrodynamic lubrication in, 191–205
Noncontact optical systems, 254
Noncontact sensors, 245, 251–254
Noncontact shape measurement, 357–359
Nonlinear ferromagnetic hysteresis, 266
Nonlinear film growth, 198–199
Normal distribution, 145
Nova Hut steel, design parameters of CR line at, 30
Nucleophilic association/dissociation mechanism, 198
Nucor Steel, 4, 6–13
  plants, 16, 19–21

O

Octave gauge chatter vibrations
  fifth, 259–262
  third, 257–259
Operator's interface upgrade solutions, 39–40
Optical inspection systems, 254
Optical triangulation, 322–323
Optimization, 141–142, 268
  caster, 246–248
  constraints, 144
  crop, *See* Crop optimization system
  formulations, 142
  of steel-rolling process, 142
  of temper mill productivity, 147
  traditional *vs.* modern approach, 142–143
  uncertainty quantification role in, 146
Optimum slab thickness of CSP, 16–17
Oxidation of iron, 91
Oxide scale
  descaling of, 93
  formation of, 91–92
  impact pressures to, 94

P

Pass schedule set-up models, 330–331
PDF, *See* Probability density functions
Pearlitic nodular core material, 67
Phase-field method, 275
Phase transformation, heat of, 164
Phenomenological models, 266
PHOENICS®, 100
Pickle line system, 234–236
  camera setup, 232, 235
  defect spreadsheet, 236
PID controller, *See* Proportional integral derivative controller
Piezoviscous Effect, 196, 200, 204
Pincher defect, 52
Plastic deformation
  in hot rolling, 130
  of strip, 135–136
Plastic flow equation, yield criterion and, 301
Plastic strain, 138
Plate mill upgrades, 55–60
Plate-Steckel configuration, 60
PLCs, *See* Programmable logic controllers
Prediction model, 271
  mechanical properties, 274
  microstructure and material properties, 272
Pressure-viscosity coefficients, 200–202
  determination of, 204–205
  for lubricants and esters, 202
Pre-temper mill stain, 233
Probability density functions (PDF), 145–146
Process models, 42, 281–283
Process shadowing, 41–42
Programmable logic controllers (PLCs), 230
Proportional integral derivative (PID) controller, 213, 215
Pulse radar sensors, 246
Pusher-type furnaces, 100
Pyrocracking factor, 75
Pyrometers, 245, 253, 350

R

Radial force measuring systems, 291
Radiation heat flux, 106
Random variables, 144–145
  capacity, 145–146
  demand, 145–146
  distributions, 145
Raw steel production, U.S., 5
RBDO, *See* Reliability-based design optimization
Recrystallization, 273
Reheat furnaces, 99–100
  computer modeling, 100–101, 271; *See also specific models*
  discharge temperature
    mechanical requirements, 101–102
    metallurgical requirements, 103–105
  exit temperature, 101–102
  slab temperature at exit from, 101–105
Reheat tunnel furnace
  of CR lines, 17
  design parameters of, 21
Reliability analysis
  probability calculation for, 145–146
  uncertainty quantification and, 144
Reliability-based design optimization (RBDO), 141, 146, 150
Reliability index, 151
Residence time determination, 110
Residual austenite content, 171
Residual stresses of strip, 129–130, 135–136, 305, 311, 314
Retained strain, 278–279
Reversing finishing mills, *See* Steckel mills
Riccati equation, 214
RM setup (RSU) functionality, 47
Roll bite, 128
  pressure distribution in, 129
  strip-thickness profiles in, 300
Roll deflection equations, 303
Roll deformation compatibility equation, 304
Roll elements
  coatings, 322
  cooling nozzles, 314
  core material, 67–68
  crowns, 148
Roll equilibrium equations, 303
Roll gap model, 256
Roll gap profile, 304–305
Roll pitch, 157
Rolling force, 120
  learning, 278
  reduction in, 202–204
Rolling friction, 122–124, 185, 187
Rolling mills
  with automatic gauge and width control, 19
  with flatness control, 19
  operation of, 49–50
  with strip profile, 19
Rolling parameters, 133–136
Rolling strip with offset from mill centerline, 344–346
Rolling temperature, 125
Roll separating forces, 303
Roll stack
  deformation model, 303–304, 360
  dimensions of, 134
Roll surface deterioration, 73
ROMETER, 324–325
ROS, *See* Run-out simulator (ROS)
ROT strip travel, *See* Run-out table strip travel
Roughing mill work rolls
  compound rolls, testing of, 68
  materials, evolution, 63–65
    from chrome steel to high-speed steel, 64–65
    early developments, 63–64
  microstructural integrity, 65, 67
  operational safety of, 66
  performance of, 65–67
  residual stress, 66–67
Run-out simulator (ROS), 157
Run-out table (ROT) strip travel
  dynamic characteristics of, 155–159
  equivalent theorem of, 156–157
  folded defect in, 155
  maximum stable threading speed on, 156–159
  similarity law for, 157–158
  simulation model, 158
  steady-state equation of motion for, 156
Runout tables (ROT) spray system characteristics, 44–45

S

Scrap prices, 10
Seamless roll technologies, 357, 359–360
Self-excited vibration, 256
Semi-endless rolling, 26
Semi-high-speed steel (Semi-HSS), 65
  production of, 67
  safe and cost-efficient use of, 68

mill practices, 68–69
roll shop practices, 69
Sendzimir mill, 360–361; *See also* 20-High Sendzimir mill
Sensors, 38, 245–246, 321, 358–359
continuous caster optimization of cut, 246–248
developments, 248–251
infrared, 245, 248, 253
and input/output upgrade solutions, 38
laser-based, 245
microwave, 245
noncontact, 245, 251–254
pulse radar, 246
scanning and positioning, 245
strip centering/camber and width measurement, 248
system examples in
finishing, 254
hot rolling, 253–254
slab casting, 252–253
techniques, 251–252
temperature measurement, 245
width measurement of slab, 248
Service-oriented architecture (SOA), 282
SeverCorr, 7–8, 20–22
Shadowing verification tools, 42
Shape
definition, 355
measurements, 357
innovations in, 358–360
noncontact, 357–359
seamless roll technologies, 357, 359–360
simulation program, 305
Shape and Crown Simulator, 342
Shape control, 357–358
actuators, 360–362
advancements in, 362–364
for cluster mill configuration, 363
multivariable techniques, 360, 362
for vertical stack mill configuration, 363
Shape factor (Q-factor), 277–278
Shapemeter–loopers, 322
Shearing
of boundary film, 198
of CR lines, 17
Ship plate, 56
SI-Flat system, 327, 358–359
Singular value decomposition (SVD) method, 363–364
Skid marks
curved skid riders impact on, 108
heating criteria for, 107
slice-to-slice method for, 107
Skid shadow effects, 107
Slab
2-D longitudinal section of, 105
heat flux into, 106
heating curves of, 108–110, 112
reheating, 16
relative thickness and length differences of, 133–134
surface scaling, 16
thermal stress modeling, 108–110
transfer furnaces, 17
Slab casters, 252–253, *See also* Medium-slab casters; Thin-slab casters
Slab sizing press (SSP)
installation, 47, 49–50
shutdown, 50
Slab temperature
at exit from furnace, 101–105
modeling, 105–108
calculation domain, 105–106
numerical formulation, 106–107
and rolling forces, 101–102
Slip zone, 125, 180, 182, 187
Solid solution mechanisms, 56
Speed regulators, digitization of, 37
Speer's theory, 103
Spin casting, 64
Spray flows, 221, 226
Spun-cast compound roll, principle of, 63
SSP, *See* Slab sizing press
Stainless pins in slab
lateral and longitudinal displacements of, 130–133
location and dimension of, 131
transverse distribution patterns of, 131–132
Statistical performance analysis for multivariable controller, 217
Steckel coiling furnace, 18
Steckel drums, tensile stresses of, 129–130, 134–135, 137
Steckel mills, 18, 128–129, 166
double-stand, 28–29
hot-rolling process of, 134–137
Steel
mechanical properties of, 271
tetrahedral phosphate molecule reaction on surface of, 198
Steel grades
different strategies for, 176–177
high carbon, 173
Steel rolling
contact geometries in, 192
optimization, 142
Stefan–Boltzmann law, 164
St1PS steel strip
energy–force and technological hot-rolling parameters for, 120
hot rolling mode of, 124–125
Straightness deviations, 287, 290
Strain rate and velocity field model, 300–301
Strengthening mechanisms, 56, 166, 169
Stresses unloading model, 305
Stressometer system, 320–321, 360
Strip
camber, 133, 136, 290
casting, 9
centerline offset of, 133
displacement measuring systems, 291–292
exit gauge, 211
heat transfer on surface of, 165
leveling methods, 297–298
measured characteristics, 351
permeability measurement, 293
plastic deformation of, 135–136
residual stresses of, 129–130, 135–136
temperature, 134–135
temperature slices, evolution of, 223
thickness, 118–119
transverse temperature distribution of, 349–352
transverse tension distribution of, 129–130, 359
width variation in, 127, 131–133
Strip canoeing, critical temperature differences of, 166–167
Strip cooling modernization, 44
Strip crown, 334
of coils, 342–345
and strip thickness profile, 329–330
Strip deflection, vacuum suction force inducement of, 359
Strip flatness, 290, 330
of coils, 342–344
control methods, 297–298
inside rolling mill, 297
outside rolling stand, 297
deadband, 330
defect types, 330
measuring systems
radial force, 291
requirements on, 293–294
Strip flatness probability, 150–153
Strip length, material properties constant over, 175
Strip manifest shape, 320
Strip modulus, 332
Strip profile, 19
calculation, 334–335
methods, 331
prediction and control models, 330–335
simplified mixed finite element method for, 331–332
tasks requiring accurate and rapid, 331
comparison of predicted and measured, 343
and flatness control, 335
model applications, 335–339
model development, 332–334
modeling control devices, 334
with offsets from mill centerline, 346
and strip crown, 329–330
thickness, 300, 308, 329–330, 334
with uniform and nonuniform roll cooling, 342–343
Strip pull force, 185–186
Strip-roll contact surfaces, 115–116
Strip shape deviations, 287
causes of, 287
classification of, 288
qualitative and quantitative assessment of, 294
Strip shape/flatness control problem, 356; *See also* Strip flatness
Strip speeds, 133, 135
Strip-strain resistance model, 117
Strip velocity, 116
Strip waviness, 287–288
bounded by curved or straight lines, 289
calculating, 321
measuring systems, 292
reasons for, 320
Strip width, 293, 352
Structure–mechanical properties relationship model, 274
Super 22H®, 85
Supervisory process control upgrade solutions, 40–41
Surface friction model, 301
Surface inspection benefits, 52
SVD method, *See* Singular value decomposition method
Switchover trials, 42–43
System modeling, 210–213

T

Tandem-finishing mill, 16, 19
Tandem mill system, 236–238
camera setup, 232, 236–237
wreck analysis, 238

Tandem rolling, 272
Tangential stress model, 117
Tangshan Guofeng minimill, design parameters of CR line, 26, 28
Telescoping, 238
Temperature control
  coiling, 45–47
  cooling, 172–173
  finishing mill predictive, 219–228
Temperature model
  boundary conditions, 165
  finishing mill, 222–223
  two-dimensional, 165
Temperature state estimation, 223–224
Temper mill productivity optimization
  formulating optimization problem, 147–148
  objective for, 147
  results and discussion, 148–150
Temper mill system, camera setup, 233–234
Tensile stresses
  of Steckel drums, 129–130, 134–135, 137
  of strip, 129–130, 135, 137
Tension stress model, 302, 310–311, 313
Thermal cracks, 75
Thermal fatigue (TF) tests, 75–76, 78
Thermo-mechanical controlled rolling (TMCR), 56–58
Thermo-mechanical control process (TMCP), 100
Thin-slab casters, 15–32
Thin wide strips
  contact stresses of, 118, 121
  hot-rolling forces and power for, 116
  hot rolling of, 115–125
  state of stress in, 116–117
Third octave gauge chatter vibration, 257–259
Timoshenko beam elements, 332, 334–336
TMCP, *See* Thermo-mechanical control process
TMCR, *See* Thermo-mechanical controlled rolling
TopPlan system, 325
Torsional chatter vibration, 256
Transformation-induced plasticity (TRIP) steel, 171
Transformation model, 273–274
Transverse equilibrium equation, 302
Triangulation lasermeters, 248
  applications of, 250
  principle of, 249
Tribocontact geometries, 192–193
Trico Steel-Decatur design parameters, 24–25
Triple-layer technology, 67
Tunnel furnace rolls
  energy considerations, 84
  options, 84–86
Tuscaloosa Steel CR line, 28–29
Twinning-induced plasticity (TWIP) steel, 171
Two-dimensional temperature model, 165

U

Ultrafast water cooling systems, 18
Ultrafine-grain microstructure steel, material properties models for, 275
Ultra-low-carbon steel, material properties models for, 275
Ultrasonic test (UT), 68–69
Ultra-thin cold rolled sheets, 179
Ultrathin strip production (UTSP) line, design parameters of, 26
Uncertainty quantification (UQ), 141, 144
  random variables, 144–145
  and reliability analysis, 144
  role in optimization, 146
Upstream drive model, 212
User interface and simulation options, 306
UT, *See* Ultrasonic test
UTSP line, *See* Ultrathin strip production line

V

Variable voltage variable frequency (VVVF) drives, 36–37
VCR/tape systems, 229, 231
VCS, *See* Video capture system
Velocity field model, 300–301
Vertical stack mill configuration, 363
VHS tapes, 229–230
Vibrational analysis systems, 253
Vibrations, mill
  fifth octave chatter, 259–262
  low-frequency forced, 256
  modeling natural resonant, 256
  third octave gauge chatter, 257–259
  torsional chatter, 256
Vibration theory, 255–256
Video capture system (VCS)
  applications, 234, 238
  camera setup and specifications, 231–233
  features of, 230
  network architecture of, 231
  technical description, 230–231
von Mises stress, 137–138, 301
VVVF drives, *See* Variable voltage variable frequency drives

W

Walking-beam-type furnaces, 100
Water-cooled rolls, 84
  heat balances for, 89–90
  heat losses for, 86–87
Water cooling systems, 18–19
Wear tests, 73–75
Web-based Level 2 systems, 282
Weld-tracking analysis and verification, 236
Wide heavy-thickness coils, 162, 167
Wide-strip mills
  contact stresses in working stands of, analysis of, 121–122
  hot rolling of steel strips in, 116
  moment and main drive power calculation of, 122–125
  rolling power calculation of, 122
Width necking, 133
  mechanical models analyzing, 128–129
  simulation using FEM, 136–137
Width variation during hot rolling, 127–139
Wilson–Walowit model, 193
Work roll (WR)
  cooling pattern, 341–342
    on strip profile, 342–343
  exaggerated elastic deformation of, 193
  flattening stiffness, 332
  roughing mill, *See* Roughing mill work rolls
  temperature, 341–342
  temperature field, 303
  thermal crown model, 303
  uniform cooling of, 343
Work roll bending (WRB), 147, 343, 345
Work roll-strip interface, 192
WR, *See* Work roll
Wuhan Iron & Steel (Group) Corporation (WISCO), 175

Y

Yield strength, 67, 134–136, 144–145, 169, 267
Yield stress drop, 311, 314

Material Science

FLAT-ROLLED STEEL PROCESSES

Advanced Technologies

Edited by Vladimir B. Ginzburg

Throughout the last two decades, the flat-steel production industry has experienced great success with the introduction of new technologies and manufacturing advances for both hot and cold steel-rolling. These improvements are resulting in significantly reduced production costs and better product quality. Recent consolidation of the steel industry—which has led to improved sharing of technological breakthroughs between plants—is creating an optimal atmosphere for the implementation of those advances.

An assessment of industry progress, **Flat-Rolled Steel Processes: Advanced Technologies** details these improvements, assembling input from 62 international contributors specializing in various areas of research and development of steel production technology and manufacturing of flat steel products. It describes the challenges and the latest solutions to problems in four major areas:

- New concepts and modernization of rolling mills
- Modeling of flat-rolling processes
- Measurement, automation, and process control
- Strip profile and flatness control

Written for a broad audience, each chapter familiarizes readers with a different aspect of the latest theoretical and practical developments in the field. With its roots in the series of technical publications that summarize and review manufacturing developments for flat-rolled steel products, this volume explores the significant developments that are modernizing automation, process control, mathematical modeling, and quality-monitoring systems in flat-rolling processes. This includes the introduction of computer-based technology in both new and existing conventional rolling mills.

Providing expert insight and analysis related to technological improvements, this book will help readers understand the current state of flat steel production, how it evolved, and its future direction.

CRC Press
Taylor & Francis Group
an informa business

6000 Broken Sound Parkway, NW
Suite 300, Boca Raton, FL 33487
270 Madison Avenue
New York, NY 10016
2 Park Square, Milton Park
Abingdon, Oxon OX14 4RN, UK

72927
ISBN: 978-1-4200-7292-1
90000
9 781420 072921
www.crcpress.com